Marco Ceccarelli
Victor A. Glazunov *Editors*

Advances on Theory and Practice of Robots and Manipulators

Proceedings of ROMANSY 2014 XX CISM-IFToMM Symposium on Theory and Practice of Robots and Manipulators

Springer

Mechanisms and Machine Science

Volume 22

Marco Ceccarelli · Victor A. Glazunov
Editors

Advances on Theory and Practice of Robots and Manipulators

Proceedings of ROMANSY 2014 XX CISM-IFToMM Symposium on Theory and Practice of Robots and Manipulators

 Springer

Editors
Marco Ceccarelli
Laboratory of Robotics
    and Mechatronics LARM
University of Cassino and South Latium
Cassino
Italy

Victor A. Glazunov
Mechanical Engineering Research
    Institute, RAS
Moscow
Russia

Printed on acid-free paper

Preface

ROMANSY 2014, the 20th CISM-IFToMM Symposium on Theory and Practice of Robots and Manipulators has been the twentieth event of a series that was started in 1973 as a first conference activity in the world on Robotics. The first event was held at International Centre for Mechanical Science (CISM) in Udine, Italy on 5–8 September 1973. It was also the first topic conference of International Federation for the Promotion of Mechanism and Machine Science (IFToMM) and it was directed not only at the IFToMM community.

The ROMANSY aim was decided at the funding meeting as a conference event representing a forum of reference for discussing the latest advances in Robotics and for facilitating contacts among research people, scholars, students, and professionals from the Industry. From the beginning the acronym ROMANSY was used to name the symposium in short by using the first letter of the words: Robots, Manipulators, and Symposium.

The aim of the ROMANSY Symposium is still focused to bring together researchers, industry professionals, and students from broad ranges of disciplines referring to Robotics, in an intimate, collegial, and stimulating environment. In 2014, after 41 years the ROMANSY event still is very attractive since we have received increased attention toward the initiative, as can be seen by the fact that this Proceedings volume contains contributions by authors from all around the world.

The funding committee that also took the responsibility for the organization of the first ROMANSY event was composed of:

Prof. A. E. Kobrinskii (USSR); Chair
Prof. L. Sobrero (Italy), Vice-Chair and CISM Director
Acad. I. I. Artboleveskii (USSR); first IFToMM President
Prof. G. Bianchi (Italy)
Prof. I. Kato (Japan)
Prof. M. S. Konstantinov (Bulgaria)
Prof. A. Morecki (Poland)
Prof. A. Romiti (Italy)
Prof. B. Roth (USA)

Prof. M. W. Thring (UK)
Dr. M. Vukobratovic (Jugoslavia)
Prof. H. J. Warnecke (Germany)
Prof. D. E. Withney (USA)
Mrs. A. Bertozzi (Italy) acting as secretary as from CISM

The funders were the first generation in ROMANSY and they have been active for several decades. Smoothly, new generations have contributed to the leadership of ROMANSY by preserving the original characters of the initiative but challenging to increase the influence and spread of the ROMANSY results within a growing world Robotics community. The current scientific committee is listed below with names of persons who are from a third generation (since they started their activity after 2000) and others, who are even pupils of the funders.

The ROMANSY series was established as cooperation between IFToMM and CISM with an initial plan to have conference events alternatively at the CSIM headquarters in Udine, Italy, and in Poland under the direct responsibility of IFToMM and CISMM leaders together with the scientific committee. Later, as it is still today, it was decided to have the conference events hosted in any world institution where the organizing chair is active. The following is the list of ROMANSY events over time:

1973:   ROMANSY 1 in Udine, Italy with chairmanship of A. E. Kobrinskii
1976:   ROMANSY 2 in Jadwisin, Poland with chairmanship of B. Roth
1978:   ROMANSY 3 in Udine, Italy with chairmanship of L. Sobrero
1981:   ROMANSY 4 in Zaborow, Poland with chairmanship of A. Morecki
1984:   ROMANSY 5 in Udine, Italy with chairmanship of G. Bianchi
1986:   ROMANSY 6 in Cracow, Poland with chairmanship of A. Morecki
1988:   ROMANSY 7 in Udine, Italy with chairmanship of G. Bianchi and A. Morecki
1990:   ROMANSY 8 in Cracow, Poland with chairmanship of A. Morecki and G. Bianchi
1992:   ROMANSY 9 in Udine, Italy with chairmanship of G. Bianchi and A. Morecki
1994:   ROMANSY 10 in Gdansk, Poland with chairmanship of A. Morecki and G. Bianchi
1996:   ROMANSY 11 in Udine, Italy with chairmanship of G. Bianchi and A. Morecki
1998:   ROMANSY 12 in Paris, France with chairmanship of A. Morecki and G. Bianchi and J. C. Guinot
2000:   ROMANSY 13 in Zakopane, Poland with chairmanship of A. Morecki and G. Bianchi
2002:   ROMANSY 14 in Udine, Italy with chairmanship of G. Bianchi and J. C. Guinot

2004:   ROMANSY 15 in Montreal, Canada with chairmanship of J. Angeles and J. C. Piedboeuf
2006:   ROMANSY 16 in Warsaw, Poland with chairmanship of T. Zielinska
2008:   ROMANSY 17 in Tokyo, Japan with chairmanship of A. Takanishi and Y. Nakamura
2010:   ROMANSY 18 in Udine, Italy with chairmanship of W. Schiehlen and V. Parenti-Castelli
2012:   ROMANSY 19 in Paris, France with chairmanship of P. Bidaud and O. Khatib

Proceedings volumes have been always published to be available also after the symposium to large pubic of scholars and designers.

This Proceedings volume contains 62 papers that have been selected after review for oral presentation and one invited lecture that prepared by Prof. Bernard Roth to celebrate the 20th anniversary event with his vision and memories. These papers cover several aspects of the wide field of Robotics concerning Theory and Practice of Robots and Manipulators.

We would like to express grateful thanks to the members of the current International Scientific Committee for ROMANSY Symposium for cooperating enthusiastically for the success of the 2014 event:

Philippe Bidaud (France)
Marco Ceccarelli (Italy)
I-Ming Chen (Singapore), as Chair of the IFToMM Technical Committee for Robotics and Mechatronics
Victor Glazunov (Russia)
Qian Huang (China)
Oussama Khatib (USA)
Vincenzo Parenti-Castelli (Italy), CISM representative
Werner Schiehlen (Germany)
Atsuo Takanishi (Japan)
Teresa Zielińska (Poland)

We thank the authors who have contributed with very interesting papers on several subjects, covering many fields of Robotics as Theory and Practice of Robots and Manipulators and additionally for their cooperation in revising papers in a short time in agreement with reviewers' comments. We are grateful to the reviewers for the time and efforts they spent in evaluating the papers with a tight schedule that has permitted the publication of this proceedings volume in time for the symposium.

We thank the Blagonravov Institute of Machines Science (known also as IMASH) of Russian Academy of Science (RAS) in Moscow for having hosted the

ROMANSY 2014 event. We express our special thanks to academician Rivner Ganiev, director of IMASH, for supporting the hosting of ROMANSY 2014 in IMASH.

We would like to thank the members of the Organizing Committee: Academician, Prof. Vasiliy Fomin; Mem. RAS., Prof. Alexandr Shiplyuk; Mem. RAS., Prof. Vacheslav Prihodko; Mem. RAS., Prof. Nikolay Bolotnik; Prof. Veniamin Goldfarb; Prof. Irina Demianushko; Prof. Vigen Arakelian; Prof. Alexandr Golovin; Prof. Sergey Yatsun; Prof. Sergey Gavryushin; Prof. Sergey Misyurin; Dr. Raphael Sukhorukov; Prof. Saygid Uvaisov; Prof. Alexey Borisov; Prof. Anrey Korabelnikov; Dr. Oleg Muguin, Dr. Constantin Salamandra; Dr. Nikolay Tatus for their help in the plans for ROMANSY 2014 in Moscow.

We also thank the support of International Federation for the Promotion of Mechanism and Machine Science (IFToMM) and the auspices of Centre for Mechanical Science (CISM). The long cooperation between IFToMM and CISM has ensured and will ensure the continuous success of ROMANSY as a unique conference event in the broad area of Robotics with tracking reached achievements and future challenges. Special thanks are expressed to IFToMM Russia that very enthusiastically supported the plan to have ROMANY in Moscow and promoted a significant participation of Russian colleagues.

We thank the publisher and Editorial staff of Springer and particularly Dr. Nathalie Jacobs, managing Editor, for accepting and helping in the publication of this volume within the book series on Mechanism and Machine Science (MMS).

We are grateful to our families since without their patience and understanding it would not have been possible for us to organize ROMANSY-2014, the 20th CISM-IFToMM Symposium on Theory and Practice of Robots and Manipulators.

Moscow, March 2014   Marco Ceccarelli
                                                                                Victor A. Glazunov

Contents

Contents xiii

Ro. Man. Sy.: Its Beginnings and Its Founders

B. Roth

Abstract This paper describes the origins of the ROMANSY series of symposia. It recounts the author's experience as one of the original founders. The emphasis is on the events leading to the first organizational meetings and the people involved in organizing the early symposia.

Keywords ROMANSY · CISM · IFToMM · Robot · Symposia

1 Introduction

My purpose in writing this paper is to record my personal recollections of the events that led to the founding of the Romansy symposia. I undertook this task at the kind invitation of Professors V. Glazunov and M. Ceccarelli. As organizers of the 20th symposium in the Romansy series, they felt it would be appropriate to mark this anniversary by adding an historical perspective. The task fell to me since, sadly, I am the last living member of the original group that conceived the project and issued the invitations to form the first Organizing Committee.

I do want to point out that Moscow is an especially appropriate venue for this 20th anniversary event since three prominent academics from Moscow, Academician I. I. Artobolevskii, Professor A. P. Bessonov and Professor A. E. Kobrinskii, played pivotal roles in Romansy's establishment and early implementations.

B. Roth (✉)
Stanford University, Standford, CA, USA
e-mail: broth@stanford.edu

2 My Voyage

Every event has many antecedents. Depending on the narrator, different founding stories start at different points in time. This paper is my version of what happened. I am fully aware that the other founders would have their own versions. Their stories would certainly overlap mine, yet this version could only be seen through my perspective. For me the essential part of the founding of Romansy began when my wife and I visited the Soviet Union for 30 days, starting April 7, 1969, under a USA-USSR Academy of Science exchange program. We were met at the airport by Professor Arcady Bessonov.

During that visit I met Professor Aaron Kobrinskii for the first time, and learned about his work in computer-aided manufacturing, vibrations, mechanisms and robotics. Most importantly, I met Academician Ivan Ivanovich Artobolevskii. I did not fully realize what an important figure Artobolevskii was until I was invited to lunch at his apartment and saw that he lived in a very prestigious location close to the Kremlin. I later found out that in addition to his academic achievements he had been elected to one of the top government bodies: the Supreme Soviet.

The next important connection for the role I was to play in the founding of Romansy occurred when we stopped for a two-week visit in Bulgaria on our way back from the USSR. Our host there was Professor Michael Konstantinov. He had been educated in a German school in Sofia, and his German was much better than his English. So, German was the language we mainly used. As an aside, his German was so beautifully and clearly spoken, that being with him was for me like attending an intensive and highly productive German refresher course.

The final steps in my personal voyage toward the formation of Romansy occurred four months later at the Second IFToMM International Congress on the Theory of Machines and Mechanisms that was held in Zakopane, Poland in September of 1969. I gave a paper on the kinematics of computer controlled manipulators that described some of the work I had been doing with my PhD student Donald Pieper. The presentation included a short film showing a computer controlled manipulator constructing a small tower of blocks while moving through an environment with obstacles that had to be avoided. It was the first autonomous manipulation demonstration that most people in the audience had ever seen. Such films are now commonplace. At that time however, it seemed excitingly new and forward looking.

At the IFToMM Congress Artobolevskii was somewhat of an aloof and imperial figure. He was housed separately and more luxuriously than the other participants. Generally he did not mix with participants during the off hours between sessions. However, when he attended technical sessions he always sat erectly in the front row and listened intently to the presentation.

When I gave my talk and showed my film he was in his usual front row seat. After my talk he came up to me, greeted me warmly and expressed, what seemed to me, very genuine admiration for my work. I could sense there was a strong interest on his part in further study on the topic of autonomous manipulation.

There were two other seemingly casual connections at this IFToMM Congress that later proved pivotal for the development of Romansy. They involved Professors Giovanni Bianchi and Adam Morecki. I had never met either of them before the Congress. Morecki was a professor at the Technical University in Warsaw who worked mainly in biomechanics and its application to medical rehabilitation. Bianchi's main interest was classical mechanics and its application to machine design. He was a professor at the Polytechnic in Milan.

The Romansy symposia were originated under the joint sponsorship of CISM and IFToMM. The founding of CISM and IFToMM both came to fruition after years of earlier discussion and organizational work. Both of these organizations were officially born at about the same time in the late 1960s. To understand the founding of Romansy it is useful to briefly review the connection of Romansy's founders to CISM and IFToMM.

3 CISM and IFToMM

CISM: The acronym is for the Italian rendering of International Center for Mechanical Sciences. Professor Luigi Sobrero was the longtime director of the Institute of Mechanics at the University of Trieste. In 1968, toward the end of a distinguished career, he succeeded in gathering enough support of eminent colleagues in Europe to establish CISM as an international institute for promoting post graduate study in the field of mechanics.

In order to foster economic growth in the region, the city of Udine gave CISM use of a palace that had been donated to it by Count Alessandro del Torso. His expressed wish was that it should be devoted to cultural activities. To this day, this palace, located in the heart of the city, provides office and meeting space for most of CISM's activities. Once established, CISM was governed by a board that consisted of representatives of member nations. One of these board members was appointed rector of CISM. It happened to be Professor Wacław Olszak who had strong ties to his native Poland and the Polish scientific community. Especially important for Romansy was his close relationship with Adam Morecki. The other direct connection between CISM and Romansy was that Giovanni Bianchi was also deeply involved in CISM's governance and had close ties to its founder Luigi Sobrero.

IFToMM: Although it has now been modified, this acronym originally stood for the International Federation for the Theory of Mechanisms and Machines. Among the most active founders of IFToMM were Artobolevskii, Bessonov, and Konstantinov. In fact Artobolevskii was the founding president of IFToMM; Bessonov held various executive positions and Konstantinov was to become IFToMM's secretary general.

The financial arrangements were a bit unusual. IFToMM was funded by dues from member countries. It had a relatively small budget and could only make token contributions to Romansy. CISM received a land subsidy from the city of

Udine, but in the main it was also funded by dues from member countries. Some of the Eastern European countries paid their CISM dues in local non-dollar convertible currency. In particular CISM had resources it could make available for meetings that were held in Poland. That combined with Adam Morecki's organizational abilities created the early pattern if alternating the venue for Romansy between Udine and Poland. It also biased the venue of many of the organizing committee meetings to Poland.

4 Founders

I have outlined the circumstances that brought me into contact with the main originators of what became the Romansy symposia. The idea to organize an international symposium on robot research was brought to me by Kobrinskii in September 1971 during the Third IFToMM World Congress held in Kupari, Yugoslavia. Kobrinskii invited me to a meeting with Professor Sobrero, the founding Secretary General of CISM, and his secretary Mrs. A. Bertozzi. In addition to the four of us there were three other participants: Artobolevskii, Konstantinov and Bianchi. The seven of us held a meeting that what would in retrospect be the founding moment of Romansy. At this meeting we agreed to organize an international symposium. It was also decided that Kobrinskii would be the chairman of the organizing committee, and Sobrero would be the vice-chairman.

Artobolevskii assured us of IFToMM's support. Sobrero was anxious to grow activities at CISM and he wanted the symposium to take place at their headquarters in Udine.

We then had to decide what to call the proposed symposium. Kobrinskii who had a quick mind and enjoyed mental puzzles suggested Robot and Manipulator Symposium with the acronym ROMANSY. Bianchi objected. He felt the acronym was too frivolous and conveyed the wrong message. At the time, I did not know Bianchi well. I remember thinking, "there goes my stereotype of Italian lovers." We discussed this for a long time. Finally Bianchi acquiesced when we agreed to write the acronym as Ro. man. sy. Later, I became very close friends with Bianchi and his family. I realized that he had been brought up in a banking family with conservative social manners. This background caused Bianchi to have a visceral rejection of Kobrinskii's brilliant idea. Slowly over the years the acronym morphed into the original suggestion. First the spaces after the periods disappeared, and we had Ro.man.sy and also RO.MAN.SY. Next the periods disappeared and we got to RoManSy. Eventually the cover of the proceeding boldly proclaimed Kobrinskii's original ROMANSY.

The original meeting in Kupari was followed by a more extensive meeting in Nieborow, Poland in May 1972. The host for this meeting was Prof. Adam Morecki. He arranged for us to meet and live in the old Radzivill Palace, which now belonged to the Polish government. This venue fostered a very relaxed country atmosphere which provided opportunities for long strolls and off-the-record conversations.

In addition to Artobolevskii, Kobrinskii, Konstantinov, the meeting was attended by Prof. Medford Thring from University College, London, Adam Morecki from the Polytechnic of Warsaw, Miomir Vukobratović from Mihajlo Pupin Institute in Belgrade, Ikiro Khato from Wasada University, Tokyo. Giovanni Bianchi represented IFToMM and Luigi Sobrero and Mrs. Anna Bertozzi represented CISM. At this meeting we prepared the call for papers for the first symposium, which was set for September 1973 at CISM in Udine.

Figure 1 Shows a photo I took at that meeting. In the front row from left to right we have Kato, Artobolevskii, Sobrero, Konstantinov, and Thring. The second row has Bianchi and Bertozzi. The third row shows Morecki flanked by two staff members. The last row has two of Morecki's staff and Vukobratović on the right.

There was a final organizing meeting that took place in Split, Yugoslavia in April of 1973. This meeting was hosted by Professors Bazjanac and Jelovac from Zagreb. This meeting was attended by the same group as at Nieborow and, in addition, Professor Hans Wanecke from the University of Stuttgart and Professor Romiti from the Polytechnic in Turin.

At the Split meeting the submitted papers were reviewed. It was decided to accept 45 papers and publish then in a volume of conference preprints. I wanted the final proceedings to be as readable as possible. So, I went through all the papers written by non English speaking authors and, where necessary, annotated them with suggested language modifications. I still recall the gratitude I received when I passed out the edited manuscripts to the authors at the symposium.

5 First Symposium

The symposium was held on September 5–8, 1973 in the beautifully frescoed main hall of the Palazio del Torso. All the papers were presented on a single track, so everyone was in the same sessions through the symposium.

After receiving the revisions, Mrs. Bertozzi arranged to have the final proceeding published as two-volume set by Springer-Verlag. The final proceedings contain the text of two Opening Lectures. The first one runs for a little over 7 pages. It is titled "The State of the Art in the field of Robots and Manipulators." It is signed A. E. Kobrinskii, Academy of Sciences of the USSR. The second one runs for two pages and is titled "Robots and Manipulators" it is signed by M. W. Thring, University of London. Whenever I look at this part of the proceedings I am reminded of what I consider the saddest event in the history of Romansy.

If there was a single person to be credited with the idea for Romansy it would be Kobrinskii. In recognition of this he was the chairman of the Organizing Committee for the first symposium. He attended all of the organizing committee meetings and was given the honor of presenting the opening lecture. It was unimaginable that he would not attend the symposium. Yet, when the scientists from the Soviet Union arrived, he was not among them. I was told that he had to cancel his trip at the last minute because his brother was stricken with an illness. It

Fig. 1 Organizing and program committee and staff, Nieborow, Poland in May 1972

was true that his trip had been cancelled at the last minute. However it had nothing to do with family illness. It was because he was not given an exit visa. I do not pretend to know the reason for this. I do know that Kobrinskii felt it was due to his Jewish origins and the Soviet Government's discriminative policies towards its Jewish citizens at that time.

These are not pleasant things to recall, especially in a paper meant to celebrate the cooperation between researchers from throughout the world. Kobrinskii is dead and so are most of the colleagues who attempted to hide the truth. In a cosmic sense the incident is meaningless. I mention it here mainly to emphasize the importance of Aaron Kobrinskii's role in Romansy's birth and to pay homage to an unusually creative colleague by acknowledging my empathy for what must have been an incredibly painful personal episode.

The rest of the symposium was uneventful and was full of good feelings and comradeship. We had achieved our goal of opening a multinational scientific exchange in the area of robotics. In addition to the two invited opening lectures, we had accepted 45 papers. The distribution according to country of these 45 papers was: USA 13, USSR 13, Japan 4, England 3, Yugoslavia 3, West Germany 3, Italy 2, Poland 2, Bulgaria 1, and France 1.

On the last day of the symposium the organizing committee was invited by Professor Sobrero to a lunch meeting in the restaurant of the upscale Astoria Hotel around the corner from CISM. I recall we were seated at a long rectangular table. Artobolevskii sat at the head and I was far away toward other end. We agreed that the symposium had been a success and that a second Romansy should be held in

Poland in 1976. The organizing committee was to have two meetings before the symposium, the first of which was to be in Warsaw in June of 1974.

The lunch went on a bit long and toward the end my mind was wandering. I was barely paying attention when Artobolevskii rose with wine glass in his hand and said, "I propose that Professor Roth should be the new chairman of the organizing committee". This was greeting with a round of applause. That was it, it was an imperial order and everyone obeyed. I was flabbergasted at Artobolevskii's action on two counts: I was both an American and the youngest person at the table. I suppose Artobolevskii must have discussed it with Sobrero and Bianchi beforehand, yet it always remained in my mind a personally generous gesture of great magnanimity on his part. I took it as both strengthening our personal connection and as a signal that Romansy had achieved a measure of Soviet-American cooperation that at the time was very much lacking in the world.

6 An Ongoing Series

The success of the first symposium led CISM and IFToMM to jointly form a permanent Technical Committee on Robots and Manipulators. This technical committee was to organize the second and all subsequent Romansy symposia. I had the honor to be the chair of this technical committee for its first years. For the second symposium the committee was:

Chairman: Prof. B. Roth (Stanford University), *Vice-Chairmen*: Prof. L. Sobrero (CISM), Prof. A. Morecki (Technical University of Warsaw). *Members*: Acad. I. I. Artobolevskii (Institute for the Study of Machines, Moscow), Prof. G. Bianchi (Technical University of Milan), Prof. I. Kato (Wasada University), Prof. A. E. Kobrinskii (Institute for the Study of Machines, Moscow), Prof. M. S. Konstantinov (High Mechanical and Electromechanical Institute, Sofia), Prof. R. B. McGhee (The Ohio State University), Prof. M. W. Thring (University of London), Mr. J. Vertut (Atomic Energy Commission, France), Prof. M. Vukobratović (Mihajlo Pupin Institute), Prof. H. J. Warnecke (University of Stuttgart). *Scientific Secretary*: Dr. K. Kędzior (Technical University of Warsaw). *Secretary*: Mrs. A. Bertozzi (CISM).

The Technical Davison of the Polish Academy of Sciences joined CISM and IFToMM's financial sponsorship, and two preparatory committee meetings for the second Romansy were held in Poland. The Second International CISM-IFToMM Symposium took place in the small village of Jadwisin near Warsaw, Poland on September 14–17, 1976. There was a volume of preprints available at the symposium.

The second Romansy was attended by 117 participants and 15 accompanying guests. They came from 4 continents and 20 countries (which doubled the 10 countries for the first symposium). The social programs included a banquet with groups of participants singing in various languages and a half-day excursion. This became the model for subsequent Romansy symposia.

For the second symposium we adopted the policy that a paper could only be published in the proceedings if it was actually presented at the symposium. I have always felt regret that this policy led to the exclusion of some good papers.

Artobolevskii passed away at the age of 71 on September 21, 1977, a year before the third Romansy. I happen to have been in the USSR at the time. I was attending a conference in Alma Ata. As soon as his death was announced everything seemed to shut down. Many participants hurried back to Moscow to attend his funeral. To me the most impressive reminder of what an important figure he was happened when the TV throughout the Soviet Union stopped its normal programs and simply played dirge music in his memory.

His colleague Prof. A. P. Bessonov had been acting as an aid-de-camp to Artobolevskii since the founding of Romansy. So, he was very knowledgeable about Romansy and was able to seamlessly take up Artobolevskii's role as a representative of the USSR on the Organizing Committee.

The third Romansy was held in Udine at CISM on September 12–15, 1978. About 8 months after the third symposium our great benefactor Prof. Luigi Sobrero passed away at the age of 69. CISM had been the crowning passion of his life, and he left it in very good shape as far as Romansy was concerned. Prof. Giovanni Bianchi had served as an aid-de-camp to Sobrero from the beginning of the Romansy discussions. After Sobrero died, he was appointed Secretary General of CISM and became the main contact between Romansy and CISM. Also, the incredibly efficient Mrs. Bertozzi was also still available. After the symposium, Professors McGhee, Thring and Warnecke left the committee, and Prof. Morecki became the chairman of the CISM-IFToMM Technical Committee on Robots and Manipulators. Prof. Bianchi became the vice chairman. The fifth Romansy was back at CISM and, accordingly, Bianchi and Morecki had switched chairman and vice chairman roles.

The sixth was back in Poland on September 9–12, 1986. This time the venue was in the city of Krakow. The symposium opened with a memorial session dedicated to the work of Jean Vertut, who had died of a heart attack at age 56. After the sixth Kato, Kobrinskii, Kędzior and I left the Organizing and Program Committee. For me, it was time to let the next generation pilot the Romansy voyage.

7 Conclusions

When Romansy was started it was the first research based conferences dealing with robot design, mechanics and control. Furthermore, before Romansy there was little or no interchange between Eastern Europe and the West on these subjects. Romansy was created on the premise of free scientific communication between all areas of the world. The fact that it achieved its original goals and continues to thrive is of great personal satisfaction to me. Even greater satisfaction for me is the great gift of the enduring and cherished friendships formed through Romansy.

Parametric Method for Motion Analysis of Manipulators with Uncertainty in Kinematic Parameters

Vahid Nazari and Leila Notash

Abstract In this paper, the motion performance of manipulators considering the uncertainty in the kinematic parameters is investigated. Interval analysis is employed to deal with the uncertainty in the kinematic parameters in the form of small uncertainty boxes. For a given range of uncertainties in the kinematic parameters, the interval linear equations are formulated to relate the velocity of joints to the end effector velocity with the Jacobian matrix. A novel approach for calculating the exact size and shape of the solution for the system of interval linear equations is presented. A 2 degrees of freedom planar serial manipulator is used as a case study to analyze the motion performance of the manipulator in the presence of uncertainties.

Keywords Interval analysis · Robot manipulators · Uncertainty · Parametric method · Parameter solution set

1 Introduction

Robot manipulators are typical of systems that are intrinsically subjected to uncertainties. The nominal relationship between the end effector pose and joints displacement is known but this relationship is not necessarily accurate due to changes in the robot hardware and uncertainties in the kinematic parameters [1]. A real robot analysis should be performed in the presence of uncertainties in the

V. Nazari (✉) · L. Notash
Department of Mechanical and Materials Engineering, Queen's University, Kingston, Canada
e-mail: nazariv@me.queensu.ca

L. Notash
e-mail: notash@me.queensu.ca

modeling of the manipulator and measurements of the kinematic parameters. The sources of uncertainties include the manufacturing tolerances of the mechanical parts, measurement error, control error, and round-off error. All types of uncertainties can be accommodated as bounded variations in the kinematic parameters.

Several methods are known for calculating the lower and upper bounds for each component of the solution set in the interval linear systems. One of the first contributions on determining the bounds of the solution set was given in [2]. It was shown that the solution set for this system is a polyhedron. More general algorithms for determining the bounds containing the exact solution were presented in [3–5]. These bounds were not necessarily identical to the exact solution. The exact solution was determined in [6] as the union of finitely many convex polytopes whose vertices were denoted by matrices with entries equal to the lower or upper bounds of the interval coefficient matrix. The shape of the solution set, in general, was a non-convex polyhedron.

The exact solution of the interval linear systems is generally complicated and not easily described. Therefore, calculation of this solution is computationally expensive and, hence, is not convenient to use for the real time application. Accordingly, the researchers are drawn to find the fastest methods to enclose the exact solution. One of the first publications on parametric interval systems for special coefficient matrices, such as symmetric and skew-symmetric matrices, was presented in [7, 8]. The characterization of the boundary of the solution set of the parametric system based on a set of inequalities was done by [9]. This approach was designed particularly for visualizing the boundary of the parametric solution set.

In this paper, the motion performance of manipulators with uncertainty in the kinematic parameters is investigated using parametric interval method. The organization of paper is as follows. The basic principles of the interval analysis and the parametric interval systems are given in Sect. 2. The proposed methodology for formulating the exact solution, which is based on parameterizing the interval linear systems, is presented in Sect. 3. The simulation results are reported in Sect. 4 and the paper is concluded in Sect. 5.

2 Parametric System of Interval Linear Equations

Interval analysis is a numerical method of representing the uncertainty in values by replacing a number with a finite range of values. An interval denoted by $[X] = [\underline{X}, \overline{X}]$ is the set of real numbers X verifying $\underline{X} \leq X \leq \overline{X}$ where $\underline{X}$ and $\overline{X}$ are the lower and upper bounds of the interval, respectively. The interval is also represented by the midpoint, X_c, and the radius, ΔX, as $[X] = [X_c - \Delta X, X_c + \Delta X]$ or $[X] = X_c + \Delta X[-1, 1]$. A real number is a special case of an interval in which $\underline{X} = \overline{X}$. The width of the interval $[X]$ is defined as $(X) = \overline{X} - \underline{X}$. The midpoint of $[X]$ is given by $m(X) = \frac{1}{2}(\overline{X} + \underline{X})$. A matrix whose entries are interval is called an interval matrix and denoted by $[\mathbf{A}]$, $\mathbf{A}_c$, is the midpoint of $[\mathbf{A}]$ whose entries are the
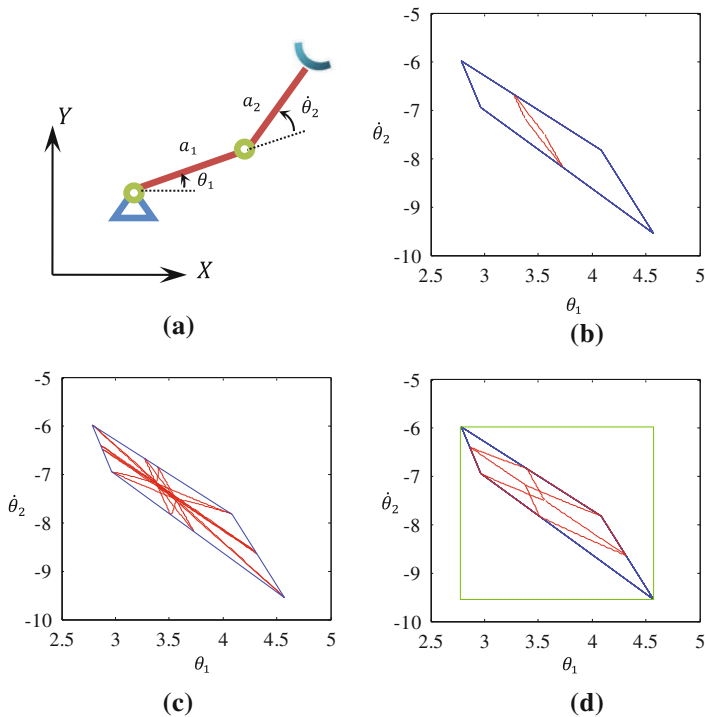
Fig. 1 a 2 DOF planar serial manipulator, **b** one of two-parameter solution sets in *red*, **c** all two-parameter solution sets in *red* and the exact solution in *blue*, **d** a three-parameter solution set in *red* and the smallest box containing the exact solution in *green*

midpoints of the corresponding entries of $[\mathbf{A}]$, the radius of the interval matrix, Δ, is defined as $\frac{1}{2}(\overline{\mathbf{A}}-\underline{\mathbf{A}})$.

In manipulators, the Jacobian matrix relates the joint velocity vector to the end effector velocity vector. Due to the uncertainty in the kinematic parameters, the relationship between the joint velocity vector and the end effector velocity vector takes the form of the interval linear system. This interval system is parameterized as $[\mathbf{J}([\mathbf{p}])]\dot{\mathbf{q}} = [\mathbf{V}([\mathbf{p}])]$ in which the entries of the Jacobian matrix and the end effector velocity vector linearly depend on parameters $[\mathbf{p}] = ([p_1], [p_2], \ldots, [p_K])$ even though in general, the entries of the Jacobian matrix and the velocity vector could be nonlinear functions of the interval parameters $[\mathbf{p}]$. The exact values of these parameters are unknown but bounded within given intervals. Considering the serial manipulator in Fig. 1a and using a linear parametric model for each entry of $[\mathbf{J}([\mathbf{p}])]$ and $[\mathbf{V}([\mathbf{p}])]$, the entries of the Jacobian matrix and the velocity vector could be defined as

$$[J_{jk}([\mathbf{p}])] = J_{jk,0} + \sum_{\mu=1}^{K} J_{jk,\mu} [p_\mu], \quad [V_j([\mathbf{p}])] = V_{j,0} + \sum_{\mu=1}^{K} V_{j,\mu} [p_\mu] \qquad (1)$$

where $J_{jk,\mu}, V_{j,\mu} \in \mathbb{R}, ; \mu = 1, \ldots, k; j = 1, \ldots, m; k = 1, \ldots, n;$ m is the task space dimension and n is the number of joints. The value of parameter K depends on the number of the interval parameters used to parameterize the interval system. The maximum number of the interval entries of $[\mathbf{J}]$ and $[\mathbf{V}]$ is mn and m, respectively. Depending on the uncertainty of the kinematic parameters in the manipulator, some entries of the Jacobian matrix and the end effector velocity vector may not be interval.

3 Parametric Method for Exact Solution

In this section, the exact solution of the interval system is calculated using solution sets obtained from parameter groups of interval systems. Depending on the number of interval parameters involved in the Jacobian matrix and the velocity vector, the exact solution will be characterized. The parameter assignment of the entries of $[\mathbf{J}]$ and $[\mathbf{V}]$ in the manipulator is performed by selecting some interval entries of either $[\mathbf{J}]$ or $[\mathbf{V}]$ as parameters $[p_\mu]$ and formulating other entries as functions of interval parameters $[p_\mu]$. All parameter assignments of the entries of $[\mathbf{J}]$ and $[\mathbf{V}]$ which lead to the same solution set are collected as one parameter group. That is, a parameter group may consist of one or several different parameter assignments.

The number of parameter groups in each interval system depends on the total number of interval entries of $[\mathbf{J}([\mathbf{p}])]$ and $[\mathbf{V}([\mathbf{p}])]$, denoted as η, and the number of interval parameters in the interval system, K. The solution sets of all parameter assignments of the interval system are checked and the parameter assignments which result in the same solution set are categorized as one parameter group. Considering a general spatial serial manipulator, to form $[\mathbf{J}] \dot{\mathbf{q}} = [\mathbf{V}]$ with η interval entries in $[\mathbf{J}]$ and $[\mathbf{V}]$ and 2 interval parameters, $K = 2$, there exist $\frac{1}{2}\sum_{i=K-1}^{\eta-1} \binom{\eta}{i} = \frac{1}{2}\sum_{i=1}^{\eta-1} \frac{\eta!}{(\eta-i)!i!}$ different parameter groups. When the number of interval parameters is $K = 3$, all the number of possible parameter groups is calculated as $\sum_{i=K-1}^{\eta-2} \frac{\binom{\eta}{i}\binom{\eta-i}{2}}{(\eta-i-2)!} = \sum_{i=2}^{\eta-2} \frac{(\eta-i-1)(\eta-i)\ldots(\eta)}{2!i!(\eta-i-2)!}$.

In this paper, once the numerical interval matrix $[\mathbf{J}]$ is calculated, the entries of $[\mathbf{J}([\mathbf{p}])]$ and $[\mathbf{V}([\mathbf{p}])]$ are expressed as linear functions of the interval parameters $[p_\mu], 1 \leq \mu \leq K$. Considering entry $[J_{jk}]$ and $[V_j]$ as linear function of $[p_\mu]$, then $[J_{jk}([p_\mu])] = J_{jk,0} + J_{jk,\mu}[p_\mu]$ and $[V_j(p_\mu)] = V_{j,0} + V_{j,\mu}[p_\mu]$. The lower and upper bounds of any interval entry $[J_{jk}] = [\underline{J_{jk}}, \overline{J_{jk}}]$ are related to those of interval parameter $p_\mu \in [\underline{p_\mu}, \overline{p_\mu}], \underline{p_\mu} \neq \overline{p_\mu}$ through the following system of linear equations

$$\begin{cases} \overline{J_{jk}} = J_{jk,0}\bar{p}_\mu + J_{jk,\mu} \\ \underline{J_{jk}} = J_{jk,0}\underline{p}_\mu + J_{jk,\mu} \end{cases} \Rightarrow \begin{bmatrix} \bar{p}_\mu & 1 \\ \underline{p}_\mu & 1 \end{bmatrix} \begin{bmatrix} J_{jk,0} \\ J_{jk,\mu} \end{bmatrix} = \begin{bmatrix} \overline{J_{jk}} \\ \underline{J_{jk}} \end{bmatrix} \tag{2}$$

The coefficients $^iJ_{jk,0}$ and $^iJ_{jk,\mu}$ are calculated by taking inverse of Eq. (2) as

$$\begin{bmatrix} J_{jk,0} \\ J_{jk,\mu} \end{bmatrix} = \begin{bmatrix} \bar{p}_\mu & 1 \\ \underline{p}_\mu & 1 \end{bmatrix}^{-1} \begin{bmatrix} \overline{J_{jk}} \\ \underline{J_{jk}} \end{bmatrix} \tag{3}$$

The same procedure is performed to formulate the entry of $[V_j]$ as a function of $[p_\mu]$. It should be noted that the entry of $[\mathbf{J}([\mathbf{p}])]$ or $[\mathbf{V}([\mathbf{p}])]$ nominated for the interval parameter must be interval. Otherwise, the matrix in Eq. (2) would be singular and the entry $[J_{jk}]$ cannot be formulated in terms of parameter $[p_\mu]$. If $[\mathbf{J}([\mathbf{p}])]$ is an $n \times n$ square matrix and non-singular for each $p_\mu \in [\underline{p}_\mu, \overline{p}_\mu], \mu = 1, \ldots, K$, $[\mathbf{J}^{-1}([\mathbf{p}])]$ exists and $[\dot{\mathbf{q}}([\mathbf{p}])] = [\mathbf{J}^{-1}([\mathbf{p}])][\mathbf{V}([\mathbf{p}])]$ is a function of K interval parameters which is continuous [9]. This parametric joint velocity vector provides the solution set for each parameter group.

When the parametric Jacobian matrix is of full-row rank, the solution which minimizes the 2-norm of the joint velocity vector is selected. If the square parametric matrix $[\mathbf{J}([\mathbf{p}])][\mathbf{J}^T([\mathbf{p}])]$ is regular for every $p_\mu \in [\underline{p}_\mu, \bar{p}_\mu]$, the minimum 2-norm solution set to the parametric system exists and is formulated as a function of interval parameters $[\dot{\mathbf{q}}([\mathbf{p}])] = [\mathbf{J}^T([\mathbf{p}])]([\mathbf{J}([\mathbf{p}])][\mathbf{J}^T([\mathbf{p}])])^{-1}[\mathbf{V}([\mathbf{p}])]$. If the manipulator has a combination of revolute and prismatic joints, the joint velocity vector is not physically consistent. If the interval entries with the same dimension are parameterized, a weighting matrix would be required to calculate the generalized (Moore-Penrose) inverse of $[\mathbf{J}([\mathbf{p}])]$ as $\mathbf{J}^{\#} = \mathbf{W}[\mathbf{J}^T([\mathbf{p}])]([\mathbf{J}([\mathbf{p}])]\mathbf{W}[\mathbf{J}^T([\mathbf{p}])])^{-1}$.

Similarly, when parametric Jacobian matrix $[\mathbf{J}([\mathbf{p}])]$ is of full column-rank and $[\mathbf{J}^T([\mathbf{p}])][\mathbf{J}([\mathbf{p}])]$ is regular for every $p_\mu \in [\underline{p}_\mu, \bar{p}_\mu]$, the least square solution set is calculated. The weighted left generalized inverse of $[\mathbf{J}([\mathbf{p}])]$ is calculated as $\mathbf{J}^{\#} = [\mathbf{J}^T([\mathbf{p}])\mathbf{W}\mathbf{J}([\mathbf{p}])]^{-1}\mathbf{J}^T([\mathbf{p}])\mathbf{W}$ if the interval entries of the Jacobian matrix are parameterized using the interval parameters with the same dimension.

4 Case Study

In this section, the 2 DOF planar serial manipulator in Fig. 1a with two revolute joints is used as a case study for the interval analysis to visualize the solution set. The manipulator has uncertainty in two joint variables θ_1 and θ_2 and the link lengths a_1 and a_2.

For the joint variables $\theta_1 = \frac{\pi}{6}$ rad and $\theta_2 = \frac{\pi}{4}$ rad, the link lengths $a_1 = a_2 = 0.5$ m, the radius of uncertainty $\frac{\pi}{180}$ rad in θ_1 and θ_2 and the radius of

uncertainty 0.010 m in link lengths, the interval Jacobian matrix is
$[\mathbf{J}] = \begin{pmatrix} [-0.760, -0.706] & [-0.497, -0.469] \\ [0.530, 0.595] & [0.110, 0.149] \end{pmatrix}$. The desired end effector velocity
is $\mathbf{V} = [v_x v_y]^T = [1 \quad 1]^T (\text{m/s})$.

If the Jacobian matrix and the end effector velocity vector are functions of two parameters $[p_1]$ and $[p_2]$, i.e., $\mu = 1, 2$, the parametric linear system will be

$$[\mathbf{J}([\mathbf{p}])] \begin{bmatrix} \dot{\theta}_1 \\ \dot{\theta}_2 \end{bmatrix} = \begin{pmatrix} [v_x([\mathbf{p}])] \\ [v_y([\mathbf{p}])] \end{pmatrix} \tag{4}$$

The parameter solution set is derived using the inverse of $[\mathbf{J}([\mathbf{p}])]$ as

$$[\dot{\theta}([\mathbf{p}])] = \begin{pmatrix} [\dot{\theta}_1([\mathbf{p}])] \\ [\dot{\theta}_2([\mathbf{p}])] \end{pmatrix} = [\mathbf{J}([\mathbf{p}])]^{-1} \begin{pmatrix} [v_x([\mathbf{p}])] \\ [v_y([\mathbf{p}])] \end{pmatrix} \tag{5}$$

Generally, the entries of the Jacobian matrix and the end effector velocity vector can be parameterized such that the entries with the consistent dimension are categorized in the same groups. In this example, the Jacobian matrix has physically consistent entries. Therefore, the parameter assignment can be performed to any entries of the Jacobian matrix. If the entries of the end effector velocity vector are interval and have the same dimension, e.g., m/s, these entries could be parameterized using an interval parameter with the same dimension, e.g., m/s. In the case study, the entries of the end effector velocity vector are not interval. Therefore, they are not functions of an interval parameter, i.e., $[V_j] = V_{j,0} = 1$, $j = 1, 2$.

Entries $[J_{12}]$ and $[J_{11}]$ are selected as the interval parameters $p_1 \in [-0.497, -0.469]$ and $p_2 \in [-0.760, -0.706]$, entries $[J_{21}]$ and $[J_{22}]$ are assigned as functions of $[p_1]$ and entries v_x and v_y are constant values 1. The interval entries of Eq. (3) are substituted into Eq. (5) and the two-parameter solution set for this parameter group is formulated as

$$\dot{\theta}(p_1, p_2) = \begin{pmatrix} \frac{-0.372[p_1] - 0.792}{1.669[p_1] - 0.792[p_2] - 1.372[p_1][p_2] + 2.291[p_1]^2} \\ \frac{2.291[p_1] - [p_2] + 1.669}{1.669[p_1] - 0.792[p_2] - 1.372[p_1][p_2] + 2.291[p_1]^2} \end{pmatrix} \tag{6}$$

Similar to the procedure in calculating the two-parameter solution set in Eq. (6), the two-parameter solution set for each parameter group is formulated. Other parameter groups are obtained by new parameter assignment of the interval entries of $[\mathbf{J}([\mathbf{p}])]$ as either $[p_1]$ or $[p_2]$ and the rest of entries as functions of $[p_1]$ and $[p_2]$. The new parameter solution set for each parameter assignment forms a parameter group. The boundary curves of the solution set for each group of parametric linear system are specified by 4 curves; two curves $\dot{\theta}(p_1, \underline{p}_2)$ and $\dot{\theta}(p_1, \bar{p}_2)$ in 2-dimensional space when p_1 varies from $\underline{p}_1$ to $\bar{p}_1$ and p_2 is set once to

the lower bound and then to the upper bound. Similarly, the other two curves $\dot{\theta}(p_2, \underline{p}_1)$ and $\dot{\theta}(p_2, \bar{p}_1)$ are formulated when p_2 varies from $\underline{p}_2$ to $\bar{p}_2$ and p_1 is set to the lower bound and the upper bound, respectively. In the resulting solution set enclosed by four curves, each curve is connected to the other two curves in two points and the two attached curves share a point. Therefore, four points $\dot{\theta}(\underline{p}_1, \underline{p}_2)$, $\dot{\theta}(\bar{p}_1, \bar{p}_2)$, $\dot{\theta}(\underline{p}_1, \bar{p}_2)$ and $\dot{\theta}(\bar{p}_1, \underline{p}_2)$ form vertices of the solution set for each parameter group. This two-parameter solution set (in red color) is illustrated in Fig. 1b and completely lies inside the exact solution (in blue color).

To characterize the exact solution, first all parameter groups which result in the same solution sets are determined and then plotted in $\dot{\theta}_1 - \dot{\theta}_2$ plane. In this example, since there are four interval entries in the Jacobian matrix, $\eta = 4$, there will exist $\frac{1}{2} \sum_{i=1}^{\eta-1} \frac{\eta!}{(\eta-i)!i!} = \frac{1}{2} \sum_{i=1}^{3} \frac{4!}{(4-i)!i!} = \frac{1}{2}(4 + 6 + 4) = 7$ different parameter groups among all possible solution sets, i.e., $2^4 = 16$. These 16 solution sets are illustrated in red color in Fig. 1c. The outer vertices of the different groups of the two-parameter solution sets are connected to form the boundary of the exact solution (in blue color). Generally speaking, when the exact solution is non-convex, the two-parameter solution sets might not be able to distinguish the indented vertices.

In the three-parameter case, each parameter group includes interval parameters $[p_1], [p_2]$ and $[p_3]$, i.e., $\mu = 1, 2, 3$. The procedure to calculate the solution set for each parameter group is similar to that of the two-parameter case. The parameter groups for three interval parameters are $\sum_{i=2}^{\eta-2} \frac{(4-i-1)(4-i)...(4)}{2!i!(4-i-2)!} = 6$. The solution set corresponding to each parameter group consists of 12 curves; the two parameters p_1, p_2 are set to either lower or upper bounds and the resulting 4 curves, which are functions of parameter p_3, are plotted when p_3 varies within the lower and upper bounds. The formulation of the solution set of the interval system including three parameters is applicable to the Jacobian matrices of the manipulators with more than 2 joints such as planar 3 DOF manipulators. The process is repeated when $[p_1], [p_3]$ are set to either the lower or upper bounds and the next 4 curves are functions of $[p_2]$. The last 4 curves are formulated as functions of $[p_1]$ when $[p_2], [p_3]$ are set to either the lower or upper bounds. The resulting 12 curves form a hypersurface which may have surfaces on the boundary surface of the exact solution.

To show the solution set for a group of parametric linear system with three interval parameters, the same example as the two-parameter case is considered. For entries $[J_{11}]$ and $[J_{12}]$ and $[J_{21}]$ as interval parameters $p_1 \in [-0.760, -0.706]$, $p_2 \in [-0.497, -0.469]$ and $p_3 \in [0.530, 0.595]$, respectively, $[J_{22}]$ as a function of $[p_1]$, and $[v_x]$ and $[v_y]$ as constant values, the three-parameter solution set is plotted in Fig. 1d. As illustrated, some edges of this solution set lie on the boundary of the exact solution. The commonly calculated smallest box containing the exact solution is depicted in Fig. 1d in green color. As shown, this solution is much larger than the exact solution.

In general, for K-parameter case, the number of curves involved to form the solution set of each parameter group is calculated to be $K \times 2^{(K-1)}$. For instance, in three-parameter case, the number of curves which forms the solution set for each parameter group is $3 \times 2^2 = 12$. It should be noted that as the size of the interval matrix, especially the interval entries of the matrix, increases, the total number of the parameter groups which have different solution sets drastically grows.

The drawback of the two-parameter solution set is that the indented vertices of the exact solution, if there is any, may be ignored. The three-parameter solution set overcomes this limitation as more curves are contributed to characterize each three-parameter solution set, and hence the actual vertices of the exact solution set are obtained. The interval analysis in this paper is performed using INTLAB [10].

5 Discussion and Conclusions

In this paper, the motion analysis of manipulators considering uncertainty in the kinematic parameters were investigated, and a novel method to identify the exact solution of joint velocities for the given end effector velocities was presented. To model the uncertainty in kinematic parameters, interval analysis was applied and the lower and upper bounds of each entry of the Jacobian matrix were determined and the interval linear equations were formulated to relate the velocity of joints to the end effector velocity. Although the range of uncertainties in the kinematic parameters was small, the accumulation effect of uncertainties caused a relatively wide solution for the velocity of the joints. The lower and upper bounds of the joint velocity components depended on the length of the links, the range of uncertainties and the configuration of the manipulator. When the manipulator is close to the singular configuration, even for small values of uncertainties, the width of joint velocity components increases. The proposed method has been implemented for the serial and parallel manipulators. Due to space limitation, only the results for a serial manipulator were reported here.

Generally, there is a trade-off between the accuracy of the solution and the computation time. The parametric interval system provides the exact solution with more computation effort. For offline analysis such as the investigation of workspace of manipulators, since the calculation time is not a concern, the parametric interval method is valuable. In real time applications, methods that are not computationally expensive are better suited. As a future work, the motion analysis of manipulators with uncertainty in the kinematic parameters, velocity limits of the joints and the joint failure will be investigated.

References

1. Roth, Z., Mooring, B., Ravani, B.: An overview of robot calibration. IEEE J. Robot. Autom. **3**, 377–385 (1987)
2. Oettli, W.: On the solution set of a linear system with inaccurate coefficients. J. Soc. Ind. Appl. Math. Series B. Numer. Anal. **2**, 115–118 (1965)
3. Hansen, E., Smith, R.: Interval arithmetic in matrix computations, part II. SIAM J. Numer. Anal. **4**, 1–9 (1967)
4. Neumaier, A.: Interval Methods for Systems of Equations. Cambridge University Press, Cambridge (1990)
5. Oettli, W., Prager, W., Wilkinson, J.: Admissible solutions of linear systems with not sharply defined coefficients. J. Soc. Ind. Appl. Math. Series B. Numer. Anal. **2**, 291–299 (1965)
6. Hartfiel, D.: Concerning the solution set of $Ax = b$ where $P \leq A \leq Q$ and $p \leq b \leq q$. Numer. Math. **35**, 355–359 (1980)
7. Jansson, C.: Interval linear systems with symmetric matrices, skew-symmetric matrices and dependencies in the right hand side. Computing **46**, 265–274 (1991)
8. Alefeld, G., Kreinovich, V., Mayer, G.: On the shape of the symmetric, persymmetric, and skew-symmetric solution set. SIAM J. Matrix Anal. Appl. **18**, 693–705 (1997)
9. Popova, E., Krämer, W.: Visualizing parametric solution sets. BIT Numer. Math. **48**, 95–115 (2008)
10. Rump, S.M.: INTLAB: INTerval LABoratory. In: Csendes, T. (ed.) Developments in Reliable Computing, pp. 77–104. Kluwer Academic Publishers, Dordrecht (1999)

Self-Adjusting Isostatic Exoskeleton for the Elbow Joint: Mechanical Design

V. A. Dung Cai and Philippe Bidaud

Abstract This paper describes the mechanical design of an active orthosis device for the human elbow joint. The device can be used in muscle stretching application to help the patient's elbow recovering its full range of motion after surgery intervention. We use a 6 degree of freedom mechanism, including an 4D parallel Delta type mechanism, to assure that the motor torque can be fully transmitted to the anatomical axis of the elbow without creating residual efforts that may limit the natural motion of the joint.

Keywords Orthosis devices · Parallel manipulators · Design · Experimental tests

1 Introduction

1.1 Related Work

Recent works on the design of exoskeletons for human anatomical joint have figured out the importance of the use of passive joints in the device's mechanism so that the whole mechanical chain will become isostatic when it is attached to the human corporel segments. Indeed, a human anatomical joint is in most cases

V. A. Dung Cai (✉)
Faculty of Mechanical Engineering, University of Technical Education,
01 Vo Van Ngan Street, Thu Duc District, Ho Chi Minh City, Vietnam
e-mail: dungcva@hcmute.edu.vn

P. Bidaud
Institut des Systèmes Intelligents et de Robotique, UPMC University Paris 06,
4 Place Jussieu, 75005 Paris, France
e-mail: bidaud@isir.upmc.fr

spatial and can not be reduced to simple elementary mechanical joints [1, 2, 9, 10]. Thus, the design of exoskeletons for functional rehabilitation must take into account the complexity of anatomical joints. A misalignment between the instantaneous anatomical axis and the actuated axis of the mechanism will create residual efforts that may limit natural motion of the joint, or even cause permanent injuries in extreme cases.

In 2006, Schiele and Van der Helm [8] presented a novel design for human arm exoskeleton which has 9 d.o.f. in total. In this design, a RPR mechanism is used at the elbow joint. Only the first rotational joint is actuated while the two other joints are passive, assuring that only the actuator torque will be transmitted to the elbow. It was followed by different original designs in literature such as [3, 5, 7, 9]. Later in 2011, Cai et al. [3] established a general design rule for exoskeletons that can be summarized as follow:

- The mechanism must have at least 3 d.o.f. in the case of planar anatomical joint. It must have at least 6 d.o.f. in the case of spatial anatomical joint.
- The number of passive joints used in the mechanism is equal to the difference between the space dimension (3 or 6) and the mobility of the anatomical joint.
- The number of actuators is the difference between the degree of freedom of the mechanism and the number of passive joints.
- Generally, for passive rehabilitation exercises, the mechanism must be designed adequately so that it can mobilize the anatomical joint in flexion or in extension by transmitting opposing torques on the two limbs of the subject. The transmitting torque orientation must be close to the that of the human anatomical axis. All other force and torque components must be minimized.

1.2 Elbow Exoskeleton

The design proposed by Schiele and Van der Helm [8] did not take into account the fact that the elbow joint, formed by the humero-ulna joint, the humero-radial joint and the proximal radio-ulna joint, is a complex spatial joint which might not be modeled by a simple serial mechanism with 2 rotation joints representing the flexion/extension and the forehand axial rotation (supination/pronation). Bottlang et al. and Ericson et al. [1, 6] figured out that the elbow kinematic should be modeled by a screw displacement axis which allow the representation of all anatomical kinematic data, which are flexion/extension, valgus/varus angles and proximal/distal, anterior/posterior displacement.

This paper describes a novel design of an active orthosis for the passive rehabilitation of elbow joint. The device kinematics is equivalent to a 3R-3P mechanism which is quasi-isotropic. The use of a Delta-type parallel mechanism not only allows the substitution of the 3 prismatic joints by bearing joints but also gives the mechanism a better torque transmission capability by its symmetric structure.
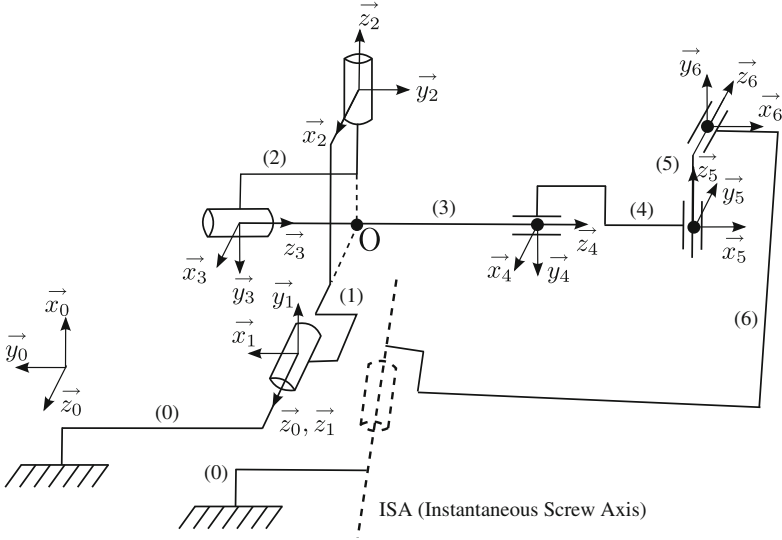
Fig. 1 Frame assignment of a 3R-3P mechanism

2 Isotropic Property

According to Chablat and Angeles [4], isotropy is always sought in the mechanical design of manipulators because it increases the robustness of the assembly and measurement errors. Isotropy also assure uniform force transmission capability, and for this reason, designers should try to use isotropic mechanisms in the design of active rehabilitation devices. Cai et al. [3] presented a knee exoskeleton with 6 d.o.f. RRRPRR mechanism which has a conditioning number around 3. However, the most commonly used mechanism is 3R-3P (A serial mechanism which includes 3 intersecting rotary joints and 3 prismatic joint). It is possible to demonstrate that the condition number of the latter is close to 1.

The Fig. 1 represents the kinematic model of a 3R-3P mechanism. By definition, the conditioning number of a matrix can be defined by the ratio between the largest and smallest singular values, which are the square roots of the eigenvalues of the positive semi-definite matrix $\boldsymbol{JJ^t}$. In this case we have a matrix $\boldsymbol{J}$ homogeneous in dimension. Thus the computation of $\boldsymbol{JJ^t}$ yields:

$$\boldsymbol{JJ^t}/_{R_2} = \begin{pmatrix} \cos^2\theta_2 & -\sin\theta_2\cos\theta_2 & 0 & 0 & 0 & 0 \\ -\sin\theta_2\cos\theta_2 & \sin^2\theta_2+1 & 0 & 0 & 0 & 0 \\ 0 & 0 & 1 & 0 & 0 & 0 \\ 0 & 0 & 0 & 1 & 0 & 0 \\ 0 & 0 & 0 & 0 & 1 & 0 \\ 0 & 0 & 0 & 0 & 0 & 1 \end{pmatrix}. \tag{1}$$

The eigenvalues of the matrix JJ^t are the roots its characteristic polynomial, which can be determined by:

$$
\begin{aligned}
P(X)_{JJ^t} &= det \begin{vmatrix}
\cos^2 \theta_2 - X & -\sin \theta_2 \cos \theta_2 & 0 & 0 & 0 & 0 \\
-\sin \theta_2 \cos \theta_2 & \sin^2 \theta_2 + 1 - X & 0 & 0 & 0 & 0 \\
0 & 0 & 1 - X & 0 & 0 & 0 \\
0 & 0 & 0 & 1 - X & 0 & 0 \\
0 & 0 & 0 & 0 & 1 - X & 0 \\
0 & 0 & 0 & 0 & 0 & 1 - X
\end{vmatrix} \\
&= det \begin{vmatrix}
\cos^2 \theta_2 - X & -\sin \theta_2 \cos \theta_2 & 0 \\
-\sin \theta_2 \cos \theta_2 & \sin^2 \theta_2 + 1 - X & 0 \\
0 & 0 & 1 - X
\end{vmatrix} \cdot det \begin{vmatrix}
1 - X & 0 & 0 \\
& 1 - X & 0 \\
0 & 0 & 1 - X
\end{vmatrix} \\
&= (1 - X)^4 (X^2 - 2X + \cos^2 \theta_2).
\end{aligned}
\tag{2}
$$

The eigenvalues of the matrix JJ^t are thus:

$$
\begin{cases}
X = 1, \\
X = 1 \pm |\sin \theta_2|
\end{cases}
\tag{3}
$$

Therefore we can obtain the conditioning number of the mechanism as follow:

$$
K = \sqrt{\frac{1}{1 - |\sin \theta_2|}}
\tag{4}
$$

where θ_2 represents the varus/valgus angular position, which is limited to 20° here. Consequently, the maximum conditioning number of the mechanism is 1.23. The mechanism is thus quasi-isotropic.

3 Mechanical Design

3.1 Kinematic Choice

Beside the quasi-isotropic property, The 3R-3P mechanism also allows the decoupling of torques and the forces, then pure torques can be transmitted to the human anatomical joint, without any linear force components which may cause sliding movements of the attaches. However, the use of prismatic joints is usually not suitable due to their massive weight and expensive cost. Then replacement mechanisms, composed by parallelograms, using only bearing joints should be considered. For that purpose, we proposed the use of Delta type parallel mechanism to substitute the 3 prismatic joints.
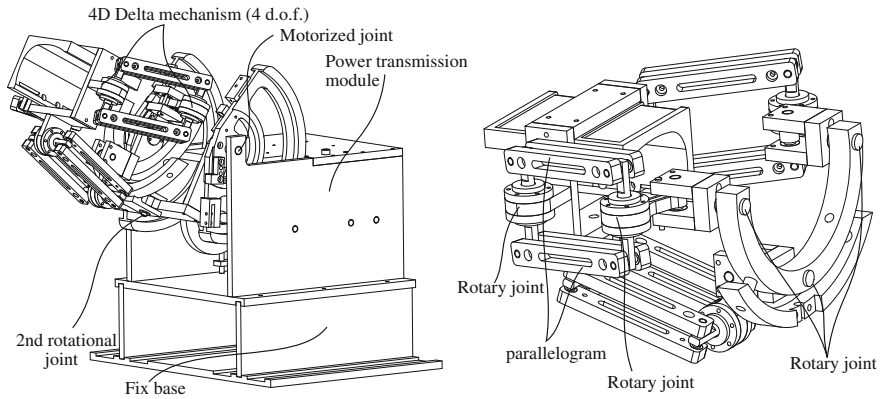
Fig. 2 a 3D computer model of the device. **b** The 4 d.o.f. delta type linkage: the close-loop mechanism is composed by 3 chains, each chain is a R-R-Pa-R mechanism

The proposed mechanism in this paper is a hybrid structure composed by 2 rotational joints in series with a 4D Delta parallel mechanism, forming a 6 degrees of freedom mechanism. With this design, the motor torque will be transmitted in the sagittal plane of the elbow, thus assuring the stability of the whole system.

3.2 Description of the Design

Figure 2 show the details of the mechanical linkage of the device. The 4D Delta type parallel linkage is composed by 3 chains. Each chain is formed by 3 rotary joints in series with a parallelogram that connects to the extremity base through a 4th rotary joints (which can be called here a R-R-R-Pa-R mechanism). The 3 first rotary joint added at each chain allow to free an additional rotational degree of freedom for the 4D Delta linkage, besides the 3 other degrees of freedom in translation. The virtual axis of rotation of this 4th degree of freedom is located near to the that of the forearm, thus allowing the elbow supination/pronation movement.

Figure 3 illustrates the transmission module. The device can provide a torque of 20 Nm through the use of a DC motor and a three-stage, backdrivable, 120:1 transmission. It comprises two high-speed friction drives followed by a low speed cable-drive. The 2nd and the 3rd stage give a torque gain 10 and 12 respectively.

The first friction drive operates through direct contact between the surface of a disk (directly fixed to the motor shaft) and 2 disk drives (of type cylinder—elastic half space contact). The elasticity is regulated by 4 compression springs pushing on the motor disk. The second friction drive is of type contact between two cylinders with parallel axes. For this 2nd stage, contact is regulated by a compression spring pushing on rollers so that slip does not occur. These systems allow the adjustment the threshold of slipping, and thus provides an extra level of safety for users.
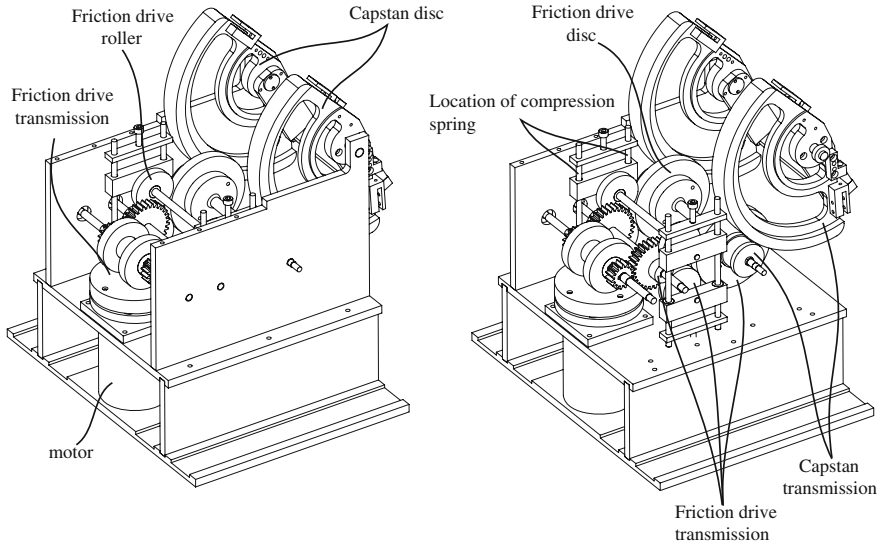
Fig. 3 The transmission module with a power ratio of 120:1
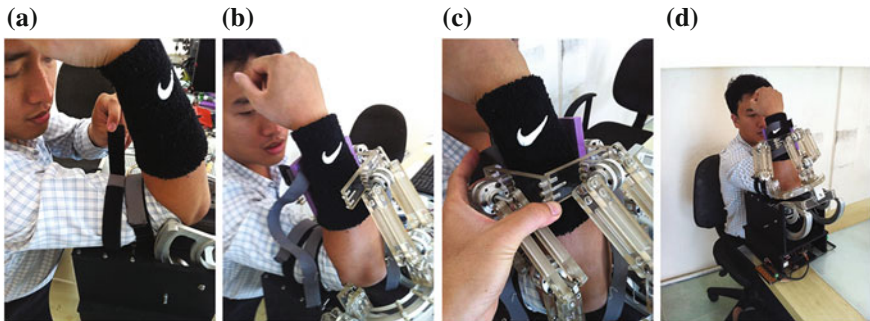
Fig. 4 Set up protocol to attach the device to the subject's limbs. **a** The subject's arm is being attached to the fixed base. **b** The forearm is being attached to the mechanism, the third mechanical chain is detached. **c** The third mechanical chain is re-attached to the mechanism. **d** End of set up protocol, the system is ready to use

4 Result

The first version of the device was manufactured, assembled and tested. Figure 4 shows the set up protocol on the user's arm. As the device is designed for muscular stretching exercises with patient having flexed elbow then the protocol must begin at full flexion. One of the 3 mechanical chains is detached at the beginning so that the rehabilitation practitioner can attach the mechanism to the user's forearm. This chain will be re-attached to the mechanism once the forearm is firmly in place.
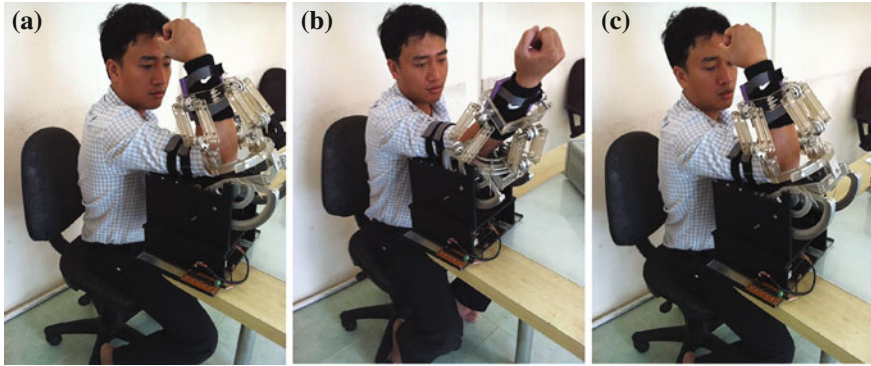
Fig. 5 Elbow stretching exercise. **a** The beginning of the exercise. **b** The device pull the elbows to a predefined position. **c** The torque set-point is set to zero, then the elbow joint can return to its initial position due to its stiffness

Preliminary results are satisfactory. We used a current sensor to monitor the motor torque and an optical encoder to measure the flexion angular position. The following algorithm was implemented for our very first experiments:

- 1st step: Pull the elbow to a certain predefined angle. The torque is controlled so that the user elbow can oscillate around this angular position.
- 2nd step: Let the elbow return to full-flexion by setting the torque set-point to zero.
- Return to the 1st step to repeat the exercise (Fig. 5).

5 Conclusion

In this paper, we presented an isostatic 6 d.o.f active orthosis device for the elbow joint. The device is composed by 2 rotational joints and a 4D Delta-type parallel mechanical linkage, assuring the stability of the whole system and keeping the mechanism's conditioning number near to 1. The first rotational joint is actuated, transmitting the motor torque to the forearm to drive the elbow in flexion-extension. Friction drive and cable drive are used to provide a safe, back-driven and high ratio mechanical power transmission. First experiments have shown the relevance of this approach. In near future, clinical trials will be realized on this device.

References

1. Bottlang, M., Madey, S.M., Steyers, C.M., Marsh, J.L., Brown, T.D.: Assessment of elbow joint kinematics in passive motion by electromagnetic motion tracking. J. Orthop. Res. 612–618 (2011)
2. Cai, V.A.D., Bidaud, P., Hayward, V., Gosselin, F.: Method for the Identification of anatomical joint motion based on a six degree of freedom electro-goniometer. In:

ROMANSY 18—Robot Design, Dynamics and Control, vol. 524, pp. 399–406, Udine-Italia (2010)
3. Cai, V.A.D., Bidaud, P., Hayward, V., Gosselin, F., Desailly, E.: Self-adjusting Isostatic exoskeleton for the human knee joint. In: Annual International Conference of the IEEE Engineering in Medicine and Biology Society, pp. 612–618 (2011)
4. Chablat, D., Angeles, J.: The computation of all 4R serial spherical wrists with an isotropic architecture. J. Mech. Des. **25**(2), 275–280 (2003)
5. Ergin, M.A., Patoglu, V.: A self-adjusting knee exoskeleton for robot-assisted treatment of knee injuries. In: IEEE/RSJ International Conference on Intelligent Robots and Systems (IROS), pp. 4917–4922 (2011)
6. Ericson, A., Arndt, A., Stark, A., Wretenberg, P., Lundberg, A.: Variation in the position and orientation of the elbow flexion axis. J. Bone Joint Surg. **85-B**(4), 538–544 (2003)
7. Jarrassé, N., Morel, G.: Formal methodology for avoiding hyperstaticity when connecting an exoskeleton to a human member. In: IEEE International Conference on Robotics and Automation (ICRA'10) (2010)
8. Schiele, A., Van der Helm, F.C.T.: Kinematic design to improve ergonomics in human machine interaction. IEEE Trans. Neural Syst. Rehabil. Eng. **14**(4), 456–469 (2006)
9. Stienen, A.H.A., Hekman, E.E.G., Van der Helm, F.C.T., Van der Kooij, H.: Self-aligning exoskeleton axes through decoupling of joint rotations and translations. IEEE Trans. Robot. **25**, 628–633 (2009)
10. Woltring, H.J., Huiskes, R., De Lange, A.: Finite centrode and helical axis estimation from noisy landmark measurements in the study of human joint kinematics. J. Biomech. **18**(5), 379–389 (1985)

Design of Ankle Rehabilitation Mechanism Using a Quantitative Measure of Load Reduction

Daisuke Matsuura, Shouta Ishida, Tatsuya Koga and Yukio Takeda

Abstract In order to achieve a desired flexion motion with adjustable load and to provide objective measure of recovery status which is important to verify the condition of therapeutic exercise to support physiotherapists, as well as to establish self-rehabilitation by patients themselves, a simple spatial rehabilitation mechanism based on an extended Oldham's coupling was employed. A kinetostatic analysis was performed to determine reasonable values of design parameters to achieve practical working range for therapeutic exercises without exerting unnecessarily large joint load. By utilizing the analysis scheme, adjustment of the joint load by attaching passive springs was also conducted, and a quantitative measure of load reduction ratio was formulated to evaluate the effectiveness of the additional springs. Reduction efficiency among several different configurations of link length was compared to search for the possibility to find an optimum design considering both compactness and safeness of the rehabilitation device.

Keywords Rehabilitation robotics · Ankle joint rehabilitation · Mechanism design · Kinetostatic analysis · Passive adaptation to spatial eccentricity of human joint

1 Introduction

In the coming highly-aged society, increasing of dependents on caregivers will become a big issue. To solve this problem, recovery and enhancement of body functions of elderly people is important, since they are likely to become bedridden due to the weakening of their lower limb. For prompt therapeutic exercises,

D. Matsuura (✉) · S. Ishida · T. Koga · Y. Takeda
Department of Mechanical Sciences and Engineering, Tokyo Institute of Technology,
2-12-1 Ookayama, Meguro-ku, Tokyo 152-8552, Japan
e-mail: matsuura@mech.titech.ac.jp

physiotherapists (PT) need effective treatment protocols based on objective measures of mobilization as well as on exerted and resistant force and torque on affected parts. With this information, PTs can decide on suitable exercise programs.

In order to carry out safe rehabilitation, inadequate conditions called *misuse* caused by unnecessary joint load should be suppressed. It is well known that human's joint has complicated structure, and its spatial movement is thus also complicated and has no constant axis of rotation [1, 2]. Many specially-designed mechanisms have been developed to adapt to the motion of joint axis, e.g. making offset to match the orthosisrotation center to user's joint [3], planar 6-DOF closed-loop mechanism [4], grooved cams and non-circular gears [5]. However, these apparatuses have to be custom-made to fit each user. This requirement can be satisfied by introducing self-adapting features e.g. a combination of two-prismatic joints [6] or a series of P-R-P joints [7], but such features entail more DOFs than the motion of target joints, and thus make the apparatuses complicated, heavy, and expensive. In addition, they cannot adapt to spatial motions.

To solve these problems, the authors have proposed an effective solution by introducing a simple spatial mechanism capable of passively adapting to an eccentricity of user's joint axis, and adjustment of exerted load by attaching passive spring [8]. As an important and practical application, dorsiflexion (DF) and plantar flexion (PF) of user's ankle joint was attempted, but design parameters have not been proofed by quantitative evaluations. In this paper, a reasonable link length to fit to user's physique while achieving practical ROM will be newly determined, and properties of additional springs to achieve effective reduction of the joint load will also be found through a kinetostatic analysis. An evaluation index of reduction ratio of the ankle joint load will be calculated regarding several different combinations of design parameter values to demonstrate the possibility to find out an optimum design regarding the compactness and safeness of the device.

2 Synthesis of the Rehabilitation Mechanism

There are four phases in typical therapeutic exercises of ankle joint which need to restore its range of motion (ROM) after tendon injury or high sprain [9]. Since the allowable range of motion and joint load in each phase are different, PTs manage ROM and joint load during the exercises based on their haptic sensations. The mechanism proposed in this paper aims to achieve suitable ROM and joint load at each phase just like PTs are doing. First, required ROM for the mechanism was determined by analyzing the movement of the human ankle joint using an optical 3D motion capture setup (MAC3D, Motion Analysis Corp.). From the result of the analysis and literature values shown in Table 1 [10–12], required angular amplitudes in plantar-dorsi and inversion–eversion axes for the mechanism have been determined to be $\pm30°$ and $\pm10°$, respectively.

Table 1 Range of motion of healthy ankle joint (unit: °)

Direction	Maximum	Functional
Plantar–Dorsi	$-20° < \theta < 45°$	$-10° < \theta < 20°$
Inversion–Eversion	$-25° < \varphi < 35°$	$-10° < \varphi < 10°$

As mentioned above, the mechanism must be capable of avoiding unnecessary joint load, namely shear, tensile and compressive force, while transmitting only torque from an input link to the ankle joint. To satisfy this requirement, Oldham's coupling mechanism can be effective. Figure 1 is a conceptual schematic drawing of the mechanism. Since the user's leg and foot are fixed on links, the user's body and the mechanism form a monolithic mechanical system. In the drawing, ankle joint is represented by a virtual joint J_7, of which location changes continuously with respect to the orientation change of the foot, and there is also a virtual link between the joints J_6 and J_7. The degrees of freedom (DOF) of the system can be calculated with Gruebler's equation,

$$F = F_s(N - 1) - \sum_{f=1}^{F_s - 1} (F_s - f)P_f. \tag{1}$$

where F_s is the DOF of the workspace, N is the number of links, and P_f is the number of joints having f-DOF. By substituting $F_s = 6$, $N = 5$, and $P_1 = 3$ and $P_2 = 2$ to the equation, DOF of the mechanism becomes 1. In contrast, when the mechanism is detached from the user's leg, the virtual link and virtual joint J_7 are disappeared, and the value of N and P_1 become 4 and 2, respectively. As the result, DOF of the mechanism becomes 6, which is the same as DOF of the workspace. This means that the mechanism is settled only when the mechanism is attached to user's leg, and can drive the user's foot with any the location and direction of the rotation center of user's ankle joint, while passively adapting to fluctuation.

3 Kinetostatic Analysis of the Mechanism

3.1 Kinematic Analysis

A kinematic analysis is performed using several parameters and coordinate systems illustrated in Fig. 1 to obtain the relationship between the input angle, θ_1, and output angle, θ_7. Although all the coordinate axes are drawn as they are parallel with each other, they can take arbitrary directions due to the actual design and spatial motion of the mechanism. The rotation of the virtual joint J_7 around $\boldsymbol{x}_7$ and $\boldsymbol{y}_7$ axes are evaluated as φ and γ, respectively. First of all, location of all joints and the distance between J_1 and J_7 are denoted as $\boldsymbol{r}_{i=1...7} = [x_i \ y_i \ z_i]^T$ and $d = \sqrt{d_x^2 + d_y^2 + d_z^2}$, respectively. Since the location of J_7 in O-XYZ coordinate can be noted as $[x_7 \ y_7 \ z_7]^T = [x_1 + d_x \ y_1 + d_y \ z_1 + d_z]^T$, that of J_3 and J_5 are described as:

Fig. 1 The special
rehabilitation mechanism and
given coordinate system
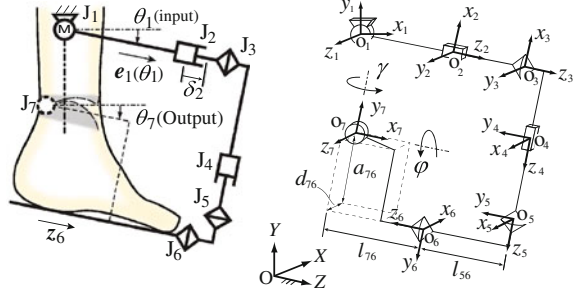
$$r_3 = \delta_2 e_1 + r_1, \quad r_5 = (r_6 - r_7) + l_{56} z_6, \tag{2}$$

where δ_2, l_{56}, e_1 and z_6 denote the displacement of joint J_2, distance between J_5 and J_6, a unit vector toward J_3 from J_1, and a unit vector toward J_5 from J_6. The coordinate rotation from $O_1 - x_1 y_1 z_1$ to $O_7 - x_7 y_7 z_7$ is written as:

$$R_x(\gamma)R_z(\varphi) = \begin{bmatrix} \cos\gamma & \sin\gamma\cos\varphi & \sin\gamma\cos\varphi \\ 0 & \cos\varphi & -\sin\varphi \\ -\sin\gamma & \cos\gamma\sin\varphi & \cos\gamma\cos\varphi \end{bmatrix}. \tag{3}$$

From the relationships between certain links, $J_2 J_3 \perp J_3 J_5$ and $J_4 J_5 \perp J_5 J_6$,

$$e_1 \cdot (r_3 - r_5) = 0, \quad z_6 \cdot (r_3 - r_5) = 0 \tag{4}$$

can be obtained. By introducing parametric representations

$$\sin\theta_7 = \frac{2k}{1+k^2}, \quad \cos\theta_7 = \frac{1-k^2}{1+k^2}. \tag{5}$$

Equation (4) is written as the following quadric polynomial;

$$k^4(A_5 - A_1) + 2k^3(A_2 - A_3) + 2k^2(2A_4 - A_5) + 2k(A_2 - A_3) + (A_1 + A_5) = 0, \tag{6}$$

where $A_{1...5}$ are constant terms determined by design parameters. For want of space, their detail is abbreviated except in case of A_1,

$$\begin{aligned}
A_1 &= d_x c(\theta_1) - d_z s(\gamma) - d_{67} s(\gamma) c(\gamma) c(\varphi) c^7(\theta_1) \\
&\quad + d_{67} c(\gamma) s(\varphi) s(\theta_1) c(\theta_1) - d_y c(\gamma) s(\theta_1) c(\theta_1) - d_x c(\gamma) c^2(\theta_1).
\end{aligned} \tag{7}$$

By solving Eqs. (5) and (6), intput–output relationship of the mechanism is calculated in such a way that output angle, θ_7, regarding given orientation angles of the ankle joint, γ and φ, and input angle, θ_1, can be obtained. In order to fit the

Table 2 Design parameters (unit: m)

Parameters	Value (m)
d_x	0.0
d_y	−0.1
d_z	0.15
l_{65}	0.053
l_{73}	0.1
a_{76}	0.1
d_{76}	−0.15

Fig. 2 Input–output relationship of the mechanism
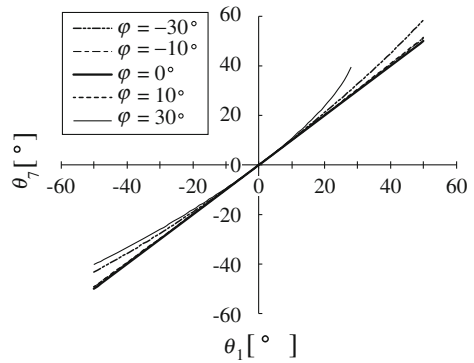
mechanism to typical adult user's physique while minimizing its volume, essential design parameters are defined as Table 2. The input–output relationship in the range of $-30° < \varphi < 30°$ while holding $\gamma = 0$ is obtained as shown in Fig. 2. By comparing Fig. 2 and typical ROM of a healthy ankle joint shown in Table 1, it can be said that the rehabilitation mechanism will achieve linear input/output relationship within the functional region, $-10° < \varphi < 10°$.

3.2 Static Analysis

In order to estimate the load exerted on the ankle joint, static analysis was performed considering the gravitational force applied to each link and the friction of the two prismatic joints. According to the free-body diagram shown in Fig. 3, equilibrium of force and moment on the links are expressed as;

(a) Equilibrium of force:

$$F_1 - F_2 + m_1 g - F_a = 0, \ F_2 - F_3 + m_2 g + F_a - F_b = 0,$$
$$F_3 - F_4 + m_3 g + F_b = 0, \ F_4 - F_5 + m_4 g = 0. \tag{8}$$

Fig. 3 Free body diagram of the proposed mechanism
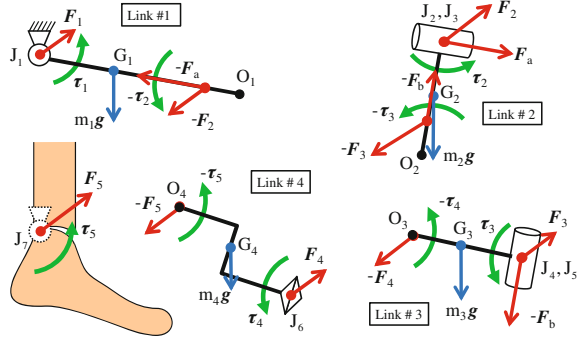
Table 3 Link mass

No.	Length (m)	Mass (kg)
1	0.30 (ℓ_{31})	0.089
2	0.25 (ℓ_{53})	0.074
3	0.05 (ℓ_{31})	0.044
4	$0.10(\ell_{76})$ $0.10(a_{76})$ $0.15(d_{76})$	0.425 + 3.075 [force sensor]

(b) Equilibrium of moment:

$$\tau_1 - \tau_2 + l_{g1} \times m_1 g - l_1 \times F_2 = 0, \quad \tau_2 - \tau_3 + l_{g2} \times m_2 g - l_2 \times F_3 = 0,$$
$$\tau_3 - \tau_4 + l_{g3} \times m_3 g - l_3 \times F_4 = 0, \quad \tau_4 - \tau_5 + l_{g4} \times m_4 g - l_4 \times F_5 = 0.$$

$$(9)$$

where $m_{1\ldots4}$ and g denote the mass of links #1,…,#4 and gravitational acceleration. l_{gi} and l_i are the vectors pointing towards the i-th center of mass, G_i, and i-th end point, O_i, from J_1, J_2, J_4 and J_6. From Eqs. (8) and (9), frictional force on the prismatic joints on J_2 and J_4 and the magnitude of ankle joint load are obtained:

$$F_a, F_b = \mu \sqrt{F_{\alpha,i}^2 + F_{\beta,i}^2} \bigg|_{i=2,4}, \tag{10}$$

$$F_{load} = \sqrt{F_{7x}^2 + F_{7y}^2 + F_{7z}^2}, \tag{11}$$

where μ is a friction coefficient which is given as $\mu = 0.2$ in the following analysis. $F_{\alpha,i}$ and $F_{\beta,i}$ are the coaxial forces with respect to each link and its orthogonal force, respectively. In order to carry out the calculation, the mass of each link shown in Table 3 were substituted. Values in the table were calculated based on the assumption that all the links were made of carbon steel. Figure 4 plots

Fig. 4 Load on the ankle joint J_7
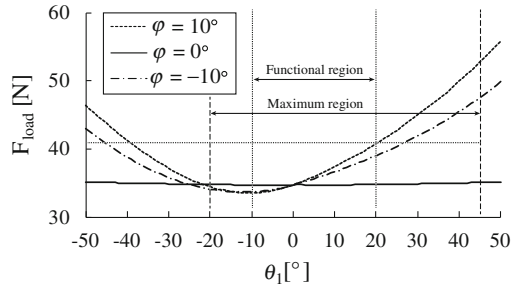
Fig. 5 Additional springs on J_2, J_3 and J_4
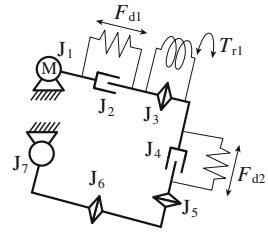
the relationship between the input angle θ_1 and the amplitude of F_{load} with respect to different inversion/eversion angles. The result indicates that the amplitude of the ankle joint load within the functional range was approximately 40 N at most.

4 Adjustment of Ankle Joint Load Using Passive Springs

Although it is difficult to completely avoid ankle load, it can be compensated by adding springs to certain joints. To select the joints to attach the springs, optimum amplitude and direction of compensation force on each joint to minimize F_{load} with respect to different θ_1 were firstly calculated. From the result of this calculation, it was found that springs on J_2, J_3 and J_4 are effective to reduce F_{load}. Since J_2 and J_4 are prismatic joints and J_3 is a revolute joint, suitable types of springs are attached as shown in Fig. 5. Next, spring coefficient and initial displacement of the three springs were determined by simply applying line-fitting to the distribution of the optimum compensation force/torque against displacement of each joint as shown in Fig. 6. The spring constant and initial length of each spring were therefore determined as shown in Table 4. The negative sign in the table indicates the direction of the spring force. In order to search for the possibility to optimize the length of each link, ankle load was calculated with several different combinations of d_y and l_{76}, 0.05 m longer and shorter ones than the original value in Table 2. The obtained ankle load in case of three different d_y is plotted in Fig. 7.

Fig. 6 Displacement/force
relationship on J_2 at different
foot orientations
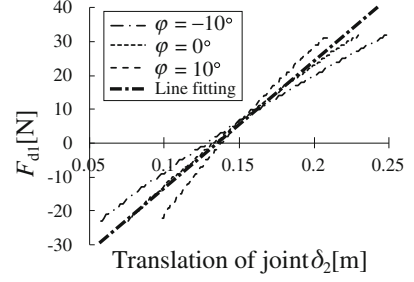
Table 4 Properties of the
springs

No.	Type	Initial displacement	Spring coefficient
J_2	Tensile	-0.13 m	375.5 N/m
J_3	Torsional	0.09 rad	39.04 Nm/rad
J_4	Tensile	-0.14 m	393.0 N/m

Fig. 7 Compensated ankle
load distribution with respect
to different link length
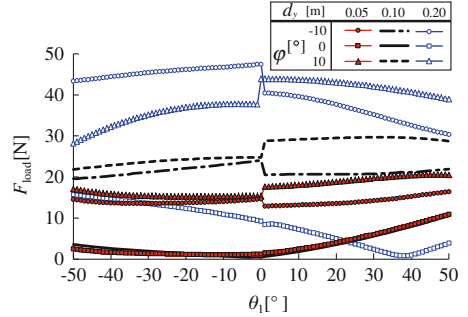
The effectiveness of each configuration on the load reduction was evaluated by an index,

$$\eta = 1 - \frac{\sum_{j=1}^{N} \left(F_{load,j} - \hat{F}_{load,j} \right)}{N \cdot F_{load}}, \tag{12}$$

where F_{load} and $\hat{F}_{load}$ are the ankle load with and without the springs at the j-th sampling and N is the number of acquired data. Based on the value of η shown in Table 5, the ankle load was reduced 91 % at most or 34 % at least by attaching the springs, and the reduction ratio can be increased by using larger d_y. In case of $\underline{d_y} = 0.20$, F_{load} was less than 20 N among entire maximum ROM. That condition is suitable for typical therapeutic exercise shown in [9]. However, there is a trade-off

Table 5 Load reduction index η (%)

Ankle inclination φ (deg)		-10	0	10
Orig $(d_y, \ell_{76}) = (0.10, 0.10)$		44	91	34
d_y (m)	Short (0.05)	-8	76	3
	Long (0.20)	63	90	57
ℓ_{76} (m)	Short (0.05)	24	89	7
	Long (0.20)	58	89	48

that increasing of link length will also enlarges the size of the rehabilitation apparatus. Optimum link length should be determined by considering both compactness and safeness. This adjustment technique can be used not only to reduce the load but also to exert a desired force. Furthermore, the resistance of a joint can be estimated by substituting the measured motion to the theoretical model. The estimated resistance will become useful information in evaluating the recovery status of joints and determining suitable rehabilitation programs for each patient.

5 Conclusion

This paper has discussed the design and analysis of a simple rehabilitation mechanism capable of adapting to fluctuation in the rotation axis and the adjusting of exerted load. The obtained results can be summarized as follows;

(1) Based on the extended Oldham's coupling mechanism, a simple spatial rehabilitation mechanism which can transmit only driving torque while adapting to changes in the axis of rotation has been proposed. The composition of the 1-DOF mechanism is very simple and thus contributes to the development of a lightweight and inexpensive rehabilitation device.

(2) A practical design of a prototype to achieve a desired working range was determined according to the result of human motion analysis experiments and literature data. Subsequently, a kinetostatic analysis considering the effects of gravitational force and friction on cylindrical joints was done to estimate the magnitude of the load on the joints.

(3) Adjustment of ankle joint load by means of springs was introduced and a practical number, location and physical properties of springs were systematically determined. The result of our theoretical analysis with the spring configuration obtained was that the load force could be reduced greater than 34 %.

(4) Possibility to determine optimum length to reduce joint load was shown by evaluating several different combination of design parameters. There is a trend that larger link length tends to achieve less joint load. However, since not only the compactness but also safeness should be paid attention to figure out practical design, those two factors should be simultaneously considered.

References

1. Malosio, M., et al.: Analysis of elbow-joints misalignment in upper-limb exoskeleton. In: IEEE International Conference on Rehabilitation Robotics, 2011
2. Gregorio, R., et al.: Mathematical models of passive motion at the human ankle joint by equivalent spatial parallel mechanisms. Med. Biol. Eng. Compu. **45**(3), 305–313 (2007)
3. Esmaeili, M., et al.: Ergonomic considerations for anthropomorphic wrist exoskeletons: a simulation study on the effects of joint misalignment. In: Proceedings of the IEEE International Conference on Intelligent Robots and Systems, pp. 4905–4910 (2011)
4. Jin, D., et al.: Kinematic and dynamic performance of prosthetic knee joint using six-bar mechanism. J. Rehab. Res. Dev. **40**(1), 39–48 (2003)
5. Teradaet, H., et al.: Developments of a Knee Motion Assist Mechanism for Wearable Robot with a Non-circular Gear and Grooved Cams. Mech. Mach. Sci. **3**(2):69–76 (2012)
6. Stienen, A.H.A., et al.: Self-aligning exoskeleton axes through decoupling of joint rotations and translations. IEEE Trans. Robot. **25**(3):628–633 (2009)
7. Cai, D., et al.: Design of self-adjusting orthoses for rehabilitation. In: Proceedings of the IASTED International Conference on Robotics and Applications, pp. 215–223 (2009)
8. Matsuura, D., et al.: Kinetostatic design of ankle rehabilitation mechanism capable of adapting to changes in joint axis. J. Robot. Mechatron. **25**(6), 1029–1037 (2013)
9. Mattacola, C.G., et al.: Rehabilitation of the ankle after acute sprain or chronic instability. J. Athl. Train. **37**(4), 413–429 (2002)
10. Gao, F., Ren, Y., et al.: Effects of repeated ankle stretching on calf muscle-tendon and ankle biomechanical properties in stroke survivors. Clin. Biomech. **26**(5), 516–522 (2011)
11. Sekiguchi, Y., et al.: The contribution of quasi-joint stiffness of the ankle joint to gait in patients with hemiparesis. Clin. Biomech. **27**(5), 495–499 (2012)
12. Lee, H., Ho, P., et al.: Multivariable static ankle mechanical impedance with relaxed muscles. J. Biomech. **44**, 1901–1908 (2011)

Characterization of the Subsystems in the Special Three-Systems of Screws

Dimiter Zlatanov and Marco Carricato

Abstract The paper examines the subspaces of a space spanned by three independent twists (or wrenches) with axes parallel to a common plane. A complete characterization of all screw cylindoids nested within a special three-system of screws is given. The results are illustrated by means of geometric models of three-dimensional projective space incorporating the Ball circle diagram of the cylindroid.

Keywords Screw systems · Projective space · Mechanism synthesis

1 Introduction

In robotic systems, the possible instantaneous motions of a rigid body, or the systems of forces acting on it, are described by a subspace of the six-dimensional vector space of twists, or wrenches. Such linear subspaces, or the underlying projective spaces, are referred to as screw systems. Screw systems were first studied in [1], but a comprehensive classification and detailed geometrical characterizations were obtained in [6]. See also [4, 5, 7, 8].

Two screw systems are *equivalent* if one can be seen as a rigid-body displacement of the other. This relation divides the space of linear subspaces of $se(3)$ into infinitely many equivalence *classes*. Geometrically similar classes are grouped into *types*: one general and a variety of special, according to [6].

D. Zlatanov (✉)
DIME, University of Genoa, Genova, Italy
e-mail: zlatanov@dimec.unige.it

M. Carricato
DIN and ICIR-HST, University of Bologna, Bologna, Italy
e-mail: marco.carricato@unibo.it

Following Gibson and Hunt [5] a screw-system class can be labeled by: its dimension; I or II, indicating whether or not there are screws of more than one finite pitch; a letter (from A to D) denoting the number (from 0 to 3) of independent infinite-pitch screws; and additional parameters. In this paper we study three-systems of B- and C-types, such as the seventh special [6], i.e., class 3–IB$(h_\circ, \gamma)$ with special pitch $h_\circ$ and angle γ.

One aspect of screw-system geometry, not yet explored in detail, is the nesting of lower-rank systems within ones of higher dimension. The key issue is the characterization of all two-systems within a three-system. (Nesting in higher-rank systems reduces to lower dimensions via reciprocity.) For each three-system, one can ask: what two-subsystem classes have representatives, and where are these two-systems located? Such questions are of theoretical value and have practical relevance in mechanism analysis and synthesis: subspaces describe end-effector freedoms under additional constraints; the orbits of $SE(3)$ action in the Grassmanian are important when trying to find serial chains with a persistent screw-system class [3].

This paper examines the subspaces of any three-system whose screw axes are parallel to a plane. For those of A types, see [2]. In the most complex cases, 3–IB$(h_\circ, \gamma)$ and 3–IB$^\circ(h_\circ)$, this is done via a novel way of representing the screws of the system as points on a plane.

2 Screws and Projective Spaces

A twist (or a wrench) is given by a pair of vectors, $(\boldsymbol{\omega}, \mathbf{v}) \in se(3)$, the body's angular velocity and the linear velocity at the origin (or $(\mathbf{f}, \mathbf{m}) \in se(3)^*$, the resultant force and moment at the origin). An element, $\boldsymbol{\xi} = (\boldsymbol{\omega}, \mathbf{v})$, of $se(3)$ (similarly $se(3)^*$) is associated with a *screw* about which the body twists (or the wrench is applied)—a line in space, $\ell(\boldsymbol{\xi})$, the screw axis, with a metric scalar, the pitch h, given by

$$h = \frac{\boldsymbol{\omega} \cdot \mathbf{v}}{\boldsymbol{\omega} \cdot \boldsymbol{\omega}}, \quad \mathbf{r}_\perp = \frac{\boldsymbol{\omega} \times \mathbf{v}}{\boldsymbol{\omega} \cdot \boldsymbol{\omega}} \tag{1}$$

where $\mathbf{r}_\perp$ is the axis point closest to the origin. Conversely, $\boldsymbol{\xi} = (\boldsymbol{\omega}, \mathbf{v}) = (\boldsymbol{\omega}, h\boldsymbol{\omega} + \mathbf{r} \times \boldsymbol{\omega})$, for any $\mathbf{r} \in \ell(\boldsymbol{\xi})$. An infinite-pitch screw is a pure direction of a translation $(0, \mathbf{v})$ (or a force couple $(0, \mathbf{m})$).

Each screw is identified with a class, $[\boldsymbol{\xi}]$, of twists obtained from each other by (real-number) scalar multiplication, i.e., it is an element of the five-dimensional *real projective space*, $[\boldsymbol{\xi}] \in P(se(3))$, generated by $se(3)$. Real projective n-space, $P(\mathbb{R}^{n+1}) = \mathbb{RP}^n$, is defined by imposing the equivalence relation $\boldsymbol{x} \sim \lambda \boldsymbol{x}$, $\lambda \neq 0$, on $\mathbb{R}^{n+1} - \{0\}$, identifying vectors that are scalar multiples. The equivalence classes can be thought of as lines through the origin in $\mathbb{R}^{n+1}$.

It is often desirable to visualize the elements of projective n-space as points of an n-manifold. One classic way is the so-called straight model, which maps $\mathbb{RP}^n$ onto $\mathbb{R}^n$ with an added hyperplane at infinity, by intersecting the lines (in $\mathbb{R}^{n+1}$) through the origin with an n-plane away from it. The *prestereographic model* [9] uses a sphere $S^n(s)$, with antipodal points O and some $s \in \mathbb{R}^{n+1}$. For a line through O not tangent to $S^n(s)$, we take the second intersection point as the image. The lines tangent to the sphere at the origin have no such second point, and so the image space needs to be augmented by "blowing-up" the origin and replacing it with a copy of $\mathbb{RP}^{n-1}$. The sphere $S^n(s)$ can then be mapped onto a hyperplane via stereographic projection from the antipode, s. If $n = 2$ this results in a plane image (a circle inversion of the straight model) with a single point at infinity and a finite point blown-up. In Sects. 4 and 5 we use two models which map a three-system onto exactly such an image: a single-point-compactified plane with one other point blown-up.

3 The Ball Circle of the General Two-System

The screw system, $\mathscr{P}^1 = P(\mathscr{A}^2)$, of a two-dimensional subspace $\mathscr{A}^2 \subset se(3)$, is classified as *general*, when it has a pair of generators, $\mathscr{A}^2 = Span\,(\xi_1, \xi_2)$, on the *principal screws* of the system, with different finite pitches, $h_1 > h_2$, and intersecting perpendicular axes. In a coordinate frame with Ox and Oy along these axes:

$$\xi_1 = (\mathbf{i}, h_i\mathbf{i}), \quad \xi_2 = (\mathbf{j}, h_2\mathbf{j}) \tag{2}$$

$$\xi = c_\theta\xi_1 + s_\theta\xi_2 = (c_\theta\mathbf{i} + s_\theta\mathbf{j}, h_1c_\theta\mathbf{i} + h_2s_\theta\mathbf{j}) \tag{3}$$

with $c_\theta = \cos\theta$, $s_\theta = \sin\theta$, where θ is the screw-axis direction angle from Ox.

It is easy to obtain the pitch and the axis location:

$$h = h_2 + Hc_\theta^2, \quad \mathbf{r}_\perp = Hc_\theta s_\theta\mathbf{k} \tag{4}$$

where $H = h_2 - h_1$. Eliminating θ we obtain

$$(p - \frac{H}{2})^2 + z^2 = \frac{H^2}{4} \tag{5}$$

the equation of a circle in the (z, p) plane. This *Ball circle*, models geometrically the relationship between screw-axis location and pitch in the cylindroid [1, 6, 9]. It can be shown to be a prestereographic model of $\mathscr{P}^1$ [9]. This reflects the fact that the angle between the (projected) axes of any two screws is subtended by the arc between their image points on the circle.

Since translations in the (z, p) plane will just shift a circle, it follows that the two-system can be represented with a circle of the same size in a plane (Z, h),
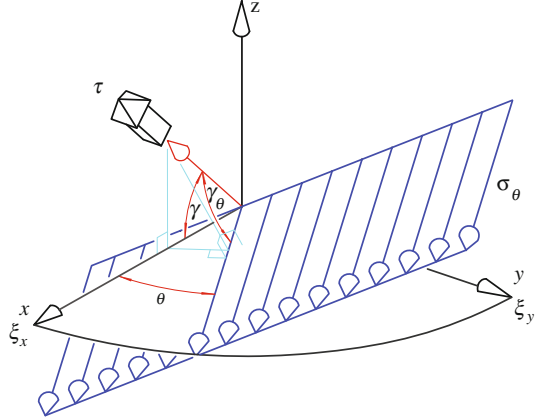
where h is the absolute pitch (rather than the relative, p) and Z is the elevation with respect to some arbitrary horizontal zero plane (rather than the central plane of the cylindroid identified with Oxy in the special coordinate system chosen above). This allows various different two-systems, with screws normal to a common direction, to be represented as circles on the same pitch-to-elevation plane.

In fact, some three-systems can be faithfully parameterized by the pair (z, p) [10]. In all such models, general two-systems appear as circles in the parameter plane. Moreover, this will be true after any change of variables which maps circles into circles, e.g., reflections, rotations, and dilations can be used. One novel such parameterization yielding a useful planar model is introduced in the following section.

4 Model and Subsystems of the Seventh-Special Three-System

A seventh-special three-system, class 3–IB$(h_\circ, \gamma)$ [5, 6], has basis and generic twist

$$\boldsymbol{\xi}_x = (\mathbf{i}, h_\circ \mathbf{i}), \quad \boldsymbol{\xi}_y = (\mathbf{j}, h_\circ \mathbf{j}), \quad \boldsymbol{\tau} = (0, c_\gamma \mathbf{i} + s_\gamma \mathbf{k}) \tag{6}$$

$$\boldsymbol{\xi} = c_\theta \boldsymbol{\xi}_x + s_\theta \boldsymbol{\xi}_y + m\boldsymbol{\tau} = (c_\theta \mathbf{i} + s_\theta \mathbf{j}, (h_\circ c_\theta + mc_\gamma)\mathbf{i} + h_\circ s_\theta \mathbf{j} + ms_\gamma \mathbf{k}) \tag{7}$$

The system's finite-pitch screws are all parallel to Oxy, Fig. 1. Those with pitch $h_\circ$ form two pencils: concurrent at O in Oxy and a Oy-parallel in the plane through Oy normal to $c_\gamma \mathbf{i} + s_\gamma \mathbf{k}$.

For the pitch and the axis location of $\boldsymbol{\xi}$ we have:
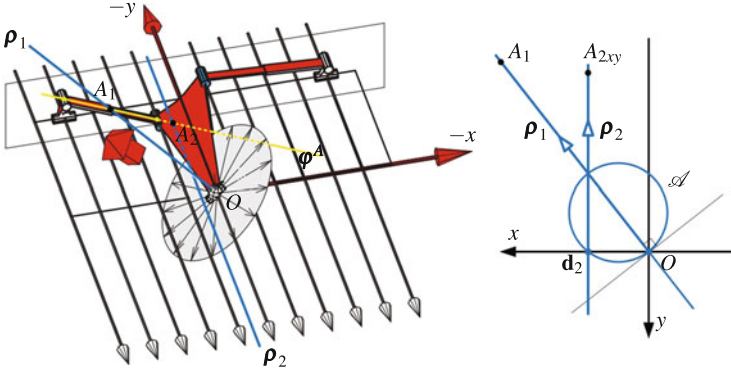
Fig. 2 The freedoms, $\mathscr{A} = Span\,(\boldsymbol{\rho}_1, \boldsymbol{\rho}_2)$, of the Exechon platform with a blocked actuator

$$h = h_\circ + p = h_\circ + mc_\theta c_\gamma \tag{8}$$

$$\mathbf{r}_\perp = \mathbf{d} + z\mathbf{k} = m(s_\theta s_\gamma \mathbf{i} - c_\theta s_\gamma \mathbf{j}) - ms_\theta c_\gamma \mathbf{k}. \tag{9}$$

We notice that almost every finite-pitch screw is defined univocally by the projection, $\mathbf{d}$, of $\mathbf{r}_\perp$ on Oxy. The only exceptions are the screws in the central $h_\circ$-pitch pencil at O, for which $\mathbf{d} = 0$. Thus we can use the plane (d_x, d_y) with point O blown up (to include the concurrent $h_\circ$-pencil) and an added single point at infinity (to represent the ∞-screw) as a model of the three-system. Moreover, since

$$\mathbf{d} = d_x\mathbf{i} + d_y\mathbf{j} = -z(\tan\gamma)\mathbf{i} - p(\tan\gamma)\mathbf{j} \tag{10}$$

this geometric representation also describes the pitch and location of the screw.

From what was said in the previous section, general two-subsystems are mapped into circles in the (d_x, d_y) plane. Each such circle must pass through O, because every two-subsystem includes a screw in the central pencil. (Every two projective two-subspaces in a three-space intersect.)

For example, the platform twists of the Exechon tripod form a 3–IB$(0, \gamma)$ system in almost every configuration, (including the singular one in) Fig. 2 [11]. If an actuator is blocked, the constraint-wrench basis can be augmented by the pure force along the leg, $\boldsymbol{\varphi}^A$, shown in Fig. 2—left with the original concurrent and planar force pencils. This leaves only a two-system of freedoms, $\mathscr{A}$, spanned by rotations $\boldsymbol{\rho}_1$ and $\boldsymbol{\rho}_2$, with axes intersected by $\ell(\boldsymbol{\varphi})^A$. In the model plane, Fig. 2—right, $\mathscr{A}$ is the circle through the image point $\mathbf{d}_2$ of $\boldsymbol{\rho}_2$, and with tangent at O perpendicular to the direction of $\boldsymbol{\rho}_1$ direction at O.

The principal screws of a general two-subsystem are represented on the circle by the antipodal points with tangents parallel to Ox. Conversely, given $h_1 > h_2$, a nested 2–IA (h_1, h_2) system is given by a circle tangent to the $(Ox$-parallel) lines $d_y = y = -(h_i - h_\circ)\tan\gamma$, $i = 1, 2$. If $h_\circ > h_1$ or $h_2 > h_\circ$, there is *no solution*,

Fig. 3 Nested general two-subsystem in 3–IB$(h_\circ, \gamma)$: *top* $h_1 > h_\circ > h_2$; *bottom* $h_1 = h_\circ$
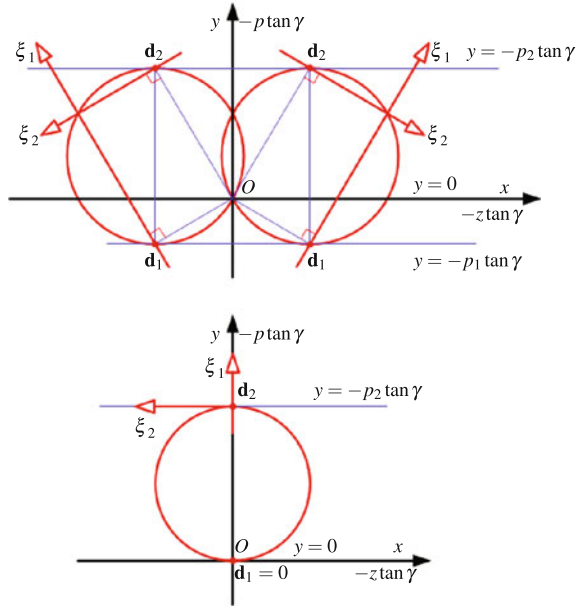
when $h_\circ = h_i$ there is a *unique solution*, and when $h_1 > h_\circ > h_2$ there are *exactly two subsystems* of this class, Fig. 3. The elevation, z, and the Oxy projection, $\mathbf{r}$, of the center are

$$z = \varepsilon\sqrt{(h_1 - h_\circ)(h_\circ - h_2)} \tag{11}$$

$$\mathbf{r} = \varepsilon\tan\gamma(2\sqrt{(h_1 - h_\circ)(h_\circ - h_2)}\mathbf{i} + (h_1 - h_2)\mathbf{k}), \quad \varepsilon = \pm 1. \tag{12}$$

The special two-subsystems are: the 2–II$(h_\circ)$ central pencil in Oxy; the IIB $(h_\circ)$ parallel pencil in a plane through Oy normal to $c_\gamma\mathbf{i} + s_\gamma\mathbf{k}$ (the abscissa axis in the model); and two representatives of each class 2–IB(β) with $\gamma < \gamma_\theta = \beta < \pi/2$, Fig. 1.

5 Model and Subsystems of the Eigth-Special Three-System

A system of class 3–IB$^\circ(h_\circ)$ (eighth-special in [6]) is spanned by $\boldsymbol{\xi}_x = (\mathbf{i}, h_\circ\mathbf{i}), \boldsymbol{\xi}_y = (\mathbf{j}, h_\circ\mathbf{j})$, and $\boldsymbol{\tau}_z = (0, \mathbf{i})$, Fig. 4. For finite-pitch normalized twists in the system,

$$\boldsymbol{\xi} = c_\theta\boldsymbol{\xi}_x + s_\theta\boldsymbol{\xi}_y + m\boldsymbol{\tau}_z = (c_\theta\mathbf{i} + s_\theta\mathbf{j}, (h_\circ c_\theta + m)\mathbf{i} + h_\circ s_\theta\mathbf{j}) \tag{13}$$

Fig. 4 The 3–IB°$(h_\circ)$ system and the plane formed by the screw axes with direction angle θ
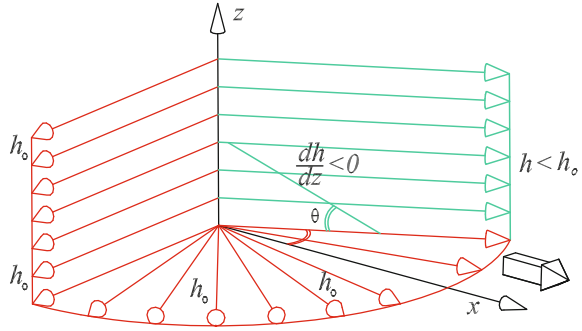
$$h = h_\circ + p = h_\circ + mc_\theta, \quad \mathbf{r}_\perp = z\mathbf{k} = -ms_\theta\mathbf{k}. \tag{14}$$

We notice that almost every screw is defined univocally by the vector

$$\mathbf{w} = w_x\mathbf{i} + w_y\mathbf{j} = mc_\theta\mathbf{i} - ms_\theta\mathbf{j} = p\mathbf{i} - z\mathbf{j}. \tag{15}$$

The only exceptions are the screws in the central $h_\circ$-pitch pencil at O, for which $\mathbf{w} = 0$, and the ∞-pitch screw. We can, therefore, model the system with the plane $(p, -z)$, supplemented with a single point at infinity (the ∞-screw) and with point $(0, 0)$ blown up (adding a copy of $\mathbb{RP}^1$, the $h_\circ$-pencil).

   This is a mirror image of the (p, z) plane, and so general two-subsystems appear as circles. As in the model of $3-IB(h_\circ, \gamma)$, all such circles pass through O, as every two-subspace intersects the concurrent pencil, another two-subspace. However, here the screw of the pencil has an axis on the tangent (rather than the normal) to the circle.

   As in the 3–IB$(h_\circ, \gamma)$ model, given $h_1 > h_2$, there are: *no subsystems* of class 2–IA(h_1, h_2) if $h_\circ > h_1$ or $h_2 > h_\circ$; exactly *one* when $h_\circ = h_1 > h_2$ or $h_1 > h_2 = h_\circ$; and exactly *two* when $h_1 > h_\circ > h_2$, Fig. 5. The centers of all cylindroids project on O and the formula for z in (11) remains valid, as is obvious from the figure.

   There are special two-subsystems of all types except IIC (only ∞-screws): one 2–II$(h_\circ)$ (the central pencil); one IIB$(h_\circ)$ (in the Oyz plane, the abscissa axis in the model); one IB° (on Ox); and two representatives of each class 2–IB(θ), Fig. 4.

6 Nested Two-Systems in the Remaining Three-Systems

We briefly review the subsystems in all other three-systems of type B, C, and D.
   A system of class 3–IB(h_x, h_y) is spanned by $(\mathbf{i}, h_x\mathbf{i})$, $(\mathbf{j}, h_y\mathbf{j})$, $(0, \mathbf{k})$. A 2–IA(h_x, h_y) cylindroid is reproduced at every point of Oxy. All other subsystems are of classes 2–IIB(h), $h_x \geq h \geq h_y$, each spanned by a cylindroid screw and $(0, \mathbf{k})$.
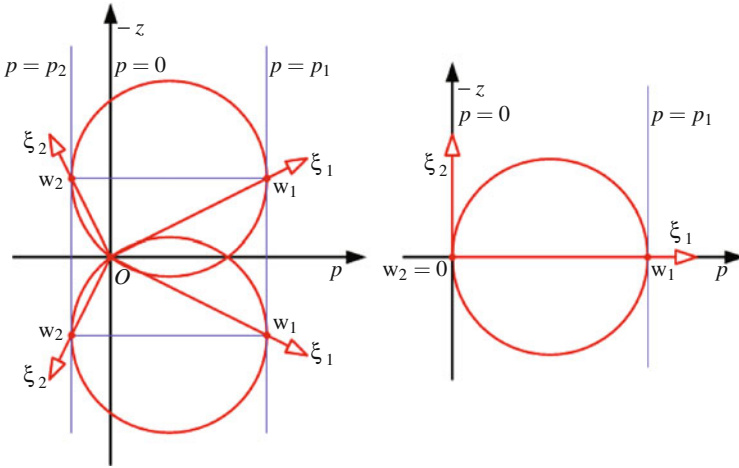
Fig. 5 Nested general two-subsystem in $3-IB°(h_\circ)$: *left* $h_1 > h_\circ > h_2$; *right* $h_2 = h_\circ$

In $3-IC(\gamma)$, a basis is $(\mathbf{i}, 0)$, $(0, \mathbf{j})$, $(0, c_\gamma \mathbf{i} + s_\gamma \mathbf{k})$. The finite pitch screws are all parallel to Ox and arranged in planes, normal to Oy, each with a 2–IIB(h) system, where $h = -y \cot \gamma$. All other subsystems are of type 2–IB(β), with $0 < \beta < \gamma$, lying in planes parallel to Ox.

A $3-IC°$ system, with basis $(\mathbf{i}, 0)$, $(0, \mathbf{i})$, $0, \mathbf{j})$, comprises all screws parallel to Ox in the Oxz plane. There is a single subsystem of each class 2–IIB(h) and 2–IB(β). There is also one helical system, 2–IB° for every z.

The subsystems in the three remaining special three-system classes are well known and trivial to characterize. In 3– IIB(h) (all h-screws in a plane), 3–IIC(h) (all parallel h-screws, and IID (the ∞-screws) they are of classes: 2–IIA(h) and 2–IIB(h); 2–IIB(h) and 2–IIC; and 2–IIC, respectively.

7 Conclusions

The paper analyzes the nesting of two-subsystems within the screw systems of rank three containing infinite-pitch screws. In the important case of the so called seventh- and eighth-special systems, $3–IB(h_\circ, \gamma)$ and $3–IB°(h_\circ)$, convenient and sophisticated plane models are used to visualize the system, to represent geometrically the relationship between pitch and axis location, and to provide a simple geometric characterization of all existing subspaces. For each of these two three-system classes, the "most general" of the special systems considered herein, it is shown that there can be no more than two screw cylindroids of any given class, and the subcases with zero, one, and two solutions are identified using the models.

References

1. Ball, R.: A Treatise on the Theory of Screws. Cambridge University Press, Cambridge (1900)
2. Carricato, M., Zlatanov, D.: Characterization of the subsystems in the general three-system of screws. In: J. Lenarcic, O. Khatib (eds.) Advances in Robot Kinematics. Springer, Berlin (2014)
3. Carricato, M., Zlatanov, D.: Persistent screw systems. Mech. Mach. Theory **73**, 296–313 (2014)
4. Donelan, P., Gibson, C.: On the hierarchy of screw systems. Acta Applicandae Mathematicae **32**(3), 267–296 (1993)
5. Gibson, C., Hunt, K.: Geometry of screw systems. Mech. Mach. Theory **25**(1), 1–27 (1990)
6. Hunt, K.: Kinematic Geometry of Mechanisms. Clarendon Press, Oxford, NY (1978)
7. Phillips, J.: Freedom in Machinery. Cambridge University Press, Cambridge (1984–1990)
8. Selig, J.: Geometric Fundamentals of Robotics. Springer, Berlin (2005)
9. Zlatanov, D.: The representation of the general three-system of screws by a sphere. Mech. Mach. Theory **49**, 315–331 (2012)
10. Zlatanov, D., Agrawal, S., Gosselin, C.: Convex cones in screw spaces. Mech. Mach. Theory **40**, 710–727 (2005)
11. Zlatanov, D., Zoppi, M., Molfino, R.: Constraint and singularity analysis of the exechon tripod. In: Proceedings of the ASME IDETC&CIE, DETC2012-71184 (2012)

Singularity Analysis of 3-DOF Translational Parallel Manipulator

Pavel Laryushkin, Victor Glazunov and Sergey Demidov

Abstract In this paper we analyze singularities of the 3-DOF translational parallel mechanism with three kinematic chains, each consisting of five revolute joints. Both Jacobian and Screw theory methods are used to determine singular points of different types. Constraint singularity is also studied.

Keywords Parallel mechanism · Three degrees of freedom · Singularity · Screw theory · Constraint singularity

1 Introduction

For last decades, the class of parallel robots is certainly attracting much attention of researchers and manufacturers. For instance, Gogu [1] has over 700 pages concerning only 2- and 3-DOF translational parallel mechanisms' topologies. However, along with undoubted advantages, several typical problems also exist for this class of manipulators.

The problem of singularities is a very common issue in parallel robots. There are some points within the workspace of a mechanism where losing a degree of freedom or uncontrollable motion of a moving plate is possible. These points are

P. Laryushkin (✉)
Bauman Moscow State Technical University,
2-ya Baumanskaya 5/1, 105005, Moscow, Russia
e-mail: pav.and.lar@gmail.com

V. Glazunov · S. Demidov
Research Institute for Machine Science of RAS,
Maly Kharitonyevsky Pereulok 4, 101990, Moscow, Russia
e-mail: vaglznv@mail.ru

S. Demidov
e-mail: chipd@rambler.ru

called singular [2]. Minimizing the number of such points [3], finding reasonable
ways to avoid them [4] and determining singularity-free zones [5] are among the
main problems in parallel mechanism design.

It is also possible to design singularity free manipulators. For translational
parallel mechanisms this topic was deeply studied in Carricato [6].

There exist several approaches in finding and classifying singularities, for
instance [7, 8]. The most popular method of finding singular points and zones is
based on Jacobian analysis [9], and Screw theory approaches [10, 11] is also used
quite often. Here we will be using a classification proposed in Gosselin and
Angeles' paper.

In this paper we present a singularity analysis of 3-DOF translational parallel
mechanism with three RRRRR legs. The mechanism was mentioned earlier as a
part of a family of translational parallel mechanisms, for instance in [12] and [13].
Later it was analyzed in detail in [14] where results of the overall kinematics,
dynamics and workspace analysis of the mechanism were presented.

2 Mechanism Overview

In this section we provide a quick overview of the analyzed parallel mechanism
and the results obtained during initial singularity analysis presented in our previous
paper.

The mechanism has three legs (or kinematic chains) with five revolute joints
each (Fig. 1).

Let $l_1 = A_iB_i$, $l_2 = B_iC_i$, $l_3 = C_iD_i$, $l_4 = D_iE_i$, $l_5 = E_iF$, $l_A = OA_i$ then the
relationship between Cartesian coordinates x, y, z and generalized coordinates
(rotation angles) θ_1, θ_2, θ_3 can be expressed using system of three equations which
we can treat as three implicit functions

$$
\begin{aligned}
f_1(x,y,z,\theta_1) &= (y - l_x \sin\theta_1)^2 + (z + l_x \cos\theta_1)^2 - l_2^2 = 0 \\
f_2(x,y,z,\theta_2) &= (z - l_y \sin\theta_2)^2 + (x + l_y \cos\theta_2)^2 - l_2^2 = 0 \\
f_3(x,y,z,\theta_3) &= (x - l_z \sin\theta_3)^2 + (y + l_z \cos\theta_3)^2 - l_2^2 = 0
\end{aligned}
\tag{1}
$$

where

$$
l_x = l_2\sqrt{1 - \left(\frac{x + l_2}{l_2}\right)^2}, \; l_y = l_2\sqrt{1 - \left(\frac{y + l_2}{l_2}\right)^2}, \; l_z = l_2\sqrt{1 - \left(\frac{z + l_2}{l_2}\right)^2}
$$

Note that we assume $l_4 = l_2$ and $l_A + l_2 = l_1 + l_3 + l_5$. These conditions
ensure that in initial position (Fig. 1) all angles between links are right angles.

Previously we have conducted a singularity research based on Jacobian and
Screw theory methods.

Fig. 1 Scheme of the
mechanism
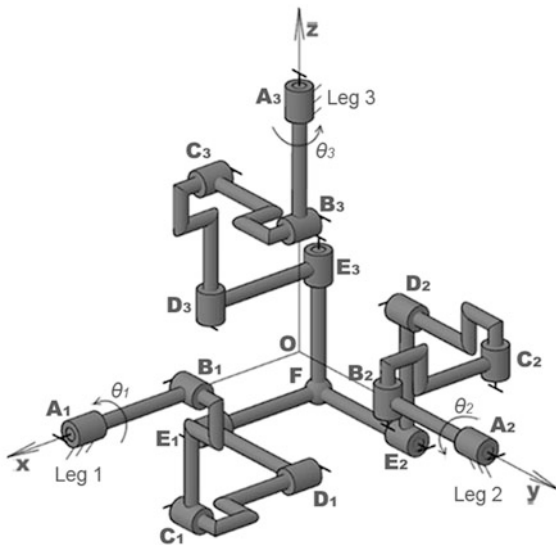
Using both methods, it was analytically discovered that Type 1 singularity (loss of moving platform mobility) can occur only at the theoretical edge of the workspace. For Type 2 singularities (uncontrollable motion of the moving platform) no analytical conditions were found, and iteration analysis was used instead. Analytical conditions for Type 3 singularities (can be treated as a manifestation of both Type 1 and Type 2 singularities simultaneously) were proven to be included in conditions for Type 1 singularities.

Iteration analysis of Type 2 singularities resulted into a statement that the mechanism has no such singularities. Later we found that is only true for two of eight possible mechanism configurations, corresponding to the number of inverse kinematics solutions, and for iteration step $0.05l_2$ that we used in our previous paper during singularity analysis.

In next two sections we present a more detailed iteration analysis of Type 2 singularities followed by analysis of constraint singularities. All numerical calculations are done in MATLAB (using built-in functions if needed), and took no longer than 787 s on a laptop with average characteristics.

3 Type 2 Singularities Analysis

We start with Jacobian analysis of Type 2 singularities. We can find partial derivatives of (1) and form the following matrix.

$$\mathbf{A} = \frac{\partial \mathbf{f}}{\partial \mathbf{x}} = \begin{pmatrix} \frac{\partial f_1(x,y,z,\theta_1)}{\partial x} & \frac{\partial f_1(x,y,z,\theta_1)}{\partial y} & \frac{\partial f_1(x,y,z,\theta_1)}{\partial z} \\ \frac{\partial f_2(x,y,z,\theta_2)}{\partial x} & \frac{\partial f_2(x,y,z,\theta_2)}{\partial y} & \frac{\partial f_2(x,y,z,\theta_2)}{\partial z} \\ \frac{\partial f_3(x,y,z,\theta_3)}{\partial x} & \frac{\partial f_3(x,y,z,\theta_3)}{\partial y} & \frac{\partial f_3(x,y,z,\theta_3)}{\partial z} \end{pmatrix} \tag{2}$$

Type 2 singularity occurs when matrix (2) is singular, i.e. $det(\mathbf{A}) = 0$.

As we mentioned earlier, we use an iteration method to find such singularities. The idea is to scan a workspace of the mechanism with a relatively small step and find a value of matrix determinant in each point. Then we assume that if for two neighbor points the determinant value have different signs ("+" and "−") than there is a some point between those two where $det(\mathbf{A}) = 0$, so Type 2 singularity occurs.

With this said and assuming iteration step is equal to $0.025l_2$ and $l_2 = 20$, we have found that for two of eight possible configurations of the mechanism's legs approximately 0.27 % of analyzed workspace points have $det(\mathbf{A}) > 0$ while all other points have $det(\mathbf{A}) < 0$. These points form three small volumes lying very close to the edge of the workspace (Fig. 2). Thus, these volumes are separated from the workspace by surfaces consisting of Type 2 singular points.

Mechanism configuration is determined by choosing the solution of inverse kinematics problem. Figure 3 illustrates two possible configurations of Leg 1 with two different values of rotation angle θ_1.

Thus having two different possible configurations for each leg with corresponding θ_i one can easily see that for any point in the workspace (except Type 1 singular points) there are eight possible configurations and eight different sets of $(\theta_{1,j}, \theta_{2,j}, \theta_{3,j})$ in total where $j = 1, 2$. For example, configuration in Fig. 1 corresponds to a set $(\theta_{1,2}, \theta_{2,2}, \theta_{3,2})$.

Figure 2 corresponds to a set $(\theta_{1,1}, \theta_{2,1}, \theta_{3,1})$. Using set $(\theta_{1,2}, \theta_{2,2}, \theta_{3,2})$ also produces only 0.27 % loss of total workspace volume, however volumes shown in Fig. 2 will be rotated by 90°.

For other six possible configurations, Type 2 singularities divide the workspace into several significantly large zones. Shape of these zones varies depending on the configuration. In Fig. 4 two "slices" of the workspace are shown. Slice (a) corresponds to a set of angles $(\theta_{1,1}, \theta_{2,1}, \theta_{3,1})$ and slice (b) corresponds to a set $(\theta_{1,2}, \theta_{2,1}, \theta_{3,1})$. Here $l_2 = 20$ and coordinate z is fixed at $z = -18$.

Darker areas present points where $det(\mathbf{A}) > 0$ and lighter areas present points where $det(\mathbf{A}) < 0$. The lightest area around does not belong to the workspace.

One can see that for set $(\theta_{1,1}, \theta_{2,1}, \theta_{3,1})$ the area separated by Type 2 singularities from the main workspace is quite insignificant while for set $(\theta_{1,2}, \theta_{2,1}, \theta_{3,1})$ it appears to be much bigger, and Type 2 singularity can occur in the middle part of the workspace. Furthermore, moving plate of real mechanism most likely will not be capable to reach the volumes shown in Fig. 2 because it requires A_iB_i, B_iC_i, and C_iD_i to be on the same line and at the same place.

Fig. 2 Volumes separated from the workspace by Type 2 singularities
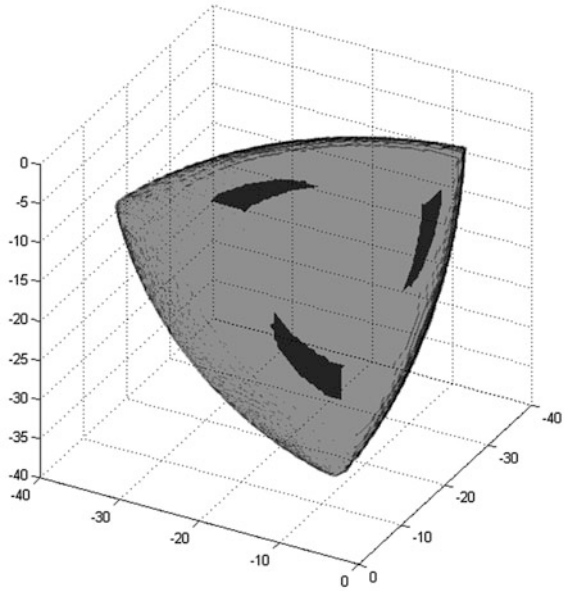
Fig. 3 Two possible configurations of Leg 1
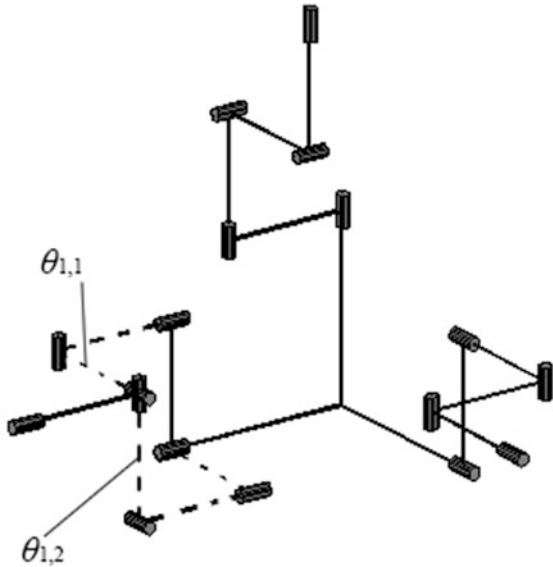
Thus, Type 2 singularities depend on mechanism configuration but undesirable configurations can be easily avoided by choosing one of two optimal configurations and corresponding set of rotation angles: $(\theta_{1,1}, \theta_{2,1}, \theta_{3,1})$ or $(\theta_{1,2}, \theta_{2,2}, \theta_{3,2})$.
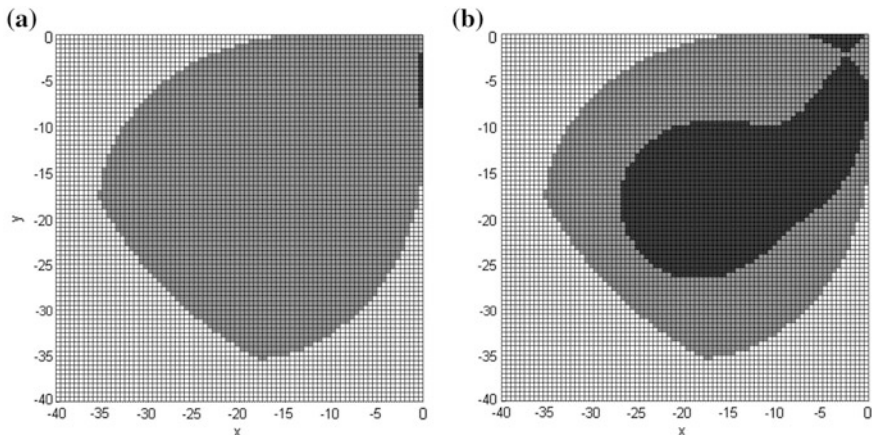
Fig. 4 Slices of the workspace at z = −18

4 Constraint Singularities Analysis

Constraint singularity is a phenomenon that arises for mechanisms with less than six degrees of freedom while legs of the mechanism have more degrees of freedom than a mechanism itself [15]. This type of singularity cannot be analyzed by Jacobian method because it deals with degrees of freedom that a mechanism normally does not have. For instance, a translational parallel mechanism can obtain a rotational degree of freedom when such singularity occurs.

In order to analyze constraint singularities, Screw theory approach must be used. We need to find screws that form a matrix of constraints.

First step is to find corresponding twists for each leg. Using Plücker coordinates, such twists for Leg 1 can be written in the form of a matrix as follows

$$
\begin{pmatrix}
1 & 0 & 0 & 0 & 0 & 0 \\
0 & \cos\theta_1 & \sin\theta_1 & 0 & -\sin\theta_1(l_A - l_1) & \cos\theta_1(l_A - l_1) \\
0 & \cos\theta_1 & \sin\theta_1 & l_x & -\sin\theta_1(x + l_5 + l_3) & \cos\theta_1(x + l_5 + l_3) \\
1 & 0 & 0 & 0 & -l_x\cos\theta_1 & -l_x\sin\theta_1 \\
1 & 0 & 0 & 0 & z & -y
\end{pmatrix}
$$

For these twists we can now find a reciprocal wrench. Doing this for each leg, we obtain three wrenches and can form a matrix of wrenches. For the discussed mechanism this matrix is

$$
\begin{pmatrix}
0 & 0 & 0 & 0 & \sin\theta_1 & -\cos\theta_1 \\
0 & 0 & 0 & -\cos\theta_2 & 0 & \sin\theta_2 \\
0 & 0 & 0 & \sin\theta_3 & -\cos\theta_3 & 0
\end{pmatrix}
$$

Fig. 5 Volume separated from the workspace by constraint singularities
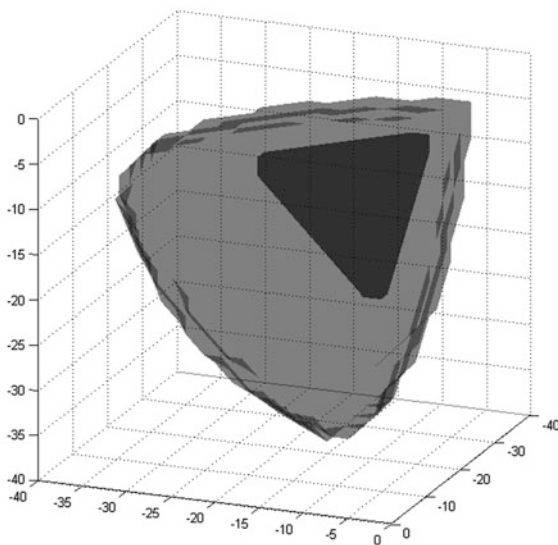
When this matrix loses its maximum rank (3 in this case) a constraint singularity occurs.

Using the same iteration approach as for Type 2 singularities analysis we have found that for sets $(\theta_{1,1}, \theta_{2,1}, \theta_{3,1})$ or $(\theta_{1,2}, \theta_{2,2}, \theta_{3,2})$ approximately 4.48 % of total workspace volume will be separated by a surface consisting of points of constraint singularity. This volume is situated at the top part of the workspace (Fig. 5).

The research shows that for other six possible configurations the workspace divided into several parts. Though, the shapes of these parts are different, such situation is clearly as unacceptable as it was with undesirable mechanism configurations when we analyzed Type 2 singularities.

The volumes shown in Figs. 2 and 5 intersect, and total theoretical workspace volume loss is 4.69 % due to both Type 2 and constraint singularities.

Thus, constraint singularities, just like Type 2 singularities, depend on mechanism configuration. Undesirable configurations can be avoided by choosing between two optimal configurations which are the same for Type 2 singularity avoidance.

5 Conclusion

In this paper the analysis of 3-DOF translational parallel mechanism (focused on Type 2 and constraint singularities) is presented. The two optimal configurations of mechanism links and corresponding sets of input rotation angles were discovered, so the total loss of the theoretical workspace volume is about 4.69 %. This

means that for actual mechanism, if designed with taking these results into account, at least 95.31 % of the workspace volume will be singularity-free with singular points of any kind only at the edge of this volume.

References

1. Gogu, G.: Structural Synthesis of Parallel Robots, Part 2: Translational. Springer, Berlin (2009)
2. Merlet, J.-P.: Parallel Robots (2nd edn.). Springer, New York (2006)
3. Arakelian, V., Briot, S., Glazunov, V.: Increase of singularity-free zones in the workspace of parallel manipulators using mechanisms of variable structure. Mech. Mach. Theory **43**(9), 1129–1140 (2008)
4. Lahouar, S., Zeghloul, S., Romdhane, L.: Singularity free path planning for parallel robots. In: Lenarcic, J., Wenger, P. (eds.) Advances in Robot Kinematics: Analysis and Design, pp. 235–242. Springer, New York (2008)
5. Li, H.D., Gosselin, C., Richard, M.J.: Determination of the maximal singularity-free zones in the six-dimensional workspace of the general Gough-Stewart platform. Mech. Mach. Theory **42**(4), 497–511 (2007)
6. Carricato, M.: Singularity-free fully-isotropic translational parallel manipulators. Dissertation, University of Bologna (2001)
7. Yang, G., Chen, I.M., Lin, W., Angeles, J.: Singularity analysis of three-legged parallel robots based on passive-joint velocities. IEEE Trans. Robot. Autom. 17(4), 413–422 (2001)
8. Zlatanov, D., Fenton, R.G., Benhabib, B.A.: A unifying framework for classification and interpretation of mechanism singularities. Asme J. Mech. Des. 117(4): 566–572 (1995)
9. Gosselin, C., Angeles, J.: Singularity analysis of closed loop kinematic chains. IEEE Trans. Robot Autom. **6**(3), 281–290 (1990)
10. Dimentberg, F.: The Screw Calculus and its Applications in Mechanics, Nauka, Moscow (trans: AD680993, Clearinghouse for Federal Tech. and Sc. Inf., Virginia) (1965)
11. Glazunov, V.A., Koliskor, ASh, Krainev, A.F., Model, B.I.: Classification principles and analysis methods for parallel-structure spatial mechanisms. J. Mach. Manuf. Reliab. **1**, 30–37 (1990)
12. Fisoli, A., Checcacci, D., Salsedo, F., Bergamasco, M.: Synthesis by screw algebra of translating in-parallel actuated mechanisms. Adv. Robot Kinemat. **7**, 433–440 (2000)
13. Lee, C.C., Herve, J.M.: Translational parallel manipulators with doubly planar limbs. Mech. Mach. Theory **41**(4), 433–455 (2006)
14. Lryushkin, P., Glazunov, V.: A new 3-DOF translational parallel manipulator: kinematics, dynamics, workspace analysis. In: Proceedings of Romansy 19—Robot design, dynamics and control, pp. 11–18. Springer (2013)
15. Zlatanov D, Bonev I, Gosselin C (2002) Constraint singularities of parallel mechanisms. In: Proceedings of the IEEE International conference. on robotics and automation, pp. 496–502

Generalised Complex Numbers
in Mechanics

J. Rooney

Abstract Three types of generalised complex number provide concise representations for spatial points and transformations useful in geometry and mechanics. The most familiar type is the ordinary complex number, $a + ib$ ($i^2 = -1$), used to represent stretch-rotations about a point in 2D space. A second type of generalised complex number is the dual number, $a + \varepsilon b$ ($\varepsilon^2 = 0$), used to represent shear transformations and inversions in 2D space. The third type of generalised complex number is the double number, $a + jb$ ($j^2 = +1$), used to represent boosts (simple Lorentz transformations) in 2D space-time. Each of the three types may be expressed in various explicit forms (Gaussian, ordered pair, matrix, parametric, exponential) for algebraic convenience, computational efficiency, and so on. Combining dual numbers with vectors and quaternions provides an efficient representation of general spatial screw displacements in 3D space.

Keywords Complex · Dual and double numbers · Stretch-rotations · Shears · Boosts

1 Introduction

Mechanics is a very extensive subject area with a long history. It encompasses not only classical mechanics but also relativistic mechanics and quantum mechanics. In the field of robotics numerous different mathematical approaches have been adopted to facilitate the modelling, analysis, and design of a large range of robot systems. However, whereas to date most such systems operate in the 'classical' régime of relatively low speed it is envisaged that the subject will expand to

J. Rooney (✉)
The Open University, Milton Keynes, UK
e-mail: j.rooney@open.ac.uk

encompass robot designs for application in ultra-high speed scenarios. In this paper the emphasis is theoretical and it explores three efficient mathematical representations of geometrical transformations relevant in both classical and relativistic mechanics. The paper simplest class on the algebraic representation of geometric transformations (stretch-rotations, shears, inversions, and boosts) in 2D space. Three types of 'generalised' complex number are compared that lead to efficient formulations of these transformations.

The Fundamental Theorem of Algebra, proves that so-called *complex numbers* of the form $a + ib$ with $i^2 = -1$ are necessary and sufficient for the solution of all polynomial equations. However, it is not commonly known that it is possible to construct two further distinct types of 'complex' number [1, 2]. These are the *dual number, $a + \varepsilon b$*, where $\varepsilon^2 = 0$, and the *double number, $a + jb$*, where $j^2 = +1$. They are not necessary for obtaining solutions to polynomial equations but they are very useful as algebraic representations in geometry, especially for some types of constructs in mechanics.

Here the algebraic representations of the three types (complex, dual, and double) are discussed in Sect. 2 and their geometric interpretation as both points and transformations in an *Argand plane* is discussed in Sect. 3. Then, in the same way that the unit complex number $\exp(i\alpha)$ can describe a rotation about a point in a plane through an angle α, the unit dual number $\exp(\varepsilon\tau)$ describes a plane shear transformation parallel to the y-axis through a shear τ, and the unit double number $\exp(j\beta)$ describes a plane boost (a simple Lorentz transformation) through a rapidity β. Similarly, non-unit complex, dual and double numbers produce stretch-rotations, stretch-shears and stretch-boosts respectively.

2 Generalized Complex Numbers

The simplest polynomial equation which does not have a real root, is the quadratic $x^2 + 1 = 0$. Its eventual solution led to the now familiar *complex numbers* $a + ib$, where a and b are reals and $i^2 = -1$. However, it is possible to start with a more general quadratic $x^2 + k_1 x + k_2 = 0$, with discriminant $D = k_1^2 - 4k_2$, and Yaglom [2] proposed a *generalized imaginary unit, E,* where $E^2 = -k_1 E - k_2$, leading to the construction of *generalized complex numbers* of the form $a + Eb$. Three different types of *generalized complex number* are possible, forming three disjoint equivalence classes, according as the discriminant D is negative, zero, or positive.

The simplest class with $D < 0$ has $k_1 = 0$, $k_2 = 1$, in which case E is denoted by $i(i^2 = -1)$, and $a + Eb$ is essentially the ordinary *complex number, $a + ib$*. Similarly, the simplest class with $D = 0$ has $k_1 = 0$, $k_2 = 0$. The imaginary unit E is then denoted by ε where $\varepsilon^2 = 0$, although ε is not itself zero nor a small quantity, and $a + Eb$ is defined as the *dual number, $a + \varepsilon b$*. The dual numbers were first introduced by Clifford [3] in a geometrical context. Finally, the simplest class with $D > 0$ has $k_1 = 0$, $k_2 = -1$. The imaginary unit E is then denoted by j where

$j^2 = +1$, although j is not the real number 1 nor -1, and $a + Eb$ is defined as the *double number, $a + jb$.*

Addition and subtraction of two numbers from the same class are performed component-wise, whereas multiplication is defined by three different multiplication rules (and hence algebras) for the product of two numbers, as follows:

$$(a_1 + ib_1)(a_2 + ib_2) = (a_1a_2 - b_1b_2) + i(a_1b_2 + a_2b_1) \quad \text{complex numbers}$$
$$(a_1 + \varepsilon b_1)(a_2 + \varepsilon b_2) = (a_1a_2) + \varepsilon(a_1b_2 + a_2b_1) \quad \text{dual numbers}$$
$$(a_1 + jb_1)(a_2 + jb_2) = (a_1a_2 + b_1b_2) + j(a_1b_2 + a_2b_1) \quad \text{double numbers}$$

A multiplicative inverse for each type of number is defined in terms of a *conjugate* and a *norm*. For the complex number these are $a - ib$ and $a^2 + b^2$ respectively, whence the inverse is $(a - ib)/(a^2 + b^2)$. For the dual number the equivalents are $a - \varepsilon b$, a^2 and $(a - \varepsilon b)/(a - \varepsilon b)(a^2)$. For the double number they are $a - jb$, $a^2 - b^2$ and $(a - jb)/(a^2 - b^2)$. The inverse exists for all nonzero complex numbers. The dual-number inverse does not exist if $a = 0$, so dual numbers of the form εb have no inverse. Similarly the double number inverse is not defined if $|a| = |b|$, so double numbers of the form $a \pm ja$ have no inverse.

The most common representations for these numbers are the standard *Gaussian* forms: $a + ib$, $a + \varepsilon b$, and $a + jb$ (Table 1), but several others are in use for the ordinary complex number, namely: ordered pair, matrix, polar, and exponential. These have analogues in the dual and double numbers. The ordered pair form for each of the three types is an obvious one. The matrix forms are obtained by treating the three fundamental quadratics $x^2 + 1 = 0$, $x^2 = 0$, and $x^2 - 1 = 0$ as matrix equations. The matrix forms of the imaginary units, i, ε and j, and the complex, dual and double numbers $a + ib$, $a + \varepsilon b$, and $a + jb$ are respectively:

$$\begin{bmatrix} 0 & -1 \\ 1 & 0 \end{bmatrix}, \begin{bmatrix} 0 & 0 \\ 1 & 0 \end{bmatrix}, \begin{bmatrix} 0 & 1 \\ 1 & 0 \end{bmatrix}, \text{ and } \begin{bmatrix} a & -b \\ b & a \end{bmatrix}, \begin{bmatrix} a & 0 \\ b & a \end{bmatrix}, \begin{bmatrix} a & b \\ b & a \end{bmatrix}$$

Note that the square of the second of these matrices is the zero matrix but it is not itself the zero matrix. Similarly the third matrix is not the unit matrix, nor its negative, yet its square is the unit matrix.

The polar forms and the exponential forms of the three types of number are expressed in terms of two real parameters referred to as *modulus* and *argument*. These are: r and θ (essentially polar coordinates) for the complex numbers; R and T for the dual numbers; and ρ and ϕ for the double numbers (Table 1).

The polar and exponential forms greatly simplify the multiplication rules, so that the modulus of the products is given by the *product* of the individual moduli, whereas the argument of the products is the *sum* of the individual arguments. Note that the exponential forms are derived by using Taylor-series expansions for functions of a generalized complex number.

Table 1 The three types of generalised complex number

	Complex	Dual	Double
Gaussian	$a + ib$	$a + \varepsilon b$	$a + jb$
Modulus	$r = \sqrt{a^2 + b^2}$	$R = a$	$\rho = \sqrt{a^2 - b^2}, \quad |a| > |b|$
			$\rho = \sqrt{b^2 - a^2}, \quad |a| < |b|$
Argument	$\theta = \tan^{-1}(b/a)$	$T = b/a, \quad a \neq 0$	$\phi = \tanh^{-1}(b/a), \quad |a| > |b|$
			$\phi = \tanh^{-1}(a/b), \quad |a| < |b|$
Polar	$r(\cos\theta + i\sin\theta)$	$R(1 + \varepsilon T)$	$\rho(\cosh\phi + j\sinh\phi), \quad |a| > |b|$
			$\rho(\sinh\phi + j\cosh\phi), \quad |a| < |b|$
Exponential	$r\exp(i\theta)$	$R\exp(\varepsilon T)$	$\rho\exp(j\phi), \quad |a| > |b|$
			$\rho j\exp(j\phi), \quad |a| < |b|$

3 Geometrical Interpretations

Treating the ordered pair forms (a, b) of the complex, dual and double numbers as the Cartesian coordinates of the points of a plane (the *Argand diagram*) the three algebras generate three different geometrical transformations on the points. The complex number algebra produces stretches, rotations and reflections, whereas the dual number algebra produces stretches, shears and inversions, and the double number algebra produces stretches and boosts.

3.1 Stretch-Rotations in a Plane

The complex-number algebra generates stretch-rotations on the points of a plane. A general point (x, y) is associated with the complex number $x + iy$. Its modulus r is the distance, $\sqrt{x^2 + y^2}$, of the point from the origin, and its argument θ is the angle between the radial line to the point and the x-axis (Fig. 1a). The lines of constant modulus are concentric circles, $x^2 + y^2 = r^2$, centred on the origin, and the lines of constant argument are straight lines passing through the origin with slope $\tan\theta$. Expressing $x + iy$ in polar form as $r(\cos\theta + i\sin\theta)$ and pre-multiplying it by another complex number with argument α and unit modulus, gives $(\cos\alpha + i\sin\alpha)r(\cos\theta + i\sin\theta) = r[\cos(\theta + \alpha) + i\sin(\theta + \alpha)]$. The equivalent in exponential form is $\exp(i\alpha)r\exp(i\theta) = r\exp[i(\theta + \alpha)]$.

The pre-multiplication increases the argument of $x + iy$ by α while leaving the modulus unchanged, and so it rotates the point about the origin through a distance $r\alpha$ along a circular arc to the new position, $x' + iy'$ (Fig. 2a). The effect of pre-multiplying by $\exp(i\alpha)$ is to rotate all points in the plane anticlockwise through the angle α. Pre-multiplication by a non-unit complex number gives a stretch-rotation of the plane (a rotation with a change of scale).
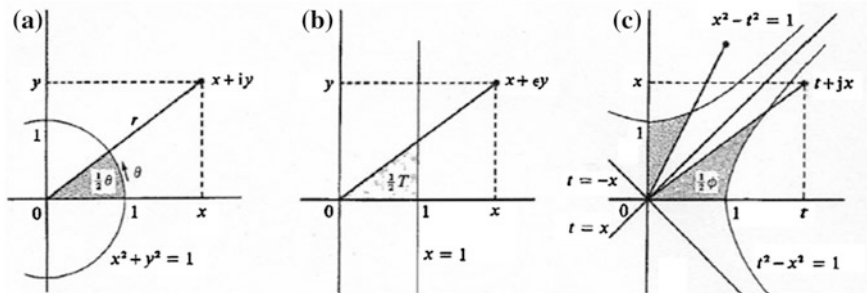
Fig. 1 The interpretation of the three types of complex number as points in a plane: **a** the complex number $x + iy$; **b** the dual number $x + \varepsilon y$; **c** the double number $t + jx$
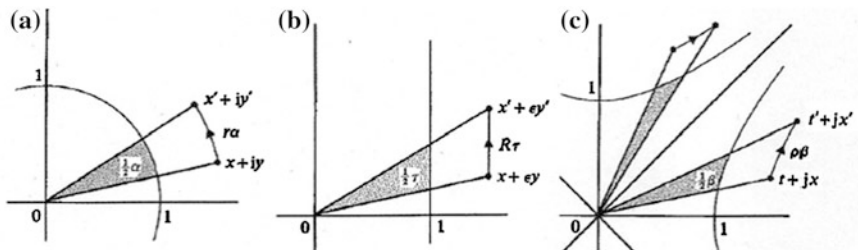
Fig. 2 The effect on a single point in a plane of: **a** unit complex-number pre-multiplication by $\exp(i\alpha)$; **b** unit dual-number pre-multiplication by $\exp(\varepsilon\tau)$; **c** unit double-number pre-multiplication by $\exp(j\beta)$

It is useful to interpret the argument θ of an ordinary complex number as twice the area of the sector of the unit circle, $x^2 + y^2 = 1$, bounded by the x-axis and the radial line to the point (Fig. 1a) [4]. Thus a rotation through α corresponds to an increase in this area by $\alpha/2$ (Fig. 2a). This interpretation more clearly demonstrates the analogies with the arguments of the dual numbers and double numbers (Sects. 3.2 and 3.3).

3.2 Shears and Inversions in a Plane

The dual-number algebra generates shear transformations of the points of a plane. A general point (x, y) is associated with the dual number $x + \varepsilon y$. Its modulus R is the $x$coordinate of the point. Its argument T is twice the area of the triangle defined by the x-axis, the line $x = 1$ (or $x = -1$ if the x coordinate of the point is negative), and the radial line to the point (Fig. 1b). The lines of constant modulus are straight lines, $x^2 = R^2$, parallel to the y-axis, whereas the lines of constant argument are straight lines passing through the origin with slope T. Pre-multiplying $x + \varepsilon y$ by

another dual number with argument τ and unit modulus, gives in polar form $(1 + \varepsilon\tau)R(1 + \varepsilon T) = R[1 + \varepsilon(T + \tau)]$. The equivalent in exponential form is $\exp(\varepsilon\tau)R\exp(\varepsilon T) = R\exp[\varepsilon(T + \tau)]$. The pre-multiplication increases the argument of $x + \varepsilon y$ by τ. Figure 2b shows that this corresponds to a translation of the point, parallel to the y-axis, through a distance $R\tau$, to the new position $x' + \varepsilon y'$. The effect of pre-multiplying by $\exp(\varepsilon\tau)$ is thus to shear the plane parallel to the y-axis through the shear τ, where the angle of shear is $\tan^{-1}\tau$. Pre-multiplication by the dual number $-(1 + \varepsilon\tau)$ with negative modulus $R = -1$ produces a shear transformation accompanied by an inversion (reflection in the origin). Also, if the pre-multiplication is by a non-unit dual number the resulting transformation is a stretch-shear of the plane (a shear with a change of scale).

3.3 Boosts in a Plane

The double-number algebra generates boost transformations of the points of a plane. These involve equal shears along x- and y-axis, that are useful in special relativistic mechanics [5]. A general point (x, y) is associated with the double number $x + jy$, but, it is better to consider the general point to be an event in 2D space-time with coordinates (t, x), where t represents time (considered as a spatial dimension), x represents a single space dimension in which motion can take place, and the system of units is chosen so that the speed of light, c, is unity. The point is then associated with the double number $t + jx$.

The points on the lines $|t| = |x|$ lie on the *light-cone* through the origin O and they are in a sense singular since they have no double-number inverse (Sect. 2). The plane is divided into four quadrants by the light-cone (Fig. 1c). The two quadrants given by $|t| > |x|$ represent *future* and *past* events of O, and consist of all points (t, x) which can be reached from O or from which O can be reached at a speed less than that of light (so $|x/t| < 1$). These are *time-like* points. The other two quadrants given by $|t| < |x|$ are *elsewhere*, and points in these regions can neither reach O nor be reached from O at a speed less than that of light (so $|x/t| > 1$). The points in these two quadrants are *space-like* points.

The double-number modulus ρ of a time-like point $t + jx(|t| > |x|)$ represents the *space-time interval*, $\sqrt{t^2 - x^2}$ between the point and the origin. The argument ϕ is twice the area of the hyperbolic sector defined by the unit *rectangular hyperbola*, $t^2 - x^2 = 1$, the t-axis, and the radial line to the point (Fig. 1c). The lines of constant modulus in the time-like quadrants are rectangular hyperbolae, $t^2 - x^2 = \rho^2$, centred on the origin with the light-cone $|t| = |x|$ as asymptotes, whereas the lines of constant argument are straight lines through the origin with slope $\tanh\phi = x/t$.

Similarly, the modulus ρ of a space-like point $t + jx(|t| < |x|)$ is $\sqrt{x^2 - t^2}$ and the argument ϕ is twice the area of the hyperbolic sector defined by the unit rectangular hyperbola, $x^2 - t^2 = 1$, the x-axis, and the radial line to the point (Fig. 1c). The lines

of constant modulus in this case are the rectangular hyperbolae, $x^2 - t^2 = \rho^2$, and the lines of constant argument are straight lines through the origin with slope coth $\phi = x/t$. Pre-multiplying $t + jx$ by another double number (from the time-like quadrants) with argument β and unit modulus, gives, in polar form: $(\cosh\beta + j\sinh\beta)\rho(\cosh\phi + j\sinh\phi) = \rho[\cosh(\phi + \beta) + j\sinh(\phi + \beta)]$ if $|t| > |x|$; $(\cosh\beta + j\sinh\beta)\rho(\sinh\phi + j\cosh\phi) = \rho[\sinh(\phi + \beta) + j\cosh(\phi + \beta)]$ if $|t| < |x|$. The exponential forms are $\exp(j\beta)\rho\exp(j\phi) = \rho\exp[j(\phi + \beta)]$, or $\exp(j\beta)$ $\rho j\exp(j\phi) = \rho j\exp[j(\phi + \beta)]$ respectively dependent on the quadrant in which $t + jx$ is located.

The pre-multiplication thus leaves the modulus ρ unchanged and increases the argument of $t + jx$ by β. By reference to Fig. 2c this clearly corresponds to a displacement of the point along an appropriate rectangular hyperbola through the space-time interval $\rho\beta$, to the new position $t' + jx'$. Time-like points remain time-like, and space-like points remain space-like. The transformation is a type of shear transformation symmetric about the line $t = x$, and known as a boost (the simplest type of *Lorentz transformation*), which is the standard connection relating the space-time coordinates of a point in a fixed frame of reference to those in a frame moving with constant velocity [5]. The latter velocity is given by $\tanh\beta$, where β itself is termed the *rapidity* [6]. Pre-multiplication by $\exp(j\beta)$ is equivalent to a boost through the rapidity β. Pre-multiplication by a unit double number, $\sinh\beta + j\cosh\beta$, from the space-like quadrants produces a boost with a reflection in one of the two lines $|t| = |x|$ representing the light-cone. If the pre-multiplication is by a non-unit double number the transformation is a stretch-boost of the plane (a boost with a change of scale).

4 Discussion and Conclusions

Three types of generalised complex number were considered in this paper, producing various types of geometric transformation. In exponential form the unit complex, dual, and double numbers $\exp(i\alpha), \exp(\varepsilon\tau)$, and $\exp(j\beta)$ generate rotations, shears and boosts respectively. These transformations have been interpreted in the *active* sense acting on the points of a plane, leaving the coordinate system fixed. For *passive* transformations acting on the coordinate system rather than on the points the appropriate complex, dual, and double numbers to use are $\exp(-i\alpha), \exp(-\varepsilon\tau)$, and $\exp(-j\beta)$ respectively. Non-unit complex, dual and double numbers produce stretch-rotations, stretch-shears, and stretch-boosts, respectively. Combinations of these transformations can be performed within a given plane by successively representing the points of the plane by the appropriate type of generalised complex number at each stage. But this must be done carefully, because combining, for example, the complex number $\cos\alpha + i\sin\alpha$ with the double number $\cosh\beta + j\sinh\beta$ by multiplying them together produces the 4D object, $\cos\alpha\cosh\beta + i\sin\alpha\cosh\beta + j\cos\alpha\sinh\beta + ij\sin\alpha\sinh\beta$. Here, as before, $i^2 = -1$ and $j^2 = +1$, but their product ij is a new object to be defined.

Combinations of complex, dual or double numbers with other algebras leads to efficient representations of more general types of transformation. For example, combining the dual number algebra with the quaternion algebra produces the dual quaternion algebra, now used widely in mechanics. Thus the dual unit quaternion [7]:

$$
\left(\cos\frac{\theta}{2} - \varepsilon\frac{S}{2}\sin\frac{\theta}{2}\right) + \left[l\sin\frac{\theta}{2} + \varepsilon\left(l\frac{S}{2}\cos\frac{\theta}{2} + l_o\sin\frac{\theta}{2}\right)\right]\mathbf{i}
$$
$$
+ \left[m\sin\frac{\theta}{2} + \varepsilon\left(m\frac{S}{2}\cos\frac{\theta}{2} + m_o\sin\frac{\theta}{2}\right)\right]\mathbf{j} + \left[n\sin\frac{\theta}{2} + \varepsilon\left(n\frac{S}{2}\cos\frac{\theta}{2} + n_o\sin\frac{\theta}{2}\right)\right]\mathbf{k}
$$

represents a general spatial screw displacement of the coordinate system about the line with direction cosines (l, m, n) and moment about the origin (l_o, m_o, n_o), through an angle θ and a distance S, where $\varepsilon^2 = 0$, $\mathbf{i}^2 = -1$, $\mathbf{j}^2 = -1$, $\mathbf{k}^2 = -1$, and $\mathbf{ijk} = -1$. Further work will explore these combinations in more detail as well as extending the generalized complex number approach to generalized hypercomplex numbers for application in 3D mechanics.

References

1. Rooney, J.: On the three types of complex number and planar transformations. Environ. Plann. B **5**, 89–99 (1978)
2. Yaglom, I.M.: Complex Numbers in Geometry. Academic Press, New York (1968)
3. Clifford, W.K.: Preliminary sketch of biquaternions. Proc. London Math. Soc. **4**(64, 65), 381–395 (1873)
4. Klein, F.: Elementary Mathematics from an Advanced Standpoint (two volumes). Dover, New York (1948)
5. Rindler, W.: Special Relativity. Wiley, New York (1966)
6. Feynman, R.P.: The Theory of Fundamental Processes. Benjamin, New York (1962)
7. Rooney, J.: A comparison of representations of general spatial screw displacement. Environ. Plann. B **5**, 45–88 (1978)

On the Perturbation of Jacobian Matrix of Manipulators

Leila Notash

Abstract The wrench capabilities of manipulators under uncertainties in parameters are examined. The forces/torques of joints are calculated utilizing the perturbed and interval forms of Jacobian matrix. The differential of Jacobian inverse and the resultant differential joint inputs are considered. Reported example parallel manipulators show the implementation of methods and the validity of distinct errors compared to uncertainties set as interval.

Keywords Parallel manipulators · Parameter uncertainty · Wrench capabilities

1 Introduction

In parallel manipulators, the mobile platform (end effector) is connected to the base by several legs that act in parallel to share the payload and control the platform motion (Fig. 1). When the number of actuated joints n is equal to the task space dimension m, $n = m$, the inverse of Jacobian matrix gives a unique solution for the vector of joint forces/torques. When $n < m$, in general, there is no solution for the joint vector and the generalized inverse results in a minimum 2-norm least square solution that minimizes the error in the required platform wrench. When $n > m$ there are infinite solutions for the joint inputs for a given wrench.

Because of the error introduced during the manufacturing and assembly processes, as well as actuator/sensor resolutions and round-off errors, generally the exact values of manipulator parameters and data are not known. Using the nominal values, the calculated characteristics of manipulators may differ from their actual performance. Calibration improves their functioning to a degree but will not result

L. Notash (✉)
Department of Mechanical and Materials Engineering, Queen's University, Kingston, Canada
e-mail: notash@me.queensu.ca

Fig. 1 Planar parallel
manipulators with
a 3 actuators; and **b** 2
actuators
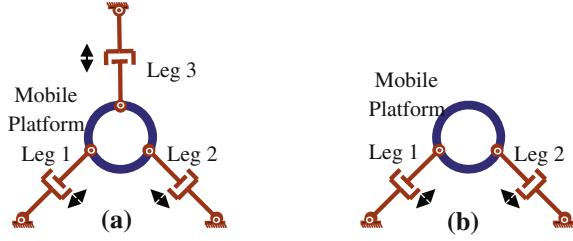
in the exact values of parameters. Hence, their performance may be degraded due
to the calculations/analyses conducted with inexact parameters/data. In addition, it
may be desired to investigate the performance of a family of manipulators for an
interval of values for the design parameters, identify all designs that fulfill the
requirements and then select the best ones (appropriate designs) for a given
application and required characteristics, e.g., [1]. Therefore, knowledge on how
the variations in parameters, with exact and inexact data/input, could affect the
manipulator performance is very valuable during their design, implementation and
operation. In Sect. 2, formulation of joint forces/torques in the presence of
uncertainties in design parameters and error in data is discussed. Simulation results
are presented in Sect. 3. Article concludes with Sect. 4.

2 Formulation of Joint Inputs with Parameter Uncertainty

For the n degrees of freedom (DOF) parallel manipulators operating within their
workspace, the $n \times 1$ vector of joint forces/torques $\boldsymbol{\tau} = \begin{bmatrix} \tau_1 & \cdots & \tau_n \end{bmatrix}^T$ is related
to the $m \times 1$ ($m \leq 6$) vector of forces and moments (wrench) $\mathbf{F}$ applied by the
platform with the $m \times n$ transposed Jacobian matrix $\mathbf{J}^T$ as

$$\mathbf{F} = \mathbf{J}^T \boldsymbol{\tau} = \begin{bmatrix} \mathbf{J}_1^T & \mathbf{J}_2^T & \cdots & \mathbf{J}_i^T & \cdots & \mathbf{J}_{n-1}^T & \mathbf{J}_n^T \end{bmatrix} \boldsymbol{\tau} = \sum_{j=1}^{n} \mathbf{J}_j^T \tau_j. \tag{1}$$

Column j of $\mathbf{J}^T$, $\mathbf{J}_j^T$, corresponds to the wrench applied on the platform by the
jth active joint. The solution of $\mathbf{F} = \mathbf{J}^T \boldsymbol{\tau}$ is

$$\boldsymbol{\tau} = \boldsymbol{\tau}_p + \boldsymbol{\tau}_h = \mathbf{J}^{\#T} \mathbf{F} + \left(\mathbf{I} - \mathbf{J}^{\#T} \mathbf{J}^T \right) \quad \mathbf{k} = \mathbf{J}^{\#T} \mathbf{F} + \mathbf{N} \boldsymbol{\lambda}$$

$$\tau_{l\min} \leq \tau_l = \tau_{pl} + \tau_{hl} = \tau_{pl} + \sum_{j=1}^{n-m} n_{lj} \lambda_j \leq \tau_{l\max} \quad \text{for} \quad l = 1, \ldots, n \tag{2}$$

where $\mathbf{J}^{\#T}$ is the Moore-Penrose generalized inverse (GI) of $\mathbf{J}^T$. If $n > m$ and the
joint vector is not physically consistent, e.g., manipulator has a combination of
actuated revolute and prismatic joints, $\mathbf{J}^{\#T} = \mathbf{W}_\tau^{-1} \mathbf{J} \left(\mathbf{J}^T \mathbf{W}_\tau^{-1} \mathbf{J} \right)^{-1}$ is the weighted

GI of full-row rank $\mathbf{J}^T$. The weighting metric $\mathbf{W}_\tau$ is chosen to have $\tau^T(\mathbf{W}_\tau \tau)$ physically consistent. The homogenous solution $\tau_h = (\mathbf{I} - \mathbf{J}^{\#T}\mathbf{J}^T)\mathbf{k} = \mathbf{N}\lambda$ vanishes when $\mathbf{J}^T$ is of full-column rank as $\mathbf{J}^{\#T}\mathbf{J}^T = \mathbf{I}$. When one or more entries of the minimum 2-norm (particular) solution $\tau_p = \mathbf{J}^{\#T}\mathbf{F}$ exceed the limit, the joint forces/torques may be adjusted by identifying the homogenous solution τ_h that would set all the joint forces/torques at or within their limits, i.e., $\tau_{\min} \le \tau_p + \tau_h \le \tau_{\max}$. For example, the novel methodology of [2] provides closed-form, minimum 2-norm least square solution for joint inputs, to recover from failures (such as exceeding joint limits), and is continuous as long as the GI is continuous, i.e., for locally constant rank $\mathbf{J}^T$.

2.1 Perturbation Bound

The uncertainty in parameters and error in data will result in perturbation of the transposed Jacobian matrix $\mathbf{J}^T$, i.e., $\tilde{\mathbf{J}}^T = \mathbf{J}^T + \mathbf{E}$. Then, the absolute error is defined as $\left\|\tilde{\mathbf{J}}^T - \mathbf{J}^T\right\| = \|\mathbf{E}\|$, and for $\|\mathbf{J}^T\| \ne 0$ the relative error is $\left\|\tilde{\mathbf{J}}^T - \mathbf{J}^T\right\|/\|\mathbf{J}^T\| = \|\mathbf{E}\|/\|\mathbf{J}^T\|$ where $\|\mathbf{J}^T\|$ is the norm of the $m \times n$ matrix $\mathbf{J}^T$, and so on. When there is a matrix $\mathbf{R}$ such that $\tilde{\mathbf{J}}^T = \mathbf{J}^T(\mathbf{I} + \mathbf{R})$ and a consistent norm is used, i.e., $\|\mathbf{J}^T\mathbf{R}\| \le \|\mathbf{J}^T\| \|\mathbf{R}\|$, then the relative error is less than or equal to the norm of $\mathbf{R}$, i.e., $\left\|\tilde{\mathbf{J}}^T - \mathbf{J}^T\right\|/\|\mathbf{J}^T\| \le \|\mathbf{R}\|$. It is noteworthy that the Frobenius norm $\|\mathbf{J}^T\|_F = \sqrt{\sum_{i=1}^{m}\sum_{k=1}^{n}|j_{ik}|^2} = \text{trace}(\mathbf{J}\mathbf{J}^T)^{1/2}$ and spectral norm (matrix 2-norm) $\|\mathbf{J}^T\|_2 = \sqrt{\lambda_{\max}(\mathbf{J}\mathbf{J}^T)} = \sigma_{\max}(\mathbf{J}^T)$, with $\lambda_{\max}(\mathbf{J}\mathbf{J}^T)$ and $\sigma_{\max}(\mathbf{J}^T)$ being respectively the largest eigenvalue and singular value of $\mathbf{J}\mathbf{J}^T$ and $\mathbf{J}^T$, are consistent.

For a given $\mathbf{F}$, $\tilde{\tau}$ will be the solution for the perturbed form of linear system (1) as

$$\mathbf{F} = \tilde{\mathbf{J}}^T\tilde{\tau} = \sum_{j=1}^{n}\tilde{\mathbf{J}}_j^T\tilde{\tau}_j. \tag{3}$$

The solution exists if and only if the GI of $\tilde{\mathbf{J}}^T$ is a continuous function of its entries, i.e., for constant rank $\tilde{\mathbf{J}}^T$. When rank $(\mathbf{J}^T)$ = rank $(\tilde{\mathbf{J}}^T)$ the perturbed Jacobian matrix $\tilde{\mathbf{J}}^T = \mathbf{J}^T + \mathbf{E}$ is an acute perturbation of $\mathbf{J}^T$. When rank $(\mathbf{J}^T) <$ rank $(\tilde{\mathbf{J}}^T)$ at least one of the singular values of $\tilde{\mathbf{J}}^T$ approach zero as $\tilde{\mathbf{J}}^T$ gets close to $\mathbf{J}^T$. Then $\tilde{\mathbf{J}}^{\#T}$, with its spectral norm $\left\|\tilde{\mathbf{J}}^{\#T}\right\|_2 = 1/\sigma_{\min}$, diverges. If $\mathbf{J}^T$ and $\tilde{\mathbf{J}}^T$ are not acute $\left\|\tilde{\mathbf{J}}^{\#T} - \mathbf{J}^{\#T}\right\|_2 \ge 1/\|\mathbf{E}\|_2$ and $\left\|\tilde{\mathbf{J}}^{\#T}\right\|_2 \ge 1/\|\mathbf{E}\|_2$ Stewart and Sun [3].

When the $n \times n$ square matrix $\mathbf{J}^T$ is nonsingular the open set of matrices $\tilde{\mathbf{J}}^T = \mathbf{J}^T + \mathbf{E}$ with $\|\mathbf{E}\| < 1/\|\mathbf{J}^{-T}\|$ are non-singular Ben-Israel and Greville [4]. For $\tilde{\mathbf{J}}^T$ to become singular, a relative perturbation of at least $\|\mathbf{E}\|/\|\mathbf{J}^T\| \geq \kappa^{-1}(\mathbf{J}^T)$ is required Stewart and Sun [3], where $\kappa(\mathbf{J}^T) = \|\mathbf{J}^T\| \, \|\mathbf{J}^{-T}\|$ is the condition number of $\mathbf{J}^T$ using a consistent matrix norm, e.g., $\kappa_2(\mathbf{J}^T) = \sigma_{\max}/\sigma_{\min}$.

2.2 Perturbation in Parameters

The effect of perturbation in n_p number of parameters could be investigated using Eq. (1) and the change in the transposed Jacobian matrix $\mathbf{J}^T$ or its generalized inverse $\mathbf{J}^{\#T}$, as well as the finite real values $\delta\mathbf{F}$ or $\delta\boldsymbol{\tau}$ as $\delta\mathbf{F} = \delta\mathbf{J}^T\boldsymbol{\tau} + \mathbf{J}^T\delta\boldsymbol{\tau}$ or $\delta\boldsymbol{\tau}_p = \delta\mathbf{J}^{\#T}\mathbf{F} + \mathbf{J}^{\#T}\delta\mathbf{F}$. The 3 dimensional $m \times n \times n_p$ array $\delta\mathbf{J}^T$ is a linear transformation (linearization) of $\mathbf{J}^T$ at the given point and is formed by n_p number of $m \times n$ matrices, with each $m \times n$ matrix containing the partial derivatives of the entries of $\mathbf{J}^T$ with respect to one of n_p parameters. Then

$$\boldsymbol{\tau}_p + \delta\boldsymbol{\tau}_p = \mathbf{J}^{\#T}(\mathbf{F} + \delta\mathbf{F}) + \delta\mathbf{J}^{\#T}\mathbf{F}. \tag{4}$$

For a given $\mathbf{F}$, $\delta\mathbf{F} = \mathbf{0}$ and $\boldsymbol{\tau}_p + \delta\boldsymbol{\tau}_p = \mathbf{J}^{\#T}\mathbf{F} + \delta\mathbf{J}^{\#T}\mathbf{F}$. The differential of perturbed Moore-Penrose GI of Jacobian matrix $d\mathbf{J}^{\#T}$ could be formulated using the change in $\mathbf{J}^T$ for (locally) constant rank $\mathbf{J}^T$ as [5]

$$d\mathbf{J}^{\#T} = -\mathbf{J}^{\#T}\,d\mathbf{J}^T\,\mathbf{J}^{\#T} + \mathbf{J}^{\#T}\mathbf{J}^{\#}d\mathbf{J}\big(\mathbf{I} - \mathbf{J}^T\mathbf{J}^{\#T}\big) + \big(\mathbf{I} - \mathbf{J}^{\#T}\mathbf{J}^T\big)\,d\mathbf{J}\,\mathbf{J}^{\#}\mathbf{J}^{\#T}. \tag{5}$$

The unique Hermitian, idempotent matrices $\mathbf{P}_{\mathbf{J}^T} = \mathbf{J}^T\mathbf{J}^{\#T}$ and $\mathbf{R}_{\mathbf{J}^T} = \mathbf{J}^{\#T}\mathbf{J}^T$ are respectively the orthogonal projectors onto the range (column) and row space of $\mathbf{J}^T$, and $\mathbf{P}_\perp = \mathbf{I} - \mathbf{J}^T\mathbf{J}^{\#T}$ and $\mathbf{R}_\perp = \mathbf{I} - \mathbf{J}^{\#T}\mathbf{J}^T$ are the projectors onto their orthogonal complements. When $\mathbf{J}^T$ is of full-row rank the second term on the right-hand side of Eq. (5) vanishes as $\mathbf{P}_\perp = \mathbf{I} - \mathbf{J}^T\mathbf{J}^{\#T} = \mathbf{0}$, and when $\mathbf{J}^T$ is of full-column rank the third term vanishes as $\mathbf{R}_\perp = \mathbf{I} - \mathbf{J}^{\#T}\mathbf{J}^T = \mathbf{0}$. When $\mathbf{J}^T$ is a full rank square matrix $d\mathbf{J}^{-T} = -\mathbf{J}^{-T}\,d\mathbf{J}^T\,\mathbf{J}^{-T}$ and both second and third terms vanish.

The perturbed least squares solution for differential $d\boldsymbol{\tau}_p$ is [6]

$$\begin{aligned} d\boldsymbol{\tau}_p = & -\mathbf{J}^{\#T}\big(\mathbf{J}^T\mathbf{J}^{\#T}\big)\,d\mathbf{J}^T\,\mathbf{J}^{\#T}\mathbf{J}^T\boldsymbol{\tau}_p - \big(\mathbf{I} - \mathbf{J}^{\#T}\mathbf{J}^T\big)\,d\mathbf{J}\,\mathbf{J}^T\mathbf{J}^{\#T}\mathbf{J}^{\#}\boldsymbol{\tau}_p \\ & + (\mathbf{J}\mathbf{J}^T)^{\#}\mathbf{J}^{\#T}\mathbf{J}^T d\mathbf{J}\big(\mathbf{I} - \mathbf{J}^T\mathbf{J}^{\#T}\big)\mathbf{F}. \end{aligned} \tag{6}$$

2.3 Interval Arithmetic's

Using interval arithmetic's, with parameters/data modelled/given as intervals, the point Jacobian matrix becomes an interval matrix $\mathbf{J}^T = [\underline{\mathbf{J}}^T, \overline{\mathbf{J}}^T] = [\mathbf{J}_c^T - \Delta\mathbf{J}^T, \ \mathbf{J}_c^T + \Delta\mathbf{J}^T]$, where $\mathbf{J}_c^T$ is the midpoint transposed Jacobian matrix. $\mathbf{F} = [\underline{\mathbf{F}}, \ \overline{\mathbf{F}}]$ and $\tau = [\underline{\tau}, \ \overline{\tau}]$ are interval vectors due to inexactness of parameters/data. If $\mathbf{J}^T = [\underline{\mathbf{J}}^T, \overline{\mathbf{J}}^T]$ does not include a singular matrix it is regular. Then, the exact/sharp lower and upper bounds of τ (e.g., interval hull of solution set) are computed for the prescribed intervals of parameters/data. The dependency among entries of $\mathbf{J}^T$ may be addressed by preconditioning, e.g., by the inverse of midpoint matrix $\mathbf{J}_c^T$, in order to tighten the solution set enclosure.

When $\mathbf{J}^T$ is a square matrix left multiplication of $\mathbf{J}^T$ with an exact or approximate inverse of the midpoint matrix $\mathbf{J}_c^{-T}$ usually results in a diagonally dominant matrix $\mathbf{J}_c^{-T}\mathbf{J}^T = \mathbf{J}_c^{-T}[\mathbf{J}_c^T - \Delta\mathbf{J}^T, \ \mathbf{J}_c^T + \Delta\mathbf{J}^T] = [\mathbf{I} - \mathbf{J}_c^{-T}\Delta\mathbf{J}^T, \ \mathbf{I} + \mathbf{J}_c^{-T}\Delta\mathbf{J}^T]$, which is almost the identity. Then, the bounds for τ are calculated solving

$$\mathbf{F}_{pcon} = \mathbf{J}_c^{-T}\mathbf{F} = \mathbf{J}_c^{-T}\mathbf{J}^T\tau = [\mathbf{I} - \mathbf{J}_c^{-T}\Delta\mathbf{J}^T, \ \mathbf{I} + \mathbf{J}_c^{-T}\Delta\mathbf{J}^T]\tau. \tag{7}$$

When the $m \times n$ matrix $\mathbf{J}^T$ is full-column rank with $n < m$, then $\mathbf{J}_c^{\#T}\mathbf{J}_c^T = \mathbf{I}_n$

$$\mathbf{J}_c^{\#T}\mathbf{F} = \mathbf{J}_c^{\#T}[\mathbf{J}_c^T - \Delta\mathbf{J}^T, \ \mathbf{J}_c^T + \Delta\mathbf{J}^T]\tau = [\mathbf{I} - \mathbf{J}_c^{\#T}\Delta\mathbf{J}^T, \ \mathbf{I} + \mathbf{J}_c^{\#T}\Delta\mathbf{J}^T]\tau. \tag{8}$$

For over-determined systems of linear equations, residual $\mathbf{r} = \mathbf{J}^T\tau - \mathbf{F}$ belongs to the orthogonal complement of the range space of $\mathbf{J}^T$ or null space of $\mathbf{J}$ as $\Re(\mathbf{J}^T)^\perp = N(\mathbf{J})$, i.e., $\mathbf{r} \in \Re(\mathbf{J}^T)^\perp$. Then, $\mathbf{J}\mathbf{r} = \mathbf{0}$ and $\mathbf{J}\mathbf{J}^T\tau - \mathbf{J}\mathbf{F} = \mathbf{0}$ [6]. Hence, the bounds for τ could also be calculated by solving the following $(m + n) \times (m + n)$ extended linear system#

$$\begin{bmatrix} \mathbf{J}^T & -\mathbf{I} \\ \mathbf{0} & \mathbf{J} \end{bmatrix} \begin{bmatrix} \tau \\ \mathbf{r} \end{bmatrix} = \begin{bmatrix} \mathbf{F} \\ \mathbf{0} \end{bmatrix} \quad \Rightarrow \quad \mathbf{J}_{ext}^T\tau_{ext} = \mathbf{F}_{ext}. \tag{9}$$

When the $m \times n$ matrix $\mathbf{J}^T$ is full-row rank with $n > m$ then $\mathbf{J}_c^T\mathbf{J}_c^{\#T} = \mathbf{I}_m$. For $\mathbf{J}\mathbf{y} = \tau$, $\mathbf{J}^T\mathbf{J}\mathbf{y} = \mathbf{J}^T\tau = \mathbf{F}$ is solved for $\mathbf{y}$ and τ is calculated from $\tau = \mathbf{J}\mathbf{y}$. Alternatively, the extended linear system of underdetermined case is used [7]

$$\begin{bmatrix} \mathbf{J} & -\mathbf{I} \\ \mathbf{0} & \mathbf{J}^T \end{bmatrix} \begin{bmatrix} \mathbf{y} \\ \tau \end{bmatrix} = \begin{bmatrix} \mathbf{0} \\ \mathbf{F} \end{bmatrix} \quad \Rightarrow \quad \mathbf{J}_{ext}^T\tau_{ext} = \mathbf{F}_{ext}. \tag{10}$$

It is noteworthy that for the point Jacobian matrix, when $\mathbf{J}^T$ is full-column or full-row rank the pertinent point matrix $\mathbf{J}_{ext}^T$ has full rank of $m + n$. For nonsingular interval $\mathbf{J}^T$, direct methods such as Gaussian elimination can produce enclosure for

Fig. 2 Parameters of planar parallel manipulators
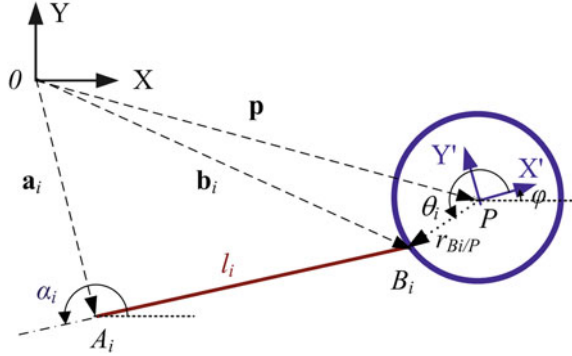
the set of exact solutions using infinite precision arithmetic. With iterative methods, the sequence of approximate solutions converge to the unique one when $\mathbf{M} = \mathbf{I} - \mathbf{J}^T$ has maximum row sum norm smaller than 1 [8].

3 Case Study

Example 1 For the redundant 2 DOF translational manipulator of Fig. 1a, with three legs and point mass platform $r_{Bi/P} = 0$ (Fig. 2), the leg attachment points A_i, $i = 1, \ldots, 3$, are at $(-2, -1.5)$, $(2, -1.5)$ and $(0, 1.5)$. For the pose $\mathbf{p} = [0 \ 0]^T$

$$\mathbf{J}^T = \begin{bmatrix} \cos \alpha_1 & \cos \alpha_2 & \cos \alpha_3 \\ \sin \alpha_1 & \sin \alpha_2 & \sin \alpha_3 \end{bmatrix} = \begin{bmatrix} -0.80000 & 0.80000 & 0 \\ -0.6000 & -0.6000 & 1.0000 \end{bmatrix} \quad (11)$$

$$\mathbf{J}^{\#T} = \begin{bmatrix} -0.6250 & -0.3488 \\ 0.6250 & -0.2488 \\ 0 & 0.5814 \end{bmatrix}. \quad (12)$$

When $\mathbf{F} = [8 \quad 10][8 \ 10]^T$ Newton's, $\tau_p = \mathbf{J}^{\#T}\mathbf{F} = [-8.4884 \quad 1.5116 \quad 5.8140]^T$ is the minimum 2-norm vector of joint forces, with a magnitude of $\|\tau_p\|_2 = 10.3990$ Newton's.

Uniformly distributed random error with bounds of ± 10 mm are added to the coordinates of A_i, then the perturbation and perturbed transposed Jacobian matrices are

$$\mathbf{E} = \begin{bmatrix} 0.0015 & -0.0023 & -0.0017 \\ -0.0021 & -0.0030 & -0.0000 \end{bmatrix},$$
$$\tilde{\mathbf{J}}^T = \begin{bmatrix} -0.7985 & 0.7977 & 0.0017 \\ -0.6021 & -0.6030 & 1.0000 \end{bmatrix}. \quad (13)$$

$\tilde{\mathbf{J}}^T$ is far from singularity as $\|\mathbf{E}\|_2/\|\mathbf{J}^T\|_2 = 0.0031 < \kappa_2^{-1}(\mathbf{J}^T) = 0.8627$. The perturbed minimum norm input is

$$\tilde{\tau}_p = \tilde{\mathbf{J}}^{\#^T}\mathbf{F} = [-8.5144\ 1.5190\ 5.7899]^T. \tag{14}$$

For the full-row rank $\mathbf{J}^T$, $\mathbf{I} - \mathbf{J}^T\mathbf{J}^{\#T} = \mathbf{0}$ and the perturbed least squares solution for $d\tau_p$ in terms of the differential of transposed Jacobian matrix $d\mathbf{J}^T$ is

$$\begin{aligned}
d\tau_p = &- \mathbf{J}^{\#T}\left(\mathbf{J}^T\ \mathbf{J}^{\#T}\right)\ d\mathbf{J}^T\ \mathbf{J}^{\#T}\mathbf{J}^T\tau_p - \left(\mathbf{I} - \mathbf{J}^{\#T}\mathbf{J}^T\right)\ d\mathbf{J}\ \mathbf{J}^T\mathbf{J}^{\#T}\mathbf{J}^{\#}\tau_p \\
&+ (\mathbf{J}\,\mathbf{J}^T)^{\#}\mathbf{J}^{\#T}\mathbf{J}^T d\mathbf{J}\left(\mathbf{I} - \mathbf{J}^T\mathbf{J}^{\#T}\right)\mathbf{F} = [-3.4593\,9.0407\,{-}4.6512]^T.
\end{aligned} \tag{15}$$

Considering an interval radius of 10 mm for the coordinates of A_i, the nominal coordinates are taken as the midpoint of corresponding interval, e.g., A_1 as $([-2.0101, -1.9899]; [-1.5101, -1.4899])$. Each interval parameter α_i, calculated using the coordinates of A_i, appears once in terms of its cosine and once in terms of its sine functions, both with the first powers. Hence, the possibility of overestimation is much lower than the case when multiple occurrences of the same interval argument happen. The interval matrices $\mathbf{J}^T$ and $\mathbf{J}^{-T}$ are

$$\mathbf{J}^T == \begin{bmatrix} [-0.8086, -0.7915][0.7915, 0.8086][-0.0068, 0.0068] \\ [-0.6075, -0.5926][-0.6075, -0.5926][0.9867, 1.0135] \end{bmatrix} \tag{16}$$

$$\mathbf{J}^{\#T} = \begin{bmatrix} [-0.6538, -0.5962][-0.3736, -0.3241] \\ [0.5962, 0.6538][-0.3736, -0.3241] \\ [-0.0193, 0.0193][0.5580, 0.6050] \end{bmatrix}. \tag{17}$$

For $\mathbf{F} = [8\ 10]^T$ Newton's, i.e., a degenerate interval of $\mathbf{F} = [[8]\ [-10, -10]]^T$, the INTLAB routine "verifylss", which is based on the 5×5 extended system in Eq. (10), was utilized with "SharpIVmult" option. The verified enclosures for the minimum norm vector of joint forces of underdetermined linear system, with infimum-supremum representation, are

$$\tau_p = [[-8.7247, -8.2509][1.2747, 1.7485][5.6006, 6.0265]]^T. \tag{18}$$

with an interval norm of $\|\tau_p\|_2 = [10.0533, 10.7469]$. Solving for $\mathbf{y}$ first results in wider bounds as $\tau_p = [[-8.9662, -8.0157][1.0367, 1.9873][5.4290, 6.2033]]^T$.

Example 2 For the 2 DOF translational manipulator of Fig. 1b at $\mathbf{p} = [0\ 0]^T$

$$\mathbf{J}^T = \begin{bmatrix} -0.8000\,0.8000 \\ -0.6000\,{-}0.6000 \end{bmatrix}, \cdots \mathbf{J}^{-T} = \begin{bmatrix} -0.6250\,{-}0.8333 \\ 0.6250\,{-}0.8333 \end{bmatrix}. \tag{19}$$

For $\mathbf{F} = [8 \; -30]^T$ Newton's, the unique vector of actuator forces is $\boldsymbol{\tau} = \mathbf{J}^{-T}\mathbf{F} = [20\,30]^T$ with a magnitude of $\|\boldsymbol{\tau}\|_2 = 36.056$ Newton's.

With uniformly distributed random error with bounds of ± 5 mm added to A_i,

$$\mathbf{E} = 1.0\mathrm{e} - 3 \times \begin{bmatrix} 0.1546 -0.2294 \\ -0.2060 -0.3058 \end{bmatrix}, \cdots \tilde{\mathbf{J}}^{-T} = \begin{bmatrix} -0.6252 -0.8329 \\ 0.6251 -0.8330 \end{bmatrix}. \quad (20)$$

and $\quad \tilde{\boldsymbol{\tau}} = \tilde{\mathbf{J}}^{-T}\mathbf{F} = [19.9866\,29.9913]^T \quad$ Newton's, $\quad \kappa_2^{-1}(\tilde{\mathbf{J}}^T) = 0.7525,$
$\|\mathbf{E}\|_2 / \|\mathbf{J}^T\|_2 = 0.0017 < \kappa_2^{-1}(\mathbf{J}^T) = 0.7500,$
$\|\mathbf{E}\|_F / \|\mathbf{J}^T\|_F = 0.0016 < \kappa_F^{-1}(\mathbf{J}^T) = 0.4800.$

The square $\mathbf{J}^T$ is full rank, hence $d\boldsymbol{\tau} = \mathbf{J}^{-T} d\mathbf{J}^T \boldsymbol{\tau} = [25.4167 \; -12.0833]^T.$

For an interval radius of 5 mm for the A_i coordinates, interval $\mathbf{J}^T$ and $\mathbf{J}^{-T}$ are

$$\mathbf{J}^T = \begin{bmatrix} [-0.8043, -0.7957][0.7957, 0.8043] \\ [-0.6037, -0.5963][-0.6037, -0.5963] \end{bmatrix} \quad (21)$$

$$\mathbf{J}^{-T} = \begin{bmatrix} [-0.6322, -0.6178][-0.8430, -0.8237] \\ [0.6178, 0.6322][-0.8430, -0.8237] \end{bmatrix} \quad (22)$$

with $\|\mathbf{I} - \mathbf{J}^T\|_\infty = [2.5915, 2.6086]$ being larger than 1. For $\mathbf{F} = [8 \; -30]^T$ Newton's, $\quad \boldsymbol{\tau} = \mathbf{J}^{-T}\mathbf{F} = [[19.6527, 20.3466][29.6525, 30.3465]]^T, \quad \|\boldsymbol{\tau}\|_2 = [35.5738, 36.5362]$ Newton's. If the joint limits are ± 30 Newton's., the solution over 30 Newton's is not acceptable for τ_2. The solution enclosure is slightly reduced using $\mathbf{J}_c^{-T}$

$$\boldsymbol{\tau} = [[19.7105, 20.2888][29.7104, 30.2886]]^T \quad (23)$$

with $\|\boldsymbol{\tau}\|_2 = [35.6540, 36.4560].$

4 Concluding Remarks

In this article, the effect of uncertainty and error in design parameters and data (sensor/actuator inputs), which exist in physical devices, on the Jacobian matrix of manipulators were investigated. The perturbed, differential and interval forms of the Jacobian matrix and their inverse/generalized inverses were examined to calculate the joint forces/torques. Planar parallel manipulators with square and rectangular Jacobian matrices (over-determined and underdetermined linear systems) were simulated. Due to space limitation, results for two cases were reported to facilitate appreciation of methods and their implementations.

References

1. Merlet, J.-P.: Interval analysis for certified numerical solution of problems in robotics. Int. J. Appl. Math. Comput. Sci. **19**(3), 399–412 (2009)
2. Notash, L.: A methodology for actuator failure recovery in parallel manipulators. Mech. Mach. Theory **46**(4), 454–465 (2012)
3. Stewart, G.W., Sun, J.-G.: Matrix Perturbation Theory. Academic Press, New York (1990)
4. Ben-Israel, A., Greville, T.N.E.: Generalized Inverses: Theory and Applications. Springer, New York (2003)
5. Golub, G.H., Pereyra, V.: Differentiation of pseudo-inverses and nonlinear least squares problems whose variables separate. SIAM J. Numer. Anal. **10**(2), 413–433 (1973)
6. Stewart, G.W.: On the perturbation of pseudo-inverses. Proj. Linear Least Squares Probl. SIAM Rev. **19**(4), 634–662 (1977)
7. Rump, S.M.: Verified bounds for least squares problems and underdetermined linear system. SIAM J. Matrix Anal. Appl. **33**(1), 130–148 (2012)
8. Moore, R.E., Kearfott, R.B, Cloud, M.J.: Introduction to Interval Analysis. SIAM (2009)

Accuracy Improvement of Robot-Based Milling Using an Enhanced Manipulator Model

Alexandr Klimchik, Yier Wu, Stéphane Caro, Benoît Furet and Anatol Pashkevich

Abstract The paper is devoted to the accuracy improvement of robot-based milling by using an enhanced manipulator model that takes into account both geometric and elastostatic factors. Particular attention is paid to the model parameters identification accuracy. In contrast to other works, the proposed approach takes into account impact of the gravity compensator and link weights on the manipulator elastostatic properties. In order to improve the identification accuracy, the industry oriented performance measure is used to define optimal measurement configurations and an enhanced partial pose measurement method is applied for the identification of the model parameters. The advantages of the developed approach are confirmed by experimental results that deal with the elastostatic calibration of a heavy industrial robot used for milling. The achieved accuracy improvement factor is about 2.4.

Keywords Robot-based milling · Elastostatic calibration · Gravity compensator

A. Klimchik (✉) · Y. Wu · A. Pashkevich
Ecole des Mines de Nantes, Nantes, France
e-mail: alexandr.klimchik@emn.fr; alexandr.klimchik@mines-nantes.fr

Y. Wu
e-mail: yier.wu@emn.fr

A. Pashkevich
e-mail: anatol.pashkevich@emn.fr

A. Klimchik · Y. Wu · S. Caro · B. Furet · A. Pashkevich
Institut de Recherche en Communications et Cybernétique de Nantes, Nantes, France
e-mail: stephane.caro@irccyn.ec-nantes.fr

B. Furet
e-mail: benoit.furet@univ-nantes.fr

S. Caro
French National Centre for Scientific Research, Nantes, France

B. Furet
University of Nantes, Nantes, France

1 Introduction

At present, the conventional CNC machines are progressively replaced in industry by robotic manipulators to perform main manufacturing tasks. For those applications, industrial robots are considered to be very competitive due to their manufacturing flexibility, large workspace and cost-effectiveness. At the same time, the robotic-based machining introduces some difficulties. For instance, link and joint compliances become non-negligible when robot is under substantial external loading. So, in order to achieve high processing accuracy, essential revision of relevant mathematical models and control strategies are required.

The stiffness modeling of robotic manipulators has been in the focus of the research community for more than 30 years [1]. There exist different approaches that are able to take into account particularities of serial and parallel manipulators [2, 3]. Among a number of existing stiffness modeling approaches, the Virtual Joint Modeling (VJM) method looks the most attractive in robotics. Its main idea is to take into account the elastostatic properties of flexible components by presenting them as equivalent localized virtual springs [4]. However the stiffness modeling of the manipulators with gravity compensators has not found enough attention yet. Another difficulty related to the stiffness modeling of robotic manipulators is the identification of their model parameters. This issue is quite new in robotics, the existing approaches are usually suitable for strictly serial manipulators only [5]. Therefore, this paper aims to obtain a sophisticated elasto-static model for heavy industrial robots with a gravity compensator and to identify their parameters.

2 Problem of the Compliance Errors Compensation

In common engineering practice, robot behavior under an external loading can be described by the following force-deflection relation [6]

$$\Delta \mathbf{t} = \left(\mathbf{J}_\theta \cdot (\mathbf{K}_\theta - \mathbf{H}_{\theta\theta})^{-1} \cdot \mathbf{J}_\theta^T \right) \cdot \mathbf{F} \tag{1}$$

where $\mathbf{J}_\theta$ and $\mathbf{H}_{\theta\theta}$ are the Jacobian and Hessian matrices respectively, the matrix $\mathbf{K}_\theta$ describes the elastic properties of the manipulator components. This model allows us to compute the end-effector deflection $\Delta \mathbf{t}$ due to the external loading $\mathbf{F}$. Since the manipulator deflection caused by the loading is known, it can be used to improve the positioning accuracy by means of error compensation technique (Fig. 1). However in practice, only geometrical parameters are provided by the robot manufacturer, while elastostatic parameters should be identified using dedicated calibration techniques. Usually the force-deflection relation (1) is rearranged in the linear model suitable for the identification procedure, which is a
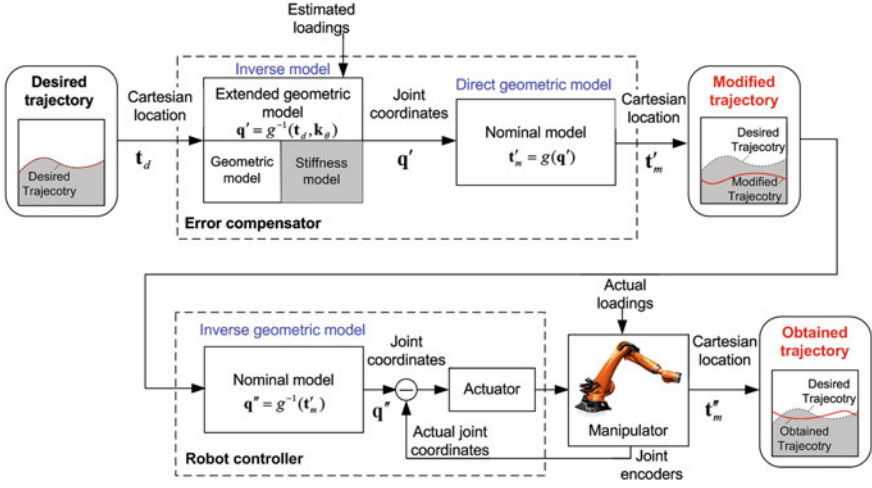
Fig. 1 Off-line compliance errors compensation strategy

linear mapping between the parameters to be identified and the end-effector displacement

$$\Delta \mathbf{t}_i = \mathbf{A}_i \, \mathbf{k}; \qquad \mathbf{A} = \left[\mathbf{J}_{1i} \mathbf{J}_{1i}^T \mathbf{F}_i, \ldots, \mathbf{J}_{ni} \mathbf{J}_{ni}^T \mathbf{F}_i \right] \quad (i = \overline{1, m}) \tag{2}$$

where the vector $\mathbf{k}$ collects elastostatic parameters of the matrix $\mathbf{k}_\theta = \mathbf{K}_\theta^{-1}$.

It should be mentioned that such a model can be efficiently applied for strictly serial manipulators (without closed-loops) while for heavy manipulators with a gravity compensator this procedure should be revised in order to take into account particularities of the stiffness model. Another difficulty is related to the gravity compensator modeling, whose parameters are usually not given.

Hence, the goal of this work is to obtain a sophisticated elastostatic model that can be used for compliance errors compensation. Accordingly, two problems should be considered: (i) developing the model for the compensator and methodology for the identification of its parameters; (ii) integration of the compensator into conventional elastostatic model and identification of its parameters.

3 Parameters of the Enhanced Manipulator Model and Their Identification

Considered industrial robot KUKA KR-270 incorporates gravity compensator that is used to balance link-weights but also affects manipulator elastostatic properties. The mechanical structure of the gravity compensator under study is presented in Fig. 2. The compensator incorporates a passive spring attached to the first and
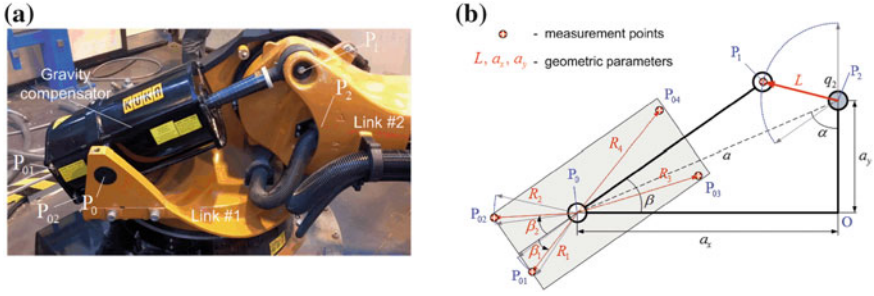
Fig. 2 Gravity compensator and its model

second links, which creates a closed loop that generates the torque applied to the second joint of the manipulator. The compensator geometrical model includes three node points P_0, P_1, P_2, which yield three principal geometrical parameters $L = |P_1, P_2|$, $a = |P_0, P_2|$, $s = |P_0, P_1|$. Let us also introduce some auxiliary parameters (such as a_x and a_y), whose geometrical meanings are described in Fig. 2. The fact that the gravity compensator affects on the second joint only allows us to replace the constant parameter K_{θ_2} in the model (1) by the non-linear one that also takes into account elasto-static properties of the compensator.

The variable s describing the compensator spring deflection can be computed as a function of the second joint coordinate q_2 as follows:

$$s^2 = a^2 + L^2 + 2\,a\,L\,\cos(\alpha - q_2) \tag{3}$$

Therefore, the equivalent stiffness of the second joint (comprising both the manipulator and compensator stiffnesses) can be expressed as

$$K_{\theta_2} = K_{\theta_2}^0 + K_c\,a\,L\left(\frac{s_0}{s}\left(\frac{a\,L}{s^2}\sin^2(\alpha - q_2) + \cos(\alpha - q_2)\right) - \cos(\alpha - q_2)\right) \tag{4}$$

where K_c is the gravity compensator stiffness, the value s_0 corresponds to the distance $|P_0, P_1|$ for the unloaded spring. This allows us to extend the classical stiffness model (1) of the serial manipulator by modifying the virtual spring parameters in accordance with the compensator properties. In this case, the Cartesian stiffness matrix $\mathbf{K}_c$ can be computed using the following expression:

$$\mathbf{K_C} = \left(\mathbf{J}_\theta \cdot (\mathbf{K}_\theta(\mathbf{q}) - \mathbf{H}_{\theta\theta})^{-1} \cdot \mathbf{J}_\theta^T\right)^{-1} \tag{5}$$

which includes both the first and second order derivatives (Jacobians and Hessians) of the functions $\mathbf{g}(\mathbf{q}, \boldsymbol{\theta})$ describing the manipulator geometry [4]. Here, the vectors $\mathbf{q}$ and $\boldsymbol{\theta}$ collect actuator coordinates and the corresponding deflections.

The equivalent stiffness of the second joint (4) depends on several geometrical parameters (L, a_x, a_y) that are unknown and should be identified using reference

points shown in Fig. 2b. By considering particularities of the experimental setup for the geometric parameters identification, where for each measurement of the point P_1 joint coordinate q_2 is given, the value of L can be computed as

$$L = \sum_{i=1}^{m} \widehat{\mathbf{p}}_i^{T} \mathbf{R} \, \widehat{\mathbf{u}}_i \bigg/ \sum_{i=1}^{m} \widehat{\mathbf{u}}_i^{T} \widehat{\mathbf{u}}_i \tag{6}$$

where $\widehat{\mathbf{p}}_i = \mathbf{p}_i - m^{-1} \sum_{i=1}^{m} \mathbf{p}_i$, $\widehat{\mathbf{u}}_i = \mathbf{u}_i - m^{-1} \sum_{i=1}^{m} \mathbf{u}_i$, $\mathbf{u}_i = [\cos q_i, \; \sin q_i, \; 0]^{T}$, $\mathbf{p}_i$ is the Cartesian coordinate vector of point P_1 for the ith measurement and m is the number of measurements and the orthogonal matrix $\mathbf{R} = \mathbf{V}\mathbf{U}^{T}$ can be obtained using the following SVD-factorization $\sum_{i=1}^{m} \widehat{\mathbf{u}}_i \widehat{\mathbf{p}}_i = \mathbf{U} \boldsymbol{\Sigma} \mathbf{V}^{T}$. The remaining geometrical parameters (a_x and a_y) are x and y coordinates of the vector

$$\mathbf{p}_0 = \frac{1}{2}\left(\mathbf{I} - \mathbf{n}\mathbf{n}^{T}\right)\left(\sum_{j=1}^{k}\sum_{i=1}^{m} \widehat{\mathbf{p}}_i^{j} \widehat{\mathbf{p}}_i^{jT}\right)^{-1} \sum_{j=1}^{k}\sum_{i=1}^{m} \widehat{s}_i^{j} \widehat{\mathbf{p}}_i^{j} + k^{-1}m^{-1}\mathbf{n}\mathbf{n}^{T}\sum_{j=1}^{k}\sum_{i=1}^{m} \widehat{\mathbf{p}}_i^{j} \tag{7}$$

where $\widehat{\mathbf{p}}_i^{j} = \mathbf{p}_i^{j} - m^{-1} \sum_{l=1}^{m} \mathbf{p}_l^{j}$, $\widehat{s}_i^{j} = \mathbf{p}_i^{jT}\mathbf{p}_i^{j} - m^{-1} \sum_{l=1}^{m} \mathbf{p}_l^{jT}\mathbf{p}_l^{j}$, $\mathbf{p}_i^{j}$ is the Cartesian coordinate vector of point P_{0j} for the ith measurement, k is the number of reference points and m is the number of measurements. Here, the vector $\mathbf{n}$ is the last column of the matrix $\mathbf{V}$ of the following SVD-factorization $\sum_{j=1}^{k}\sum_{i=1}^{m} \widehat{\mathbf{p}}_i^{j} \widehat{\mathbf{p}}_i^{jT} = \mathbf{U}\boldsymbol{\Sigma}\mathbf{V}^{T}$.

Since all geometrical parameters are known, the elastostatic ones can be identified. To take into account the compensator influence while retaining the approach developed for serial robots without compensators, manipulator elastostatic parameters can be identified into two steps. The first step aims to compute the extended set of elastic parameters that includes all equivalent virtual springs for the second joint by using the standard least-square technique

$$\mathbf{k} = \left(\sum_{i=1}^{m} \mathbf{B}_i^{(p)^{T}} \mathbf{B}_i^{(p)}\right)^{-1} \cdot \left(\sum_{i=1}^{m} \mathbf{B}_i^{(p)^{T}} \Delta\mathbf{p}_i\right) \tag{8}$$

where the vector $\Delta\mathbf{p}_i$ is the small displacement of the end-effector under the external loading $\mathbf{F}_i$, matrix $\mathbf{B}_i^{(p)}$ is a rearranged matrix $\mathbf{A}_i$ that integrates positional components only and considers the shape and meaning of vector $\mathbf{k}$. The second step deals with the identification of the gravity compensator parameters and compliance of joint #2 that can be obtained from the following equation

$$\begin{bmatrix} K_{\theta_2}^{0} & K_c & s_0 \cdot K_c \end{bmatrix}^{T} = \left(\sum_{i=1}^{m_q} \mathbf{C}_i^{T}\mathbf{C}_i\right)^{-1}\left(\sum_{i=1}^{m_q} \mathbf{C}_i^{T}K_{\theta_{2i}}\right) \tag{9}$$

where m_q is the number of different angles q_2 in the experimental data,

$$\mathbf{C}_i = \begin{bmatrix} 1 & -aL \cdot \cos(\alpha - q_{2i}) & aL/s \cdot \left(aL/s^2 \cdot \sin^2(\alpha - q_{2i}) + \cos(\alpha - q_{2i}) \right) \end{bmatrix} \quad (10)$$

In order to ensure high calibration efficiency, the design of experiments should be considered while choosing measurement configurations. To the best of our knowledge, the best results for particular industrial applications can be achieved by using the test-pose based approach [7], which reduces optimal pose selection to the following optimization problem:

$$\mathrm{trace} \left(\mathbf{A}_0^{(p)} \sum_{j=1}^{m_q} \left(\sum_{i=1}^{m} \mathbf{A}_i^{j(p)^T} \mathbf{A}_i^{j(p)} \right)^{-1} \mathbf{A}_0^{(p)^T} \right) \rightarrow \min_{\{\mathbf{q}_i, \mathbf{w}_i\}} \quad (11)$$

Here matrix $\mathbf{A}_0^{(p)}$ has the same structure as matrix $\mathbf{A}_i^{(p)}$, but is defined by the desired test pose configuration $\mathbf{q}_0$ and the external loading $\mathbf{F}_0$. The values of $\mathbf{q}_0$, $\mathbf{F}_0$ are usually related to a typical machining configuration and force generated by the tool-workpiece interaction. Such an approach allows us to ensure the highest positioning accuracy after compensation compliance errors caused by the technological process.

Using theoretical results presented in this section, it is possible to obtain a sophisticated elasto-static model that can be used for further error compensation. In the next section, these results are used to obtain the stiffness model of the KUKA KR-270 robot.

4 Experimental Results and Comparison Analysis

The main geometric parameters of the gravity compensator are L, a_x and a_y (see Fig. 2). They can be identified by using relative locations of points P_0 and P_1 with respect to point P_2. Since the adopted geometric model is a planar one, here the laser tracker base frame is defined in a particular way in order to ensure that the marker locations relative to the XY-plane are not significant. Another important issue is related to the selection of the marker point locations on the rigid part of the gravity compensator. To ensure high identification accuracy, these markers should be located on the opposite sides of the compensator rotational axis, such that the optimal conditions $\sum_{j=1}^{k} R_j \cos \beta_j = 0$ and $\sum_{j=1}^{k} R_j \sin \beta_j = 0$ are satisfied. To increase the identification accuracy, four marker points are used in the calibration experiments and are denoted as P_{01}, P_{02}, P_{03} and P_{04}, respectively. Their locations are shown in Fig. 1, where the radii $R_1 = R_3$ and $R_2 = R_4$, and the angles $\beta_3 = \pi + \beta_1$ and $\beta_4 = \pi + \beta_2$. The measurement data have been obtained using a Leica laser-tracer for the set $q_2 = \{0°, -30°, -60°, -90°, -120°, -140°\}$. The values of the identified geometrical parameters and corresponding confidence intervals are given in Table 1.

Table 1 Identification results for the compensator geometric parameters

	L (mm)	a_x (mm)	a_y (mm)
Value	184.72	685.93	123.30
CI	±0.06	±0.70	±0.69
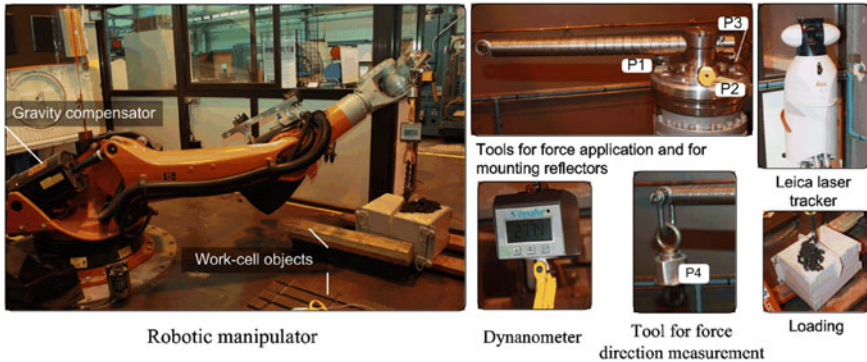
Fig. 3 Experimental setup for manipulator elastostatic calibration

For the identification of manipulator elastostatic parameters, 15 measurement configurations (with 5 different values for q_2) were obtained based on the industry oriented performance measure (10), for which the Cartesian coordinates of the reference points (P_1, P_2 and P_3) were measured three times (before and after the loading). The corresponding experimental setup is illustrated in Fig. 3. The desired elastostatic parameters have been obtained using a two-step identification procedure. On the first step, the base and tool transformations have been computed. On the second step, all measurement data as well as the obtained base and tool transformations have been used for the identification of the manipulator elastostatic parameters. Corresponding numerical results are given in Table 2.

To show the advantages of the developed approach, the manipulator accuracy after calibration has been compared for two distinct plans of calibration experiments. The first one has been obtained using the industry-oriented performance measure and implements enhanced numerical routines. In this case, the manipulator was presented as a quasi-serial chain, and the calibration data were obtained using the enhanced partial pose measurements. The second plan used measurement configurations that were selected semi-intuitively, in accordance with some kinematic performance measures [5]. A relevant manipulator model corresponding to the strict serial architecture, and the calibration data were obtained using conventional full-pose measurements.

Using these two sets of calibration data, the identification yielded two slightly different sets of manipulator parameters (Table 2). Then, the obtained parameters (both sets) may be used to compute the end-effector positions for the validation configurations (that were not used in both identification routines). Comparing these

Table 2 Manipulator elastostatic parameters obtained using different approaches, [μrad/Nm]

	k_1	k_2	k_3	k_4	k_5	k_6
The results obtained in this work	0.623	Inline media	0.416	2.786	3.483	2.074
Dumas et al. 2011 [5]	3.798	0.248	0.276	1.975	2.286	3.457

Table 3 The manipulator accuracy improvement after elastostatic error compensation

Criterion	Before compensation	After compensation		Improvement factor	
		Dumas et al. 2011 [5]	(This work)	Dumas et al. 2011 [5]	(This work)
max [mm]	8.28	1.77	0.78	4.6	10.4
RMS [mm]	5.90	1.27	0.53	4.6	11.1

results with the corresponding position measurements, it is possible to evaluate the "calibration quality" and relevant plans of the experiments.

For comparison purposes, the manipulator accuracy improvement due to elastostatic errors compensation has been studied based on the error analysis before and after compensation. Relevant results are shown in Table 3, where the maximum and RMS values of the distance-based residuals are provided. As follows from the obtained results, using the identified elastostatic parameters, it is possible to compensate 91.2 % of the end-effector deflections (in average). In general, the manipulator positioning accuracy has been improved by a factor of 11.1 compare to a non-compensated robot. Compare to the previous results, the compensation efficiency has been increased by a factor of 2.4 using almost the same number of configurations, which is also referred to as the accuracy improvement factor. Hence, the above presented analysis shows the advantages of theoretical contributions presented in this work. The developed calibration technique allows us to increase essentially the manipulator positioning accuracy under external loading using a reasonable number of measurement configurations. It should be noted that the obtained elastostatic parameters can be used for elaso-dynamic analysis.

5 Conclusion

The paper deals with the accuracy improvement of a heavy industrial robot used for milling operations. It provides a sophisticated geometric/elastostatic model for quasi serial manipulators with gravity compensator and techniques for the identification of their model parameters. In order to improve the identification accuracy, design of experiments technique based on industry oriented performance measure was used. The advantages and practical significance of the proposed approach have been shown by experimental results and a comparison analysis. The improvement factor is about 2.4.

References

1. Salisbury, J.K.: Active stiffness control of a manipulator in Cartesian coordinates. In: Decision and Control including the Symposium on Adaptive Processes, IEEE, pp. 95–100 (1980)
2. Kövecses, J., Angeles, J.: The stiffness matrix in elastically articulated rigid-body systems. Multibody Sys. Dyn. **18**(2), 169–184 (2007)
3. Merlet, J.-P., Gosselin, C.: Parallel mechanisms and robots. In: Siciliano, B., Khatib, O. (eds.) Springer Handbook of Robotics, pp. 269–285. Springer, Berlin (2008)
4. Pashkevich, A., Klimchik, A., Chablat, D.: Enhanced stiffness modeling of manipulators with passive joints. Mech. Mach. Theory **46**(5), 662–679 (2011)
5. Dumas, C., Caro, S., Garnier, S., Furet, B.: Joint stiffness identification of six-revolute industrial serial robots. Robot. Comput. Integr. Manuf. **27**(4), 881–888 (2011)
6. Klimchik, A., Bondarenko D., Pashkevich A., Briot, S., Furet, B.: Compensation of tool deflection in robotic-based milling. In: ICINCO 2012, pp 113-122 (2012)
7. Klimchik, A., Wu, Y., Pashkevich, A., Caro, S., Furet, B.: Optimal selection of measurement configurations for stiffness model calibration of anthropomorphic manipulators. Applied Mechanics and Materials **162**, 161–170 (2012)

Design and Optimization
of a Tripod-Based Hybrid Manipulator

Dan Zhang and Bin Wei

Abstract In this paper, a novel 3DOF hybrid manipulator 3PU*S-PU is proposed based on the general function (Gf) set theory. After discussing the advantages of this new type of manipulator, the kinematic and Jacobian matrix of this manipulator are first analyzed, then the kinematic performances which include stiffness/compliance and workspace are analyzed and optimized, and the multi-objective optimization on the compliance and workspace is subsequently conducted.

1 Introduction

Type synthesis for parallel manipulators is a vital important task for the future parallel manipulator developments, analysis and applications, and the type synthesis for the parallel manipulators is and still will be a main issue for many scholars and its related applications. Type synthesis can simply put as this way: using various methods to combine the advantages of serial and parallel manipulators to design new application-orientated mechanisms. Furthermore, if we want to design a new type of parallel manipulator, we cannot just stick to the conventional joints, i.e. prismatic joint, revolute joint, universal joint and spherical joint. We can use, for example, parallelogram (Pa joint) or pure-translational universal joint (U* joint, U* joint can also be seen as a special parallelogram) or the double parallelogram (Pa2 joint) as a leg or part of structure instead of conventional fixed length leg or actuated leg, because the parallelogram structure has higher stiffness compared to the conventional legs. Obviously, parallelogram has

D. Zhang (✉) · B. Wei
University of Ontario Institute of Technology, 2000 Simcoe Street North,
Oshawa, ON L1H 7K4, Canada
e-mail: Dan.Zhang@uoit.ca

two links acting in parallel, which can distribute the loads whereas the normal leg just has one leg, so the stiffness can be improved for the parallelogram structure based parallel robotics. In addition, by using a parallelogram, the tilting angle or rotation capacity can also be improved [1]. Until now, numerous methods have been proposed to provide guidance for designing new type of parallel manipulators for the purpose of further improving parallel manipulators' performances. The most common way to design a new parallel manipulator is the one that based on the Chebychev-Grübler-Kutzbach formula and then enumerate all the possibilities, which is a cumbersome work. In [2], the systematic enumeration method which is based on the idea that some of the functional requirements of desired mechanisms are transformed into structural characteristics is proposed; in [3], the theory of groups of displacements is used to develop some new architecture of four DOF (3T1R) fully-parallel manipulators by resorting to the parallelograms, each parallelogram based structure is treated as a "motion generator", and by combing different motion generators, new types of parallel manipulators can be generated; similarly in [4], two identical kinematic chain that serve as a Schonflies-Motion Generator is proposed as a kinematic chain for the parallel manipulator, which also employed the parallelograms. Recently, the general function (Gf) set theory was proposed for the type synthesis of parallel manipulators, and our new proposed manipulator is based on this method. The detail steps and procedures of applying the Gf set theory can be found in [5]. Based on the Gf set theory, a number of three degrees of freedom parallel manipulators can be derived, but some of them are not useful at all. Among them, one is 3PU*S-(CR)$_o$ parallel manipulator and another is 3PU*S-(RC)$_o$ parallel manipulator, but these parallel manipulators have a rotation axis perpendicular to the moving platform, i.e. they have two rotations, one of them is to rotate about Z axis, which is not what we wanted, what we wanted is two rotations about X and Y axes, i.e. two rotation axes parallel to the moving platform. In [6], a hybrid head mechanism 4UPS-PU was proposed to serve as the head section of a groundhog-like mine rescue robot, the unique feature of that mechanism is that a central passive P-U type limb was incorporated in the mechanism so that it can constrain the whole structure to be three degrees of freedom, i.e. two rotations about X and Y axes and one translation along Z axis, inspired by the design in [6], we changed the middle passive leg from the original to the PU type, this passive leg consists of a universal joint attached to the moving platform and a passive link fixed to the base, by this way the manipulator has three desired degrees of freedom, i.e. two rotations about X and Y axes, and one translation along Z axis.

The novelty of our new proposed 3PU*S-PU manipulator can be concluded as follows: firstly, by employing the U* joint, the stiffness of this parallel manipulator can be greatly improved; secondly, by changing the structure of the middle passive leg, i.e. changing the dof of the middle passive leg, the whole parallel manipulator can be reconfigured, for example, if we remove the middle passive leg, the three dof mechanism will turn to six dof.
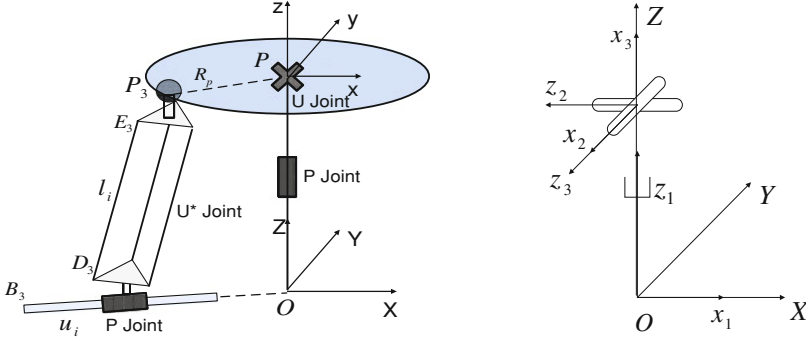
Fig. 1 Kinematic structures of 3PU*S-PU mechanism and central passive leg

2 Kinematic and Jacobian Analysis of the Mechanism

The 3PU*S-PU mechanism is shown in Fig. 1. The moving platform is connected to the base by three active legs P-U*-S and one central passive leg P-U. In the active leg, the pure-translational universal joint U* (fixed leg structure) is used instead of conventional leg. This U* joint is connected to the base and moving platform by a prismatic joint and a spherical joint, respectively. There is passive leg in the middle consisting of a universal joint and a passive link. There are two purposes of using this passive leg, one is to constrain the moving platform to have only three degrees of freedom, which are rotations about X and Y axes and translation along Z axis, another is to further increase the stiffness of this parallel manipulator [7]. By actuating these three prismatic joints on the guide ways, the moving platform can achieve desired motions.

The guide ways intersect at the point O of the fixed coordinate system. The coordinates of $B_i (i = 1, 2, 3)$ and P_i with respect to the fixed coordinate system $O(X, Y, Z)$ and moving coordinate system $P(x, y, z)$ are denoted as ^oB_i and ^PP_i, respectively; the coordinates of P_i with respect to the fixed coordinate system are denoted as ^oP_i. Then ^oP_i can be written as follows:

$$^oP_i = \begin{bmatrix} x^o_{pi} \\ y^o_{pi} \\ z^o_{pi} \end{bmatrix} = R_e{}^PP_i + {}^oP = \begin{bmatrix} -R_p \cos\theta_i \sin\theta_y \\ R_p \sin\theta_i \sin\theta_x - R_p \cos\theta_i \cos\theta_x \cos\theta_y \\ z_e + R_p \cos\theta_x \sin\theta_i + R_p \cos\theta_i \cos\theta_y \sin\theta_x \end{bmatrix} \tag{1}$$

Differentiate the above equation yields:

$$\begin{bmatrix} \delta x^o_{pi} & \delta y^o_{pi} & \delta z^o_{pi} \end{bmatrix}^T = [J_i] \begin{bmatrix} \delta\theta_x & \delta\theta_y & \delta\theta_z & \delta x & \delta y & \delta z_e \end{bmatrix}^T \tag{2}$$

From the vector loop equation, the following equation can be obtained:

$$^oP_i - {}^oB_i - u_in_i = l_is_i \tag{3}$$

where u_i is the actuated input, n_i is the unit vector pointing along the rails, l_i is the length of the U* link, s_i is the unit vector pointing along the link D_iE_i. Dot multiplying Eq. (3) with itself can yield the inverse kinematic solution. Since

$$l_i^2 = (x_{pi}^o - R_b\cos\alpha_i + u_i\cos\alpha_i)^2 + (y_{pi}^o - R_b\sin\alpha_i + u_i\sin\alpha_i)^2 + (z_{pi}^o)^2 \tag{4}$$

Take the derivative of Eq. (4) with respect to x_{pi}^o, y_{pi}^o and z_{pi}^o, and rearrange the equations yields the following:

$$\partial u_i = J_{parallel}[\,\delta\theta_x \quad \delta\theta_y \quad \delta\theta_z \quad \delta x \quad \delta y \quad \delta z_e\,]^T \tag{5}$$

The central passive leg can be viewed as serial component. The kinematic structure of the central passive leg is shown in Fig. 1. The Jacobian matrix of the central passive leg of the mechanism J_{serial} can be expressed as follows [7]:

$$J_{serial} = \begin{bmatrix} zeros(3,1) & e_{42} & e_{43} \\ e_{41} & e_{42} \times r_{42} & e_{43} \times r_{43} \end{bmatrix} \tag{6}$$

The Jacobian matrix of the whole mechanism can be written as $J_{parallel}J_{serial}$ [6].

3 Compliance Modeling and Optimization

Due to space limitation, the general derivation process of the Cartesian compliance matrix is as follows. Based on the principle of virtual work [7], one has the following equation:

$$(J_{co}J_{serial})^T\tau = J_{serial}^Tw \tag{7}$$

where τ is the vector of actuator forces, w is the force or torque applied to the moving platform, and

$$J_{co} = \left[\begin{bmatrix} \frac{l_{1x}}{l_1} & \frac{l_{1y}}{l_1} & \frac{l_{1z}}{l_1} \end{bmatrix}[J_1] \quad \begin{bmatrix} \frac{l_{2x}}{l_2} & \frac{l_{2y}}{l_2} & \frac{l_{2z}}{l_2} \end{bmatrix}[J_2] \quad \begin{bmatrix} \frac{l_{3x}}{l_3} & \frac{l_{3y}}{l_3} & \frac{l_{3z}}{l_3} \end{bmatrix}[J_3] \right]^T$$

An actuator compliance matrix C is defined as:

$$C\tau = \Delta\rho \tag{8}$$

where $\Delta\rho$ is the joint displacement. Equation (7) can be rewritten as follows:

$$\Delta\rho = C(J_{co}J_{serial})^{-T}J_{serial}^{T}w \tag{9}$$

Further, for a small displacement vector $\Delta\rho$, one has

$$\Delta\rho = J_{co}\Delta c \tag{10}$$

where Δc is a vector of small Cartesian displacement and rotation [7]. Plug Eq. (10) into (9), and rearrange the equation, the following can be derived,

$$\Delta c = J_{serial}(J_{co}J_{serial})^{-1}C(J_{co}J_{serial})^{-T}J_{serial}^{T}w \tag{11}$$

So the Cartesian compliance matrix is obtained as follows:

$$C_c = J_{serial}(J_{co}J_{serial})^{-1}C(J_{co}J_{serial})^{-T}J_{serial}^{T} \tag{12}$$

In order to implement the optimization process, the objective function should be first established.

(1) Objective function: $ObjF = \sum_{i=1}^{6} C_c(i,i)$

(2) Design variables and constraints are as follows:

$R_P \in [0.04, 0.15]\text{m}, R_b \in [0.4, 0.6]\text{m}, l_i \in [0.35, 0.5]\text{m}, angle1 \in [15°, 45°],$
$angle2 \in [15°, 45°]$

where R_b and R_p are the radii of the base and moving platform, $angle1$ is the angle between X axis and OB_1, and $angle2$ is between x axis and PP_1. The optimization result of the global compliance using DE is illustrated in Fig. 2.

By using differential evolution (DE) optimization algorithm, the optimal parameters are obtained as follows after about 50 generations, and illustration of the configuration of the mechanism after optimization is shown in Fig. 3.

$[R_P, R_b, L, angle1, angle2] = [0.15\,\text{m}, 0.5716\,\text{m}, 0.35\,\text{m}, 0.2740\,\text{rad}, 0.2995\,\text{rad}]$

4 Global Condition Index of the Mechanism

One found that making the parallel mechanisms have the maximum workspace volume could sometimes lead to bad kinematic performances, and later the global condition index [8] was proposed for workspace optimization in order to have a so

Fig. 2 Optimization result of global compliance
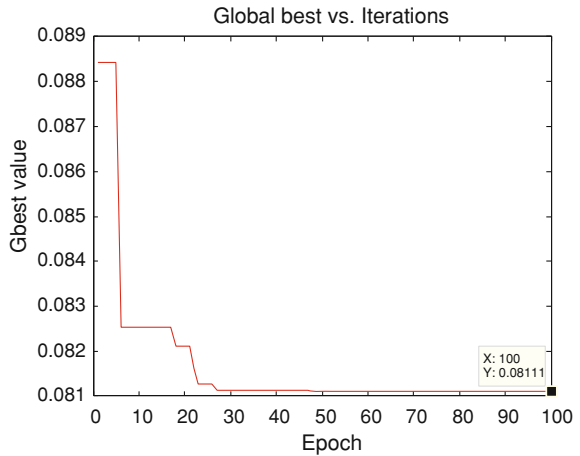
Fig. 3 The 3PU*S-PU mechanism after optimization
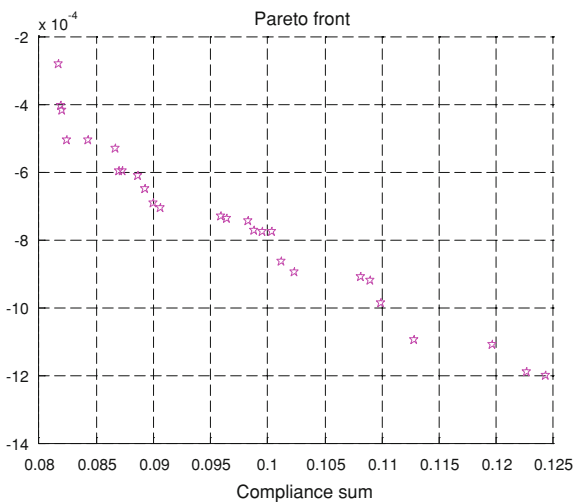
called "well-conditioned workspace". Here the index is used as an objective function for workspace optimization. The derivation process for the index is briefly described as follows: firstly, many points n_{total} are randomly selected in the possible workspace; secondly, we need to check whether each point falls inside of the workspace, this can be done by solving inverse kinematic for each actuated input to see if the prismatic joint is in the range of guide ways; thirdly, determine the kinematics condition index KCI for every point that falls in the workspace; finally, the global condition index η can be obtained by multiplying KCI and the possible workspace volume (pwv), then dividing by the total number of previously selected points n_{total}:
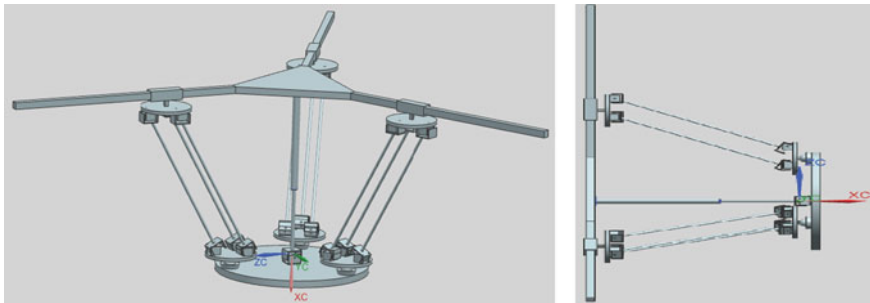
Fig. 4 Pareto front

$$\eta = pwv \cdot KCI/n_{total} \tag{13}$$

Using similar method, i.e. we can use GA, DE or PSO to single optimize the global condition index to have the maximum well-conditioned workspace, here we are not doing this anymore, we are straight going to the multi-objective optimization for the stiffness and workspace due to the fact that the stiffness and workspace normally conflict to each other.

5 Multi-objective Optimization

Normally, when the stiffness of the parallel manipulator is increased, the workspace of the parallel manipulator will be affected, and vice versa. One should always compromise between these two and find the optimal solution according to our specific design requirements and preferences. Here the objective function for the stiffness and workspace can be written as the sum of the leading diagonal elements of the compliance matrix and global condition index, respectively.

$$ObjF1 = \sum_{i=1}^{6} C_c(i,i);$$
$$ObjF2 = pwv \cdot KCI/n_{total}$$

After optimization, the Pareto front of compliance and global condition index is illustrated in Fig. 4. One can see that the compliance sum and the global condition index conflict to each other, which means if we want to have higher stiffness, we have to sacrifice the workspace, so the results are comprised. And one can see that there is no single optimum value, the optimal solution is not just one solution but rather several solutions, which are called non-dominated solutions. We can select from those results based on our requirements, different requirements may select different values, i.e. if we want higher stiffness and the workspace is not important,

Table 1 Typical results for objective functions and the corresponding design variables

R_P	R_b	L	$angle1$	$angle2$	Compliance sum	Global condition index
0.1491	0.4153	0.3547	0.3721	0.3735	0.0843	−0.0005
0.1489	0.4174	0.3881	0.3997	0.3656	0.1012	−0.0008
0.1498	0.4162	0.3619	0.3795	0.3733	0.0870	−0.0005
0.1486	0.4192	0.4265	0.4237	0.3746	0.1227	−0.0012

then we can select those higher value for stiffness and sacrifice some workspace. Here we give four typical results for the objective function and the corresponding design variables as shown in Table 1.

6 Conclusion

A novel 3DOF hybrid manipulator 3PU*S-PU which is based on the Gf set theory is proposed and analyzed. The advantages of this new type of manipulator are first briefly described, and then the relatively most important kinematic performances, i.e. stiffness/compliance and workspace, are analyzed and optimized by resorting to the differential evolution algorithm, finally, the multi-objective optimization on the compliance and workspace of the mechanism is implemented based on the Pareto front theory. The novelty of this new proposed Gf set based manipulator can be concluded as follows: firstly, by changing the original passive leg to PU type, the manipulator therefore has desired three degrees of freedom, secondly, by changing the structure of the middle passive leg, the whole parallel manipulator can be reconfigured, thirdly, by applying U* joints as three limbs instead of the conventional limbs, the stiffness of this hybrid/parallel manipulator can be greatly improved. The future work will focus on the nonlinear control of this new parallel manipulator based on the Lagrangian dynamics.

References

1. Liu, X.J., Wang, J.S., Pritschow, G.: A new family of spatial 3-DoF fully-parallel manipulators with high rotational capability. Mech. Mach. Theory **40**, 475–494 (2005)
2. Tsai, L.W.: Mechanism design: enumeration of kinematic structures according to function. CRC Press, Boca Raton (2001)
3. Salgado, O., Altuzarra, O., Petuya, V., et al.: Type synthesis of a family of 3T1R fully-parallel manipulators using a group-theoretic approach. In 12th IFToMM world congress on the theory of machines and mechanisms, Besancon, pp. 18–21 (2007)

4. Angeles, J., Caro, S., Khan, W., et al.: The kinetostatic design of an innovative Schonflies motion generator. Proc. Inst. Mech. Eng. Part C, J. Mech. Eng. Sci. **220**(C7), 935–944 (2006)
5. Gao, F., Yang, J.L., Ge, Q.D.: Gf set theory for the type synthesis of parallel manipulators. Science Press, Beijing (In Chinese) (2010)
6. Zhang, D., Gao, Z.: Hybrid head mechanism of the groundhog-like mine rescue robot. Robotics Comput. Integr. Manuf. **27**, 460–470 (2011)
7. Zhang, D.: Kinetostatic analysis and optimization of parallel and hybrid architectures for machine tools. Dissertation, Laval University (2000)
8. Stamper, R., Tsai, L.W., Walsh, G.: Optimization of a three DOF translational platform for well-conditioned workspace. In Proceedings of the IEEE international conference on robotics and automation, pp. 3250–3255 (1997)

Moving Mechanism Design and Analysis of Suspension Insulator Inspection Robot

Shujun Li, Hongguang Wang, Shichao Xiu, Xiaopeng Li and Zhaohui Ren

Abstract To drive synchronously and simply control system of insulator inspection robot, a single-driving moving mechanism of suspension insulator inspection robot is designed. The parallel transmission mechanism is designed to drive two sets of impeller shafts synchronously by single motor, which achieves synchronizing movement. Analysis and simulation are completed to verify structural parameters and kinematic performance of the moving mechanism. It is also discussed that the application of differential drive systems to obtain synchronizations of the driving branches and adjustment of structural errors of insulator strings.

Keywords Inspection robot · Moving mechanism · Parameter design · Analysis and simulation

S. Li (✉) · S. Xiu · X. Li · Z. Ren
College of Mechanical Engineering and Automation, Northeastern University,
Shenyang 110004, People's Republic of China
e-mail: shjunli@mail.neu.edu.cn

S. Xiu
e-mail: shchxiu@mail.neu.edu.cn

X. Li
e-mail: xpli@mail.neu.edu.cn

Z. Ren
e-mail: zhhren@mail.neu.edu.cn

S. Li · H. Wang
State Key Laboratory of Robotics of China, Shenyang 110016, China
e-mail: hgwang@sia.ac.cn

1 Introduction

Insulator deterioration of extra-high-voltage (EHV) transmission lines has a potential damage to the reliability of power supply, and online detection of insulator has important practical value. At present, many domestic and foreign researchers focus on the development of robotic detection devices, which accomplish insulator detection on live line instead of manual operation by line workers. Regarding the study of early detection of insulators in the 1980s [1, 2], Japan's Sumitomo Electric Machinery Co., Ltd. presented a patent of a poor insulator detection device, which can automatic crawl and detect double insulator string by mechanical automatic walking equipments [3]. In 1990s, many research works were published about online automatic cleaning and testing for EHV transmission line insulator [4–7]. Korea Electric Power Research Institute (KE-PRI) developed an automatic operation insulators robot for cleaning and inspection of insulator strings in 2006 [8]. This robot mechanism consists of upper and lower fixed frame body, middle cleaning mechanism and two picking mechanisms. During 2008 and 2009, KEPRI designed a kind of suspension insulator inspection robot [9]. The robot mechanism is dominated by a crawling module which is a combination of three legs, and the movement of each group impeller is drived by the motor individually. Crawling mechanism of the robot system is compact and light weight. In 2010, KEPRI produced the physical prototype of the robot and conducted experiments and testing on the transmission line [10]. This paper presents a crawling detection robot mechanism formed by two sets of single-impeller. The mechanism can drive two sets of impeller shaft synchronously by parallel transmission driven by single motor, which achieves synchronized movement. Analysis and simulation were completed to get structural parameters and kinematic performance of the moving mechanism.

2 Configuration Design of the Mechanism

2.1 Configuration Arrangement of the Overall Robot System

Suspension insulator inspection robot consists of impeller rotary moving mechanism, detection mechanism, and guiding mechanism. The mechanism sketch of the overall robot system is shown in Fig. 1, in which 1, 2, 3 and 4 is the impeller rotary movement mechanism, 5 and 6 is timing belt, 7 and 8 is a pair of transmission gear, 9 is the transmission mechanism of gear detection mechanism, 10 is the probe of detection mechanism, 11 is the detection mechanism of suspension insulator inspection robot and 12 is the insulator.
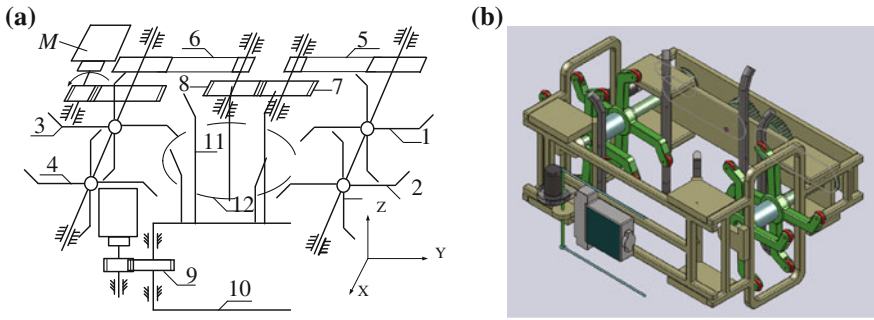
Fig. 1 The mechanism sketch, **a** 2D mechanism sketch **b** The 3D assembly model

2.2 Works of Suspension Insulator Inspection Robot

Works of impeller rotary moving mechanism: A motor *M* drives the impeller 3 and 4 through one pair of gears, drives gears 7 and 8 by timing belt 6, and drives the impeller 1 and 2 through timing belt 5, which makes suspension insulator inspection robot rise as a whole (or to balance gravity). The robot can be stopped in any position, so that the detection mechanism can implement inspect operation.

3 Parameter Design of the Mechanism

The length of impeller: as shown in Fig. 2, *a* is the Length of the impeller arms, the dotted line with an arrow is the movement direction of the impeller, *L* is the distance between the two insulators (*L* is also known as the height insulators), and *l* is the distance between adjacent impeller claws.

When $l = L$, impeller rotary moving mechanism can just stride over the insulator body skirt flash, and there is no impact force. So, the Length of the impeller claws *a* can be determined.

$$a = \sqrt{l^2/2} \tag{1}$$

The main dimensions of suspension insulators are structural height (*H*) and disc diameter (*D*), the design object in this paper is XP-210 suspension disc insulators with $H = 170$ (mm) and $D = 180$ (mm). Because $L = H = 170$ mm, make $l = L$, so $a = 120$ mm.

The distance between the two output axes of the impeller: as shown in Fig. 3, *d* is the distance between the two output axes of impellers, d_{min} and d_{max} are the maximum and minimum values of the distance.

Fig. 2 The schematic diagram of the optimal size of the impeller
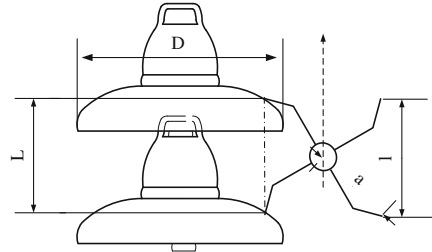
Fig. 3 The limit position diagram of the distance between the output shaft
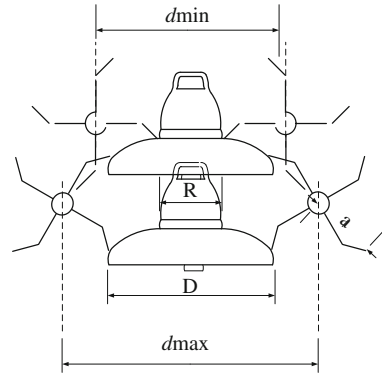
As shown in Fig. 3, $d_{\min}$ can be got:

$$d_{\min} = R + 2a \tag{2}$$

where, R is the diameter of the insulator iron cap.

The maximum distance between the two output shafts $d_{\max}$ is:

$$d_{\max} = D + \sqrt{2}a \tag{3}$$

Because $R = 140$ (mm) and $D = 280$ (mm), from formula (2) and formula (3), $d_{\min} = 380$ mm, $d_{\max} = 450$ mm. The value of d is in the range between $d_{\min}$ and $d_{\max}$, in order to reduce the weight of the robot system and get compact construction, so $d = 400$ (mm).

4 Kinematic Analysis of Suspension Insulator Inspection Robot

4.1 Geometry Modeling of Walking Track

The surface of the insulator sheds can be approximated as a conical surface. The coordinate of insulator's sheds is shown in Fig. 4.

Fig. 4 Coordinate of insulator's sheds
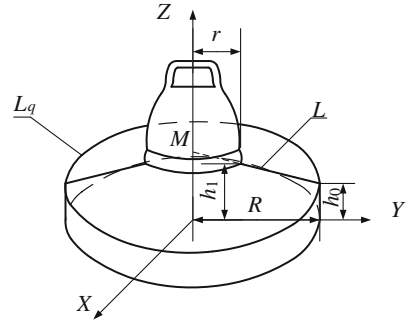
As shown in Fig. 4, L_q is the alignment of insulator sheds conical surface, L_n is the bus bar, L_n goes through two points (R, h_0) and (r, h_1), vertex M is the intersection of the axis Z and the bus bar L_n. Where, $r = \frac{1}{2}d = 60$ mm, $R = \frac{1}{2}D = 140$ mm, $h_0 = 57$ mm, $h_1 = 80$ mm. After the calculation, formula (4) can be obtained:

$$z = 97.25 - 0.2875y \qquad (4)$$

Formula (4) is the equation of bus bar L_n, and the coordinates of the vertices M is (0, 0, 97.25).

$$\begin{cases} x^2 + y^2 = 19600 \\ z = 57 \end{cases} \qquad (5)$$

Formula (5) is the equation of alignment L_q. For the conical surface equation, when vertex M, bus equation and alignment equation are known, so the conical surface equation can be deduced:

$$x^2 + y^2 - \frac{[140(97.25 - z)]^2}{40.25^2} = 0 \qquad (6)$$

The contact position of impeller is taken $x = \pm 42$ according to the structure design, walking trajectory equation of the rotating small wheel of impeller rotary moving mechanism is described in formula (7):

$$z = 97.25 - 0.2875\sqrt{y^2 + 1764} \qquad (7)$$

Fig. 5 Coordinate of main
moving mechanism
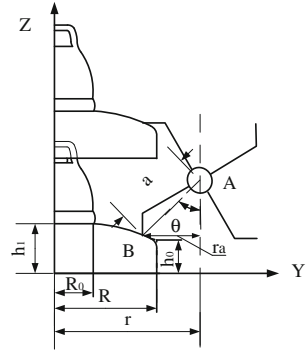
4.2 Kinematic Analysis

$r = d/2 = 200$ mm, $R = D/2 = 140$ mm, $R_0 = D_0/2 = 60$ mm, $h_0 = 57$ mm, $h_1 = 80$ mm, $a = 120$ mm. The coordinate of main moving mechanism of suspension insulator inspection robot is shown in Fig. 5; A is the center of impeller, B is the touching position of impeller and insulator. $r = d/2 = 200$ mm, $R = D/2 = 140$ mm, $R_0 = D_0/2 = 60$ mm, $h_0 = 57$ mm, $h_1 = 80$ mm, $a = 120$ mm. The relationship between position A of the moving mechanism and rotation angle θ of the impeller is established.

From Fig. 5, formula (8)–(10) can be deduced.

$$y_A = r \tag{8}$$

$$z_A = a\cos\theta + z_B \tag{9}$$

$$y_B = y_A - a\sin\theta \tag{10}$$

According to formula (7), coordinate expression of point B can be got as:

$$z_B = 97.25 - 0.2875\sqrt{y_B^2 + 1764} \tag{11}$$

The main moving mechanism position of suspension insulator inspection robot can be calculated.

$$\begin{cases} y_A = r \\ z_A = a\cos\theta + 97.25 - 0.2875\sqrt{(r - a\sin\theta)^2 + 1764} \end{cases} \tag{12}$$
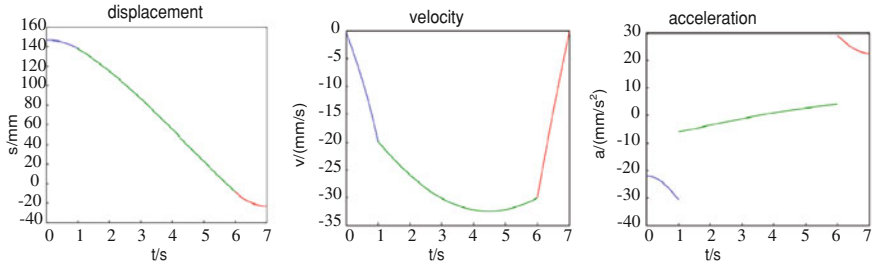
Fig. 6 The displacement, velocity and acceleration of the moving mechanism

It is known that the motor speed is 5(r/min), work time $t = 7$ s. The transmission ratio between drive motor and the output shaft is 2:1, so the rotation speed of the impeller mechanism is 2.5(r/min).

The rotation speed of the impeller mechanism is $\pi/12$ (rad/s), supposed that the motor accelerates to rated speed 1 s, so from rated speed to static is also 1 s. When position varies from $\theta_0 = 0.25\pi$ to $\theta_1 = 0.75\pi$, displacement, velocity and acceleration variation graphs of main moving mechanism are shown as in Fig. 6.

As shown in Fig. 6, the displacement stroke of the moving mechanism is probably 170 (mm), which accords with the distance L between two insulators in line insulator string (i.e. the height of insulators H). And the velocity of mechanism is no mutation, which indicates that the design of the moving mechanism is reasonable. Although the acceleration of the main moving mechanism occur mutations, it is permitted for the DC servo motor.

5 Mobile Detection Process Simulation of Suspension Insulator Inspection Robot

For impeller rotating mechanism, the motion characteristics (displacement, angular velocity and angular acceleration of the output shaft) in detection z are simulated. Simulation results are consistent with the motor speed, and the centroid position of the impeller changes continuously as shown in Fig. 7a. The velocity changed and the acceleration shocked between 3 and 4 s, because suspension insulator inspection robot is just transited from a contact with one insulator to a contact with two insulators during this time, which accords with the actual operating conditions. Simulation results (Fig. 7) show good motion characteristics of the mechanism.

Fig. 7 The motion
characteristics of the impeller
rotating mechanism
movement detection,
a displacement, **b** velocity,
c acceleration
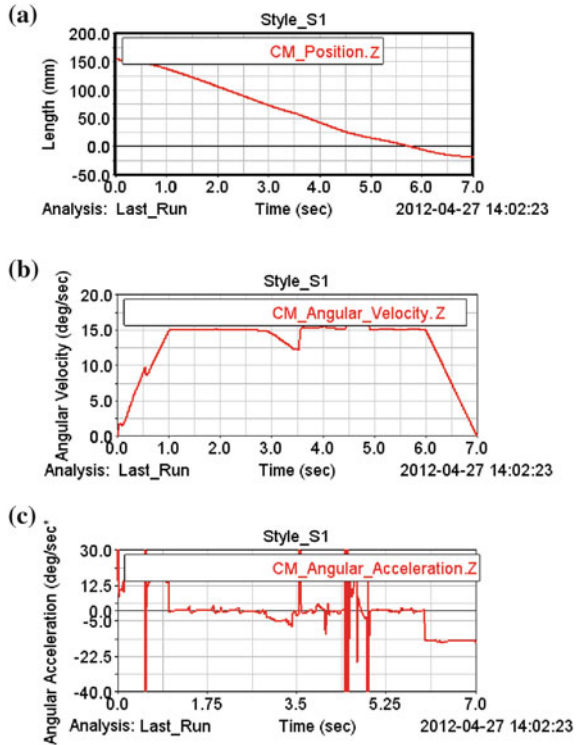
6 Conclusions

Analysis indicated that the moving mechanism of single-driving suspension insulator inspection robot designed in this paper can satisfy the operational requirements of suspension insulator detection, and can also achieve the crawling operations along the suspension V-shaped and L-shaped insulator string without considering manufacturing errors and mounting errors of the insulator string. It is necessary to verify the actual working ability of the moving mechanism by physical prototype experiment for suspension insulator inspection robot.

References

1. Devine, C.W.: Method and apparatus for testing insulators. U.S. Patent, no. 4.266.184 (1981)
2. Naito, K., Irie, T., Fujita, H., Kato, S.: Faulty insulator detector for transmission line. NGK Rev. **44**, 11–25 (1982)
3. Toshio, I., Toshiharu, M., Tetsuji, I.: Detector for defective insulator. Japan Patent, no. 57194364 (1982)
4. Bellerive, J.P.: Performance of porcelain insulators: forty years of experience at Hydro-Quebec. In: Canadian Electrical Association, Transmission Section, Spring Meeting, Montreal, Canada (1990)
5. Pairs, L.: Equipment to carry out maintenance operations, particularly washing, on insulator chains of high voltage electric lines. U.S. Patent, no. 5.119.851 (1992)
6. Yi, H., Jiansheng, C.: The research of the automatic washing-brushing robot of 500 kV DC insulator string. In: Proceedings of International Conference on Transmission and Distribution Construction and Live Line Maintenance, pp. 411–424 (1993)
7. Vaillancourt, G.H., Bellerive, J.P., StJean, M., Jean, C.: New live line tester for porcelain suspension insulators on high-voltage power lines. IEEE Trans. Power Deliv. **9**(1), 208–219 (1994)
8. Park, J.-Y., Cho, B.-H., Byun, S.-H.: Development of automatic cleaning robot for live-line insulators. In: IEEE 11th International Conference on Transmission and Distribution Construction, Operation and Live-line Maintenance, ESMO, pp. 1–4 (2006)
9. Park, J.-Y., Lee, J.-K., Cho, B.-H.: Development of inspection robot system for live-line suspension insulator strings in 345 kV power transmission lines. Control Autom. Syst. **6**, 2062–2065 (2008)
10. Park, J.-Y., Lee, J.-K., Cho, B.-H., Oh, K.-Y.: Development of advanced insulator inspection robot for 345 kV suspension insulator strings. In: Proceedings of the International MultiConference of Engineers and Computer Scientists, Hong Kong (2010)

Design of 4-DOF Parallelogram-Based RCM Mechanisms with a Translational DOF Implemented Distal from the End-Effector

A. Gijbels, D. Reynaerts and E. B. Vander Poorten

Abstract Numerous passive and active tool holders for minimally invasive surgery consisting of a remote center of motion (RCM) mechanism with four degrees of freedom (DOFs) have been developed. These are mostly serial mechanisms composed of three 1-DOF RCM mechanisms and a 1-DOF translation stage. In the vast majority, the translation stage is implemented proximal to the end-effector resulting into a heavy and voluminous end-effector. To provide easier access to the surgical site and facilitate use of multiple instruments and holders, this work elaborates on the design of 4-DOF parallelogram-based RCM mechanisms featuring a 1-DOF translation mechanism implemented distal from the end-effector. Kinematical design rules to develop such mechanisms are derived. Guidelines on how to apply these design rules and three interesting embodiments are given.

Keywords RCM mechanisms · Minimally invasive surgery · Robotics

1 Introduction

The shift towards less invasive surgical procedures is an ongoing trend in medicine. Minimally invasive surgery (MIS) is performed inside the patient's body using instruments that are inserted through small incisions in the body wall. Compared to open surgery, MIS results in less pain, trauma and recovery time for the patients. Disadvantages of MIS for the surgeon include reduced dexterity and poor vision. This has led to the development of numerous passive and active tool holders to assist surgeons during MIS [1].

A. Gijbels (✉) · D. Reynaerts · E. B. Vander Poorten
Department of Mechanical Engineering, University of Leuven, Leuven, Belgium
e-mail: gijbels@kuleuven.be

Fig. 1 During MIS, the tool shaft is allowed to move with four DOFs. The two translational DOFs in the plane tangential to the body wall could cause damage to the tissue
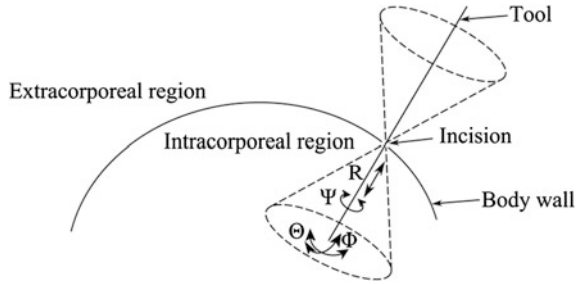
The incision ports used in MIS act as a kind of kinematical constraint on the mobility of the surgical tools. The incision port limits the degrees of freedom (DOFs) of the tool shaft from six to four (Fig. 1). These will be referred in the following as two rotations Θ and Φ about the incision, a rotation Ψ around the tool's axis and a translation R along the direction of the tool's axis and through the incision. A good tool holder provides undiminished access to these four DOFs while adhering to the two kinematical constraints and as such prevents excessive forces between the tool shaft and the surrounding tissue. However, it is undesirable to implement any physical joint at the incision because of spatial constraints, limited accessibility and sterilization issues. The rotational DOFs are rather implemented by virtue of a remote center of motion (RCM). An RCM is a fixed point in space about which a part of a mechanical system can rotate and which is located distal from any joint [2]. It is imperative to have an RCM located at the incision. Likewise, the translational DOF should be implemented using one or multiple joints located distal from the incision.

2 State-of-the-Art RCM Implementation

An RCM can be implemented through software (virtual RCM) or mechanically (mechanical RCM). A virtual RCM is realized through coordinated joint control of a multi-DOF robot. A mechanical RCM is realized with a specially designed mechanism, called a RCM mechanism. Virtual RCMs have as benefit that the location of the RCM can be easily adapted i.e. reprogrammed. However, many researchers advocate the use of mechanical RCMs [1]. First, using a mechanical RCM minimizes the number of actuators and thus the complexity of the system. Second, in case of a power failure, the tool holder maintains the RCM and therefore the tool cannot cause any harm to the tissue surrounding the incision.

Numerous RCM mechanisms have been reported in literature [3]. They can be grouped into serial and parallel mechanisms. Parallel RCM mechanisms have as advantage a high inherent stiffness. Furthermore, it is often easy to incorporate the actuation of all DOFs at the base of the mechanism, which limits the mechanism's inertia. This typically results in a high-bandwidth system. Serial RCM mechanisms
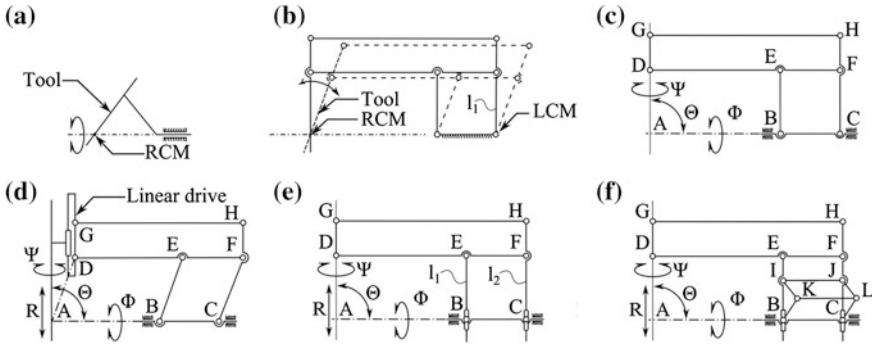
Fig. 2 State-of-art parallelogram-based RCM mechanisms

are popular because of their mechanical simplicity, easy control and larger and more isotropic workspace per mechanism volume.

Serial multi-DOF RCM mechanism are composed out of different 1-DOF RCM mechanisms. Zong et al. introduced six types of such mechanisms. Especially the revolute joint and double-parallelogram RCM mechanism are very popular. In case of a revolute joint (Fig. 2a), all points on the axis of a revolute joint, excluding the points enclosed within the joint, can be considered as RCMs. Figure 2b shows a double-parallelogram RCM mechanism. Here, two parallelograms copy the rotation of a linkage l_1 about a local center of motion (LCM) distal from the tool. By doing so the tool will rotate about the RCM.

A popular 3-DOF RCM mechanism for MIS tool holders combines two 1-DOF revolute joint RCM mechanisms to implement rotations Φ and Ψ and a 1-DOF double-parallelogram RCM mechanism to implement the Θ-rotation (Fig. 2c) [4]. A linear drive mechanism is commonly added proximal to the end-effector to create a translational DOF (Fig. 3d). Mechanisms like the one of Taylor are widely applied because of their simplicity and relatively large workspace. However, for many MIS applications, such a heavy and voluminous end-effector is undesirable. For example, in microsurgical applications where instruments needs to move in a highly confined space below a voluminous microscope [5]. When space is an issue, it is desirable to use a 4-DOF RCM mechanism with a translational DOF implemented distal from the end-effector. Only a few mechanisms of this type have been reported. These mechanisms all consist of a prismatic joint at points B and C (Fig. 2e). In order to guarantee a stable RCM, the translations of linkages l_1 and l_2 need to be synchronized. This is done either actively by using two synchronized actuators [6] or passively by adding a synchronization mechanism (Fig. 2f) [4]. However, calculating the number of DOFs of the latter mechanism shows that it is in fact overconstrained. DOFs R and Θ are only decoupled when the opposing linkages are equal in length or when play or flexibility is introduced into the mechanism. Such mechanism characteristics are disadvantageous in applications where precision matters.
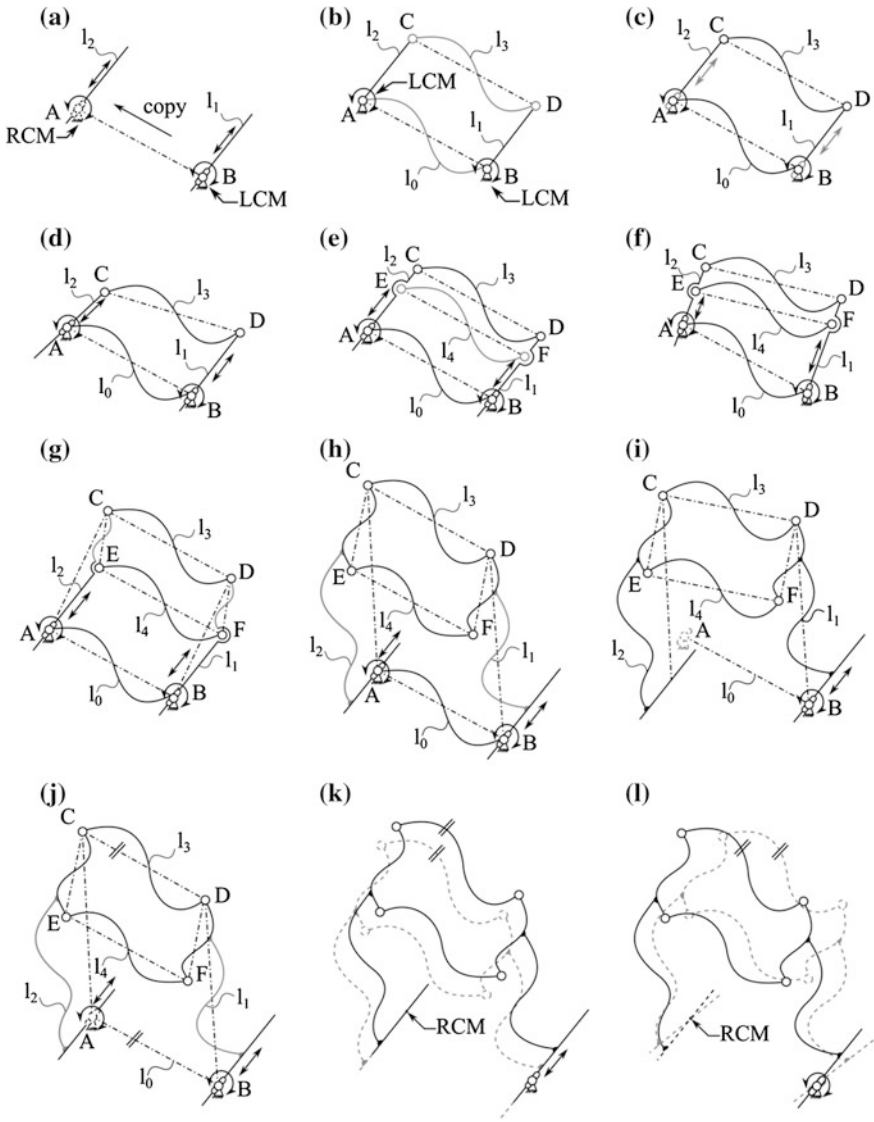
Fig. 3 Derivation of the kinematical design rules to copy motions R and Θ from a distal linkage l_1 at an LCM to a linkage l_2 at a stable RCM

3 Kinematical Design Rules for Stable 4-DOF Parallelogram-Based RCM Mechanisms with a Distal Translational DOF

This section is dedicated to the derivation of kinematical design to develop stable 4-DOF parallelogram-based RCM mechanisms with a translational DOF implemented distal from the end-effector. DOFs Φ and Ψ are omitted in this derivation since their implementation, using a 1-DOF revolute joint RCM mechanism, is trivial. Therefore, the goal is to derive kinematical design rules to copy motions R and Θ from a distal linkage l_1 at an LCM to a linkage l_2 at a stable RCM (Fig. 3a). The prismatic and revolute joint at the RCM are dashed in this figure to indicate that these components are non-physical. The derivation is split into two steps. First, two LCMs are considered to derive the design rules to copy motions R and Θ from one LCM to another. Second, the kinematical design rules are derived to transform one of the LCMs into a stable RCM.

In the absence of a translational DOF, the orientation of linkage l_1 can be copied to linkage l_2 by coupling the linkages in a parallelogram configuration ACDB using two arbitrarily shaped linkages l_0 and l_3 and four revolute joints (Fig. 3b). A prismatic joint at points A and B is needed to add the translational DOF at both LCMs (Fig. 3c). Unfortunately, the resulting mechanism has three instead of two DOFs. The third DOF destabilizes parallelogram ACDB and therefore desynchronizes the linkages' rotation and translation (Fig. 3d). An additional linkage l_4 connected to l_1 and l_2 with revolute joints F and E respectively eliminates this third DOF (Fig. 3e). Hereby, a new parallelogram ECDF is formed, which forces l_1 and l_2 to remain parallel at all times. It must be mentioned that linkage l_4 cannot guarantee at all times identical translations of l_1 and l_2. A transition of parallelogram ACDB into an isosceles trapezoid is possible when ACDB reaches a rectangular shape (Fig. 3f). When forming an isosceles trapezoid, l_1 and l_2 will translate with identical magnitude but in opposite direction. This issue will be dealt with later on in this derivation. Since linkages l_1 and l_2 were chosen to be straight, joints A, E and C and joints B, F and D respectively are collinear. This is however an unnecessary kinematical constraint. When linkages l_1 and l_2 are equally bended and non-collinear joints are used, the motions of l_1 and l_2 can still be synchronized (Fig. 3g). In fact, to guarantee motion synchronization between l_1 and l_2, it is sufficient that the two prismatic joints are initially chosen parallel and that parallelograms ACDB and ECDF exist and share the opposing linkages l_1 and l_2. These conditions result in a general mechanism (Fig. 3h) to copy motions R and Θ from one LCM to another.

Next, one could remove the physical joints at A when trying to create an RCM if this would not introduce an additional DOF into the mechanism as shown in Fig. 3i. Such extra DOF destabilizes the imaginary parallelogram ACDB and desynchronizes the motion of l_1 and l_2 (Fig. 3i). It is sufficient that linkage l_3 and the imaginary linkage l_0 remain parallel in order to synchronize the motions of l_1 and l_2 (Fig. 3j). This condition guarantees a stable RCM for both translations
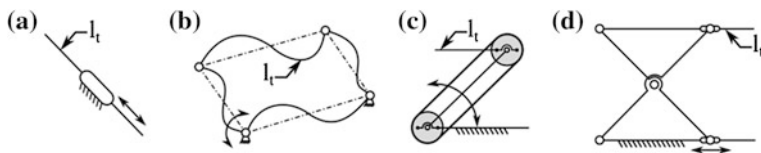
Fig. 4 Embodiments of 1-DOF translation mechanisms. **a** Prismatic joint. **b** Parallelogram. **c** Synchronous transmission. **d** Lift mechanism [2]

(Fig. 3k) and rotations (Fig. 3l) of these linkages. Note that by definition, this kinematical condition also keeps the imaginary parallelogram ACDB from transforming into an isosceles trapezoid. In order to comply with this kinematical condition, it is mandatory that the orientation of linkage l_3 remains unchanged for any motion of linkages l_1 and l_2. This can be done by connecting linkage l_3 rigidly to a 2-DOF translation mechanism. Both parallel and serial 2-DOF translation mechanisms exist. Figure 4 depicts four examples of 1-DOF translation mechanisms that can be connected in series to form a 2-DOF translation mechanism. The translating linkages, at which connections must be made, are indicated as l_t.

4 Guidelines on How to Apply the Kinematical Design Rules

Figure 5 demonstrates how to apply the derived kinematical design rules when developing a stable 2-DOF parallelogram-based RCM mechanism with a translational DOF implemented distal from the end-effector.

Step 1   Choose an arbitrary but appropriate location for a RCM and a LCM consisting of a revolute and prismatic joint

Step 2   Connect parallel linkages l_1 and l_2 to the LCM and the RCM respectively

Step 3   Position revolute joints C and D at a convenient arbitrary but equal relative position with respect to the RCM and the LCM respectively. Connect joints C and D with a linkage l_3. Note that this in fact implements a virtual parallelogram ACDB

Step 4   Introduce revolute joints E and F and linkages l_4, l_5 and l_6 to form an arbitrary but appropriate parallelogram ECDF

Step 5   Unite linkage l_5 with linkage l_1 and linkage l_6 with linkage l_2 using arbitrary but appropriate rigid connections

Step 6   Choose a 2-DOF translation mechanism and rigidly connect its 2-DOF translation linkage l_t rigidly to linkage l_3

Figure 5g and h demonstrate the stability of RCM for a translation and a rotation of linkage l_1 respectively.
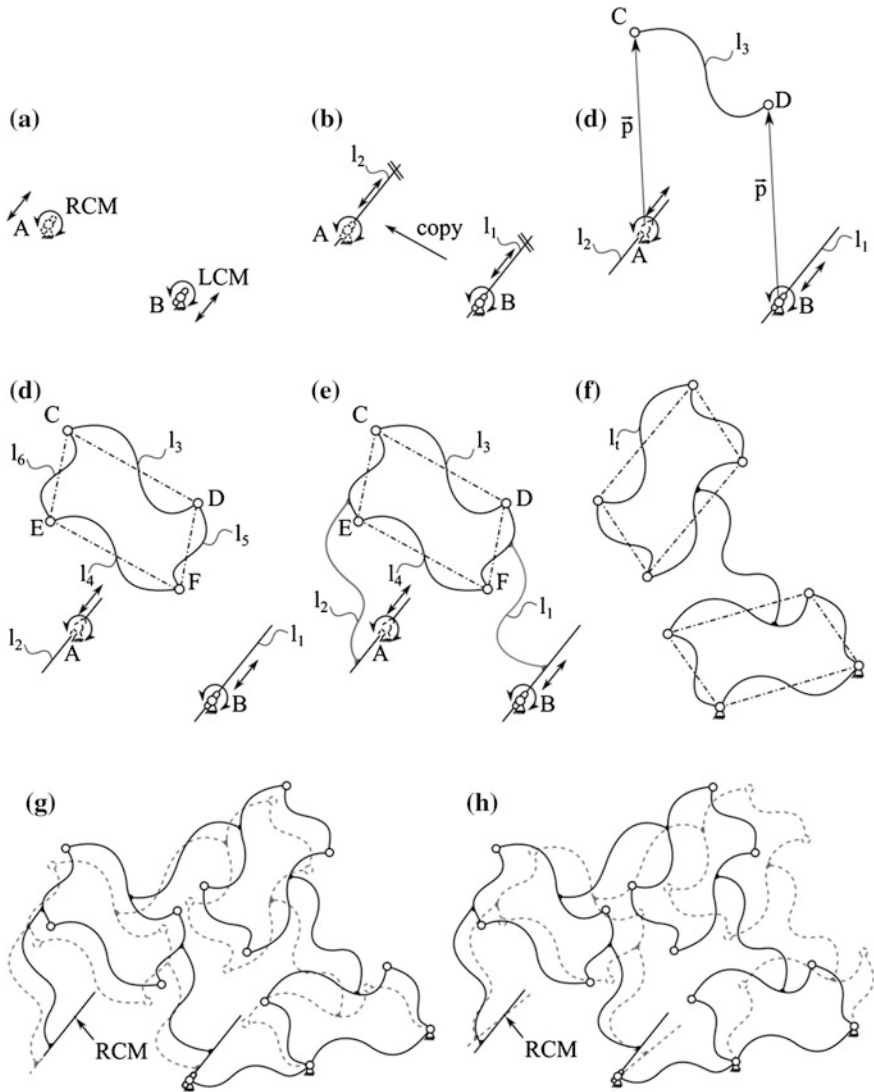
Fig. 5 Guidelines on how to apply the derived kinematical design rules. **a** Step 1. **b** Step 2.
c Step 3. **d** Step 4. **e** Step 5. **f** Step 6. **g** Translation. **h** Rotation

Figure 6 depicts three examples of stable 4-DOF parallelogram-based RCM
mechanisms with a distal translational DOF. Figure 6a shows an embodiment with
two stacked parallelograms as a 2-DOF translation mechanism [5]. The second
embodiment uses two prismatic joint mechanisms in series as a 2-DOF translation
mechanism (Fig. 6b). Notice that in this embodiment, the RCM and revolute joints
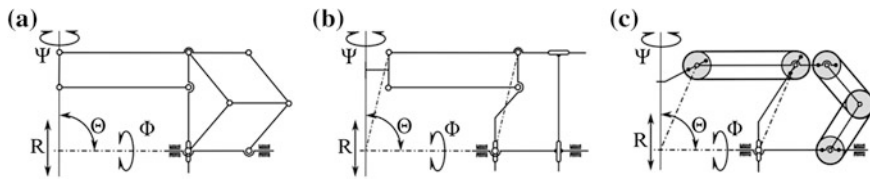
Fig. 6 Three embodiments of a stable 3-DOF parallelogram-based RCM mechanism with a distal translational DOF

C and E are chosen non-collinear. This results in an even smaller end-effector. The third embodiment uses two synchronous transmissions in series as a 2-DOF translation mechanism (Fig. 6c). Note that an additional synchronous transmission replaces parallelogram ECDF.

5 Conclusion

RCM mechanisms are widely used as tool holders for MIS interventions. When aligning the RCM with the incision into the body damage to surrounding tissue can be kept to a minimum. Many mechanisms adopt a serial parallelogram-based configuration with a bulky translational DOF implemented at the end-effector. For many MIS applications where only limited working space is available at the level of the incision, implementing the translational DOF distal from the end-effector is more favorable. So far, only a limited number of such mechanisms does exist, current designs have limitations in achievable precision and RCM stability. This paper derives kinematical design rules to develop stable 4-DOF parallelogram-based RCM mechanism with a translational DOF distal from the end-effector. Guidelines on how to apply these kinematical design rules were presented and three examples of such mechanisms were given. While the current derivation focused on combinations of revolute joints and a double-parallelogram mechanism, future work will study how other types of 1-DOF RCM mechanisms can be employed to create compact 4DOF RCM mechanisms.

References

1. Taylor, R., Stoianovici, D.: Medical robotics in computer-integrated surgery. IEEE Trans. Robot. Autom. **19**, 765–781 (2003)
2. Zong, G., et al.: Classification and type synthesis of 1-DOF remote center of motion mechanisms. Mech. Mach. Theory **43**, 1585–1595 (2008)
3. Kuo, C.H., et al.: Kinematic design consideration for MIS robots: an overview. The Int. J. Med. Robotics Comput. Assist. Surg. **8**, 127–145 (2012)
4. Taylor, R., et al.: RCM robot for surgery. US patent 5397323 (1995)

5. Gijbels, A., et al.: Design and realisation of a novel robotic manipulator for retinal surgery. Int. Conf. Intell. Robot. Syst. (2013)
6. Davies, B., et al.: Neurobot: a special-purpose robot for NeuroSurgery. Int. conf. Robot. Autom. (ICRA), 4103–4108 (2000)

Rotational Axes Analysis of the 2-RPU/SPR 2R1T Parallel Mechanism

Yundou Xu, Shasha Zhou, Jiantao Yao and Yongsheng Zhao

Abstract This paper presents a novel 2-RPU/SPR 2R1T parallel mechanism, which has one translational degree of freedom (DOF) and two rotational DOFs. The properties of the rotational axes of the mechanism are analyzed by using screw theory, and the results show that the 2-RPU/SPR mechanism has two rotational continuous axes. The position analysis of the 2-RPU/SPR mechanism is also carried out. The proposed 2R1T mechanism has very simple kinematic model, which reduces difficulties in calibrating kinematic parameters.

Keywords 2R1T parallel mechanism · Screw theory · Continuous rotation axes · Position analysis

1 Introduction

The 2R1T parallel mechanism (PM) is an important category of the lower-mobility PMs [1], which has one translational DOF and two rotational DOFs. Since Hunt proposed the 3-RPS parallel mechanism in 1983 [3], the 2R1T lower-mobility PM has attracted a lot of attention. For instance, Z3 head (3-PRS mechanism) in machine tool [10], the parallel part of the Exechon kinematically equal to a 2-UPR-SPR PM, these are typical examples of success. The 2R1T PM was also implemented in many applications such as telescope application, motion simulator [8] micro-manipulator, and coordinate measuring machine [6]. Therefore, the

Y. Xu (✉) · S. Zhou · J. Yao · Y. Zhao
Parallel Robot and Mechatronic System Laboratory, Yanshan University, Qinhuangdao 066004, Hebei, People's Republic of China
e-mail: ydxu@ysu.edu.cn

Y. Zhao
e-mail: yszhao@ysu.edu.cn
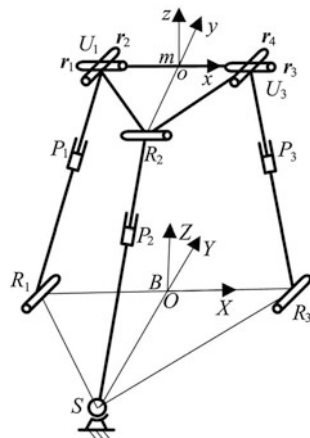
kinematics analysis, dimensional synthesis [9], singularity analysis [5] and
dynamics analysis [2] of the 2R1T parallel mechanism have been extensively
studied. The notation of R denotes a revolute pair, P a prismatic pair, S a spherical
joint, and U a universal joint.

For the 2R1T PM, two translational motions are restricted, the rotational axes
cannot be chosen arbitrarily, which is also called as incomplete rotation. Instan-
taneous rotational axes and continuous rotational axes are two types of rotational
axes of the PM. If the moving platform can only rotate around the rotational axes
in a specified pose, such axes are rotational instantaneous axes. Otherwise, the
moving platform can rotate around the rotation axes continually, the rotational
axes are named rotational continuous axes. Some investigations on the rotation
axes of the 2R1T PM can be found [4], and the analysis results show that the 2-
PRS/PRRU parallel mechanism without parasitic motion has two continuous
rotational axes, the 2-UPR/SPR overconstrained PM has also two continuous
rotational axes [7]. However, except the above-mentioned two kinds of 2R1T PMs,
very few 2R1T PMs with two continuous rotational axes have been reported.
Therefore, a novel 2R1T PM with two continuous rotational axes will be proposed,
and the properties of rotational axes will be analyzed.

2 Rotational Axes Analysis of a 2-RPU/SPR Parallel Mechanism

As shown in Fig. 1, a novel 2-RPU/SPR 2R1T PM is composed of a moving
platform, a fixed base, two RPU supporting limbs, and a SPR supporting limb. The
three points, S, R_1, and R_3, on the base constitute an isosceles triangle with
$SR_1 = SR_3$. Another three points, U_1, R_2, and U_3, on the moving platform also
constitute an isosceles triangle with $R_2U_1 = R_2U_3$. The limb RPU connects the

moving platform to the base by a U joint on the moving platform at U_i ($i = 1, 3$), an actuated P joint along the limb, and the R joint on the base at R_i in sequence. The axis of the U joint within the $R_1P_1U_1$ limb, proximal to the base, is denoted by r_1, and that closes to the moving platform is denoted by r_2. The axis of the U joint within the $R_3P_3U_3$ limb, proximal to the base, is denoted by r_3, and that closes to the moving platform is denoted by r_4. The SPR limb connects the moving platform to the base by the R joint on the moving platform at R_2, an actuated P joint along the limb, and the S joint on the base at S in sequence.

For the RPU limb, the axis of the R joint is parallel to the axis of the U joint connecting to the base, the axis of the actuated P joint is perpendicular to the axis of the R joint, the axes of the R joints of two UPR limbs are parallel to each other, and r_1 and r_3 are aligned. The axis of the R joint within the SPR limb is parallel to r_1 and r_3.

When the mechanism is in the initial configuration, the points R_1, R_3, U_1, and U_3 are located on a same plane, and the plane is perpendicular to the planes SR_1R_3 and $U_1R_2U_3$, the vector $\boldsymbol{Oo}$ is also perpendicular to the planes SR_1R_3 and $U_1R_2U_3$, in which O and o are mid-points of R_1R_3 and U_1U_3 respectively. The vector $\boldsymbol{SO}$ is parallel to the axis of the R joint within the RPU limb.

For the purpose of analysis, a fixed coordinate frame B: O-XYZ is attached at point O on the base, with Y-axis pointing along vector $\boldsymbol{SO}$ and X-axis parallel to vector $\boldsymbol{R_1R_3}$. A moving coordinate frame m: o-xyz is attached at point o on the moving platform, with x-axis pointing along vector $\boldsymbol{U_1U_3}$, y-axis parallel to vector $\boldsymbol{R_2o}$, and z-axis perpendicular to the plane $U_1R_2U_3$, just as shown in Fig. 1.

2.1 Rotational Axes Analysis of PM in the Initial Configuration

When moving platform in the initial configuration, in the fixed frame B, the coordinate of point R_i is $[x_{Ri}\ \ 0\ \ 0]^T$, the coordinate of point U_i is $[x_{Ui}\ \ y_{Ui}\ \ z_{Ui}]^T$, the coordinate of S is $[0\ \ y_S\ \ 0]^T$, the coordinate of point R_2 is $[x_{R2}\ \ y_{R2}\ \ z_{R2}]^T$.

The twist system of limb $R_iP_iU_i$ with respect to the fixed frame B is given by

$$\begin{cases} \$_{i1} = [0\ \ 1\ \ 0\ \ 0\ \ 0\ \ -x_{Ri}]^T \\ \$_{i2} = [0\ \ 0\ \ 0\ \ L_i\ \ 0\ \ N_i]^T \\ \$_{i3} = [1\ \ 0\ \ 0\ \ 0\ \ -z_{Ui}\ \ 0]^T \\ \$_{i4} = [0\ \ 1\ \ 0\ \ z_{Ui}\ \ 0\ \ -x_{Ui}]^T \end{cases} \qquad (1)$$

where $[L_i\ 0\ N_i]^T$ denotes the unit vector along the axis of prismatic joint within the limb $R_iP_iU_i$.

The constraint wrenches supplied by the limb $R_iP_iU_i$ can be identified in the fixed frame B as

$$\begin{cases} \$_{i1}^r = [\,0 \quad 0 \quad 0 \quad 0 \quad 0 \quad 1\,]^T \\ \$_{i1}^r = [\,0 \quad 1 \quad 0 \quad z_{Ui} \quad 0 \quad \lambda\,]^T \end{cases} \tag{2}$$

where $\$_{i1}^r$ denotes a constraint couple, whose direction is parallel to the Z-axis, $\$_{i2}^r$ denotes a constraint force that is parallel to the Y-axis and passes through point U_i, and λ is an arbitrary value.

The twist system of limb SP_2R_2 with respect to the fixed frame B is given by

$$\begin{cases} \$_{21} = [\,1 \quad 0 \quad 0 \quad 0 \quad 0 \quad y_S\,]^T \\ \$_{22} = [\,0 \quad 1 \quad 0 \quad 0 \quad 0 \quad 0\,]^T \\ \$_{23} = [\,0 \quad 0 \quad 1 \quad -y_S \quad 0 \quad 0\,]^T \\ \$_{24} = [\,0 \quad 0 \quad 0 \quad 0 \quad M_2 \quad N_2\,]^T \\ \$_{25} = [\,1 \quad 0 \quad 0 \quad 0 \quad -z_{R2} \quad y_{R2}\,]^T \end{cases} \tag{3}$$

where $[0 \ M_2 \ N_2]^T$ denotes the unit vector along the axis of $\underline{P}$ joint within the limb SP_2R_2.

The constraint wrench supplied by the limb SP_2R_2 can be identified in the fixed frame B as

$$\$_{21}^r = [\,1 \quad 0 \quad 0 \quad 0 \quad 0 \quad y_S\,]^T \tag{4}$$

where $\$_{21}^r$ denotes a constraint force that is parallel to the x-axis and passes through point S.

The twist system of the 2-R$\underline{P}$U/S$\underline{P}$R 2R1T PM with respect to the fixed frame B can be calculated as

$$\begin{cases} \$_1^{pm} = [\,0 \quad 0 \quad 0 \quad 0 \quad 0 \quad 1\,]^T \\ \$_2^{pm} = [\,0 \quad 1 \quad 0 \quad 0 \quad 0 \quad 0\,]^T \\ \$_3^{pm} = [\,1 \quad 0 \quad 0 \quad 0 \quad -z_{U1} \quad 0\,]^T \end{cases} \tag{5}$$

where $\$_1^{pm}$ denotes a translational DOF along Z-axis, $\$_2^{pm}$ denotes a rotational DOF, whose axis is parallel to the Y-axis and passes through point O, that is, points along vector SO, and $\$_3^{pm}$ also denotes a rotational degree of freedom, whose axis points along vector U_1U_3.

The configuration of 2-R$\underline{P}$U/S$\underline{P}$R parallel mechanism is shown in Fig. 2 after the moving platform rotates only around the Y-axis in the fixed frame B.

The constraint wrenches supplied by the limb $R_iP_iU_i$ can be identified in the fixed frame B as

Fig. 2 The configuration after rotation around the Y-axis in frame B

$$\begin{cases} \$_{i1}^r = \begin{bmatrix} 0 & 0 & 0 & n_{12} & 0 & -l_{12} \end{bmatrix}^T \\ \$_{i2}^r = \begin{bmatrix} 0 & 1 & 0 & z_{Ui}' & 0 & -x_{Ui}' \end{bmatrix}^T \end{cases} \tag{6}$$
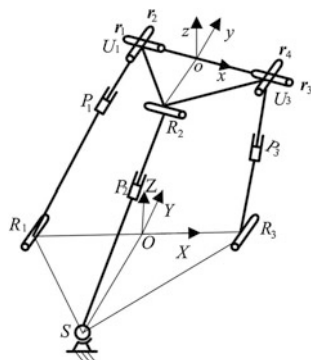
where $\begin{bmatrix} l_{12} & 0 & n_{12} \end{bmatrix}^T$ denotes the unit vector of r_1 and r_3 after the moving platform's rotation around the Y-axis in fixed frame B, $\begin{bmatrix} x_{Ui}' & 0 & z_{Ui}' \end{bmatrix}^T$ denotes coordinate of points U_i in the fixed frame B.

The constraint wrench supplied by the limb SP_2R_2 can be identified in the fixed frame B as

$$\$_{21}^r = \begin{bmatrix} l_{12} & 0 & n_{12} & -n_{12}y_S & 0 & l_{12}y_S \end{bmatrix}^T \tag{7}$$

where $\begin{bmatrix} n_{12} & m_{22} & -l_{12} \end{bmatrix}^T$ is the direction cosines of the axis of $\underline{P}$ joint within the limb SP_2R_2.

Thus, the twist system of the 2-RPU/SPR PM with respect to the fixed frame B can be calculated as

$$\begin{cases} \$_1^{pm} = \begin{bmatrix} 0 & 0 & 0 & n_{12} & 0 & -l_{12} \end{bmatrix}^T \\ \$_2^{pm} = \begin{bmatrix} 0 & 1 & 0 & 0 & 0 & 0 \end{bmatrix}^T \\ \$_3^{pm} = \begin{bmatrix} l_{12} & 0 & n_{12} & 0 & n_{12}x_U' - l_{12}z_U' & 0 \end{bmatrix}^T \end{cases} \tag{8}$$

The configuration of 2-RPU/SPR parallel mechanism is shown in Fig. 3 after the moving platform rotates around the x-axis in the moving frame m.

In this situation, the twist system and the constraint wrenches of limb $R_iP_iU_i$ do not change compared with the situation that the PM is the initial configuration.

The constraint wrench supplied by the limb SP_2R_2 can be identified in the fixed frame B as

Fig. 3 The configuration after rotation around the x-axis in frame m
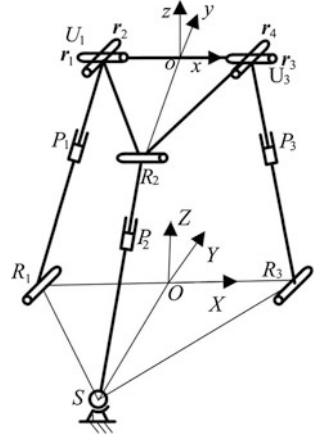
Fig. 4 The configuration after rotation around the Y-axis and the moving x-axis

$$\$_{21}^r = \begin{bmatrix} 1 & 0 & 0 & 0 & 0 & y_S \end{bmatrix}^T \tag{9}$$
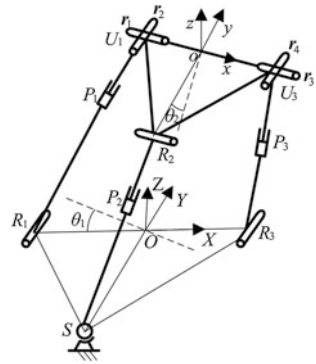
where $\begin{bmatrix} 0 & y_S' & 0 \end{bmatrix}^T$ denotes coordinate of point S in the fixed frame B after the moving platform's rotation around the x-axis in moving frame m.

As a result, the twist system of the 2-R$\underline{P}$U/S$\underline{P}$R PM with respect to the fixed frame B can then be obtained as

$$\begin{cases} \$_1^{pm} = \begin{bmatrix} 0 & 0 & 0 & 0 & 0 & 1 \end{bmatrix}^T \\ \$_2^{pm} = \begin{bmatrix} 0 & 1 & 0 & 0 & 0 & 0 \end{bmatrix}^T \\ \$_3^{pm} = \begin{bmatrix} 1 & 0 & 0 & 0 & -z_{U1} & 0 \end{bmatrix}^T \end{cases} \tag{10}$$

The configuration of 2-R$\underline{P}$U/S$\underline{P}$R parallel mechanism is shown in Fig. 4 after the moving platform rotates around the fixed Y-axis and the moving x-axis simultaneously.

The constraint wrenches of limb $R_iP_iU_i$ are the same as the wrenches when the PM in the configuration after the moving platform rotates around the Y-axis in the fixed frame B.

The constraint wrench supplied by the limb SP_2R_2 can be identified in the fixed frame B as

$$\$_{21}^r = \begin{bmatrix} l_{12} & 0 & n_{12} & -n_{12}y_S & 0 & l_{12}y_S \end{bmatrix}^T \tag{11}$$

which is also identical with that in the situation when the PM in the configuration after the moving platform rotates around the Y-axis in the fixed frame B.

Obviously, the twist system of the PM is also expressed as

$$\begin{cases} \$_1^{pm} = \begin{bmatrix} 0 & 0 & 0 & n_{12} & 0 & -l_{12} \end{bmatrix}^T \\ \$_2^{pm} = \begin{bmatrix} 0 & 1 & 0 & 0 & 0 & 0 \end{bmatrix}^T \\ \$_3^{pm} = \begin{bmatrix} l_{12} & 0 & n_{12} & 0 & n_{12}x'_{U1} - l_{12}z'_{U1} & 0 \end{bmatrix}^T \end{cases} \tag{12}$$

From the above analysis, it can be seen that the Y-axis in the fixed frame B and the x-axis in the moving frame m are always the rotational axes of the moving platform, so the Y-axis in the fixed frame B and the x-axis in the moving frame m are two continuous rotational axes of the PM.

3 Position Analysis of the 2-R<u>P</u>U/S<u>P</u>R Parallel Mechanism

Since the fixed Y-axis and moving x-axis are two continuous rotational axes of the PM, the homogeneous transformation matrix from the moving frame m to the fixed frame B can be described directly as

$$\begin{aligned} {}_m^B\mathbf{T} &= Rot(\mathbf{Y}, \theta_1)Trans(0 \quad 0 \quad d)Rot(\mathbf{x}, \theta_2) \\ &= \begin{pmatrix} \cos\theta_1 & 0 & \sin\theta_1 & 0 \\ 0 & 1 & 0 & 0 \\ -\sin\theta_1 & 0 & \cos\theta_1 & 0 \\ 0 & 0 & 0 & 1 \end{pmatrix} \begin{pmatrix} 1 & 0 & 0 & 0 \\ 0 & 1 & 0 & 0 \\ 0 & 0 & 1 & d \\ 0 & 0 & 0 & 1 \end{pmatrix} \begin{pmatrix} 1 & 0 & 0 & 0 \\ 0 & \cos\theta_2 & -\sin\theta_2 & 0 \\ 0 & \sin\theta_2 & \cos\theta_2 & 0 \\ 0 & 0 & 0 & 1 \end{pmatrix} \\ &= \begin{pmatrix} \cos\theta_1 & \sin\theta_1\sin\theta_2 & \sin\theta_1\cos\theta_2 & d\sin\theta_1 \\ 0 & \cos\theta_2 & -\sin\theta_2 & 0 \\ -\sin\theta_1 & \cos\theta_1\sin\theta_2 & \cos\theta_1\cos\theta_2 & d\cos\theta_1 \\ 0 & 0 & 0 & 1 \end{pmatrix} \end{aligned} \tag{3}$$

where θ_1 and θ_2 represent the angles that the moving platform rotates around the Y-axis and x-axis, respectively, and d denotes the displacement that the moving platform translates along the z-axis in the moving frame m.

The position vectors of U_1, R_2 and U_3 can then be obtained in the fixed frame B as

$$
\begin{cases}
U_1^B = [x_{U1}c\theta_1 + z_{U1}s\theta_1 c\theta_2 + ds\theta_1 - z_{U1}s\theta_2 - x_{U1}s\theta_1 + z_{U1}c\theta_1 c\theta_2 + dc\theta_1]^T \\
R_2^B = [x_{R2}c\theta_1 + y_{R2}s\theta_1 s\theta_2 + z_{R2}s\theta_1 c\theta_2 + ds\theta_1 y_{R2}c\theta_2 - z_{R2}s\theta_2 \\
\qquad - x_{R2}s\theta_1 + y_{R2}c\theta_1 s\theta_2 + z_{R2}c\theta_1 c\theta_2 + dc\theta_1]^T \\
U_3^B = [x_{U3}c\theta_1 + z_{U3}s\theta_1 c\theta_2 + ds\theta_1 - z_{U3}s\theta_2 - x_{U3}s\theta_1 + z_{U3}c\theta_1 c\theta_2 + dc\theta_1]^T
\end{cases}
\tag{14}
$$

Then, the length of there actuated limbs can be obtained as

$$
\begin{cases}
l_i = \sqrt{(^Bx_{Ui} - x_{Ri})^2 + {}^By_{Ui}^2 + {}^Bz_{Ui}^2}, \; i = 1, 3 \\
l_2 = \sqrt{{}^Bx_{R2} + (^By_{R2} - y_S)^2 + {}^Bz_{R2}^2}
\end{cases}
\tag{15}
$$

4 Conclusion

In this paper, a novel 2R1T mechanism 2-RPU/SPR is proposed, and rotational axes of the PM are analyzed, the results show that the proposed mechanism has two rotational continuous axes, which are the Y-axis fixed on the fixed platform and x-axis fixed on the moving platform, respectively. The relationship between the pose of the moving platform and the length of actuated limbs can be established easily. In a word, the 2-RPU/SPR 2R1T mechanism proposed has simple kinematic model, which can reduce the difficulties in kinematic parameters calibration.

References

1. Carretero, J.K., Nahon, M., Gosselin, C.M., Buckham, B.: Kinematic analysis of a three-dof parallel mechanism for telescope applications. In: ASMN Design Automation Conference, Sacramento (1997)
2. Farhat, N., Mata, V., Page, A., Valero, F.: Identification of dynamic parameters of a 3-DOF RPS parallel manipulator. Mech. Mach. Theory **43**, 1–17 (2008)

3. Hunt, K.H.: Structural kinematics of in-parallel-actuated robot arms. ASME J. Mech. Transm. Autom. Des. **105**, 705–712 (1983)
4. Huang, Z., Tao, W.S., Fang, Y.F.: Study on the kinematic characteristics of 3-DOF in-parallel actuated platform mechanisms. Mech. Mach. Theory **31**, 999–1007 (1996)
5. Joshi, S.A., Tsai, L.W.: Jacobian analysis of limited-DOF parallel manipulator. ASME J. Mech. Des. **124**, 254–258 (2002)
6. Liu, D., Che, R., Li, Z., Luo, X.: Research on the theory and the virtual prototype of 3-DOF parallel-link coordinating machine. IEEE T Instrum. Meas. **52**, 119–125 (2003)
7. Li, Q.C., Chen, Q.H., Wu, C.Y., Huang, Z.: Geometrical distribution of rotational axes of 3-[P][S] parallel mechanisms. Mech. Mach. Theory **65**, 46–57 (2013)
8. Pouliot, N.A., Nahon, M.A., Gosselin, C.M.: Motion simulation capabilities of three-degrees-of-freedom flight simulators. J Aircraft **35**, 9–17 (1988)
9. Tsai, M.S., Shiau, T.N., Tsai, Y.J., Chang, T.H.: Direct kinematic analysis of a 3-PRS parallel mechanism. Mech. Mach. Theory **38**, 71–83 (2003)
10. Wahl, J.: Articulated tool head. WIPO Patent No. WO/2000/025976 (2000)

Recursive and Symbolic Calculation of the Stiffness and Mass Matrices of Parallel Robots

Sébastien Briot and Wisama Khalil

Abstract This paper presents a symbolic and recursive calculation of the stiffness and mass matrices of parallel robots. In order to reduce the computational time required for simulating the elastodynamic behavior of robots, it is necessary to minimize the number of operators in the symbolic model expression. Some algorithms have been proposed for the rigid case or for parallel robots with lumped springs. In this paper, we extend the previous works to parallel robots with distributed flexibilities. The proposed algorithm, that takes advantage of recursive calculations for the computation of the Jacobian matrices defining the kinematic constraints, is used to compute the natural frequencies of a robot developed at IRCCyN: the NaVARo.

Keywords Parallel robots · Flexibilities · Natural frequencies

1 Introduction

The large computational time required for calculating the natural frequencies of a robot prevents to use them in many applications, such as real-time control, design optimization process, etc. To decrease the computational cost, this paper focuses

S. Briot (✉) · W. Khalil
IRCCyN, UMR CNRS 6597, Nantes, France
e-mail: Sebastien.Briot@irccyn.ec-nantes.fr

W. Khalil
e-mail: Wisama.Khalil@irccyn.ec-nantes.fr

S. Briot · W. Khalil
École Centrale de Nantes, Nantes, France

(a) **(b)** **(c)**
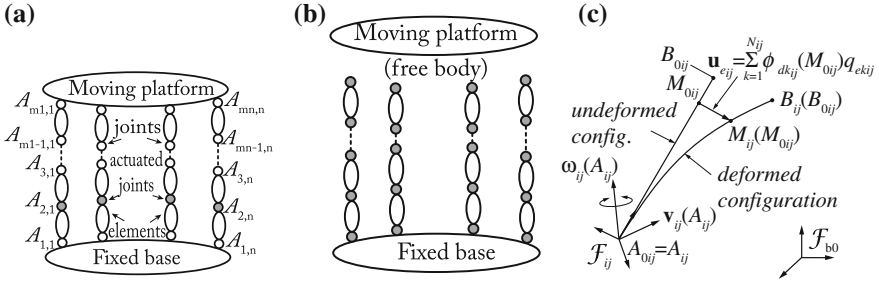
Fig. 1 A general parallel robot composed of flexible elements. **a** Kinematic chain. **b** Virtual tree structure. **c** A single flexible link

on the efficient symbolic computation for the stiffness and mass matrices of flexible parallel robots. This approach could be combined with model reduction methods [6, 9, 10], but this is not the main goal of that paper.

For the computation of the robot natural frequencies, two main approaches are generally proposed (see [11] for a large literature review): (i) lumped modeling [13, 18] and (ii) modeling using distributed flexibilities [2, 3, 7, 16, 17]. The lumped modeling is generally simpler to use by non-experts in finite element methods but, to obtain a correct model accuracy, higher number of elements is required, thus increasing the computational time.

Contrary to lumped modeling, using distributed flexibilities allows the improvement of the model accuracy. However, such methods require highly-skilled users. In [2, 16, 17], some general methodologies are proposed. In the case of closed-loop mechanisms, some Jacobian matrices are computed that allow taking into account the kinematic dependencies. However, such general method-ologies are not specifically designed for parallel robots and they do not guarantee the minimization of the number of operators for the symbolic computation of the model. To the best of our knowledge, a systematic procedure to compute the mass and stiffness matrices (using distributed flexibilities) of parallel robots with a minimal numbers of operators has never been proposed.

The present work aims at filling this gap. In order to minimize the number of operations, the Jacobian matrices defined in the principle of virtual powers (*PVP*) are computed using recursive algorithms. For computing the stiffness and mass matrices of parallel robots, the approach proposed in [5] is adapted. It proposes to (1) convert the parallel robot into a virtual system defined by a tree-structure robot composed of the kinematic chains of the actual robot for which all joints (passive and active) are considered actuated and a free body (the platform which is con-sidered as rigid) (Fig. 1), (2) compute the elastodynamic model of this new virtual system, and (3) finally, close the loops by using the *PVP*.

This method is effective, systematic, can be applied to any parallel robot.

2 Stiffness and Mass Matrices for the Virtual System

Let us consider a parallel robot composed of one rigid fixed base (denoted as element 0), one rigid moving platform and n legs, each leg being a serial kinematic chain composed of $(m_i - 1)$ elements[1] connected by m_i joints of coordinates q_{ik} (revolute, prismatic or fixed joints—$i = 1, \ldots, n$) located at points A_{ik} ($k = 1, \ldots, m_i$—Fig. 1a). The j-th element of the i-th leg is denoted by ij and its displacement can be parameterized by the coordinates $^{ij}\mathbf{t}_{ij}$[2] which represents the twist of the body ij at the origin of the local frame $\mathscr{F}_{ij}$ (Fig. 1c) and $\dot{\mathbf{q}}_{e_{ij}}$ that are the generalized velocities characterizing the elastic displacement of the body ij

$$^{ij}\mathbf{t}_{e_{ij}}(M_{ij}) = \boldsymbol{\Phi}_{ij}(M_{0ij})\dot{\mathbf{q}}_{e_{ij}} \tag{1}$$

where $^{ij}\mathbf{t}_{e_{ij}}(M_{ij})$ is the deformation twist due to the body elasticity that can be parameterized using truncated series of Rayleigh-Ritz shape functions $\boldsymbol{\Phi}_{ij}$ [4].

The vector of generalized coordinates of the tree-structure is given by $\mathbf{q}_t = \left[\mathbf{q}_{t_1}^T \cdots \mathbf{q}_{t_n}^T\right]^T$, where $\mathbf{q}_{t_i}$ regroups all joint variables (denoted as $\mathbf{q}_{p_i}^T = [q_{i1} \ldots q_{im_i}]$) and elastic generalized coordinates $\mathbf{q}_{e_i}^T = \left[\mathbf{q}_{e_{i1}}^T \cdots \mathbf{q}_{e_{i,m_i}}^T\right]$ for the real i-th leg.

The Lagrangian of the tree structure system can be expressed as:

$$L_t = \frac{1}{2}\sum_{i,j}\left(\left[^{ij}\mathbf{t}_{ij}^T \ \ \dot{\mathbf{q}}_{e_{ij}}^T\right]\mathbf{M}_{ij}\begin{bmatrix}^{ij}\mathbf{t}_{ij} \\ \dot{\mathbf{q}}_{e_{ij}}\end{bmatrix} - \mathbf{q}_{e_{ij}}^T\mathbf{K}_{ij}\mathbf{q}_{e_{ij}}\right) \tag{2}$$

where $\mathbf{M}_{ij}$ and $\mathbf{K}_{ij}$ are the mass and stiffness matrices of the link ij whose full expressions in the most compact form are given in [4, 15]. To express the Lagrangian as a function of $\mathbf{q}_t$ and $\dot{\mathbf{q}}_t$, let us express the displacement of the element ij frame located at A_{ij} using the following equations obtained by a recursive algorithm [4]

$$^{ij}\mathbf{t}_{ij} = \mathbf{J}_{t_{ij}}\dot{\mathbf{q}}_t \text{ with } \mathbf{J}_{t_{ij}} = {}^{ij}\mathbf{T}_{i(j-1)}\mathbf{J}_{t_{i(j-1)}} + \boldsymbol{\Phi}_{\mathbf{q}_{eij}} + \mathbf{A}_{ij} \text{ and} \tag{3}$$

$$\boldsymbol{\Phi}_{\mathbf{q}_{eij}} = \begin{bmatrix}\mathbf{0} & \cdots & {}^{ij}\overline{\mathbf{R}}_{i(j-1)}\boldsymbol{\Phi}_{i(j-1)}(A_{ij}) & \cdots & \mathbf{0}\end{bmatrix}, \mathbf{A}_{ij} = \begin{bmatrix}\mathbf{0} & \cdots & {}^{ij}\mathbf{a}_{ij} & \cdots & \mathbf{0}\end{bmatrix} \tag{4}$$

where $\mathbf{a}_{ij}$ is the unit twist describing the joint ij axis [4] and, in $\boldsymbol{\Phi}_{\mathbf{q}_{eij}}$ ($\mathbf{A}_{ij}$, resp.), the term $^{ij}\overline{\mathbf{R}}_{i(j-1)}\boldsymbol{\Phi}_{i(j-1)}(A_{ij})$ ($^{ij}\mathbf{a}_{ij}$, resp.) is located at the columns corresponding to the variables $\dot{\mathbf{q}}_{e_{i(j-1)}}$ ($\dot{q}_{ij}$, resp.). Moreover, in the previous expressions,

---

[1] Note that each robot link can be composed of one element or several elements.
[2] In what follows, the preceding superscript "ij" denotes that the vector is given in the frame $\mathscr{F}_{ij}$.

$$
{}^{ij}\overline{\mathbf{R}}_{i(j-1)} = \begin{bmatrix} {}^{ij}\mathbf{R}_{i(j-1)} & \mathbf{0} \\ \mathbf{0} & {}^{ij}\mathbf{R}_{i(j-1)} \end{bmatrix}, \quad {}^{ij}\mathbf{T}_{i(j-1)} = {}^{ij}\overline{\mathbf{R}}_{i(j-1)} \begin{bmatrix} \mathbf{I_3} & -{}^{i(j-1)}\hat{\mathbf{r}}_{i(j-1)}(A_{ij}) \\ \mathbf{0} & \mathbf{I_3} \end{bmatrix} \quad (5)
$$

where $\mathbf{I_3}$ is the (3×3) identity matrix, ${}^{ij}\mathbf{R}_{i(j-1)}$ is the rotation matrix between frames $\mathscr{F}_{ij}$ and $\mathscr{F}_{i(j-1)}$, ${}^{i(j-1)}\hat{\mathbf{r}}_{i(j-1)}(A_{ij})$ is the cross-product matrix associated with the vector ${}^{i(j-1)}\mathbf{r}_{i(j-1)}(A_{ij})$, i.e. the position of point $A_{ij} \equiv B_{i(j-1)}$ in $\mathscr{F}_{i(j-1)}$ (Fig. 1c).

Finally, a global Jacobian matrix $\mathbf{J}_{ij}$ defined such as $\begin{bmatrix} {}^{ij}\mathbf{t}_{ij}^T & \dot{\mathbf{q}}_{e_{ij}}^T \end{bmatrix}^T = \mathbf{J}_{ij}\dot{\mathbf{q}}_t$ can be computed as $\mathbf{J}_{ij}^T = \begin{bmatrix} \mathbf{J}_{t_{ij}}^T & \mathbf{O}_{\mathbf{q}_{eij}}^T \end{bmatrix}$ where $\mathbf{O}_{\mathbf{q}_{eij}}$ is defined such that $\dot{\mathbf{q}}_{e_{ij}} = \mathbf{O}_{\mathbf{q}_{eij}}\dot{\mathbf{q}}_t$.

Introducing $\begin{bmatrix} {}^{ij}\mathbf{t}_{ij}^T & \dot{\mathbf{q}}_{e_{ij}}^T \end{bmatrix}^T = \mathbf{J}_{ij}\dot{\mathbf{q}}_t$ into (2) leads to

$$
L_t = \frac{1}{2}\sum_{i,j}\left(\dot{\mathbf{q}}_t^T\mathbf{J}_{ij}^T\mathbf{M}_{ij}\mathbf{J}_{ij}\dot{\mathbf{q}}_t - \mathbf{q}_t^T\mathbf{O}_{\mathbf{q}_{eij}}^T\mathbf{K}_{ij}\mathbf{O}_{\mathbf{q}_{eij}}\mathbf{q}_t\right) = \frac{1}{2}\left(\dot{\mathbf{q}}_t^T\mathbf{M}_t\dot{\mathbf{q}}_t - \mathbf{q}_t^T\mathbf{K}_t\mathbf{q}_t\right) \quad (6)
$$

where $\mathbf{M}_t$ and $\mathbf{K}_t$ are the mass and stiffness matrices of the tree structure.

Adding the contribution of the rigid platform into (6), the Lagrangian of the total system can be written as:

$$
\begin{aligned}
L &= \frac{1}{2}\left(\begin{bmatrix} \dot{\mathbf{q}}_t \\ \mathbf{t}_p \end{bmatrix}^T \begin{bmatrix} \mathbf{M}_t & \mathbf{0} \\ \mathbf{0} & \mathbf{M}_p \end{bmatrix} \begin{bmatrix} \dot{\mathbf{q}}_t \\ \mathbf{t}_p \end{bmatrix} - \begin{bmatrix} \mathbf{q}_t \\ \mathbf{x}_p \end{bmatrix}^T \begin{bmatrix} \mathbf{K}_t & \mathbf{0} \\ \mathbf{0} & \mathbf{0} \end{bmatrix} \begin{bmatrix} \mathbf{q}_t \\ \mathbf{x}_p \end{bmatrix}\right) \\
&= \frac{1}{2}\left(\dot{\mathbf{q}}_g^T\mathbf{M}_g\dot{\mathbf{q}}_g - \mathbf{q}_g^T\mathbf{K}_g\mathbf{q}_g\right)
\end{aligned} \quad (7)
$$

$\mathbf{M}_p$ is the mass matrix of the rigid platform and $\mathbf{x}_p$ represents the platform displacement ($\mathbf{t}_p$ its twist). $\mathbf{M}_g$ and $\mathbf{K}_g$ are the total mass and stiffness matrices of the virtual system. $\mathbf{q}_g^T = \begin{bmatrix} \mathbf{q}_t^T & \mathbf{x}_p^T \end{bmatrix}$ is its vector of generalized coordinates.

3 Stiffness and Mass Matrices for the Parallel Robot

It is now necessary to determine one possible subset of generalized coordinates for the parallel robot. Using (3) for computing the twist ${}^{i,m_i}\mathbf{t}_{i,m_i}$ of the tip of leg i:

$$
{}^{i,m_i}\mathbf{t}_{i,m_i} = \mathbf{J}_{t_{i,m_i}}^i\dot{\mathbf{q}}_{t_i} \quad (8)
$$

where $\mathbf{J}_{t_{i,m_i}}^i$ can be obtained from $\mathbf{J}_{t_{i,m_i}}$ by extracting the columns corresponding to the vector $\dot{\mathbf{q}}_{t_i}^T = \begin{bmatrix} \dot{\mathbf{q}}_{p_i}^T, \dot{\mathbf{q}}_{e_i}^T \end{bmatrix}$, i.e. the vector stacking all variables of the leg i.

As the leg extremity is also linked to the rigid platform, its twist can be related to the platform twist $\mathbf{t}_p$ via the rigid body displacement relation:

$$^{i,m_i}\mathbf{t}_{i,m_i} = \mathbf{J}_p^i \mathbf{t}_p, \text{ where } \mathbf{J}_p^i = ^{i,m_i}\overline{\mathbf{R}}_0 \begin{bmatrix} \mathbf{I}_3 & -{}^0\hat{\mathbf{p}}_i \\ \mathbf{0} & \mathbf{I}_3 \end{bmatrix} \tag{9}$$

in which ${}^0\hat{\mathbf{p}}_i$ is the cross product matrix of vector ${}^0\mathbf{p}_i$ that characterizes the position of the attachment point A_{i,m_i} w.r.t. the platform center (Fig. 1a) and ${}^{i,m_i}\overline{\mathbf{R}}_0$ is the (6×6) rotation matrix between the global frame and the local frame $\mathscr{F}_{i,m_i}$.

Thus, the following set of equations can be obtained:

$$\begin{bmatrix} \mathbf{J}_{t_1,m_1}^1 & \cdots & \mathbf{0} \\ \vdots & \ddots & \vdots \\ \mathbf{0} & \cdots & \mathbf{J}_{t_n,m_n}^n \end{bmatrix} \begin{bmatrix} \dot{\mathbf{q}}_{t_1} \\ \vdots \\ \dot{\mathbf{q}}_{t_n} \end{bmatrix} - \begin{bmatrix} \mathbf{J}_p^1 \\ \vdots \\ \mathbf{J}_p^n \end{bmatrix} \mathbf{t}_p = \mathbf{0} \Leftrightarrow \mathbf{J}_t \dot{\mathbf{q}}_t - \mathbf{J}_p \mathbf{t}_p = \begin{bmatrix} \mathbf{J}_t & -\mathbf{J}_p \end{bmatrix} \begin{bmatrix} \dot{\mathbf{q}}_t \\ \mathbf{t}_p \end{bmatrix}$$
$$= \mathbf{J}_g \dot{\mathbf{q}}_g = \mathbf{0} \tag{10}$$

where $\mathbf{J}_g$ is a $(rn \times n_{q_g})$ matrix, $n_{q_g} > rn$ ($r = 6$ for a spatial robot, $r = 3$ for a planar robot). This means that a subset $\dot{\mathbf{q}}_d$ of rn variables in vector $\dot{\mathbf{q}}_g$ is linked to the others. This subset is not unique. As most of parallel robots have identical legs, an idea is to put in $\dot{\mathbf{q}}_d$ the last r components $\dot{\mathbf{q}}_{t_i}^f$ of each vector $\dot{\mathbf{q}}_{t_i}$ which can be decomposed into two parts $\dot{\mathbf{q}}_{t_i}^T = \begin{bmatrix} \dot{\mathbf{q}}_{t_i}^{0T} & \dot{\mathbf{q}}_{t_i}^{fT} \end{bmatrix}$:

$$-\begin{bmatrix} \mathbf{J}_{t_1,m_1}^{f1} & \cdots & \mathbf{0} \\ \vdots & \ddots & \vdots \\ \mathbf{0} & \cdots & \mathbf{J}_{t_n,m_n}^{fn} \end{bmatrix} \begin{bmatrix} \dot{\mathbf{q}}_{t_1}^f \\ \vdots \\ \dot{\mathbf{q}}_{t_n}^f \end{bmatrix} = \begin{bmatrix} \mathbf{J}_{t_1,m_1}^{01} & \cdots & \mathbf{0} & -\mathbf{J}_p^1 \\ \vdots & \ddots & \vdots & \vdots \\ \mathbf{0} & \cdots & \mathbf{J}_{t_n,m_n}^{0n} & -\mathbf{J}_p^n \end{bmatrix} \begin{bmatrix} \dot{\mathbf{q}}_{t_1}^0 \\ \vdots \\ \dot{\mathbf{q}}_{t_n}^0 \\ \mathbf{t}_p \end{bmatrix} \Leftrightarrow \mathbf{J}_t^f \dot{\mathbf{q}}_t^f$$
$$= \mathbf{J}_{tp} \dot{\mathbf{q}}. \tag{11}$$

This can be rewritten as

$$\dot{\mathbf{q}}_t^f = \left(\mathbf{J}_t^f\right)^{-1} \mathbf{J}_{tp} \dot{\mathbf{q}} = \begin{bmatrix} \mathbf{J}_{d_{1,1}} & \cdots & \mathbf{J}_{d_{1,n}} & \mathbf{J}_{d_{1,n+1}} \\ \vdots & \ddots & \vdots & \vdots \\ \mathbf{J}_{d_{n,1}} & \cdots & \mathbf{J}_{d_{n,n}} & \mathbf{J}_{d_{n,n+1}} \end{bmatrix} \dot{\mathbf{q}} = \mathbf{J}_d \dot{\mathbf{q}}. \tag{12}$$

If the coordinates $\dot{\mathbf{q}}_{t_i}^f$ are those of the last elastic element of the leg (which is most often the case), the k-th column of matrix $\mathbf{J}_{t_{il}}^{fi}$ corresponds to a unit twist that describes the displacement of the leg extremity due to the k-th coordinate of $\mathbf{q}_{t_i}^f$, i.e. [12]

$$\mathbf{J}^{fi}_{t_{il}} = \begin{bmatrix} {}^{i,m_i}\mathbf{R}_{il} & -{}^{i,m_i}\mathbf{R}_{il}{}^{il}\hat{\mathbf{p}}_{il} \\ \mathbf{0} & {}^{i,m_i}\mathbf{R}_{il} \end{bmatrix} \qquad (13)$$

where ${}^{i,m_i}\mathbf{R}_{il}$ is the rotation matrix between the local frame linked at element i, m_i and the local frame linked at element il and ${}^{il}\hat{\mathbf{p}}_{il}$ is the cross product matrix of the vector ${}^{il}\mathbf{p}_{il}$ that characterizes the position of the leg extremity with respect to the frame linked at element il. Thus its inverse is equal to

$$\left(\mathbf{J}^{fi}_{t_{il}}\right)^{-1} = \begin{bmatrix} {}^{i,m_i}\mathbf{R}^T_{il} & \hat{\mathbf{p}}^{i,m_i}_{il}\mathbf{R}^T_{il} \\ \mathbf{0} & {}^{i,m_i}\mathbf{R}^T_{il} \end{bmatrix} \qquad (14)$$

which does not require much calculation. Finally, from (12) and the definition of $\dot{\mathbf{q}}^T_g = \left[\dot{\mathbf{q}}^T_{t_1}, \ldots, \dot{\mathbf{q}}^T_{t_n}, \mathbf{t}^T_p\right]^T$, the matrix $\mathbf{J}$ defined such that $\dot{\mathbf{q}}_g = \mathbf{J}\dot{\mathbf{q}}$ can be computed.

Introducing $\dot{\mathbf{q}}_g = \mathbf{J}\dot{\mathbf{q}}$ into (7) leads to:

$$L = \frac{1}{2}\left(\dot{\mathbf{q}}^T\mathbf{J}^T\mathbf{M}_g\mathbf{J}\dot{\mathbf{q}} - \mathbf{q}^T\mathbf{J}^T\mathbf{K}_g\mathbf{J}\mathbf{q}\right) = \frac{1}{2}\left(\dot{\mathbf{q}}^T\mathbf{M}\dot{\mathbf{q}} - \mathbf{q}^T\mathbf{K}\mathbf{q}\right) \qquad (15)$$

from which the natural frequencies f_i $(i = 1, \ldots, n_{q_g} - rn)$ of the parallel robot can be computed as $f_i = \sqrt{eig\left(\mathbf{M}^{-1}\mathbf{K}\right)}/(2\pi)$. It should be noticed that obviously, matrices $\mathbf{M}$ and $\mathbf{K}$ depend on the robot configuration.

To automatize the calculation of the mass and stiffness matrices of the robot, for each computation, the elements of a vector or a matrix containing at least one mathematical operation are replaced by an intermediate variable. This variable is written in an output file which contains the model. The elements that do not contain any operations are not modified. The obtained vectors and matrices are propagated in the subsequent equations. Consequently, at the end, the model is obtained as a set of intermediate variables. Those that have no effect on the desired output can be eliminated. This algorithm has been successfully implemented with Mathematica.

4 Case Study: The NaVARo

The NaVARo is a 3-*dof* planar parallel manipulator developed at IRCCyN (Fig. 2a) and composed of 3 identical legs and one moving platform made up of 3 segments E_1P, E_2P and E_3P rigidly linked at point P. The i-th leg contains four links connected with five revolute joints in such a way that $A_iB_iC_iD_i$ is a parallelogram linkage, $i = 1, 2, 3$. The base frame $\mathscr{F}_b(O, \mathbf{x}_0, \mathbf{y}_0, \mathbf{z}_0)$ (not shown in Fig. 2b) is defined such as point O is located at the geometric centre of the equilateral triangle $A_1A_2A_3$. Frame $\mathscr{F}_p(P, \mathbf{x}_p, \mathbf{y}_p, \mathbf{z}_p)$ is attached to the moving platform. In the home configuration shown in Fig. 2, $\mathscr{F}_b$ and $\mathscr{F}_p(P, \mathbf{x}_p, \mathbf{y}_p, \mathbf{z}_p)$
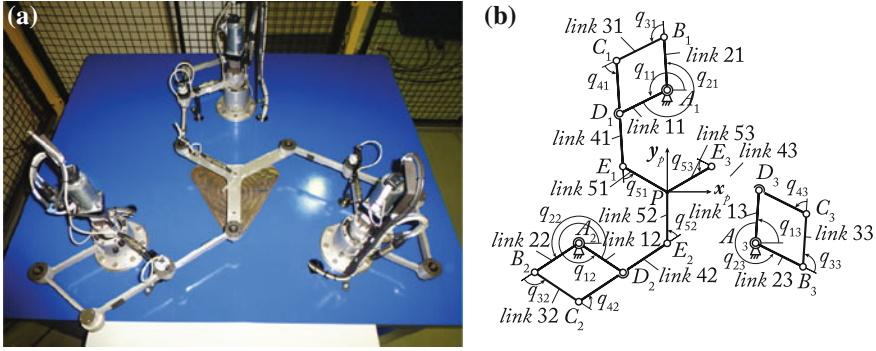
Fig. 2 The NaVARo. **a** Prototype of the NaVARo. **b** Shematics of the NaVARo

Table 1 MDH parameters of the i-th leg and characteristics of the beam cross-sections

ji	$a(ji)$	σ_{ji}	γ_{ji}	b_{ji}	α_{ji}	d_{ji} (m)	θ_{ji}	r_{ji}
$1i$	0	0	γ_i	0	0	$d_1 = 0.4041$	$q_{1i} - \gamma_i$	0
$2i$	0	0	γ_i	0	0	$d_1 = 0.4041$	$q_{2i} - \gamma_i$	0
$3i$	$2i$	0	0	0	0	$d_3 = 0.2100$	q_{3i}	0
$4i$	$3i$	0	0	0	0	$d_4 = 0.2100$	q_{4i}	0
$5i$	$4i$	0	0	0	0	$d_5 = 0.4200$	q_{5i}	0
link	A_{ij} (m^2)	$I_{y_{ij}}$ (m^4)	$I_{z_{ij}}$ (m^4)	$I_{p_{ij}}$ (m^4)	$I_{0_{ij}}$ (m^4)			
$1i, 2i, 3i, 4i$	$2.4 \cdot 10^{-4}$	$1.152 \cdot 10^{-8}$	$2.000 \cdot 10^{-9}$	$1.352 \cdot 10^{-8}$	$5.902 \cdot 10^{-9}$			
$5i$	$4 \cdot 10^{-4}$	$3.333 \cdot 10^{-8}$	$5.333 \cdot 10^{-8}$	$8.666 \cdot 10^{-8}$	$1.123 \cdot 10^{-8}$			

(attached to the moving platform) coincide. (x_p, y_p) are the Cartesian coordinates of point P expressed in frame $\mathscr{F}_b$ and θ_p is the orientation angle of the platform (the angle between $\mathbf{x}_0$ and $\mathbf{x}_p$).

Three double clutches are mounted to the base at points A_i, $i = 1, 2, 3$, in order to actuate either angle q_{1i} or angle q_{2i}. As a consequence, the NaVARo has 8 actuation modes [1, 14]. Therefore, the platform can be moved throughout the workspace without reaching any parallel singularity thanks to a judicious actuation scheme. The kinematics of the i-th leg is described by the modified Denavit-Hartenberg parameters (MDH) [12] given in Table 1, in which $\gamma_i = \pi/2$ if $i = 1$, $\gamma_i = -5\pi/6$ if $i = 2$ and $\gamma_i = -\pi/6$ if $i = 3$. Besides, the circumradius of the moving-platform is equal to 0.2027 m, i.e., $l_{5i} = 0.2027$ m. Each link, of rectangular cross-section, is made up of duraluminum alloy. Table 1 gives their cross-section area and inertia.

In the experimental setup, the rotation of links $1i$ and $2i$ about point A_i, $i = 1, 2, 3$, is locked thanks to the double clutch mechanisms. A single 3D beam element is used to model links $1i$, $2i$, $3i$ and $5i$ while two 3D beam elements of equal lengths are used to model links $4i$, the latter being twice longer than the former.

Table 2 Comparison of the natural frequencies obtained with Cast3 M and Matlab

(Hz)	f_1		f_2		f_3		f_4		f_5	
	Cast3 M	Matlab	Cast3 M	Matlab	Cast3 M	Matlab	Cast3 M	Matlab	Cast3 M	Matlab
Pose (a)	44.10	44.10	44.10	44.10	53.98	53.98	60.63	60.63	95.62	95.62
Pose (b)	45.71	45.71	45.71	45.71	54.58	54.58	65.35	65.35	97.92	97.92
Pose (c)	36.98	36.98	49.31	49.31	53.37	53.37	67.28	67.28	91.80	91.80
Pose (d)	40.17	40.17	50.32	50.32	52.99	52.99	67.36	67.36	91.52	91.52
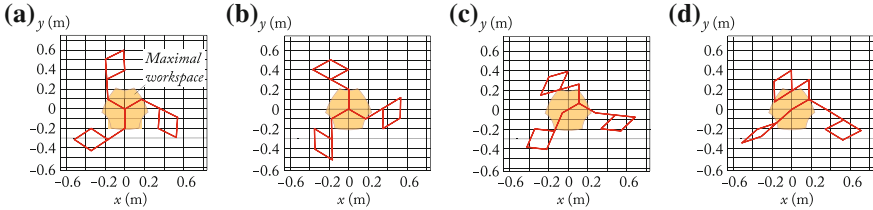
Fig. 3 The four test poses $\{x_p, y_p, \theta_p\}$ (positions in meters, orientation in radian). **a** $\{0, 0, 0\}$. **b** $\{0, 0, -\pi/3\}$. **c** $\{0.12, 0.07, -\pi/3\}$. **d** $\{0.18, 0.11, -\pi/3\}$

Thus, the NaVARo is modelled as a spatial mechanism and its model contains 144 generalized coordinates, among which only 90 are independent (see Sect. 3). The model has been calculated using the proposed procedure and compiled into C code to obtain the robot natural frequencies. The computation involve the use of 36183 '+' or '−'and 37341 '*' or '/' operators, while 21383 variables are defined.

To the best of our knowledge, there exist no works that try to minimize the number of operators in the elastodynamic models of parallel robots. Therefore, the efficiency of the proposed solution may be difficult to analyze. However, for reasons of comparison, the obtained frequencies were validated by means of an equivalent model developed using Cast3 M software [8]. For the simulations, Cast3 M gives the result after around 6 s of computation while our model send the results in around 0.01 s (for a Pentium 4 2.70 GHz, 8Go of RAM). Both models give the same values for the first 90 natural frequencies of the NaVARo. Table 2 gives the first 5 natural frequencies of the NaVARo for the 4 robot postures shown in Fig. 3.

5 Conclusions

The paper has presented a symbolic and recursive calculation of the stiffness and mass matrices of parallel robots. The proposed algorithm, that takes advantage of recursive calculations for the computation of the Jacobian matrices defining the kinematic constraints, is used to compute the natural frequencies of a robot developed at IRCCyN: the NaVARo. Results have shown that the proposed model was able to give the same values as a FEA software for the first 90 natural frequencies of the NaVARo but in a considerably reduces computational time (around 0.01 s for our model while FEA results were obtained in several sec.).

References

1. Arakelian, V., Briot, S., Glazunov, V.: Increase of singularity-free zones in the workspace of parallel manipulators using mechanisms of variable structure. Mech. Mach. Theory **43**(9), 1129–1140 (2008)
2. Bauchau, O.: Flexible Multibody Dynamics. Springer, Berlin (2011)
3. Boyer, F., Khalil, W.: An efficient calculation of the flexible manipulator inverse dynamics. Int. J. Robot. Res. **17**(3), 282–293 (1998)
4. Boyer, F., Khalil, W., Benosman, M., LeVey, G.: Robot manipulators. modeling, performance, analysis and control, chap. 7: modeling and control of flexible robots, pp. 337–394. In: Proceedings of Control Systems, Robotics and Manufacturing Series. ISTE (2007)
5. Briot, S., Khalil, W.: Recursive and symbolic calculation of the elastodynamic model of flexible parallel robots. Int. J. Robot. Res. (2014) (In Press)
6. Briot, S., Pashkevich, A., Chablat, D.: Reduced elastodynamic modelling of parallel robots for the computation of their natural frequencies. In: Proceedings of World Congress in Mechanism and Machine Science, p. 13 (2011)
7. Cammarata, A., Condorelli, D., Sinatra, R.: An algorithm to study the elastodynamics of parallel kinematic machines with lower kinematic pairs. ASME Transactions Journal of Mechanisms and Robotics **5**(1), 1138-1145.(2013)
8. Castem3000: The castem software webpage. http://www-cast3m.cea.fr. (2012) Accessed Nov 2012
9. Craig, R.: Structural Dynamics. Wiley, New York (1981)
10. Craig, R.R., Bampton, M.C.C.: Coupling of substructures for dynamic analysis. AIAA J. **6**(7), 1313–1319 (1968)
11. Dwivedy, S., Eberhard, P.: Dynamic analysis of flexible manipulators, a litterature review. Mech. Mach. Theory **41**(7), 749–777 (2006)
12. Khalil, W., Dombre, E.: Modeling, Identification and Control of Robots. Hermes Penton, London (2002)
13. Khalil, W., Gautier, M.: Modeling of mechanical systems with lumped elasticity. In: Proceedings of the IEEE International Conference on Robotics and Automation, pp. 3965–3970. San Francisco, CA, USA (2000)
14. Rakotomanga, N., Chablat, D., Caro, S.: Kinetostatic performance of a planar parallel mechanism with variable actuation. In: Proceedings of Advances in Robot Kinematics (2008)
15. Shabana, A.: Dynamics of flexible bodies using generalized newton-euler equations. J. Dyn. Syst. Meas. Contr. **112**, 496–503 (1990)
16. Shabana, A.: Dynamics of Multibody Systems. Cambridge University Press, Cambridge (2005)
17. Stachera, K., Schumacher, W.: Automation and Robotics, chap. 15: Derivation and Calculation of the Dynamics of Elastic Parallel Manipulators. I. Tech Education and Publishing, Vienna (2008)
18. Wittbrodt, E., Adamiec-Wójcik, I., Wojciech, S.: Dynamics of Flexible Multibody Systems. Springer, Berlin (2006)

Kinematics, Dynamics, Control and Accuracy of Spherical Parallel Robot

Sergey Kheylo and Victor Glazunov

Abstract This paper deals with the kinematical and dynamical properties of parallel spherical manipulators with three degrees of freedom. Accelerations, dynamics, control and accuracy are considered. Algorithm of control is based on the inverse problem of dynamics and allows minimizing deviations of coordinates, velocities and accelerations.

Keywords Spherical parallel mechanism · Dynamics · Control · Accuracy

1 Introduction

Spherical mechanisms are used as orienting devices, machine tools, medical equipments, etc. The first works were focused on the mechanisms of one degree of freedom and open kinematic chain [1]. It was one of the first monographs dealing with the spherical mechanisms.

Furthermore these mechanisms were applied in parallel robots that contain several kinematic chains [2–6]. A lot of publications describe 3-dof spherical parallel mechanisms. Such 3-dof spherical parallel mechanism is composed of three limbs connecting a moving platform (end-effector) to a fixed base and all the axes of kinematic pairs intersect at one point [7]. But not all the mentioned axes

S. Kheylo (✉)
Moscow State University of Design and Technology, Sadovnicheskaya, 33/1, Moscow, Russia
e-mail: Sheilo@yandex.ru

V. Glazunov
Mechanical Engineering Research Institute of RAS, M. Khariton'evsky per. 4, Moscow, Russia
e-mail: Vaglznv@mail.ru
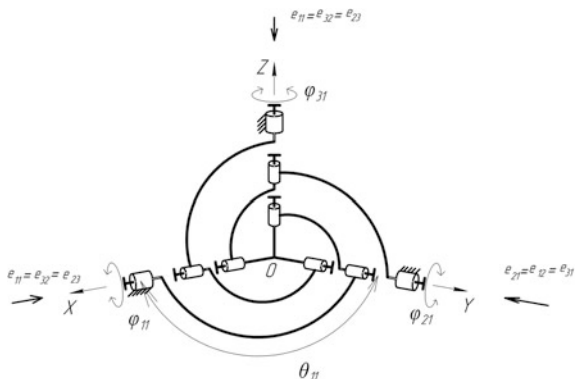
may intersect at a single point. An intermediate rotating kinematic pair can be
replaced by three pairs with parallel axes. [8–10].

Spherical mechanisms were subjects of many publications dealing with the
structure [6, 7], the problem of positions and velocities and workspace modeling
[11], problems of optimization and design [12, 13], dynamical analysis and sin-
gularity analysis [14].

However, not all the important problems have been addressed earlier. These
concern the problem of accelerations and accuracy. Besides, the problem of
control is very important [15]. This article is devoted to these issues. Proposed
algorithm is based on concept of minimized deviations of coordinates, velocities
and acceleration, using inverse problems of dynamics

2 Mechanism Configuration

In the considered spherical mechanism with three kinematic pairs in each chain
(Fig. 1), the input link is connected to the engine. The output link is a platform that
revolves around three axes intersecting at a point O. The output coordinates are
angles of rotation of the platform α, β, γ around the axes, whose relative positions
are described by a fiction kinematic chain (Fig. 2a). The generalized coordinates
are angles φ_{11}, φ_{21}, φ_{31}. Each of the three kinematic chains has three joints with
intersecting axes.

Let us associate the output link of the mechanism with a moving coordinate
system ξ, η, ζ, whose axes are situated along the main inertia axes of this link.
Therefore for the orientation angles ($\alpha = \beta = \gamma = 0$) the directions of the axes ξ,
η, ζ coincide with directions of the axes x, y, z, respectively. The constrain
equations are derived from geometry of mechanism, transfer matrixes absolute and
moving coordinate systems.

The constrain equations for a spherical mechanism with three kinematic chains
can be represented by the following system:
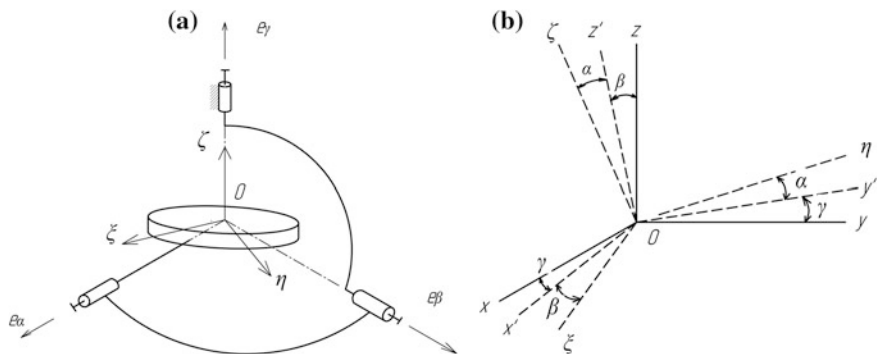
Fig. 2 The angles α, β, γ: **a** fiction kinematic chain, **b** coordinate systems

$$F_1 = \text{tg}\,\varphi_{11} + \frac{\cos\alpha \cdot \sin\gamma \cdot \sin\beta - \cos\gamma \cdot \sin\alpha}{\cos\alpha \cdot \cos\beta} = 0 \ ; \quad F_2 = \frac{\sin\beta}{\cos\gamma \cdot \cos\beta} - \text{tg}\,\varphi_{21} = 0;$$

$$F_3 = \text{tg}\,\varphi_{31} + \frac{\cos\gamma \cdot \sin\alpha \cdot \sin\beta - \cos\alpha \cdot \sin\gamma}{\cos\alpha \cdot \cos\gamma + \sin\alpha \cdot \sin\beta \cdot \sin\gamma} = 0$$

$$(1)$$

3 Dynamical Analysis

Differentiating these expressions (1) with respect to t, we obtain a system of equations of velocities of the input and output links:

$$\frac{\partial F_i}{\partial \alpha}\dot{\alpha} + \frac{\partial F_i}{\partial \beta}\dot{\beta} + \frac{\partial F_i}{\partial \gamma}\dot{\gamma} + \frac{\partial F_i}{\partial \varphi_{i1}}\dot{\varphi}_{i1} = 0 \tag{2}$$

Differentiating the Eq. (1) again with respect to t, we obtain equations of accelerations:

$$\frac{\partial F_1}{\partial \varphi_{11}}\ddot{\varphi}_{11} = \frac{\partial^2 F_1}{\partial \alpha^2}\dot{\alpha}^2 + 2\frac{\partial^2 F_1}{\partial\alpha\partial\beta}\dot{\alpha}\dot{\beta} + 2\frac{\partial^2 F_1}{\partial\alpha\partial\gamma}\dot{\alpha}\dot{\gamma} + \frac{\partial^2 F_1}{\partial\beta^2}\dot{\beta}^2 + 2\frac{\partial^2 F_1}{\partial\beta\partial\gamma}\dot{\beta}\dot{\gamma} + \frac{\partial^2 F_1}{\partial\gamma^2}\dot{\gamma}^2$$

$$+ \frac{\partial^2 F_1}{\partial\varphi_{11}^2}\dot{\varphi}_{11} + \frac{\partial F_1}{\partial\alpha}\ddot{\alpha} + \frac{\partial F_1}{\partial\beta}\ddot{\beta} + \frac{\partial F_1}{\partial\gamma}\ddot{\gamma}\ldots$$

$$(3)$$

The equation of motion of a spherical mechanism with three degrees of freedom has the following form (mass of the arc shaped links are ignored):

$$J_\xi \cdot \underset{\xi}{\ddot{\varphi}} = M_1 \cdot \frac{\partial\varphi_{11}}{\partial\varphi_\xi} + M_2 \cdot \frac{\partial\varphi_{21}}{\partial\varphi_\xi} + M_3 \cdot \frac{\partial\varphi_{31}}{\partial\varphi_\xi} + \dot{\varphi}_\eta \cdot \dot{\varphi}_\zeta \cdot \left(J_\zeta - J_\eta\right) \qquad (4)$$

where $J_\xi = J_\eta$, J_ζ are the inertia moments in respect to the axes ξ, η, ζ; M_1, M_2, M_3, are the moments in the drives, $\frac{\partial\varphi_{ij}}{\partial\varphi_\xi}$ are variable coefficients, $\ddot{\varphi} = \dot{\omega}_\xi$, $\dot{\varphi}_\xi = \omega_\xi$, $\underset{\eta}{\ddot{\varphi}}$, $\dot{\varphi}_\eta$, $\underset{\zeta}{\ddot{\varphi}}$, $\dot{\varphi}_\zeta$ are the projections of accelerations and velocities on the axes ξ, η, ζ. Other equations are similar. The torques are determined using the algorithm represented in [15]. Let $\mathbf{r_i}$ be the vector perpendicular to the axes of the passive joints of the i-th chain. This vector has coordinates r_{ix}, r_{iy} r_{iz} and $r_{i\zeta}$, $r_{i\eta}$, $r_{i\xi}$ in the absolute and moving coordinate systems correspondingly. It may be shown that:

$$\omega_\xi \cdot \mathbf{r}_{i\xi} + \omega_\eta \cdot \mathbf{r}_{i\eta} + \omega_\zeta \cdot \mathbf{r}_{i\zeta} = \omega_{i1} \cdot (x_{i1}\mathbf{r}_{ix} + y_{i1}\mathbf{r}_{iy} + z_{i1}\mathbf{r}_{iz}) \qquad (5)$$

where ω_ξ, ω_η, ω_ζ are projections of velocity of the output link to the axes ξ, η, ζ, x_{i1}, y_{i1}, z_{i1} are the coordinates of the unite vector $\mathbf{e_{i1}}$ (Fig. 1).

Then from (5) the variable coefficients can be determined. By this we take into account that $y_{i1} = 0$, $z_{i1} = 0$ (Fig. 1).

$$\frac{\partial\varphi_{11}}{\partial\varphi_\xi} = \frac{\omega_{11}}{\omega_\xi} = \frac{\mathbf{r}_{1\xi}}{\mathbf{r}_{1x}}; \quad \frac{\partial\varphi_{11}}{\partial\varphi_\eta} = \frac{\omega_{11}}{\omega_\eta} = \frac{\mathbf{r}_{1\eta}}{\mathbf{r}_{1x}}; \quad \frac{\partial\varphi_{31}}{\partial\varphi_\eta} = \frac{\omega_{31}}{\omega_\eta} = \frac{\mathbf{r}_{3\eta}}{\mathbf{r}_{3z}} = 0 \qquad (6)$$

Other coefficients have similar forms.

The velocities $\dot{\alpha}$, $\dot{\beta}$, $\dot{\gamma}$ may be obtained from linear equations:

$$\omega_\xi = \dot{\alpha} \cdot \alpha_\xi + \dot{\beta} \cdot \beta_\xi + \dot{\gamma} \cdot \gamma_\xi, \ldots, \omega_\zeta = \dot{\alpha} \cdot \alpha_\zeta + \dot{\beta} \cdot \beta_\zeta + \dot{\gamma} \cdot \gamma_\zeta \qquad (7)$$

where $(\alpha_\xi, \alpha_\eta, \alpha_\zeta)$ are the projections of the unit vector $\mathbf{e_\alpha}$ of the joint corresponding to the velocity $\dot{\alpha}$ (Fig. 2a), $(\beta_\xi, \beta_\eta, \beta_\zeta)$ and $(\gamma_\xi, \gamma_\eta, \gamma_\zeta)$ are defined analogously.

4 Control of the Manipulator

Control of parallel manipulators is one of the most important problems. There are different approaches to solve this problem. The applied algorithm is based on the inverse problems of dynamics [15].

The desired laws of the coordinates of the mobile platform are described by equations $\alpha_T(t)$, $\beta_T(t)$, $\gamma_T(t)$.

The task is to minimize the errors $\Delta\alpha = \alpha_T(t) - \alpha(t)$, $\Delta\beta = \beta_T(t) - \beta(t)$, $\Delta\gamma = \gamma_T(t) - \gamma(t)$, where $\alpha(t)$, $\beta(t)$, $\gamma(t)$ are the actual coordinates of the mobile platform.
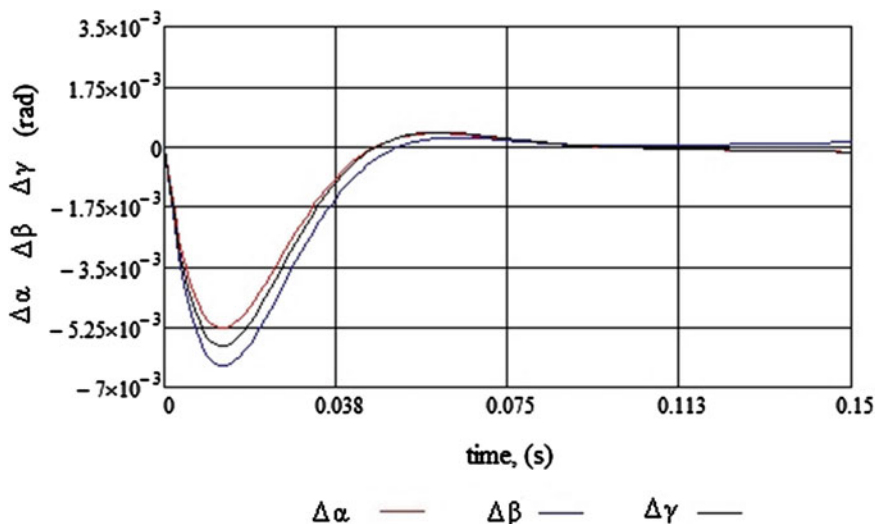
Fig. 3 The simulation result of displacement

Equations of errors are

$$\ddot{\Delta}\alpha + K_D\dot{\Delta}\alpha + K_P\Delta\alpha = 0, \ldots, \ddot{\Delta}\gamma + K_D\dot{\Delta}\gamma + K_P\Delta\gamma = 0 \qquad (8)$$

where K_D, K_P are the feedback coefficients. The value feedback gains coefficients are determined according the theory robotic control [15].

According to Eq. (8) the actual accelerations become:

$$\ddot{\alpha} = \underset{T}{\ddot{\alpha}} + K_D(\dot{\alpha}_T - \dot{\alpha}) + K_P(\alpha_T - \alpha), \ldots, \ddot{\gamma} = \underset{T}{\ddot{\gamma}} + K_D(\dot{\gamma}_T - \dot{\gamma}) + K_P(\gamma_T - \gamma) \quad (9)$$

The laws of errors is described oscillatory second-order systems, which control time is minimize. Let us consider an example: the desired laws of the coordinates of the moving platform are $\alpha_T(t) = 0.1 \cdot \sin(\omega\ t)$, $\beta_T(t) = 0.11 \cdot \sin(\omega\ t)$, $\gamma_T(t) = 0.12 \cdot \sin(\omega\ t)$. Moment of inertia $J_\xi = J_\eta = 0.0012$ kg·m^2, $J_\zeta = 0.002$ kg·m^2, $K_D = 120$, $K_P = 7200$. Result of the simulation is presented on Fig. 3. The maximal errors are about $6 \cdot 10^{-3}$ rad.

5 Accuracy of the Manipulator

The full differential of input-output equation can be written:
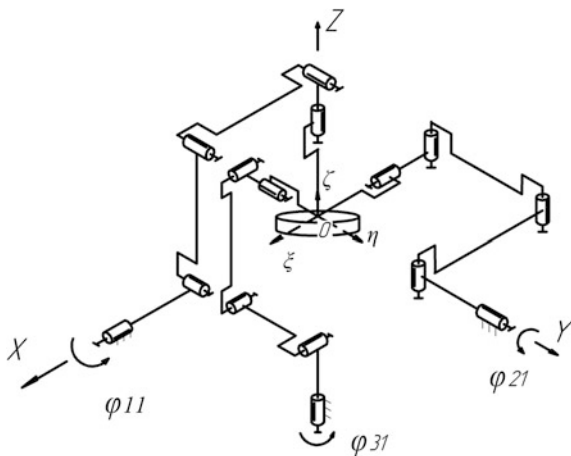
$$\frac{\partial F_i}{\partial \alpha} \delta\alpha + \frac{\partial F_i}{\partial \beta} \delta\beta + \frac{\partial F_i}{\partial \gamma} \delta\gamma + \frac{\partial F_i}{\partial \theta_{i1}} \delta\theta_{i1} + \frac{\partial F_i}{\partial \theta_{i2}} \delta\theta_{i2} + \frac{\partial F_i}{\partial \varphi_{i1}} \delta\varphi_{i1} = 0 \qquad (10)$$

where θ_{i1}, θ_{i2} are the angels between the axes of kinematic pairs (Fig. 1).

According to the linear theory of accuracy, we assume increment in the actuators are equal to zero: $\delta\varphi_{11} = \delta\varphi_{21} = \delta\varphi_{31} = 0$. Therefore the system of equations can be represented as:

$$\frac{\partial F_i}{\partial \alpha} \delta\alpha + \frac{\partial F_i}{\partial \beta} \delta\beta + \frac{\partial F_i}{\partial \gamma} \delta\gamma + \frac{\partial F_i}{\partial \theta_{11}} \delta\theta_{i1} = -\left(\frac{\partial F_i}{\partial \theta_{12}} \delta\theta_{i2} + \frac{\partial F_i}{\partial \varphi_{11}} \delta\varphi_{i1} \right) \qquad (11)$$

Thus, knowing the deviations of angles between the axes of kinematic pairs we can determine the deviations of the position of the output link.

For example, if errors are: $\theta_{11} = 0.01$ rad, $\theta_{12} = 0.005$ rad, $\theta_{31} = 0.01$ rad, $\theta_{i2} = 0.0075$ rad, $\theta_{12} = 0.005$ rad, $\theta_{22} = 0.005$ rad, $\theta_{23} = 0.005$ rad, then the deviations of the position of the output link are $\delta\alpha = 0.012$ rad, $\delta\beta = 0.017$ rad, $\delta\gamma = 0.005$ rad.

6 Prototyping of the Manipulator

We considered the mechanism where all the axes of the kinematic pairs intersect at a single point. But one rotating kinematic pair can be replaced by three pairs with parallel axes. [8–10]. Thus, we introduce a mechanism with five kinematic pairs in each kinematic chain [9, 10] (Fig. 4).

Fig. 5 Prototype of spherical mechanism with three kinematic chains
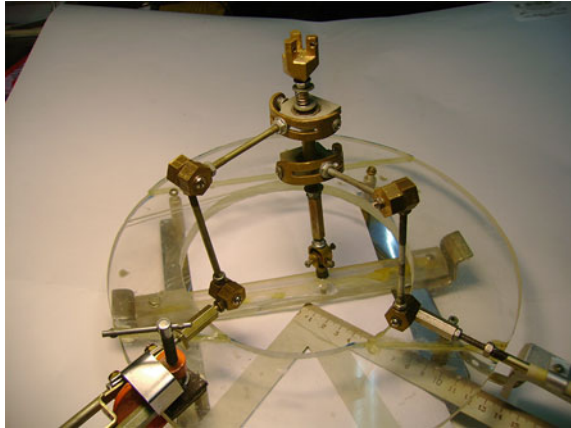
One of versions of spherical mechanisms with five kinematic pairs in any chain is prototyped One of the versions of spherical mechanism with five kinematic pairs in two kinematic chains and three kinematic pairs in one kinematic chain is prototyped (Fig. 5).

7 Conclusion

In this article, the problem of kinematics and dynamics of the spherical parallel manipulator is considered. Dynamical properties are analyzed applying the virtual work principle. Algorithm of control is based on the inverse problem of dynamics and allows minimizing deviations of coordinates, velocities and accelerations. Our further work will focus on determination of workspace of the prototype (Fig. 5).

References

1. Dobrovolsky, V.V.: Theory of Spherical Mechanisms, Moscow (in Rus.) (1947)
2. Merlet, J.P.: Parallel Robots, 2nd edn. Kluwer Academic Publishers, Boston (Springer) (2000)
3. Kong, X., Gosselin, C.: Type Synthesis of Parallel Mechanisms. Springer, Berlin (2007)
4. Ceccarelli, M.: Fundamentals of Mechanics of Robotic Manipulations. Kluwer Academic Publishers, Dordrecht (2004)
5. Glazunov,V., Koliskor, A., Krainev, A., Model, B.: Classification principles and analysis methods for parallel-structure spatial mechanisms. J. Mach. Manuf. Reliab. (Allerton Press Inc.) **1**, 30–37 (1990)

6. Glazunov, V.: Principles of the construction and analysis of spatial parallel structure mechanisms. J. Mach. Manuf. Reliab. (Allerton Press Inc.) **1,** 10–15 (1995)
7. Kong, X., Gosselin, C.M.: Type synthesis of three-degree-of-freedom spherical parallel manipulators. Int. J. Robot. Res. **23**(3), 237–245 (2004)
8. Huda, S., Takeda, Y.: Dimension synthesis of 3-URU pure rotation parallel mechanism with respect to singularity and workspace. In: 12th IFToMM World Congress, Becasson, pp. 235–242 (2007)
9. Kheylo, S., Glazunov, V., Kulemkin, Y., Ephros, V.: (2013) Analysis of accelerations and nonlinear oscillations of spherical mechanism of parallel structure. J. Mach. Manuf. Reliab. **42**, 184–191
10. Kheylo, S., Glazunov, V., Minh, T.N.: (2013) Acceleration and nonlinear oscillations of parallel spherical mechanism. In: Proceeding of the 3rd IFToMM International Symposium on Robotics and Mechatronics, Singapore, pp. 504–513
11. Gosselin, C.M., Angeles, J.: The optimum design of spherical three degree of freedom parallel manipulator. Trans. ASME J. Mech. Des. **111**, 202–207 (1989)
12. Larochelle, P.M.: Design of 3-DOF spherical robotic mechanism. In: 9th IFToMM Word Congress on the Theory of Machines and Mechanism, Milan, Italy (1995)
13. Liu, X.J., Jin, Z.L., Gao, F.: Optimum design of 3-DOF spherical parallel mechanism with respect to the conditioning and stiffness indices. Mech. Mach. Theory **35**(9), 257–1267 (2000)
14. Gosselin, C.M., Wang, J.: Singularity loci of a special class of spherical three-degree-of-freedom parallel mechanisms with revolute actuators. Int. J. Robot. Res. **21**(7), 649–659 (2002)
15. Craig, J.J.: Introduction to Robotics: Mechanics and Control, 2nd edn. Addisson-Wesley, Reading (1989)

Dynamics and Control of a Two-Module Mobile Robot on a Rough Surface

N. Bolotnik, M. Pivovarov, I. Zeidis and K. Zimmermann

Abstract A two-module (two-body) locomotion system moving along a straight line on a rough horizontal plane is considered. The motion of the system is excited by a periodic change in the distance between the bodies. Friction between the bodies and the plane obeys Coulomb's law. The conditions for the system to be able to start moving from a state of rest and the steady-state motion are studied. The friction force acting on the system is assumed to be small as compared with the excitation force, and the method of averaging is applied to the equation of motion of the system's center of mass. On the basis of the averaged equation, necessary and sufficient conditions subject to which the system can start moving from a state of rest in a dry friction environment are obtained. The excitation law that implies a piecewise quadratic time history of the distance between the bodies is considered. For this excitation law, the system can start moving from a state of rest if the bodies have different masses and the times of increase and decrease of the distance between them do not coincide. Closed-form expressions for the steady-state velocity of the system's center of mass are obtained and investigated as a function of the parameters of the system and the excitation law. The maximum magnitudes of the steady-state velocities and the respective values of the parameters are found. An experimental prototype of the robot under consideration was built. The experimental results demonstrate qualitative agreement with the theoretical predictions.

N. Bolotnik
Institute for Problems in Mechanics of the Russian Academy of Sciences, 101 bld. 1
Vernadsky Ave, Moscow 119526, Russia
e-mail: bolotnik@ipmnet.ru

M. Pivovarov · I. Zeidis (✉) · K. Zimmermann
Department of Technical Mechanics, Technische Universitaet Ilmenau, Max-Planck-Ring
12, 98693 Ilmenau, Germany
e-mail: igor.zeidis@tu-ilmenau.de

M. Pivovarov
e-mail: michail.pivovarov@arcor.de

K. Zimmermann
e-mail: klaus.zimmermann@tu-ilmenau.de

1 Introduction

A two-body system excited by a periodic change in the distance between the bodies is a simple model of bio-inspired limbless worm-like locomotors. Such systems can move progressively in nonlinear resistive environments. This principle of motion can be used for mini-sized biomimetic mobile robots. This paper is closely related to studies [3, 4, 6] in which the motion of a two-body system in a dry friction environment was considered. In [3], the system is controlled by a periodically changing force of interaction between the bodies, while in [4, 6], the rate of change in the distance between the bodies is taken as the control variable. In [3, 4], explicit expressions are obtained for the average velocity of the system relative to the environment, and the optimal control parameters that maximize this quantity are found. The conditions, subject to which the system can move progressively in an isotropic dry friction environment, were analyzed in [6]. A number of problems related to the locomotion of two-body systems in anisotropic dry friction environments are solved in [7]. In our paper, we investigate a two-body system excited by a periodic change in the distance between the bodies and moving in an isotropic Coulomb friction environment for the case of low friction. Two-body systems are a simplest class of limbless (snake-like and worm-like) multilink artificial locomotors. For a review of publications on the motion planning, control, and optimization of multilink locomotors see, e.g., [2, 5].

2 Mechanical System and Basic Assumptions

Consider a model of a locomotion system shown in Fig. 1.

The system consists of two bodies coupled by a prismatic joint that allows the bodies to move translationally relative to each other along a rectilinear guide (the axis of the joint). We will indicate the bodies of the system by numbers 1 and 2. The joint is actuated by a drive that increases or decreases the distance between the bodies according to a prescribed law. The forces generated by the drive are the internal forces acting between the system's components. The bodies of the system interact with an environment that resists their motion with the forces depending on the velocities of the bodies relative to the environment. These forces are external with respect to the system. The forces generated by the drive change the velocities of the system's bodies relative to each other and relative to the environment, which causes change in the environmental forces acting on the system. Thus, by controlling the relative motion of the system's components we can change the external
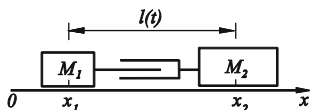
Fig. 1 Two-body system with a prismatic joint

forces acting on the system, controlling thereby the motion of the entire system in the environment. In what follows, we confine ourselves to the case where both bodies and the entire system move along a horizontal straight line that coincides with the axis of the joint. In this case, the bodies of the system can be treated as point masses. Let M_1 and M_2 denote the masses of bodies 1 and 2, respectively; x_1 and x_2 the coordinates characterizing the positions of the bodies on the line of their motion relative to a point O fixed on this line; l the coordinate of body 2 relative to body 1 ($l = x_2 - x_1$); $F_i(\dot{x}_i)$ ($i = 1, 2$) the friction forces acting on the bodies.

We assume that the time history $l(t)$ of the relative motion of bodies 1 and 2 is prescribed and that the drive of the joint perfectly sustains this law. In terms of mechanics, this means that the motion of the system is subject to a time-varying constraint defined by the relation

$$x_2(t) - x_1(t) = l(t). \tag{1}$$

The constrained system has one degree of freedom, and its configuration can be completely defined by the coordinate of a single characteristic point of the system. It is natural and convenient to characterize the motion of the system by the motion of its center of mass, the coordinate of which relative to the point O is defined by

$$X = \frac{M_1 x_1 + M_2 x_2}{M}, \qquad M = M_1 + M_2. \tag{2}$$

Use Eqs. (1) and (2) to express the coordinates x_1 and x_2 in terms of X and l:

$$x_1 = X - \frac{M_2}{M} l \quad x_2 = X + \frac{M_1}{M} l. \tag{3}$$

According to the linear momentum principle, the motion of the center of mass of the system under consideration is governed by the equation

$$M\dot{V} = F_1\left(V - \frac{M_2}{M} u\right) + F_2\left(V + \frac{M_1}{M} u\right), \tag{4}$$

$$V = \dot{X}, \quad u = \dot{l}. \tag{5}$$

The right-hand side of Eq. (4) expresses the resultant of the external forces acting on the system. The variable u occurring in this equation can be interpreted as the control variable for the system under consideration.

For what follows, we assume that the excitation law $l(t)$ is T-periodic, i.e., $l(t + T) = l(t)$ and that the period T is prescribed. Hence, the control function $u(t)$ is also T-periodic and, in addition, has zero average over the period.

3 Non-dimensionalization

Introduce the dimensionless variables (marked by asterisks) for Eq. (4) as follows:

$$t^* = \frac{t}{T}, \ V^* = \frac{T}{L}V, \ u^* = \frac{T}{L}u, \ F_i^*(V^*) = \frac{1}{kMg}F_i\left(\frac{L}{T}V^*\right), \ m_i = \frac{M_i}{M}, \ i = 1, \ 2,$$

(6)

where k is the coefficient of friction, g is the acceleration due to gravity, and L is defined as a quantity coinciding in order of magnitude with the amplitude of oscillation of the variable l:

$$L \sim \max_t \ l(t) - \min_t \ l(t).$$

(7)

We assume that the friction between the bodies and the environment is Coulomb's dry friction. Then

$$F_i^*(\dot{x}_i^*) = m_i F^*(\dot{x}_i^*), \qquad F^*(\dot{x}_i^*) = \begin{cases} -\operatorname{sgn}\dot{x}_i^*, & \text{if } \dot{x}_i^* \neq 0, \\ -\Phi^*, & \text{if } \dot{x}_i^* = 0, \end{cases} \quad \Phi^* \in (-1, \ 1) \ \ (8)$$

Proceeding in Eq. (4) to the dimensionless variables and then omitting the asterisks, we arrive at the equation

$$\dot{V} = \varepsilon\, G(V,t), \ \ G(V,t) = m_1 F(V - m_2 u(t)) + m_2 F(V + m_1 u(t)), \ \ \varepsilon = \frac{kgT^2}{L}.$$

(9)

The function $G(V, t)$ is 1-periodic in t, since $u(t)$ is 1-periodic in t, the parameter ε characterizes the ratio of the force of friction to the force of interaction between the bodies of the system produced by the drive. Without loss of generality we will assume $m_2 > m_1$. If $m_2 < m_1$, we apply the change of variables $(m_1, m_2, u) \to (m_2, m_1, -u)$. This means that we invert the direction of the coordinate axis along the line of motion of the system and renumber the bodies. This change of variables preserves the right-hand side of Eq. (9). We do not consider the case where $m_1 = m_2$, because in this case, $G(0, t) \equiv 0$ for any $u(t)$, and the system cannot be set in motion from a state of rest.

4 Excitation Mode

We confine ourselves to the piecewise quadratic excitation mode that is characterized in the dimensionless variables by the function $l(t)$ defined as follows:

$$
l(t) = \begin{cases}
t^2/\tau, & 0 \leq t < \tau/2, \\
-(t-\tau)^2/\tau + \tau/2, & \tau/2 \leq t < \tau, \\
-\tau(t-\tau)^2/(1-\tau)^2 + \tau/2, & \tau \leq t < (1+\tau)/2, \\
\tau(t-1)^2/(1-\tau)^2, & (1+\tau)/2 \leq t < 1,
\end{cases} \quad \text{for } 0 < \tau \leq 1/2,
$$

(10)

$$
l(t) = \begin{cases}
t^2(1-\tau)/\tau^2, & 0 \leq t < \tau/2, \\
-(1-\tau)(t-\tau)^2/\tau^2 + (1-\tau)/2, & \tau/2 \leq t < \tau, \\
-(t-\tau)^2/(1-\tau) + (1-\tau)/2, & \tau \leq t < (1+\tau)/2, \\
(t-1)^2/(1-\tau), & (1+\tau)/2 \leq t < 1,
\end{cases}
$$

(11)

for $1/2 < \tau \leq 1$.

To represent these expressions in the dimensional variables according to Eq. (6), we should replace formally the variables l, t, and τ in Eqs. (10) and (11) by l/L, t/T, and τ/T, respectively. It can be shown that the maximum absolute value of the rate $\dot{l}$ is equal to L/T in the dimensional units and to 1 in the dimensionless units. Hence, when non-dimensionalizing, we defined the period T as a unit of time, and the maximum absolute value of the relative velocity of the system's bodies as a unit of velocity.

The functions $l(t)$ and $u(t) = \dot{l}(t)$ are plotted in Fig. 2.

5 Low Resistance Averaged Equation

In what follows, we assume that the parameter ε in Eq. (9) is small, while the function $G(V, t)$ has an order of unity. The right-hand side of Eq. (9) is 1-periodic in t. Then the method of averaging [1] can be applied to Eq. (9). According to this method, the time-varying Eq. (9) is replaced by the time-invariant averaged equation

$$
\dot{v} = \varepsilon\,\bar{G}(v), \quad \bar{G}(v) = \int_0^1 G(v,t)dt = \int_0^1 \left[m_1 F(v - m_2 u(t)) + m_2 F(v + m_1 u(t)) \right] dt.
$$

(12)
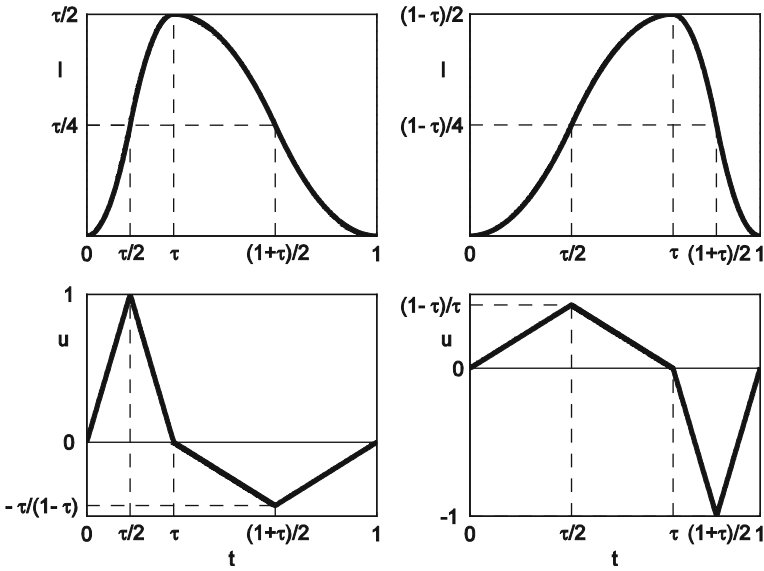
Fig. 2 Time histories of l and u

The solution $v(t)$ of the averaged Eq. (12) provides an acceptable approximation to the solution $V(t)$ of the primary Eq. (9).

The evolution of the velocity from the value $v = 0$ to the steady-state value is governed by the equation

$$\dot{v} = \varepsilon \bar{G}(v) = \varepsilon \begin{cases} (m_2 - m_1)(1 - 2\tau) - 2\left(\dfrac{m_1^2\tau^2 + m_2^2(1 - \tau)^2}{m_1 m_2 \tau}\right)v, & 0 < \tau \leq 1/2, \\[4mm] (m_2 - m_1)(1 - 2\tau) - 2\left(\dfrac{m_2^2\tau^2 + m_1^2(1 - \tau)^2}{m_1 m_2 (1 - \tau)}\right)v, & 1/2 < \tau < 1. \end{cases}$$

(13)

According to this equation, the system moves rightward for $\tau < 1/2$ and leftward for $\tau > 1/2$. The system cannot start moving from a state of rest if $\tau = 1/2$. For $\tau \neq 1/2$, the velocity $v(t)$ approaches its steady-state value exponentially as $t \to \infty$. The steady-state velocity v_* is defined as a root of the equation $\bar{G}(v_*) = 0$. Figure 3 plots the maximum of the absolute value of the steady-state velocity $|v_*|_{\max}$ as a function of m_1 for $0 < m_1 < 1/2$.

From Fig. 3 it is seen that there exists an optimal value of $m_1 \approx 0.28$ that corresponds to the maximum steady-state velocity.

Fig. 3 The maximum steady-state velocity $|v_*|_{max}$ versus m_1
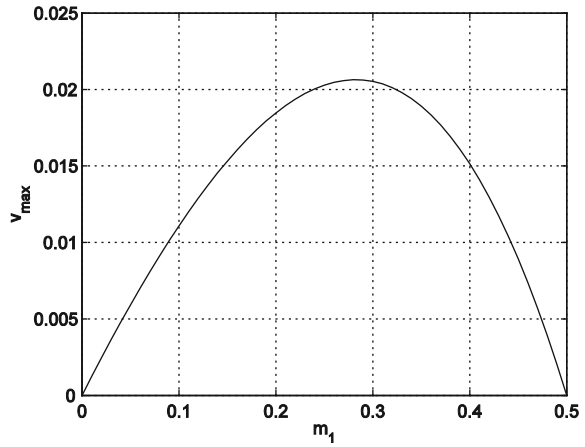
Fig. 4 Prototype of the mobile robot
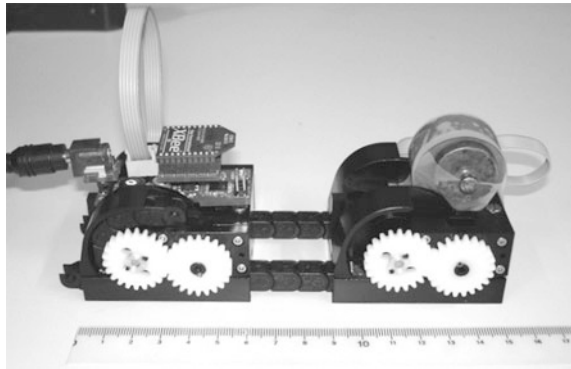
6 A prototype of the Mobile Robot and the Experiments

A prototype of the locomotion system under consideration is shown in Fig. 4.

This prototype was built at Technische Universitaet Ilmenau. The masses of bodies 1 and 2 are $M_1 = 0.125$ kg and $M_2 = 0.245$ kg, respectively, the coefficient of friction $k = 0.065$, and the distance by which the bodies of the system can move apart is max $_t l(t) -$ min $_t l(t) = 2$. The excitation period and the switching time are defined as $T = 0.37$ s and $\tau = 0.12$ s, respectively. For this case, $\varepsilon = 0.71$. The steady-state velocity of the robot measured in the experiment is $V_{exp} = 0.54$ cm/s, while the calculation in accordance with the averaged equation of motion yields $V_{theor} = 0.63$ cm/s.

7 Conclusion

The system under consideration can move progressively, if the bodies have different masses and the times of increase and decrease in the distance between them during the period do not coincide. The motion changes in direction if the bodies of the system change in place or the difference between the times of increase and decrease in the distance between the bodies changes in sign. A prototype based on the principles described above was built, and the experiments demonstrated an acceptable qualitative agreement with the theoretical predictions.

References

1. Bogolybov, N.N., Mitropolski, Y.A.: Asymptotic methods in the theory of nonlinear oscillations. Gordon and Breach Science, New York (1961)
2. Bolotnik, N., Pivovarov, M., Zeidis, I., Zimmermann, K.: The undulatory motion of a chain of particles in a resistive medium. ZAMM **91**, 259–275 (2011)
3. Chernousko, F.L.: The optimum rectilinear motion of a two-mass system. J. Appl. Math. Mech. **66**, 1–7 (2002)
4. Chernousko, F.L.: Analysis and optimization of the rectilinear motion of a two-body system. J. Appl. Math. Mech. **75**, 493–500 (2011)
5. Chernousko, F.L., Bolotnik, N.N., Figurina, T.Yu.: Optimal control of vibrationally excited locomotion systems. Regular Chaotic Dyn. **18**, 85–99 (2013)
6. Wagner, G.L., Lauga, E.: Crawling scallop: friction-based locomotion with one degree of freedom. J Theor Biol. **324**, 42–51 (2013)
7. Zimmermann, K., Zeidis, I., Behn, C.: Mechanics of Terrestrial Locomotion. Springer, Berlin (2009)

Shaking Force and Shaking Moment Balancing in Robotics: A Critical Review

Vigen Arakelian

Abstract The continuous demand for increased operation speeds of manipulators challenges designers with various issues. One of them is the vibration in the base due to the shaking force and shaking moment. Thus, it is desirable that a high-speed manipulator will be balanced in order to reduce the variable dynamic loads transmitted to the frame. Various design concepts for balancing of manipulators are available in the literature. The aim of this paper is to propose a critical review of shaking force and shaking moment balancing methods used in robotics.

Keywords Shaking force · Shaking moment · Static balancing · Dynamic balancing · Reactionless manipulator · Optimal motion planning

1 Introduction

It is known that a high-speed mechanical system with unbalance shaking force/moment transmits substantial vibration to the frame. Thus, a primary objective of the balancing is to cancel or reduce the variable dynamic loads transmitted to the frame and surrounding structures. The reduction of vibrations leads to the increased accuracy of manipulators [1], which is the major advantage of the balancing.

Different approaches and solutions devoted to the shaking force and shaking moment balancing have been developed and documented for one degree of

V. Arakelian (✉)
Institut de Recherche en Communications et Cybernétique de Nantes (IRCCyN), UMR CNRS 6592, Nantes, France
e-mail: Vigen.Arakelyan@irccyn.ec-nantes.fr

V. Arakelian
Department of Mechanical and Control Systems Engineering, Institut National des Sciences Appliquées de Rennes (INSA), Rennes, France

freedom mechanisms [2–5]. A new field for their applications is the design of mechanical systems for fast manipulation, which is a typical problem in advanced robotics.

The balancing of manipulators is generally carried out by two steps: (i) the cancellation (or reduction) of the shaking force and (ii) the cancellation (or reduction) of the shaking moment.

2 Shaking Force Balancing

The review of methods devoted to the shaking force balancing of manipulators showed that five principal approaches can be distinguished.

2.1 Shaking Force Balancing by Adding Counterweights in Order to Keep the Total Centre of Mass of Moving Links Stationary

In the case of open-chain manipulators the balancing of shaking force start from the outermost link and add a counterweight to it bring the center of mass of this link on the preceding joint axis. Such a balancing process must be repeated sequentially until the center of mass of the whole chain will be at the fixed pivot [6]. It is obvious that the adding of a supplementary mass as a counterweight is not desirable because it leads to the increase of the total mass, overall size of the manipulator and the efforts in joints. That is why in many constructions of industrial robots the masses of the motors are often used as counterweights [7].

With regard to the parallel manipulators, the purpose is the same: by adding counterweights keep the total centre of mass of moving links stationary. However, it is easier to carry out such a balancing in planar parallel manipulators [8] than in spatial parallel manipulators [9].

2.2 Shaking Force Balancing by Adding Auxiliary Structures

The different approaches have developed in order to keep the total centre of mass of moving links stationary by adding auxiliary structures.

In [6] the parallelograms, as auxiliary structures, were used in order to create the balanced manipulators. The three links are added to form parallelograms and then used to identify the center of mass. For the 3-link mechanism, the system consists of parallelograms in two layers: the first layer has two parallelograms

while the second layer has one. As it mentioned in the cited paper, this procedure can be extended to *n* links.

The pantograph has also been used in order to balance the shaking force of the Delta robot [10, 11]. The different solutions were proposed: by adding a pantograph to each leg or by adding a pantograph connected with the center of mass localized by using the parallelograms.

2.3 Shaking Force Balancing by Elastic Components

These studies are focused on optimum force balancing of a five-bar parallel manipulator with combination of a proper distribution of link masses and the springs connected to the driving links. The force balancing is formulated as an optimization problem such that a mean-square-root of the sum-squared values of bearing and spring forces. However, it should be noted that the springs connected to the driving links produce elastic forces which are the internal forces and the added springs cannot have any influence on the shaking force minimization due to the inertia of the moving links. Nevertheless, they influence on the gravitational forces and the input torques which are also included in the objective function. In the mentioned studies, the authors overlook this fact [12, 13].

2.4 Shaking Force Balancing by Adjustment of Kinematic Parameters

This study deals with the synthesis of the balanced five-bar mechanism via changing the geometric and kinematic parameters of the mechanical structure. The shaking force balancing leads to the conditions which are traditionally satisfied by the redistribution of moving masses. In the mentioned studies the link's mass is considered unchanged and the lengths and the mass centers of the links are determined in order to carry out the shaking force balancing. Thus, a new kinematic chain is obtained which is fully force balanced. With regard to the trajectory planning, the authors propose to assume the given positions of the end effector of the mechanism by the controllers of servomotors. As it is rightly mentioned in these studies, the proposed design approach will change the workspace, so some regions of the original workspace may not be reachable. The drawback of this approach is that the designers, firstly, set the structural and kinematic tasks, then the dynamic optimization. It is really rare such a situation when it is necessary to impose the fixed values of moving masses and then to find the kinematic parameters of the mechanism [14].

This approach was also applied on the design of a spatial three-degree-of-freedom parallel manipulator [15]. The theoretical results were obtained, which was not feasible for real application.

It seems that the combined optimization including mass and geometric parameters will be more attractive for a wide range of applications of this technique.

2.5 Shaking Force Minimization via Centre of Mass Acceleration Control

Solution developed in [16] was based on the optimal control of the robot links centre of masses. The aim of the suggested method consists in the fact that the manipulator is controlled not by applying end-effector trajectories but by planning the displacements of the total mass centre of moving links. The trajectories of the total mass centre of moving links are defined as straight lines and are parameterized with "bang-bang" displacement law. Such a control approach allows the reduction of the maximum value of the centre of mass acceleration and, consequently, the reduction in the shaking force. It should be mentioned that such a solution is also very favourable for reduction of input torques because it is carried out without adding counterweights.

3 Shaking Moment Balancing

With regard to the shaking moment balancing of manipulators, the following approaches were developed.

3.1 Shaking Moment Balancing by Counter-Rotation

The concept of the shaking moment balancing by counter-rotation was studied for the first time in [17]. This approach was developed further in the various studies devoted to the balancing of 1-dof mechanisms and later in [8, 18–21] to multi-dof mechanisms.

As it was rightly pointed out in [22], this technique leads to the unavoidable increase in the initial mass, as well as the mechanism dimensions and the price paid for complete shaking moment balancing is unjustifiably high.

Taking into account this criticism, in [23–28], a new design concept was proposed, studied and optimized for light-weight shaking moment balancing by gears. The aim of this concept is to assume both the functions of counter-rotation and counterweight simultaneously, and help reduce the mass of the resulting mechanism.

At the end of this subsection it should be noted that the major disadvantage of the balancing technique by counter-rotation is the need for the connection of gears

to the oscillating links. The oscillations of the links of the manipulator will create noise unless expensive anti-backlash gears are used. Anti-backlash gears are devices that bias the gear always to favour one side of the tooth through spring action. Regardless of the direction of movement, they should always 'push' up against the same side of the tooth. They are basically comprised of two gears that are spring-loaded in opposing directions. One gear is attached to the mechanism being moved, the other simply 'floats' to provide the bias.

3.2 Shaking Moment Balancing with Modules Based on Dynamically Balanced Four-Bar Linkages

In this case, the complete shaking force and shaking moment balancing is carried out without any separate counter-rotation. It becomes possible thanks to the synthesis of fully balanced four-bar linkages. It was shown that a four-bar linkage having specific geometric parameters and assuming some report between the lengths of links can be fully balanced only by optimal choice of mass and inertia parameters of moving links. This principle is also practicable when the input angular velocity of the four-bar linkage is variable. Thus, the various structures of manipulators are designed by special legs constructed with modules based on dynamically balanced four-bar linkages [29–32].

3.3 Shaking Moment Balancing by Generating Optimal Trajectories of Moving Links

In [33] a redundant 3-DOF manipulator is designed in which the system center mass is fixed by optimal redistribution of masses and the dynamics of the system is decoupled. The letter feature simplified the planning of optimal motions in order to balance the shaking moment of the manipulator. A similar study is carried out in [34].

The study [35] deals with a novel scheme for motion planning of a dual-arm free-floating planar manipulator where one arm is commanded to perform desired tasks while the other provides compensating motions to keep the base inertially fixed.

Shaking moment balancing by prescribed rotation of the end-effector was proposed in [36–38]. The shaking moment of 3-DOF planar parallel manipulator [36] was cancelled using two approaches: thought proper choice of inertia and geometric parameters and using appropriate motion planning. The shaking moment of the SCARA-type robots with 4-DOF has been vanished by prescribed velocity of the end-effector [37]. Taking into account that the two angles of the linear positioning don't depend on the orientation angle, it was proposed to balance the shaking moment of the robot by rotation of the end-effector during its linear displacement. The advantage of such a balancing is simplicity because the

complete balancing of the shaking moment is achieved without important design modifications. The major drawback is the increasing the inertia moment of the end-effector in order to compensate the inertia moment all other rotating links. A similar approach has been applied on the PAMINSA manipulator in [38].

3.4 Shaking Moment Balancing by Adding an Inertia Flywheel Rotating with a Prescribed Angular Velocity

It is well known that after shaking force balancing the shaking moment applied on the base is constant relative to any point, i.e. for a given position of the manipulator it has the same value for any point of the base. Taking into account this property the shaking moment of any planar manipulator can be balanced by adding an inertia flywheel rotating with a prescribed angular velocity [39]. A similar approach based on the active balancing of the shaking moment of the Delta robot by three additional rotating inertia flywheels was discussed in [10].

It should be noted that the new balanced structures were also developed. In [40] a dynamically balanced 3-DoF planar parallel manipulator was presented and tested. The manipulator is composed of two independently force-balanced five-bar linkages pivoted to the base and coupled with an end-effector link. In this manipulator each leg was balanced separately, which was made possible by distributing the inertia of the platform on each of its attachment points [39, 41].

In [42] a novel 3-DOF parallel mechanism referred to as the parallelepiped mechanism was developed. Counterweights and counter-rotations were used to dynamically balance the proposed mechanism.

The design of a dynamically balanced redundant planar 4-RRR parallel manipulator was also presented together with the design approaches of adapting a given kinematic architecture and of composing it from known balanced architectures [43].

The complete shaking force and shaking moment balancing of planar parallel manipulators with prismatic pairs [44] and with variable payload [32, 45] were also studied.

Finally, it should be noted that the various optimization methods were also applied in order to reduce the dynamic loads due to the shaking force and shaking moment of manipulators [46–50].

4 Conclusion

The survey of investigations into the shaking force and shaking moment balancing of manipulators showed that not only the known methods of linkage balancing found further development but new approaches were also proposed. The counter-rotation balancing, which seemed to be essential technique in linkage balancing is

not so indispensable in robotics. It seems promising the design of reactionless manipulators with dynamically balanced modules, as well as the balancing by generation optimal motions of moving links of manipulators.

With regard to the various optimization techniques, it is obvious that they can be a useful tool for designers. Nevertheless, it is important to pay attention to the physical interpretation of the obtained results in order to avoid the possible errors.

Finally, it should be noted that although quite rich theoretical results the practical applications of developed balancing methods are fairly limited.

The strict space limitations did not permit the inclusion in this review of all the works worthy of attention. The list of references is in no way complete, but it covers the major part of the literature. In the future, a similar review with full references and more detailed discussion will be presented as a paper to an appropriate journal.

References

1. Foucault, S., Gosselin, C.M.: On the development of a planar 3-Dof reactionless parallel mechanism. In: Proceeding of the ASME Design Engineering Technical Conferences and Computers and Information in Engineering Conference, Montreal, Sept 29–Oct 2 2002
2. Lowen, G.G., Berkof, R.S.: Survey of investigations into the balancing of link-ages. J. Mech. **3**, 221–231 (1968)
3. Lowen, G.G., Tepper, F.R., Berkof, R.S.: Balancing of linkages: an update. Mech. Mach. Theory **18**(3), 213–230 (1983)
4. Arakelian, V., Dahan, M., Smith, M.R.: A historical review of the evolution of the theory on balancing of mechanisms. In: Proceeding of the International Symposium on History of Machines and Mechanisms - HMM2000 / Edited by Marco Ceccarelli, Kluwer Academic Publishers, Boston, pp. 291–300 (2000)
5. Arakelian, V., Smith, M.R.: Shaking force and shaking moment balancing of mechanisms: a historical review with new examples. Trans ASME J. Mech. Des. **127**, 334–339 (2005)
6. Agrawal, S.K., Fattah, A.: Reactionless space and ground robots: novel design and concept studies. Mech. Mach. Theory **39**, 25–40 (2004)
7. Bayer, A. and Merk, G.: Industrial robot with a weight balancing system. EP Patent 2 301 727, 24 Aug 2011
8. Menschaar, H., Ariens, A., Herder, J., Bakker, B.: Five-bar mechanism with dynamic balancing means and method for dynamically balancing a five-bar mechanism. Patent WO2006080846, 2 Aug 2006
9. Gosselin, C. M.: Gravity compensation, static balancing and dynamic balancing of parallel mechanisms. In: Smart Devices and Machines for Advanced Manufacturing, Springer, pp. 27–48 (2008)
10. Van der Wijk, V., Herder, J.L.: Dynamic balancing of Claver's Delta robot. In: Proceeding of the 5th International Workshop on Computational Kinematics, Computational Kinematics, Springer, pp. 315–322 (2009)
11. Herder, J.L., Van der Wijk, V.: Force balanced delta robot. Patent NL2002839, 11 Nov 2010

12. Alici G., Shirinzadeh, B.: Optimum force balancing with mass distribution and a single elastic element for a five-bar parallel manipulator. In: Proceeding of International Conference Robotics Automation, Taipei, pp. 3666–3671, 14–19 Sept 2003
13. Alici, G., Shirinzadeh, B.: Optimum force balancing of a planar parallel manipulator. J. Mech. Eng. Sci. **217**(5), 515–524 (2003)
14. Ouyang, P.R., Zhang, W.J.: Force balancing of robotic mechanisms based on adjustment of kinematic parameters. Trans ASME. J. Mech. Des. **127**, 433–440 (2005)
15. Zhang, D., Gao, F., Hu X., Gao, Z.: Static balancing and dynamic modelling of a three-degree-of-freedom parallel kinematic manipulator. In: Proceeding of International Conference Robotics Autommation, Shanghai, pp. 3211–3217, 9–13 May 2011
16. Briot, S., Arakelian, V., Le Baron, J.-P.: Shaking force minimization of high-speed robots via centre of mass acceleration control. Mech. Mach. Theory **57**(November), 1–12 (2012)
17. Berestov L.V.: Comparative analysis of the reactions in the kinematic pairs of the four-bar linkages for the different methods of balancing (Russian). J. Mech. Mach. n°52, 61–70 (1977)
18. Fattah, A., Agrawal, S.K.: On the design of reactionless 3-DOF planar parallel mechanisms. Mech. and Mach. Theory **4**(1), 70–82 (2006)
19. Coelho T.A.H., Yong L, Alves V.F.A.: Decoupling of dynamic equations by means of adaptive balancing of 2-DOF open-loop mechanisms. Mech. Mach. Theory **39**(8), 871–81 (2004)
20. Arakelian, V., Smith, M.R.: Design of planar 3-DOF 3-RRR reactionless parallel manipulators. J. Mechatron. **18**, 601–606 (2008)
21. Acevedo, M., Ceccarelli, M., Carbone, G.: Application of counter-rotary counterweights to the dynamic balancing of a spatial parallel manipulator. Appl. Mech. Mater. **162**, 224–233 (2012)
22. Kochev, I.S.: General theory of complete shaking moment balancing of planar linkages: a critical review. Mech. and Mach. Theory **35**, 1501–1514 (2000)
23. Herder, J.L., Gosselin, C.M.: A counter-rotary counterweight (CRCW) for light-weight dynamic balancing. In: Proceeding of the ASME Design Engineering Technical Conferences and Computers and Information in Engineering Conference, Salt Lake City, pp. 659–667, 28 Sept–2 Oct 2004
24. Van der Wijk, V., Herder, J. L.: Dynamic balancing of mechanisms by using an actively driven counter-rotary counter-mass for low mass and low inertia. In: Proceeding of the Second International Workshop on Fundamental Issues and Future Research Directions for Parallel Mechanisms and Manipulators, Montpellier, pp. 241–251 (2008)
25. Van der Wijk, V., Herder, J. L.: Double pendulum balanced by counter-rotary counter-masses as useful element for synthesis of dynamically balanced mechanisms. In: Proceeding of the ASME International Design Engineering Technical Conferences and Computers and Information in Engineering Conference, Brooklyn, 3–6 August 2008
26. Van der Wijk, V., Herder, J. L.: Guidelines for low mass and low inertia dynamic balancing of mechanisms and robotics. Advances in Robotics Research, **4**, 21–30 (2009)
27. Van der Wijk, V., Herder, J. L., Demeulenaere, B.: Comparison of various dynamic balancing principles regarding additional mass and additional inertia. Trans. ASME. J. Mech. Robot. **1**, 9 p (2009)
28. Van der Wijk, V., Demeulenaere, B., Gosselin, C., and Herder, J. L.: Comparative analysis for low-mass and low-inertia dynamic balancing of mechanisms. Trans. ASME. J. Mech. Robot. **4**, 031008 (2012)
29. Richard, R., Gosselin C.M.: On the development of reactionless parallel manipulators. In: Proceeding of the ASME Design Engineering Technical Conferences and Computers and Information in Engineering Conference, Baltimore, 10–13 Sept 2000
30. Gosselin, C.M., Coté, G., Wu, Y.: Synthesis and design of reactionless three-degree-of-freedom parallel manipulators. IEEE Trans. Robot. Autom. **20**(2), 191–199 (2004)
31. Wu, Y., Gosselin, C.M.: Synthesis of reactionless spatial 3-DOF and 6-DOF mechanisms without separate counter-rotations. Int. J. Robot. Res. **23**(6), 625–642 (2004)

32. Lecours, A., Gosselin, C.M.: Reactionless two-degree-of-freedom planar parallel mechanisms with variable payload. Trans. ASME. J. Mech. Robot. **2**, 041010-1–041010-7 (2010)
33. Papadopoulos, E., Abu-Abed, A.: Design and motion planning for a zero-reaction manipulator. In: Proceeding of the IEEE International Conference on Robotics and Automation, San Diego, pp. 1554–1559 (1994)
34. He, G., Lu, Z.: Optimal motion planning of parallel redundant Mechanisms with Shaking Force Reduction. In: Proceeding of the IMACS conference, Beijing, pp. 1132–1139, 4–6 Oct 2006
35. Agrawal, S.K., Shirumalla, S.: Planning motions of a dual-arm free-floating manipulator keeping the base inertially fixed. Mech. Mach. Theory **30**(1), 59–70 (1995)
36. Fattah, A., Agrawal, S.K.: On the design of reactionless 3-DOF planar parallel mechanisms. Mech. Mach. Theory. **41**(1), 70–82 (2006)
37. Arakelian, V., Briot, S.: Dynamic balancing of the SCARA robot. In: Proceedings of the 17th CISM-IFToMM Symposium on Robot Design, Dynamics, and Control (Romansy 2008), Tokyo, 5–9 July 2008
38. Briot, S., Arakelian, V.: Complete shaking force and shaking moment balancing of the position-orientation decoupled PAMINSA manipulator. In: Proceeding of the IEEE/ ASME International Conference on Advanced Intelligent Mechatronics, Singapore, 14–17 July 2009
39. Arakelian, V., Smith, M.: Design of planar 3-DOF 3-RRR reactionless parallel manipulators. Mechatronics **18**(10), 601–606 (2008)
40. Foucault, S., Gosselin, C.M.: Synthesis, design, and prototyping of a planar three degree-of-freedom reactionless parallel mechanism. AMSE J. Mech. Des. **126**, 992–999 (2004)
41. Wu, Y., Gosselin, C.M.: On the dynamic balancing of mult-dof parallel mechanisms with multiple legs. Trans. AMSE J. Mech. Des. **129**(2), 234–238 (2007)
42. Wu, Y., Gosselin, C.M.: Design of reactionless 3-DOF and 6-DOF parallel manipulators using parallelepiped mechanisms. IEEE Trans. on Robot. **21**(5), 821–833 (2005)
43. Van der Wijk, V., Krut, S., Pierrot, F., Herder, J.L.: Design and experimental evaluation of a dynamically balanced redundant planar 4-RRR parallel manipulator. Int. J. Robot. Res. **32**, 744–759 (2013)
44. Briot, S., Bonev, I.A, Gosselin, C.M, Arakelian, V.: Complete shaking force and shaking moment balancing of planar parallel manipulators with prismatic pairs. J. Multi-body Dyn. **222**(Part K, 1), pp. 43–52 (2009)
45. Van der Wijk, Herder, J.L.: Force balancing of variable payload by active force-balanced reconfiguration of the mechanism. In: Proceeding of the ASME/IFToMM International Conference on Reconfigurable Mechanisms and Robots, London, pp. 323–329, 22–24 June 2009
46. Xi, F.: Dynamic balancing of hexapods for high-speed applications. Robotica **17**, 335–342 (1999)
47. Alici, G., Shirinzadeh, B.: Optimum dynamic balancing of planar parallel manipulators. In: Proceeding of the IEEE International Conference on Robotics and Automation, New Orleans, pp. 4527–4531, April 2004
48. Alici, G., Shirinzadeh, B.: Optimum dynamic balancing of planar parallel manipulators based on sensitivity analysis. Mech. Mach. Theory **41**, 1520–1532 (2006)
49. Ilia, D., Cammarata, A., Sinatra R.: A novel formulation of the dynamic balancing of five-bar linkages. In: Proceeding of the 12th World Congress in Mechanism and Machine Science, Besançon, 18–21 June 2007
50. Buganza, A, Acevedo, M.: Dynamic balancing of a 2-DOF 2RR planar parallel manipulator by optimization. In: Proceeding of the 13th World Congress in Mechanism and Machine Science, Guanajuato (2011)

Investigation into the Influence of the Foot Attachment Point in the Body on the Four-Link Robot Jump Characteristics

S. Jatsun, O. Loktionova, L. Volkova and A. Yatsun

Abstract In this paper the settlement scheme of the four-link jumping robot is submitted, the mathematical model of movement of object in which the jump of the device is presented in the form of sequence of phases is developed, dependences between the jump characteristics and the position of the point of fixing of a foot are received.

1 Introduction

Nowadays the mobile robotic systems are widely used in inspection, repairing, dismantling, transportations and rescue operations, especially when the latter appear to be dangerous and potentially hazardous or being conducted in least accessible areas. Relatively new but rapidly developing area of robotics is construction of devices that are able to move above the surface. Such a great demand

S. Jatsun (✉) · L. Volkova · A. Yatsun
Department of Theoretical Mechanics and Mechatronics, South-West State University,
Kursk, Russia
e-mail: teormeh@inbox.ru

L. Volkova
e-mail: mila180888@yandex.ru

A. Yatsun
e-mail: ayatsun@yandex.ru

O. Loktionova
South-West State University, Kursk, Russia
e-mail: teormeh@inbox.ru

of this area of robotics is easily explained by device's increased ability to move cross-country, on rough or uneven terrain and the possibility of their use for military intelligence purposes, buildings examination and monitoring the environment after natural and technological disasters.

Devices that are able to move above the surface are being researched by many scientists, such as S. Kesner, G. Zeglin, S. Dubowsky, P. Fiorini, M. Kovac, D. Floreano, M. Raibert, V. Lapshin, S. F. Jatsun, S. Komarov, N. Miskaktin and many others [1–8]. At the same time, hopping devices dynamics, modes of their movement and jump stages are not studied enough, which significantly limits the possible use of these devices. Therefore, the crucial tasks nowadays are the investigation of device's dynamic motion regimes with regard to the positioning parameters and acceleration before the lift-off from the surface, dynamic effects arising from the implementation of the jump, development of parameters calculation methods of the device and synthesis of control laws for realization of the required characteristics of the jump.

2 Mathematical Model of the Jumping Apparatus

Jumping apparatus, analytical model of which is presented in Fig. 1, consists of the links 1–4, link 1 is the foot, links 2 and 3 are the leg, and link 4 is the body [7, 8]. Links 4 and 2 hold drives 5 and 6 of the rotational motion, respectively; they provided rotation the links 3 and 1 relatively to the links 4 and 2. Link 2 also holds drive 7 of the progressive movement, allowing parts 2 and 3 move relative to each other. The jump of the apparatus is considered in the vertical plane Oxy with a horizontal rough absolutely rigid surface, which belongs to the axis Ox.

There has been developed an apparatus jump realization method (Fig. 2). During stages 1–3 there is the positioning of the object for the jump, the body of the robot interacts with the surface and accelerating module consisting of links 1–3 changes its position relative to the body for jump realization under a demanded angle to the horizon. At a stage 1 links 1, 2 and 3 rotate in the body so that the link 2 is settled down under a demanded angle to the horizon. The second stage is characterized by rotation of a link 1 to the point where it is paralleled to the side of the body on which points interact with a surface. During the third stage links 1 and 2 move forward from the body until link 1 interacts with surface. The fourth stage corresponds to acceleration of the device during which the link 1 appears on a surface, and links 3 and 4 move with an increasing speed at the expense of sliding pair. The stage 5 is described by robot movement above the surface, links 1 and 2 are thus involved in the body. Stages 6 and 7 describe an object landing on the body and its positioning until the body won't reach steady position on a surface. And the stage 7 can be observed if the device lands on one point of the body, otherwise after a stage 6 the object is ready to realization of the following jump.

While developing mathematical model of the device the following assumptions were accepted. It is considered that all links of the device are absolutely rigid
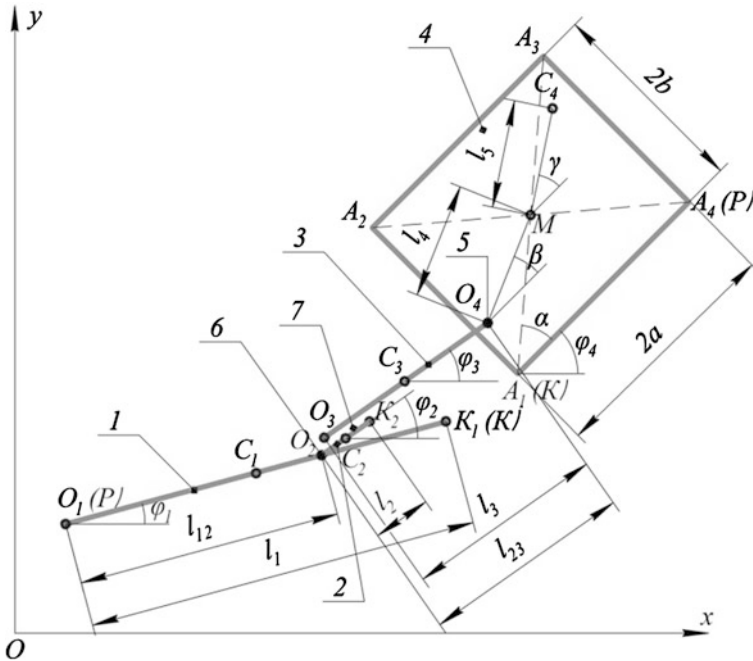
Fig. 1 Settlement scheme of the jumping apparatus

bodies, links 1–3 represent cores lengths l_i, $i = 1-3$, and link 4 is the rectangle $A_1A_2A_3A_4$ sizes the $2a \times 2b$. The centers of mass of links $i = 1-3$ are located in the centers C_i of their symmetry. The body's center of mass is a point C_4 displaced with respect to the center of symmetry of a rectangle (the point M) on distance l_5 at an angle γ. Length of a leg is defined by distance l_{23} between points O_2 and O_4, position of the point O_4 in the body is set by distance l_4 and an angle β.

There has been developed a mathematical model of interaction of links 1 and 4 with the surface considering jump stages. The assumption taken states that at interaction of each link with a surface as the centers of normal reaction of a surface the extreme points with the support elements of the corresponding link which have been conditionally designated K and P. If interaction of a link 1 or 4 to a surface occurs in one point, this point becomes a point of normal reaction forces application. Friction force in both cases arises only in one contact point K and is described by the following formula:

$$F_{frK} = \begin{cases} -fN_K\mathrm{sgn}(\dot{x}_K), & \text{if } \dot{x}_K \neq 0; \\ -F_0, & \text{if } \dot{x}_K = 0, \ |F_0| \leq fN_K; \\ -fN_K\mathrm{sgn}(F_0), & \text{if } \dot{x}_K = 0, \ |F_0| > fN_K, \end{cases} \tag{1}$$

where F_0 is a horizontal projection of total force, except dry friction force, enclosed to the link interacting with a surface; f is a sliding friction coefficient; N_K

is the normal reaction in a point K; $\dot{x}_K$ is the speed of point K along axis Ox. At interaction of one of links 1 or 4 with a surface four options of movement of object (substage) are possible: (1) the link is not movably on a surface and interacts with it in two points $(N_K > 0) \wedge (N_P > 0) \wedge (|F_0| \leq fN_K)$; (2) the link interacts with a surface in two points and moves along an axis Ox $(N_K > 0) \wedge (N_P > 0)$ $\wedge(\dot{x}_K \neq 0)$; (3) the link contacts with a surface in one motionless point $(N_K > 0) \wedge (N_P = 0) \wedge (|F_0| \leq fN_K)$; (4) the link interacts with a surface in one point which moves along an axis Ox $(N_K > 0) \wedge (N_P = 0) \wedge (\dot{x}_K \neq 0)$.

Movement of each link of the device is described by three coordinates x_{Ci}, y_{ci}, φ_i, $i = 1-4$, where x_{Ci}, y_{Ci} are the projections of position of the center of mass of the link to axes Ox and Oy, φ_i is the angle of inclination of the link to the positive direction of a horizontal axis, for the body an angle φ_4 represents an angle under which the side A_1A_4 of the body is inclined to an axis Ox. Thus, total number of the coordinates defining position of the robot, is equal $W = 12$. At the same time constrains of two types are imposed on the mechanism:

(1) constantly operating constrains s = 7 determined from the kinematic scheme of the robot. Six constrains describe ratios between projections of positions of the centers of mass of links 2–4 and the same parameters of the first link, and the seventh constrain is caused by that links 2 and 3 represent prismatic joint;
(2) periodically arising constrains l caused by sequence of stages of a jump and interaction with a supporting surface.

Thus, the number of degrees of device freedom is determined by a following formula $n = W - s - 1$. The length n of a vector $\bar{q}$ of the generalized coordinates is a variable. In a general view for m substage ($m = 1 \ldots 4$) k stage ($k = 1 \ldots 7$) of a jump a generalized coordinates vector can be written as follows: $\bar{q}_{km} = (q_1 \ldots q_n)^T$.

At a stage 4 when the link 1 contacts the surface, the generalized coordinates vector $\bar{q} = \begin{pmatrix} x_{C1} & y_{C1} & \varphi_1 & \varphi_2 & \varphi_4 \end{pmatrix}^T$ is used for the description of device position on the surface Oxy without l constrains. The generalized coordinates vector is described as $\bar{q} = \begin{pmatrix} x_{C4} & y_{C4} & \varphi_1 & \varphi_2 & \varphi_4 \end{pmatrix}^T$ at the stages of a jump when the body of the robot interacts with a surface or the object is flying . Taking into account the pattern of friction force that describes object links interaction with a surface and types of link movements at jump stages we should remember that for each stage there are specific conditions for object's presence at each substage, specific l constrains and the generalized coordinates that form a $\bar{q}$ vector.

For the sake of analysis convenience, the differential equations system of jumping device movement, calculated with Lagrange equation of the second kind, can be presented in a matrix form.

$$A_{km}(g)\,\ddot{g} + B_{km}(g)D(\dot{g})\dot{g} + C_{km}(g)\dot{g}_6\dot{g}_8 = Q_{km}. \qquad (2)$$

Thus instead of a vector $\bar{q}$ of the generalized coordinates the generalized matrix-column g representing a matrix of eight coordinates by means of which it is
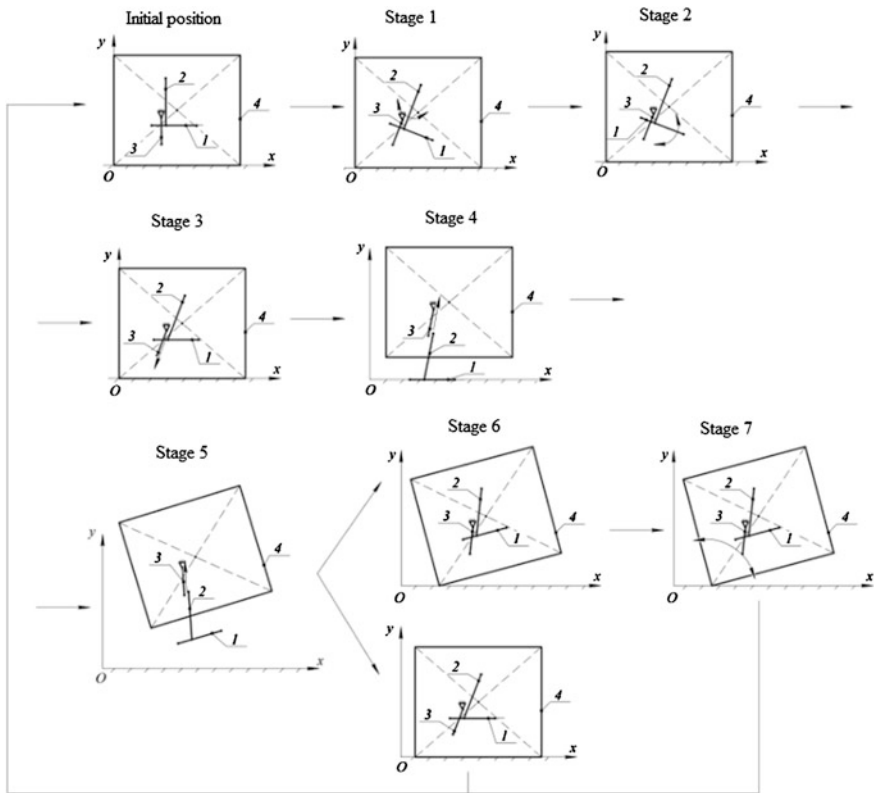
Fig. 2 Methodology of the jump

possible to describe object movement at any stage of a jump is used: $g_1 = x_{C4}$, $g_2 = y_{C1}$, $g_3 = x_{C4}$, $g_4 = y_{C4}$ are coordinates of the centers of mass of links 1 and 4, $g_5 = \varphi_1$, $g_6 = \varphi_2$ and $g_7 = \varphi_4$ are angles of rotation of the corresponding links, $g_8 = l_{23}$ is the length of a foot of the device. Matrixes of coefficients $A_{km}(g)$, $B_{km}(g)$, $C_{km}(g)$ and generalized forces Q_{km} are defined at each substage m of all stages k of movement of the robot according to the developed technique of a jump, $D(\dot{g})$ is a diagonal matrix of the first derivative coordinates g.

3 Results of Mathematical Model

The jump of the device is program-controlled, and control is exercised at stages 1–5, the moments and force, created by drives 5, 6 and 7 respectively are the operating influences (see Fig. 2). As operating influences will consider moments M_{43}, M_{21}, generated drives 5 and 6, and force F_{32} generated drive 7. In this article it is accepted that these influences are piecewise-constant functions, numerical
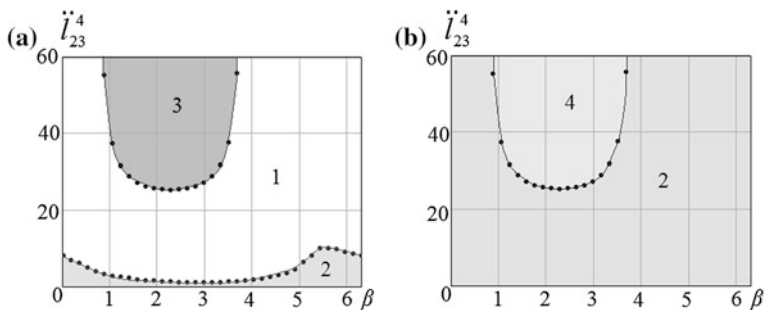
Fig. 3 Dynamic modes of acceleration: **a**–$f = 0.9$; **b**–$f = 0.7$; 1—two points of contact without slipping; 2—two points of contact with slipping; 3—one point of contact without slipping; 4—one point of contact with slipping

Fig. 4 Influence on height and length of a jump of acceleration of retraction of links 1 and 2 in flight
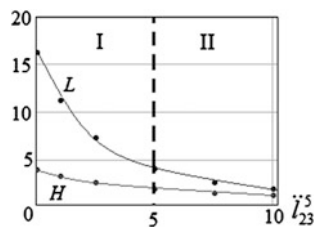

values of which at each stage of the jump are constant. Transition to dimensionless sizes using scaling coefficients of mass $M_0 = 0.05$ kg, time $T_0 = 0.1$ s, distances $L_0 = 0,1$ m is carried out for generalization of modeling results. Geometrical and inertial parameters of the robot: $m_{i\,=\,1-3} = 1$, $m_4/m_{i=1-3} = 5$, $a = 1$, $b = 1$, $l_1 = 0.5$, $l_2 = 0.9$, $l_3 = 0.9$, $l_{12} = 0.5$, $l_{23}^{min} = 0.4$.

It is established that four modes of acceleration are possible: at interaction of a link 1 with a surface in one and two points with slipping and without it (Fig. 3), where $\ddot{l}_{23}^4$ is the acceleration that moves links 3 and 4 at a stage 4, the top index corresponds to stage number. Areas of parameters at which acceleration occurs without slipping and capsizing are defined, also it is revealed that with increase of an angle φ_2^0 a foot inclination to a surface, the relations of the body mass to the mass of other links $m_4/m_{i\,=\,1-3}$ at $m_1 + m_2 + m_3 + m_4 = const$, the coefficient of friction f, reduction of distances l_{23}^0 and l_4 the range of accelerations $\ddot{l}_{23}^4$ without slipping and capsizing extends.

Dependences of height and length decrease of the jump on acceleration of links retraction of a foot in flight are received: at small accelerations height and length of a jump decrease curvilinearly, at large accelerations of retraction the law of decrease of characteristics of a jump asymptotically aspires to direct (Fig. 4).

At uniformly accelerated foot retraction at a flight stage the device rotates in the direction, opposite to the moment created by force of retraction, except for cases when the line of action of this force passes through point C_4. Values of an angle φ_4
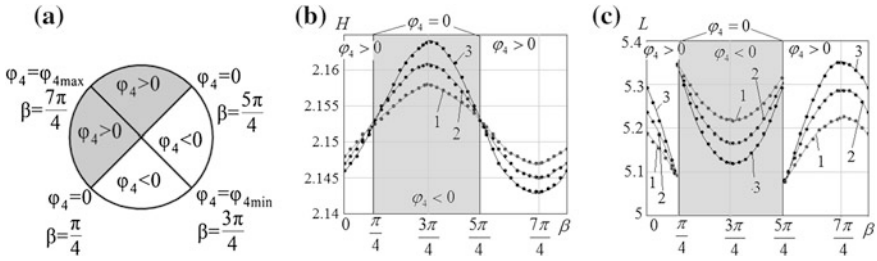
Fig. 5 Dependences of characteristics of a jump on the position of a point O_4: **a**—$\varphi_4(\beta)$; **b**—$H(\beta)$; **c**—$L(\beta)$; 1—$l_4 = 0.1$; 2—$l_4 = 0.15$; 3—$l_4 = 0.2$

Fig. 6 The diagram of modes of a landing at $l_4 = 0.1$, $\dot{l}_{23}^0 = 4$, $\varphi_2^0 = \pi/4$
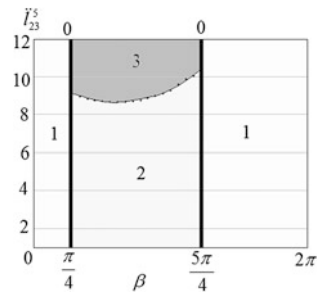
that are formed at the beginning of stage 6, change at a variation β in the range of $0 \ldots 2\pi$ under the sinusoidal law, the max value of an angle φ_{4max} is observed at $\beta = \varphi_2^0 + 3\pi/2$, and the min value $\varphi_{4\ min}$ at $\beta = \varphi_2^0 + \pi/2$, in the considered case $\varphi_2^0 = \pi/4$ (Fig. 5a). Values φ_{4max} and φ_{4min} increase on the module in proportion to increasing distance l_4. Body rotation in flight leads to sinusoidal dependence of height of a jump on an angle β, max value is observed at the smallest angle of rotation of the body in flight, and the min value at the greatest angle, that is visible according to Fig. 5b. Function $L(\beta)$ has discontinuous character and consists of three areas, discontinuities between which correspond $\beta = \varphi_2^0$ and $\beta = \varphi_2^0 + \pi$, when rotation of the body in flight doesn't carried out (Fig. 5c).

Body rotation in flight leads to various modes of a landing that is shown in Fig. 6.

In case when rotation occurs clockwise at big accelerations of retraction of links of a foot, at the end of a jump there will be a device overturn on 90^0 regarding the initial position, A_4 is the first point of a landing, A_3 is the second point of a landing (area 3). If there is no rotation in flight, or rotation is occurres counterclockwise or clockwise at small values of acceleration of retraction, at the end of the jump the object will be on the same side of the body with which the jump was carried out. The first and second points of a landing will change thus, in the first case the landing is carried out at the same time on two points A_1A_4 of the body (area 0), in the second case A_1 is the first point of a landing, A_4 is second point of a landing (area 1), for the third case is characteristic that the first point of a landing is A_4, the

second is A_1 (area 2). Character of the landing diagram is correct irrespective of values of varied parameters φ_2^0, l_4, $m_4/m_{i=1-3}$, and the initial speed of a stage of flight $\dot{l}_{23}^0$.

4 Conclusion

This article presents the four-link jumping robot consisting of the body, the foot formed by two links, and feet. The jump of the device is presented in the form of sequence of stages, each stage is characterized by certain types of link movements. For the following device there has been developed the mathematical model consisting of systems of the differential equations describing movement of the robot on each of stages with regard to the constrains imposed on system. According to this mathematical model numerical modeling of a jump of the device is carried out. Considering the results of mathematical modeling modes of acceleration and a landing of this device are revealed, regularities of jump characteristics from the position of a point of fixing of a foot in the body are received. This dependences can be used in design of the jumping robots that use a foot as the jumping module.

References

1. Kovac M., Schlegel M., Zufferey J.-C., Floreano D.: Steerable miniature jumping robot. Auton. Robot **28**, 295–306 (2010)
2. Dubowsky S., Kesner S., Plante J., Boston P.: Hopping mobility concept for search and rescue robots. J. Indus. Robot **35**(3), 238–245 (2008)
3. Lapshin, V.V.: Motion control of a legged machine in the supportless phase of hopping. Int. J. Robot. Res. **4**, 327–337 (1991)
4. Raibert, M.: Legged robots. Commun. ACM. **29**(6), 499–514 (1986)
5. Uniroo, Z.G.: A One-Legged Dynamic Hopping Robot, p.65. Massachusetts Institute of Technology, USA (1991)
6. Tammepõld, R., Fiorini P., Kruusmaa, M.: Attitude Control of Small Hopping Robots for Planetary Exploration: theory and Simulations, p. 1–8. ESA/ESTEC, Netherlands (2011)
7. Komarov, S.S., Miskaktin, N.I.: Stabilizacia lvigenia prygayushih pnevmouprugih roborov. Vestnik Ufimskogo gosudarstvennogo aviacionnogo tehnicheskogo universiteta. **11**(2), 97-104 (2008)
8. Jatsun, S.F., Volkova, L.Y.: Modelirovanie dvigeniya mnogozvennogo prygayushego robota I issledovanie ego harakteristik. Izv. RAN. TiSU **4**, 137–149 (2013)

Numerical Detection of Inactive Joints

Marek Wojtyra

Abstract Inactive joints are the joints that cannot perform relative motion due to structural limitations in a mechanism. They are usually introduced in order to eliminate redundant constraints. A joint can be inactive in the whole range of the mechanism motion or only in selected configurations. A numerical method of detection of inactive joints is presented. The method is based on multibody system approach and utilizes the constraint Jacobian matrix. The ability to perform relative motion is investigated and inactivity of joints in both regular and singular configurations is discussed. A numerical example is provided.

1 Introduction

Redundant constraints existence within the mechanism structure, combined with manufacturing imperfections of the mechanism parts or thermal loads, usually results in introduction of unwanted self-stresses and thus additional joint loads [1–3]. Consequently, the level of joint friction increases which—especially in robotic systems—causes problems with accurate controlling of the mechanism [4].

Modeling and simulation of overconstrained mechanisms is also impeded. It is impossible to find unique values of joint reaction forces using rigid body models [5–9]. Moreover, in the case of joint friction, the rigid body model does not lead to a unique solution of the direct dynamics problem [10].

The mechanisms intentionally designed to avoid redundant constraints are sometimes called rational mechanisms [11] or exact constraint designs [1]. Since

M. Wojtyra (✉)
Institute of Aeronautics and Applied Mechanics, Warsaw University of Technology,
Warsaw, Poland
e-mail: mwojtyra@meil.pw.edu.pl

overconstrained structures of robotic mechanisms are often unwelcome, the designers of parallel manipulators frequently propose structures without redundant constraints.

One of the method of constraint redundancy elimination consists in introduction of idle mobilities. The idle mobility is a potential mobility of a joint that is not used by the mechanism, under the hypothesis of perfect manufacturing and assembling precision [12]. When all motilities of a joint are idle, the joint is regarded as an inactive joint. Inactive joints are present in some types of structures of parallel manipulators [12–14]. Sometimes inactive joints are introduced to mathematical model of an overconstrained mechanism in order to avoid computational problems associated with the presence of redundant constraints [15].

It should be noted that introduction of inactive joints makes no contribution to the movement of the mechanism, however, it changes the number of over-constraints as well as the reaction forces in the joints [14]. In particular, when all redundant constraints are eliminated, the problem of joint reactions indeterminacy disappears [8].

When inactive joints are introduced in order to relax redundant constraints, their inactivity is observed in the whole range of mechanism motion. On the other hand, mechanism—that in regular configurations has no inactive joints—may reach a singular position, called a lock-up configuration [16] or stationary configuration [17], at which one or more joints become inactive.

In the case of designing structures of parallel manipulators' legs, the inactive joints are introduced deliberately, after thorough examination of the manipulator kinematics, thus there is no need to detect them. However, in the case of modeling and simulation of large and complicated multibody mechanisms or trusses, which were designed less carefully or even automatically generated, a method of automatic detection of inactive joints would be welcome. Such a method would be also useful in the detection and analysis of lock-up configurations of robotic mechanism as well as more general multibody systems.

This contribution presents a proposition of a numerical method of detection of inactive joints. A typical for multibody systems analyses approach, based on the constraint Jacobian matrix investigation, is adopted. The proposed method can be easily automated and applied to arbitrarily large and complex system.

2 Numerical Detection of Inactive Joints

2.1 Coordinates, Constraints and Jacobian Matrix

Let us consider a multibody system, consisting of rigid parts, whose configuration is described by n dependent generalized coordinates $\mathbf{q}$. Let us assume that constraints imposed on generalized coordinates are represented by a set of m scalar algebraic equations, which can be concisely written in a matrix form:

$$\mathbf{\Phi}(\mathbf{q}) = \mathbf{0}_{m \times 1}. \tag{1}$$

In further considerations absolute Cartesian coordinates [16, 18], often used in multibody modeling, are utilized. The main reason for choosing this type of coordinates is the fact that, in this approach, all kinematic pairs are treated in the same way, i.e. each pair is represented as a subset of Eq. (1). Moreover, for any moving body, information about its position and velocity is explicitly present in vectors $\mathbf{q}$ and $\dot{\mathbf{q}}$ (there is no need for recursive calculations).

The constraint Eq. (1) can be differentiated with respect to time to obtain constraints for velocities:

$$\mathbf{\Phi_q}(\mathbf{q}) \, \dot{\mathbf{q}} = \mathbf{0}_{m \times 1}, \tag{2}$$

where $\mathbf{\Phi_q}$ is the constraint Jacobian matrix of $m \times n$ size. In nonsingular configurations of the mechanism rank r of the Jacobian matrix is equal to m, if there are no redundant constraints, and is less than m when the mechanism is overconstrained.

2.2 Feasible Velocities of Bodies

For any movable mechanism $r = rank(\mathbf{\Phi_q})$ is less than n, thus there exist infinitely many vectors $\dot{\mathbf{q}}$ that satisfy Eq. (2). If the multibody system forms an unmovable structure (e.g., a truss), $r = n$ and $\dot{\mathbf{q}} = \mathbf{0}$ is the only solution.

Let matrix $\mathbf{N}$ of size $n \times (n{-}r)$ be defined as a basis for the null space of $\mathbf{\Phi_q}$, so that:

$$\mathbf{\Phi_q} \, \mathbf{N} = \mathbf{0}. \tag{3}$$

In accordance with Eq. (2), any feasible vector of multibody system velocities can be represented as a linear combination of columns of matrix $\mathbf{N}$:

$$\dot{\mathbf{q}} = \mathbf{N} \, \mathbf{\sigma}, \tag{4}$$

where column vector $\mathbf{\sigma}$ consists of coefficients of the linear combination.

When absolute coordinates are used, a global reference frame π_0 is established on the mechanism basis, and body-fixed local reference frames π_i are embedded in the other bodies. For a planar system comprising of b bodies (only planar mechanisms are considered henceforth, however the presented ideas are valid for spatial systems as well), the vector of coordinates $\mathbf{q}^T = \left[\mathbf{q}_1^T \ldots \mathbf{q}_i^T \ldots \mathbf{q}_b^T\right]$ consists of body-related subvectors $\mathbf{q}_i^T = \left[\mathbf{r}_i^T \quad \varphi_i\right]$, where $\mathbf{r}_i$ and φ_i represent the position and orientation of the local reference frame π_i with respect to the global frame π_0, respectively (note that $n = 3b$).

The feasible linear velocity of body i local frame origin ($\mathbf{v}_i$) and the feasible angular velocity of body i (ω_i) can be acquired from vector $\dot{\mathbf{q}}$, i.e., calculated as:

$$\begin{bmatrix} \mathbf{v}_i \\ \omega_i \end{bmatrix} = \dot{\mathbf{q}}_i = \begin{bmatrix} \mathbf{N}_i^v \\ \mathbf{N}_i^\omega \end{bmatrix} \boldsymbol{\sigma}, \tag{5}$$

where matrices $\mathbf{N}_i^v$ and $\mathbf{N}_i^\omega$ consist of rows of $\mathbf{N}$ associated with linear and angular motion of body i, respectively.

2.3 Method of Checking Ability to Perform Relative Motion

When searching for relative velocity of two bodies, linear velocities $\mathbf{v}_i$ and $\mathbf{v}_j$ cannot be compared directly, since origins of local frames i and j usually do not coincide. However, at each considered configuration, for each body k of the mechanism, it is possible to define an auxiliary point A_k which is rigidly connected to body k (the point moves along with the body) and—at the considered moment— coincides with the origin of the global frame. The linear velocity of point A_k can be calculated as:

$$\mathbf{v}_k^A = \mathbf{v}_k - \boldsymbol{\Omega}\,\mathbf{r}_k\,\omega_k = \left(\mathbf{N}_k^v - \boldsymbol{\Omega}\,\mathbf{r}_k\,\mathbf{N}_k^\omega\right)\boldsymbol{\sigma}, \qquad \boldsymbol{\Omega} = \begin{bmatrix} 0 & -1 \\ 1 & 0 \end{bmatrix}. \tag{6}$$

Now, taking into account feasible velocities of two bodies i and j, i.e. bodies that form an investigated kinematic pair, one can calculate feasible relative velocity of these bodies.

$$\begin{bmatrix} \mathbf{v}_{ij} \\ \omega_{ij} \end{bmatrix} = \begin{bmatrix} \mathbf{v}_i^A \\ \omega_i \end{bmatrix} - \begin{bmatrix} \mathbf{v}_j^A \\ \omega_j \end{bmatrix} = \begin{bmatrix} \mathbf{N}_i^v - \boldsymbol{\Omega}\,\mathbf{r}_i\,\mathbf{N}_i^\omega - \mathbf{N}_j^v + \boldsymbol{\Omega}\,\mathbf{r}_j\,\mathbf{N}_j^\omega \\ \mathbf{N}_i^\omega - \mathbf{N}_j^\omega \end{bmatrix} \boldsymbol{\sigma} = \mathbf{U}_{ij}\,\boldsymbol{\sigma}. \tag{7}$$

The velocity constraints given by Eq. (2) are satisfied for any choice of coefficients $\boldsymbol{\sigma}$, hence the relative motion of bodies i and j must be investigated for all vectors $\boldsymbol{\sigma}$. It is clear that when $\mathbf{U}_{ij} = \mathbf{0}$, the relative motion is impossible. In such a case, the joint formed by bodies i and j is inactive. Thus, to decide whether or not the investigated joint is active, it is sufficient to calculate matrix $\mathbf{U}_{ij}$ and inspect whether it consists of zeros only.

2.4 Comments and Remarks

The proposed method of detection of inactive joints acts only locally, i.e. it does not inform whether a joint classified as inactive at configuration $\mathbf{q}^*$ holds this property in the whole range of the mechanism motion or is inactive only in the

isolated point $\mathbf{q}^*$ at which the mechanism reaches lock-up configuration. To distinguish a permanent inactivity of joint from a temporary inactivity, the inspection should be repeated at a neighboring configuration $\mathbf{q}^* + \delta\mathbf{q}$.

Usually, to detect a lock-up configuration some driving constraints must be formulated [16]. The method proposed here does not require driving constraints. It is worth noting that, when no driving constraints are formulated, rank of the Jacobian matrix does not change at lock-up position. Nevertheless, by inspecting inactivity of joints, it is possible to detect that configuration is somehow special (lock-up), even though rank of the constraint Jacobian does not degenerate.

The proposed method may be amended in order to detect idle mobilities within joints with more than one degree of freedom. The amendment would consist in a convenient, i.e. joint-related selection of points A_i and A_j and appropriate rotation of local frames. In that way relative motion in joint-specific directions could be investigated.

3 Examples

For brevity and clarity a simple mechanism is analyzed, however, the discussed method of detection of inactive joints can be used for arbitrarily complex system.

The proposed method was utilized to investigate a mechanism presented in Fig. 1. The mechanism consists of the basis 0 and five moving bodies 1–5. The bodies are connected by five revolute joints (A, B, C, D, E) and two translational joints (K, L). The mechanism has one degree of freedom. The absolute coordinates that describe the mechanism form a vector consisting of $n = 15$ elements: $\mathbf{q} = \begin{bmatrix} \mathbf{r}_1^T & \varphi_1 & \mathbf{r}_2^T & \varphi_2 & \mathbf{r}_3^T & \varphi_3 & \mathbf{r}_4^T & \varphi_4 & \mathbf{r}_5^T & \varphi_5 \end{bmatrix}^T$.

Each revolute joint, formed by bodies i and j at point P, is represented by constraint equations of the form:

$$\boldsymbol{\Phi}^r = \mathbf{r}_i + \mathbf{R}_i \mathbf{s}_P^{(i)} - \mathbf{r}_j - \mathbf{R}_j \mathbf{s}_P^{(j)} = \mathbf{0}, \qquad \mathbf{R}_k = \mathbf{R}_k(\varphi_k) = \begin{bmatrix} \cos\varphi_k & -\sin\varphi_k \\ \sin\varphi_k & \cos\varphi_k \end{bmatrix},$$

(8)

where $\mathbf{s}_P^{(k)}$ is the position vector of point P in the local reference frame π_k and $\mathbf{R}_k$ is the direction cosine matrix ($\mathbf{r}_i$ and $\mathbf{r}_j$ are expressed in the global frame π_0).

Each translational joint, formed by bodies i and j, is represented by constraint equations of the form:

$$\boldsymbol{\Phi}^t = \begin{bmatrix} \left(\mathbf{r}_j + \mathbf{R}_j \mathbf{s}_Q^{(j)} - \mathbf{r}_i - \mathbf{R}_i \mathbf{s}_P^{(i)} \right)^T \mathbf{R}_j \mathbf{v}_{ij}^{(j)} \\ \varphi_i - \varphi_j - \psi_{ij} \end{bmatrix} = \mathbf{0}_{2\times 1},$$
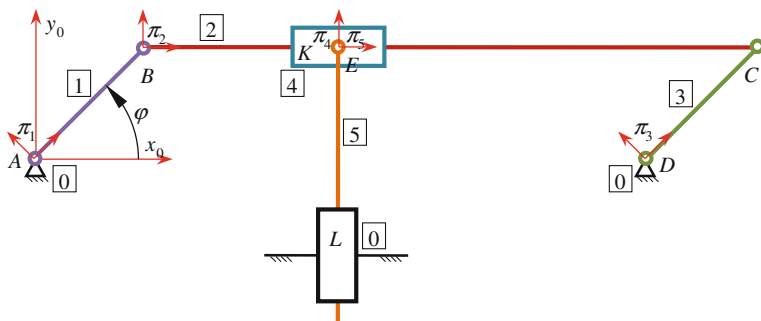
(9)

Fig. 1 Bodies, joints and reference frames of the investigated mechanism

where points P_i and Q_j lie on the axis of relative joint motion, vector $\mathbf{v}_{ij}$ is perpendicular to this axis and ψ_{ij} is a constant angular value.

Equation (8) for five revolute joints and Eq. (9) for two translational joints constitute constraint equations for the whole system ($m = 14$ scalar equations):

$$\mathbf{\Phi}(\mathbf{q}) = \begin{bmatrix} \mathbf{\Phi}_A^{rT} & \mathbf{\Phi}_B^{rT} & \mathbf{\Phi}_C^{rT} & \mathbf{\Phi}_D^{rT} & \mathbf{\Phi}_E^{rT} & \mathbf{\Phi}_K^{tT} & \mathbf{\Phi}_L^{tT} \end{bmatrix}^T = \mathbf{0} \qquad (10)$$

The constraint Jacobian $\mathbf{\Phi_q}$ is a matrix of size 14×15 (details of its derivation are omitted). The Jacobian matrix was evaluated for different configurations of the mechanism, represented by different values of angle φ (see Fig. 1). For each investigated configuration of the mechanism matrix $\mathbf{N}$ was calculated, and then—for each joint—matrices $\mathbf{U}_{ij}$ were computed. Finally, inactive joints were detected.

For several investigated regular configurations, i.e. for $0 < \varphi < \pi/2$, it was found that no redundant constraints exist, since constraint Jacobian is a full rank matrix ($r = 14$), and consequently, matrix $\mathbf{N}$ is of size 15×1. In every investigated regular configuration matrix $\mathbf{U}_{45}$ (that corresponds to joint E) was a zero matrix of size 3×1. All other matrices $\mathbf{U}_{ij}$ were nonzero matrices. As a result, revolute joint E was detected as the only inactive joint. These results agree with the outcome of an intuitive inspection of the mechanism—it is clear that body 4 cannot rotate with respect to body 5.

The results obtained for configuration described by $\varphi = \pi/2$ were different. This configuration, depicted in Fig. 2a, can be classified as a lock-up or stationary configuration, since body 5 cannot continue its upward motion. It should be emphasized that the configuration is not regular, nevertheless, the constraint Jacobian is a full rank matrix. As a result, matrix $\mathbf{N}$ is of size 15×1 and matrices $\mathbf{U}_{ij}$ are of size 3×1. The rank of $\mathbf{\Phi_q}$ does not suggest that the configuration is somehow special, however, the search for inactive joint does. It was found that this time two joints are inactive: the revolute joint E and the translational joint L. Note that a careful inspection of the mechanism reveals that in the considered configuration it is pointless to actuate joint L.
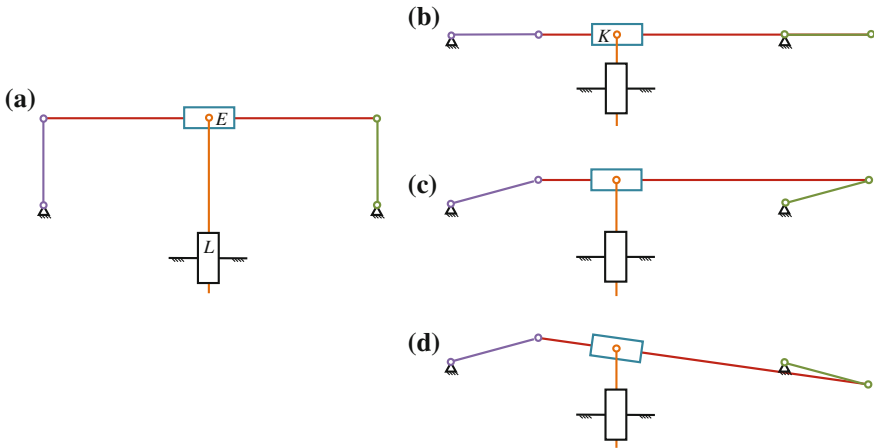
Fig. 2 Investigated configurations of the mechanism

Completely different results are obtained for configuration described by $\varphi = 0$, shown in Fig. 2b. This position of mechanism is singular, since the parallelogram formed of bodies 0, 1, 2 and 3 attains bifurcation configuration [16]. For $\varphi = 0$, the rank of the Jacobian matrix decreases to $r = 13$, which means that constraint dependency arises. Consequently, matrix $\mathbf{N}$ is of size 15×2 and matrices $\mathbf{U}_{ij}$ are of size 3×2. In the considered configuration matrix $\mathbf{U}_{24}$ (that corresponds to translational joint K) is a zero matrix, and all other matrices $\mathbf{U}_{ij}$ are nonzero. It should be stressed that joint E, which was inactive in all previous cases, becomes active for $\varphi = 0$. On the contrary, the translational joint K, which was active so far, becomes inactive. As it is shown in Fig. 2c, d, at the bifurcation configuration the mechanism can switch from parallel to skew assembly mode, which explains the possible activity of joint E.

The results obtained for $\varphi = 0$ and $\varphi = \pi/2$ show that detection of inactive joints may be helpful in singular configurations analysis.

4 Conclusions

A numerical method of detection of inactive joints was developed. The method conforms with multibody system approach to modeling of mechanisms and can be easily generalized to the case of spatial systems. After slight modifications, the method can be used to detect idle mobilities within joints with more than one relative degree of freedom. Potentially, the method can be used in analysis of mixed truss-mechanism systems. It was shown that in some situations the state of activity of a joint can change, thus the proposed method may be helpful in the analysis of singular configurations. This issue, however, needs to be further investigated.

References

1. Blanding, D.L.: Exact Constraint Machine Design Using Kinematic Principles. ASME Press, New York (1999)
2. Brouwer, D.M., Boer, S.E., Meijaard, J.P., Aarts, R.G.K.M.: Optimization of release locations for small self-stress large stiffness flexure mechanisms. Mech. Mach. Theory **64**, 230–250 (2013). doi:10.1016/j.mechmachtheory.2013.01.007
3. Olędzki, A.: Basics of Theory of Machines and Mechanisms (in Polish). WNT, Warsaw (1987)
4. Morecki, A., Oderfeld, J.: Theory of Machines and Mechanisms (in Polish). PWN, Warsaw (1987)
5. García de Jalon, J., Gutiérrez-López, M.D.: Multibody dynamics with redundant constraints and singular mass matrix: existence, uniqueness, and determination of solutions for accelerations and constraint forces. Multibody Sys. Dyn. **30**, 311–341 (2013). doi:10.1007/s11044-013-9358-7
6. Song, S.M., Gao, X.: The mobility equation and the solvability of joint forces/torques in dynamic analysis. ASME J. Mech. Des. **114**, 257–262 (1992). doi:10.1115/1.2916940
7. Wojtyra, M.: Joint reaction forces in multibody systems with redundant constraints. Multibody Sys. Dyn. **14**, 23–46 (2005). doi:10.1007/s11044-005-5967-0
8. Wojtyra, M.: Joint reactions in rigid body mechanisms with dependent constraints. Mech. Mach. Theory **44**, 2265–2278 (2009). doi:10.1016/j.mechmachtheory.2009.07.008
9. Wojtyra, M., Frączek, J.: Comparison of selected methods of handling redundant constraints in multibody systems simulations. ASME J. Comput. Nonlinear Dyn. **8**, 021007-1–021007-9 (2013). doi:10.1115/1.4006958
10. Frączek, J., Wojtyra, M.: On the unique solvability of a direct dynamics problem for mechanisms with redundant constraints and Coulomb friction in joints. Mech. Mach. Theory **46**, 312–334 (2011). doi:10.1016/j.mechmachtheory.2010.11.003
11. Reshetov, L.N.: Designing of Rational Mechanisms, 2nd edn. Mechanical Engineering, Moscow (1972)
12. Gogu, G.: Structural Synthesis of Parallel Robots. Part 4: Other Topologies with Two and Three Degrees of Freedom. Springer, Netherlands (2011)
13. Kong, X., Gosselin, C.M.: Type synthesis of three-degree-of-freedom spherical parallel manipulators. Int. J. Robot. Res. **23**, 237–245 (2004). doi:10.1177/0278364904041562
14. Kong, X., Gosselin, C.M.: Type synthesis of 4-DOF SP-equivalent parallel manipulators: a virtual chain approach. Mech. Mach. Theory **41**, 1306–1319 (2006). doi:10.1016/j.mechmachtheory.2006.01.004
15. Majou, F., Gosselin, C.M., Wenger, P., Chablat, D.: Parametric stiffness analysis of the orthoglide. Mech. Mach. Theory **42**, 296–311 (2007). doi:10.1016/j.mechmachtheory.2006.03.018
16. Haug, E.J.: Computer Aided Kinematics and Dynamics of Mechanical Systems. Allyn and Bacon, Boston (1989)
17. Yan, H.S., Wu, L.I.: The stationary configurations of planar six-bar kinematic chains. Mech. Mach. Theory **23**, 287–293 (1988)
18. Nikravesh, P.E.: Computer-Aided Analysis of Mechanical Systems. Prentice Hall, Englewood Cliffs (1988)

Quasi-Static Motions of a Three-Body Mechanism Along a Plane

I. Borisenko, F. Chernousko and T. Figurina

Abstract Quasi-static motion of a three-body system along a horizontal plane in the presence of dry friction is considered. The control forces are due to pairwise interaction between the bodies. For the quasi-static motion, the control forces should be chosen so that the equilibrium conditions hold for each body and, hence, for the entire system. The quasi-static motions, for which one of the bodies is moving, while the other two bodies are in a state of rest, are described. It is shown that if the products of the weight of each body by the corresponding friction coefficient satisfy the triangle inequalities, then each body can be quasi-statically moved to any prescribed position in the plane, whereas the other two bodies are at rest. Thus, quasi-static controllability of the system, subject to the aforementioned assumptions about the parameters, is proved. An optimal control problem for the moving body is solved, and the shortest (minimizing the work against friction) trajectory is shown to be a two-link broken line or a straight line segment. An algorithm for transferring the system to a given state is presented. The results obtained can be used for designing control strategies for mobile robotic systems.

Keywords Multibody mechanism · Control · Optimization · Dry friction · Robotics

I. Borisenko · F. Chernousko · T. Figurina (✉)
Institute for Problems in Mechanics RAS, Moscow, Russia
e-mail: t_figurinal@mail.ru

I. Borisenko
e-mail: IgorNB.mail@gmail.com

F. Chernousko
e-mail: chern@ipmnet.ru

1 Introduction

This paper is closely related to the studies that deal with the motions of robotic systems with variable configuration in resistive media. The control variables in such systems are either the forces acting between the components of the system or the rate at which the generalized coordinates that characterize the relative positions of these components change. When the configuration of the system changes, the velocities of its components, in the general case, change too, which causes a change in the external resistance forces.

One of the classes of systems outlined above are multilink systems moving along a horizontal plane, subject to dry friction. In papers [1–3] control problems for two-link and three-link systems that form an open chain of consecutively connected bodies are solved. It was proved that these multilink systems can be driven to any prescribed position in a plane by alternating slow (quasi-static) and fast motions.

There were also studied the quasi-static motions of multilink systems in the plane in the presence of dry friction forces, i.e., the motions where accelerations and velocities can be neglected. The control forces in a quasi-static motion coincide in order of magnitude with the forces of friction. It was proved [4] that multilink systems with at least four links can move quasi-statically along a straight line, whereas two-link systems are quasi-statically uncontrollable and their motion is fully preset by the initial position [5]. A three-link system of star-like type, as well as a three-link system with consecutive connection of the links can be moved to any position in the plane [6]. However, these motions are rather complex because of the kinematic constraints between vertices of the system.

In this paper, a three-body locomotion system on which no kinematic constraints are imposed is considered. The forces of interaction between the bodies are taken as the control forces. Dry friction forces act between the contact points and the plane. The system under consideration can be a model of a mobile robot that can move along a plane. Since the system has three contact points, it is statically determinate.

2 Equation of a Quasi-static Motion

Let us consider the system consisting of three point masses M_i, $i = 1, 2, 3$, on a horizontal plane (Fig. 1). Between each pair of masses M_i, control forces act. The system is a model of a mobile robot that can move along a plane, and we study possible quasi-static motions of the system.

Dry friction force $\mathbf{F}_i$ exerted upon point M_i of mass m_i is given by equations

Fig. 1 Three-body
mechanism
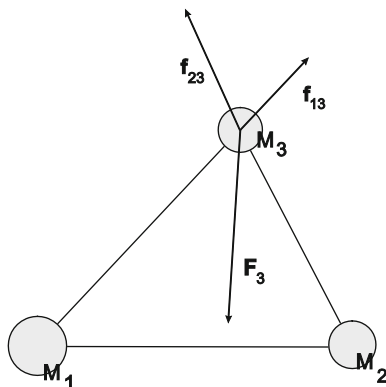
$$\mathbf{F}_i = -k_i m_i g \frac{\mathbf{v}_i}{|\mathbf{v}_i|}, \ \ \mathbf{v}_i \neq 0, \quad |\mathbf{F}_i| \leq k_i m_i g, \ \mathbf{v}_i = 0, \tag{1}$$

where $\mathbf{v}_i$ is the velocity of point M_i, k_i is the friction coefficient, and g is the gravity acceleration. For any pair of indices $i \neq j$, we have the interaction control force $\mathbf{f}_{ij}$ acting from point M_i upon point M_j and directed along $M_i M_j$

$$\mathbf{f}_{ij} = -\mathbf{f}_{ji}, \quad \mathbf{f}_{ij} \times (\mathbf{r}_i - \mathbf{r}_j) = 0, \quad i, j = 1, 2, 3, \quad i \neq j \tag{2}$$

where $\mathbf{r}_i$ is the radius-vector of M_i. We consider only such control forces $\mathbf{f}_{ij}$ that lead to quasi-static motion of each point M_i. In such motions, the equilibrium equations hold

$$\mathbf{F}_i + \mathbf{f}_{ji} - \mathbf{f}_{ik} = 0, \quad i \neq j \neq k, \quad i, j, k = 1, 2, 3. \tag{3}$$

From Eqs. (2), (3), it follows

$$\sum_{i=1}^{3} \mathbf{F}_i = 0, \quad \sum_{i=1}^{3} \mathbf{r}_i \times \mathbf{F}_i = 0. \tag{4}$$

It is shown that if forces $\mathbf{F}_i$ satisfy Eq. (4), then forces $\mathbf{f}_{ij}$ exist such that Eq. (3) hold. Suppose the parameters of the system satisfy the following triangle inequality

$$k_1 m_1 + k_2 m_2 \geq k_3 m_3 \tag{5}$$

and two other analogous inequalities that differ from (5) by the permutation of indices. It can be shown that (5) is a necessary condition for the possibility to move mass M_3.

3 Quasi-Static Motions with One Moving Point

Let us find all quasi-static motions such as two masses of the system (for example, M_1 and M_2) do not move, whereas the third mass (M_3) moves. Let D be the intersection of the circles with centers at points M_1 and M_2 and radii $ak_2m_2/(k_3m_3)$, $ak_1m_1/(k_3m_3)$ respectively, where a is the distance between the fixed points. The radii of the circles are the distance a between the fixed points multiplied by the ratio of the maximal friction forces at the fixed points to the maximal friction force at the moving point. Set D is not empty, according to inequality (5).

Proposition 1 *Quasi-static motion of mass M_3, with points M_1 and M_2 fixed, is possible iff the straight line containing point M_3 and parallel to its velocity intersects set D.*

Corollary *Under conditions (5) the system consisting of three masses M_1, M_2, and M_3 is quasi-statically controllable, i.e., can be quasi-statically brought to any preset position.*

4 Optimal Quasi-static Motions

Let us consider optimal control problem for the moving mass. Let two points A and B be fixed on the plane. It is required to move quasi-statically mass M_3 from point A to point B with minimal work against friction, i.e., to construct the trajectory of quasi-static motion for mass M_3 with the minimum length. If the straight line AB intersects set D, then the trajectory with the minimum length is the segment AB.

Proposition 2 *If the intersection of the setDwith the straight line AB is empty, then the trajectory with the minimum length for mass M_3quasi-statically moving from pointAto pointB,is polygonal chain ACB.The line segments ACandBCbelong to the supporting straight lines of set D; here, pointAand set Dare located on different sides of straight lineBC, and pointBand setDare located on different sides of straight lineAC(Fig.2).*

The algorithm for the displacement of the three—body system from any initial position to any given terminal one is presented. At any moment, only one mass M_i is moving, and each mass moves only during one time interval. There exist six ways of displacement, corresponding to six possible permutations of mass numbers. If permutation (i, j, k) is chosen, then points M_i, M_j, M_k move one after another, while two other masses are at rest. During each time interval the moving mass follows along the shortest trajectory which is either a straight line or a polygonal chain of two line segments, according to Proposition 2. Comparing these six ways of displacement, the algorithm corresponding to the minimum work can be chosen.
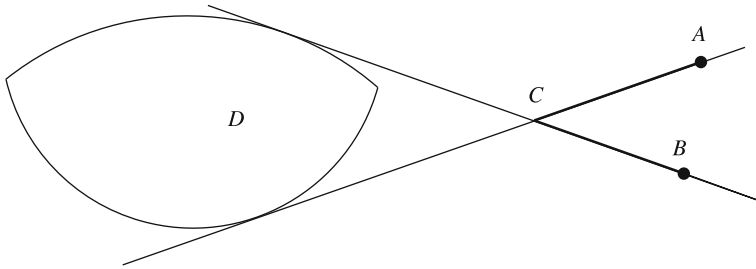
Fig. 2 Optimal trajectory

5 Conclusions

Quasi-static motions of a three-body system on a horizontal plane in the presence of dry friction is analyzed. Interaction forces between each pair of bodies are considered as controls. The case in which one body is moving whereas two others are at rest is considered. It is shown that, if the triangle inequality for the masses and friction coefficients holds, then the moving body can be relocated from any initial position to any terminal one. Optimal trajectory (minimizing the work against friction along the trajectory) is found and is proved to be a polygonal chain of one or two line segments. Quasi-static controllability of the system is established. The algorithm for relocating of the system to the given state is presented. The results obtained can be used for the development of control for mobile robotic systems.

References

1. Chernousko, F.L.: Controllable motions of a two-link mechanism along a horizontal plane. J. Appl. Math. Mech. **65**(4), 578–591 (2001)
2. Chernousko, F.L.: The motion of a three-link system along a plane. J. Appl. Math. Mech. **65**(1), 15–20 (2001)
3. Chernousko, F.L.: Snake-like locomotion of multilink mechanisms. J. Vib. Control **9**(1–2), 237–256 (2003)
4. Chernousko, F.L.: The wavelike motion of a multilink system on a horizontal plane. J. Appl. Math. Mech. **64**(4), 518–531 (2000)
5. Figurina, T.Y.: Quasi-static motion of a two-link system along a horizontal plane. Multibody Sys. Dyn. **11**(3), 251–272 (2004)
6. Figurina, T.Y.: Controlled slow motions of a three-link robot on horizontal plane. J. Comput. Syst. Sci. Int. **44**(3), 473–480 (2005)

Control Design for 3D Flexible Link Mechanisms Using Linearized Models

Erfan Shojaei Barjuei, Paolo Boscariol, Alessandro Gasparetto,
Marco Giovagnoni and Renato Vidoni

Abstract This paper presents an approach to the optimal control of a spatial flexible mechanism. A highly accurate dynamic model of the system is briefly resumed. Then, in order to be able to employ the classical optimal control theory, a linearization of the model with consideration of gravity force is done. After that the chosen optimal control is described, and the most important results of the simulation are presented and discussed.

Keywords Flexible links mechanisms · Dynamic model · Spatial mechanism · Control

1 Introduction

Robot motion control is an important criterion for robot manufactures, so the current investigations are focused on increasing the robot performance, robot cost reduction, safety improvements, and increasing new functionalities. Therefore,

E. S. Barjuei (✉) · P. Boscariol · A. Gasparetto · M. Giovagnoni
DIEGM, University of Udine, Udine, Italy
e-mail: erfan.shojaei@uniud.it

P. Boscariol
e-mail: paolo.boscariol@uniud.it

A. Gasparetto
e-mail: gasparetto@uniud.it

M. Giovagnoni
e-mail: giovagnoni@uniud.it

R. Vidoni
Faculty of Science and Technology, University of Bolzano, Bolzano, Italy
e-mail: renato.vidoni@unibz.it

there is a need to continuously improve the mathematical models and control methods in order to achieve conflicting requirements, such as performance increasing of a weight-reduced robot, with lower mechanical stiffness and more involved vibration modes.

Vibration control of flexible mechanisms as a subset of robot motion control is still an open issue in scientific researches [18]. A large amount of work has been carried out in the field of flexible mechanism modeling, analysis, and control since the early 1970s. Several techniques are currently available for modeling flexible mechanisms. Most researchers have concentrated their investigation on the describing of accurate mathematical models both for single body and multi-body system [1, 7, 18]. The classical approaches applied in flexible multi-body systems deals with mechanisms featuring large displacement and small deformations. Two main techniques have been adopted in literature [7, 8, 11–15]: the Finite Element Method (nodal approach) and the Assumed Mode Method (modal approach). Rigid body and elastic motion coupling effects have been considered in different works and approaches, firstly by considering only the effect of the rigid body motion on the elastic deformation [11, 14] and then by considering also the effect of the elastic deformation on the rigid body motion [15]. Floating Frame of Reference (FFR) formulation [16, 17] is the consequence of these works.

In this paper a linearized model is developed with the aim of designing model-based control techniques for spatial flexible link mechanisms. Linear models are often used to develop control strategies for this class of mechanism, including robust control [6], model predictive control [2–4] and sliding mode control [10], just to cite a few notable works on the subject. The accuracy of the linearization procedure introduced in this paper is measured by a comparison with the nonlinear model, and its use is demonstrated through the development of a LQR position and vibration control.

2 Dynamic Model of a Flexible Mechanism

One of the most studied problems in flexible robotics is dynamic modeling. Differently to conventional rigid robots, the elastic behavior of flexible robots makes the mathematical deduction of the models, which govern the real physical behavior, quite difficult. Here the method used for accurate modeling of the systems with large displacements and small elastic deformation is based on the Equivalent Rigid Link System (ERLS) concept which first was introduced for a planar mechanisms [9], and then expanded to spatial environment in [19, 20] which is briefly recalled in this section. According to the work [5], the ERLS-FEM dynamic model for flexible-link mechanisms is described by the ODE system of equations:

$$
\begin{bmatrix} \boldsymbol{M} & \boldsymbol{MJ} \\ \boldsymbol{J}^T\boldsymbol{M} & \boldsymbol{J}^T\boldsymbol{MJ} \end{bmatrix} \begin{bmatrix} \ddot{\boldsymbol{u}} \\ \ddot{\boldsymbol{q}} \end{bmatrix} = \begin{bmatrix} -2(\boldsymbol{M}_{G1}+\boldsymbol{M}_{G2})-\alpha\boldsymbol{M}-\beta\boldsymbol{K} & -\boldsymbol{M}\dot{\boldsymbol{J}} & -(\boldsymbol{M}_{C1}+2\boldsymbol{M}_{C2}+\boldsymbol{M}_{C3})-\boldsymbol{K} \\ \boldsymbol{J}^T(-2(\boldsymbol{M}_{G1}+\boldsymbol{M}_{G2})-\alpha\boldsymbol{M}) & -\boldsymbol{J}^T\boldsymbol{MJ} & -\boldsymbol{J}^T(\boldsymbol{M}_{C1}+2\boldsymbol{M}_{C2}+\boldsymbol{M}_{C3}) \end{bmatrix} \begin{bmatrix} \dot{\boldsymbol{u}} \\ \dot{\boldsymbol{q}} \\ \boldsymbol{q} \end{bmatrix}
$$
$$
+ \begin{bmatrix} \boldsymbol{M} & \boldsymbol{I} \\ \boldsymbol{J}^T\boldsymbol{M} & \boldsymbol{J}^T \end{bmatrix} \begin{bmatrix} \boldsymbol{g} \\ \boldsymbol{f} \end{bmatrix}
$$

$$
(1)
$$

in which $\boldsymbol{M}$ is the mass matrix, $\boldsymbol{J}$ is the Jacobian matrix of the manipulator, $\boldsymbol{M}_{G1}$ and $\boldsymbol{M}_{G2}$ are the Coriolis contribution terms, $\boldsymbol{K}$ is the stiffness matrix, and $\boldsymbol{M}_{C1}$, $\boldsymbol{M}_{C2}$ and $\boldsymbol{M}_{C3}$ are the terms introduced by the centrifugal terms of acceleration. $\boldsymbol{f}$ is the vector of nodal forces, $\boldsymbol{g}$ is the gravity vector, $\boldsymbol{q}$ is the vector of rigid displacements and $\boldsymbol{u}$ is the vector of nodal displacements. Rayleigh damping has been considered in the model, through α and β constants.

3 Linearized Model

The dynamic model represented by Eq. (1) is nonlinear, due to the quadratic relation between the nodal acceleration and the velocities of the free coordinates. Thus it cannot be used to design a linear-model based control. In order to develop a state-space form linearized version of the dynamic system of Eq. (1) a linearization procedure has been developed. First of all, Eq. (1) can be written in the following form, by defining a state vector $\boldsymbol{x}(t)$ and an input vector $\boldsymbol{v}(t)$:

$$
\boldsymbol{A}(\boldsymbol{x}(t))\dot{\boldsymbol{x}}(t) = \boldsymbol{B}(\boldsymbol{x}(t))\boldsymbol{x}(t) + \boldsymbol{C}(\boldsymbol{x}(t))\boldsymbol{v}(t)
$$

In which matrices $\boldsymbol{A}$, $\boldsymbol{B}$ and $\boldsymbol{C}$ do not depend on $\boldsymbol{v}(t)$. If $\boldsymbol{x}_e$ is a steady equilibrium point for the system in Eq. (1), a linearization procedure can be set by applying a Taylor series expansion:

$$
\boldsymbol{A}(\boldsymbol{x}_e + \Delta\boldsymbol{x}(t))(\dot{\boldsymbol{x}}_e + \Delta\dot{\boldsymbol{x}}(t)) = \boldsymbol{B}(\boldsymbol{x}_e + \Delta\boldsymbol{x}(t))(\boldsymbol{x}_e + \Delta\boldsymbol{x}(t)) \\ + \boldsymbol{C}(\boldsymbol{x}_e + \Delta\boldsymbol{x}(t))(\boldsymbol{v}_e + \Delta\boldsymbol{v}(t)) \quad (2)
$$

Since $\boldsymbol{x}_e(t)$ is an equilibrium point for the system, the following equation holds:

$$
\boldsymbol{B}(\boldsymbol{x}_e)\boldsymbol{x}_e + \boldsymbol{C}_e(\boldsymbol{x}_e)\boldsymbol{v}_e = \boldsymbol{A}(\boldsymbol{x}_e)\dot{\boldsymbol{x}}_e = 0 \quad (3)
$$

Therefore the system linearized around the equilibrium point can be written as:

$$
\boldsymbol{A}(\boldsymbol{x}_e)\Delta\dot{\boldsymbol{x}}(t) = \left[\boldsymbol{B}(\boldsymbol{x}_e) + \left(\frac{\partial\boldsymbol{B}}{\partial\boldsymbol{x}}\bigg|_{\boldsymbol{x}=\boldsymbol{x}_e} \times \boldsymbol{x}_e \right) + \left(\frac{\partial\boldsymbol{C}}{\partial\boldsymbol{x}}\bigg|_{\boldsymbol{x}=\boldsymbol{x}_e} \times \boldsymbol{v}_e \right) \right] \Delta\boldsymbol{x}(t) + \boldsymbol{C}(\boldsymbol{x}_e)\Delta\boldsymbol{v}(t)
$$

$$
(4)
$$

The matrices in Eq. (4) are constant, so we have obtained a linear model in the form:

$$A\Delta\dot{x}(t) = B\Delta x(t) + C\Delta v(t) \tag{5}$$

The constant matrices A and B can be evaluated as:

$$A = \begin{bmatrix} M & MJ & 0 & 0 \\ J^T M & J^T MJ & 0 & 0 \\ 0 & 0 & I & 0 \\ 0 & 0 & 0 & I \end{bmatrix}_{x=x_e} \tag{6}$$

$$B = \begin{bmatrix} -2M_G - \alpha M - \beta K & 0 & -K & B_{14} \\ J^T(-2M_G - \alpha M - \beta K) & 0 & 0 & B_{24} \\ I & 0 & 0 & 0 \\ 0 & I & 0 & 0 \end{bmatrix}_{x=x_e} \tag{7}$$

in which:

$$B_{14} = -\frac{\partial K}{\partial q} \times u_e + \frac{\partial F_g}{\partial q} \tag{8}$$

$$B_{24} = -\frac{\partial J^T}{\partial q} \times F_g + J^T \times \frac{\partial F_g}{\partial q} \tag{9}$$

Matrix C remains unchanged after the linearization process, since it is composed of only zeros and ones. Equation (5) can be brought to the most common form of a Linear Time Invariant (LTI) model by using the simple relations $F_{lin} = A^{-1}B$ and $G_{lin} = A^{-1}C$:

$$\begin{cases} \Delta\dot{x}(t) = F_{lin}\Delta x(t) + G_{lin}v(t) \\ y(t) = H_{lin}x(t) + D_{lin}v(t) \end{cases} \tag{10}$$

4 Reference Mechanism

The mechanism chosen as the basis of the simulations is a L-shape mechanism, made by two steel rods, connected by a rigid aluminum joint (Fig. 1). The rotational motion of the first link, which is rigidly connected to the motor, can be imposed through a torque-controlled actuator. The whole mechanism can swing in 3D environment, so the effects of gravity on both the rigid and elastic motion of the mechanism can be considered and taken into account in the formulation.
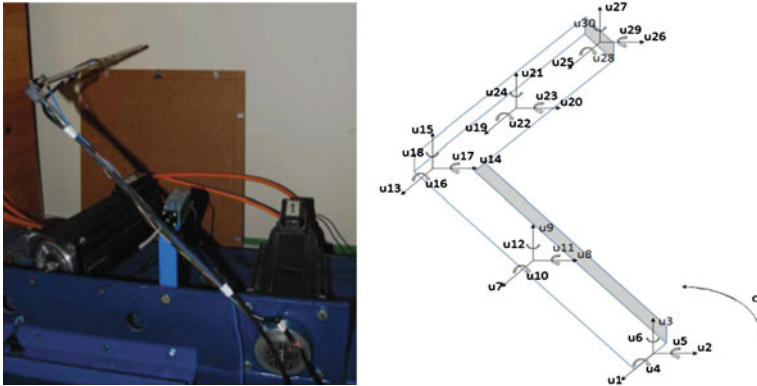
Fig. 1 The mechanism built in the laboratory for the experimental validation of the model (*left*), FEM discretization and nodal displacements (*right*)

The mechanism shown in Fig. 1 is made by two aluminum beam whose length is 0.5 m, and their square section is 8 mm wide. Two Euler-Bernoulli finite elements have been used for each link (Fig. 1). Since each finite element has 12 degrees of freedom, every link has 18 degrees of freedom. After assembling the 2 links and considering the constraints fixed by the kinematic couplings and neglecting one of the nodal displacements in order to make the system solvable (see [20]), the resulting system is described by 24 nodal elastic displacements and one rigid degree of freedom, as shown in Fig. 1.

4.1 Accuracy of the Linearized Model

In order to estimate the accuracy of the linearized model, a comparison between the impulsive response for linear and nonlinear models is set. The mechanisms is fed with a 5 Nm torque impulse applied to the crank with 0.1 s delay. The initial configuration has been arbitrarily chosen as $q_{eq} = 0$ deg, but similar results can be obtained for any choice of the linearization configuration of the mechanism. The comparison is set in terms of rigid displacement q and of nodal displacement u_8, but it could be extended also to all the other nodal displacements belonging to the model leading to similar results. As it can be seen from Fig. 2 the linearized model shows a very high level of accuracy, both in terms of q displacement and nodal displacement u_8. It can be noticed that the impulsive response of the two models lead to two very similar responses, since the error, defined as the difference between the two responses, is almost negligible.
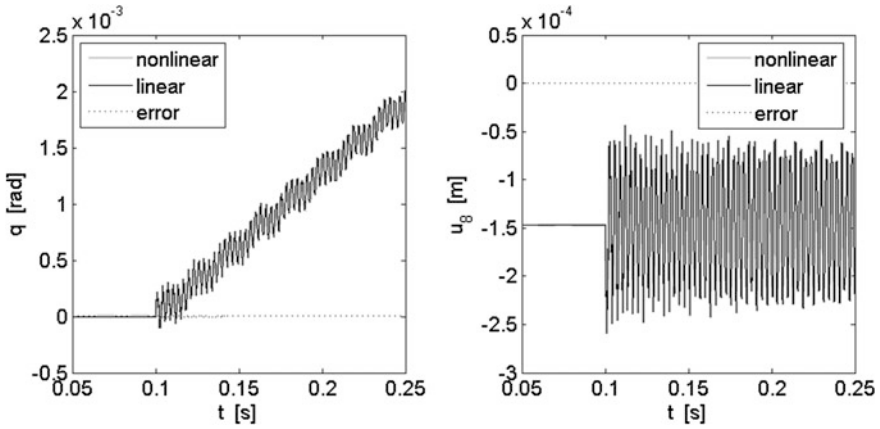
Fig. 2 Impulsive response: comparison between nonlinear and liner model: angular position q (*left*), nodal displacement u_8 (*right*)

5 Results

The linearized dynamic model of the system, obtained in Sect. 4 Eq. (10), can be used to synthesize an optimal LQR controller. The output vector y was defined to be the full state vector (i.e. H was taken as the identify matrix).

The goal is to determine the control action $\tau(t)$, which allows minimizing the performance index W, defined as:

$$W = \int_0^\infty \left[y^T(t)Qy(t) + \tau^T(t)L\tau(t) \right] dt = \int_0^\infty \left[x^T(t)H^TQHx(t) + \tau^T(t)L\tau(t) \right] dt \quad (12)$$

Q and L matrices are used to tune the control system, by defining the weight of each value of the state vector $x(t)$ and of control action $\tau(t)$ on the cost function c. The resulting gain matrix K can be evaluated using the well-known results of optimal control theory [12].

The results of two numerical tests are reported in Figs. 3 and 4. The results refer to two test case: in the first one only the angular position q is weighted in matrix Q, while in the second one also the elastic displacements are weighted. The initial position of the L-shape mechanisms is taken as $q = 90°$. A step reference input with amplitude $\Delta q = 4$ deg with 0.05 s delay was given to the mechanisms actuator which is an electrical motor. Our aim is to reach the defined position for the rigid DOF coordinate with a limited amplitude of vibrations.

Figure 3 shows the step response of the free coordinate (left) and the torque produced by the actuator (right). The amplitude of nodal vibrations u_7 and u_{12} are shown in Fig. 4. All the simulations have been run with the linear controller acting on the nonlinear mechanism. It can be seen that the LQR control can achieve a good vibration damping: the amplitude of nodal displacement are kept constant
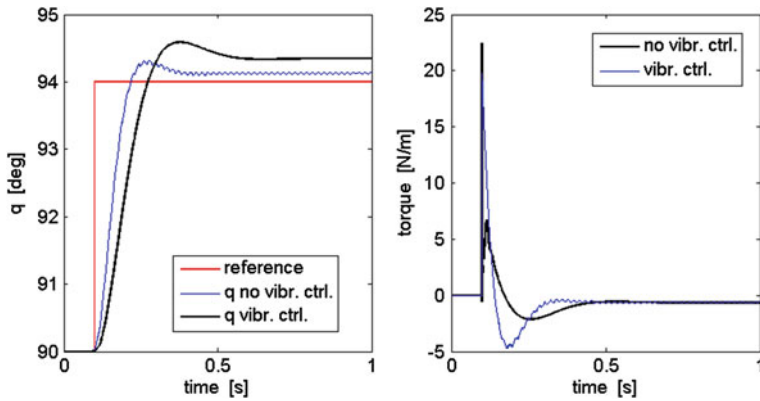
Fig. 3 LQR control: angular position (*left*), applied torque (*right*), with and without vibration control
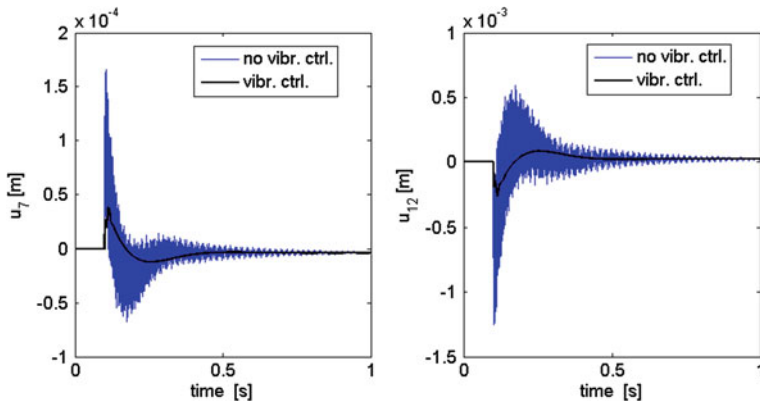
Fig. 4 LQR control: time evolution of elastic displacements u_7 and u_{12}, with and without vibration control

within 0.5 s approximately. The angular displacement q can track quite well the reference signal, but with a constant error. This could be reduced by introducing an integral action in the controller.

6 Conclusion

In this work a linearized model for spatial flexible link mechanism has been developed. The dynamic model can account for gravity acting on any direction. The accuracy of the linearized model is evaluated trough a comparison with the response of the nonlinear model. The linearization procedure allows to develop model-based control strategies for this class of mechanisms. A model design procedure has been

applied to build a LQR position and vibration control. The results show that the synthesized LQR produces fast response with a good vibration damping.

References

1. Benosman, M., Boyer, F., Le Vey, G., Primault, D.: Flexible links manipulators: from modelling to control. J. Intell. Robot. Syst. **34**(4), 381–414 (2002)
2. Boscariol, P., Gasparetto, A., Zanotto, V.: Vibration reduction in a flexible link mechanism trough the synthesis of an MPC controller. Mechatronics (2009) ICM 2009. IEEE International Conference on IEEE (2009)
3. Boscariol, P., Gasparetto, A., Zanotto, V.: Active position and vibration control of a flexible links mechanisms using model-based predictive control. J. Dyn Syst Meas Control **132**(1), 014506-1–014506-4 (2010)
4. Boscariol, P., Zanotto, V.: Design of a controller for trajectory tracking for compliant mechanisms with effective vibration suppression. Robotica **30**(1), 15–29 (2012)
5. Boscariol, P. Gasparetto, A. Giovagnoni, M., Moosavi A.K., Vidoni R.: On the modeling of flexible-link robots: First experimental validation of an ERLS-FEM dynamic model. Mechatronics (ICM), International Conference on IEEE, pp. 298–302 (2013)
6. Caracciolo, R., Richiedei, D., Trevisani, A., Zanotto, V.: Robust mixed-norm position and vibration control of flexible link mechanisms. Mechatronics **15**(7), 767–791 (2005)
7. Dwivedy, S.K., Eberhard, P.: Dynamic analysis of flexible manipulators, a literature review. Mech. Mach. Theory **41**(7), 749–777 (2006)
8. Ge, S.S., Lee, T.H., Zhu, G.: A nonlinear feedback controller for a single-link flexible manipulator based on a finite element model. J. Robot. Syst. **14**(3), 165–178 (1997)
9. Giovagnoni, M.: A numerical and experimental analysis of a chain of flexible bodies. J. Dyn. Syst. Meas. Control **116**(1), 73–80 (1994)
10. Huang, An-Chyau, Yuan-Chih Chen: Adaptive sliding control for single-link flexible-joint robot with mismatched uncertainties. Control Systems Technology, IEEE Transactions on 12.5, 770–775 (2004)
11. Kalra, P., Sharan, A.M.: Accurate modelling of flexible manipulators using finite element analysis. Mech. Mach. Theory **26**(3), 299–313 (1991)
12. Kirk, D.E.: Optimal Control Theory: An Introduction. Courier Dover Publications, New York (2012)
13. Martins, J.M., Mohamed, Z., Tokhi, M.O., Sa da Costa, J., Botto, M.A.: Approaches for dynamic modelling of flexible manipulator systems. IEE Proc Control Theory Appl **150**(4), 401–411 (2003)
14. Naganathan, G., Soni, A.H.: Nonlinear modeling of kinematic and flexibility effects in manipulator design. J. Mech. Trans. Autom. Des. **110**(3), 243–254 (1988)
15. Nagarajan, S., Turcic, D.A.: Lagrangian formulation of the equations of motion for elastic mechanisms with mutual dependence between rigid body and elastic motions: Part I—element level equations. J. Dyn. Syst. Meas. Control **112**(2), 203–214 (1990)
16. Shabana, A.: Flexible multibody dynamics: Review of past and recent developments. Multibody Syst. Dyn. **1**(2), 189–222 (1997)
17. Shabana, A. A.: Dynamics of Multibody Systems. Cambridge University Press, Cambridge (2005)
18. Tokhi, O., Azad, A.K.M.: Flexible robot manipulators: Modelling, simulation and control. Inst. Eng. Technol. 1–20 (2008)
19. Vidoni, R., Gasparetto, A., Giovagnoni, M.: A method for modeling of three-dimensional flexible mechanisms based on an equivalent rigid-link system. J. Vibr. Control (2012)
20. Vidoni, R., Gasparetto, A., Giovagnoni, M.: Design and implementation of an ERLS-based 3-D dynamic formulation for flexible-link robots. Robot. Comput. Integr. Manuf. **29**(2), 273–282 (2013)

Walking on Slippery Surfaces: Generalized Task-Prioritization Framework Approach

Milutin Nikolić, Borovac Branislav and Mirko Raković

Abstract Like humans, bipedal robots can easily fall on slippery and low-friction surfaces. In order to avoid costly breakdowns, fall avoidance is of major importance. Recently reported generalized task-prioritization framework enables us to impose dynamical inequality constraints on the robot motion, which we used to create quasi-static walk using task prioritization. Created walking is tested on high- and low-friction surfaces and resulting walking patterns are observed.

Keywords Task prioritization · Walking · Low friction · Contact constraints

1 Introduction

In view of the fact that future robots will act in the immediate environment of humans, such as offices, apartments, hospitals, etc., "the living and working coexistence" of men and robots seems to be inevitable. Since the environment of humans is well suited for the way the humans move, legged locomotion brings itself as a natural choice. However, like humans, bipedal robots can easily fall over or slip on slippery surface. Changes in gait on slippery surfaces are topic of numerous biomechanical papers [2]. When robot is walking on slippery surface, it can change its locomotion pattern so it doesn't slide [1]. For example it can intentionally perform shorter locomotion steps or reduce the walking speed. However, in order to do so, relationship between friction coefficient and step length (walking speed) has to be established, and those parameters

M. Nikolić (✉) · B. Branislav · M. Raković
Faculty of Technical Sciences, University of Novi Sad, Novi Sad, Serbia
e-mail: Milutinn@uns.ac.rs

B. Branislav
e-mail: Borovac@uns.ac.rs

M. Raković
e-mail: rakovicm@uns.ac.rs

have to be changed artificially. In Kaita et al. [4] authors have calculated minimum friction coefficient for a given walking pattern, and then modified walking pattern in order to further minimize that coefficient. It would be of great interest if a robot could simply be provided with friction coefficient, so that the control system would automatically adapt walking pattern, and thus be able to perform the walk as close to the nominal as possible, while still avoiding slipping. For such a purpose, the task prioritization framework introduced in [3, 5] could be extended and used.

Task prioritization framework allows redundant robot to perform multiple tasks where secondary tasks are handled without interfering with the primary ones. Control methodology was based on successive null-space projections where each task is performed in null-space of all higher priority tasks. However that framework was well-suited only for tasks of equality type. Avoiding slipping is inequality type task, since magnitude of tangential contact force has to be lower than the product of the friction coefficient and the normal contact force. Also, keeping zero moment point (ZMP) within the supporting area (vital for walking) is of inequality type. The way of resolving this with possibility of prioritizing inequalities as well is described in [6]. In this paper constraints were introduced on kinematic level so these dynamical constraints cannot be included.

One of the most recent generalizations of this framework [7] has showed us how dynamical constraints can be included in the framework. Authors kept ZMP between predefined bounds, and the robot was able to reject the disturbance without predefining compensation movement. We will try to employ such a framework in this paper.

In Sect. 2, the generalized framework has been briefly introduced. In Sect. 3, simulation results are presented to demonstrate the behavior of the system on high and low friction surface. Conclusions are given in Sect. 4.

2 Generalized Framework

In this section we introduce the framework presented in [7]. Let us consider a robotic system consisting of n links. The coordinate, velocity, and acceleration at the i-th joint are denoted by $q_i, \dot{q}_i, \ddot{q}_i$. The joint is driven by the torque τ_i. The equation governing the system dynamics is:

$$\mathbf{H}\,\ddot{\mathbf{q}} + \mathbf{h}_0 = \boldsymbol{\tau} \tag{1}$$

where $\mathbf{H}$ is a positive definite inertia matrix, $\mathbf{h}_0$ is the vector that comprises the velocity and gravitation effects, $\ddot{\mathbf{q}}$ is vector of joint accelerations and $\boldsymbol{\tau} = [\tau_1, \tau_2, \ldots, \tau_n]^T$ is vector of joint driving torques. Let us suppose that goal is to control the system described by (1) to fulfill p tasks given by:

$$\mathbf{A}_i\,\ddot{\mathbf{q}} = \mathbf{b}_i \text{ or } \mathbf{A}_i\,\ddot{\mathbf{q}} \preccurlyeq \mathbf{b}_i \tag{2}$$

depending on task nature (equality or inequality-type task). The size of the matrix $\mathbf{A}_i$ is $m_i \times n$, with $m_i \cdot n$, and the length of the vector $\mathbf{b}_i$ is m_i. The tasks are prioritized,

whereby the first task has the highest and the p-th the lowest priority. A higher-priority task will be realized without regard to the lower priority ones. Although this form of task representation looks deficient, it can represent wide variety of tasks. Any task written in forms $\mathbf{f}(\mathbf{q}, t) = \mathbf{x}_{des}$ or $\mathbf{f}(\mathbf{q}, \dot{\mathbf{q}}, t) = \mathbf{x}_{des}$ can be represented in form (2) by differentiating with respect to time once (for the second case) or twice (for the first case). This class of tasks can be illustrated by the example of reaching a point in the space around the robot. Inequality tasks of form $\mathbf{f}(\mathbf{q}, t) \preceq \mathbf{x}_{limit}$ and $\mathbf{f}(\mathbf{q}, \dot{\mathbf{q}}, t) \preceq \mathbf{x}_{limit}$ can be represented in form (2) using Taylor expansion up to a second derivative. Also, system can be constrained, for example contact with the environment, which can also be represented in form (2), where constraint matrices would be denoted by $\mathbf{A}_0$ and $\mathbf{b}_0$. The objective is to find an appropriate torque τ which needs to be applied to (1) so that the p tasks set by (2) are fulfilled. According to [7] procedure for determining torques is shown by Algorithm 1. Also, importance of matrix $\mathbf{A}_i \mathbf{H}^{-1/2}$ was demonstrated so the whole procedure was rewritten in such a manner. The modified task matrices are $\mathbf{B}_i = \mathbf{A}_i \mathbf{H}^{-1/2}$, while modified vector of joint acceleration is $\ddot{\mathbf{r}} = \ddot{\mathbf{q}}$ and modified vector of velocity and gravitational effects is $\mathbf{p} = \mathbf{H}^{-1/2} \mathbf{h}_0$. Null space of constraint is $\mathbf{N}_c$ while modified torque induced by constraint is denoted by $\mathbf{T}_c$. Null space of all tasks preceding current task is denoted by $\mathbf{N}_{prev}$ and modified torque which needs to be applied in order to fulfill all tasks preceding current one is $\mathbf{T}_{prev}$. Matrix $\mathbf{C}$ and vector $\mathbf{d}$ are used in order to include inequality tasks in the framework. Set S contains indexes of inequalities that are strictly fulfilled after the optimization and the set $\bar{S}$ contains indexes of inequalities that have reached the equality sign.

Algorithm 1 Procedure for determining control torques

1: $\mathbf{N}_c \leftarrow \mathbf{I}; \mathbf{T}_c \leftarrow \mathbf{0}; \ \mathbf{C} \leftarrow [\ ]; \mathbf{d} \leftarrow [\ ];$

2: **if** system constrained **then** $\mathbf{N}_c \leftarrow \mathbf{I} - \mathbf{B}_0^+ \mathbf{B}; \mathbf{T}_c \leftarrow \mathbf{B}_0^+ (\mathbf{b}_0 + \mathbf{B}_0 \mathbf{p});$

3: **for** Each task i **do**

4:      **if** task of inequality type **then**

5:          **if** system feasible **then**

6:              $\mathbf{C} \leftarrow \begin{bmatrix} \mathbf{C} \\ \mathbf{B}_i \end{bmatrix}; \mathbf{d} \leftarrow \begin{bmatrix} \mathbf{d} \\ \mathbf{b}_i \end{bmatrix};$ **continue;**

     Solve: minimize $\| \mathbf{B}_i \ddot{\mathbf{r}} - \mathbf{b}_i \|_2^2$

7:             subject to: $\ddot{\mathbf{r}} + \mathbf{p} = \mathbf{T}_c + \mathbf{N}_c \mathbf{T}_{prev} + \mathbf{N}_c \mathbf{N}_{prev} \mathbf{u}$
                               $\mathbf{C}\ddot{\mathbf{r}} \preceq \mathbf{d}$

8:      $\mathbf{T}_{prev} \leftarrow \mathbf{T}_{prev} + \mathbf{N}_{prev} \mathbf{u}; \bar{S} \leftarrow \{k \mid \mathbf{C}_k \ddot{\mathbf{r}} = d_k\}; S \leftarrow \{k \mid \mathbf{C}_k \ddot{\mathbf{r}} < d_k\};$

9:      $\mathbf{N}_{prev} \leftarrow \mathbf{N}_{prev} \left(\mathbf{I} - \left(\begin{bmatrix} \mathbf{B}_i \\ \mathbf{C}_{\bar{S}} \end{bmatrix} \mathbf{N}_c \mathbf{N}_{prev} \right)^+ \begin{bmatrix} \mathbf{B}_i \\ \mathbf{C}_{\bar{S}} \end{bmatrix} \mathbf{N}_c \mathbf{N}_{prev} \right); \mathbf{C} \leftarrow \mathbf{C}_S; \mathbf{d} \leftarrow \mathbf{d}_S;$

10: **Endfor**

11: $\tau \leftarrow \mathbf{H}^{1/2} \mathbf{T}_{prev}$

2.1 Constraints on Contact Forces

In maintaining stable contact the vertical component of ground reaction force has to be positive, CoP of each contact must not be on the edge of the contact area to avoid foot inclination. That can be written as:

$$F_z > F_{z|MIN}; \; |M_y| < ZMP_{x|MAX}F_z; \; |M_x| < ZMP_{y|MAX}F_z \tag{3}$$

where F_x, F_y, F_z, M_x and M_y are components of ground reaction force and torque. $ZMP_{x|MAX}$ and $ZMP_{y|MAX}$ are maximal ZMP position in x and y directions. $F_{z|MIN}$ is minimal vertical ground reaction force. Although it just has to be above zero, we have chosen $F_{z|MIN} = 50\ N$ in order to provide safety margin. Ground reaction force can be calculated using d'Alambert's principle $\mathbf{F} = \sum m_i \mathbf{a}_i$, where m_i is the mass and $\mathbf{a}_i$ is the acceleration of i-th segment. Since accelerations of the segments are linear in joint accelerations, then the force is linear in joint accelerations as well. As a result, inequalities (3) can be written in required form (2).

In order to avoid slipping, (Coulomb friction is assumed) constraint in quadratic form $\left(F_x^2 + F_y^2 \leq \mu^2 F_z^2 \right)$ has to be fulfilled, but in this form it cannot be included in Algorithm 1. In order to include it in the framework, tighter linear bounds which ensure that no slipping occurs are created:

$$\sqrt{2}|F_x| < \mu F_z; \; \sqrt{2}|F_y| < \mu F_z \tag{4}$$

Using d'Alambert's principle, it can be shown that these constraints can be represented in form (2), which enables us to include them in the Algorithm 1.

3 Simulation Results

In this section we present the simulation results obtained by applying the proposed prioritization framework on a complex and redundant humanoid robot. Firstly first, we describe briefly the model, and then present the simulation results illustrating the influence of friction coefficient on walking.

The humanoid model is very similar to the models already used by the same authors [7, 8]. It consists of two 7-DoF legs, two 4-DoF arms (wrist joint is omitted) and 1-DoF head. Thus, the model of the robot has 23 joints in total. Taking into account additional 6 coordinates needed to describe position of robot in world coordinate frame, the overall number of DoFs for mechanism is 29.

The simulation results are related to the quasi-static robotic walk. A quasi-static robotic walk means that the center of mass (CoM) is always above supporting area. The walk will consist of two distinctive phases; during the first where robot moves its CoM above the center of one of the feet, while the second phase represents

swing phase, where robot moves its foot from one position to the other while maintaining CoM above the foot which is in contact with the ground. By changing the support area by moving the feet the robot is able to move forward. During those two phases robot performs a list of tasks split in several groups based on their importance and function, starting from a group which enables self-collision and fall avoidance. The task of the highest priority is keeping the torques at all joints between saturation values. The task of second highest priority is to keep coordinates at each joint between the upper $\mathbf{q}_u$ and lower limits $\mathbf{q}_l$, T represents preview time interval. These two tasks written in form of (2) are:

$$\begin{bmatrix} \mathbf{H}^{1/2} \\ -\mathbf{H}^{1/2} \end{bmatrix} \mathbf{T}_{p+1|pref} \preccurlyeq \begin{bmatrix} \boldsymbol{\tau}_{sat} \\ \boldsymbol{\tau}_{sat} \end{bmatrix}; \; \frac{T^2}{2} \begin{bmatrix} \mathbf{0}_{23\times6} & \mathbf{I}_{23\times23} \\ \mathbf{0}_{23\times6} & -\mathbf{I}_{23\times23} \end{bmatrix} \ddot{\mathbf{q}} \preccurlyeq \begin{bmatrix} \mathbf{q}_u - \mathbf{q} - \dot{\mathbf{q}}T \\ -\mathbf{q}_l + \mathbf{q} + \dot{\mathbf{q}}T \end{bmatrix} \quad (5)$$

Third task of this group was to maintain stable contact between the feet and the ground (inequalities (3)). At first two simulated cases (walk on high friction surface with nominal speed and walk on low friction surface with reduced speed) inequalities (4) were neglected. In the last one (walk on low-friction surface with nominal speed), all the constraints were are included.

Second group of tasks is comprised of tasks of moving center of mass and swinging leg (if in swing phase). The first task of this group was to maintain the CoM above the desired position. In stepping phase, additional task is that robots foot has to follow given trajectory. Task matrices are:

$$\mathbf{A}_4 = \mathbf{J}_{CM|xy}, \; \mathbf{b}_4 = \ddot{\mathbf{x}}_{4|des} - \dot{\mathbf{J}}_{CM|xy}\dot{\mathbf{Q}}; \; \mathbf{A}_5 = \mathbf{J}_{foot}, \; \mathbf{b}_5 = \ddot{\mathbf{x}}_{5|des} - \dot{\mathbf{J}}_{foot}\dot{\mathbf{Q}}; \quad (6)$$

where $\mathbf{J}_{CM|xy}$ and $\mathbf{J}_{foot}$ represents the Jacobian associated with the CoM in the x and y directions and Jacobian associated with the foot, while $\ddot{\mathbf{x}}_{4|des}$ and $\ddot{\mathbf{x}}_{5|des}$ denote the desired acceleration of CoM and foot respectively. Desired trajectories of the CoM and the foot are obtained using qubic spline, where initial, middle and final positions are given. Last group of tasks were posture-related. First was that the robot should keep the torso at the constant height without changing its orientation. The last one was that the robot should keep its joint angles as close as possible to the middle of joint motion range in order to minimize joint movement.

3.1 Simulated Cases

Proposed approach was tested by simulation of walking in three different cases. In the first one, walk is performed on high-friction surface ($\mu = 0.9$) which would serve as benchmark. Resulting walking pattern is shown in Fig. 1. It is important to note that no care about sliding was taken ((4) is omitted). Since the walk is performed on high-friction surface no slipping appeared. During simulation (25 s) the robot managed to cover 2.5 m, step length was 0.25 m and duration was 2.35 s.
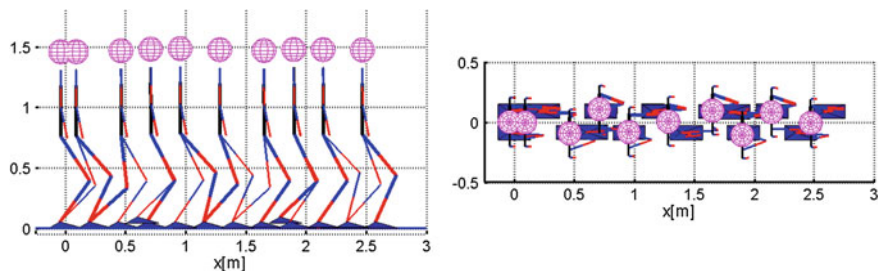
Fig. 1 Walk on high-friction surface with neglected sliding
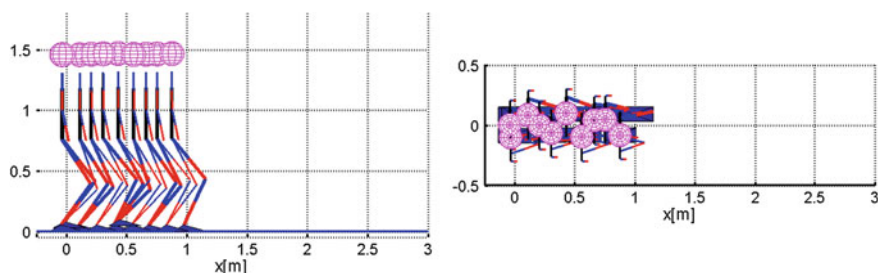
Fig. 2 Walk on low-friction surface with neglected sliding

In the second case, walking on low-friction surface ($\mu = 0.2$) was performed, without taking care of the friction and sliding. When walking with same speed as in previous case, the robot fell down due to the slipping of the feet. When landing the swinging foot, it had tendency to slip forwards, causing the robot to fall. In order to avoid slip, the step length was reduced to 0.15 m. While transferring CoM from above back foot to above front foot, back foot was sliding, so the step duration of this phase was increased 3.8 s (105 %). Results of the simulation are shown in Fig. 2. It can be seen that with shorter step length and increased stepping time the robot managed to cover only 0.9 m during the same time.

For the third case walking on low-friction surface ($\mu = 0.2$) was performed with friction constraint (4) introduced, while stepping duration and step length remain same as in benchmark case. Figure 3 shows the results and it can be noticed that it closely resembles Fig. 1. Robot managed to cover distance of 2.5 m during the 25 s. On Fig. 4, positions of feet, desired and obtained positions of CoM as well as ZMP position during the walk are shown. One can clearly notice that CoM follows almost the same trajectory when walking on high and low-friction surfaces, although robot had to comply with additional constraints induced by low-friction surface. It can be noticed that during the walk on low-friction surface there was still some foot sliding and twisting, but that only occurred during the touch-down of the swinging foot when no special care was taken regarding swinging leg. That did not compromise the walk, but, interestingly, the distance covered was increased by about 0.04 m. In the Fig. 4 it can be seen that ZMP is always within
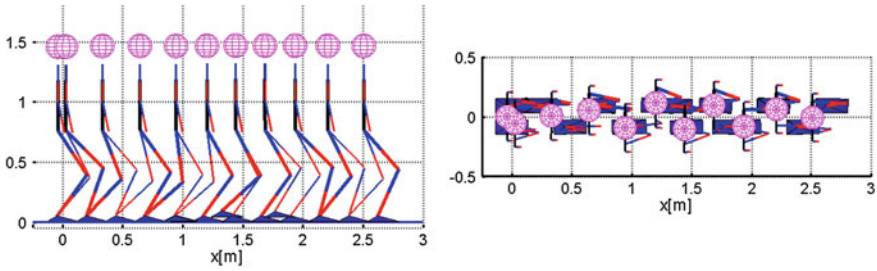
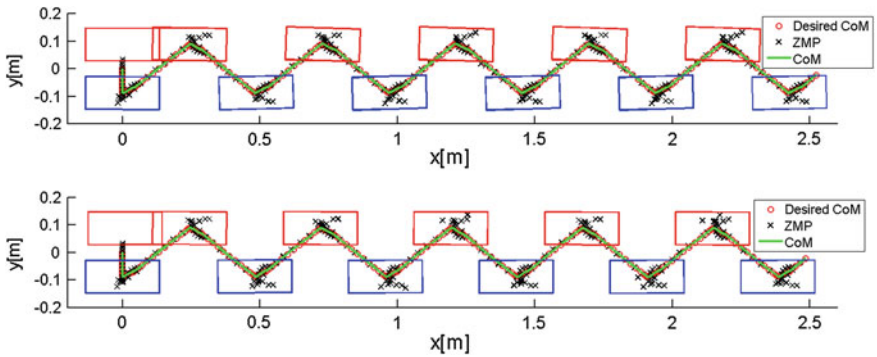**Fig. 3** Walk on low-friction surface with sliding constraint introduced

Fig. 4 ZMP and CoM during walk on low-(*above*) and high-friction (*below*) surfaces

supporting polygon which is ensured by introduced dynamical constraints (3). Also, one can see that CoM follows closely desired path,[1] while ZMP slightly oscillates around it due to induced inertial forces.

4 Conclusion

In this paper we used generalized and improved task prioritization scheme to create a walk appropriate for slippery surface. Prioritized tasks in form of equalities and inequalities are introduced, so that the robot was able to perform walking. The control scheme was tested on high and low-friction surfaces. Since the generalized task prioritization framework enables us to impose dynamical inequality constraints we were able to secure feet-ground contact. The ZMP was always within support polygon, the vertical component of ground reaction force had always higher intensity than predefined minimal value and horizontal components were

---

[1] Desired CoM path during double support phase follows line which connects centers of the feet.

constrained to prevent slipping. Without introduction of constraints on horizontal components of ground reaction force, the robot had to walk with shorter step length and increased step duration. When the constraints were introduced, walking was performed same way as on high-friction surface. There was some minimal slipping during touchdown of the swinging foot but that did not affect the walk.

Although friction coefficient is unknown, by setting it to some estimated value, framework will create appropriate walking pattern. Naturally, next step is to create dynamically balanced walk which is not quasi-static and this will be our next task.

References

1. Park, J.H., Kwon, O.: Reflex control of biped robot locomotion on a slippery surface. In: Proc. IEEE-Robotics and Autonomous Systems/RSJ International Conference on Robotics and Automation, Seoul, May 2001
2. Cham, R., Redfern, M.S.: Changes in gait when anticipating slippery floors. Gait Posture **15**(2), 159–171 (2002)
3. Sentis, L., Khatib, O.: Task-oriented control of humanoid robots through prioritization. In: Proceeding of IEEE-Robotics and Autonomous Systems/RSJ International Conference Humanoid Robots, Santa Monica, November 2004
4. Kajita, S., Kaneko, K., Harada, K., Kanehiro, F., Fujiwara, F., Hirukawa, H.: Biped walking on a low friction floor. In: IEEE/RSJ International Conference on Intelligent Robots and Systems (IROS 2004), vol. 4, pp. 3546–3552, Sendai, Oct 2004
5. Sentis, L., Khatib, O.: Synthesis of whole-body behaviors through hierarchical control of behavioral primitives. Int. J. Humanoid Robot. **2**(4), 505–518 (2005)
6. Kanoun, O., Lamiraux, F., Wieber, P.-B.: Kinematic control of redundant manipulators: generalizing the task-priority framework to inequality task. IEEE Trans. Robot. **27**(4), 785–792 (2011)
7. Nikolić, M., Borovac, B., Raković, M., Savić, S.: A further generalization of task-oriented control through tasks prioritization. Int. J. Humanoid Robot. **10**(3), 1–29 (2013)
8. Borovac, B., Nikolić, M., Raković, M.: How to compensate for the disturbances that jeopardize dynamic balance of a humanoid robot? Int. J. Humanoid Robot. **8**(3), 533–578 (2011)

Autonomous Robot Control in Partially Undetermined World via Fuzzy Logic

S. Yu. Volodin, B. B. Mikhaylov and A. S. Yuschenko

Abstract The paper presents a fuzzy logic approach to the mobile robot control in the undetermined environment. Initially, a 3D computer vision system has to process available information and identify the objects using a fuzzy classifier. The fuzzy controller is to plan out and correct the robot trajectory to avoid the obstacles unknown beforehand. The experimental investigation has proved that the proposed algorithms are efficient.

1 Introduction

Nowadays in robotics the autonomous mobile robot control in the partially undetermined environment is the challenge that requires an urgent solution. The proposed robot control system enables solving one of the problems i.e. avoiding the previously unknown obstacles both indoors and outdoors. The 3D computer vision systems may serve for avoidance recognition. Such systems are capable to recognize the objects appeared in the working space and appreciate their dimension and coordinates. It allows the robot to plan the necessary maneuver to avoid the obstacles and correct the trajectories of movement. Information the control system receives from the 3D computer vision systems, usually, is incomplete and fuzzy. That is why the on-board fuzzy algorithms to identify the obstacles are to be

S. Yu. Volodin · B. B. Mikhaylov · A. S. Yuschenko (✉)
Bauman Moscow State Technical University, Center "Robototechnika", Izmaylovskaya sq., 7, 105037 Moscow, Russia
e-mail: robot@bmstu.ru

applied to the robot movement control. The control algorithms also become fuzzy. So the fuzzy logic approach may be effectively applied to solve both problems the working scene identification and the movement of robot control.

2 3D Computer Vision System

Applying the structural light to 3D computer video system (CVS) may solve the task of 3D vision. The system consists of high definition TV-camera and pulse source to generate a special light flat matrix on the work scene. Consequently the CVS forms 3D description of the real work scene, as Cartesian coordinates data file. Moreover, the CVS forms a set of the elementary triangles, each including three nearest points of scene.

The obstacles recognition requires that the points are determined with coordinates having the level exceeding the threshold over zero. The scene segmentation for the separate objects is fulfilled by the algorithm based on the analysis of normal vectors of elementary triangles [1].

To plan the robot movement in the space with unknown obstacles the appreciation of the scene relief is not enough. The identification of the objects is necessary to realize the algorithms previously entered the robot knowledge base. These algorithms are based on the comparison of the object fuzzy features detected on the work scene with those of accessed in the database. At first, the fuzzification procedure should be applied to the geometric features measured by computer vision system such as D—the distance for the obstacle, W—the width of the object, L, R—the distances from the main axis of robot platform to the left or to the right edge of the obstacle, H—the height of the obstacle etc.

Note that a geometric description of the obstacles and the separate objects may demand the special robot movements of cognitive type to obtain the relevant information to determine the type of unknown object. An analysis of the typical situation for indoor operation proved the need for determining the types of the obstacles such as *Wall, Door, Threshold, Block*, etc. The database contains the typical obstacles with the vectors of fuzzy features obtained from the CVS. Among them there are coordinates and an object dimension, a mutual disposition of the objects, their geometrical characteristics, etc. For example, *the object is extensive, flat, horizontal, not high, to the right, not distant*, etc. The linguistic variables allow the user easily to continue the list of the possible objects using their characteristic features.

The fuzzy features allow object identification as well when the object description is incomplete for obstacles or shadows. In these cases the cognitive behavior of robot may be planned to seek the relevant information for the object classification. For example, for appropriate observation the robot vision system may require a special position.

The identification algorithms are the fuzzy logic inference using the previously determined classification rules and fuzzy features of the reference model of objects

contained in the knowledge base. The base also contains the production rules of object classification and the corresponding maneuvers representation. The fuzzy features of the objects are represented by the membership functions for the corresponding linguistic variables. These functions are to be correlated with the technical characteristics of robot and its computer vision system. For example, the robot dimension itself determines the meaning 'the doorway width is enough'. The dimension of the robot platform determines the meaning '*the obstacle height is not enough*'. The meaning '*the obstacle is distant*' is restricted by the CVS characteristics. The membership functions of the linguistic variables are to be assigned beforehand during the calibration procedure of the 3D CVS as a part of a definite mobile robot [2].

The fuzzy classifier realized the Mamdany fuzzy inference procedure to determine the type of the object [3]. The first maximum approach is applied at the defuzzification stage. Both the choice of the fuzzy features for object classification and that of the production rules and membership functions depend on the task under consideration. It may be different depending on the importance of those either another features for the task to be fulfilled by the robotic system.

The situation in the working scene, in general, may be represented as a kind of fuzzy chart where the binary relations between all the objects have been determined. Robot is one of these objects. Such a fuzzy chart allows the robot control system to determine its own position in relation for the benchmarks.

The important peculiarity of the mobile robot control system is in the fact that the scale of the image is continuously changing due the robot movement. That is why the membership functions for mobile robot sensing system depend on the distance. In this case the 3D membership functions have been introduced [3].

3 Mobile Robot Behavior in the 3D External World

It seems quite possible to use the term "behavior" for autonomous mobile robot operation in the partially undetermined world. We can represent the pattern of behavior determined by the characteristic situation as the production rules "*if the situation is S_i then the tactics is T_i*". The *tactics* here is the list of production rules of typical patterns of behavior represented with the linguistic variables. These rules determine the previously described robot movement for any typical situation. For example, "*if the obstacle is near and to the left then go around slow and anticlockwise*". The typical movement (*go around slow and anticlockwise*) in its turn also may be determined by a list of production rules contained in the database [4]. Such a data base allows the user to develop the new tactics such as "to pursuit the moving objects", "move to the prescribed object", "pass the doorway", "go around the obstacle" etc.

In general, the tactics of robot behavior may be determined with a task frame: <current situation> <robot characteristics> <tactics name> <the objects and obstacles> <the conditions of the operation feasibility>.

Robot characteristics such as dimension parameters (weight, power of drivers, possible velocity etc.) are contained in the database. These characteristics together with the features of the environment (relief, ground parameters, obstacles types) determine the possibility of the prescribed operation feasibility. The latter may include also the post condition to be met after completing the operation such as a stable robot position. The feasibility conditions for operation such as the objects persecution or the obstacle avoidance are to be classified beforehand in accordance with their features.

When some slots of the operation frame are empty the robot itself has to plan a movement of cognitive type to find the necessary information [5] e.g. the parameters of the doorway to pass through. The cognitive operations are also contained in the robot knowledge base as a list of fuzzy production rules.

4 Experimental Investigation

We supposed that the most of indoor situations might be represented as a combination of the following typical objects: "Wall", "Threshold", "Block", "Left angle", "Right angle", "Doorway" (Fig. 1). Each object detected by the 3D computer vision system is classified as one of the typical objects via the fuzzy inference procedure discussed above. Then the desirable movement trajectory may be planned.

The following linguistic variables were introduced: "*The object position*" (*to the right, to the left, in the centre*); "*The object height*" (*tall, middle, low*) "*The object width*" (*wide, compact*), "*Distance to the object*" (*dangerous, safety, the edge of the vision area*). The diversity of the terms of the linguistic variables may be easily expanded, if necessary.

The experiment has been conducted in the laboratory using a small mobile robot equipped with the 3D vision system described above.

As mentioned above, the scale of CVS image based on the robot platform was changing during the robot movement. So it is important to take into consideration the membership functions as being the functions of current distance to the obstacle. So for the terms of the linguistic variable "*object height*" the membership functions are formed taking in consideration the angle of the TV camera arrangement on the robot board (Fig. 2). The object classified as *tall* on the edge of the vision area may be classified as *middle* at the distance dimension. The same is for the linguistic variable "*object position*". The object situated at *the centre* may be found as *to the right* at small distance (Fig. 3). It makes possible to plan the maneuver beforehand e.g. to begin planning the walk round the block at the safe distance from the obstacle.

The identification of the obstacles has been developed in accordance with the prescribed classification rules e.g. "*slow and wide object is a Threshold*"; "*slow and compact object is a Block*"; "*Tall or middle object to the left is a Left angle*"; "*Tall and wide object in the center is a Wall*". Note that the features conjunction
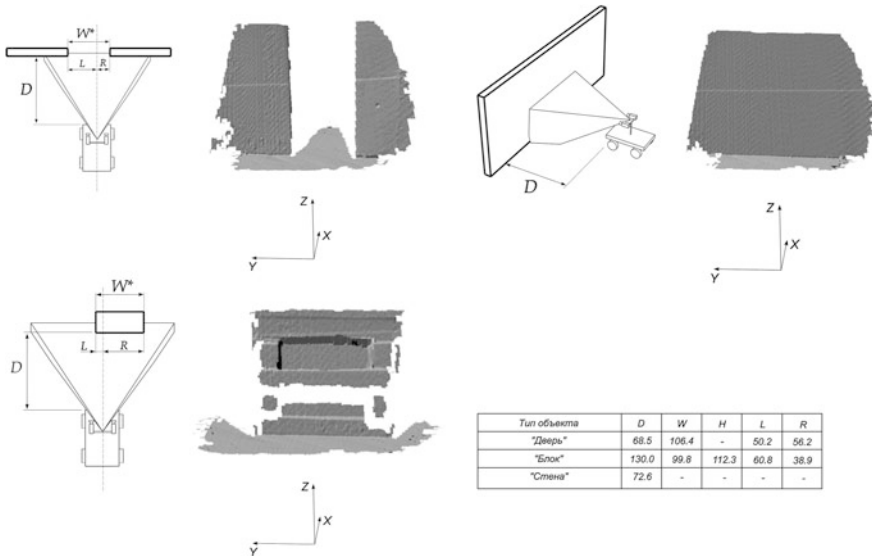
Тип объекта	D	W	H	L	R
"Дверь"	68.5	106.4	-	50.2	56.2
"Блок"	130.0	99.8	112.3	60.8	38.9
"Стена"	72.6	-	-	-	-

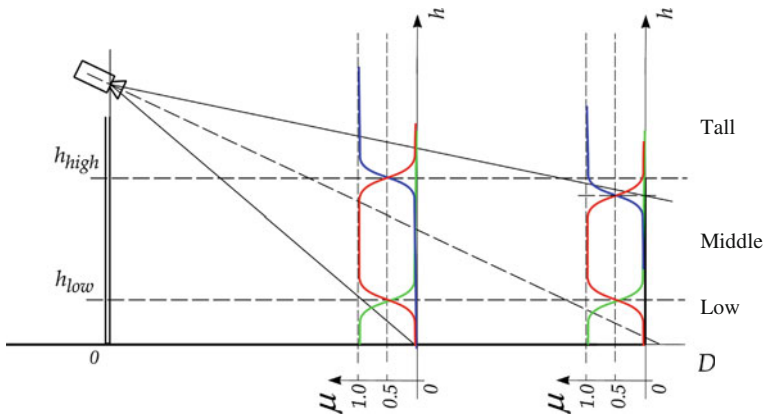**Fig. 1** The typical obstacles and their parameters

Fig. 2 Membership functions "Tall", "Middle", "Low"

related both to the object features and to its position leads to description of the situation on the whole using the description of separate objects. An example of the real experiment is presented in Fig. 1 where the robot has determined the object "The doorway" as "*The tall object to the left* (*Left angle*) and *The tall object to the right* (*Right angle*) *almost at the same distance*". To perform the operation: "To walk into the doorway" the feasibility condition of the operation "*The doorway is*

Fig. 3 Membership
functions "To the left", "In
the center", "To the right"
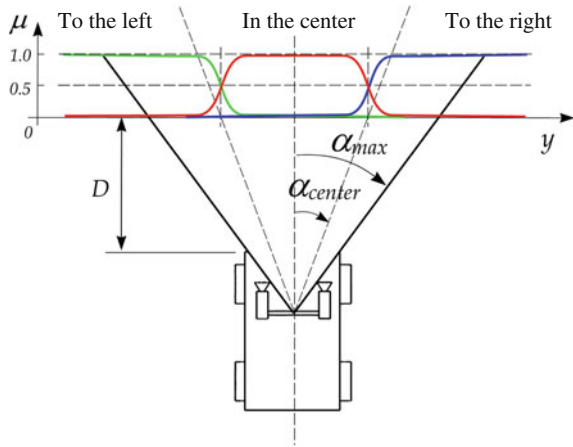
Fig. 4 Membership
functions "To the left", "In
the centre", "To the right" as
the functions of the distance
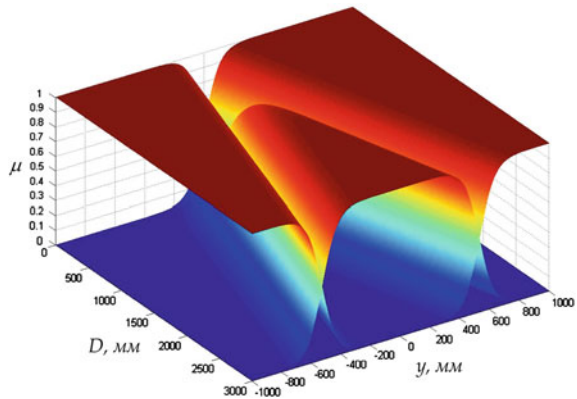
free" is to be examined. The condition is not fulfilled in the case the system has
found another obstacle (Block, for example) between the Left and the Right
angles.

After the situation has been completely determined the necessary trajectory
may be planned as a sequence of the typical operations contained in the database
as described above.

Figure 4 shows the membership functions "To the left", "To the right", "In the
centre" as functions of distance. Such representation allows the robot movement to
be planned beforehand with its no-interruption operation. Such control mode can
improve the safety of operations and eliminate the possibility of collision. It may
be of great importance when the moving objects appear, thus allowing to correct
the trajectory and to avoid the possible collision.

5 Conclusion

The experiments prove that the proposed algorithms of information processing and mobile robot control are efficient. It has been shown that the obstacles identification procedures based on the fuzzy logic inference are quite effective in the indoor navigation when most of the adequately represented obstacles can be included in the list of fuzzy features beforehand. The fuzzy control system allows robot to fulfill the stated task autonomously in partly determined environment.

References

1. Mikhaylov, B.B., Nguen An Van: Identification of polyhedral space objects. S-Pb Univ. Vedomosty **5**:103–108 (2013)
2. Mikhaylov B.B., Volodin, Yu.S., Orlov A.V.: Calibration of 3D computer vision system. In: Proceedings of the of 16th Conference on "Extreme Robotics", S-Pb, pp. 314–322 (2005)
3. Volodin, Yu.S.: The 3D-computer vision system for object identification. In: Proceedings of the 15th Conference on "Extreme Robotics", S-Pb, pp. 324–330 (2004)
4. Yuschenko, A.S., Mikhaylov, B.B., Volodin, Yu.S.: Fuzzy obstacles classification by modile robot using 3D computer vision system. In: Proceedings of the 6th Conference "Integrated Models and Soft Computing in Artificial Intelligence", Kolomna, pp. 372–380 (2011)
5. Yuschenko, A.S.: Fuzzy logic in mobile robots control systems. Vestnik BMSTU, Priborostroenie **6**, 29–43 (2012)

Laplacian Trajectory Vector Fields for Robotic Movement Imitation and Adaption

Thomas Nierhoff, Sandra Hirche and Yoshihiko Nakamura

Abstract Vector field methods for trajectory following are generally computed offline before execution and thus only applicable to static trajectories. In contrast this paper introduces Laplacian trajectory vector fields (LTVF) as a computationally efficient method for creating convergent vector fields towards a discretized reference trajectory. In case of environmental changes both the vector field and the reference trajectory can be quickly recomputed. The conducted experiment uses a HRP-4 robot in order to display the applicability to daily life problems.

Keywords Manipulators · Trajectory · Vector fields

1 Introduction

Vector fields are a standard method for reactive trajectory adaption, allowing one to calculate a desired movement vector for any point in space while avoiding obstacles and maintaining a desired movement behavior. Probably the oldest and most used vector fields in robotics are potential fields [1, 2], focusing on collision avoidance in both static and non-static environments by superimposing repellent forces from each obstacle. Other approaches have the goal of a safe physical interaction with a

T. Nierhoff (✉) · S. Hirche
Faculty of Electrical Engineering, Institute for Information-Oriented Control (ITR),
Technische Universität München, 80290 Munich, Germany
e-mail: tn@tum.de

S. Hirche
e-mail: hirche@tum.de

T. Nierhoff · Y. Nakamura
Department of Mechano-Informatics, University of Tokyo, 7-3-1 Hongo, Bunkyo-ku,
Tokyo 113-8656, Japan
e-mail: nakamura@ynl.t.u-tokyo.ac.jp

human user [3], goal convergence in constrained environments [4] or global convergence towards closed curves [5]. A recent trend focusing on imitation learning incorporates the modulation of a dynamical system [6, 7], thus overcoming the problem of getting stuck in a local minimum and being able to encode more complex movements. An elaborate approach for convex-shaped obstacle avoidance while maintaining the shape of a goal-driven motion is presented in [8].

Most of the presented vector field methods for trajectory following are learnt offline and assume the underlying trajectory not to be changed during execution. Yet in the presence of large disturbances or environmental changes this can cause undesired and possibly diverging trajectories [9]. An alternative option presented in this paper is to recompute the trajectory and recalculate the resulting vector field for faster convergence.

The contribution of this paper is a method to construct converging vector fields for arbitrarily, discretized trajectories. Regarding computational complexity, the vector field is recalculated quickly whenever the trajectory has to be updated. Convergence of the integral curves along the trajectory towards an end point can be ensured by interpolating between multiple first-order dynamical systems. Continuity of the vector field within specified bounds is proven. Because the vector field depends only on a few parameters its calculation can be automated fully and combined with a Programming by Demonstration approach as shown in the experiment using an HRP-4 robotic platform.

2 Approach

2.1 Laplacian Vector Fields

Let a trajectory be the combination of a path $\mathbf{P} = [\mathbf{p}(t_1), \mathbf{p}(t_2), \ldots, \mathbf{p}(t_n)]^T \in \mathbb{R}^{n \times m}$ with n sampling points $\mathbf{p}(t_i)$ and associated temporal information $t_i \in \mathbb{R}$. For simplicity, $\mathbf{P} = [\mathbf{p}(t_1), \mathbf{p}(t_2), \ldots, \mathbf{p}(t_n)]^T$ is rewritten as $\mathbf{P} = [\mathbf{p}_1, \mathbf{p}_2, \ldots, \mathbf{p}_n]^T$. The trajectory consists of trajectory segments τ_i defined as the line segment between two subsequent sampling points $\mathbf{p}_i, \mathbf{p}_{i+1}, i \in \{1, \ldots, n-1\}$, see Fig. 1. Every trajectory segment has a mid point $\mathbf{p}_{m,i} = \frac{\mathbf{p}_i + \mathbf{p}_{i+1}}{2}$, lying on the hyperplane h_i with corresponding normal vector $\mathbf{n}_i = \frac{\mathbf{p}_{i+1} - \mathbf{p}_i}{\|\mathbf{p}_{i+1} - \mathbf{p}_i\|}$. The vector fields for the remainder of this paper are of the general form

$$\dot{\mathbf{p}} = \mathbf{A}_i \mathbf{p} + \mathbf{b}_i, \tag{1}$$

with $\mathbf{A} \in \mathbb{R}^{m \times m}, \mathbf{b} \in \mathbb{R}^m$. For the i-th trajectory segment, they can be split up as

$$\begin{aligned} \mathbf{A}_i &= \mathbf{A}_{\|i} + \mathbf{A}_{\perp i}, \\ \mathbf{b}_i &= \mathbf{b}_{\|i} + \mathbf{b}_{\perp i}, \end{aligned} \tag{2}$$
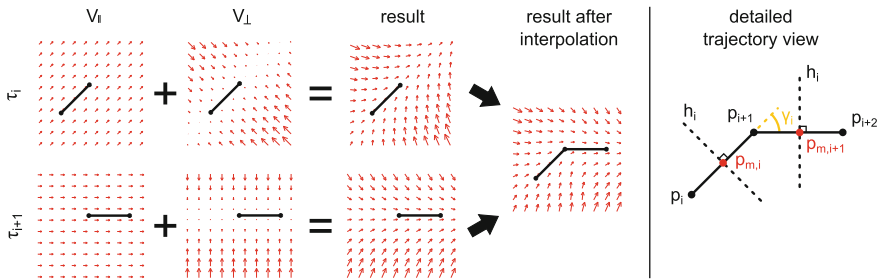
Fig. 1 Vector field example for a trajectory consisting of two segments τ_i and τ_{i+1}. *Left side* Calculated vector field both after superposition and split up into individual parallel and orthogonal vector fields. *Right side* Schematic view

consisting of a parallel vector field $V_{\|i} = \{\mathbf{A}_{\|i}, \mathbf{b}_{\|i}\}$ responsible for guiding an object along the trajectory and an orthogonal vector field $V_{\perp i} = \{\mathbf{A}_{\perp i}, \mathbf{b}_{\perp i}\}$ for convergence towards the trajectory in case of a sudden disturbance. In order to calculate the elements of the vector fields, we define an orthonormal basis in $\mathbb{R}^m$ with basis vectors $\mathbf{a}_{j,i}, j \in \{1, \ldots, m\}$ such that $\mathbf{a}_{1,i}$ coaligns with $\mathbf{p}_{i+1} - \mathbf{p}_i$. It is assumed that the eigenvectors $\mathbf{e}_{j,i}$ of $\mathbf{A}_i$ coincide with $\mathbf{a}_{j,i}$. The scalar values $\lambda_{\|j,i}$ and $\lambda_{\perp j,i}$ denote the eigenvalues of $\mathbf{A}_{\|i}$ and $\mathbf{A}_{\perp i}$. Then the parallel vector field $V_{\|i}$ has to fulfill the conditions

$$\lambda_{\|1,i} = \lambda_{\|2,i} = \cdots = \lambda_{\|m,i} = 0,$$
$$\dot{\mathbf{p}}(\mathbf{p}_{m,i}) = \frac{\mathbf{p}_{i+1} - \mathbf{p}_i}{t_{i+1} - t_i} > 0, \tag{3}$$

that is a vector field with constant velocity parallel to the i-th trajectory segment. The orthogonal vector field $V_{\perp i}$ has to fulfil the condition

$$\lambda_{\perp 1,i} = 0,$$
$$\lambda_{\perp 2,i} = \lambda_{\perp 3,i} = \cdots = \lambda_{\perp m,i} < 0, \tag{4}$$
$$\dot{\mathbf{p}}(\mathbf{p}_{m,i}) = 0,$$

i.e. the line through $\mathbf{p}_i, \mathbf{p}_{i+1}$ being the only stable set of equilibrium points. By defining $\mathbf{A}_{\|i}$ and $\mathbf{b}_{\|i}$ as

$$\mathbf{A}_{\|i} = \mathbf{0},$$
$$\mathbf{b}_{\|i} = \frac{\mathbf{p}_{i+1} - \mathbf{p}_i}{t_{i+1} - t_i}, \tag{5}$$

it suffices (3). A heuristic approach is used to find a solution that suffices (4). By remembering that

$$\dot{\mathbf{p}} = \mathbf{A}_{\perp i}\mathbf{p} + \mathbf{b}_{\perp i}, \tag{6}$$

one can create the equation system

$$
\begin{aligned}
\dot{\mathbf{p}}(\mathbf{p}_{m,i}) &= 0, \\
\dot{\mathbf{p}}(\mathbf{p}_{m,i} + \mathbf{a}_{1,i}) &= 0, \\
\dot{\mathbf{p}}(\mathbf{p}_{m,i} + \mathbf{a}_{q,i}) &= -\kappa_i \mathbf{a}_{q,i}, \quad \forall q \in \{2, \ldots, m\}
\end{aligned}
\tag{7}
$$

and solve it for the variables in $\mathbf{A}_{\perp i}$ and $\mathbf{b}_{\perp i}$ in order to construct the orthogonal vector field. The strength parameter $\kappa_i > 0$ adjusts the influence of the orthogonal vector field $V_{\perp,i}$, accounting for the rate at which any object converges back to the trajectory after a disturbance. Note that the norm of any vector $\mathbf{v}_{\perp i}$ caused the vector field $V_{\perp i}$ is directly proportional to the minimal distance $d_{m,i}$ to the line through $\mathbf{p}_{i+1}, \mathbf{p}_i$ as

$$\|\mathbf{v}_{\perp i}\| = d_{m,i}\kappa_i. \tag{8}$$

When moving along a trajectory, an interpolation scheme according to (9) with the weighting factor $w_i \in [0, 1]$ blending over the vector fields of subsequent trajectory segments is proposed in order to avoid discontinuities

$$\dot{\mathbf{p}} = w_i(\mathbf{A}_i + \mathbf{b}_i) + (1 - w_i)(\mathbf{A}_{i+1} + \mathbf{b}_{i+1}). \tag{9}$$

The trajectory segment τ_i is defined by the two points $\mathbf{p}_i, \mathbf{p}_{i+1}$, the trajectory segment τ_{i+1} by $\mathbf{p}_{i+1}, \mathbf{p}_{i+2}$. Let the projection of an object position onto the τ_i segment be $\mathbf{p}_{p,i}$ and its relative length $r_i = \frac{\|\mathbf{p}_{p,i} - \mathbf{p}_i\|}{\|\mathbf{p}_{i+1} - \mathbf{p}_i\|}$. The interpolation scheme weight w_i is given as

$$
\begin{aligned}
r_{i'} &= |r_i - 0.5|, \\
r'_{i+1} &= |r_{i+1} - 0.5|, \\
w'_i &= \frac{r'_{i+1}}{r_{i'} + r'_{i+1}},
\end{aligned}
\tag{10}
$$

with the offset of 0.5 moving the moment of switching to the hyperplane h_i. Note that this interpolation scheme is only well defined for intersection angles γ_i

$$\gamma_i = \arccos\left(\frac{(\mathbf{p}_{i+2} - \mathbf{p}_{i+1}) \cdot (\mathbf{p}_{i+1} - \mathbf{p}_i)}{\|\mathbf{p}_{i+2} - \mathbf{p}_{i+1}\|\|\mathbf{p}_{i+1} - \mathbf{p}_i\|}\right) < \frac{\pi}{2}, \tag{11}$$

The approach can be readily combined with Laplacian Trajectory Editing [10], allowing one to deform the underlying trajectory proactively while still being able to recompute the new vector field quickly. For collision avoidance, one can use an arbitrary superimposing method, for example potential fields or the method in [8].

2.2 Convergence

Two aspects of convergence are investigated: Transition convergence (any point **s** either on the hyperplang h_i or in between h_i and h_{i+1} eventually converges to h_{i+1}) and point converge (any point on the last hyperplane h_{n-1} or beyond convergence to the last point $\mathbf{p}_n$). By combining both convergence properties one can thus ensure that a point moving along the trajectory eventually converges to $\mathbf{p}_n$.

To prove transition convergence, the vector field $\dot{\mathbf{p}}(\mathbf{s})$ always has to point in direction of $\mathbf{n}_{i+1}$ as

$$\dot{\mathbf{p}}(\mathbf{s})^T \mathbf{n}_{i+1} > 0. \tag{12}$$

By decomposing $\dot{\mathbf{p}}(\mathbf{s})$ as

$$\dot{\mathbf{p}}(\mathbf{s}) = w_1(\mathbf{v}_{\|i} + \mathbf{v}_{\perp i}) + w_2(\mathbf{v}_{\|i+1} + \mathbf{v}_{\perp i+1}), \tag{13}$$

it accounts both for the orthogonal/parallel components of the vector fields V_i, V_{i+1} and a interpolation scheme with weights w_1, w_2. Looking at the geometric properties, (12) can be rewritten as

$$\begin{aligned} w_1(\|\mathbf{v}_{\|i}\| \cos(\gamma_i) - \|\mathbf{v}_{\perp i}\| \sin(\gamma_i)) + w_2\|\mathbf{v}_{\|i+1}\| > 0, \\ w_1(\|\mathbf{v}_{\|i}\| \cos(\gamma_i) - d_{m,i}\kappa_i \sin(\gamma_i)) + w_2\|\mathbf{v}_{\|i+1}\| > 0. \end{aligned} \tag{14}$$

The minimal values of (14) are given for $w_1 = 1, w_2 = 0$, resulting in

$$\|\mathbf{v}_{\|i}\| \cos(\gamma_i) > d_{m,i}\kappa_i \sin(\gamma_i). \tag{15}$$

Equation (15) is a necessary condition for transition convergence. Depending on the intersection angle γ_i it defines an admissible region around the trajectory segment whose extent can approach ∞ for $\gamma_i \to 0$ in the limiting case or 0 for $\gamma_i \to \frac{\pi}{2}$.

Point convergence for $\mathbf{p}_n$ can be achieved by creating a vector field V for the last trajectory segment such that it fulfills

$$\begin{aligned} \lambda_{1,n} = \lambda_{2,n} = \cdots = \lambda_{m,n} < 0, \\ \dot{\mathbf{p}}(\mathbf{p}_n) = 0, \end{aligned} \tag{16}$$

that is a point attractor for $\mathbf{p}_n$ which can be created following the idea in (7). The proof is analogous to the one for transition convergence.

2.3 Spatial Bounds Approximation

Whereas conservative spatial bounds of the deviation of the integral curve C from the reference path can be given which hold for any $\kappa_i > 0$, a good approximation can be made under the assumption of $\gamma_i \approx 0$ and $\|\mathbf{v}_{\|i+1}\| \approx \|\mathbf{v}_{\|i}\|$. Then for an object starting from the hyperplane h_1 with an initial distance $d_{m,1}$ to the trajectory—see (8)—the resulting distance $d_{m,s}$ when passing the hyperplane h_s can be calculated as

$$
\begin{aligned}
d_{m,s} &= d_{m,1} - \int_C V_\perp dx, \\
&\approx d_{m,1} \prod_{i=1}^{s} exp(-\kappa_i \Delta t_i), \\
&\approx d_{m,1} \prod_{i=1}^{s} exp(-\kappa_i \frac{\|\mathbf{p}_{m,i+1} - \mathbf{p}_{m,i}\|}{\|\mathbf{v}_{\|i}\|}),
\end{aligned}
\tag{17}
$$

with $\int_C$ as the integral over the integral curve C and Δ_t as the time required to traverse from the hyperplane h_i to h_{i+1}.

3 Experimental Evaluation

The experiment consists of a movement imitation task where a button has to be pressed while avoiding an obstacle. To adapt to environmental changes, LTVF and Laplacian trajectory editing [10] are combined with a Programming by Demonstration (PbD) framework [11, 12]: Whereas the PbD framework produces a prototypic (i.e. regressed) trajectory, Laplacian trajectory editing is used to deform the prototypic trajectory in case of large environmental changes. Subsequently, LTVF are used to create movements converging to the prototypic trajectory in case of small disturbances (e.g. a slightly varied starting position).

The human hand movement is recorded at a frame rate of 200 Hz using a Vortex motion capture system. Five demonstration rollouts are performed in which the hand is moved from various starting positions through a narrow tunnel to press a button, see Fig. 2a. All demonstrations are aligned in the temporal domain using Dynamic Time Warping. Then Gaussian Mixture Regression gives a prototypic trajectory with corresponding spatial covariance matrix Σ_i for the i-th sampling point. The spatial variance is used to determine the strength parameter $\kappa_i \propto \frac{1}{\sqrt{\det \Sigma_i}}$ of the vector field. This ensures quick convergence towards the trajectory wherever the spatial variance is low, corresponding to constrained sections of the trajectory. On the other hand a high variance implicitly assumes free space, resulting in low values of κ_i. Shown in Fig. 2b are the five rollouts (orange trajectories). The colorful tube is centered around the prototypic trajectory.

(a)

(b)   **(c)**

κ = 3.3

κ = 8.6e-3

(d)
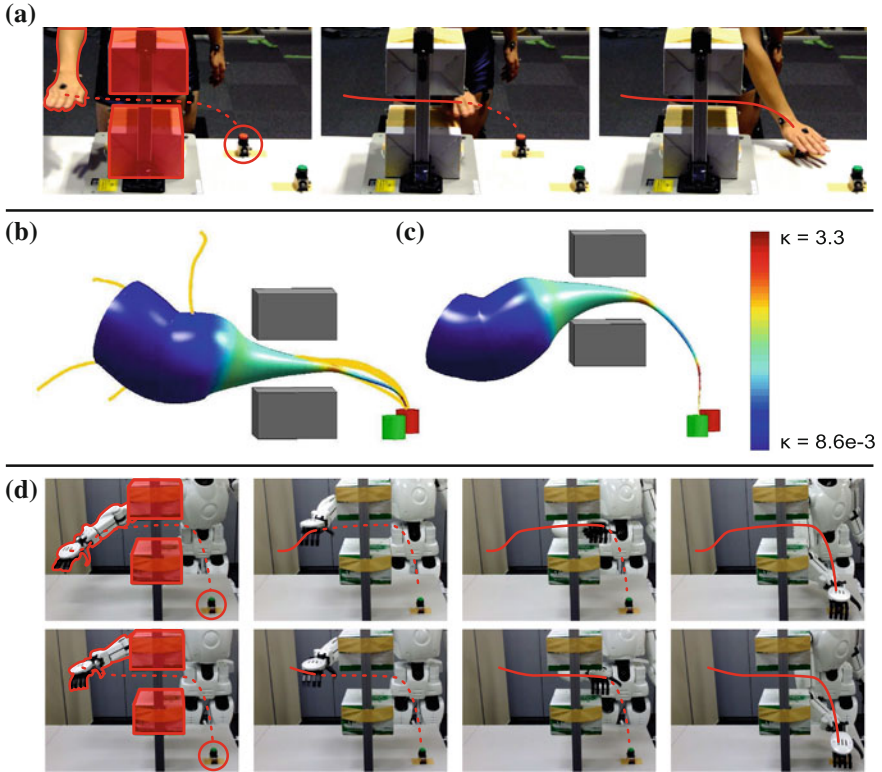
Fig. 2 Experimental results. Human demonstration (**a**), processed results (**b**), adaption to a changed environment (**c**) and adapted movement using a HRP-4 robot (**d**). Highlighted in (**a**) and (**d**) in *red* are the human/robot arm, two boxes representing the obstacle, the button to be pressed and the hand trajectory

The color of the tube represents the vector field strength κ_i whereas the tube diameter is directly proportional to the distance $d_{m,s}$ in (17). The result is a funnel in which convergence according to the spatial bounds approximation can be guaranteed. Adaption to a varied environment (varied obstacle position, different button to press) can be achieved by retargeting the trajectory using Laplacian trajectory editing, see Fig. 2c. Figure 2d shows the reproduction of only two trajectories from different starting positions using a HRP4 robotic platform.

4 Discussion

Experiments show how the presented approach can be readily combined with other approaches and applied to robotic movement imitation problems. Differing from other approaches based on Gaussian mixture models which have to learn the

mixture model for every new trajectory, no learning is necessary when using LTVF. This makes the approach applicable for real-time applications where online trajectory modifications are necessary. Because at any time instance the vector field has to be computed based only on two adjacent trajectory segments, its computational complexity is independent of the shape or length of the trajectory. Moreover, tight spatial boundaries can be specified which are helpful for collision prediction and avoidance. A drawback is that methods based on Gaussian mixture models like Dynamic Movement Primitives have useful theoretical properties in terms of global stability and robustness to disturbances. Convergence for LTVF on the other hand can be shown only on a local scale. Hence any disturbance large enough may lead to divergent behavior, making it necessary to recompute the reference trajectory. Differing from Gaussian mixture models which are generally time-independent, the presented approach is time-variant as one has to keep track of the object's current trajectory segment. This can be used to resolve issues regarding self-intersecting paths.

5 Conclusion and Future Work

This paper presents a generic method to construct convergent vector fields towards a discretized reference trajectory. In case the trajectory is retargeted, the vector field can be reconstructed quickly without the need of an explicit optimization routine. The guaranteed convergence, low computational complexity and large spatial adaption range makes it predestined to be used with other approaches for collision avoidance and vector field adaption.

Future work will be focused on an improved version extending the presented approach to continuous trajectories.

References

1. Barraquand, J., Langlas, B., Latombe, J.C.: Numerical potential field techniques for robot path planning. IEEE Trans. Syst. Man Cybern. **22**, 224–241 (1992)
2. Khatib, O.: Real-time obstacle avoidance for manipulators and mobile robots. Int. J. Robot. Res. **5**(1), 90–98 (1986)
3. Pistillo, A., Calinon, S., Caldwell, D.G.: Bilateral physical interaction with a robot manipulator through a weighted combination of flow fields. In: IEEE IROS, pp. 3047–3052 (2011)
4. Lindemann, S., La Valle, S.: Smoothly blending vector fields for global robot navigation. In: IEEE CDC, pp. 3353–3559 (2005)

5. Gonçalves, V.M., Pimenta, L.C.A., Maia, C.A., Dutra, B.C.O., Pereira, G.A.S.: Vector fields for robot navigation along time-varying curves in n -dimensions. IEEE Trans. Rob. **26**(4), 647–659 (2010)
6. Ernesti, J., Righetti, L., Do, M., Asfour, T., Schaal, S.: Encoding of periodic and their transient motions by a single dynamic movement primitive. In: IEEE-RAS Humanoids, pp. 57–64 (2012)
7. Hersch, M., Guenter, F., Calinon, S., Billard, A.: Dynamical system modulation for robot learning via kinesthetic demonstrations. IEEE Trans. Rob. **24**(6), 1463–1467 (2008)
8. Khansari-Zadeh, S.M., Billard, A.: A dynamical system approach to realtime obstacle avoidance. Auton. Robots **32**(4), 433–454 (2012)
9. Calinon, S., D'halluin, F., Sauser, E.L., Caldwell, D.G., Billard, A.: Learning and reproduction of gestures by imitation. IEEE Robot. Autom. Mag. **17**(2), 44–54 (2010)
10. Nierhoff, T., Hirche, S.: Fast trajectory replanning using Laplacian mesh optimization. In: ICARCV, pp. 154–159 (2012)
11. Calinon, S., D'Halluin, F., Sauser, E.L., Caldwell, D.G., Billard, A.G.: Learning and reproduction of gestures by imitation: an approach based on hidden Markov model and Gaussian mixture regression. IEEE Robot. Autom. Mag. **17**(2), 44–54 (2010)
12. Muehlig, M., Gienger, M., Hellbach, S., Steil, J.J., Goerick, C.: Task-level imitation learning using variance-based movement optimization. In: IEEE ICRA, pp. 1177–1184 (2009)

Trajectory Planning of Redundant Planar Mechanisms for Reducing Task Completion Duration

Emre Uzunoğlu, Mehmet İsmet Can Dede, Gökhan Kiper,
Ercan Mastar and Tayfun Sığırtmaç

Abstract In the industry there is always a demand to shorten the task completion durations in order to maximize the efficiency of the operation. This work aims to provide a solution to minimize the task completion duration for planar tasks by introducing kinematic redundancy. An example setting of a redundant planar mechanism is considered and an algorithm developed for resolving redundancy order to minimize task completion duration is discussed based on this mechanism.

Keywords Trajectory planning · Redundant manipulator · Redundancy resolution

1 Introduction

Kinematically redundant manipulators have numerous advantages over the sufficient manipulators since they can provide the task designer with infinite number of solutions that can achieve the same primary task. Self-motion of the redundant

E. Uzunoğlu (✉) · M. İ. C. Dede · G. Kiper
Department of Mechanical Engineering, İzmir Institute of Technology,
35430 Izmir, Turkey
e-mail: emreuzunoglu@iyte.edu.tr

M. İ. C. Dede
e-mail: candede@iyte.edu.tr

G. Kiper
e-mail: gokhankiper@iyte.edu.tr

E. Mastar · T. Sığırtmaç
Coşkunöz Metal Form Endüstri ve Ticaret A.Ş., R&D Department,
16159 Bursa, Turkey
e-mail: emastar@coskunoz.com.tr

T. Sığırtmaç
e-mail: tsigirtmac@coskunoz.com.tr

manipulator, which has no effect on primary task [4], is used to achieve subtasks (e.g. singularity avoidance, minimizing total joint motion). Redundancy resolution algorithms that allow the ability to optimize for various criteria using subtask controllers have been proposed in literature. Redundancy resolution in velocity making use of pseudo-inverse approaches has been widely used in various subtask controls such as singularity avoidance [10], joint velocity minimization [7], obstacle avoidance [1, 2], mechanical joint limit avoidance [8], and manipulability [3]. In addition, different redundancy resolution approaches have been proposed including in velocity level [5] and in acceleration level [9]. Examples presented above address optimization for various sub-tasks. However, in this work, our focus is on reducing the total task completion duration with maximum allowable accelerations.

The motivation of this paper is to use the advantage of extra degrees of freedom (DoF) of redundant manipulators to develop trajectory generation algorithm to achieve higher acceleration motions in global task space in order to reduce the operation time. Shortening the operation time as much as possible is crucial since it will increase the productivity of the machine. As a fact, in many industrial and robotic applications that include sharp curves in their paths, robot's acceleration performance is required to be as high as possible not to lose much time at the curves. However, in industrial settings, where the manipulators have large work-space, higher accelerations at the tip of the manipulator will call for higher force/torque demands from the actuators of the manipulator. Nevertheless, mechanisms that have higher inertia cannot achieve high acceleration motions since it results in poor precision and may create physical damage in the mechanism due to high amplitude vibrations. Therefore, there are limitations for maximum allowable accelerations for high inertia manipulators. This study claims that making the system kinematically redundant, by integrating a mechanism with lower inertial characteristics, can be used for operation time reduction with the proposed algorithms in this paper. Next section provides a general description of a redundant mechanism for planar tasks. Following this, algorithm developed for redundancy resolution in order to minimize the end-effector task completion time is presented. Algorithm is devised from the work of [6], which comprises designing the velocity profiles separately for two mechanisms to impose a desired joined velocity profile generation of end point.

2 Planar Redundant Mechanism for Higher Acceleration Motion

Planar redundant manipulator that is used in aimed trajectory generation algorithms is composed of two mechanisms that have independently controlled two DoFs in planar space. As illustrated in Fig. 1, the secondary mechanism, with relatively smaller workspace, is mounted onto the primary mechanism, which has

Fig. 1 Redundant
mechanism
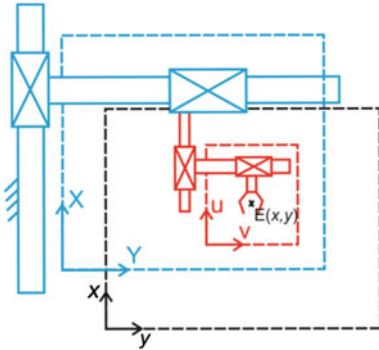
lower acceleration capabilities due to its higher inertial properties. End-effector is assembled on the second mechanism, which will project the desired output $E(x, y)$ of motion as a result of unified motions of the two mechanisms.

Motion of the primary mechanism is indicated with capital X and Y, while the secondary mechanism's motion occurs along u and v axes. The workspace location of u and v axes, which is shown in red in Fig. 1 depends on the position of X and Y axes. End-effector path in this case is defined with respect to the global coordinates which are x- and y-axes. It should be noted that, since the designated system is planned to be used in industrial applications, such as machining tools, the end effector velocity is limited for application type. For example, during operation, mounted tool will be most likely required to have relatively lower speed limit below the maximum achievable speed of mechanism for proper operation.

3 Trajectory Planning Algorithm

Trajectory planning algorithm is developed to achieve the main task, which is position tracking of end-effector provided in global workspace. In general, the algorithm uses advantage of higher acceleration capabilities of secondary, low weight mechanism to reach maximum allowed velocity of end point, E, as quickly as possible. Unlike defining a main task and subtasks for redundant mechanisms, this algorithm comprises trajectory planning and control of two different mechanisms simultaneously. A possible solution to achieve a high acceleration trajectory planning algorithm for redundant manipulator can be determined in velocity profile generation level. In this algorithm, end-effector velocity profile is designed to have trapezoidal velocity profile with highest possible acceleration for end-effector as proposed in [6]. Main aim is to shorten task completion duration compared to the conventional machine with only two axes.

The main function of the algorithm is to deploy end-effector position demands extracted from G-codes segments on redundant machining device (RMD) to utilize formerly mentioned capabilities. Trajectory planning algorithm is to be used as a
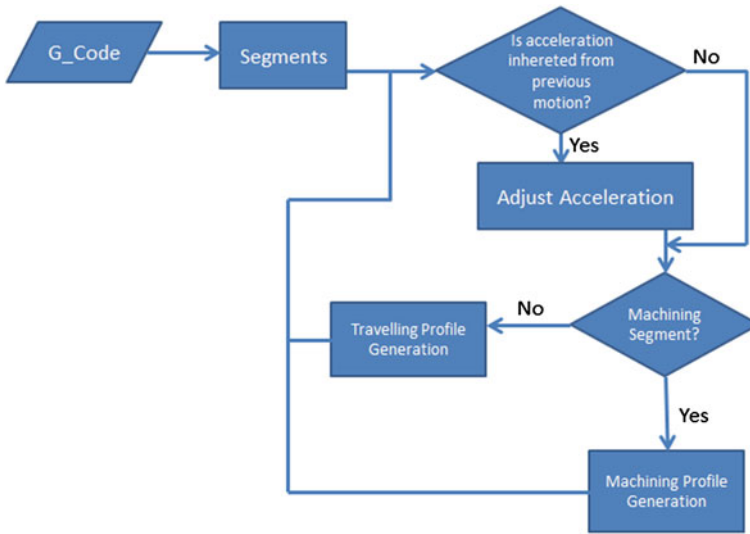
Fig. 2 Flowchart of trajectory planning algorithm

built-in function in between G-code extractions of RMD and machine controller, which is typically a CNC system. The input data for motion planning are extracted from G-codes as segments in two categories: machining segments or travelling segments. In machining segments, the maximum speed of end-effector, or machining tool specifically, is limited by machining process type specifications. On the other hand, the travelling segments are created as positioning of tool before or in between machining segments with maximum motion capabilities of RMD. After the segments are created, the algorithm creates motion profiles sequentially with respect to the presented flowchart in Fig. 2. Segments data are fed as input to the motion planning scheme, which contain information about motion (distance travelled, start and end points of segment) and segment type. At first, the algorithm checks if there are any motions on the primary and secondary mechanisms from previous segments while the end-effector is kept at a constant position, which is further discussed in next sections. After that, if necessary, when acceleration adjustment is completed, the algorithm generates the velocity profile according to motion limitations for either travelling or machining segments.

In this study, the acceleration of the primary axes are designed to be limited with 9.81 m/s^2 for primary mechanism and 49.05 m/s^2 for secondary mechanism, and end-effector velocity is limited with 40 m/min. The maximum velocities are set 200 m/min for primary mechanism, and 100 m/min for secondary mechanism. Position demands delivered to secondary mechanism were held within workspace limitations as predesigned between ±50 mm along both u and v axes.
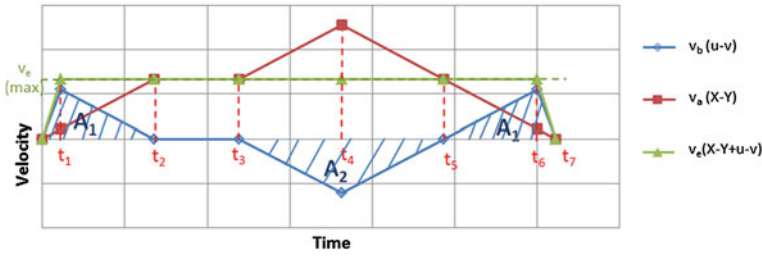
Fig. 3 Velocity level motion generation for machining segments

3.1 Velocity Profile Generation for Machining Segment

A machining segment represents the motions that the end-effector follows during working on a workpiece. With redundancy resolution, this is achieved by adding two independently created velocity profiles for primary mechanism, v_a, along X–Y axes and secondary mechanism, v_b, along u–v axes to obtain the end-effector velocity profile. A continuous velocity profile, which is usually a small part G-code sequence, is illustrated in Fig. 3. This velocity profile is applicable in cases where distance to be traveled is long enough to achieve proposed method. When distance is not enough to reach the maximum allowable velocity limits, a triangle velocity profile of the end-effector is used. Velocity of the end-effector is limited with v_e (max), which is the velocity limit for the designated machining process. Profile generation is designed such that secondary mechanism is designated to start motion at the center of its workspace, which is marked in red (Fig. 1).

After v_e(max) is reached with combined accelerations of the two mechanisms, velocities of the two mechanisms are consistently regulated to preserve end-effector velocity at v_e(max) until time t_6. The duration that end-effector reaches its maximum velocity, t_1, is found by the combined acceleration of two mechanism which are primary axis limit, a_a, and secondary axis limit, a_b (Eq. 1).

$$t_1 = t_7 - t_6 = \frac{v_{e(\text{max})}}{a_a + a_b} \tag{1}$$

Secondary mechanism, after t_1 seconds, decelerates at with a $-a_a$ value and comes to a full stop at t_2. After the primary mechanism reaches the v_e(max) at t_2, the velocity of both mechanisms are kept constant until t_3. Velocity of primary mechanism exceeds the end-effector velocity between t_3 and t_5 in order to retract secondary mechanism to the center of its workspace. Thus, when the total motion is completed, relative position of secondary mechanism will be at the center of its workspace to be ready for the next motion segment. Advantage of this algorithm is that the acceleration and deceleration are much higher at the beginning and termination of the motion, which shortens the total task completion duration.
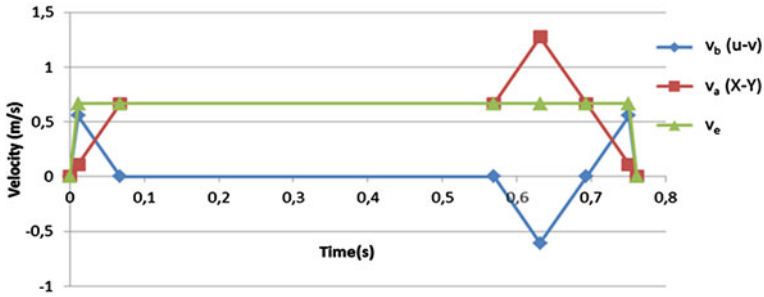
Fig. 4 Velocity level motion generation for 0.5 m machining distance

Distance traveled by secondary mechanism as identified by A_1 and A_2 in Fig. 3 is calculated as presented in Eq. (2), where $A_2 = 2 \times A_1$.

$$A_1 = \frac{1}{2}a_b t_1^2 + \frac{1}{2}a_a(t_2 - t_1)^2; \quad A_2 = \frac{1}{2}a_b(t^*)^2 \tag{2}$$

t^* is the duration between t_5 and t_3. which is calculated in Eq. (3).

$$t^* = t_1 \cdot \sqrt{1 + \frac{a_a}{a_b}\left(\frac{a_e}{a_a} - 1\right)^2} \tag{3}$$

Time elapsed during constant velocity is calculated from required distance to be travelled, d_T, as represented in Eq. (4).

$$(t_3 - t_2) = \frac{d_T}{v_{e(\max)}} - (2t_2 + t_1 + t^*) \tag{4}$$

Motion planning of a machining segment with a traveling distance of 0.5 m for the end-effector is presented in Fig. 4. Motion is generated with respect to the described algorithm in this section for continuous motion of end-effector. According to calculations, the task is completed in 0.761 s with a maximum velocity of 40 m/min. When compared with task completion duration (0.818 s) of the conventional mechanism, there is a 6.97 % time gain. Although time reduction magnitudes for longer-distance machining are smaller, for a task with many smaller-distance contours, algorithm results in remarkably higher reductions in total.

3.2 Velocity Profile Generation for Travelling Segment

Travelling segments are reserved for motions generated for moving end-effector or machining tool to the desired initiation coordinates of the machining process.
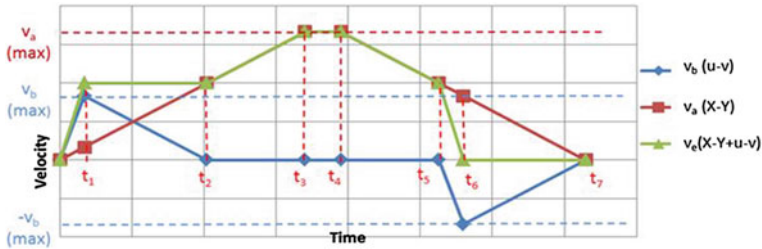
Fig. 5 Velocity level motion generation for travelling segment

Travelling segments are planned between machining segments if there is an offset between termination and initiation coordinates of sequences of G-codes. Like in machining segment, travelling velocity profile generation is carried out for primary mechanism velocity, v_a, along X–Y axes and secondary mechanism, v_b, along u–v axes. In travelling velocity profiles, maximum acceleration duration and velocity generated by secondary mechanism is limited due to its workspace.

In Fig. 5, the velocity profiles generated for travelling segment are drawn according to primary and secondary mechanisms' velocity limits, $v_a(\max)$ and $v_b(\max)$. $v_a(\max)$ is set by primary mechanism's maximum velocity and $v_b(\max)$ is chosen to preserve secondary mechanism's motions inside its workspace. During $t_0 - t_1$, secondary mechanism accelerates with maximum acceleration and decelerates with the same acceleration magnitude of the primary mechanism to stop at its workspace limit. As a result of this, the velocity of end-effector is kept constant while secondary mechanism decelerates and comes to a stop.

Since at initiation and termination secondary mechanism should be located at it center point, distance travelled by end effector is calculated from motion of primary mechanism. Therefore, the t_3 and t_4 time values are determined by conventional trapezoidal velocity calculations using the maximum velocity and acceleration limits of primary mechanism and required distance to be travelled by end-effector.

The velocity limit of secondary axes $v_b(\max)$ is chosen to preserve secondary mechanism's motions inside its workspace. Thus, t_1 and duration between t_6 and t_5, is found by using the acceleration limit of the secondary mechanism $t_1 = v_{b\max}/a_b$. t_2 is calculated by Eq. (5), which is also the equal to duration between t_7 and t_5.

$$t_2 = \frac{(a_b + a_a)t_1}{a_a} \tag{5}$$

During the deceleration of end-effector, secondary mechanism moves in the reverse direction of the end-effector motion with its maximum acceleration initiating from the limit of its workspace. This results in a faster deceleration of the end-effector and the end-effector reaches the travelling segment's termination location. However, at t_6, while the end-effector completes its designated motion, the primary and secondary mechanisms still move. The motion on each
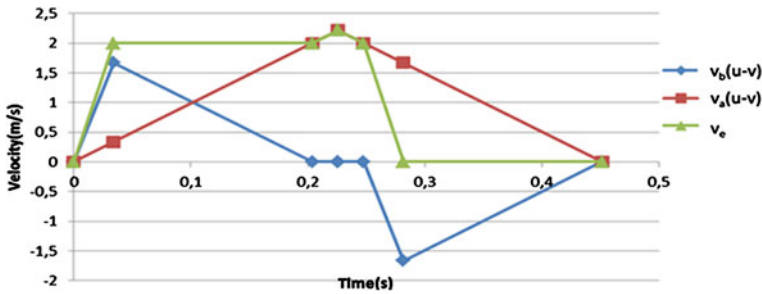
Fig. 6 Velocity level motion generation for 0.5 m travelling distance

mechanism from t_6 to t_7 is described to hold the end-effector position constant while retracting the secondary mechanism to the center of its workspace. This is achieved by demanding 9.81 m/s^2 acceleration from both mechanisms in different directions. Primary mechanism velocity is designed to have a trapezoidal profile with maximum acceleration (9.81 m/s^2) and maximum speed (200 m/min) between $t_0 - t_7$. At the end of the motion described in Fig. 5, from t_6 to t_7, end-effector does not move and reaches its motion termination location. This may be seen as a loss of time. However, for any machining operation, there should be a time interval to cut into the workpiece and this dead time can be utilized for this purpose.

For the numerical example, motion planning of a travelling segment with a traveling distance of 0.5 m of the end-effector is presented in Fig. 6. The calculations show that the travelling segment task is completed in 0.4515 s with a maximum velocity of 132.88 m/min for primary mechanism. As it can be deduced from Fig. 6, there is 0.17 s of time gain (dead time) that can be used for initiation of the cutting process of tool. As a result, there will be time reduction from total completion of sequences of RMD's process.

4 Conclusion

Conventional machines that have larger workspaces suffer in providing higher accelerations while preserving their precision specifications due to moving higher inertia components during the execution of the task. In this work, kinematic redundancy is proposed to enhance the acceleration capability for executing the same task with larger workspace limits. An example case study is carried out for planar motion. An algorithm is generated and discussed to distribute the global motion demand to the primary mechanism and secondary mechanism. Advantage of the algorithm is proved by numerical examples conducted for both machining and travelling segments. This algorithm also has an advantage with respect to pseudo-inverse methods that numerical calculation load is less since this method

uses only simple algebraic calculations rather than dealing with matrix inversions. This method also guarantees that maximum allowable acceleration is achieved throughout the task to minimize total task execution duration. However, algorithm has a practical disadvantage that jerks are not infinite as utilized in this study. Thus, effects and compensation for these effects will be investigated.

References

1. Chen, J.L., Liu, J.S., Lee, W.C., Liang, T.C.: On-line multi-criteria based collision-free posture generation of redundant manipulator in constrained workspace. Robotica **20**, 625–636 (2002)
2. Guo, Z.Y., Hsia, T.C.: Joint trajectory generation for redundant robots in an environment with obstacles. In: IEEE International Conference on Robotics and Automation, Cincinnati, U.S.A, pp. 157–162 (1990)
3. Maaroof, O., Gezgin, E., Dede, M.İ.C.: General subtask controller for redundant robot manipulators. In: 12th IEEE International Conference on Control, Automation, Jeju Island, Korea (2012)
4. Nakamura, Y.: Advanced Robotics Redundancy and Optimization. Addison-Wesley Pub. Co., Massachussetts (1991)
5. Rajiv, V.D., James, A.E., Scott, M.: Real-time implementation of an optimization scheme for seven-degree-of-freedom redundant manipulators. IEEE Trans. Robot. Autom. **1**(5), 579–588 (1991)
6. Sartorio, F.: Machine tool and manipulator devise adapted to be mounted on such machine. Patent No: US 2004/0025761 A1 (2004)
7. Seraji, H.: Task options for redundancy resolution using configuration control. In: IEEE Conference on Decision and Control, Brighton, vol. 3, pp. 2793–2798 (1991)
8. Tatlıcıoğlu, E., Braganza, D., Burg, T.C., Dawson, D.M.: Adaptive control of redundant robot manipulators with subtask objectives. Robotica **27**(6), 873–881 (2009)
9. Wang, J., Li, Y., Zhao, X.: Inverse kinematics and control of a 7-dof redundant manipulator based on the closed-loop algorithm. Int. J. Adv. Rob. Syst. **7**(4), 1–9 (2010)
10. Yoshikawa, T.: Analysis and control of robot manipulators with redundancy. In: Proceedings of First International Sympossium on Robotics Research, MIT Press, Cambridge, pp. 735–748 (1984)

Design Choices in the Development of a Robotic Head: Human-Likeness, Form and Colours

**Scean Mitchell, Gabriele Trovato, Matthieu Destephe,
Massimiliano Zecca, Kenji Hashimoto and Atsuo Takanishi**

Abstract The design of what a robot could look like is a matter of growing importance. Variations of style, size, shape and colour open endless design possibilities. It is important to create a look that poses no visual uncanny valley effects on the human user and that is appropriate to potentially serve in different job areas in human society. In this paper we want to share the methods applied in the design of a new head for the humanoid robot KOBIAN-R. Our creation process is similar to that of the product design process taking into account the psychology of shape, colour and functionality to name a few. Following the creative process we conducted some surveys to assess our new design. Feedback data from participants from a diverse age range and cultural backgrounds are a precious input towards the future development of this robotic head.

Keywords Robot design · Prototyping · Service robots · Humanoid robots

1 Introduction

As humanoid robots enter our everyday life, it is necessary to think ahead about the acceptability and effectiveness of a robots' external appearance. Face-to-face communication was once person to person; even person to animal, and now it has

S. Mitchell · M. Destephe · M. Zecca · K. Hashimoto
Faculty of Science and Engineering, Waseda University, #41-304, 17 Kikui-cho,
Shinjuku-ku, Tokyo 162-0044, Japan

G. Trovato
Graduate School of Advanced Science and Engineering, Waseda University,
Shinjuku-ku, Japan

A. Takanishi (✉)
Department of Modern Mechanical Engineering and Humanoid Robotics Institute (HRI),
Waseda University, Shinjuku-ku, Japan
e-mail: contact@takanishi.mech.waseda.ac.jp

reached a stage where it is person to machine. Usually when we consider person to person communication, the face is one of the primary areas of focus [15]. The human face can relay an important amount of information about emotion as well as other non spoken messages. For this reason, robotic face aesthetic design must be thought carefully. The dimensions of the head, and the presence and number of facial features can heavily influence the perception of humanness in robot heads [3]. Human-like cues can potentially have a positive effect on acceptance [4].

Recently, some humanoid heads are built with a large number of DoF, such as KOBIAN-R [7], and design aesthetics are on the rise thanks to carefully designed anthropomorphic robot heads like are Snackbot [8–10]. Different humanoid heads can be identified based on a character design space diagram of cartoon illustrated face types [2, 11]. This measurement system has also been used and modified to help the robotic industry categorize robot faces. The parameters are Realistic/Objective, Iconic/Subjective, and Abstract [1, 16]. A few examples of realistic robotic faces are [5, 6, 13].

Is human-likeness in humanoid robots a goal that is necessary to achieve? If we intend human-likeness as a concept inclusive of the ability of moving like humans, understanding human society rules and adapting to a human environment, then the answer is certainly positive. If we intend human-likeness as just appearance, then we should make sure that such an appearance does not cause a negative effect on humans' acceptance of the robot.

Our final purpose is to create and refine a head that can appeal to the public. In the present study, we compare a new humanoid robot head design with two existing robot heads and gather comments from an international audience, and we studied the role of colour in identifying the hypothetical robots job in the society.

The rest of the paper is organised as follows: in Sect. 2 the concept behind the design is introduced; experiments are carried out in Sect. 3 and results are discussed in Sects. 4 and 5 concludes the paper.

2 Development of a New Head

2.1 Requirements and Constraints

The head to be developed should have both an active function (expressing emotions, conveying information actively) and a passive function (give a context and background information about the status of the robot). It should also convey positive feelings as friendliness, trust, kindness and safety, through its looks. One more constraint is the application: as it has to be mounted on KOBIAN, it should match with the rest of the body and appear as robot-like more than human-like. This constraint influences details such as the colour of the face and the presence of an artificial skin. We discussed the factors with a professional designer, and various head sketches from simple to highly detailed were considered. Designs

ranged from life like human, symbolic, character, anthropomorphic, mechanical and simplified futuristic styles. Materials to be used were also discussed, such as soft rubbery material verses metal, or hard plastics.

2.2 Influence of Nature in Design

What determined the definition of the final version was the influence of nature in design. Our idea is to make the robot have a mix of nature design motifs, a simplified representation of human form, mechanical commercial product styling and likeable popular culture characteristics.

Based on this we refined our sketches (Fig. 1). In order to lower the uncanny valley effect we simplified this new design by removing excess biological human details. This should always be done to prevent a robotic design from crossing the line from visually acceptable to biologically eerie, due to a less than perfect life like representation. It is important to omit or simplify and stylise biological details like hair, pore glands, soft imitation skin material and adult like facial structures.

Then, we mixed functional and subtle nature-inspired design (Fig. 2). The reason for this is that nature inspired forms are documented in the design industry to be functional, pleasing to the eye and stimulating. Details like soft curves and circles found in cut sections of wood, water ripples and the smooth surface of a rounded stone, have appeal in the consumer product market.

Eyes are a highly important feature for interaction, as Oculesics is one separate category of Kinesics. Though not yet implemented, we plan to add around the lens a symbolic eyelash to soften the look and allow blinking behaviour.

Lips and eyebrows were kept in the 3D stylized form. Both parts should be soft (using silicon-like material such as the Dragonskin used for KOBIAN-R) and allow smooth movements; we decided to make them as removable (attached by magnets). In the case of the lips, this means that inside the mouth there will be just a smooth surface: there should not be any intrusions entering the surface.

These design decisions were taken in order to keep a more natural or close to natural interface: something the human viewer is used to interact with. By keeping lips and eyebrows on 3D physical plane, we can manage keep the sense of natural facial emotional communication, in a physical sense. The reason for this is supported by natural human face to face interaction that is already a part of natural day to day life. This starts from the early stages of childhood where babies are naturally drawn to the facial features of others as a primary mode of communication which continues through one's life [15]. These parts, as previously said, must go through a process of simplification and become more symbolic rather than realistic. For instance, organic details such as the tongue should be avoided.

The refined digital design sketches were followed by the creation of the solid body data using 3D modelling and CAD software. The data was then 3D printed and checked for any minor surface discrepancies. In order to remove aggressive lines and angles, the printed parts were hand sanded. This way of producing
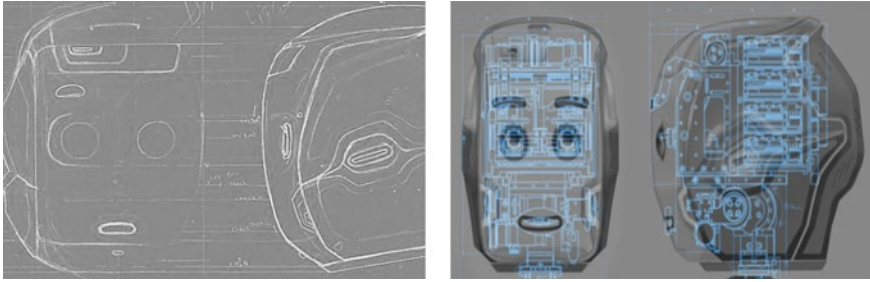
Fig. 1 Early planning sketches (*left*) and CAD 3D design (*right*)

Fig. 2 Nature product design influence

objects is done in product design to convey non-threatening and approachable forms. The final result is just a container, with no sensing capabilities. As such, the model is very generic and the technique and design style are something that can be applicable in other researches too.

3 Results

The evaluation of the head consisted in a questionnaire divided in two parts:

1. Comparison of the new head with two other robotic heads.
2. Investigation on the use of colour.

All the pictures used for the new design are photos of the real prototype with some retouching such as colour overlay. In total, 45 subjects (32 male, 13 female) participated in this experiment: 14 Americans, 11 Japanese, 8 Europeans and a few from other countries. Average age was 33.3; standard deviation 11.9. As the questionnaire was made through a web survey, it was possible to gather participants from several countries.

3.1 Human Likeness

The first part was focused on human-likeness. We displayed three humanoid head types differing in likeness: KOBIAN-R, our new head design and HRP-4C
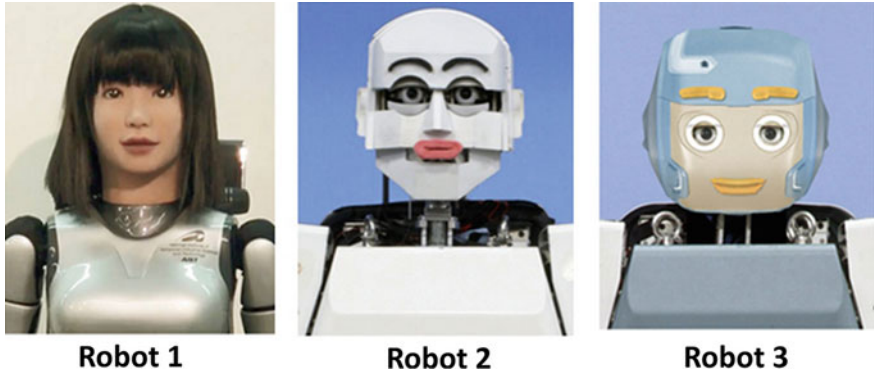
Fig. 3 The three robot heads, as they were presented in the survey, without specific labels

Table 1 Comparison of percentage of preference for the robotic heads

Robot	Comfortable (%)	Would like to use at home (%)	Do not like (%)
HRP-4C	15.6	20.0	53.3
KOBIAN-R	8.9	6.7	35.6
New head	75.6	73.3	11.1
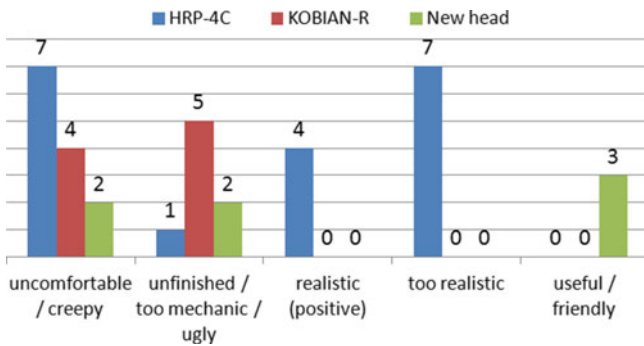
Fig. 4 Comments gathered on the three robot heads

(Fig. 3). We specifically wanted to compare the new design with one very realistic robotic face and with the current design of the head of KOBIAN, which is non-realistic. All of the faces were shown in the survey with their neutral expression and on purpose without labels.

Table 1 shows that the preference for the new head is quite clear. Therefore, it is important to understand the reasons that led to this preference. The subjects were asked to leave some comments freely. We categorised those comments in the labels shown in Fig. 4.

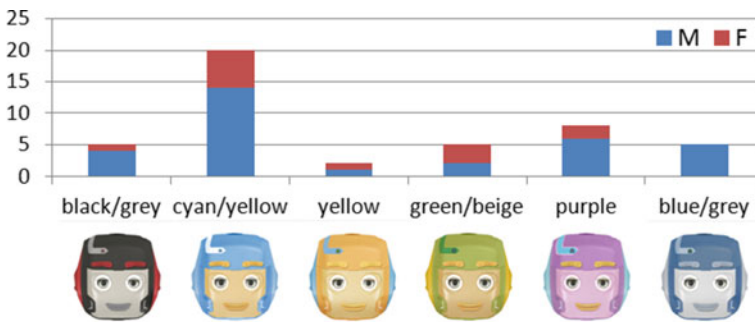**Fig. 5** Possible choices of different colours of the new head

Fig. 6 Preferred colour by gender

3.2 Preference on Colours

The second part of the questionnaire was focused on finding out which colour of the new head is preferred by subjects, and the association of each colour with a job type that the robot could hypothetically do. The choices were presented as in Fig. 5, and results are shown in Fig. 6. The cyan/yellow combination (Robot 2) was the most selected, however gender-related differences can also be noticed, as in some cases (black/grey (Robot 1) and blue/grey (Robot 6) the percentage of preference by female subjects is very low. These results confirm the ones obtained in the survey reported in a previous publication (Mitchell et al. [12]. Further investigation in Table 2 gives us suggestions about how to customise the robot for different targets. The best job/colour combinations are highlighted.

4 Discussion

Regarding the survey on human likeness, a few interesting point of discussion can be seen analysing the graph in Fig. 4:

- Uncomfortable and creepy are adjectives used mostly about HRP-4C and to a lesser extent, about KOBIAN-R, while the design of the new head does not cause such discomfort.

Table 2 Association of head colours with possible role in society

Cleaning	8	13	17	11	10	15
Sales	6	8	8	1	9	15
Nature	2	5	10	30	5	4
Elderly helper	2	17	13	8	13	8
Child care	2	21	13	8	17	5
Theme park	4	11	16	10	18	8
Security	28	3	3	6	2	15

- HRP-4C's head is the most realistic and human-like, and the comments about human-likeness were divided between positive and negative. As the negative ones ("too realistic") were more common than the positive, we believe that realism in human-likeness is the main reason of discomfort.
- Negative comments KOBIAN-R are mainly due to the raw/mechanical appearance. This is more evidence that supports our view that robots should be designed with shapes aesthetically inspired by nature.
- The last column of the graph in Fig. 4 contains comments not related to appearance, but rather on usefulness and perceived friendliness of a hypothetical robot using the new head. This seemed to be a consequence of the appearance. In this regard, interaction mechanisms described in The Media Equation [14] seem related, as human perception of a machine can be influenced by indirect factors, such as, in this case, just facial design.

As for the survey on colours, study on such small details may seem done for its own sake; however, these subtle variations could make the difference, in a future society, between a product that gets sold and a product that does not get sold. In our previous investigation [12], we also found out that children have their own taste regarding robots seen as toys. Even in the case of applying a robot in a public role, we should be careful to consider the implication of a colour in the particular culture. For instance, the colour green, depending on the context or on the culture, can be associated to nature, to spring, to envy or poison.

5 Conclusion

In this study, we described the nature inspired design of a new head for humanoid robot. The results of a comparison with two other, more human-like robotic heads show that human-likeness is not always perceived as positive by humans and therefore design should be carefully considered. It is also investigated how colour

styles can be useful in establishing ideas for personal market preferences and job types. Through all these design features, using a product design method with interesting shapes, we believe that a robot will potentially get a better acceptance and have a wider range and role in tomorrow's society. These studies gave us a direction to follow. For the future, we are planning to mount the real prototype on the body of the robot KOBIAN-R and evaluate it again through metrics like Bartneck's Godspeed scales. Furthermore, a study on lights and colours will be carried out. As lights of different colours can convey different messages depending also on the context, the ability of displaying lights is important for improving communication capabilities of the robot.

References

1. Blow, M. et al.: The art of designing robot faces: dimensions for human-robot interaction. In: ACM Proceedings of 1st Annual Conference on HRI, pp. 331–332 (2006)
2. Chang, W.C., Wu, T.Y.: Exploring types and characteristics of product forms. Int. J. Des. **1**(1), 3–14 (2007)
3. DiSalvo, C.F et al.: All robots are not created equal: the design and perception of humanoid robot heads. In: Proceedings of the 4th Conference on Designing Interactive Systems: Processes, Practices, Methods, and Techniques, pp. 321–326. ACM, New York (2002)
4. Duffy, B.R.: Anthropomorphism and the social robot. Robot. Auton. Syst. **42**, 177–190 (2003)
5. Hashimoto, T., Kato, N., Kobayashi, H.: Development of educational system with the android robot SAYA and evaluation. Int. J. Adv. Rob. Syst. **8**(3), 51–61 (2011)
6. Kaneko, K., Kanehiro, F., Morisawa, M., Miura, K., Nakaoka, S., Kajita, S.: Cybernetic human HRP-4C. In: 9th IEEE-RAS International Conference on Humanoid Robots, pp. 7–14 (2009)
7. Kishi, T. et al.: Development of expressive robotic head for bipedal humanoid robot. In: Intelligent Robots and Systems (IROS), pp. 4584–4589 (2012)
8. Lee, M.K. et al.: The snackbot: documenting the design of a robot for long-term human-robot interaction. In: Proceedings of HRI 2009, pp. 7–14 (2009)
9. Leite, I., Martinho, C., Pereira, A., Paiva, A.: iCat: an affective game buddy based on anticipatory mechanisms. In: Proceedings of the 7th International Joint Conference on Autonomous Agents and Multiagent Systems (AAMAS '08), vol. 3, pp. 1229–1232
10. Lütkebohle, I., Hegel, F., Schulz, S., Hackel, M., Wrede, B., Wachsmuth, S., Sagerer, G.: The bielefeld anthropomorphic robot head flobi. ICRA **3–7**, 3384–3391 (2010)
11. McCloud, S.: Understanding Comics: The Invisible Art. Harper Collins Publisher, Inc., New York (1993)
12. Mitchell, S. et al.: Shaping the form of tomorrows robotic faces. In: Workshop on Design of Human Likeness in HRI, from Uncanny Valley to Minimal Design, 8th ACM/IEEE International Conference on Human-Robot Interaction (HRI), pp. 14–18 (2013)
13. Oh, J., Hanson, D., Kim, W., Han, Y., Kim, J., Park, I.: Design of android type humanoid robot albert HUBO. IROS **2006**, 1428–1433 (2006)

14. Reeves, B., Nass, C.: The media equation: how people treat computers, television and new media like real people and places. University Press, Cambridge (1996)
15. Russell, J.A.: Is there universal recognition of emotion from facial expressions? A review of the cross-cultural studies. Psychol Bull **115**(1), 102–141 (1994). doi:10.1037/0033-2909.115.1.102
16. Wodehouse, A.J., Ion, W.J.: Information use in conceptual design: existing taxonomies and new approaches. Int J Des **4**(3), 53–65 (2010)

Hopping Robot Using Pelvic Movement and Leg Elasticity

Takuya Otani, Kazuhiro Uryu, Masaaki Yahara, Akihiro Iizuka, Shinya Hamamoto, Shunsuke Miyamae, Kenji Hashimoto, Matthieu Destephe, Masanori Sakaguchi, Yasuo Kawakami, Hun-ok Lim and Atsuo Takanishi

Abstract Analysis of human running has revealed that the motion of the human leg can be modeled by a compression spring because leg's joints behave like a torsion spring. In addition, the pelvic movement in the frontal plane contributes to the increase in jumping force. We therefore assumed that human-like running, which requires higher output power than that of existing humanoid robots, could be realized based on these characteristics. Hence, we developed a model composed of a body mass, a pelvis and a rotational joint leg, and fabricated the leg by incorporating a stiffness adjustment mechanism that uses two leaf springs. In this way, we were able to achieve a human-like joint stiffness, which could be adjusted by varying the effective length of one of the leaf springs. We achieved hopping by resonance of the pelvic movement and joints' elasticity.

Keywords Humanoid · Hopping · Human motion analysis

T. Otani · K. Uryu · M. Yahara · A. Iizuka · S. Hamamoto · S. Miyamae
Graduate School of Science and Engineering, Waseda University, Shinjuku, Tokyo, Japan

T. Otani
Research Fellow at the Japan Society for the Promotion of Science, Chiyoda-ku, Japan

K. Hashimoto
Research Institute for Science and Engineering, Waseda University, Shinjuku, Japan

M. Destephe · A. Takanishi (✉)
Faculty of Science and Engineering, Waseda University, Shinjuku, Japan
e-mail: contact@takanishi.mech.waseda.ac.jp

M. Sakaguchi · Y. Kawakami
Faculty of Sport Sciences, Waseda University, Shinjuku, Japan

M. Sakaguchi
Faculty of Kinesiology, University of Calgary, Calgary, AB, Canada

H. Lim
Faculty of Engineering, Kanagawa University, Kanagawa-ku, Japan

H. Lim · A. Takanishi
Humanoid Robotics Institute (HRI), Waseda University, Shinjuku, Japan

1 Introduction

In a previous study, we developed a biped humanoid robot to simulate human motions, which we named WABIAN-2R (WAseda BIpedal humANoid-No. 2 Refined) [1]. The robot can be used to understand the mechanism of the human body [2] and to test welfare devices [3]. If the robot could be made to mimic human hopping and running, it would be possible to realize more human motions.

This robot, however, is limited to walking. In human running, the joints of the standing leg require about 1,000 W [4], which is higher than the power of the WABIAN-2R actuator. Some biped robots are capable of running; for example, ASIMO can run at a speed of 9 km/h [5], and MABEL at a speed of 11 km/h [6]. Compared to a human sprinting at a speed of 36 km/h [7] and jogging at a speed of 14 km/h [8], the running speeds of those biped robots are lower and we would like to get closer to those higher human speeds.

To solve this problem, we propose the utilization of lower body movement which is a human characteristic in running. Human running can be modeled by a Spring Loaded Inverted Pendulum (SLIP) model, which is composed of a body mass and spring leg inspired by the linear relationship between the ground reaction force and the vertical body displacement during running (McMahon et al. [9]. This model describes human running in a simple, straightforward way and is used on the studies of running robots. Moreover, the knee and ankle joints of the standing leg act like torsion springs which emerge the leg stiffness [10]. Furthermore, an important characteristic that has not yet been reported is that a human pelvic movement in the frontal plane can help to increase takeoff forces. Considering the above, our aim was to mimic human pelvic movement and joint stiffness using elastic bodies to reproduce its high power.

In this paper, we propose a running model that is a combination of a traditional SLIP model and a pelvis. We then describe a hopping robot using this model. We developed a mechanism comprising two leaf springs for adjusting the joint stiffness and implemented it in the new leg. We completed a hopping experiment with a real hopping robot.

This paper is organized as follows. In Sect. 2, we describe the development of the hopping robot. In Sect. 3, we present the experiment and its results. Finally, in Sect. 4, we draw our conclusions from the results and discuss about the future works.

2 Development of a Hopping Robot

2.1 Model of Human Running

In previous studies, the human leg during running was modeled by the traditional SLIP model, which is composed of a body mass and compression spring. Moreover, human has the characteristics that the knee and ankle joints of the standing

Fig. 1 Scheme of a new model
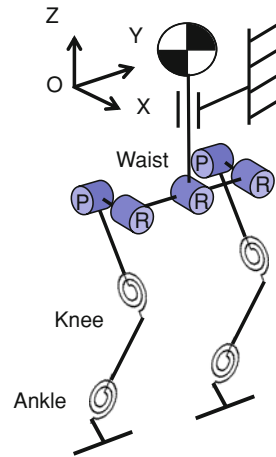
leg act like torsion springs [10]. In an attempt to identify other characteristics of human running motion that could be useful for robot design, we conducted a series of motion capture experiments with human subjects. Based on the human motion analysis, we found that the human pelvic sine movement in the frontal plane can help to increase takeoff forces.

We propose a new model which is composed of a body mass, a pelvis, and spring legs (Fig. 1). In this model, the knee and ankle joints of the standing leg act like torsion springs and the pelvic sine movement causes the resonance for hopping.

## 2.2 Development of Pelvis Mimicking Human Pelvic Movement

We aim to develop a hopping robot that can successfully execute a hopping motion using real hardware. We determined the requirements for velocity and torque in the hip roll joint based on human running data [8]. We also fixed the requirements for the velocity of the pelvis roll joint based on human running data [11]. To the best of our knowledge, no work has previously been conducted on the torque of the pelvis roll joint. We calculated these requirements by substituting appropriate values in the mentioned model.

We chose a 150-W DC motor (Maxon Co., Ltd.), a timing belt, and a harmonic drive to actuate the pelvis and hip joints (Fig. 2).

2.3 Model of Joint Stiffness Adjustment Mechanisms

During the stance phase of human running, the joints alternately lengthen and shrink like a spring. As mentioned above, the leg stiffness and joint stiffness vary

Fig. 2 Developed pelvis
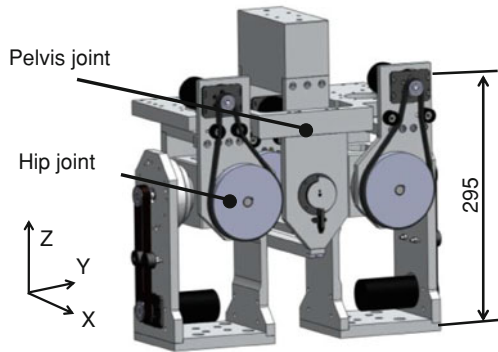

Table 1 Joint stiffness requirements

	Max. [Nm/deg]	Min. [Nm/deg]
Knee	10	7
Ankle	10	9

according to the running speed. We targeted the running speed between 4 and 10 m/s. The joint stiffness requirements are given in Table 1.

There are several ways of mimicking joint stiffness. For example, one can use an actuator to control like a spring, implementation of a spring, and a combination of these methods. During human running, each joint of the leg requires more than 1,000 W [4]. However, the output of the DC motors used in the legs of WABIAN-2R is 150 W, which is much lower than the required power of the human leg joint. If motors with higher power are used, their size and weight would make it difficult to mimic a human leg. Although hydraulic actuators can be used to produce the required high output, huge and heavy pumps are needed. It is therefore very difficult to realize human running by using existing actuators.

Hence, we considered the possibility of mimicking this characteristic by using a compression coil spring, a torsion spring, or a leaf spring for the elastic bodies. To mimic the variation of the joint stiffness with the running speed, we used a leaf spring for easy adjustment of the stiffness by varying the distance between a supporting point and a load point. Figure 3 is a scheme of the proposed joint stiffness adjustment mechanism. The load point is fixed on Link A and the leaf spring is fixed on Link B via the joint axis. When a force is applied to Link A, the force is transmitted to the leaf spring through the load point. Link A then rotates in accordance with the deformation of the leaf spring. By this means, we could adjust the joint stiffness by changing the position of the load point. The theoretical formula for the joint stiffness is as follows:

$$K_j = \frac{T}{2\sin^{-1}\left(\frac{Tl}{6EI}\right)} \tag{1}$$
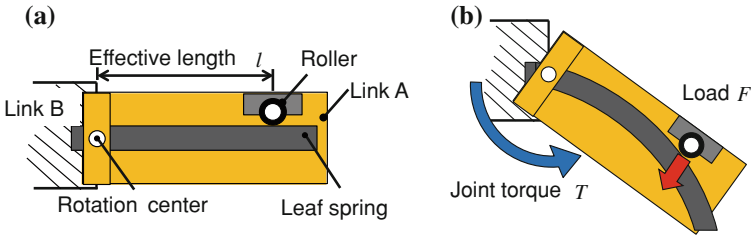
Fig. 3 Scheme of the joint stiffness adjustment mechanism. When the load is applied to *Link A*, the force is transmitted to the leaf spring through the load point. *Link A* therefore rotates in accordance with the deformation of the leaf spring. The joint stiffness can thus be varied by changing the distance between the supporting point on *Link A* and the load point on *Link B*. **a** No load, **b** Loaded

where K_j is the joint stiffness, T is the joint torque, l is the effective length of the leaf spring, E is the Young's modulus of the leaf spring, and I is the area moment of inertia of the leaf spring.

2.4 Development of Rotational Joint Leg

The joint stiffness adjustment mechanism can change its stiffness. However, in mimicking low joint stiffness, it was difficult to install the leaf spring in the leg which is about as big as that of a human. We need to position the load point far from the supporting point. Moreover, the leaf spring could not withstand the force when its thickness was reduced to decrease the stiffness. This leaf spring joint stiffness adjustment mechanism could therefore not be used to achieve the required joint stiffness.

To solve this problem, we incorporated an additional leaf spring in the mechanism. We show the schematic view of the joint stiffness adjustment mechanism with two leaf springs in Fig. 4. The modified mechanism is comprised two units of the previous one, but the stiffness of only one of the leaf springs is adjustable. This was because the stiffness adjustment mechanism occupied much space. By this means, the stiffness of the knee and ankle joints can be adjusted over a wide range and the mechanism can be installed in the leg (Fig. 5). The theoretical formula for the joint stiffness using two leaf springs is as follows:

$$K_{j'} = \frac{T}{2\left\{\sin^{-1}\left(\frac{Tl_1}{6E_1 I_1}\right) + \sin^{-1}\left(\frac{Tl_2}{6E_2 I_2}\right)\right\}} \tag{2}$$
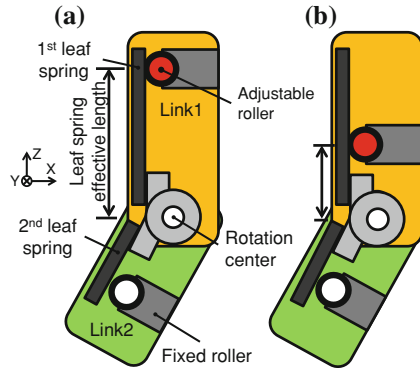
Fig. 4 Joint stiffness adjustment mechanism with two leaf springs. The mechanism basically comprises two units of the previous mechanism, but the stiffness of only one of the *leaf springs* is made adjustable because the adjustment mechanism occupies much space. By this means, the joint stiffness can be adjusted over a wide range and the mechanism can be installed inside the leg. **a** Low joint stiffness, **b** High joint stiffness
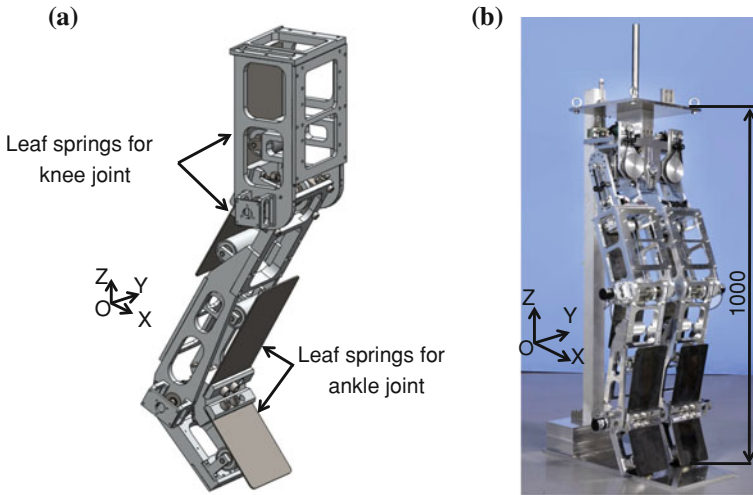
Fig. 5 Rotational joint leg. The joint stiffness adjustment mechanisms with two *leaf springs* are installed in the knee and ankle joints to mimic the joint stiffness similar to that of a human. **a** CAD, **b** Overview

where K_j' is the joint stiffness, T is the joint torque, and l_1 and l_2, E_1 and E_2, and I_1 and I_2 are respectively the effective lengths, Young's modulus, and area moment of inertia of the two leaf springs. The values of the design stiffness of the knee and ankle joints are given in Table 2.

Table 2 Design value of the joint stiffness adjustment mechanism with two leaf springs

	Adjustable [Nm/deg]	Fixed [Nm/deg]	Joint [Nm/deg]
Knee	10 ∼ 42	24	7 ∼ 16
Ankle	16 ∼ 28	28	9 ∼ 12

Fig. 6 Height displacement on hopping experiment. The robot hopped when the displacement of the mass was greater than 0 mm
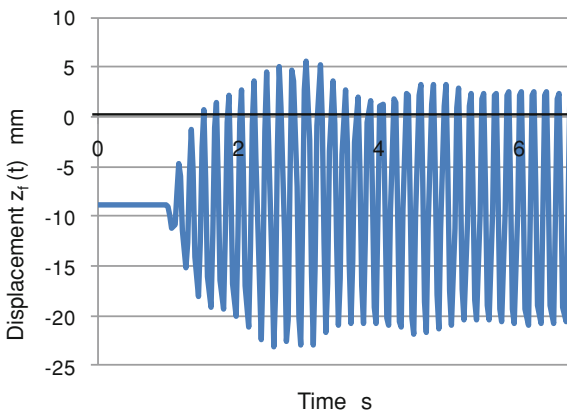
3 Hopping Experiment

We tested hopping by resonance using the pelvic oscillation movement. At the beginning of the experiment, the robot stood with its one leg. Then, the robot started moving its pelvis. The pelvis oscillation movement is expressed as follows:

$$\theta_{\text{pelvis}}(t) = \begin{cases} A\sin(\omega t) & \text{for } z_f(t) \leq 0 \text{ (stancephase)} \\ 0 & \text{for } z_f(t) > 0 \text{ (flightphase)} \end{cases} \tag{3}$$

where A is the pelvic rotation amplitude, ω is the natural frequency, t is the time of the stance phase and $z_f(t)$ is the vertical mass displacement. In this experiment, the pelvic rotation amplitude was 1°. The knee and ankle joint stiffness were 7 and 9 Nm/deg, respectively. The robot motion is restricted to the vertical direction with linear guides. When the leg rose off the ground, the mass displacement was 0 mm. This indicated that the robot hopped when the displacement of the mass was greater than 0 mm.

The results of the experiment are shown in Fig. 6. We successfully performed a continuous hopping by the pelvic sine movement. We intend to use larger pelvic movement and hip pitch joint for higher hopping.

4 Conclusion

In this paper, we described the development of a hopping robot with a pelvis and a joint stiffness adjustment mechanism that uses two leaf springs to mimic the joint stiffness of a human leg during running. The new mechanism is able to adjust the joint stiffness by variation of the effective length of leaf springs. By this means, the joint stiffness can be adjusted over a wide range and the mechanism can be installed in the leg. We evaluated the performance of the new mechanism and confirmed that it produced a joint stiffness similar to that of a human. The robot could achieve hopping by resonance, which confirmed that the mechanism could be used for human-like hopping and running.

We note that the leg only mimics the motion of a human leg in the standing phase. In the flight phase, a human bends the knee of the swing leg to prevent its hitting the ground before lifting the foot forward, and to decrease the moment of inertia of the leg. By mimicking this motion, we would be able to realize human-like running.

References

1. Hashimoto, K., Takezaki, Y., Hattori, K., Kondo, H., Takashima, T., Lim, H.O., Takanishi, A.: A study of function of the human's foot arch structure using biped humanoid. In: Robotics Proceedings of the 2010 IEEE/RSJ International Conference on Intelligent Robots and Systems, pp. 2206–2211 (2010)
2. Hashimoto, K., Takezaki, Y., Motohashi, H., Otani, T., Kishi, T., Lim H.O., Takanishi A.: Biped walking stabilization based on Gait analysis. In: Proceedings of the 2012 IEEE International Conference on Robotics and Automation, 154–159 (2012)
3. Ogura, Y., Aikawa, H., Shimomura, K., Kondo, H., Morishima, A., Lim, H.O., Takanishi. A.: Development of a humanoid robot capable of leaning on a walk-assist machine. In: Proceedings of the first IEEE/RAS-EMBS 2006 International Conference on Biomedical Robotics and Biomechatronics, p. 299 (2006)
4. Dalleau, G., Belli, A., Bourdin, M., Lacour, J.R.: The spring-mass model and the energy cost of treadmill running. Eur. J. Appl. Physiol. **77**, 257–263 (1998)
5. Takenaka, T., Matsumoto, T., Yoshiike, T., Shirokura, S.: Running gait generation for biped robot with horizontal force limit. JRSJ **29**(9), 93–100 (2011)
6. Grizzle, J.W., Hurst, J., Morris, B., Park, H.W., Sreenath, K.: MABEL, a new robotic bipedal walker and runner. In: 2009 American Control Conference, pp. 2030–2036 (2009)
7. Endo, T., Miyashita, K., Ogata, M.: Kinetics factors of the lower limb joints decelerating running velocity in the last phase of 100 m race. Japan J. Phys. Educ. Hlth. Sport Sci. **53**, 477–490 (2008). (in Japanese)

8. Ferber, R., Davis, I.M., Williams III, D.S.: Gender differences in lower extremity mechanics during running. Clin. Biomech. **18**(4), 350–357 (2003)
9. McMahon, T., Cheng, G.: The mechanics of running: how does stiffness couple with speed? J. Biomech. **23**, 65–78 (1990)
10. Gunther, M., Blickhan, R.: Joint stiffness of the ankle and the knee in running. J. Biomech. **35**, 1459–1474 (2002)
11. Schache, A.G., Branch, P., Rath, D., Wrigley, T., Bennell, K.: Three-dimensional angular kinematics of the Lumbar spine and Pelvis during running. Hum. Mov. Sci. **21**, 273–293 (2002)

A Robotic Head that Displays Japanese "Manga" Marks

Tatsuhiro Kishi, Hajime Futaki, Gabriele Trovato, Nobutsuna Endo, Matthieu Destephe, Sarah Cosentino, Kenji Hashimoto and Atsuo Takanishi

Abstract This paper describes the development of a robotic head with ability to display marks commonly used in "manga" (Japanese comics). To communicate with humans, robots should have an expressive facial expression ability for indicating its inner state. Our previous research suggests that, robots can express its emotion clearly if it perform facial expressions that can adapt with the cultural background of the communication partner. As a first step, we focus on making expressions for Japanese people. Manga mark is a unique and famous way of emotion expression in Japanese culture. In a previous preliminary experiment, we determined facial expressions for the robot KOBIAN-R with manga marks. Those expressions included four manga marks as "Cross popping veins" for "Anger", "Tear mark" for "Sadness", "Vertical lines" for "Fear" and "Wrinkle" for "Disgust". A new head that express these marks was developed. Flexible full color LED matrix display and mechanism for indicating black lines were implemented. Experimental evaluation shows that the new robotic head has over 90 % average emotion recognition rates by 30 Japanese participants for each of the six emotions.

T. Kishi (✉) · H. Futaki · G. Trovato · S. Cosentino
Graduate School of Science and Engineering, Waseda University, Waseda, Japan
e-mail: contact@takanishi.mech.waseda.ac.jp

T. Kishi
Research Fellow, Japan Society for the Promotion of Science, Chiyoda-ku, Japan

N. Endo
Graduate School of Engineering, Osaka University, Osaka, Japan

M. Destephe · A. Takanishi
Faculty of Science and Engineering, Waseda University, Waseda, Japan

K. Hashimoto
Research Institute for Science and Engineering, Waseda University, Waseda, Japan

A. Takanishi
Humanoid Robotics Institute (HRI), Waseda University, Waseda, Japan

1 Introduction

In our elderly society there is a growing need of robots that can perform not only simple tasks instead of humans but that can also support humans daily life including medical and nursing. In order to support humans both physically and psychologically, robot should communicate with human fluently. Communication between humans is achieved through both verbal and non-verbal information. Non-verbal information performs an important role and especially facial expression is important [1]. Therefore, robot should have understandable facial expression ability for indicating its inner state in order to achieve a fluent communication with a human.

Many robots with some facial expression ability have been developed, such as EMYS [2], Albert-HUBO [3] and Geminoid [4]. We have also developed a robotic head for KOBIAN-R (Fig. 1) that can express exaggerate facial expressions (Fig. 2). That head has 24 DoFs and electro luminescence sheet for blue facial color. Our previous research [5] shows that exaggerated expressions with wide movable range of facial parts and exaggerate facial color are effective for the robotic head to express emotion understandably. However, for all these robotic heads it is difficult to obtain high recognition rates for the expressions of all the six basic [6] emotions. In fact, the average recognition rates of KOBIAN-R was 68.5 %.

One of the probable reasons for that usually robots facial expressions are not culture-specific. Previous study shows that when human recognize the emotions from facial expressions, there is a aspect of cultural background [7, 8, 9] and our previous study suggested that this is also true in robotic facial expressions [10]. Therefore, in order to achieve expressions that are easy to understand, robot should express facial expressions that adapt to different cultural backgrounds. For the first step of this study, we focus on Japanese culture. Japanese comic ("manga") marks is unique and widely used way for expressing emotions in Japan. The potential advantages of their use were proved in our previous research [10]. In our preliminary study, we obtained facial expressions with manga marks with sufficiently high recognition rates for Japanese (Figs. 3 and 4). We defined these expressions as a model to use with Japanese people. In this paper, we describe the development of the new robotic head that aims to improve even more recognition rates for Japanese people through implementing these manga marks.
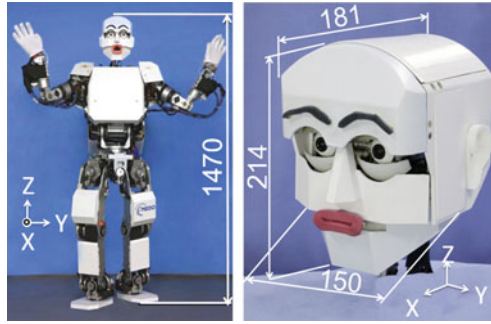
Fig. 1 KOBIAN-R and its head
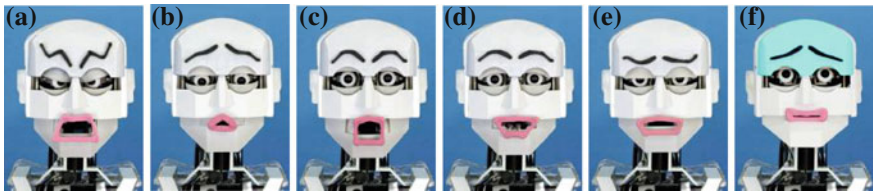
Fig. 2 Facial expressions of KOBIAN-R. **a** Anger, **b** Sadness, **c** Surprise, **d** Happiness, **e** Disgust, **f** Fear
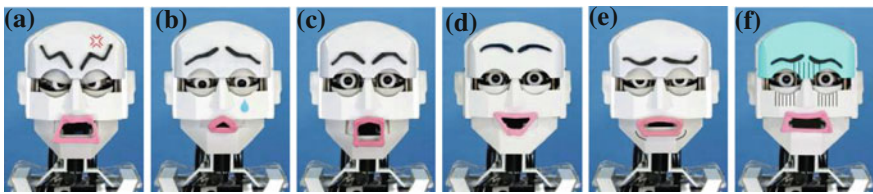
Fig. 3 Model facial expressions (Photo edited). **a** Anger, **b** Sadness, **c** Surprise, **d** Happiness, **e** Disgust, **f** Fear
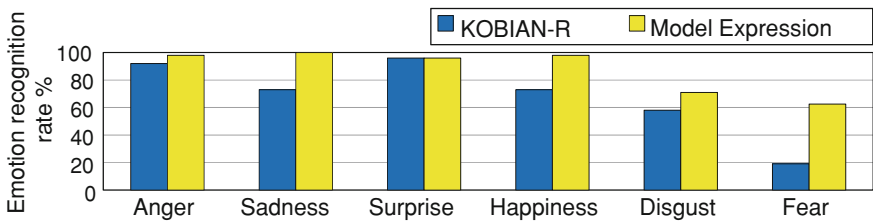

Fig. 4 Emotion recognition rates of model expression

2 Hardware Development of Expressing Manga Marks

The model expressions were designed using red "Cross popping veins" for "Anger" and black "Vertical lines" for "Fear" should be expressed on forehead. Blue "Tear mark" and black "Vertical lines" for "Fear" for "Sadness" should be expressed on cheeks. Black marks as "Wrinkle" for "Disgust" should be expressed under the lip ends.

First, we tried to implement all of these expressions with LED or liquid crystal displays. However, we couldn't implement the black color for "Vertical lines" or "Wrinkle" with high contrast by this method. In addition, there are no commercial liquid crystal displays or LED displays that bend on the curved surface of the head cover. Therefore, we decided to develop two mechanisms for expressing these marks. One is a full color LED matrix display for expressing red and blue marks for "Anger" and "Sadness." The other is the mechanism with a sheet with black lines for "Disgust" and "Fear". Especially, the new forehead mechanism is consisted of five layers structure (Fig. 5). Between the magnet for moving eyebrows on the outer and inner head case, light diffusion sheet, LED display for expressing marks and EL display for expressing facial color are placed. Those mechanisms are implemented as Fig. 6. LED displays are implemented on forehead and cheeks. Sheet mechanisms for black marks are implemented on the forehead, the cheek and the jaw. The outer dimension of the new robotic head was almost same as that of Japanese adult female and total weight was 3.0 kg. We named the whole body emotion expression robot with this new head as KOBIAN-RII (KOBIAN-Refined II).

2.1 LED Display for Expressing "Cross Popping Veins" and "Tear Mark"

Required size of mark expressing area of LED display was not smaller than 35 × 48 mm. As for the mount place's space limit, the device size including control area should be no larger than 35 × 110 mm. In addition, the area LEDs are mounted should be bent along the face surface, the area around LEDs or backside of it couldn't be used for mounting other parts. Furthermore, on the forehead, the device is placed between the magnets which drives the eyebrow. Therefore, the thickness of the device should be as thin as possible. Size of LED itself and the pitch defines the preciseness of marks and thickness of the sheet. We used the 1 × 1 and 0.2 mm thick LED, which is smallest full color LED in the world (SMLP34RGB2 W by ROHM) and placed them in 2 mm pitch on both X and Y axes. In the expression area, 24 × 16 LEDs were placed (Fig. 7). In order to minimize the control part of the device, the active matrix control was used for controlling the image. Active matrix is implemented with two 12ch full color LED drivers and three shift registers. Brightness of each RGB color can be controlled in
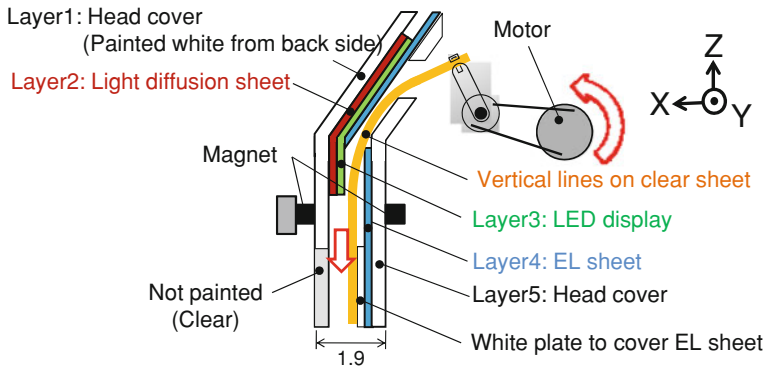
Fig. 5 Layer structure of forehead
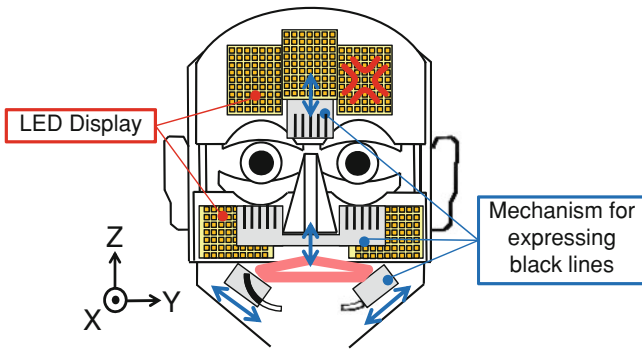
Fig. 6 Placement of the mechanisms for manga marks
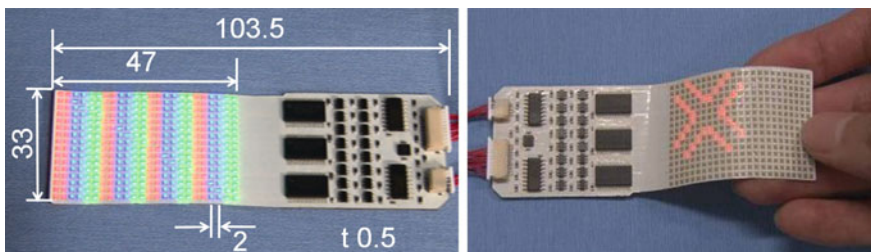
Fig. 7 Full color LED matrix display that has high flexibility

16 bit level. Image on the display can be controlled via SPI connection. The refresh rate is 10 ms. SPI signal is input from the motor controller unit which is already mounted on the robotic head for controlling motors (Fig. 8). Five displays (three on the forehead, one on each cheek) were mounted on the new head.
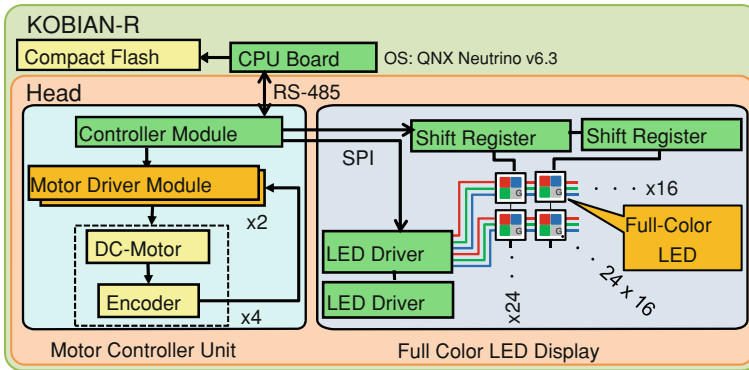
Fig. 8 Control system of the LED matrix display

2.2 Mechanism for Expressing "Vertical Lines" and "Wrinkle"

As the light emitting device can't express black color with high contrast, we decided to design a new mechanism for expressing black marks for expressing "Vertical lines" and "Wrinkle" for "Fear" and "Disgust". "Vertical lines" for "Fear" should be displayed on the forehead and on the cheeks. These are achieved with mechanisms of a clear sheet, on which black lines are printed (Fig. 9), which moves pushed and pulled on front and back of the head case. Especially on the forehead, the sheet is pushed and pulled by link and come out from back of the LED display. "Wrinkle" for "Disgust" is achieved by a mechanism in which a black plate is pushed and pulled in and out of window-like non painted part of the jaw front cover (Fig. 5).

3 Experimental Evaluation

We conducted a questionnaire for evaluating the facial expression ability of the new robotic head. 30 Japanese subjects (15 men and 15 women, average age was 20.9, S.D. 1.27) joined the experiment. Picture of facial expression of KOBIAN-RII used in the experiment is shown in Fig. 10 and the result is shown in Fig. 11. As no effective manga marks were found for "Surprise" and "Happiness", the results without marks were only shown. Results show that over 80 % emotion recognition rate was obtained for each six basic emotion. The average rate was 92.2 %.

Especially, the rates for "Anger", "Sadness" and "Surprise" were 100 %. Though the rate for "Fear" of KOBIAN-R was only 27 %, the one of KOBIAN-RII increased to 80 %. Focusing on the effect of manga marks, the results show
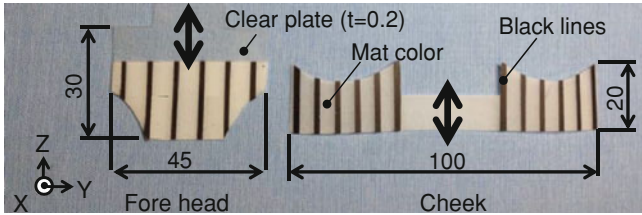
Fig. 9 Sheet with *black line*
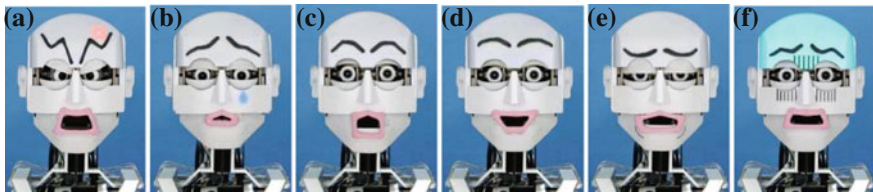
Fig. 10 Facial expression of KOBIAN-RII. **a** Anger, **b** Sadness, **c** Surprise, **d** Happiness, **e** Disgust, **f** Fear
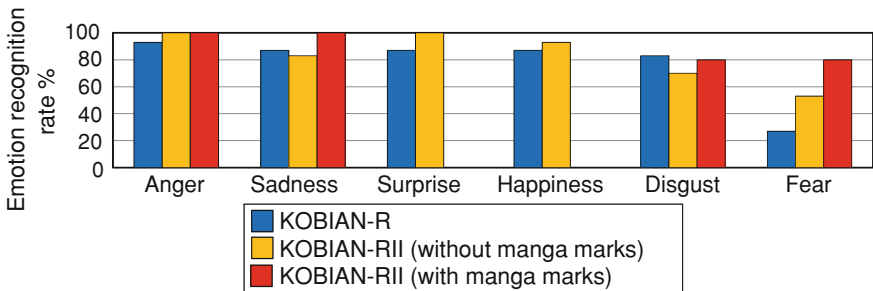
Fig. 11 Emotion recognition rates of KOBIAN-RII. For "Surprise" and "Happiness", we couldn't find effective manga marks

that all of them were effective for emotion expression. With "Tear mark", the emotion recognition rate for "Sadness" increased from 83 to 100 %. With "Wrinkle", the rate for "Disgust" increased from 70 to 80 %. We couldn't find the increase of emotion recognition rate for "Anger" because the rate was still 100 % without the mark expression. Figure 12 shows "Fear" expressions with the combination of manga marks achieved by KOBIAN-RII. Figure 13 shows the difference of the emotion recognition rates for them. Emotion recognition rate for the facial expression without "manga" marks was only 37 %. On the other hand, recognition rate of the facial expression with blue facial color was 53 % and the one of the facial expression with "Vertical lines" was 73 %. This shows that "Vertical lines" are more effective than blue facial color for expressing "Fear".
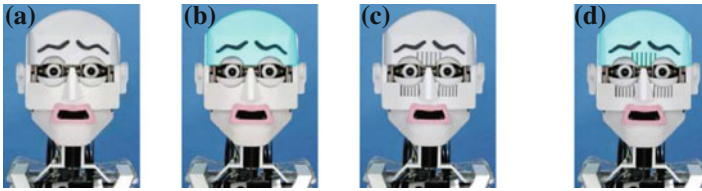
Fig. 12 "Manga" marks for expressing "Fear". **a** No marks, **b** Facial color, **c** Verticle lines, **d** Facial color + vertical lines
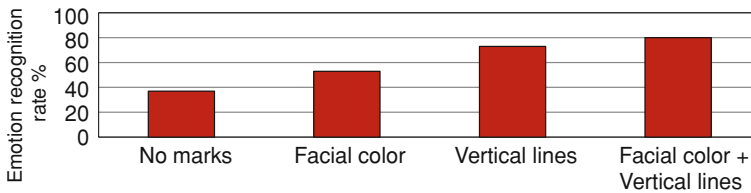
Fig. 13 Difference of emotion recognition rate for "Fear" depends on the "manga" marks

Furthermore, with the combination of blue facial color and "Vertical lines" emotion recognition rate increased to 80 %. This suggests the effectiveness of combination of manga marks for expressing understandable facial expressions.

4 Conclusions and Future Work

In order to improve the facial expression ability of KOBIAN-R, our goal is to develop a robot whose facial expression can adapt to different cultural backgrounds. As a first step, we focused on Japanese culture and found effectiveness of using Japanese comic ("manga") marks in making the expression clearer. In order to display "manga" marks on the curved surface on the face cover on the robotic head, we developed the full color LED matrix display for expressing red "Cross popping veins" mark for "Anger" and blue "Tear" mark for "Sadness." In addition, we developed a mechanisms consisting in a sheet with black lines for expressing black "Vertical lines" for "Fear" and "Wrinkle" for "Disgust." The result of experimental evaluation shows that the new robotic head for KOBIAN-RII had over 80 % emotion recognition rates for each of the six basic emotions and suggested the positive effect of using manga marks on the robotic head for expressing emotions clearly for Japanese. In the future, we would like to evaluate the effect of cultural background or age.

References

1. Mehrabian, A.: Silent Message. Wadsworth, Belmont (1991)
2. Kędzierski, J., et al.: EMYS—emotive head of a social robot. Int. J. Soc. Robot. **5**(2), 237–249 (2013)
3. Oh, J. et al.: Design of android type humanoid robot Albert HUBO. In: Proceedings of the 2006 IEEE/RSJ International Conference on Intelligent Robots and Systems, pp. 1428–1433 (2006)
4. Ishiguro, H., et al.: Building artificial humans to understand humans. J. Artif. Organs **10**(3), 133–142 (2007)
5. Kishi, T. et al.: Development of expressive robotic head for bipedal humanoid robot. In: Proceedings of the 2012 IEEE/RSJ International Conference on Intelligent Robots and Systems, pp. 4584–4589 (2012)
6. Ekman, P., et al.: Constants across cultures in the face and emotion. J. Pers. Soc. Psychol. **17**(2), 124–129 (1971)
7. Shimoda, K., et al.: The intercultural recognition of emotional expressions by three national racial groups: english, italian and japanese. EJSP **8**, 169–179 (1978)
8. Koda, T.: Cross-cultural evaluations of avatar facial expressions. In: Workshop on Enculturating Conversational Interfaces IUI (2008)
9. Masaki, Y., et al.: Are the windows to the soul the same in the East and West? Cultural differences in using the eyes and mouth as cues to recognize emotions in Japan and the US. J. Exp. Soc. Psychol. **43**(2), 303–311 (2007)
10. Trovato, G. et al.: A cross-cultural study on generation of culture dependent facial expressions of humanoid social robot. In: Proceedings of the 4th International Conference on Social Robotics, pp. 35–44 (2012)

Terrain-Adaptive Biped Walking Control Using Three-Point Contact Foot Mechanism Detectable Ground Surface

Kenji Hashimoto, Hyun-jing Kang, Hiromitsu Motohashi, Hun-ok Lim and Atsuo Takanishi

Abstract In this study we describe a terrain-adaptive biped walking control using a new biped foot mechanism with the capability of detecting ground surface. The foot system consists of three spikes each of which has an optical sensor to detect ground height. A robot modifies a foot-landing motion along the vertical axis and about pitch and roll axes according to sensor values, and this enables the robot to walk on unknown uneven terrain. Verification of the proposed control was conducted through experiments with a human-sized humanoid robot WABIAN-2R.

Keywords Humanoid robot · Foot mechanism · Uneven terrain · Ground adaptation

1 Introduction

The final goal of this research is to develop a biped walking technology to realize a stable walk on uneven terrain in real environment. One solution when walking on unexpected ground surface is to detect obstacles and ground surface conditions by

K. Hashimoto (✉)
Research Institute for Science and Engineering, Waseda University, Tokyo, Japan
e-mail: contact@takanishi.mech.waseda.ac.jp

H. Kang · H. Motohashi
Graduate School of Science and Engineering, Waseda University, Tokyo, Japan

H. Lim
Faculty of Engineering, Kanagawa University, Kanagawa, Japan

H. Lim · A. Takanishi
Humanoid Robotics Institute (HRI), Waseda University, Tokyo, Japan

A. Takanishi
Faculty of Science and Engineering, Waseda University, Tokyo, Japan

using external sensors such as a laser range finder, stereo cameras and so on [1, 2]. Most vision sensors, however, have some measurement errors. Therefore, a biped robot equipped with external sensors should have an ability to walk on unknown uneven terrain with 20 mm height, considering the distance from the ground surface to the position where sensors are mounted.

There are many previous works on biped stabilization controls on uneven terrain [3–5]. Most of them assume that a biped robot can maintain large support polygons on uneven terrain. Small unevenness and irregularities in outdoor surfaces, however, make it difficult for biped robots with rigid, flat soles to maintain large support polygons, meaning that such robots easily lose their balance even when they use stabilization controls. To deal with these problems, we have developed a new biped foot system, WS-1R (Waseda Shoes—No. 1 Refined) [5], which can maintain large support polygons on uneven terrain by only a hardware mechanism. Its weight is 2.0 kg, and it is heavier than usual rigid, flat soles. Therefore, it will be better for a biped robot to deal with uneven terrain from both sides of hardware mechanisms and controls.

In this approach, a biped foot system, WAF-2 (Waseda Anthropomorphic Foot—No. 2) [6], has been proposed, which can absorb foot-landing impact and detect ground height. It, however, assumes that a robot maintains large support polygons with four spikes at each corner of the foot. It's possible to maintain four-point contact on even ground but it's almost impossible to maintain it on uneven terrain.

In this paper, we propose a terrain-adaptive walking control using three-point contact foot mechanism which can detect ground unevenness. A robot modifies a foot-landing motion along the vertical axis and about pitch and roll axes according to sensor values, and this enables the robot to walk on unknown uneven terrain. This paper is organized as follows. Section 2 describes the details of the foot system design, and Sect. 3 describes the terrain-adaptive control by using the foot system developed. In Sect. 4, experimental results are shown. Section 5 provides conclusions and future work.

2 Three-Point Contact Foot Mechanism Detectable Ground Surface

It is difficult to maintain a large support polygon on uneven terrain with rigid, flat soles due to the lack of plane contact. In this research, we deal with ground undulation by adopting three-point contact with the ground. While walking on uneven ground, it is difficult to maintain four-point contact, and support polygons are not determined uniquely in some cases. The number of contact point should be three to determine support polygons uniquely. The proposed biped foot system has three spikes at each corner of the foot, and it maintains three-point contact on both even and uneven terrain.

The biped foot system developed is shown in Fig. 1. Its size is almost the same as that of the rigid, flat feet of WABIAN-2R (Waseda Bipedal Humanoid—No. 2
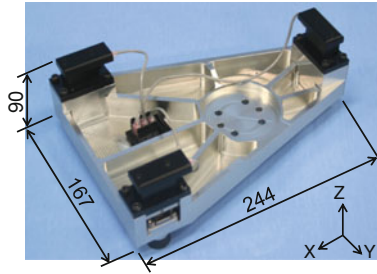
Fig. 1 New biped foot mechanism with three spikes each of which has an optical distance sensor unit to detect ground height. The foot weighs 1.3 kg
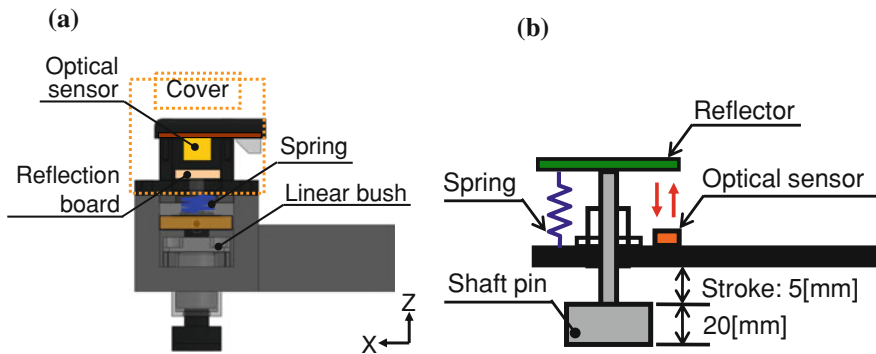
Fig. 2 Mechanical structure of foot spike. **a** Actual foot mechanism structure. **b** Schematic view

Refined) [7], and it weighs 1.3 kg. The thickness of the operating spike is 20 mm as shown in Fig. 2, so it can avoid convex surface up to 20 mm and adapt to ground undulation. We use optical sensors to detect ground height because it is lighter and smaller than linear encoders. The optical distance sensor unit is covered because optical sensor is weak at external light. The spikes at three edges contact the ground earlier than the foot's base part. Then, the distance between the ground surface and the base part can be detected by measuring the displacement of the spike with optical sensors.

3 Terrain-Adaptive Biped Walking Control Using Three-Point Contact Foot Mechanism

In this method, a support polygon can be formed by three-point contact on uneven terrain. A robot modifies a foot-landing motion along the vertical axis and about pitch and roll axes according to sensor values, and this enables a biped robot to

Axis	Double Support Phase	Swing phase		Double Support Phase	Stance phase		Double Support Phase
		first half	last half		first half	last falf	
z	Preset Pattern	Preset Pattern	Control phase	Holding phase	Returning phase	Preset Pattern	Preset Pattern
Roll	Holding phase	Returning phase	Control phase	Holding phase	Holding phase	Holding phase	Holding phase
Pitch	Holding phase	Returning phase	Control phase	Holding phase	Holding phase	Holding phase	Holding phase

Fig. 3 Timing chart of terrain-adaptive biped walking control

walk on unknown uneven terrain. The proposed control consists of the following three key points:

(i) Landing pattern modification along the vertical axis
(ii) Landing pattern modification about pitch and roll axes
(iii) Returning to a preset walking pattern at each step

Figure 3 shows the timing chart of the proposed terrain-adaptive control during one walking cycle. One walking cycle is divided into seven parts, and the foot position and orientation are controlled during each phase as follows:

- Control phase: a foot-landing pattern is modified according to sensor values of the 3-point contact foot mechanism.
- Holding phase: modified position and orientation at the last step are held.
- Returning phase: foot position and orientation return to a preset walking pattern.

In the last half of a swing phase, a foot-landing pattern is modified to follow uneven terrain. The modified position and orientation are held during the stance phase. The foot position along the vertical axis returns to the preset pattern in the first half of a stance phase, and the foot orientation about pitch and roll axes returns in the first half of a swing phase. We also use a virtual compliance control to reduce a foot-landing impact [8].

3.1 Landing Pattern Modification Along the Vertical Axis

A foot-landing motion along the vertical axis is modified according to sensor values. In case of the sensor stroke is Δl, while the sensors are shortened by Δl, terrain height is detected by comparing an actual and a theoretical sensor length. A theoretical sensor length $\Delta x_{th}(t)$ for a biped robot walking on even terrain is described as follows:

(i)

$$\Delta l + \bar{z}_{leg}(t) < z_{waist}(t)$$

$$\Delta x_{th}(t) = 0 \tag{1}$$

(ii)

$$\Delta l + \bar{z}_{leg}(t) \geq z_{waist}(t)$$

$$\Delta x_{th}(t) = \Delta l + \bar{z}_{leg}(t) - z_{waist}(t) \tag{2}$$

where $\bar{z}_{leg}(t)$ is the height of the foot in the reference walking pattern, and $z_{waist}(t)$ the height of the robot's waist. Variables are also depicted in Fig. 4.

Foot movement along the vertical axis is modified by feeding back landing height error $e(t)$ at each control cycle. Foot height displacement along the vertical axis, $H(t)$, is calculated as follows:

$$e(t) = \Delta x_{th}(t) - \Delta x_{ac}(t) \tag{3}$$

$$H(t) = H(t - \Delta t) - K_e \cdot e(t - \Delta t) \tag{4}$$

where $e(t)$ is landing height error, $\Delta x_{th}(t)$ theoretical sensor length, $\Delta x_{ac}(t)$ actual sensor length, Δt the control cycle of 1 ms, H(t) foot height displacement along the vertical axis, and K_e gain.

3.2 Landing Pattern Modification About Pitch and Roll Axes

A foot motion about pitch and roll axes is modified according to two sensors' values, and a foot orientation is modified around the landing point of the spike. The modification angle $\theta(t)$ is calculated as follows:

$$\theta(t) = \sin^{-1}\left\{ \Delta x_{ac}(t) \middle/ \sqrt{\Delta x_{ac}(t)^2 + L^2} \right\} \tag{5}$$

where $\theta(t)$ is modification angle, and L the distance between two sensors. Variables are also shown in Fig. 5.

Sensor values are obtained at every 1 ms, and the average of displacement amount is calculated at every 10 ms to reduce noise effects. The modification amounts are added to a preset walking pattern.
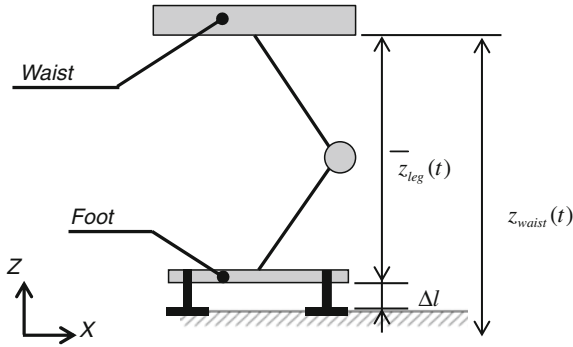
Fig. 4 Definition of variables
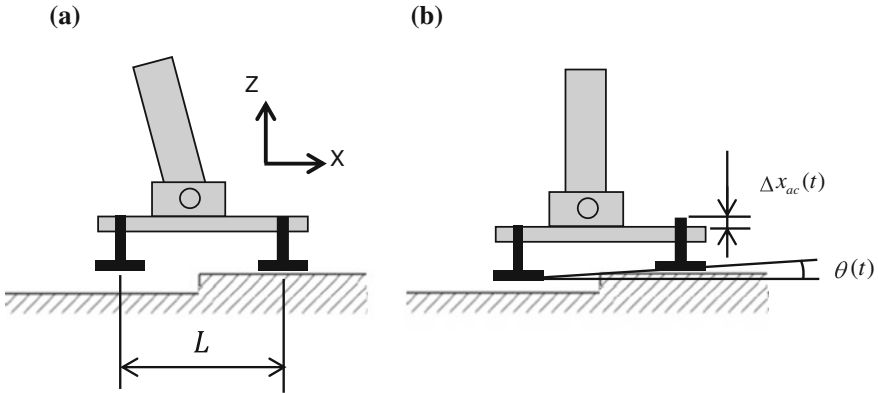
Fig. 5 Modification about pitch and roll axes. **a** Before contacting the ground. **b** Just after contacting the ground

3.3 Returning to a Preset Walking Pattern at Each Step

Modification displacement in the vertical direction at the end of a swing phase is maintained during the double support phase, and a foot movement along the vertical axis returns to a preset walking pattern during the first half of a stance phase. Roll and pitch displacements obtained at the end of a swing phase are held during the stance phase, and the roll and pitch foot movements return to a preset walking pattern in the first half of the swing phase. A quintic polynomial is used to generate returning motion because we can arbitrarily set position, velocity and acceleration values of starting and end points.

(a) **(b)**
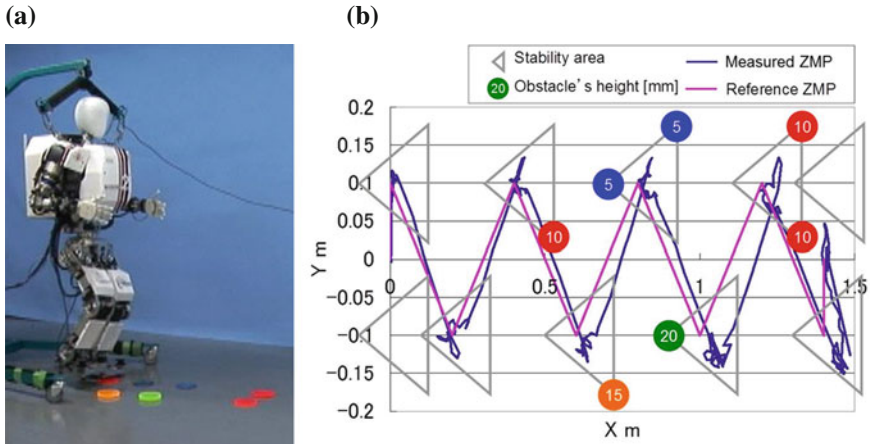
Fig. 6 Walking experiment on uneven terrain with random obstacles. The maximum height of the obstacles is 20 mm. Its walking cycle is 1.0 s/step and its step length is 200 mm/step. **a** Experimental photo. **b** ZMP trajectories

(a) **(b)**
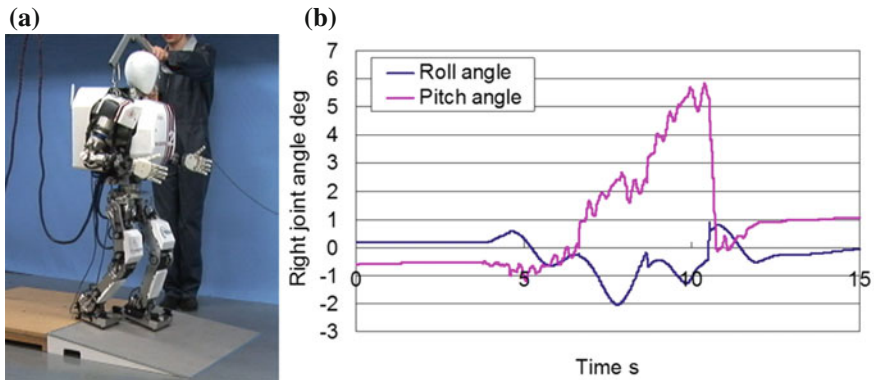
Fig. 7 Walking experiment on 7.0° slope. Its walking cycle is 1.0 s/step and its step length is 200 mm/step. **a** Experimental photo. **b** Modification angle of right foot

4 Evaluation Experiments

We conducted evaluation experiments to verify the effectiveness of the proposed terrain-adaptive control by using a biped humanoid robot WABIAN-2R.

First we randomly placed acrylic boards whose maximum thickness was 20 mm as shown in Fig. 6a. WABIAN-2R walked stably forward on such uneven terrain by using the control we developed. Figure 6b shows ZMP trajectories, and we can find that they are inside support polygons during walking.

The terrain-adaptive control also can be applied to an inclined surface. We performed a walking experiment on an inclined surface of 7.0° as shown in Fig. 7a. The walking cycle was 1.0 s/step, and the step length was 200 mm/step. The robot started to land on the slope from the 3rd step. The robot finished climbing down the slope at the 7th and 8th step, and a stable walk on inclined surface was realized. Figure 7b shows modified foot angles, and about 7.0° modification is confirmed about the pitch axis.

5 Conclusions

We aimed a stable biped walking on unknown uneven terrain and developed a terrain-adaptive control using a new biped foot mechanism with three spikes each of which has an optical distance sensor unit to detect ground height. A robot modifies a foot-landing motion along the vertical axis and about pitch and roll axes according to sensor values, and this enables a biped robot to walk on uneven terrain.

Through walking experiments, we confirmed the effectiveness of the proposed method that maintained a support polygon on uneven terrain with bump and slope, and WABIAN-2R succeeded in walking on uneven terrain with the mixture of bump up to 20 mm. In this study we generated a walking pattern offline, but integrating walking pattern generation is our future work to change ZMP trajectories during walking on uneven terrain.

References

1. Yagi, M., Lumelsky, V.J.: Biped robot locomotion in scenes with unknown obstacles. In Proceeding of the 1999 IEEE International Conference on Robotics and Automation, pp. 375–380 (1999)
2. Michel, P., Chestnutt, J., Kagami, S., Nishiwaki, K., Kuffner, J., Kanade, T.: GPU-accelerated real-time 3D tracking for humanoid locomotion and stair climbing. In: Proceedings of the 2007 IEEE/RSJ International Conference on Intelligent Robots and Systems, pp. 463–469 (2007)
3. Hirai, K., Hirose, M., Haikawa, Y., Takenaka, T.: The development of Honda humanoid robot. In: Proceedings of the 1998 IEEE International Conference on Robotics and Automation, pp. 1321–1326 (1998)

4. Park, J.H., Chung, H.: ZMP Compensation by on-line trajectory generation for biped robots. In: Proceedings of the 1999 IEEE System, Man and Cybernetics, pp. 960–965 (1999)
5. Hashimoto, K., Sugahara, Y., Lim, H.O., Takanishi, A.: Biped landing pattern modification method and walking experiments in outdoor environment. J. Robot. Mechatron. **20**(5), 775–784 (2008)
6. Yamaguchi, J., Takanishi, A., Kato, I.: Experimental development of a foot mechanism with shock absorbing material for acquisition of landing surface position information and stabilization of dynamic biped walking. In: Proceedings of the IEEE International Conference on Robotics and Automation, pp. 2892–2899 (1995)
7. Ogura, Y., Shimomura, K., Kondo, H., Morishima, A., Okubo, T., Momoki, S., Lim, H.O., Takanishi, A.: Human-like walking with knee stretched, heel-contact and toe-off motion by a humanoid robot. In: Proceedings of the 2006 IEEE/RSJ International Conference on Intelligent Robots and Systems, pp. 2497–2502 (2006)
8. Sugahara, Y., Hosobata, T., Mikuriya, Y., Lim, H.O., Takanishi, A.: Realization of stable dynamic walking by a parallel bipedal locomotor on uneven terrain using a virtual compliance control. In: Proceedings of the 2003 IEEE/RSJ International Conference on Intelligent Robots and Systems, pp. 595–600 (2003)

Biped Walking on Irregular Terrain Using Motion Primitives

Mirko Raković, Branislav Borovac, Milutin Nikolić and Srđan Savić

Abstract Effective and efficient motion of humanoid robots is a prerequisite for their activity in the unstructured environment. It is of great importance to enable the walk on uneven ground surface. This work presents a method for the synthesis and realization of the online modifiable robot walk that is adjustable to the partially unknown configuration of ground surface. Walk is composed of tied simple movements—primitives which are parameterized with established relationship with overall motion parameters. Proposed approach was tested by simulation and it was demonstrated that it is possible to generate a online modifiable dynamically balanced walk. For such walk is tested the ability to adapt to uneven configuration to uneven terrain.

Keywords Biped locomotion · Motion primitives · Irregular terrain

1 Introduction

Usual example of dynamic and unstructured environment is the living and working environment of humans, but it also can be scene of catastrophic events with ruins and debris. While walking is such environments we do not have precise

M. Raković (✉) · B. Borovac · M. Nikolić · S. Savić
Faculty of Technical Sciences, Trg D. Obradovica 6, 21000 Novi Sad, Serbia
e-mail: rakovicm@uns.ac.rs

B. Borovac
e-mail: borovac@uns.ac.rs

M. Nikolić
e-mail: milutinn@uns.ac.rs

S. Savić
e-mail: savics@uns.ac.rs

information about the configuration of the terrain and we can't be confident how the surrounding will act. These are the reasons why the robots have to have the ability to adapt and to online modify the walk for successful activity in our environment.

Neurological studies of human walk Breniere and Bril [1], Keenan and Evans [2] have shown that certain modes of legs motion become the patterns, which are during execution modified to adapt to the instantaneous situation. We propose same concept. Straight forward walking on flat surface should be synthesized and used as basic motion pattern which can be modified and adapted to the terrain conditions, even during execution, to suit new requirements.

This is why we proposed that biped basic walking pattern is composed of simple parameterized movements—primitives. Overall walk parameters i.e. speed, step length, height of the leg during the swing phase, and the motion direction should be able to change primitive execution even if initiated during motion. It is achieved by introducing relationship between overall parameters and parameters of the primitives. However, any change of primitive execution should not endanger dynamic balance which must be permanently ensured.

2 Existing Approaches and Motion Primitives

The first approach to the synthesis of dynamically balanced gait is semi-inverse method introduced by Vukobratović and Juričić [3]. Methods that have appeared afterwards represent just modifications and upgrading.

With the majority of modern humanoid robots the gait is generated by prescribing the desired position of the feet on the ground Morisawa et al. [4], Perrin et al. [5] along the path by which the robot should walk, while additionally ensuring its dynamic balance. In order to preserve dynamic balance of the system it is necessary to assign a reference trajectory for the zero-moment point (ZMP) and the motion of the rest of the system is calculated to satisfy it.

Besides, the application of primitives for the generation of movements is not an entirely new approach, but different authors define primitives in different ways. In Schaal [6], the author introduced the notion of Dynamic Movement Primitives (DMP), defined as the desired state of the kinematics of the extremities, obtained by prescribing in advance the values of the angles, angular velocities and angular accelerations for each robot joint. In Hauser et al. [7] there is a library in which each primitive represents one step. Based on the preset requirements and current state of the robot, a new step which corresponds to the requirements is selected from the library. In Zhang et al. [8], the leg motion primitives are obtained by segmenting and modifying the movements recorded from man.
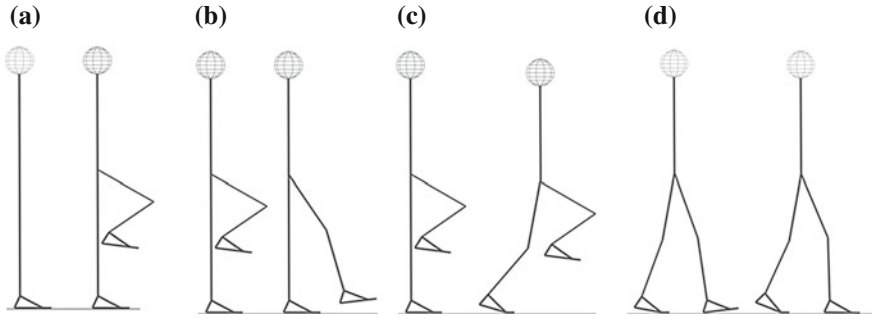
Fig. 1 Stick diagrams of the primitives: **a** leg bending, **b** leg stretching, **c** inclining the robot forward, **d** making the foot surface contact

2.1 Notion of Motion Primitives

The approach presented here differs in several important points from those mentioned above. We define primitive as a simple movement which is realized by simultaneous and synchronized motion of a number of joints. Illustrative examples are presented in Fig. 1. The complex motion (i.e. walking) is composed by combining and tying different primitives, without having a reference trajectory that was prescribed in advance.

Each primitive is parameterized, so that a form of the realization is adjusted by choosing the appropriate parameters, even during execution. There are no limitations in the defining of new primitives, either in the number of parameters or in the number of joints that will be activated. Every primitive can be considered as a movement to be realized on the basis of the task assigned and the current situation. To define execution trajectory, we propose to associate coordinate frame to a particular link of the kinematic chain performing the primitive and then to assign the target positions to which is necessary to bring it by the realization of the selected primitive. Another important point is smooth continuation of tied primitives.

For the gait synthesis, we introduced five primitives realized by the legs, along with one realized by the trunk and one by the arms. The primitives that are realized by the legs in the single-support phase are: bending of the leg in the swing phase, stretching of the leg in the swing phase, and inclining the robot forward. The primitives realized during the double-support phase are: making the foot surface contact after the heel strike, and transferring the body weight onto the subsequent supporting leg. The primitives that are realized by the trunk and arms are: maintenance of the trunk upright posture, and arms swinging during the walk.

The trunk is used to keep the upright posture and at the same time to maintain dynamic balance. However, the maintenance of dynamic balance is of higher priority, and task assigned to trunk at each time instant depend on ZMP position whose desired position is predefined for each primitive. If actual ZMP distance from its desired position exceeds threshold, it has been considered dynamic
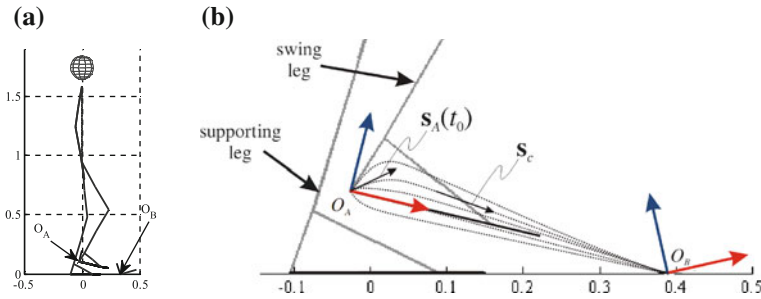
Fig. 2 Stick diagram of the robot for leg stretching: **a** robot posture with the preset target position O_B to which the coordinate frame on the heel tip O_A should be brought **b** possible paths of O_A for different initial velocities

balance is jeopardized, and the trunk is used to return the ZMP back, to prevent the system from falling down. When dynamic balance is not jeopardized, it is possible to tackle the task of correcting deviations of the trunk from its upright position.

2.2 Primitives Smooth Tying

Let us assume that the locomotion mechanism moves and that the primitive realized by the leg in swing phase has just been completed, so that at the beginning of execution of the next primitive the leg is not at rest. While walking, the robot finds itself in such a situation when, in the single-support phase (Fig. 2a), the leg bending is ended, and the realization of leg stretching is about to start. The vector $\mathbf{r}_A$ represents the instantaneous position of the coordinate frame O_A (in Fig. 2a) it is the heel tip, while the vector $\mathbf{r}_B$ represents the target position (defined by the coordinate frame O_B) to which O_A is to be brought. In view of the fact that the swing leg in the given moment is moving, it is necessary to determine first the desired velocity at point A. i.e. $\mathbf{s}_A = [\mathbf{v}_A \quad \boldsymbol{\omega}_A]^T$ of the coordinate frame O_A to ensure that the leg stretching follows smoothly after the just completed leg bending.

The trajectory (as well as the velocity $\mathbf{s}_A$ in each moment) by which the foot is to move from the starting position O_A to the target position O_B depends on the intensity and direction of the velocity $\mathbf{s}_A^0$ at the starting moment t_{p0}. Figure 2b shows a set of possible paths from O_A to O_B.

The desired velocity $\mathbf{s}_A$ is calculated as:

$$\mathbf{s}_A(t_i) = (1 - b(t_i)) \cdot \mathbf{s}_A^0 + b(t_i) \cdot [\, v_{int} \cdot \mathbf{p}_e^{ort} \quad \omega_{int} \cdot \mathbf{o}_e^{ort} \,]^T$$

where $\mathbf{p}_e^{ort}$ and $\mathbf{o}_e^{ort}$ represent the orts of the $\mathbf{p}_e = \mathbf{p}_B - \mathbf{p}_A$ and $\mathbf{o}_e = \mathbf{o}_B - \mathbf{o}_A$ i.e. the position and orientation between $\mathbf{r}_A$ and $\mathbf{r}_B$. The coefficient b changes during the prescribed time interval from 0 to 1. This ensures smooth tying of primitives by
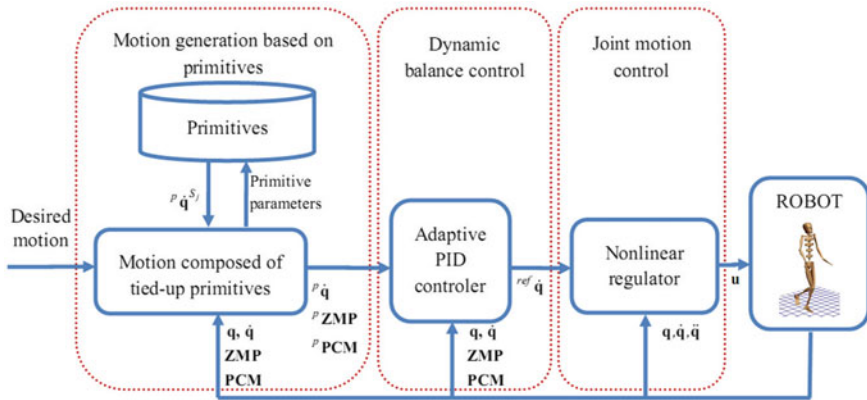
Fig. 3 Block diagram of the robot control for realization of the motion synthesized

a gradual change of the velocity $\mathbf{s}_A(t)$ from the initial value $\mathbf{s}_A^0$ to the value that will lead the frame O_A to the target position.

Intensities of the linear and angular velocities v_{int} and ω_{int} are dependent on the cruising speeds v_c and ω_c, which are set by the primitive parameters. To ensure the leg gradual stopping the intensities of the velocities v_{int} and ω_{int} are to be reduced when O_A comes close to the target. Having thus determined $\mathbf{s}_A(t_i)$, and using inverse kinematics, the desired joint angular velocities can be calculated.

2.3 Joints Motion Control and Preservation of Dynamic Balance

For control synthesis we propose cascade control loop as shown in Fig. 3. The inputs to the first block are parameters of the desired overall motion. In this block, the primitives are combined by calling the functions for each primitive used. To check the fulfillment of the conditions for starting and ending the realization of each primitive the inputs to this block are also the feedback values of the robot instantaneous state (angles and angular velocities, along with the current positions of ZMP and vertical projection of the mass centre-PCM). The outputs from the first block are the desired values of joint angular velocities $^{des}\dot{\mathbf{q}}(t_i)$ as well as the desired positions of ZMP and PCM. The role of the second block is to ensure the maintenance of dynamic balance which is performed by corrections of the desired angular velocities $^{des}\dot{\mathbf{q}}(t_i)$.

Corrections are determined on the basis of the desired and the current values of ZMP and PCM, as well as of the current values of the joint angles and angular velocities $\mathbf{q}$ and $\dot{\mathbf{q}}$. The corrections of the angular velocities depend on the deviations of ZMP and PCM from the desired values that are generated online with

respect to current position of feet. In Vukobratović et al. [9] was shown that the movements of the ankle joint in one direction and of the hip in the other direction ensured a very efficient control of the positions of PCM and ZMP. An different approach can be seen at Peuker et al. [10].

After determining the reference angular joint velocities $^{ref}\dot{\mathbf{q}}(t_i)$ the voltages of the motors have to be calculated. For realization of this motion we used nonlinear regulator which is a combination of feedback linearization, sliding mode control and disturbance estimator [11].

3 Online Modifiability and Adaptability of Walk

As a overall walk parameters we introduced: walk speed W_S, height to which the foot is lifted during the swing phase F_H, step length S_L, and walking direction W_D. All these parameters can be changed within an predefined range, but the basic walk with the parameters: $W_S = 1$, $F_H = 1$, $S_L = 1$, $W_D = 0$ should be synthesized first.

The gait speed (W_S) has a direct influence on the speed of execution of each primitive, F_H influences the height to which the foot is to be lifted during leg bending, the step length (S_L) influences the parameters for leg stretching. The desired gait direction W_D, (the turn angle with respect to the x axis of the fixed coordinate frame) influences also the parameters of the primitive for leg stretching.

The synthesis of one half-step is performed in four phases involving the execution of the corresponding primitives that are realized by the legs. Also, for each phase is given the desired goal position of the PCM. Simultaneously with the primitives that are realized by the legs, irrespective of the current phase, the primitive for keeping the trunk in an upright position and the primitive for arms swinging are constantly executed during the walk.

Figure 4 shows the stick diagrams of the robot, disposition of the feet, and positions of the ZMP and PCM during the realization of the basic motion by the previously described procedure. The trajectories of ZMP and PCM were all the time inside the support area, i.e. the robot's dynamic balance was constantly preserved.

Figure 5 presents the case when the robot is online adjusting the pace, direction of the walk and height of the foot during the swing phase in order to pass between the tables and step over the bar on the ground. It can be seen that walk combined from primitives is online modified by changing the overall parameters of walk.

In Fig. 6. is shown the walk of a robot over the irregular terrain. The terrain is uneven with different heights of the ground surface. The starting and ending conditions for primitives execution made possible for robot to adapt to such a terrain. At the end of first half-step ground is 2 cm above the initial ground level, at the end of second half-step it is 3 cm above the ground level, and finally, during
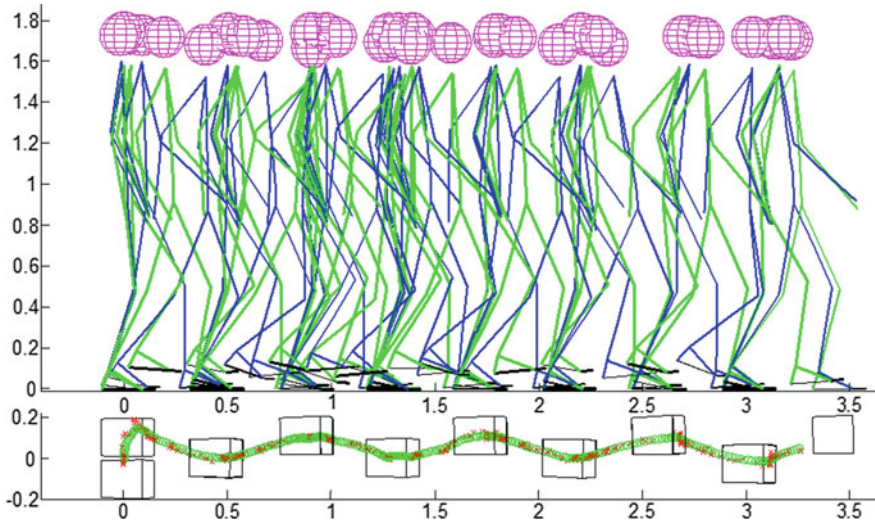
Fig. 4 Stick diagram of the robot, positions of the feet, and the trajectories of ZMP and PCM for the basic walk
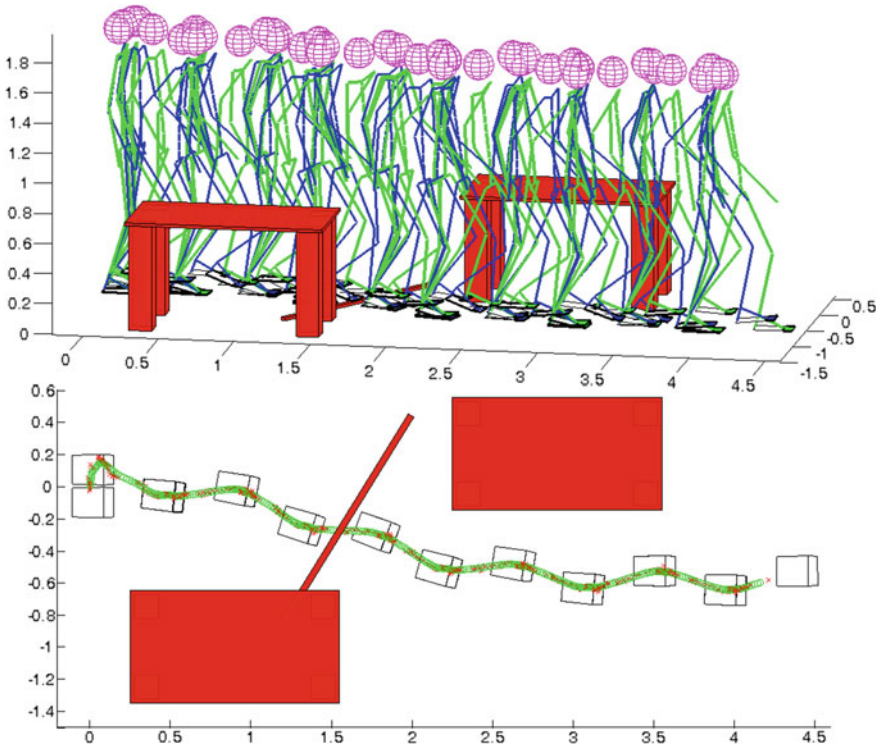
Fig. 5 Example of on-line change of the walking direction, foot height during the swing phase and speed to pass around the obstacles
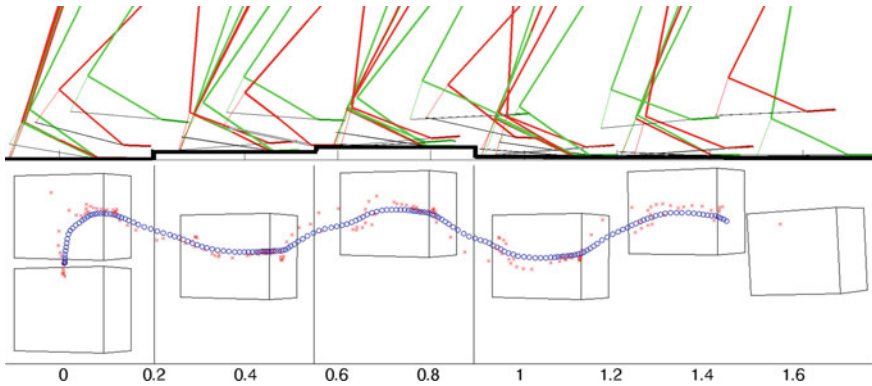
Fig. 6 Stick diagram of the robots' legs, positions of the feet, and the trajectories of ZMP (*crosses*) and PCM (*circles*) for t he case when robot is walking on uneven terrain with unknown terrain configuration

third step it is 1 cm above the ground level. The robot performed walk without knowing in advance the configuration of the terrain.

4 Conclusion

In this work we proposed use of primitive based bipedal walk for motion in unstructured and irregular environment. The walk was composed of tied primitives without exact reference to be followed. Motion was generated online and modified according to current situation. The preservation of dynamic balance was also secured by monitoring the deviation of the actual ZMP from its desired position.

The main achievement of this paper is that has been shown that walk combined from primitives can easily be performed and modified online by simply changing parameters of the overall motion (turn left or right, step over obstacle, …). This was achieved by establishing the relationship between the primitive parameters and the parameters of the overall motion which can be estimated, for example, from visual information (robot can see obstacle in front of it and estimate its size and position). The presented approach is also robust and adaptable to unknown terrain configuration because primitive will be executed only if its execution is feasible i.e. if conditions for primitive execution exist. This enables versatile and robust walk.

References

1. Breniere, Y., Bril, B.: Development of postural control of gravity forces in children during the first 5 years of walking. Exp. Brain Res. **121**(3), 255–262 (1998)
2. Keenan, T., Evans, S.: An introduction to child development. SAGE Publications Limited, Los Angeles (2009)
3. Vukobratovic, M., Juricic, D.: Mathematical modeling of a bipedal walking system. In: Proceedings ASME Winter Annual Meeting, pp 26–30 (1972)
4. Morisawa, M., Harada, K., Kajita, S., Nakaoka, S., Fujiwara, K., Kanehiro, F., Kaneko, K., Hirukawa, H.: Experimentation of humanoid walking allowing immediate modification of foot place based on analytical solution. In: IEEE International Conference on Robotics and Automation, 2007, pp 3989–3994 (1972)
5. Perrin, N., Stasse, O., Lamiraux, F., Kim, Y.J., Manocha, D.: Realtime footstep planning for humanoid robots among 3d obstacles using a hybrid bounding box. In: IEEE International Conference on Robotics and Automation (ICRA), 2012. IEEE, pp. 977–982 (2012)
6. Schaal, S.: Dynamic movement primitives-a framework for motor control in humans and humanoid robotics. In: Adaptive Motion of Animals and Machines, pp. 261–280. Springer, Tokyo (2006)
7. Hauser, K., Bretl, T., Harada, K., Latombe, J.-C.: Using motion primitives in probabilistic sample-based planning for humanoid robots. In: Algorithmic Foundation of Robotics VII, pp. 507–522. Springer, Heidelberg (2008)
8. Zhang, L., Bi, S., Liu, D.: Dynamic leg motion generation of humanoid robot based on human motion capture. In: Intelligent Robotics and Applications, pp. 83–92. Springer, Heidelberg (2008)
9. Vukobratović, M., Herr, H., Borovac, B., Raković, M., Popovic, M., Hoffmann, A., Jovanović, M., Potkonjak, V.: Biological principles of control selection for a humanoid robot's dynamic balance preservation. Int. J. Humanoid Rob. **05**(04), 639–678 (2008)
10. Peuker, F., Maufroy, C., Seyfarth, A.: Leg-adjustment strategies for stable running in three dimensions. Bioinspirat. Biomimetics 7(3) (2012)
11. Slotine, J.-J.E., Li, W. et al.: Applied nonlinear control, vol. 1, 1st edn. Prentice Hall, New Jersey (1991)

Experimental Investigation of Human Exoskeleton Model

V. G. Gradetsky, I. L. Ermolov, M. M. Knyazkov, E. A. Semyonov and A. N. Sukhanov

Abstract This paper describes a kinematic model of a human arm exoskeleton for which direct and inverse kinematics are solved. The results of experimental research are also delivered.

1 Introduction

Contemporary studies in the field of the exoskeleton research and development allow us to estimate perspectives of using such devices in human activities: medical research and treatment, sports, space research, virtual reality applications etc. The great interest is represented by the studies describing control techniques for such robotic devices designed for different human limbs and also studies describing the interaction between human-operator and robotic device. The design of an exoskeleton often appears to be a multilink system which provides unloading power during its operation [1] or even additional force to operator [2]. The additionally controlled force is used as a feedback in virtual environment applications [3, 4] and in research on force-torque loading from exoskeleton components to operator [5]. Such devices are often used in medical treatment after limbs

V. G. Gradetsky · M. M. Knyazkov · E. A. Semyonov · A. N. Sukhanov
Institute for Problems of Mechanics, Russian Academy of Sciences,
Vernadskogo 101, block 1, Moscow 119526, Russia
e-mail: gradet@ipmnet.ru

I. L. Ermolov (✉)
Robotics and Mechatronics Department, MSTU "STANKIN",
Vadkovsky per. 3A, Moscow 127994, Russia
e-mail: ermolov@stankin.ru

traumas or for telemechanics. Along with mathematical modeling of multilink systems selection of correct control system is an important part. The type of the control system depends on the exoskeleton's technical parameters, operational modes and the field of its application. The most prospective type of the interface between an operator and an exoskeleton is electromiografical (EMG) control technique [6–10]. This approach includes reading data from operator's muscles by using EMG-sensors and applying Hill-model which predicts muscle force as a function of human muscle's neuroactivity level. Researchers often use genetic algorithms to control an exoskeleton device and optimize its control model.

In telemechanics exoskeletons are used in master-slave control of different manipulators which are situated far away from an operator. These devices are essential for microsurgery, space researches and military forces.

Kinematic research is essential for developing exoskeletons. Our paper is devoted to mathematical model of the exoskeleton arm.

2 Mathematical Model of the Exoskeleton Arm

One of the basic tasks for developing control system for a such multibody device as an exoskeleton is estimation of its position error due to links and joints tolerances. These errors depend on linear and angular dimensions' errors, type of the actuator, type of motion system, materials and sensors, integrated in the construction. General coordinates input error is caused by control system and causes output shaft of the actuator:

$$\Delta q_j = \frac{\Delta \varphi_j}{U_j},$$ (1)

where $\Delta \varphi_j$—motor shaft rotation error, U_j—gear ratio of the actuator.

The object of our research was the physical model of the exoskeleton arm designed in the Robotics and Mechatronics laboratory of the Institute for Problems of Mechanics of the Russian Academy of Sciences [11]. It is a multibody structure with 4 degrees of freedom. The kinematics of the device is presented on Fig. 1.

The virtual model of the designed exoskeleton is shown on Fig. 2.

In order to describe mathematical model of the designed exoskeleton it is necessary to solve the forward and inverse kinematics tasks. The forward kinematics means finding the rotation matrix and the position vector of the multibody system as functions of general coordinates [12, 13]. To find the rotation matrix and the position vector we used 4×4 DH matrixes technique. Here is the algorithm of local coordinate's definition (Fig. 1b) for further combination of $(i-1)$-coordinate system $O_{i-1}X_{i-1}Y_{i-1}Z_{i-1}$ with i-coordinate system $O_iX_iY_iZ_i$:

Rotation around Z_{i-1}-axis with q_i-angle (X_{i-1}- and X_i-axes should be parallel);
Moving along Z_{i-1}-axis with d_i (X_{i-1}- and X_i-axis should coincide);
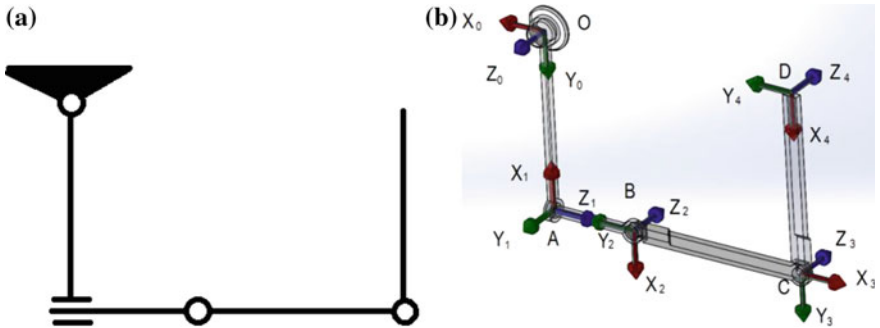
Fig. 1 The kinematics of the exoskeleton arm (**a** the kinematic structure, **b** local coordinates definition)
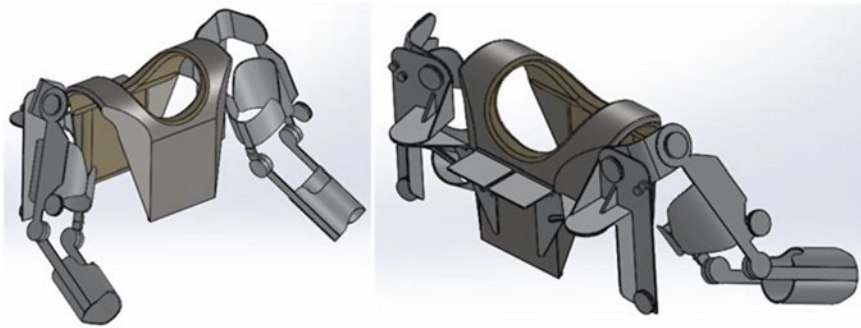
Fig. 2 Designed exoskeleton for human arms

Moving along X_{i-1}-axis with a_i (points O_{i-1} and O_i should coincide);
Rotation around X_{i-1}-axis with α_i-angle ($O_iX_iY_iZ_i$ and $O_{i-1}X_{i-1}Y_{i-1}Z_{i-1}$ coordinate systems should coincide).

Here is the transition matrix 4×4 for combination ($i-1$)-coordinate system with i-coordinate system:

$$
A_{i,i-1} = \begin{vmatrix}
\cos(q_i) & -\cos(\alpha_i)\sin(q_i) & \sin(q_i)\sin(\alpha_i) & a_i\cos(q_i) \\
\sin(q_i) & \cos(\alpha_i)\cos(q_i) & -\cos(q_i)\sin(\alpha_i) & a_i\sin(q_i) \\
0 & \sin(\alpha_i) & \cos(\alpha_i) & d_i \\
0 & 0 & 0 & 1
\end{vmatrix} \quad (2)
$$

We can find the following transformation matrixes in each joint of the exoskeleton:

$$
\begin{cases}
A_{0A} = \begin{vmatrix} C_1 & 0 & S_1 & L_1C_1 \\ S_1 & 0 & -C_1 & L_1S_1 \\ 0 & 1 & 0 & 0 \\ 0 & 0 & 0 & 1 \end{vmatrix} \\[4pt]
A_{AB} = \begin{vmatrix} C_2 & 0 & -S_2 & 0 \\ S_2 & 0 & C_2 & 0 \\ 0 & -1 & 0 & L_2 \\ 0 & 0 & 0 & 1 \end{vmatrix} \\[4pt]
A_{BC} = \begin{vmatrix} C_3 & -S_3 & 0 & L_3C_3 \\ S_3 & C_3 & 0 & L_3S_3 \\ 0 & 0 & 1 & 0 \\ 0 & 0 & 0 & 1 \end{vmatrix} \\[4pt]
A_{CD} = \begin{vmatrix} C_4 & -S_4 & 0 & L_4C_4 \\ S_4 & C_4 & 0 & L_4S_4 \\ 0 & 0 & 1 & 0 \\ 0 & 0 & 0 & 1 \end{vmatrix}
\end{cases} \tag{3}
$$

where $C_i = \cos(\varphi_i)$, $S_i = \sin(\varphi_i)$.

To find the final transformation matrix we should product these matrixes (3):

$$A_{0D} = A_{0A}A_{AB}A_{BC}A_{CD}, \tag{4}$$

$$
A_{0D} = \begin{vmatrix} n_x & s_x & a_x & X_D \\ n_y & s_y & a_y & Y_D \\ n_z & s_z & a_z & Z_D \\ 0 & 0 & 0 & 1 \end{vmatrix} = \begin{bmatrix} T_{rot} & b^T \\ 0\ \ 0\ \ 0 & 1 \end{bmatrix}, \tag{5}
$$

where T_{rot} is rotation matrix. $b = (\ X_D, \quad Y_D, \quad Z_D\ )$ is radius-vector of the working point (D) of the exoskeleton.

$$
T_{rot} = \begin{vmatrix} C_4(C_1C_2C_3 - S_1S_3) - S_4(C_1C_2S_3 + S_1C_3) & -S_4(C_1C_2C_3 - S_1S_3) + C_4(C_1C_2S_3 + S_1C_3) & -S_2C_1 \\ C_4(S_1C_2C_3 + C_1S_3) - S_4(S_1C_2S_3 - C_1C_3) & -S_4(S_1C_2C_3 + C_1S_3) + C_4(S_1C_2S_3 - C_1C_3) & -S_2S_1 \\ C_4S_2C_3 - S_4S_2S_3 & -S_4S_2C_3 + C_4S_2S_3 & C_2 \end{vmatrix}
$$

$$(6)$$

Coordinates of the point D are:

$$
\begin{cases}
X_D = L_4(C_4(C_1C_2C_3 - S_1S_3) - S_4(C_1C_2S_3 + S_1C_3)) + L_3(C_1C_2C_3 - S_1S_3) + L_2S_1 + L_1C_1 \\
Y_D = L_4(C_4(S_1C_2C_3 + C_1S_3) - S_4(S_1C_2S_3 - C_1C_3)) + L_3(S_1C_2C_3 - C_1S_3) - L_2C_1 + L_1S_1 \, . \\
Z_D = L_4(C_4S_2C_3 - S_4S_2S_3) + L_3S_2C_3
\end{cases}
$$

$$(7)$$

Fig. 3 Elbow component of exoskeleton
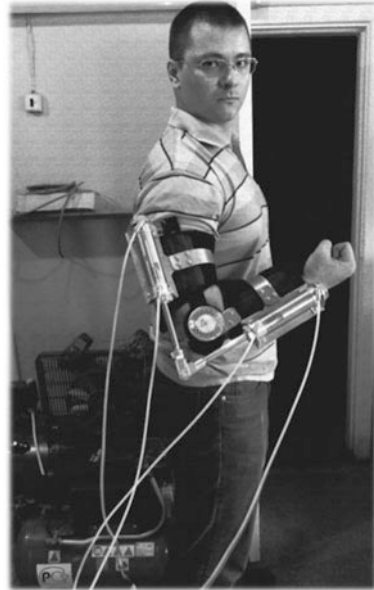
The rotation matrix (6) and coordinates of the point (D) are the forward kinematics solution.

The inverse kinematics is the problem of finding generalized coordinates to produce the given position and orientation of the construction. If we have the rotation matrix (6) and coordinates of the point (D) we can find φ_i-angles:

$$
\begin{cases}
\varphi_1 = \text{arctg}\left(\frac{a_y}{a_x}\right) \\
\varphi_2 = \text{arctg}\left(\frac{-a_x}{a_z \cos\varphi_1}\right) \\
\varphi_3 = \arccos\left(\frac{(L_4 n_z - z_D)\cos\varphi_1}{L_3 a_x}\right) \\
\varphi_4 = \text{arctg}\left(\frac{s_z \cos\varphi_3 - n_z \sin\varphi_3}{s_z \sin\varphi_3 - n_z \cos\varphi_3}\right)
\end{cases}
. \tag{8}
$$

The system (8) is the inverse kinematics solution. It is useful if we already know the rotation matrix and coordinates of the end-point.

3 Experimental Results

Experimentation was done in Robotics and Mechatronics Laboratory of Institute for Problems of Mechanics.

Fig. 4 Exoskeleton lifts
10 kg load

Table 1 Exoskeleton
performance in various
modes

Working mode	Operation time (s)
Free load	1.5
2.5 kg load	1.7
10 kg load	3.2

During experimentation physical model of exoskeleton-arm based on pneumatic drives was explored. Figure 3 presents elbow component of exoskeleton and Fig. 4 shows exoskeleton in working mode.

This exoskeleton was constructed using standard arm's orthosis. The latter was additionally equipped with 2 Ø32 pneumatic drives with 80 mm stroke. The overall weight of a system was 4.1 kg.

Within our experimentation the time of exoskeleton's links operation was measured for 120° angular motion. This was done for both free-load functioning and with a load of 10 kg applied.

The results are presented in Table 1.

The experiment shows that operation time is dependent from a load. To improve the operation time a torque sensor in the joint and a controlled valve are needed. In this case the elbow's controller will get torque, pressure level and angle as input data and will calculate opening time for the valve. Thus we will be able to control the angle and the operation time. The future work is to create the shoulder part of the exoskeleton and verify its kinematics.

4 Conclusion

This paper presents mathematical model of human arm exoskeleton. The direct and inverse kinematics tasks are solved for this model. Experiments performed on elbow part of exoskeleton.

References

1. Ward, J., Sugar, T., Standeven, J., Engsberg, J.: Stroke survivor gait adaptation and performance after training on a powered ankle foot orthosis. 2010 IEEE international conference on robotics and automation, Anchorage Convention District, 3−8 May 2010, Anchorage, Alaska, USA
2. Sledd, A., O'Malley, M.: Performance enhancement of a haptic arm exoskeleton, Mechanical Engineering and Materials Science. Proceedings of 14 Symposium of haptic interfaces for virtual environment and teleoperator systems, 2006
3. Frisoli, A., et al.: A force-feedback exoskeleton for upper-limb rehabilitation in virtual reality. Appl. Bionics Biomech. **6**(2), 115–126 (2009)
4. Frisoli, A., et al.: A new force-feedback arm exoskeleton for haptic interaction in virtual environments. Proceedings of Eurohaptics conference, 2005 and symposium on haptic interfaces for virtual environment and teleoperator systems, 2005. World Haptics 2005
5. Mistry, M., Mohajerian, P., Schaal, S.: Arm movement experiments with joint space force fields using an exoskeleton robot. Proceedings of the 2005 IEEE, 9th International conference on rehabilitation robotics, 28 June–1 July 2005, Chicago, IL, USA
6. Cavallaro, E., et al.: Real-time myoprocessors for a neural controlled powered exoskeleton arm. IEEE Trans. Biomed. Eng. **53**(11), 2387–2396 (2006)
7. Pang, M., Guo, S., Song, Z.: Study on the sEMG driven upper limb exoskeleton rehabilitation device in bilateral rehabilitation. J. Robotics Mechatron. **24**(4), 585–594 (2012)
8. Hidalgo, M., Sanchez, A., Tene, G.: Fuzzy control of a robotic arm using EMG signals, Department of Automatization and Industrial Control (2005)
9. Jain, R.K., Datta, S., Majumder, S.: Design and control of an EMG driven IPMC based artificial muscle finger. Second international conference on innovative computing technology (INTECH 2012) 18–20 Sept. 2012, Casablanca, Morocco
10. Saponas, T.S., Tan, D.S., Morris, D., Balakrishnan, R.: Demonstrating the feasibility of using forearm electromyography for muscle-computer Interfaces, CHI 2008, 5–10 April, Florence, Italy
11. Gradetsky, V., Kalinichenko, S., Kravchuk, L., Lopashov, V.: Modular design and mechatronic approaches to the exoskeleton system. Lecture notes of the ICB seminars biomechanics. Biomechanics of the musculoskeletal system medical robotics, pp. 260–269. Polska Akademia Nauk, Warsaw (2000)
12. Gradetsky, V., Knyazkov, M., Semyonov, E., Ermolov, I., Kryukova, A., Sukhanov, A.: The designing of the exoskeleton leg with pneumatic drives. Proceedings of the 16th international conference on climbing and walking robots and the support technologies for mobile machines, July 2013, pp 19–27
13. Gradetsky, V., Knyazkov, M., Semyonov, E., Ermolov, I., Kryukova, A., Sukhanov, A.: Motion control algorithms for the exoskeleton equipped with pneumatic drives. Proceedings of the 16th international conference on climbing and walking robots and the support technologies for mobile machines, July 2013, pp. 27–34

Underactuated Finger Mechanism for LARM Hand

M. Zottola and M. Ceccarelli

Abstract An underactuated mechanism is designed for improving grasping adaptability of LARM Hand fingers. The proposed design is presented with numerical results of simulations for operation characterization and design feasibility.

1 Introduction

Manipulation of objects with fingered robotic hands is an aspect which involves many applications, also in industry and service contexts and it attracts still great interest as indicated for example in [2, 6, 14].

Since a recent past, in order to develop anthropomorphic finger mechanisms researchers have used two different approaches: complex mechanisms in order to perform manipulation tasks with high dexterity, or design of mechanisms with a reduced number of degrees of freedoms (DOFs) and actuators with less performances but a fairly simplified device operation.

Using underactuated mechanisms it is possible to achieve an adaptive grasp that mimics the human grasping action for which it is possible to consider two kinds of structures, namely using flexibility of links or designing underactuated mechanisms as pointed out in [9]. A mechanism is defined underactuated when its number of actuators is smaller than the number of degrees of freedom of the mechanism. It is possible to identify two types of underactuated finger

M. Zottola · M. Ceccarelli (✉)
LARM: Laboratory of Robotics and Mechatronics, University of Cassino and South Latium, Cassino, FR, Italy
e-mail: ceccarelli@unicas.it

mechanisms, depending on whatever a tendon or link transmission is used. Examples of tendon finger mechanisms are reported in [4, 10, 13]. A finger mechanism with tendons is presented in [1], while a pulley-cable solution is described in [5].

When large grasping forces are required, underactuated linkage mechanisms are usually preferred, like for example in [11], where a 1-DOF mechanism with suitable four-bar linkages and flexible elements is used to move all phalanxes of fingers, in [18], where an underactuated linkage with force control is studied or in [19], where a 5 fingered underactuated prosthetic hand is reported.

Since the end of 1990s at LARM in Cassino design and research activities have been carried out in order to design a low-cost easy-operation robotic hand with anthropomorphic fingers, denominated LARM Hand [7].

In this paper the design of a new underactuated finger mechanism has been proposed for LARM Hand, as focused on requirements referring to 1-DOF, anthropomorphic grasp, and mechanism's compact size.

2 LARM Hand

Last version of LARM Hand is reported in Fig. 1a, with three 1-DOF fingers, a palm, and a standard flange for connection with robots [7]. The size of this prototype is 1.2 times larger than an average human hand. The physical sizes of the phalanx bodies is given by height 2 cm with length of 6, 3.7 and 3.5 cm for phalanx 1, 2 and 3, respectively [8]. The actuation system consists of three DC motors with a reduction gear train on each axis. A 1-DOF human-like finger mechanism for LARM Hand was designed as in the scheme in Fig. 1b. Each finger is composed of a cross two four-bar linkage. Phalanx 1 is the input bar of the first four-bar linkage and is also the base frame of the second four-bar linkage. Phalanx 2 is the input bar of the second four–bar linkage and it is also the coupler of the first four-bar linkage. Phalanx 3 is the coupler of the second four-linkage. The LARM design for finger mechanism is characterized by link ratios in Table 1 with limited grasping adaptability. In order to improve the capability of grasping objects with different sizes and shapes, solutions with underactuated mechanism have are considered [16].

3 Problems for Adaptable Grasps

The articulated finger mechanism in LARM Hand IV is composed of rigid links, so that the phalanxes have predetermined grasping configurations. A finger mechanism has no possibility to adapt its configuration to the shape of grasped objects, with the exception of those sizes and shapes that have been considered during the design process for predetermined finger grasping configuration. In order to
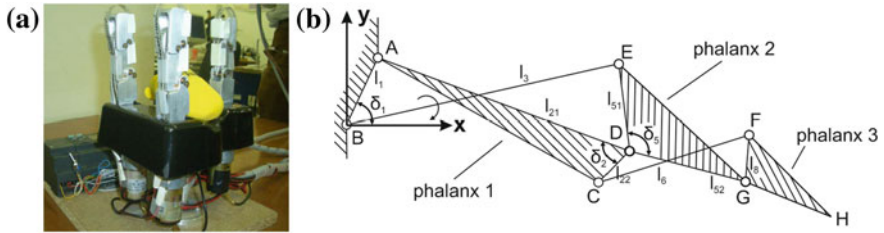
Fig. 1 LARM hand IV: **a** Prototype built in 2007; **b** Finger mechanism's scheme [7]

Table 1 Structural parameters of the LARM hand in Fig. 1

[mm]								[deg]		
l_1	l_{21}	l_{22}	l_3	l_{51}	l_{52}	l_6	l_8	δ_1	δ_2	δ_5
8.8	24.1	3.9	28.5	6	19.9	25	6.9	83.5	51	129
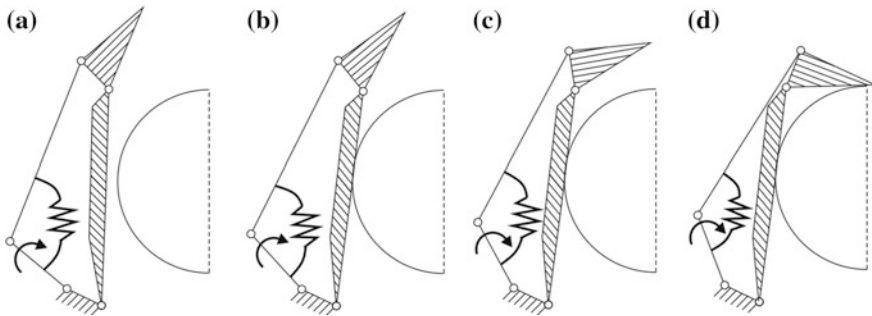
Fig. 2 An example of a closing sequence **a–d** of an underactuated 2-DOFs finger mechanism

improve the capability of grasping objects with different sizes and shapes, a solution with underactuated mechanism can be used.

Self-adaptive fingers envelope objects to be grasped by adapting mechanism configuration to their shape with only one actuator and without complex control strategies. While a finger closes against an object, the configuration of the finger is determined at any time by external constraints that are associated with the object. When the object is fully grasped, the force generated by the actuator is distributed among all phalanges as pointed out in [12]. As an example a closing sequence of an underactuated 2-DOFs finger is shown in Fig. 2, in order to illustrate the concept of underactuation for grasping. The finger is actuated through the smaller link, as shown by the arrow in the figure. Since there are 2-DOFs and 1 actuator, 1 elastic element must be used. Thus, a spring is aimed to maintain the finger fully extended. In Fig. 2a, the finger is in its initial configuration and the finger mechanism behaves as a four-bar linkage. In Fig. 2b, the first phalanx makes

contact with the object. In Fig. 2c, the second phalanx moves with respect to the first one and the finger closes against the object since the first phalanx is constrained by the object. During this phase, the actuator produces the force that is required to stress the spring. Finally, in Fig. 2d, both phalanges are in contact with the object and the finger has completed the shape adaptation phase. The actuator force is distributed among the two phalanges in contact with the object. It should be noted that the sequence occurs with a continuous motion of the actuator as pointed out in [12].

Due to different shapes or positions of objects, sometimes a distal phalanx will be in contact with the object before the proximal phalanx. In addition it is possible to reach singular positions, where the grasp is not stable and the finger could lose contact with the object, as explained in [3].

In order to obtain an underactuated finger for LARM Hand, it is possible to slightly modify the articulated mechanism shown in Fig. 1b. The goal is to preserve the main features of LARM Hand design concerning with a 1-DOF mechanism structure with anthropomorphic grasping behavior and a mechanism size that permits a mechanical design within the finger body during all grasping phases.

4 A Proposed Underactuated Finger Mechanism

In order to design a new 1-DOF underactuated finger for LARM Hand, new kinematic mechanisms have been developed by using considerations in [9]. In [20] in order to obtain a new underactuated finger mechanism for LARM Hand a mechanism search has been reported to identify several possible solutions.

The selected solution for a new finger mechanism is shown in Fig. 3. It is composed by 8 links and 9 revolute joints. Phalanxes are respectively links 2, 6 and 8. This mechanism has a limited manufacturing complexity because of the reduced number of bodies and linkage design. Because of underactuation this mechanism is able to grasp objects with different shapes remaining within the finger body during its movement. The closure sequence of the finger motion grasping a cylinder is reported in Fig. 4 as a characteristic operation example.

The mechanism operation can be described according to characteristic situations for specific contacts through suitable virtual equivalent mechanisms as used in [15–17]. Namely, equivalent mechanisms can be identified for the cases: no phalanxes in contact; only phalanx 1 in contact with an object; phalanxes 1 and 2 in contact. Referring to the first situation, a phalanx is free when there is no contact force and torque acts on it. Generally a phalanx is free before it will touch an object. In this case, links that are connected by spring can be considered as a single virtual link. Here links 3 and 4 can be considered as acting as one virtual link 9 as shown by dashed line segment BD in Fig. 3b. Link 6 and 7 can be considered as another virtual link 10 through segment FI. Therefore, the proposed finger mechanism can be simplified as the equivalent mechanism Fig. 3b, which recall the original linkage in LARM Hand, shown in Fig. 1b. In the second situation,
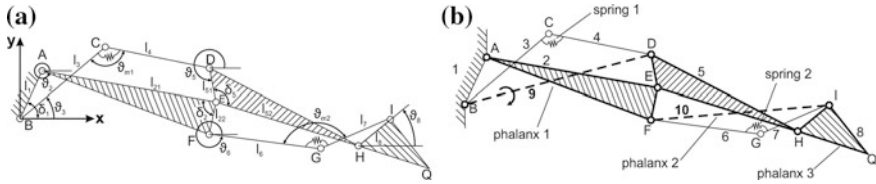
Fig. 3 A new underactuated solution for LARM hand fingers: **a** Scheme with structural parameters; **b** Equivalent mechanisms during functioning
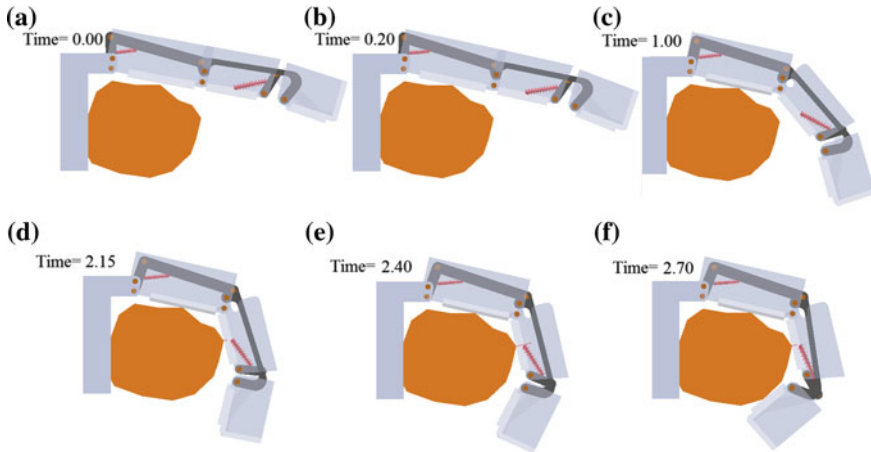
Fig. 4 A closure sequence of **a–f** object grasping by finger mechanism in Fig. 1

phalanx 1 is stopped while phalanxes 2 and 3 are free. In this case, link 2 and joints E and F are fixed and they act as a virtual base as shown in Fig. 3b. Spring 1 will start to be deformed because of motor push. But spring 2 will be not activated because phalanxes 2 and 3 are free. Links 6 and 7 can still be considered as one single virtual link 10. Thus, the finger mechanism can be simplified as the equivalent mechanism in Fig. 3b. When phalanx 2 is stopped because in contact with object, link 6 and joints E, F and G are fixed and phalanxes 1 and 2 act as a virtual base. Thus, also spring 2 will start to be deformed.

A characterization of the new finger mechanism has been worked out through simulation in ADAMS environment. Considering the design criteria and finger mechanical design in Fig. 5, structural parameters have been determined as reported in Table 2, referring to the kinematic scheme in Fig. 3a.

From values of Table 2 a CAD model has been built in Solidworks, as shown in Fig. 4. In ADAMS model joint friction and friction between objects surface and phalanxes have been defined as reported in Table 3. This table reports also mechanical parameters for springs that are used in underactuated DOFs.
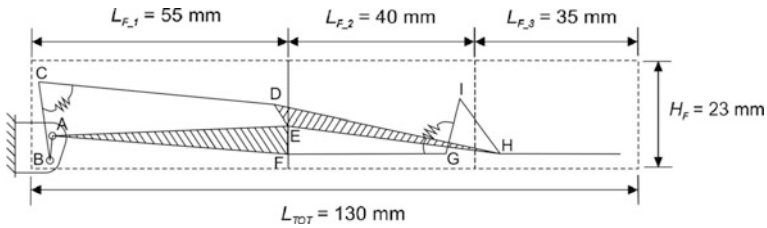
Fig. 5 Finger mechanical design with phalanxes dimensions and embedded mechanism

Table 2 Structural parameters, referring to kinematic scheme in Fig. 3a

[mm]										[deg]		
l_1	l_{21}	l_{22}	l_3	l_4	l_{51}	l_{52}	l_6	l_7	l_8	δ_1	δ_2	δ_5
5.4	50.8	6	17	51.3	5.4	46.5	34.3	12.3	14.5	83.5	87.7	128.6

Table 3 Friction values and springs mechanical parameters

Friction	Joints	Object—Phalanx	Springs	
Static	0.1	2	Stiffness [N/mm]	0.2
Dynamic	0.01	1.1	Damping [N*s/mm]	1

5 Simulation Results for a Characterization

Referring to Fig. 6, from each simulation in ADAMS environment it is possible to determine contact force values F_{c0}, F_{c1}, F_{c2}, F_{c3}, actuation torque τ at joint B, joints reactions R_a, R_b, R_c, R_d, R_e, R_f, R_g, R_h, R_i as depending of friction parameters, contact point accelerations a_{f1}, a_{f2}, a_{f3} and spring deformations from initial length Δ_1 and Δ_2. Several simulations have been worked out in grasping different objects with closure sequences of 1, 4 and 5 s duration.

Results in Figs. 7 and 8 are reported for the case in Fig. 4 for a 3 s grasping action with a generally shaped rigid object made of aluminum of a 3 N weight when an input motion is given with a sinusoidal law. Figure 7 shows results of contact and reaction forces from which it is easy to identify the corresponding configurations (b), (d), (f) in Fig. 4, when phalanxes 1, 2 and 3 reach contact. In (b) configuration forces on phalanx 1 and palm are about 0.5 N, while in (d) forces on palm and phalanx 2 reach about 20 N. The maximum reaction force is reached at E joint with a value of 170 N. The maximum values of phalanxes contact point accelerations are computed of about 500.00 mm/s^2 for contacts of phalanx 1 and about 1,100.00 mm/s^2 during phalanx 2 and 3 contacts.

In Fig. 8a torque history recalls the situation for the contact and reactions forces as depending from them, with a maximum value of 2.48 Nmm. In Fig. 8b
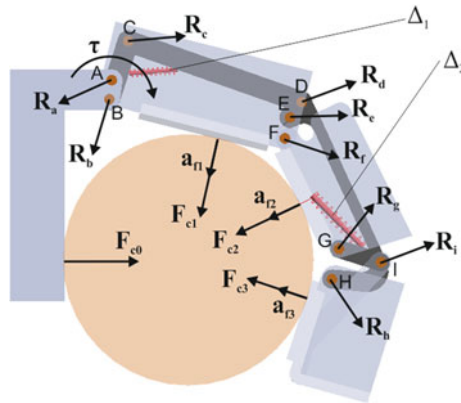
Fig. 6 Finger scheme with variables that are calculated in ADAMS simulations
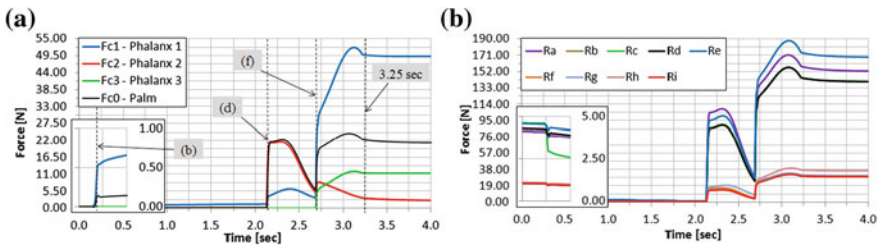
Fig. 7 Simulation results for the grasping test in Fig. 4: **a** Contact forces on phalanxes and palm; **b** Joint reaction forces
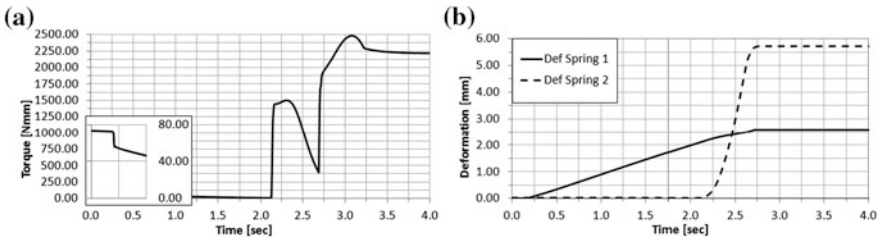
Fig. 8 Simulation results for the grasping test in Fig. 4: **a** Input torque; **b** Spring deformations

deformation history of the two springs in the mechanism is reported with their maximum elongation of 2.59 and 5.71 mm that are reached when also phalanx 3 is in contact with the object at the final grasp configuration.

Referring to Figs. 1b and 3a with Tables 1 and 2 it is possible to compare the finger mechanism of LARM Hand with the new underactuated finger mechanism.

6 Conclusions

An underactuated mechanism is presented as an evolution from the linkage design of the original LARM Hand finger. The kinematic design is characterized by underactuation that is obtained by springs as passive actuators between two connected links and by permitting a motion of the whole mechanism still within the finger body. The smooth human-like operation is tested through numerical simulations that give results for a characterization of a feasible implementation as shown also in functionality first tests of a prototype.

References

1. Bhatti S.: Design of a multiple finger prosthetic hand with a passive adaptive grasp system, EE 4BI6 electrical engineering biomedical capstones, Paper 28, Hamilton (2010)
2. Bicchi, A.: Hands for dexterous manipulation and robust grasping: a difficult road toward simplicity. IEEE Trans. Robot. Autom. **16**, 652–662 (2000)
3. Birglen, L., Gosselin, C.M.: On the force capability of underactuated fingers. In: Proceedings of the 2003 IEEE International Conference on Robotics and Automation (ICRA), vol. 1, pp. 1139–1145, Sept. (2003)
4. Birglen, L., Lalibertè, T., Gosselin, C.: Underactuated Robotic Hands. Springer, Berlin (2008)
5. Cabas, R., Cabas, L.M., Balaguer, C.: Optimized design of the underactuated robotic hand. In: Proceedings of the 2006 IEEE International Conference on Robotics and Automation (ICRA), pp. 982–987. Orlando, May (2006)
6. Carbone, G.: Grasping in Robotics. Springer, Dordrecht (2013)
7. Carbone, G., Ceccarelli, M.: Design of LARM hand: problems and solutions. J. Control Eng. Appl. Inform. **10**(2), 39–46 (2008)
8. Ceccarelli, M., Rodriguez, N.E., Carbone, G.: Optimal design of driving mechanism in a 1-DOF anthropomorphic finger. Mech. Mach. Theory **41**(8), 897–911 (2005)
9. Ceccarelli, M., Tavolieri, C., Lu, Z.: Design considerations for underactuated grasp with a one D.O.F. anthropomorphic finger mechanism. In: Proceedings of International Conference on Intelligent Robots and Systems IROS 2006, pp. 1611–1616. Beijing, Oct. (2006)
10. Crisman, J.D., Kanojia, C., Zeid, I.: Robot arm end-effectors. US patent 5570920 (1996)
11. Gosselin, C.M., Lalibertè, T.: Underactuated mechanical finger with return actuation. US patent 5762390, June 1998
12. Lalibertè, T., Birglen, L., Gosselin, C.: Underactuation in robotic grasping hands. Mach. Intell. Robot. Control **4**, 1–11 (2002)
13. Mullen, J.F.: Mechanical hand. US patent 3694021, Sept. 1972
14. Siciliano, B., Kathib, O.: Springer Handbook of Robotics, Part D, Chapter 28. Springer, Heidelberg (2008)
15. Wu, L., Ceccarelli, M.: A numerical simulation for design and operation of an underactuated finger mechanism for LARM hand. Int. J. Mech. Based Des. Struct. Mach. **37**, 86–112 (2009)
16. Wu, L., Carbone, G., Ceccarelli, M.: Designing an underactuated mechanism for a 1 active DOF finger operation. Mech. Mach. Theory **44**, 336–348 (2008)
17. Yao, S., Ceccarelli, M., Carbone, G., Zhan, Q., Lu, Z.: Analysis and optimal design of an underactuated finger mechanism for LARM hand. Front. Mech. Eng. **6**, 332–343 (2011)
18. Zhang, W., Zhao, D., Chen, Q., Du, D.: Linkage under-actuated humanoid robotic hand with control of grasping force. Inf. Control Autom. Robot. (CAR) **2**, 417–420 (2010)

19. Zhao, J., Jiang, L., Shi, S., Cai, H., Liu, H., Hirzinger, G.: A five-fingered underactuated prosthetic hand system. In: Proceedings of the 2006 IEEE International Conference on Mechatronics and Automation, pp. 1453–1458. Luoyang, June (2006)
20. Zottola, M.: Design of an underactuated LARM finger mechanism for robotic hand. Master's thesis, University of Cassino and South Latium, Cassino (2013)

Design and Kinematic Analysis of a Novel Cable-Driven Parallel Robot for Ankle Rehabilitation

Runtian Yu, Yuefa Fang and Sheng Guo

Abstract In this paper, a novel cable-driven parallel robot based on the motion characteristics of human ankle joint is proposed for ankle rehabilitation. Because of the novel mechanical design of the equivalent spherical joint and platform, the mechanism centre of rotations can easily match the ankle axes of rotations, which is an advantage over some existing rehabilitation robots. The mechanism design is described and the kinematics are studied, then the workspace of the robot under ankle rehabilitation working mode is analyzed. Finally, a reality model of the parallel robot simulated under the ADAMS environment. It shows the design can well meet the needs of ankle joint rehabilitation requirements.

Keywords Ankle rehabilitation · Cable-driven · Parallel robot · Kinematics · Simulation

1 Introduction

Ankle sprains can occur in everyday activities or athletic events, especially, those professional basketball and soccer players tend to suffer from more ankle sprains than ordinary people. In addition, the stroke and the traffic accident causes a large increase in patients with lower limb disability who need to perform specific

R. Yu · Y. Fang (✉) · S. Guo
Department of Mechanical Engineering, Beijing Jiaotong University,
Beijing, People's Republic of China
e-mail: yffang@bjtu.edu.cn

R. Yu
e-mail: 12121337@bjtu.edu.cn

S. Guo
e-mail: shguo@bjtu.edu.cn

movements driven by motor and carry on rehabilitation training. If the patients cannot be treated timely and thorough, it is possible to cause repeated sprains and loss of function. In recent years, with the development of economy, people pay more attention to the health and quality of life so that the disabled have an increasing demand on the rapid ankle rehabilitation. The study on the robot of ankle rehabilitation has aroused widespread attention of scientific researchers.

In the last decade, a number of robotic devices for ankle physiotherapy have been proposed. Liu et al. [1] discussed the 3-RSS/S parallel robot with three DOFs (degree of freedom) for ankle rehabilitation. Bian et al. [2] proposed a 2-RRR/ UPRR parallel robot for ankle rehabilitation and analyzed its kinematics. One of the successful active foot orthoses is the MIT's Anklebot, an actuated exoskeleton that users wear while walking over ground, proposed by Roy et al. to train stroke survivors to overcome common foot drop and balance problems [3]. In 1999, The State University of New Jersey developed the "Rutgers Ankle" [4], based on a 6-DOF Stewart platform that applies variable forces and virtual reality exercises on the patient's foot, can perform any complicated spatial motions including three-dimensional rotation. But it is too complicated to be commercially available. Dai and Zhao [5] proposed a 3 or 4-DOF parallel robots with a central strut for ankle rehabilitation and analyzed the mobility and the stiffness. Later on, a 2-DOF parallel robot with a central strut as well was developed and studied by Saglia et al. [6]. However, all the forgoing robots have the same problems: the robot axes of rotation are far offset from the ankle axes of rotation, which is likely to cause secondary sprain; Majority of ankle rehabilitation robots make use of rigid rods as the driving elements. Hence, due to limitations of the hinge angle, working space is reduced. In addition, the harmful impact will be easily produced by rigid rods during rehabilitation training process causing the patient anxious.

The existing rehabilitation robots are far from perfect. It is still not an easy task to design a robot to possess reasonable performance with simple structure. In addition, there are no cable-driven robots for ankle rehabilitation in literatures. Hence, based on the above discussed, a novel cable-driven ankle rehabilitation robot is proposed with several advantages as follows:

1. The robot has 3-DOF rotations such that it can fully meet the requirements of ankle rehabilitation.
2. The robot center of rotation match the ankle axes of rotation as closely as possible so as to avoid the secondary sprain during operation.
3. The cable-driven robot increases its work space and also avoids the inertial impact from rigid bars.
4. The flexibility of the system is enhanced by designing a special redundancy scheme.

2 Design of the Ankle Rehabilitation Robot

2.1 Ankle's Motion Characteristics

The human ankle joint complex is one of the major weight bearing structures in the body, which bears the whole weight of the body when a person stands and walks. If translations in the ankle motion are ignored, then the ankle motion can be described as rotations of a ball joint about X, Y, Z three directions, as shown in Fig. 1. The actual ankle movement is more complex. Thanks to previous work, the estimated range of motion of the ankle in each direction is given in Table 1 [7]. It is worthy of noting that the range of motion can vary greatly among different persons.

Based on the above analysis, robot for ankle rehabilitation should be designed to be able to achieve three rotations of ankle movement. The maximum allowable rotational ranges should satisfy the requirements in Table 1 to ensure the safety of auxiliary rehabilitation.

2.2 Brief Introduction of the Rehabilitation Robot

To solve the above mentioned problems of the existing robots, this paper proposes a cable-driven ankle rehabilitation robot, as shown in Fig. 2a. In the figure, R represents revolute pair; P represents prismatic pair. The rehabilitation robot can rotate around three axes and consists of a frame, a moving platform and constraint limbs. By controlling the four linear actuators and the rotation of redundant motor, desired motions can be achieved. In Fig. 2b, shortening (elongating) linear actuator 1 and 2, or elongating (shortening) linear actuator 3 and 4 will make the moving platform rotate around x-axis; meanwhile shortening (elongating) linear actuator 2 and 3, or elongating (shortening) linear actuator 1 and 4 will make the moving platform rotate around y-axis. The redundant motor on the lower frame drive the constraint limb and make the moving platform rotate around the z axis. When redundant motor is self-locked, the robot turns to be a two degrees of freedom robot. Since the cable can only apply force in one direction, it is necessary to implement a redundant actuators to finish closing force of the moving platform. To achieve "n-DOF" montions, a cable-driven robot needs "n + 1" actuators [8]. Such we use four cables to pull the moving platform. The novel design of the constraint limb which is equivalent to a spherical pair and the adjustable double-deck moving platform ensure that the center of rotation coincides with one of the ankle joint. The flexible cable of the robot increases the working space of the system and avoids inertial impaction during rehabilitation.
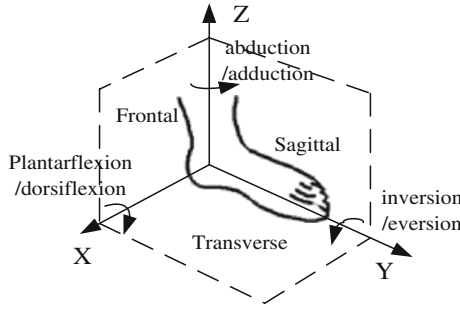
Fig. 1 Some definitions about ankle rotation

Table 1 The ankle range of motion [7]

Type of motion	Maximum allowable motion
Dorsiflexion	20.3°–29.8°
Plantarflexion	32.6°–40.8°
Inversion	14.5°–22.0°
Eversion	10.0°–17.0°
Abduction	15.4°–25.9°
Adduction	22.0°–36.0°
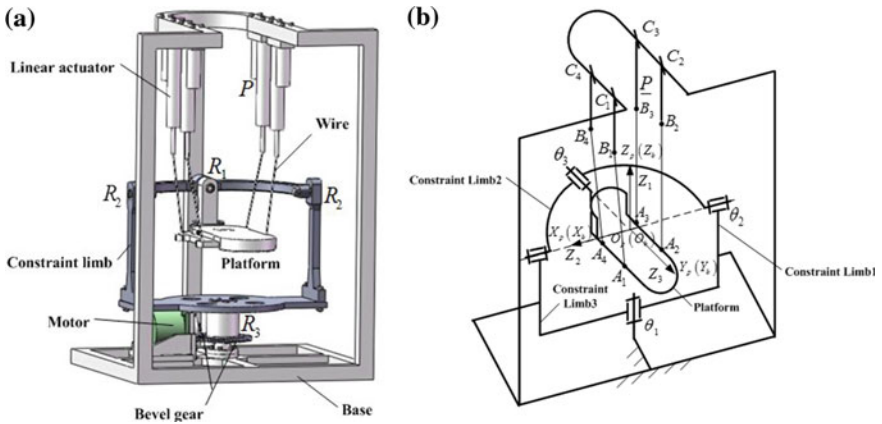
Fig. 2 **a** The model of cable-driven parallel robot for ankle rehabilitation. **b** The kinematic diagram of the robot for ankle rehabilitation

3 Inverse Kinematics

Figure 2b depicts the geometrical model of the robot. The reference frames $K_b(X_bY_bZ_bO_b)$ and $K_p(X_pY_pZ_pO_p)$ are attached at the base and the moving platform respectively, and locate at the rotational center of the moving platform. A_i is the joint of cable i and moving platform, B_i is the joint of cable i and the end of linear actuator i. C_i is the joint of linear actuator i and the frame, ${}^bR_p$ represents the orientation or rotation matrix of the moving platform with respect to the fixed base, q_i is the displacement of linear actuator, L_{AB} is the length of cable, $L_i(A_i \rightarrow B_i)$ is the vector of the cable, i represents the number of cables. In the subsequent modeling process, assuming that the cable is always tensioned, in elastic and in the zero gravity status. Euler angles are used to describe the orientation of the moving platform. With reference to the fixed coordinates system, if the moving coordinate system rotates an angle α about X-axis, rotates an angle β about Y-axis, and rotates an angle γ about Z-axis, the orientation of the moving platform ${}^bR_p$ can be expressed as follows:

$$ {}^bR_p = R_Z(\gamma)R_X(\alpha)R_Y(\beta) \tag{1} $$

where, $c\alpha = \cos\alpha$, $s\alpha = \sin\alpha$ and so forth.

The inverse kinematics problem can be stated as follows: given the orientation (α, β, γ) of the moving platform, the displacements (q_1, q_2, q_3, q_4) of the linear actuators and rotation angle q of driving motor are calculated. The coordinates of the points A_i ($i = 1, 2, 3, 4$) attached at the moving platform and expressed in the reference frame $X_bY_bZ_bO_b$, can be calculated using the known orientation matrix ${}^bR_p$ and the coordinates of the same points but expressed in the frame $X_pY_pZ_pO_p$, as follows:

$$ a_i^b = {}^bR_p a_i^p = [\, ax_i \quad ay_i \quad az_i \,]^T , \quad i = 1, 2, 3, 4 \tag{2} $$

B_i and C_i can be expressed as b_i^b and c_i^b, respectively in fixed coordinate system $X_bY_bZ_bO_b$. According to the constraint relations, we can get the following equation:

$$ (b_i^b - a_i^b) \cdot (b_i^b - a_i^b) = l_{AB}^2 \tag{3} $$

$$ (c_i^b - b_i^b) \cdot (c_i^b - b_i^b) = q_i^2 , \quad i = 1, 2, 3, 4 \tag{4} $$

From Eqs. (3) and (4), we can get q_1, q_2, q_3, q_4.

Parameter	Value
L_{AB}	0.175 m
a_1^p	$[0.070, 0.070, -0.090]^T$
a_2^p	$[-0.070, 0.070, -0.090]^T$
a_3^p	$[-0.070, -0.070, -0.090]^T$
a_4^p	$[0.070, -0.070, -0.090]^T$
c_1^b	$[0.095, 0.045, 0.310]^T$
c_2^b	$[-0.095, 0.045, 0.310]^T$
c_3^b	$[-0.095, -0.045, 0.310]^T$
c_4^b	$[0.095, -0.045, 0.310]^T$

Table 2 The Architectural parameters of the robot

4 Workspace Analysis

Work space of a robot manipulator is the working volume, whose size is an important indicator to measure the performance of a robot. Configuration parameters of the robot are shown in Table 2.

The linear actuator's stroke is limited to be 100 mm, the motion range of passive joints have also been considered. For cable-driven robot, Due to the unidirectional feature of the cable tension force, work space is affected not only by cable length, but also the tension values. It need to be ensured that the tension of each cable remain between the minimum pre-tightening force and maximum permissible force, and that the forces and moments acting on the moving platform should be balanced.

Force and torque equilibrium equation of the ankle rehabilitation robot's moving platform can be expressed as follows:

$$JT + F = 0 \tag{5}$$

where, $J = \begin{bmatrix} J_1 & J_1 & J_1 & J_1 \end{bmatrix} \in R^{3 \times 4}$ is the cable matrix.

$$J_i = \frac{\left(^bR_p\,^{o_p}A_i\right) \times \left(^{o_b}B_i - ^bR_p\,^{o_p}A_i\right)}{\left\|^{o_b}B_i - ^bR_p\,^{o_p}A_i\right\|} \tag{6}$$

T represents tension vector of the cables, $T = \begin{bmatrix} t_1 & t_2 & t_3 & t_4 \end{bmatrix}^T \in R^4$, F represents complex moment vector, acting on moving platform.

Based on the consistent solving strategy of m DOF parallel robot's workspace driven by n cables. The mass and tension parameters of the moving platform are as follows: m = 5 kg, $t_{i,min} = 5\,N$, $t_{i,max} = 200\,N$. According to the flowchart of feasible workspace' solving method [9], the feasible workspace of ankle rehabilitation robot's wrench is programmed as Fig. 3.
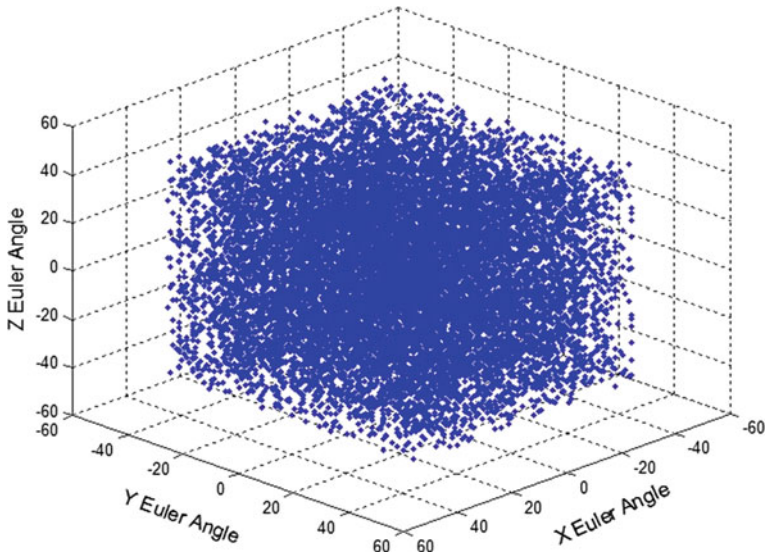
Fig. 3 The feasible workspace of the robot under the condition of wrench balance

Table 3 The workspace limits of the ankle rehabilitation robot	Direction of motion	Workspace limits (°)
	Dorsiflexion/plantarflexion	40
	Inversion/eversion	44
	Abduction/adduction	45

The numerical solutions of the feasible workspace of the moving platform under the condition of wrench balance are shown in Fig. 3. The result shows that the allowable rotation around any one of the three axes is highly dependent on the angular displacements at the other two axes.

By analyzing various 'slice' of the workspace, the maximum achievable angular displacement in each direction are given in Table 3. Comparing with the data in Table 1, it can be seen that the rotational ranges of the robot satisfy the required angle range of ankle.

5 Simulation

To meet the requirements of the ankle recovery, this paper selects a set of suitable mechanical parameters as shown in Table 2. Based on these parameters, the model of ankle recovery facility is constructed, and is imported into ADAMS system for kinematics simulation. The recovery exercises adopt the method of passive recovery movement according to the recovery therapy and requirements of physical therapists. As required by the physical therapist, the movement includes
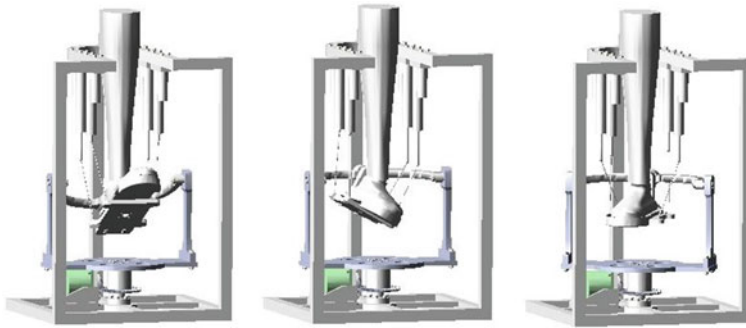
Fig. 4 The ankle rehabilitation robot are making the movement of dorsiflexion, inversion and abduction
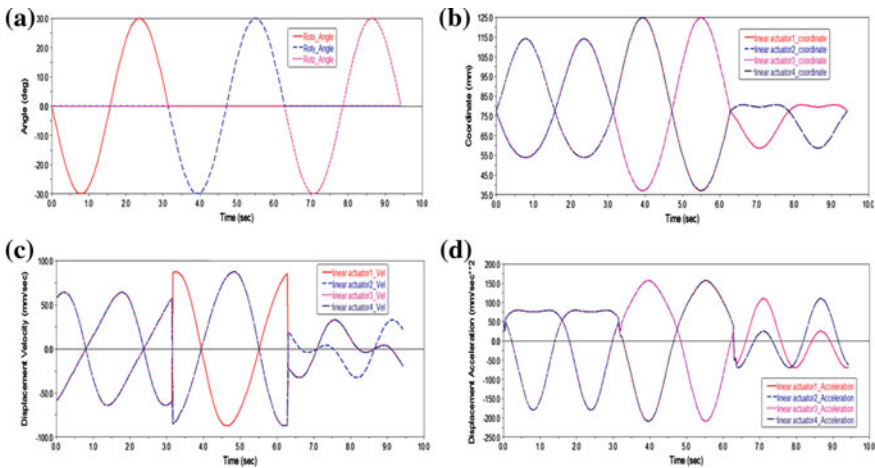
Fig. 5 **a** The variation curve of the moving platform rotation angle **b** The variation curve of low end's coordinate of linear actuator. **c** Velocity variation of linear actuators. **d** Acceleration variation of linear actuators

dorsiflexion/plantar flexion, inversion/eversion and adduction/adduction in 10 s. In the process of simulation, the moving platform will move around X, Y, Z axes in turn at ±30-degree angle on the hypothesis that the angle along the axis is varied in sine function. The cycle time is 3.14 s, and the total time for simulation is 9.42 s. The corresponding simulation results are as follows:

(1) Orientation simulation
    Fig. 4. Shows the robot is making the movement of dorsiflexion, inversion and abduction.
(2) The result of the inverse kinematics simulation is shown in Fig. 5.
(3) The simulation results show that the angle displacements about X, Y, Z axes can reach the design requirements in Table 3.

Figure 5 illustrate rotational angles, low end's coordinate, velocity and acceleration curves of four linear actuators. As a whole, every curve is smooth. This indicates that the robot can move smoothly in this range.

The result of the simulation indicates that the robot can achieve the motion pattern of the ankle rehabilitation exercises. The orientation workspace of the moving platform, can meet the requirements set by the exercise.

6 Conclusion

In this paper, a new cable-driven robot for ankle rehabilitation is proposed. The novel mechanical design of the equivalent spherical joint and platform guarantees the performances in terms of torque and load capacity while ensuring that the mechanism axes of rotation match the ankle axes of rotation as closely as possible and maintaining a simple structure. Then, the analysis of kinematic and workspace has confirmed that the robot can meet the motion requirements of ankle. Finally, a reality model of the parallel robot simulated under the ADAMS environment, the result of which also indicates this mechanism can meet the needs of ankle rehabilitation.

References

1. Liu, G.Q., Gao, J.L., Yue, H.: Design and kinematics analysis of parallel robots for ankle rehabilitation. In: IEEE/RSJ International Conference on Intelligent Robots and Systems, pp 253–258 (2006)
2. Bian, H., Liu, Y.H., Liang, Z.C., Zhao, T.S.: A novel 2-RRR/UPRR Robot for ankle rehabilitation and its kinematics. Robot **32**(1), 6–12 (2010)
3. Roy, A., Krebs, H.I., Williams, D.J., Bever, C.T.: A novel robot for ankle rehabilitation. IEEE Trans. Rob. **25**(3), 569–582 (2009)
4. Girone, M., Burdea, G.M., Bouzit, V., et al.: A stewart platform based system for ankle telerehabilitation. Auton. Robots **10**(3), 203–212 (2001)
5. Girone, M., Burdea, G., Bouzit, M.: Rutgers ankle orthopedic rehabilitation interface. In: Proceeding of the ASME DSC, vol. 67, 305–312 (1999)
6. Saglia, J.A., Tsagarakis, N.G., Dai, J.S., Caldwell, D.G.: A high performance 2-dof over-actuated parallel mechanism for ankle rehabilitation. In: IEEE International Conference on Robotics and Automation, pp 2180–2186 (2009)
7. Tsoi, Y.H., Xie, S.Q.: Design and control of a parallel robot for ankle rehabilitation. Int. J. Intell. Syst. Technol. Appl. **8**, 100–113 (2010)
8. Pham, C.B., Yeo, S.H., Yang, G.: Force-closure workspace analysis of cable-driven parallel mechanisms. Robot Mach. Theory **2**, 53–69 (2006)
9. Liu, X., Qiu, Y.Y., Chen, S.Y.: Proofs of existence conditions for workspace of wire-driven parallel robots and a uniform solution strategy for the workspaces. J. Mech. Eng. **46**(7), 27–34 (2010)

Position/Force Control of Medical Robot Interacting with Dynamic Biological Soft Tissue

V. Golovin, M. Arkhipov and V. Zhuravlev

Abstract Most applications of position/force control theory relate to the machining but not to a technique where a tool interacts with patient's soft tissue. In medicine the compliant motion is more necessary then strict program one. Firstly it refers to noninvasive restorative medicine, namely to various massage and extremities movement in joints. In the present paper the position/force control of robot interacting with inertial viscoelastic biological soft tissue is considered. In this practical case the number of contact force components is less then the number of robot degrees of freedom. These investigations can be used for medical robot control.

Keywords Position/force control · Medical robot and biological soft tissue

1 Introduction

The position/force control theory appears in contact tasks to account not only program motion but desired force interaction with environment. Significant contribution to the development of the position/force control theory is made by scientists of the Serbian school under the leadership of Miomir Vukobratovic [1].

The theory applications are in general in area of machinery. However the necessity to consider the compliance interaction with biological soft tissue arises in problems of medical robotics including noninvasive restorative medicine [2]. There is direct compliance interaction of robot with soft tissue during various massage or by means of levers for extremities movements in joints. In these procedures compliance movement is more essential than strict program one.

V. Golovin (✉) · M. Arkhipov · V. Zhuravlev
Moscow State Industrial University, Moscow, Russia
e-mail: medicalrobot@mail.ru

Depending on the procedure complexity the various soft tissue models and control methods are used. The description of inertial and viscoelastic properties of soft tissue is necessary for more fine solutions.

The employment of multilink manipulation robots for restorative medicine is a very promising trend [3].

2 Soft Tissues Dynamic Characteristics

Soft tissue can be presented as an anisotropic, multilayered, nonlinear, inertial, viscoelastic, plastic and non-stationary environment in the most general models. The nonlinear properties especially evident for soft tissues overlaying the rigid bones. Some soft tissues characteristics are described in monograph [4].

The elasticity coefficient on the soft tissue characteristic part, which is close to the linear one, is in the range of 500–5000 N/m and soft tissue viscosity coefficient is in the range of 10–100 Ns/m.

The data on soft tissue inertia were obtained in experiments with high-speed video camera use.

On Fig. 1 the experimental curves of transition processes of relaxed forearm front surface deformation by ball are shown. On the soft tissue the balls of diameter 7 and 20 mm fall from the height 13 mm.

The soft tissue dynamic model in one-dimensional case can be given in the impedance form:

$$m\ddot{x} + \mu\dot{x} + kx = F, \tag{1}$$

where m, μ, k are the mass, the viscosity coefficient and the soft tissue elasticity coefficient accordingly.

Let us approximate the soft tissue characteristics in experiments (Fig. 1) using an impedance models. In these experiments for $k = 1000$ N/m we have $m = 0.1$ kg, $\mu = 10$ Ns/m.

Experiments described above represent soft tissues dynamics using transients. There are methods of soft tissue dynamics description in frequency region [5].

3 Position/Force Control of Robot Interacting with Dynamic Environment

The theory of position/force control of robot interacting with dynamic environment is expounded within the framework of analytical mechanics in monograph [1].

The robot interacting with the dynamic environment can be presented by the following differential equation:
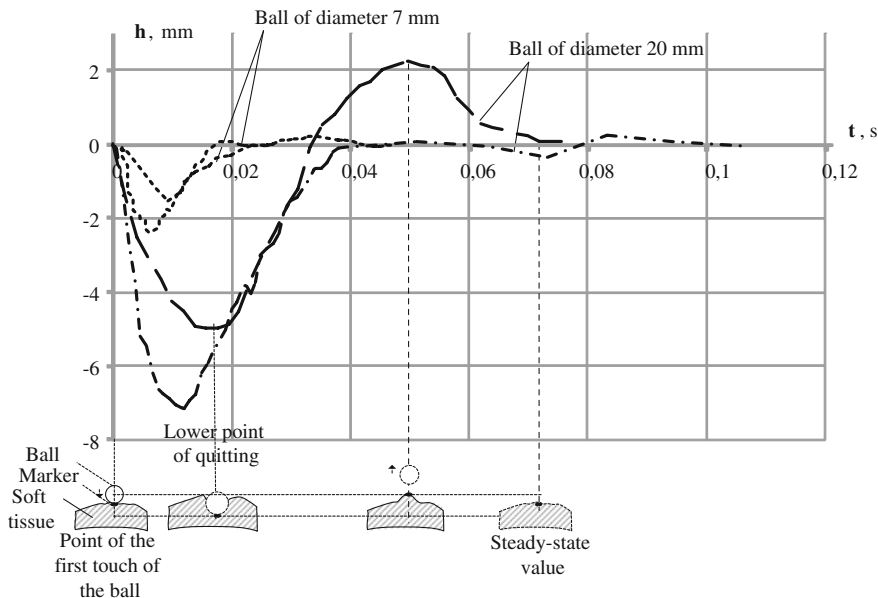
Fig. 1 The transition processes of relaxed forearm front surface deformation by ball

$$M(\boldsymbol{q})\,\ddot{\mathbf{q}} + h(\boldsymbol{q}, \dot{\boldsymbol{q}}) = \tau + J^T(\boldsymbol{q})\mathbf{F}, \tag{2}$$

the environment dynamics can be described by the following differential equation:

$$M(\boldsymbol{q})\,\ddot{\mathbf{q}} + L(\boldsymbol{q}, \dot{\boldsymbol{q}}) = -S^T(\boldsymbol{q})\mathbf{F}, \tag{3}$$

where $\boldsymbol{q}, \dot{\boldsymbol{q}}, \ddot{\boldsymbol{q}} \in R^n$ are the vectors of the generalized coordinates of position, velocity and acceleration accordingly, $H(\mathbf{q}) \in R^{n \times n}$ is the matrix characterizing inertial properties of the manipulator, $\mathbf{h}(\mathbf{q}, \dot{\mathbf{q}}) \in R^n$ is the vector characterizing gravitational, centrifugal, Coriolis' forces, $M(\mathbf{q}) \in R^{n \times m}$ is the matrix character-izing inertial properties of the environment, $\mathbf{L}(\mathbf{q}, \dot{\mathbf{q}}) \in R^m$ is the vector charac-terizing viscoelastic properties of the environment and its weight, $\tau \in R^n$ is the vector of the input control, $\mathbf{F} \in R^m$ is the vector of the forces operating on the end link (tool) of the manipulator from outside the environment, $S(\mathbf{q}) \in R^{m \times m}$ is the nonsingular matrix.

The robot control goal is to synthesize the control law $\tau(t)$ that provides the following:

$$\boldsymbol{q}(t) \to \boldsymbol{q}_0(t), \; \dot{\boldsymbol{q}}(t) \to \dot{\boldsymbol{q}}_0(t), \; \boldsymbol{F}(t) \to \boldsymbol{F}_0(t), \; , \; t \to \infty. \tag{4}$$

Let the model with the assigned transients in generalized coordinates $\boldsymbol{q}(t)$ is described by a linear differential equation of the second order:

$$\ddot{\boldsymbol{q}} + k_1\dot{\boldsymbol{q}} + k_2\boldsymbol{q} = 0, \tag{5}$$

or in deviations $\boldsymbol{e}_q = \boldsymbol{q}_0(t) - \boldsymbol{q}(t)$:

$$\ddot{\mathbf{e}}_q + k_1\dot{\mathbf{e}}_q + k_2\mathbf{e}_q = 0, \tag{6}$$

where k_1 и k_2 are $n \times n$ matrix providing necessary quality transients of coordinates $\boldsymbol{q}(t)$.

We have:

$$\ddot{\boldsymbol{q}} = \ddot{\boldsymbol{q}}_0 - \ddot{\boldsymbol{e}}_q = \ddot{\boldsymbol{q}}_0 + k_1\dot{\boldsymbol{e}}_q + k_2\boldsymbol{e}_q. \tag{7}$$

To guarantee the necessary quality transients the control law should be as follows:

$$\boldsymbol{\tau} = H(\boldsymbol{q})(\ddot{\boldsymbol{q}}_0 + k_1\dot{\boldsymbol{e}}_q + k_2\boldsymbol{e}_q) + h(\boldsymbol{q}, \dot{\boldsymbol{q}}) - J^T(\boldsymbol{q})\boldsymbol{F}. \tag{8}$$

This is a control law of system having feedback loops with respect to $\boldsymbol{q}, \dot{\boldsymbol{q}}, \boldsymbol{F}$.

The task of force stabilization can be determined as a guarantee of condition: $\boldsymbol{F}(t) \to \boldsymbol{F}_0(t)$, $t \to \infty$ and the necessary quality transients defined by the differential equation:

$$T\dot{\boldsymbol{e}}_F + \boldsymbol{e}_F = 0, \tag{9}$$

where $\boldsymbol{e}_F(t) = \boldsymbol{F}_0(t) - \boldsymbol{F}(t)$,

T is time constants matrix providing necessary quality transients of forces.

From Eq. (9) we have:

$$T\dot{\boldsymbol{F}} = T\dot{\boldsymbol{F}}_0 + \boldsymbol{e}_F.$$

Integrating we obtain:

$$\boldsymbol{F} = \boldsymbol{F}_0 + \frac{1}{T}\int_{t_0}^{t} \boldsymbol{e}_F(\omega)d\omega. \tag{10}$$

If environment dynamic parameters are known and $m = n$ then one of the control laws of system having feedback loops with respect to $\boldsymbol{q}, \dot{\boldsymbol{q}}, \boldsymbol{F}$ can be the following:

$$\boldsymbol{\tau} = H(\boldsymbol{q})M^{-1}(\boldsymbol{q})[-\mathbf{L}(\boldsymbol{q}, \dot{\boldsymbol{q}}) - S^T(\boldsymbol{q})(\boldsymbol{F}_0 + \frac{1}{T}\int_{t_0}^{t} \boldsymbol{e}(\omega)d\omega)] + h(\boldsymbol{q}, \dot{\boldsymbol{q}}) - J^T(\boldsymbol{q})\boldsymbol{F}.$$

$$\tag{11}$$

If $m < n$, then it is proposed to part the vector q into two subvectors:

$$q^{(1)} \in R^{n-m} \text{ and } q^{(2)} \in R^m, \; q = \begin{pmatrix} q^{(1)} \\ q^{(2)} \end{pmatrix}, \quad (12)$$

so that

$$M(\mathbf{q})\mathbf{q} = M_1\left(q^{(1)}\right)q^{(1)} + M_2\left(q^{(2)}\right)q^{(2)}, \quad (13)$$

where $M_1(q) \; \varepsilon \; R^{m \times (n-m)}$ and $M_2(q) \; \varepsilon \; R^{m \times m}$ are submatrix of matrix $M(q)$.

In this case, when $m < n$, the requirement $F(t) \to F_0(t)$ can be guarantee only for m robot degrees of freedom with respect to coordinates $q_0^{(2)}(t)$. So it is necessary to have the following conditions:

$$q^{(1)}(t) \to q_0^{(1)}(t), \; \dot{q}^{(1)}(t) \to \dot{q}_0^{(1)}(t), \; t \to \infty. \quad (14)$$

These conditions must be performed to guarantee the necessary quality transients of coordinates $q^{(1)}(t)$, determined by the differential equation:

$$\ddot{e}_{q1} + k_1\dot{e}_{q1} + k_2 e_{q1} = 0, \quad (15)$$

where $e_{q1} = q_0^{(1)}(t) - q^{(1)}(t)$, k_1 and k_2 are $n\text{-}m \times n\text{-}m$ matrix guaranteeing the necessary quality transients.

We also assume the transients $F(t)$ are defined by the following model:

$$\frac{1}{T}\dot{\mathbf{e}}_F + \mathbf{e}_F = 0 \text{ and } \mathbf{F} = \mathbf{F}_0 + \frac{1}{T}\int_{t_0}^{t} e_F(\omega)d\omega. \quad (16)$$

Let us introduce the notation:

$$\mathbf{W}(\mathbf{q},\dot{\mathbf{q}},t,\mathbf{F}) = -M_2^{-1}(\mathbf{q})[\mathbf{L}(\mathbf{q},\dot{\mathbf{q}}) + S^T(\mathbf{q})\mathbf{F} + M_1(\mathbf{q})(\ddot{\mathbf{q}}_1^0 + k_1\dot{\mathbf{e}}_{q1} + k_2\mathbf{e}_{q1})], \quad (17)$$

$$\ddot{\mathbf{q}}_c(\mathbf{F}) = \begin{pmatrix} \ddot{\mathbf{q}}_0^{(1)} + k_1\dot{\mathbf{e}}_{q1} + k_2\mathbf{e}_{q1} \\ W(\mathbf{q},\dot{\mathbf{q}}, t, \mathbf{F}) \end{pmatrix}. \quad (18)$$

We have the following equations of robot and environment:

$$H(\mathbf{q})\ddot{\mathbf{q}}_c(F) + \mathbf{h}(\mathbf{q},\dot{\mathbf{q}}) = \boldsymbol{\tau} + J^T(\mathbf{q})\left(\mathbf{F}_0 + \frac{1}{T}\int_{t_0}^{t} e_F(\omega)d\omega\right), \quad (19)$$

$$M(\boldsymbol{q})\,\ddot{\mathbf{q}}_c + \mathbf{L}(\boldsymbol{q}, \dot{\boldsymbol{q}}) = -S^T(\boldsymbol{q})\left(\mathbf{F}_0 + \frac{1}{T}\int\limits_{t_0}^{t} \mathbf{e}_F(\omega)d\omega\right). \qquad (20)$$

Performing algebraic transformations on matrices we find the control law:

$$\boldsymbol{\tau} = H(\boldsymbol{q})\,\ddot{\mathbf{q}}_c(\mathbf{F}) + h(\boldsymbol{q}, \dot{\boldsymbol{q}}) - J^T(\boldsymbol{q})\left(\mathbf{F}_0 + \frac{1}{T}\int\limits_{t_0}^{t} \mathbf{e}_F(\omega)d\omega\right). \qquad (21)$$

This is one of the control laws of system having feedback loops with respect to $\boldsymbol{q}, \dot{\boldsymbol{q}}, \mathbf{F}$ and integral of the force deviation $\boldsymbol{e}_F$. Let us consider the next chapter the ability to control medical robot using proposed control law.

4 Control of Massage Robot Interacting with the Dynamic Soft Tissue

Let us consider the control of robot interacting with inertia soft tissue. As well as robot with press motion on soft tissue can be modeled by one-drive robot, the robot with shear motion of soft tissue can be modeled by two-drive robot (Fig. 2).

In this task the position/force control aim consists in realization of movement along x axis with assigned constant speed while providing assigned force along y axis.

On Fig. 2 the following designations are introduced: τ_x and τ_y are the input control, F_x and F_y are resistance forces of soft tissue in directions axes x and y.

$$\begin{aligned} F_x &= \mu \cdot \dot{x} + f \cdot F_y \cdot \text{sgn}\dot{x} \\ F_y &= m_y \ddot{y} + \mu \cdot \dot{y} + k \cdot y, \end{aligned} \qquad (22)$$

where k is soft tissue elasticity coefficient, μ is soft tissue viscosity coefficient, f is coefficient of friction of the robot tool relatively soft tissue. The mass m_y is soft tissue part which characterizes dynamic properties of soft tissue in transient process of robot interaction with soft tissue. If the transition process is close to the aperiodic one with response time T then $m_y = k \cdot T^2$. If for soft tissue $k = 1000$ N/m and $T = 0.1$ s, then $m_y = 0.1$ kg. Let us introduce the following vectors and matrix calculated for this example:

Fig. 2 The scheme of planar robot interacting with soft tissue
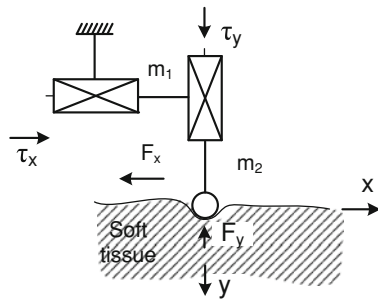
$$\mathbf{q} = \begin{pmatrix} x \\ y \end{pmatrix}, \; H(q) = \begin{pmatrix} m_1 + m_2 & 0 \\ 0 & m_2 \end{pmatrix}, \; \mathbf{h}(q,\dot{q}) = \begin{pmatrix} \mu \cdot \dot{x} \\ 0 \end{pmatrix}, \; \mathbf{L}(q,\dot{q}) = \begin{pmatrix} 0 \\ k \cdot y \end{pmatrix},$$

$$J^T(q) = \begin{pmatrix} -f \cdot \mathrm{sgn}\dot{x} & 0 \\ 0 & -1 \end{pmatrix}, \; S^T(q) = \begin{pmatrix} 0 & 0 \\ 0 & 1 \end{pmatrix}, \; \mathbf{F} = \begin{pmatrix} F_y \\ F_y \end{pmatrix}.$$

Then the robot control laws are as follows:

$$\tau_x = (m_1 + m_2)(k_1 \dot{e}_x + k_2 e_x) + \mu \cdot \dot{x} + f \cdot \left(F_0 + \frac{1}{T} \int_{t_0}^{t} e_F(\omega)d\omega \right) \cdot \mathrm{sgn}\dot{x}, \quad (23)$$

$$\tau_y = \left(\frac{m_2}{m_y} + 1 \right) \left(F_0 + \frac{1}{T} \int_{t_0}^{t} e_F(\omega)d\omega \right) + \frac{m_2}{m_y}(\mu \cdot \dot{y} + k \cdot y). \quad (24)$$

The control laws take into account the parameters of the manipulator and soft tissue, suggest feedbacks loops with respect to $q, \dot{q}, \mathbf{F}$ and integral of the force, that allows identify robot controller structure.

Measurement and the introduction in control law changing soft tissues parameters such as m_y, k, μ, f are problematic in the general case. These are tasks of adaptive position/force control.

The simplified model of robot interacting with soft tissues in tool direction axis is considered in [4]. The robot performing massage and extremities movement techniques has been developed at Moscow State Industrial University. The force module containing a strain sensor is mounted on the end link. The position/force control with force training is implemented to expand possibilities of the standard robot [4].

5 Conclusion

The robots for restorative medicine should have position/force control and consider features of the environment with which they interact. The position/force control taking into account soft tissue dynamics is necessary for robot control in fine massage techniques, speed methods, for example for vibration and impulse mobilization massage techniques, especially during the deformation of massive areas of the body. The research results allowed identifying the structure of the robot controller. The experimental investigations of soft tissues and extremities properties and adaptive position/force control development are required.

References

1. Vukobratovic, M., Surdilovic, D., Ecalo, Y., Katic, D.: Dynamics and robust control of robot—environment interaction. Monograph series in the World scientific publishing under the title «New Frontiers in Robotics». World Scientific Publishing Company, Singapore (2009)
2. Golovin, V.: Robot for massage. In: Proceedings of JARP, 2nd Workshop on Medical Robotics. Heidelberg, (1997)
3. Jones, K.C., Du, W.: Development a massage robot for medical therapy. In: Proceedings of the IEEE/ASME International Conference on Advanced Intelligent Mechatronics (AIM'03), p. 1096–110. Kobe, 23–26 July 2003
4. Golovin, V., Zhuravlev, V., Arkhipov, M.: Robotics in Restorative Medicine: Robots for Mechanotherapy. p. 280. LAP LAMBERT Academic Publishing GmbH & Co. KG, Saarbrücken (2012)
5. Timanin, E., Eremin, E.: Mechanical impedance of biological soft tissues: possible models. Russian J. Biomech. **3**(4), 78–86 (1999)

Biomimicking a Brain-Map Based BCF Mode Carangiform Swimming Behaviour in a Robotic-Fish Underwater Vehicle

Abhra Roy Chowdhury and S. K. Panda

Abstract The objective of this paper is to biomimic a rectilinear swimming behaviour propulsion mechanism of a carangiform robotic fish with impressive speeds and show its exceptional characteristics in the fluid environment. Major kinematic parameters analysed from Lighthill (LH) mathematical model are chosen as major parameters to be adapted. Parameter information is drawn from a brain map similar to fish memory. Based on an environment based error signal robotic fish selects the proper parameter/s value showing adaptive behaviour. A DES methodology has been used to model the brain-kinematic-map, then integrated with a set-point control to track the brain map generated reference command for fish–tail undulation. Parameter adaptation for the three parameters have been shown to successfully emulate fish swimming. Joint-position tracking results are found to be satisfactory as the error converges in quick time.

1 Introduction

Considering the propulsive features of existing fish modes [1], a novel propulsive mechanism that integrates 2-joint, 3-link body caudal fin *BCF* carangiform fish [1, 2]—like swimming with modular links and fin movements has been proposed [2]. We demonstrate that fishes use an alternative strategy for rectilinear swimming across large distances over impressive speed, the combination of the kinematic variables [1, 2] such as caudal amplitude (CA), propulsive wavelength (PW) and tail-beat frequency (TBF) on the robotic fish can reveal the way fishes manage

A. R. Chowdhury (✉) · S. K. Panda
National University of Singapore, Engineering Drive 3, Singapore, Singapore
e-mail: abhra.roychowdhury@nus.edu.sg

to energy efficient swimming. Kinematic studies [1] and experimental results [2] have shown that most carangiform fishes are believed to swim by creating a trailing-edge vortex that remains attached to the caudal-fin tail as it translates through a stroke. Nearly every vertebrate including carangiform fishes sensory system consists of multiple brain maps [3]. Each map has many neuron populations with distinct physiological traits and found to handling different sensory kinematic parameters [1, 2]. Each of the kinematic parameter correspond to a stream of information that are stimulated to be combined or modulated across these brain maps to evoke the adaptive behavior in response to a changing stimulus. The two significant parameters that are varied to adapt these signals are their TBF and CA. These parameters when combined in a unique way result in different body waves physiologically reflected in the overall fish swimming.

Various underwater swimming robots with neuro-muscular pattern signals [3] are studied and implemented in many other research papers to obtain different swimming behaviors [4] have been reported in literature. The research proposed a neuromechanical model implementation of pattern generators for gait modulation [3, 5] through velocity and direction in an amphibious salamander robot [3]. Swimming behaviour is seen to be dominated by kinematic parameters like TBF and/or CA. These have also been used as control variables to regulate the speed [1, 2, 6]. State machine [7] based gait transition is used to define neurological systems in biology as state transitions can realize gait transition successfully [5]. A Smooth gait transition of a robotic fish swimming motion using a FSM based method has been proposed [6]. Gait transition realization from forward swimming to turning by a combination of time and event. A temporal FSM based gait transition method was investigated for a quadruped robot [8]. The locomotion gait involves event enforcing and synchronization successfully.

2 System Model

The dynamic equations of the 6 degree of freedom (DoF) robot are obtained using, the Lagrange-Euler formulation [9]. Therefore, the vehicle's three translational and three rotational motions derived from the momentum conservation laws defined in usual notation [10] are expressed as a condensed non-linear equations of motion in earth fixed coordinate (ve):

$$M_{ve}(q,\eta,\zeta)\ddot{\xi} + C_{ve}(q,\eta,\zeta)\dot{\xi} + D_{ve}(q,\eta,\zeta)\dot{\xi} + g_{ve}(q,\eta) = F_{[ve]} \qquad (1)$$

where $\xi = [\eta^T, x_t^T]^T$ M_{ve} is vehicle inertia matrix including the added inertia, C_{ve} is Coriolis-centripetal matrix, D_{ve} is damping (hydrodynamic) matrix, g_{ve} is gravity matrix, F_{ve} is propulsion force vector, η is position and orientation vector [x, y, z, ϕ, θ, ψ] in earth fixed coordinate and v is linear and angular velocity vector [u, v, w, p, q, r] and q is joint angle variable in body fixed coordinate [9, 10].

2.1 Lighthill Equation and Kinematic Parameters

Lighthill [8] in his *slender body theory* reported about the inviscid flow around a slender fish whose cross-section varies along its length. It results into swimming movements in a direction transverse to its direction of undulatory caudal tail movement. Supporting this flow value conditions the motion of a standing wave displacement vector $y(x, t)$ was introduced as a empirical expression. The fish body is represented by a planar spline curve [2, 8] due to the propulsive wave behavior as lateral curvature in spine and musculature.

$$y_{body}(x, t) = [(c_1 x + c_2 x^2)][sin(kx + \omega t)] \tag{2}$$

where y_{body} is the transverse displacement of body, x is the displacement along main axis, k is the body wave number ($k = 2\pi/\lambda$), λ is the body propulsive wave (PW), c_1 and c_2 are linear and quadratic wave amplitude envelope respectively (CA). ω is the tail-beat frequency (TBF). Lateral velocity $w(x, t)$ [2] resulting due to it can be written as

$$w(x, t) = \frac{\partial h}{\partial t} + U\left(\frac{\partial h}{\partial x}\right) \tag{3}$$

where U is the mean forward speed.

3 DES Based Brain Map and Control Architecture

Translating a biology based behavior of a vertebrate [3] fish to a mobile robot is challenging. Present system is built on a behavior-based approach called subsumption architecture [11] which is well braced by a vast ethology community. Behaviors [11], are organized in layers made up of individual finite state machine according to a predefined priority of action. This structure has an edge to allow robustness to perturbations and shorter reaction times in a complex environment. It is similar to the present set-point control system integrated with the DES aided behaviour model to adapt a real-time dynamic environment with only joint-position sensing capabilities. Different swimming behaviours are shown by the biological fish in response to different stimuli [3] needs arising due to food search, predator escape, successful reproduction etc. [1]. Each of these different life motives are supported by kinematic priorities follow actions like straight swimming, turning (C turn, S turn), sudden start/stop and so on [6]. A DES [7] model of forward swimming behaviour is presented here shown in Fig. 1.

These correspond to a stream of information that are stimulated to be combined or modulated across the brain maps to evoke the adaptive behavior in response to a changing stimulus. We emulate these kinematic changes in the robotic fish by
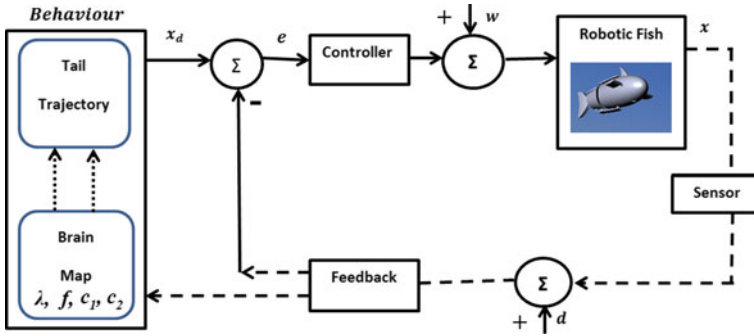
Fig. 1 Block diagram of Kinematic brain-map based Behaviour Control scheme
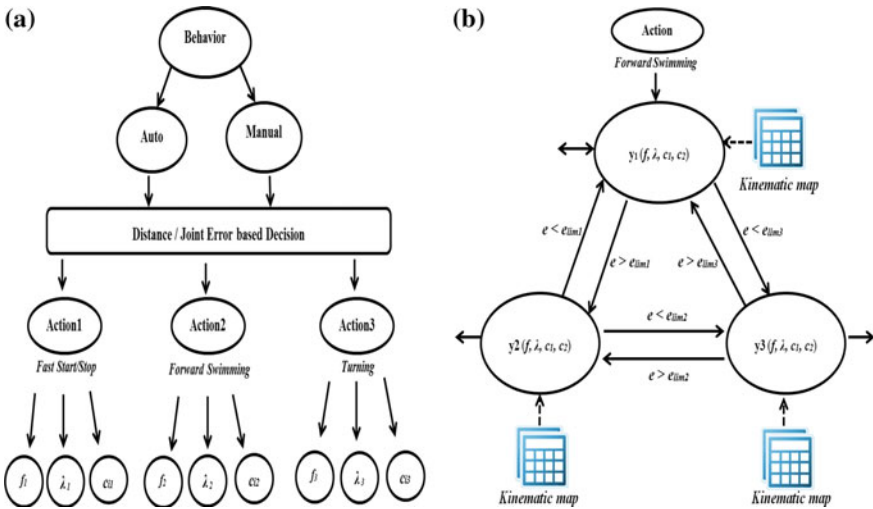
Fig. 2 Behaviour architecture using DES model. **a** Sub-sumption architecture automata. **b** DES model of error based action selection

modulating the major kinematic parameters [1, 2] TBF(ω), PW(λ) and CA (c_1, c_2) based on a priority logic decision. These kinematic parameters values are obtained from open-loop experiments and lie in the operating range of the robot. These values are grouped into distinct look-up tables from which they are accessed based an action or priority state. The logic decision variables are chosen based on a feedback error signal e from joint position sensors (in operational space). The graph model is shown below.

The coordination of the brain-map system can be modeled as a discrete-event system (DES) [7] occurring asynchronously over time. DES behaviour of stimuli selection is realized by Finite State Machines (FSMs). They represent a centralized mathematical behavior sub-sumption model. As shown in Fig. 2a it has been used

Fig. 3 Error based action
selection algorithm

Algorithm 1 Error Based Parameter Switching

Require: $\mid e(t)_{ub} - e(t)_{lb} \mid \leq e_{lim}$
Ensure: $e = y_{sp} - y$
1:   $y \leftarrow 1$
2:   **if** $\mid (e - e_s) \mid \leq e_{lim}$ **then**
3:     $e_s = e$
4:     $f = f_1$
5:   **else if** $\mid (e - e_s) \mid \geq e_{lim}$ **then**
6:     $e_s = e$
7:     $f = f_2$
8:   **else if** $e_{lim} \leq \mid (e - e_s) \mid \leq e_{lim}$ **then**
9:     $e_s = e$
10:    $f = f_3$
11:     $where y = (c_1 x_i + c_2 x_i^2) sin(kx + 2\pi f_i t_i)$
12: **end if**

to describe a neurological system. DES based brain kinematic-map model has been used to design and analyze the coordination of the distinct environment based stimuli corresponding to different major kinematic variables. Each stimulus is represented by a state. Based on a purpose (food, predator escape etc.) is tagged to a kinematic parameter or a combination of parameters mention in Lighthill equation [2]. Switching action takes place between two states as the biological species use memory maps in their brain [3] to use a data (pre-recorded or experience) for a present event. Here, we try to emulate the same brain mechanism.

3.1 Error Based Action Selection

We have shown to implement the action based on a outer feedback loop error signal (position or velocity) to the DES model. In uncertain environment, a feedback error signal coming to the PID controller is used by the brain map to decide state priority. This approach is environment based as the feedback signal from operational space helps to select/switch a transition to another suitable action state. As mentioned in the adaptation algorithm 1 in Fig. 2b and depicted in Fig. 3, we select a change in state only when the error bound is greater or less than a given limit to achieve a desired speed profile. Adaptation here refers to select the apt kinematic parameter corresponding to the suitable environment based stimuli.

It is necessary to identify set of states (including an initial state), set of events, and transition structure of system based on kinematic parameters. The robotic fish behaviour is modeled as a DES which specifies set of states, set of events and the transition function of the system [7]. Formally, a DES is represented by an automaton or generator. The sequence of events called a string is formed by concatenating events. Events are function of LH kinematic parameters and event transition is based on a error function algorithm given in Fig. 3. The generator is deterministic in the sense that if an event occurs the transition leads the system to unique system state.

4 Kinematic Behaviour Based Tracking Control

## 4.1 Tail Beat Frequency and Phase Shift

This parameter adaptation is important because TBF, PW, CA play important role in generating thrust created by the undulating body wave [1, 2, 8]. For example in the case of TBF, using one value of constant TBF will use a level of energy and control signal whereas if the adpatation/modulation concept is brought into existence it allows choosing distinct values at different time periods based on environment feedback stimuli. That means lesser energy used for control effort for a given distance. The forward swimming velocity increases with the raise of TBF. Further after reaching a peak velocity at the given frequency a descending pattern follows. This results embodies the fact that efficient swimming speed is achieved only at a given frequency further increasing which will result into a waste of energy. As shown in Fig. 4a we took three intervals for $u = 0.12$ m/s at $f = 0.1$ Hz, $u = 0.115$ m/s at $f = 0.64$ Hz) and $u_{max} = 0.138$ m/s at $f = 0.33$ Hz for the kinematic profile obtained for the robot [2] at 1.1BL/s (body length per second). Figure 4d shows the change in phase angle at the changing TBF parameters. In this paper, forward velocity, u results were obtained by varying the oscillating frequency or the tail-beat frequency parameter fixed at different values of wavelength and amplitude. Other parameters are kept at $c_1 = 0.002$, $c_2 = 0.00835$, and $\lambda = 0.5$.

4.2 Caudal Amplitude Shift

The existing second order amplitude envelop is chosen to produce three body-waves by three distinct values of c_1 and c_2 shown in Fig. 4b. In practice, oscillatory-amplitude-based speed control method adjusts the transverse movement at a constant oscillating frequency (at $\lambda = 1.4$ m and $f = 0.5$) to change the changed thrust and swimming speed. The variation of these two combined kinematic parameters TBF and CA is shown in Fig. 4d using the brain-kinematic map information and DES switching logic based on tail position error. Both kinematic parameters change at different time-sequences like in real fish in real-time environment to generate forward propulsion. The overall improvement in path traveled using the Lighthill's algorithm is over 14 % [2]. The choice of the CA between two speed limits also depend on TBF at a fixed wavelength [2]. Joint Position tracking and its tracking error signal response for the control scheme are depicted in Fig. 4e, f respectively with respect to a simple trajectory reference signal to yield satisfactory convergence rates. Controller tuning algorithm and control methodology improvement will be explored in future. The above simulation results verify the real time carangiform fish kinematic behaviour studies reported by Dewar [1, 2] biomimicked in a robotic fish within the framework of Lighthill theory [8].
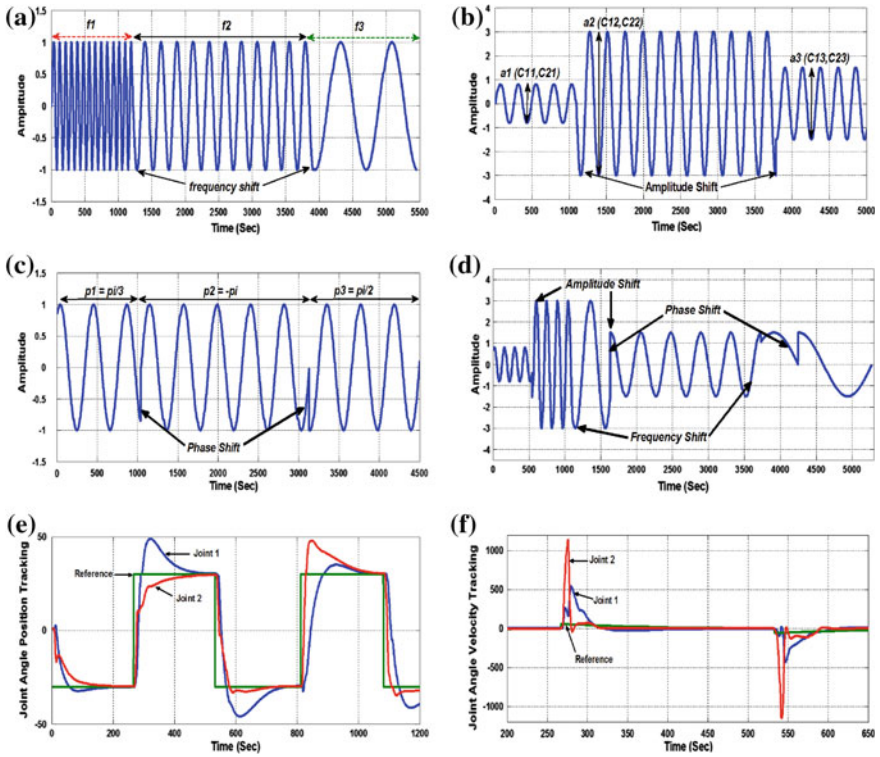
Fig. 4 Kinematic parameter adaptation and joint position tracking. **a** TBF shift. **b** CA shift. **c** Phase shift. **d** TBF and CA sync shift. **e** Joint angle. **f** Joint angle velocity
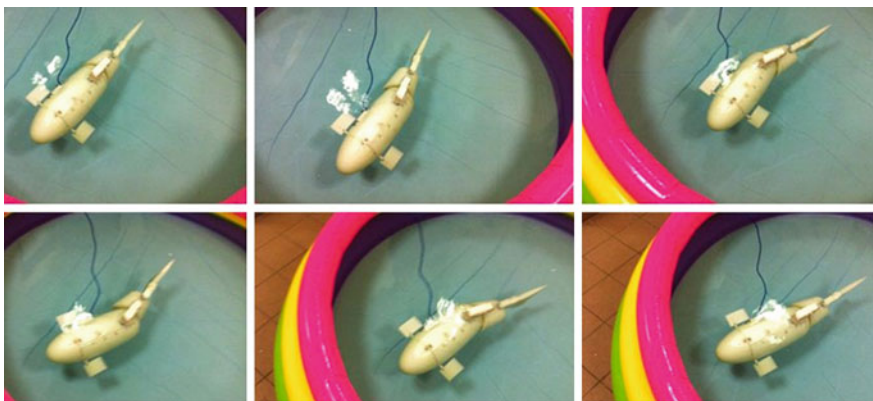
Fig. 5 Robotic fish swimming modes

Robotic fish project with different swimming modes is shown in Fig. 5. Its implementation is carried out in MATLAB and Simulink. The yaw-axis servo-motor is a Hitec HS-5646WP (11.3 kg cm/6 V) used in all the joints. Arduino-Uno with ATMEGA328P serves as central processing unit for the robotic fish. The mechanical CAD design and animation has been implemented with the help of the Solidworks and MATLAB Sim-Mechanics, VRML (3D motion).

5 Conclusions

Present research work translates biology based behaviour of a vertebrate fish to a mobile robot in a dynamic environment. A DES based brain map model consisting of major kinematic parameters information is made. Integrating it with a set-point control methodology demonstrates behaviour stimuli based adaptation in a robot. Joint position tracking signal shows a satisfactory convergence rate. The built prototype is a 74 cm long, weighs 4.5 kg, BCF (Body Caudal Fin) mode 6 DOF fishlike underwater robot with a horizontal caudal fin (tail).

References

1. Dewar, H., Graham, J.: Studies of Tropical Tuna Swimming Performance in a Large Water Tunnel—Kinematics. J. Exp. Biol. **192**(1), 45–59 (1994) (CA, pp. 1–9, 1996)
2. Abhra, R.C., Prasad, B., Vishwanathan, V., Kumar, R., Panda, S.K.: Implementation of a BCF mode bio-mimetic robotic fish underwater vehicle based on Lighthill mathematical model. In: 2012 IEEE ICROS International Conference on Control, Automation and Systems, Korea, pp. 437–442
3. Metzner, W., Juranek, J.: A sensory brain map for each behavior? Proc. Natl. Acad. Sci. U.S.A. **94**(26), 14798–14803 (1997)
4. Righetti, L., Ijspeert, A.J.: Programmable central pattern generators: an application to biped locomotion control. In: Proceedings of the 2006 IEEE BIOROB, 2006
5. Liu, A., Yu, Z.X., Ge, Z.K.: Gait transition of quadruped robot using time sequence control based on finite-state machine. Mechatron Robot Control Autom Manuf Appl Mech **24**, 2799–2804
6. Wang, M., Yu, J., Tan, M., Zhang, G.: A CPG-based sensory feedback control method for robotic fish locomotion. In: Proceedings of the 30th Chinese Control Conference 22–24 July 2011, Yantai, China (2011)
7. Brandin B.A., Wonham W.M.: Modular supervisory control of timed discrete-event systems. In: Proceedings of the 32nd Conference on Decision and Control San Antonio, Texas Dec 1993 (1993)
8. Lighthill, M.J.: Note on the swimming of slender fish. J. Fluid Mech. **9**, 305317 (1960)
9. Fossen, T.I.: Handbook of Marine Craft Hydrodynamics and Motion Control. Wiley, Hardcover (2011). ISBN 978-1-1199-9149-6, Kindle: avaialble at www.amazon.com

10. Abhra, R.C., Kumar, V., Prasad, B., Kumar, R., Panda, S.K.: Bio-harmonized dynamics model for a biology inspired carangiform robotic fish underwater vehicle. In: Proceedings of 19th IFAC World Congress, vol. 19, Capetown (2014)
11. Rooks, R.A.: How to build complete creatures rather than isolated cognitive simulators. In: Architectures for Intelligence, Conference Proceeding 22nd, Carnegie-Mellon University, Carnegie Symposium on Cognition (1988)

Variable Inertia Muscle Models
for Musculoskeletal Dynamics

Minyeon Han and F. C. Park

Abstract We proposes a general framework for musculoskeletal dynamic simulation that takes into account changes in muscle inertia that occur during movement. We first develop a general shape-varying muscle mass model in which muscle deformations are modeled via linear volume-preserving transformations, and derive a corresponding muscle mass matrix and Jacobian in a Lagrangian setting. A dynamic musculoskeletal model is then constructed, in which each muscle is segmented into multiple segments that are each modeled using our earlier muscle deformation model. To improve computational efficiency, a spline-based dynamics algorithm based on interpolating sampled values of the system mass matrix is developed. Case studies involving planar arms with multiple shape-varying muscles attached demonstrate the feasibility and computational advantages of our proposed method for musculoskeletal modeling and simulation.

Keywords Musculoskeletal simulation · Deformable volumetric muscle model · Riemannian geometry · Geometric interpolation

1 Introduction

Muscles comprise the majority of mass in many body segments. Existing musculoskeletal simulators typically model muscles as rigid bodies, by lumping the muscle mass with its body segment, and then performing a multibody dynamic simulation. Somewhat surprisingly, there has been little previous work on simulation methods that explicitly take into account the changing muscle mass distribution during movement, and the overall effect of these shape-varying muscles on

M. Han · F. C. Park (✉)
Robotics Laboratory, Seoul National University, Seoul 151-744, Korea
e-mail: fcp@snu.ac.kr

rigid body inertias. In recent work with significant implications for musculoskeletal simulation, Pai [1] showed that the traditional approach of lumping the muscle mass with the body segment, and performing a standard rigid body dynamics simulation, can incur considerable errors. In short, as the muscle length varies during movement, the corresponding muscle mass also moves accordingly and clearly affects the overall system inertia. Examining both monoarticular and biarticular muscle models that span a single revolute joint, Pai shows that these errors can be quite large and nonuniform, dependent on both the skeletal posture and joint velocities, and that they will likely not cancel themselves even if, e.g., effects such as soft tissue behavior and muscle wobble are included.

As Pai himself points out, the models used in [1] are of the simplest variety, in which a muscle is modeled as a line and does not take into account the volumetric shape of the muscle. Moreover, given that failure to take into account the effect of muscle masses on system inertia can lead to large errors, even for single joint systems, the consequences for whole-body musculoskeletal dynamic simulation are potentially significant. On the other hand, the computational difficulties in simulating the dynamics of such a high-dimensional, highly constrained multibody system also cannot be ignored. For example, musculoskeletal dynamic simulations are used extensively in designing exercise bicycles and rowing machines, which involve numerous closed chains subject to a variety of contact constraints.

In this paper we extend Pai's mode so that the system inertia correctly reflects the changes in the muscle's length and shape during movement. We assume that shape deformations are volume-preserving, and propose a multisegment muscle model. An interpolation-based, computationally efficient algorithm for approximately integrating the dynamics is also proposed, that respects the intrinsic geometry [2] of system inertias (e.g., symmetric, positive-definite). After briefly reviewing Pai's model, we provide details of our shape-varying muscle model, and a brief overview of our approximate dynamics algorithm, followed by numerical experiments on a simple arm simulation.

2 Shape Varying Muscle Mass Model

2.1 Single Segment Model

In Pai [1] a muscle is modelled as a line segment of uniformly distributed mass along its length, with a total mass of μ_m. Following standard convention the muscle is regarded as a unit actuator whose behavior is determined by its length and time derivative of length. Denote the joint angles of the musculoskeletal system by $\theta \in \mathbb{R}^n$, and let $p \in \mathbb{R}^3$ be a material point of the muscle, parametrized by some intrinsic non-dimensional material coordinate $s \in [0, 1]$ ($s = 0$ at the muscle origin and $s = 1$ at the point of attachment). The value of s is assumed to remain fixed for a given material point even when the muscle stretches. The point velocity $\dot{p}$ is
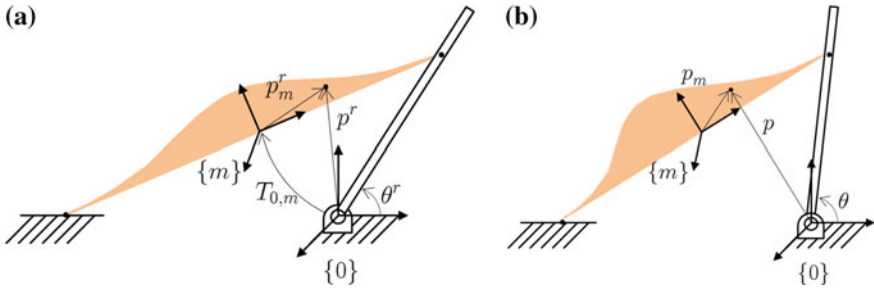
Fig. 1 1-DOF shape varying muscle mass model. **a** Reference state with *joint angle* $= \theta^r$. **b** Deformed state with *joint angle* $= \theta$

assumed to be linearly related to the system's joint velocity $\dot{\theta}$ via the muscle Jacobian $J_m(s)$, as $\dot{p} = J_m(s)\dot{\theta}$. For space reasons we omit the derivation, but the muscle mass matrix $\mathcal{I}_m$ becomes

$$\mathcal{I}_m = \mu_m \int_0^1 J_m(s)^\mathrm{T} J_m(s)\, ds. \tag{1}$$

We now extend Pai's model so that the muscle inertia varies according to both changes in the muscle length and shape deformations. We assume that all shape deformations of the muscle are volume-preserving linear transformations, and that points on the muscle can be expressed as a function of θ. The muscle shape shown in Fig. 1a is taken to be the reference. The frames $\{0\}$ and $\{m\}$ respectively represent the fixed frame and moving muscle frame. To represent the location of a point p^r on the reference muscle in frame $\{0\}$ frame coordinates, the rigid body motion $T_{0,m} \in SE(3)$ describing frame $\{m\}$ relative to $\{0\}$ is needed, together with p_m^r, the description of the muscle point in moving frame $\{m\}$ coordinates. Figure 1b illustrates the displacement of p^r to p as the joint angle is changed from θ^r to θ. In terms of the moving frame $\{b\}$, the reference point $p_m^r \in \mathbb{R}^3$ is displaced to $p_m \in \mathbb{R}^3$ as follows:

$$p_m = T(l)p_m^r, \tag{2}$$

where $T(l)$ is an element of the Special Linear group $SL(3)$ (i.e., the set of 3×3 real matrices of unit determinant), and l is the muscle length divided by the length of the reference muscle.

Now taking into account the joint angle θ, a reference material point p^r on the muscle is then assumed to be deformed via the following 4×4 affine transformation $T(\theta)$:

$$\begin{bmatrix} p \\ 1 \end{bmatrix} = T^A(\theta) \begin{bmatrix} A(l(\theta)) & 0 \\ 0 & 1 \end{bmatrix} \begin{bmatrix} p^r \\ 1 \end{bmatrix}, \tag{3}$$

where $T^A \in SE(3)$ is the earlier $T_{0,m}$ of Fig. 1, and $A(l(\theta)) \in SL(3)$ defines the muscle shape deformation.

We now derive the muscle mass matrix based on the above affine transformation matrix $T(\theta)$. Differentiating Eq. (3) with respect to time, we obtain the muscle Jacobian matrix as follows:

$$\begin{bmatrix} \dot{p} \\ 0 \end{bmatrix} = \begin{bmatrix} \frac{\partial T}{\partial \theta_1} \begin{bmatrix} p^r \\ 1 \end{bmatrix} & \cdots & \frac{\partial T}{\partial \theta_n} \begin{bmatrix} p^r \\ 1 \end{bmatrix} \end{bmatrix} \dot{\theta} \triangleq J_m \dot{\theta}. \tag{4}$$

From above the kinetic energy of the muscle can be written

$$K_m = \frac{1}{2} \int_v \rho \dot{p}^T \dot{p} \, dv \tag{5}$$

where $dv' = \det(T) \, dv$ and ρ is the muscle density. The (i, j) entry of the muscle mass matrix is therefore given by

$$M_{ij} = \text{tr}\left(\rho \frac{\partial T}{\partial \theta_i} \int \begin{bmatrix} p^r \\ 1 \end{bmatrix} \begin{bmatrix} p^r \\ 1 \end{bmatrix}^T dv' \frac{\partial T^T}{\partial \theta_i} \right). \tag{6}$$

From the above we can observe that the mass matrix is defined by the moment of the reference muscle volume, which is fixed, and a partial derivative of $T(\theta)$. The mass matrix can now be straightforwardly calculated from the partial derivatives of $T(\theta)$.

2.2 Multi-Segment Model

Real muscles can assume a variety of shapes during deformation, and it is in practice difficult to model muscle deformations using a single volume-preserving linear transformation. In this subsection we describe a method for dividing a muscle into several segments, and applying a transformation matrix for each segment. We illustrate our method with a three segment muscle model (see Fig. 2) with initial ($s = 0$) and final ($s = 1$) muscle shapes given.

In the figure M_i, m_i, $\{i\}$, and p_i respectively denote the ith muscle segment, a point in M_i, a local coordinate frame attached to M_i, and the position of m_i in the local coordinate frame. We further assume that the muscle is fixed at coordinate frame $\{1\}$ (also the global coordinate frame) and that relative motion between the local frames is linear; for this purpose we assume adjacent local frames are attached to each other via a prismatic joint.
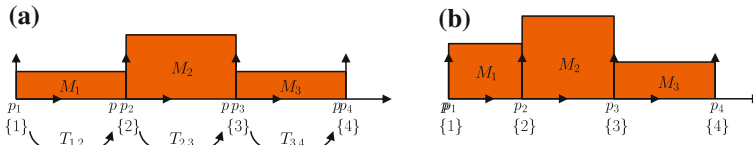
Fig. 2 Muscle shape data **a** $s = 0$ **b** $s = 1$

For space reasons we are unable to show the complete derivation, but we finally obtain the deformation of M_i in global coordinates as follows:

$$\begin{bmatrix} m_i'(s) \\ 1 \end{bmatrix} = \prod_{j=1}^{i-1} T_{j,j+1}(s) \begin{bmatrix} \frac{l_i(s)}{l_i(0)} & 0 & 0 \\ 0 & \frac{l_i(0)}{l_i(s)} & 0 \\ 0 & 0 & 1 \end{bmatrix} \begin{bmatrix} m_i(0) \\ 1 \end{bmatrix}. \tag{7}$$

The total muscle mass matrix can be constructed by combining the mass matrices of each muscle segment as shown above.

3 Dynamics Algorithm

The most direct way to derive the dynamic equations for our musculoskeletal system is to formulate the associated Lagrangian:

$$L(\theta, \dot{\theta}) = \frac{1}{2} \dot{\theta}^{\mathrm{T}} M(\theta) \dot{\theta} - V(\theta), \tag{8}$$

where $\theta \in \mathbb{R}^n$ denotes the joint vector, the first term corresponds to the total kinetic energy of the system, and the second term denotes the total potential energy. The $n \times n$ symmetric positive-definite matrix $M(\theta)$ is denoted the mass matrix. For our musculoskeletal systems, the total kinetic energy is obtained by summing the kinetic energy contributions of each muscle segment. As the shape of the muscle mass varies with the motion, this will influence the kinetic energy of the muscle. Recall also that in our model the muscle mass shape over each segment is determined from the overall muscle length, and from the choice of volume-preserving transformation over the segment. The muscle length is in turn determined by the joint angles; hence, the total kinetic energy can be expressed as a function of the joint vector θ and its derivative $\dot{\theta}$. For similar reasons the total potential energy $V(\theta)$ can also be expressed as a function of θ.

Substituting the above Lagrangian into the Euler-Lagrange equations then leads to the equations of motion. The mass matrix $M(\theta)$ here should not be confused with the usual mass matrix for rigid multibody systems; it involves determining the kinetic energy contributions of each shape-varying muscle mass segment, and its

evaluation is computationally highly intensive. Moreover, the remaining terms in the dynamic equations depend on the derivatives of the mass matrix, making real-time numerical integration of the dynamics extremely difficult. In the next section we describe a method for evaluating the dynamics in real-time, based on a B-spline approximation of the mass matrix.

3.1 Mass Matrix Approximation

Since evaluating the mass matrix $M(\theta)$ for arbitrary values of θ is a highly computationally intensive task, we propose an interpolation-based method, in which $M(\theta)$ is evaluated a priori at uniformly sampled values of θ_i, $i = 1, \ldots, N$, and for arbitary values of θ, $M(\theta)$ is approximated by appropriately interpolating between the two nearest sampled values to θ. For this purpose we require a means of interpolating between two symmetric positive-definite matrices, or two elements of the manifold $\mathcal{P}(n)$. As has been pointed out in the related literature, e.g., [3], ad hoc methods for interpolating between two elements of $\mathcal{P}(n)$ can have the undesirable property of being local coordinate-dependent, and also failing to preserve certain invariant features of $\mathcal{P}(n)$ (for example, given two elements $P_1, P_2 \in \mathcal{P}(n)$ with $\det P_1 = \det P_2$, one would like for an interpolating curve $P(t)$ between P_1 and P_2 to preserve the determinant).

   The Riemannian geometry of $\mathcal{P}(n)$ has been extensively studied in the literature, e.g., [3, 4], and we refer the reader to the literature for details. One convenient means of interpolating on $\mathcal{P}(n)$ using the Euclidean space notion of B-splines is as follows. Suppose we wish to determine $M \in \mathcal{P}(n)$ by appropriately interpolating among the control points $C_i \in \mathcal{P}(n)$ that are nearest to M. Then

$$M(\theta) = \arg \min_{M} \sum_i w_i(\theta) \operatorname{dist}(M, C_i)^2, \tag{9}$$

where w_i denotes a B-spline basis function, and $\operatorname{dist}(\cdot, \cdot)$ denotes a distance metric on $\mathcal{P}(n)$. Various distance metrics for $\mathcal{P}(n)$ are introduced in [5].

4 Experiments

In order to test the accuracy of our approximate dynamics algorithm, we consider a two-DOF planar closed chain system that structurally resembles the musculo-skeletal structure of a planar arm (see Fig. 3). For convenience we assume all the link lengths and masses are of value 1. The rigid body dynamic equations are derived analytically, in particular the mass matrix $M(\theta)$, and the results are compared with those obtained from our approximate dynamics algorithm.

Fig. 3 Three-bar 2-DOF
linkage
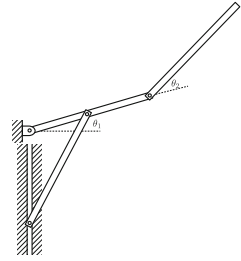
We first extract 100 mass matrix samples (essentially 100 points in $P(n)$), by uniformly sampling along θ_1 and θ_2 in ten intervals, at $\frac{\pi}{5}$ radians per interval. We then determine 100 B-spline control points such that the B-spline mass matrix approximation (essentially, a two-dimensional surface in $P(n)$ parametrized by θ_1 and θ_2) passes through these 100 sampled points in $P(n)$. We then randomly generate 1,000 samples of (θ_1, θ_2), and compare the values of the approximated mass matrix at these samples with the actual mass matrix. We also generate random samples of $\dot{\theta}$, and compare the values of the approximated Coriolis forces with the actual Coriolis forces as determined from the analytical equations of motion.

In order to compare the accuracy of approximated values, we define the error ratios for the mass matrix and Coriolis force values respectively as

$$e_M = \frac{\|M(\theta) - \tilde{M}(\theta)\|}{\|M(\theta)\|} \tag{10}$$

$$e_C = \frac{\|C(\theta, \dot{\theta})\dot{\theta} - \tilde{C}(\theta, \dot{\theta})\dot{\theta}\|}{\|C(\theta, \dot{\theta})\dot{\theta}\|}. \tag{11}$$

Figure 4 shows the histogram for the error ratios.

In the case of the mass matrix computations, the average of the error ratio is less than 0.1 %, and the maximum value is less than 1 %. Even if we use only 100 samples, the mass matrix can be reconstructed quite accurately. The error ratios for the Coriolis forces are somewhat larger, but these originate from the scale of the Coriolis terms; the absolute error still remains small because the Coriolis forces themselves are comparatively small.

The accuracy of the approximate dynamics can be further improved by increasing the sample size. To determine the extent of the improvements, we quadruple the number of samples by decreasing by half the sampling interval along each of the two joints θ_1 and θ_2. A comparison of the results obtained for 400 samples with those for 100 samples is given in Table 1; the improvements in accuracy are clearly evident. Moreover, the sample size does not affect computational performance during the reconstruction process; this process requires only the weighted average of a fixed number of control points, which in turn depends on the degrees of freedom of the system and the degree of the B-spline, and not on the scale of the control points.
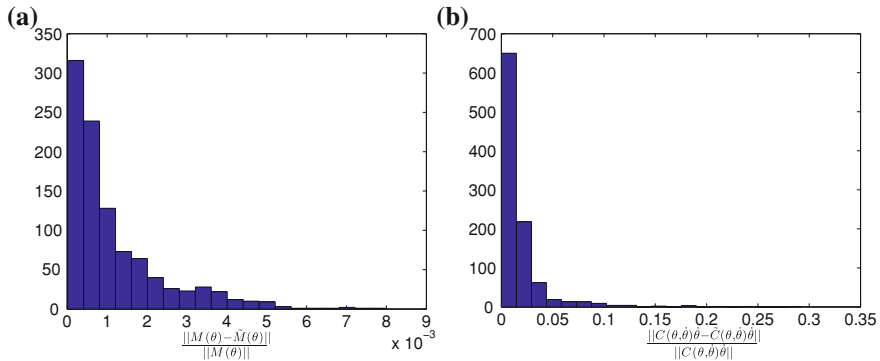
Fig. 4 Error ratio histogram using intrinsic Riemannian metric. **a** Mass matrix error ratio. **b** Coriolis term error ratio

Table 1 Error ratio from 400 mass matrices interpolation

Metric	AVG(e_M) (%)	MAX(e_M) (%)	AVG(e_C) (%)	MAX(e_C) (%)
Cholesky metric	0.0034	0.0316	0.1515	11.7976
Log-Euclidean metric	0.0051	0.0519	0.2098	6.9240
Riemmanian metric	0.0056	0.0568	0.2611	7.7334

5 Conclusion

In this paper we have proposed a shape-varying muscle mass model for musculoskeletal simulation. In contrast to existing algorithms that assumes the muscle as a rigid body to be lumped with the nearest link, our model takes into account the changes in inertia that occur during movement, as a result of the time-varying changes in the muscle mass distribution. We show that our model can be applied to various muscle shapes including fusiform and convergent muscles. Using our model and a newly proposed approximate dynamics program, it is possible to perform more accurate dynamic simulations of musculoskeletal model, and also perform, e.g., motion optimization in a computationally tractable way.

We emphasize that the shape varying muscle model employed in our work is but one possible formulation, and that several variations are possible, e.g., allowing for more general affine transformations, rather than volume-preserving linear transformations, to describe the muscle deformations. We do not make any claims about the biomechanical accuracy of the explicit choices made in our model. Rather, our intent is to provide a general and computationally efficient dynamic model that takes into account muscle shapes and their effect on inertias, and offers enough flexibility to adjust any parameter values and mapping choices so as to best fit any available muscle data while being computationally tractable and accurate to some user-specified resolution.

References

1. Pai, D.K.: Muscle mass in musculoskeletal models. J. Biomech. **43**(11), 2093–2098 (2010)
2. Muller, A., Maisser, P.: Lie group formulation of kinematics and dynamics of constrained MBS and its application to analytical mechanics. Multibody Sys. Dyn. **9**(4), 311–352 (2003)
3. Fletcher, P.T., et al.: Riemannian geometry for the statistical analysis of diffusion tensor data. Sig. Process. **87**(2), 250–262 (2007)
4. Smith, S.T.: Covariance, subspace, and intrinsic Cramer-Rao bounds. IEEE Trans. Signal Process. **53**(5), 1610–1630 (2005)
5. Dryden, I.L., Koloydenko, A., Zhou, D.: Non-Euclidean statistics for covariance matrices, with applications to diffusion tensor imaging. Ann. Appl. Stat. **3**(3), 1102–1123 (2009)

UGV Epi.q-Mod

**Giuseppe Quaglia, Luca G. Butera, Emanuele Chiapello
and Luca Bruzzone**

Abstract This paper presents the functional design and the related detailed mechanical design embodiment of UGV Epi.q-Mod, which is a new version of the Unmanned ground vehicles Epi.q. UGVs Epi.q are mobile robots used for surveillance/reconnaissance/transport operations and they are based on a hybrid wheeled-legged locomotion system. The locomotion system consists of three-wheeled units with epicyclical mechanism capable of switching between wheeled and legged locomotion even without an active control intervention, depending on the dynamic condition of the vehicle. The main characteristic of this robot is the application of the modular approach that allows to generate different architectures based on functional requirements.

Keywords Unmanned ground vehicle · Mobile robot · Hybrid locomotion · Modular UGV

G. Quaglia (✉) · L. G. Butera · E. Chiapello
Department of Mechanical and Aerospace Engineering, Politecnico di Torino, Turin, Italy
e-mail: giuseppe.quaglia@polito.it

L. G. Butera
e-mail: luca.butera@polito.it

E. Chiapello
e-mail: emanuele.chiapello@studenti.polito.it

L. Bruzzone
Department of Mechanics and Design of Machines (DIMEC), University of Genova,
Genoa, Italy
e-mail: bruzzone@dimec.unige.it

1 Introduction

An Unmanned Ground Vehicle (UGV) is defined as any piece of mechanized equipment that moves across the surface of the ground and serves as a means for carrying or transporting something, but explicitly does not carry a human being [5].

The use of UGVs is growing very rapidly in several fields because they have many potential applications and the demand for them is ever increasing. The exploitation of UGVs ranges from planetary exploration, police operations, military operations such as reconnaissance, surveillance and target acquisition, industrial and home usage, to special intervention tasks such as rescue operations.

UGVs are used also in hazardous sites and this use is gaining popularity because they can be sent ahead or in place of humans, act on the surroundings with a manipulator arm or other active means attached to an arm, collect data about the environment, and send it back to the operator without risks for humans. UGVs are classified based upon their main characteristics, such as locomotion mode, control strategy and intended operating area.

This paper presents the functional and the embodiment design of UGV Epi.q-Mod, and is organized as follows. Section 2 introduces the UGV operational and technical requirements while the design methodology of the UGV Epi.q family is showed in Sect. 3. Section 4 describes the functional principle of the robot locomotion unit. The new modular architecture and the embodiment design of the UGVEpi.q-Mod are discussed in Sect. 5, whereas the last section, Sect. 6, presents the conclusions and the future developments of the robot.

2 UGV Operational and Technical Requirements

Currently many UGV architectures are presented by industry, research institutes and universities and each vehicle is designed in order to fulfill specific operational and technical requirements.

An important field of application is military application, however UGVs are used in others important operational fields like security and surveillance, for monitoring hazardous locations, agriculture and planetary exploration.

The category of UGVs covers a wide range of capabilities and degrees of autonomy, but in general an unmanned ground vehicle, and in particular a tele-operated or autonomous ground vehicle, has to fulfill the following technological requirements:

- *Mobility*: this is the term used to describe the ability of the vehicle to travel across an uneven terrain without any information from sensors or others devices. In literature the mobility of a UGV is often expressed in terms of the ratio between the size of an obstacle (both negative and positive) and the height of the vehicle.
- *Energy*: One of the most important key factors of a UGV is the energy source, and especially the rate at which it can be utilized. The power train system must be

able to support mobility and the others technical requirements in the most efficient way.

- *Recognition*: Sensors, computers, and software modules are used for the fundamental UGV capability that is to acquire knowledge about the working environment and the internal status of the robot. There is a broad variety of sensors that can be used on UGVs. There are sensors used for a simple measuring and others for a complex measuring in order to acquire information about environmental characteristics and the vehicle's motion.
- *Human–robot interaction*: HRI is the interdisciplinary study of interaction dynamics between humans and robots. In particular the human–computer interfaces are important because they allow to manage the vehicle in a simpler way and how humans will interact with a team of robots.
- *Communication*: This covers how a specific set of information is transported from one electronic device to another. A teleoperated vehicle, for example, needs a very high-bandwidth, low-latency and high-reliability communication system because any delay in the communication system can generate a problem during the supervision of the vehicle.

3 UGV Epi.q Family

In general, on the basis of their locomotion systems, mobile robots can be classified in wheeled [7], tracked [6] and legged [1]. Moreover, hybrid solutions with various combinations of wheels, tracks and legs are possible. An overview of robotic locomotion systems is outlined in [3].

UGVs Epi.q are vehicles that can be used for surveillance and reconnaissance operations. The main characteristic of this robot family is its hybrid wheeled-legged locomotion system, even if each robot is different from the others due to its peculiarities, that influence its performance [13]. The locomotion system consists of three-wheeled units with an epicyclical mechanism capable of switching between wheeled and legged locomotion without an active control intervention, depending on the dynamic condition of the vehicle.

The first prototype was Epi.q-1 [9], designed and built by a team from Politecnico di Torino—Department of Mechanics. Epi.q-1 is a mobile robot designed to move small robotic devices, such as mini robotic arms. The Epi.q-1 peculiarity is its driving unit. The driving unit can be switched from a closed configuration, suitable for motion in narrow spaces, to an open configuration, useful to traverse higher obstacles, and vice versa. Epi.q-2 [2] was the first robot designed in collaboration between Politecnico di Torino and Università di Genova. Differently from the first versions, the locomotion units employ a new mechanism, based on an epicyclical mechanism, that is simpler and more compact than Epi.q-1. The driving unit ability to change configuration has been removed because the related mechanical complexity was not repaid by significant benefits in terms of performance for most applications. Epi.q-TG FWD and Epi.q-TG AWD were

respectively the second and the third prototypes designed and built in collaboration between Politecnico di Torino and Università di Genova [11]. With respect to Epi.q-2, the mechanical design has been refined in order to improve performance and reliability. Epi.q-Lizard [4] is the second to last vehicle designed and it is characterized by a higher level of modularity. It is composed of two identical frame modules and each one is equipped with two locomotion modules. The two frame modules are connected by a central passive longitudinal revolute joint that lets the robot adapt to ground unevenness and obstacles.

Epi.q-Mod is the last version of UGVs Epi.q and it is the subject of this paper. The main characteristic of this version is the application of the modular approach to the single driving unit that allows to generate different configurations based on functional requirements.

The main advantages of UGVs Epi.q are the high level of mobility and the low energy consumption. The locomotion system, thanks to an epicyclical mechanism and its mechanical efficiency, allows the robot to change locomotion mode, from rolling on wheels (advancing mode) to rotating legs (automatic climbing mode) according to local friction and dynamic conditions. The transition between advancing mode and automatic climbing mode occurs in presence of obstacles and also when the robot is moving on a slope that exceeds a limit value or when the robot is accelerating over a limit value, as discussed in [10].

Another important characteristic is the modular approach that, starting from the modules, allows several alternatives to be generated, which can be evaluated and compared. Moreover, from a manufacturing point of view, the modular approach allows robots to be built that fulfill various operative requirements, without the need to redesign the whole robot.

4 UGVEpi.q-Mod Driving Unit

The peculiar feature of UGVs Epi.q is their three-legged locomotion unit (Fig. 1), with three radial wheels mounted at the end of each leg. The transmission system is based on an epicyclical mechanism. Its frame, whose angular velocity is Ω, represents the planetary carrier and houses:

- one sun gear connected to the input shaft, with angular velocity ω_i,
- three idler gears,
- three planetary gears connected to the three wheels, with angular velocity ω_w.

The locomotion unit frame can rotate with respect to the robot frame and the relation between its angular velocities is expressed by the Eq. (1):

$$\omega_i = \frac{z_p}{z_s}\omega_w + \frac{z_s - z_p}{z_s}\Omega \tag{1}$$
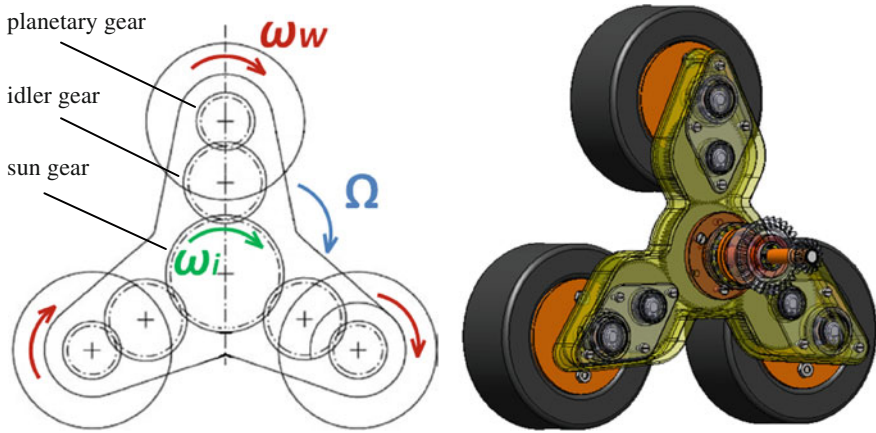
Fig. 1 Epi.q locomotion unit
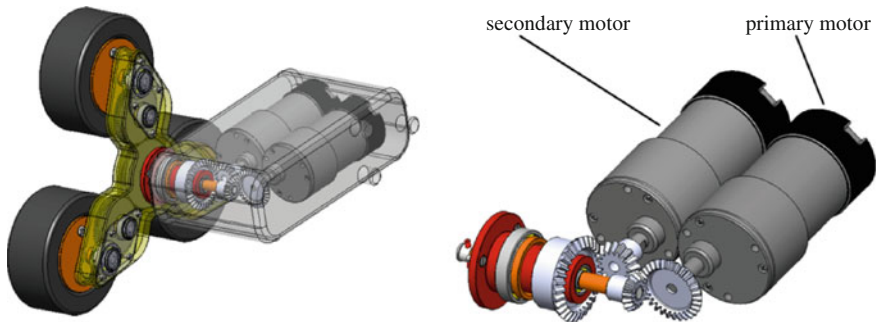
Fig. 2 Epi.q-Mod 2 M driving unit

where z_s is the tooth number of the sun gear and z_p is the tooth number of the planetary gears. If the torque required for moving on wheels exceeds the torque required for moving on legs, the locomotion unit switches from wheeled locomotion to legged locomotion, and vice versa.

In wheeled locomotion (advancing mode) the robot weight and the contact between the two lower wheels and the ground constrain the angular position of the locomotion unit frame. When the robot bumps against an obstacle, the friction between the front wheel and the obstacle stops the rotation of the front wheel; consequently, the locomotion unit starts to rotate around the front wheel axis, allowing the robot to climb over the obstacle (automatic climbing mode). Further details can be found in [11].

The main difference between the UGV Epi.q-Mod and the others UGVs Epi.q is the installation of two driving motors on the driving unit (Fig. 2). One motor, defined the primary motor, is connected to the input shaft of the sun gear while the
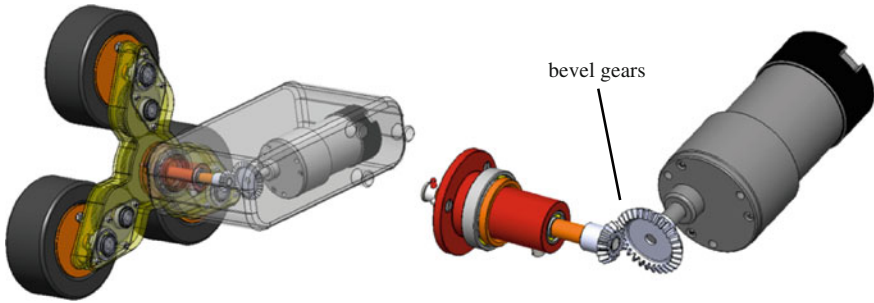
Fig. 3 Epi.q-Mod 1 M driving unit

secondary motor is connected to the planetary carrier. This solution provides a full control of the planet carrier movement during the legged locomotion. The presence of two motors causes the loss of the automatic switching from advancing to climbing mode and require a more complex sensing and control architecture, but is an interesting solution for applications where a full control of the robot motions, both for climbing and descending obstacles, is required.

The design of the driving unit also allows the installation of a single primary motor (Fig. 3), bearing in mind that the bevel gears of the input shaft must be replaced. Obviously this last solution ensures the movement of the vehicle but with a reduced control of the vehicle during the legged locomotion.

5 UGV Epi.q-Mod Functional and Embodiment Design

In this section of the paper, the first part presents the functional design of a solution of UGV Epi.q-Mod. A version, called Epi.q-Mod PSU, with a suspension system is also shown. In the second part the mechanical design embodiment of the vehicle is described.

The Epi.q-Mod (Fig. 4) measures $160 \times 540 \times 330$ mm (height $\times$ length $\times$ width) and is similar to the UGVs Epi.q prototypes, but with respect to the previous versions, it has a higher level of modularity. It is composed of four identical frame modules, each one equipped with one locomotion unit. The frame modules are connected to the central case (for batteries and electronic devices) by joints that let the robot adapt to ground unevenness and obstacles. The front modules are actuated while the rear modules can be actuated or not. The robot center of gravity is low-rise, increasing the stability margin and allowing the robot to negotiate steeper slopes both frontward, backward and sideways; moreover the robot is symmetrical with respect to a horizontal plane, so it can continue walking even after an overturn.

Thanks to its modularity, the robot can be reconfigured on the basis of the specific task requirements; for example, Epi.q-Mod PSU is a solution with a

Fig. 4 Epi.q-Mod
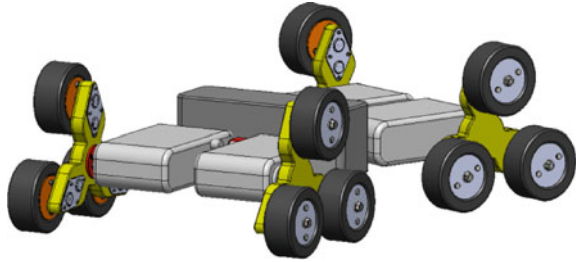
Fig. 5 Epi.q-Mod PSU
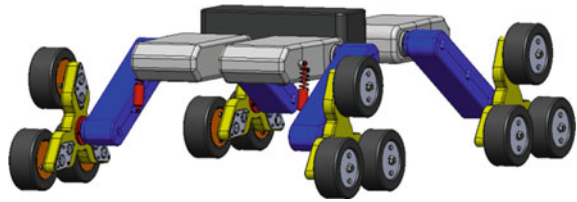
passive suspension system (Fig. 5). It loses the symmetry with respect to the horizontal plane and the capability of operating after an overturn, but it gains the ability of climbing higher steps and obstacles.

Every module carries one locomotion units that is actuated by two direct current motoreducers. The primary transmission system has a gearmotor (12 V maximum voltage, 0.18 Nm maximum torque, 200 rpm maximum speed) connected to the locomotion unit input shaft by bevel gears (16/16 teeth, 0.8 mm module); the secondary transmission system has a gearmotor (12 V maximum voltage, 0.25 Nm maximum torque, 12 rpm maximum speed) connected to the planetary carrier by a bevel gears (15/30 teeth, 1 mm module). The motors are positioned with their axes along the robot's longitudinal direction to avoid the use of belts and to reduce the robot's transversal width (Fig. 6).

The frame modules are realized using aluminum alloy plates (5 mm of thickness), joined by M3 screws. The locomotion unit frame is composed of two aluminum alloy shells (one flat, one hollow) connected by screws, and hosts the seven toothed wheels of the epicyclical mechanism. The epicyclical mechanism of the locomotion unit consists of a solar gear with 80 spur teeth, three idler gears with 72 spur teeth, and three planetary gears with 20 spur teeth; all the gears have a 0.5 mm module and are realized in steel.

In terms of performance, the robot is able to:

- move on the horizontal plane with a linear speed of about 10 km/h,
- climb a flight of stairs, for example, at the speed of one step every 4 s.
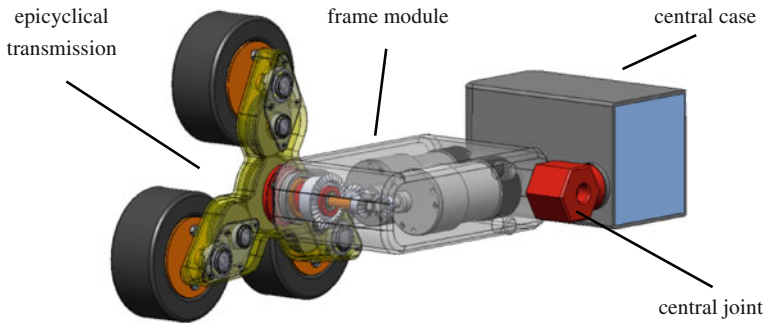
Fig. 6 Epi.q-Mod embodiment design

6 Conclusions

The paper presents the new version of the UGVs Epi.q. This prototype is the last development stage of the UGV Epi.q family of small-scale ground robots for surveillance and inspection tasks. Their hybrid legged-wheeled locomotion principle, compared to other robots with similar obstacle crossing capabilities, appears advantageous in terms of mobility and energy consumption.

Besides the constructive refinements of the locomotion units, the main novelty of this version is the strong tendency to modularity, in fact UGV Epi.q-Mod is composed of four identical frame modules with different possible internal layouts.

The benefits of the modular conception are evident. The most important of these is the possibility of adapting the robot to the specific task requirements. Furthermore, only a small set of spare parts is necessary, and this reduces the overall maintenance costs. Future steps will be to create a prototype of the robot and carry out experimentation on the vehicle. Following this, most of the future research efforts will be devoted to the integration of an intelligent navigation system for autonomous operation.

References

1. Aucouturier, J.J., Ikeuchi, K., et al.: Cheek to chip: dancing robots and AI's future. IEEEIntell. Syst. **23**(2), 74–84 (2008). doi:10.1109/MIS.2008.22
2. Bozzini, G., Bruzzone, L., et al.: Design of the small mobile robot Epi.q-2. In: Proceedings of AIMETA (2009)
3. Bruzzone, L., Quaglia, G.: Review article: locomotion systems for ground mobile robots in unstructured environments. Mech. Sci. **3**, 49–62 (2012). doi:10.5194/ms-3-49-2012
4. Bruzzone, L., Quaglia, G., et al.: Epi.q Lizard: a modular ground mobile robot. In: Proceedings of AIMETA (2013)
5. Gage, D.W.: UGV history 101: a brief history of Unmanned Ground Vehicle (UGV) development efforts. Unmanned Syst. Mag. **13**(3), 9–16 (1995)

6. Klinker, S., Lee, C.G.-Y., et al.: Destination moon and beyond for the micro rover Nanokhod. In: Proceedings of DGLR International Symposium "To Moon and beyond" (2007)
7. Morin, P., Samson, C.: Motion control of wheeled mobile robots. In: Springer Handbook of Robotics. Springer, Heidelberg (2008). doi:
8. National Research Council: Technology Development for Army Unmanned Ground Vehicles. The National Academies Press, Washington (2002)
9. Quaglia, G., Appendino, S., et al.: Design of a minirobot with transformable locomotion. In: Proceedings of AIMETA (2007)
10. Quaglia, G., Maffiodo, D., et al.: Epi.q-1.2: a new hybrid mobile mini robot. In: Proceedings of RAAD 2008, 17th International Workshop on Robotics in Alpe Adria Danube Region (2008)
11. Quaglia, G., Bruzzone, L., et al.: Epi.q-TG: mobile robot for surveillance. Ind. Robot: Int. J. **38**(3), 282–291 (2011). doi:10.1108/01439911111122789
12. Quaglia, G., Oderio, R., et al.: Epi.q robots, mobile robots-current trends. In: Gacovski, Z. (ed.) InTech (2011). doi:10.5772/27050
13. Quaglia, G., et al.: New frontiers for Epi.q robot family. In: Proceedings of RAAD 2012, 21st International Workshop on Robotics in AlpeAdria Danube Region (2012)

Six-Link In-pipe Crawling Robot

S. Jatsun, O. Loktionova and A. Malchikov

Abstract The paper describes the design and principles of locomotion of six-link mobile robot for monitoring pipelines with varying diameter. The description of the mathematical model of the robot movements in various modes of working is presented.

1 Introduction

Today, pipelines are the main element of the transportation systems for transfer gaseous, liquid substances and solids in the form of solutions, over long distance. In the process of maintaining operating condition of pipelines the monitoring of inner surface of pipe it is needed. Actively developing and promising solution for those tasks it is use of a snake—and worm-like principles of locomotion of robots to move in confined spaces of pipelines [1–7].

The important task in design of mobile robots is to consider the effects of interaction devices with external environment [8–10] the dynamic effects of the robot body moving by the electric motor.
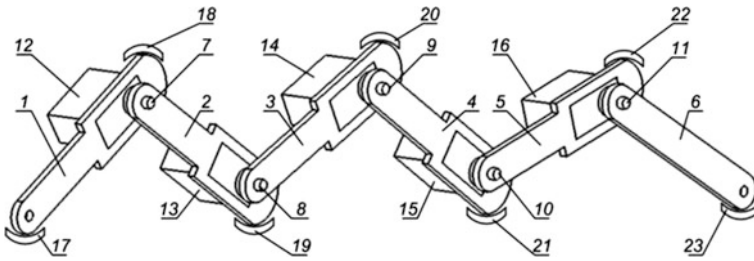
S. Jatsun (✉) · A. Malchikov
Department of Theoretical Mechanics and Mechatronics, South-West State University, Kursk, Russia
e-mail: teormeh@inbox.ru

A. Malchikov
e-mail: zveroknnp@gmail.com

O. Loktionova
South-West State University, Kursk, Russia
e-mail: teormeh@inbox.ru

Fig. 1 Scheme of in-pipe robot's structure

This paper presents the mathematical models of the in-pipe crawling robot movements in different mode and comparison of the results of mathematical modeling and data from experiments.

2 Structure and Description of In-pipe Crawling Robot's Motion Principle

Initially we have to take a look at structure and robot's motion principle in the peace of straight pipeline.

The main body of mobile in-pipe crawling robot is made by six articulated segments—links, and between these links set up joints 7–12, which are settled by electric motors. These electric motors provide angular displacement for each segment of this robot. In the joints and at the end of links it contains support element with inboard contact sensor (Fig. 1).

Interaction of support elements 17, 18 and 19 are provided by rotation of robot's link in joint 7–11 by electro motor. Interactions of support elements are determined by inboard contact sensors and the data transmitted to the robot control system. Further actuators 12–16 move link to the desired angle for a given initial position of the robot.

Initial position of the robot is defined as follows. Any pair of robot's segments (for example 1 and 2) should remain in contact with the surface of pipe wall, but other links of robot are angularly situated on zero degree relatively to each other.

Robot should occupy the initial position when the electric motors get power from the power source.

The algorithm for straight-line motion of robot shown in Fig. 2.

As is clear from Fig. 2, on the basic principle of robot's motion along the pipeline there will be periodically exit affixation due to friction force at the contact points of robot with pipeline surface. In this case, the interaction force between support elements and surface of pipe is provided by the wedging of link robot. In this case the interaction force between support elements and surface of pipe is provided by wedging of link of the robot inside the pipeline.

Fig. 2 Algorithm of in-pipe
robot straight-line motion
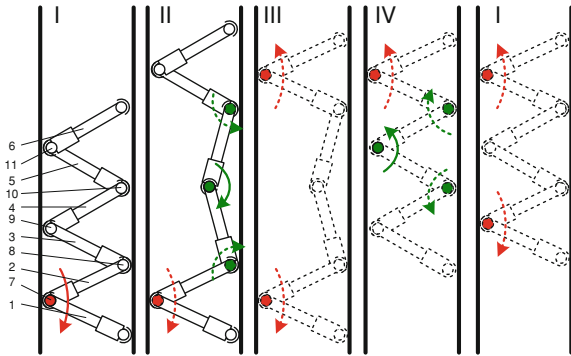
We should be attentive to these things, at the first, robot's motion can be happen in deformation processes at the contact points. And the second one is similar to the first fact, that the robot is moving along vertical line or sloping surface, there may be deformation.

For the purpose of dynamics research for controlled objects, mathematical modeling motions of this are developed. After analyzing the motion algorithm of this object, we can divide two basic functional parts. The first condition is fixation of object in pipeline by wedging of link inside of pipeline and the other condition is the movement of center mass along the direction of motion. Note that while robot is trying to get it is own position, only one electric motor will be working. But, while the robot is in action, the amount of working electric motors is two at least.

3 Mathematical Modeling of In-pipe Robot in the Fixation Mode

The scheme for mathematical model for fixation mode is shown in Fig. 3.

The indexes in illustrated scheme of fixation model are as the following: G—gravitational force, in these case, direction of this force is vertically down and put the centre of entire force system; m_ig—gravitational force of i-th link; R_{12}—reaction of joints A_2; R_{32}—reaction of joints A_3; which attached at angle β to normal of second link, α— angle between links and horizontal line; F_{fr}^{A3}—friction force, which allowing the robot to keep its position under the action of gravity. To be able to obtain a solution for this system, we assume that points A_2 and A_1 do not have friction force. Based on our experimental studies of the behavior of the system (as discussed at length in paper [11]) we draw a conclusion that making that assumption does not result in a significant simulation error (in a sense that the results of the simulation, made with this model, agree with the results obtained from the experimental study), while makes the analytical derivation of the
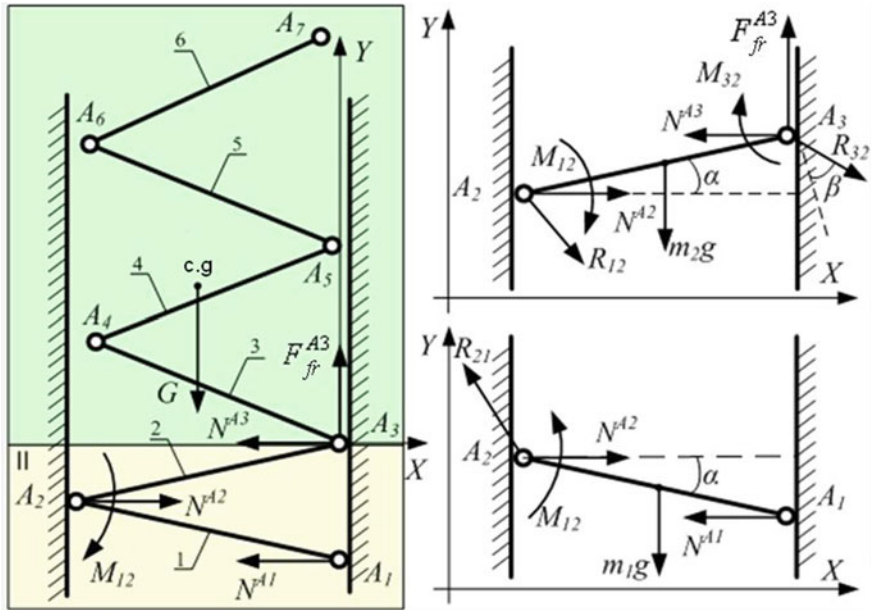
Fig. 3 Scheme of fixation model of robot

equations of motion significantly easier. Thus point A_3 has generalized friction force that is determined as:

$$F_{fr} = k(N^{A1} + N^{A2} + N^{A3}), \tag{1}$$

where N^{A1}, N^{A2}, N^{A3}—normal reaction forces, k—coefficient of dry friction force.

Let's consider that lengths of each link are equal l, and will take a look at statics balance of segment 1 and 2.

$$\begin{cases} N^{A2} - N^{A1} - R_{21}^x = 0; \\ R_{21}^y + m_2 g = 0; \\ -M_{12} + m_1 g \frac{d}{2} + N^{A1} l \sqrt{1 - \left(\frac{d}{l}\right)^2} = 0. \end{cases} \tag{2}$$

$$\begin{cases} N^{A2} - N^{A3} + R_{12}^x + R_{32} \cdot \cos(\beta - \alpha) = 0; \\ F_{fr} - m_1 g - R_{12}^y - R_{32} \cdot \sin(\beta - \alpha) = 0; \\ M_{12} + M_{32} + m_2 g \cdot \frac{l}{2} \cos(\alpha) - F_{fr} l \cos(\alpha) - \\ -N^{A3} l \cdot \sin(\alpha) + R_{32} \cos(\beta) \cdot l = 0; \end{cases} \tag{3}$$

where $m_1 g$ $m_2 g$—gravitational force of segment A_1 A_2, and A_2 A_3; M_{12}, M_{32}—torques between links of robot 1–2, and 3–2; R_{12}, R_{32}—reaction in the joints, which have two components R^x and R^y.

Fixation of robot is provided by due to dry friction force at the point A_3.

$$F_{fr} = \begin{cases} k\left(\sum_{i=1}^{3} N^{Ai}\right) sign(\dot{y}), & if \quad \dot{y} \neq 0; \\ F_{sum}, & if \quad \dot{y} = 0 \quad u \quad |F_0| \leq k\left(\sum_{i=1}^{3} N^{Ai}\right); \\ k\left(\sum_{i=1}^{3} N^{Ai}\right) sign(F_{sum}) & if \quad \dot{y} = 0 \quad |F_{sum}| > k\left(\sum_{i=1}^{3} N^{Ai}\right); \end{cases} \tag{4}$$

where F_{sum}—total force, except dry friction force, N^{Ai}—normal reaction force at the point A_i.

When the magnitude of friction force, which provides by electric motor torque, less than the gravity along axis A_3Y, robot slips through the pipe. For this case the equation of motion can be shown as following:

$$M\ddot{y} = F_{fr}^{A3} - G - \mu\dot{y}, \tag{5}$$

where M—total mass of robot, G—gravitational force, μ—coefficient viscous resistance.

Torques $M_{23} = \frac{C_m I_2^r}{i_{red}}, M_{34} = \frac{C_m I_3^r}{i_{red}}$, which are provided by electric motors can be written by the equation of each electric motor as the following:

$$L_r \frac{dI_r}{dt} + r_r I_r + C_e \dot{\phi} \cdot i_{red} = U, \tag{6}$$

where L_r and r_r—inductance and active resistance; C_e and C_e—proportional coefficients; ϕ—angular angle of segment; i_{red}—transmission ratio of gear; I_r—current in coil of electric motor; U—voltage for motor, formed by automatic control system.

4 Mathematical Model of the Mobile Robot in the Move Mode

When moving the center of gravity of the robot, generally it will use 4 drive device (actuator 1 is required to maintain the fixed state). Considering the simplest case, when the movements of links are affected by the drive torque 8 and 9. Design scheme of mode motion of the links are shown in Fig. 4.

To obtain the equations of motion we have written Lagrange equations describing the system with two degrees of freedom, and Kirchhoff's circuit laws for the motors' coils, and then we worked out the derivation from there.

Fig. 4 Design scheme of the robot in move mode
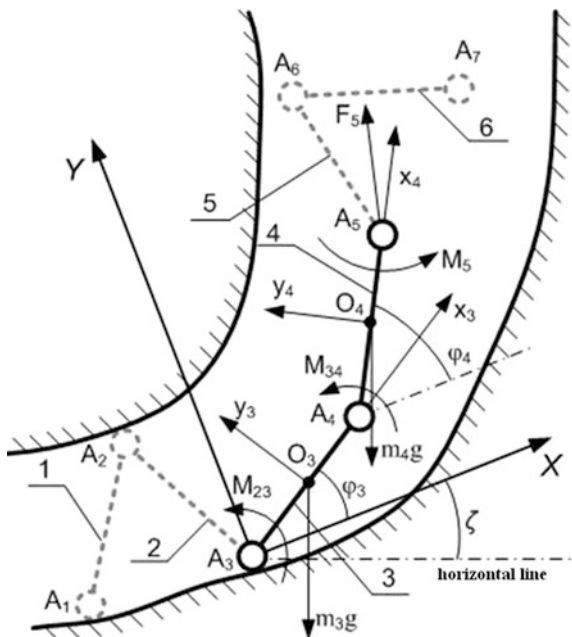
$$
\begin{cases}
\underset{3}{\ddot{\varphi}}\left(J_{A_3} + m_3 l_3^2\right) + \frac{1}{2} m_4 l_3 l_4 \underset{4}{\ddot{\varphi}} \cos(\varphi_3 - \varphi_4) + \frac{1}{2} m_4 l_3 l_4 \dot{\varphi}_4^2 \sin(\varphi_3 - \varphi_4) \\
= M_{23} - M_{fr}^3 + F_5 l_4 \sin(\alpha_5 - \varphi_3) + m_4 g l_4 \cos(\zeta + \varphi_3) + m_3 g \frac{l_3}{2} \cos(\zeta + \varphi_3); \\
\underset{4}{\ddot{\varphi}}\left(J_{A_4} + \frac{m_4 l_4^2}{4}\right) + \frac{1}{2} m_4 l_3 l_4 \underset{3}{\ddot{\varphi}} \cos(\varphi_3 - \varphi_4) - \frac{1}{2} m_4 l_3 l_4 \dot{\varphi}_3^2 \sin(\varphi_3 - \varphi_4) \\
= M_{34} - M_{fr}^4 + M_5 + F_5 l_4 \sin(\alpha_5 - \varphi_4) + m_4 g \frac{l_4}{2} \cos(\zeta + \varphi_4); \\
L_r \frac{dI_r^3}{dt} + r_r I_r^3 + C_e \dot{\varphi} *_3 \cdot i_{\text{red}} = U_3; \\
L_r \frac{dI_r^4}{dt} + r_r I_r^4 + C_e \dot{\varphi} *_4 \cdot i_{\text{red}} = U_4;
\end{cases}
\tag{7}
$$

where φ_3, φ_4—the generalized coordinates, angles of links, $\dot{\varphi}*_3 = \varphi_3 - \xi$ and $\dot{\varphi}*_4 = \varphi_4 - \varphi_3$—angles relative displacement of links, J_{A3}, J_{A4}—moments of inertia, m_3, m_4 l_3, l_4—mass and length of robots links; F_5 and M_5 reduced power and reduced moment acting on the system units, α_5—angle application of external force F_5; M_{23} and M_{34}—torques produced by motors. Based on the Coulomb's model of friction, the torque produced by friction force can be written as the following:

$$
M_{fr} = \begin{cases}
M^{\text{fr.stat}} \text{sign}(\dot{\varphi}_3), & \text{if} \quad \dot{\varphi}_3 \neq 0; \\
\sum M_3^{\text{ext}}, & \text{if} \quad \dot{\varphi}_3 = 0 \quad \text{and} \quad \left|\sum M_3^{\text{ext}}\right| \leq M_3^{\text{fr.stat}}; \\
M^{\text{fr.stat}} \text{sign}(\sum M_3^{\text{ext}}), & \text{if} \quad \dot{\varphi}_3 = 0 \quad \left|\sum M_3^{\text{ext}}\right| > M_3^{\text{fr.stat}},
\end{cases}
\tag{8}
$$

where $\sum M_3^{\text{ext}}$—the sum of external moments acting pivotal connection $M^{\text{fr.stat}}$—torque of static friction.

To reduce the effects of dynamic contact interaction, and process control locking device decided to use elastic support elements, equipped with contact switch.

5 Conclusion

Development of robots using principle motion based on the variable shape of the body is impossible without the study of the dynamics of movement, the effects of interaction the robot with pipe surface and the elaboration of algorithms for robot motion.

Adequacy of the mathematical models of the mobile robot, which presented in this paper, was confirmed experimentally and it is can be used to calculate structure parameters and for designing of mobile in-pipe crawling robot.

References

1. Brunete, A.: Drive modules for pipe inspection microrobots. In: Brunete, A., Hernando, M., Gambao, E. (eds.) 2004 IEEE International Conference on Mechatronics and Robotics, Aachen (2008)
2. Chernousko, F.L.: Snake-like locomotion of multilink systems. J. Vibr. Control (2002)
3. Dertien, E.: Development of an inspection robot for small diameter gas distribution mains. In: Dertien, E., Stramigioli, S., Pulles, K. (eds.) 2011 IEEE International Conference on Robotics and Automation Shanghai International Conference Center, Shanghai, pp. 5044–5049 (2011)
4. Hirose, S.: Biologically inspired robots: snake-like locomotors and manipulators. Oxford University Press, Shigeo Hirose (1993). ISBN 0-19-856261-6
5. Hollinger, G.: Genetic optimization and simulation of a piezoelectric pipe-crawling inspection robot. In: Hollinger, G., Briscoe, J. (eds.) Proceedings IEEE International Conference on Robotics (2005)
6. Sigurd, A.: A snake-like robot for internal inspection of complex pipe structures (PIKo). In: Sigurd, A., Fjerdingen, P., Transeth, A. (eds.) The 2009 IEEE/RSJ International Conference on Intelligent Robots and Systems, Louis, USA. pp 5665–5671
7. Sun, L., Lu, L., Qin, X., Gong, Z.: Micro robot for detecting wall cracks of pipe. In: Proceedings of the 6-th International Conference CLAWAR 2003, Catania, Italy, pp. 643–650 (2003)
8. Malchikov, A.V.: Investigation of movements of planar six-link in-pipe crawling mobile robot. In: Malchikov, A.V., Jatsun, S.F., Rublev, S.B. (eds.) Proceedings of the Samara Scientific Center, Russian Academy of Sciences, Samara, №4 (5), pp. 1263–1265 (2012)
9. Jatsun, S.F.: Automated mobile system for diagnosis of variable diameter pipelines. In: Jatsun, S.F., Malchikov, A.V. (eds.) Automation and Modern Technology, Moscow, №12, pp. 3–8 (2012)

10. Jatsun, S.F.: Dynamic support elements crawling robots for movement on inclined surfaces. In: Jatsun, S.F., Malchikov, A.V., Zhakin, A.I. (eds.) Proceedings of the South–West State University, Kursk, №2(41), part.1, pp 89–95 (2012)
11. Malchikov, A.V.: Experimental investigation the fixation process of in-pipe mobile robot. In: Malchikov, A.V., Jatsun, S.F. (eds.) Actual Questions of Science: Proceedings of the VIII International Scientific and Practical Conference, Moscow, pp. 29–33 (2013)

Dynamics Model of STB Projectile Loom

Assylbek Jomartov, Skanderbek Joldasbekov and Gakhip Ualiyev

Abstract In this paper we develop a dynamic model of STB projectile loom. STB projectile loom is a complex machine, containing various types of cyclic mechanisms and the mechatronic devices. A dynamic model of STB projectile loom allows analysis of the dynamics for different speeds of the main shaft of the loom. For practical modeling of the dynamics of the STB projectile loom is applied package software SimulationX. SimulationX is a multidisciplinary software for modeling complex physical and technical facilities and systems. Dynamic model of the STB projectile loom on software package SimulationX allows taking into account backlash at the joints and nodes, the force of resistance and electric motor performance.

Keywords Dynamics · STB loom · Model · SimulationX

1 Introduction

One of the main tasks in the development of textile machinery, is to increase the rapidity looms, consequently, their productivity. With increasing of speeds looms, dynamic loads on their separate mechanisms and moving joints sharply increasing. In these circumstances, identification of the weakest points and elements of the loom is a priority for the dynamic calculation.
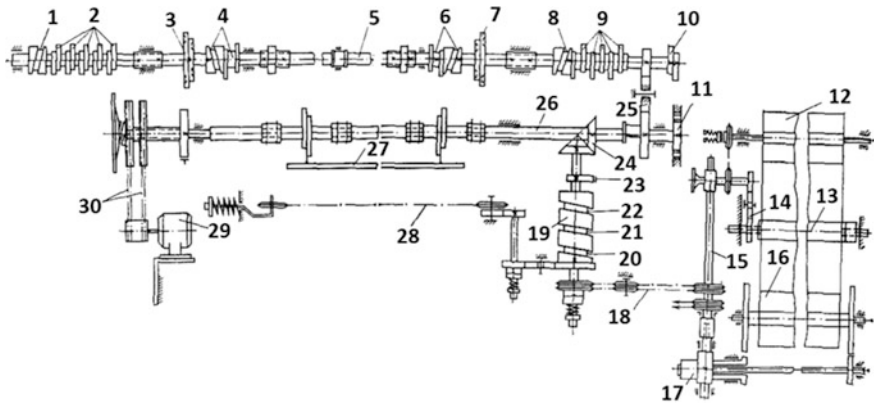
The STB projectile loom consists of a large number of structurally different mechanisms. This is cam, lever, gear, friction and combined cyclic mechanisms.

A. Jomartov (✉) · S. Joldasbekov · G. Ualiyev
Institute Mechanics and Mechanical Engineering, Almaty, Kazakhstan
e-mail: legsert@mail.ru

S. Joldasbekov
e-mail: dgpimmash@mail.ru

Fig. 1 The structural scheme of STB projectile loom

The modern STB projectile loom contains the various mechatronic devices: device for automatic removal of faulty weft, electromechanical drive warp yarns, electronic controllers, servos, etc. All this allows STB projectile loom to work without the participation of the weaver, so there is reason to assume STB projectile loom is the mechatronic system.

Real mechanical system has an infinite number of degrees of freedom. Idealization of real mechanical system when it is displayed by the dynamic model depends on many factors [1−4]. Suggesting that inertial parameters of the system (or mass moments of inertia) are concentrated at separate points or sections that are connected inertialess, elastic, dissipative constraints, it is possible to make a dynamic model with a limited number of degrees of freedom [5−10].

2 Dynamic Model of STB Projectile Loom

Let's consider the creation of a dynamic model of STB projectile loom based on structural scheme. The structural scheme of STB projectile loom [11], shown in Fig. 1, which shows the main units and mechanisms, where denoted: #1—the drive of mechanism for pushing of projectile weft from right receiving box; #2—the drive of mechanisms of right receiving box; #3—the drive of mechanism of right scissors; #4—the drive of mechanism of right formation hem; #5—upper shaft, #6—the drive of mechanism of left formation hems; #7—the drive of mechanism of left scissors; #8—the drive of mechanism for pushing of projectile weft; #9— the drive of mechanism of upper left box; #10—the drive mechanisms of a brake and a compensator weft; #11—roller locking mechanism; #12—goods shaft; #13—Scalo; #14—the drive of scalo; 15—lower shaft; #16—warp beam; #17— differential; #18—the drive of lower shaft; #19—cross shaft of left weft box; #20–23—the drives of mechanisms respectively: left weft box, opener of springs
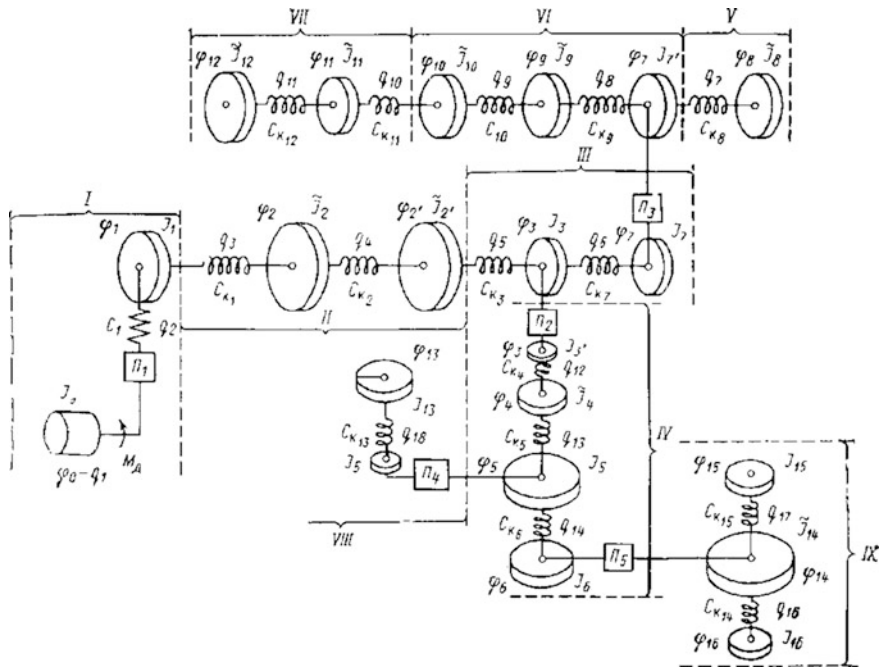
Fig. 2 Dynamic model of STB projectile loom

of projectile weft, lifting of projectile weft, opener springs thread catcher, picking mechanism; #24—transmission from the main shaft to the cross shaft of left weft box; #25—transmission from the main shaft to the upper shaft; #26—the main drive shaft of loom; #27—beam of sley; #28—conveyor of projectiles weft; #29—electric motor of the main drive shaft of loom; #30—V-belt drive transmission of the main drive shaft of loom.

We consider the task of constructing a dynamic model of STB projectile loom to study performance and interaction of separate mechanisms in terms of improving overall system productivity [11−13]. Dynamic model of STB projectile loom is considered as a multimass torsional vibrational mechanical system. Inertial and elastic properties of the elements are included as appropriate reduced values. Distributed along the shaft moments of inertia are reduced to the relevant sections of shaft of loom.

We represent the dynamic model of STB projectile loom in the form of chain (see Fig. 2).

The basis of the model is the main shaft of the loom from which are driven by all its mechanisms. Rotation of asynchronous AC motor with a moment of inertia $J_0 = const$ of the rotor and pulley is transmitted to the main shaft through a belt drive Π_1 with stiffness c_1 to pulley and crossbar of the friction clutch with moment of inertia $J_1 = const$ (group mechanisms—I). The main shaft the loom consisting of separate parts different length and torsional stiffness $c_{k_1}, c_{k_2}, c_{k_3}, c_{k_7}$. The following

is a sley mechanism, moments of inertia $\tilde{J}_2$ which are variable, because drives are cam rocker mechanism (group mechanisms—II). From the bevel gear Π_2, the moment of inertia which is designated $J_3 = const$, the rotation is transmitted to the left cross camshaft of weft box. From it driven mechanisms whole group variable and constant structure associated with laying weft threads.

Shaft section at the left end with the torsional stiffness c_{k_7} ending helical gear Π_3 with inertia $J_7 = const$ (group mechanisms—III). Mechanisms and details of the left weft box associated with the camshaft, form a group IV.

By the mechanism of V-th group are cam-lever mechanisms of compensation and braking weft a permanent structure with cams and variable moment of inertia $\tilde{J}_8$. Torsional stiffness of the upper shaft section from the drive gear to the cams is denoted c_{k_8}. By VI-th group mechanisms upper left box assigned mechanisms: the returners of the weft yarn with opener of returners of springs, left scissors, centering device, left weft controller, the total reduced variable moment of inertia which is denoted by $\tilde{J}_9$ a dynamic model. Torsional stiffness of the upper section of the shaft from the drive gear is denoted c_{k_9}. The mechanisms of left formation hems and thread catcher are assigned in this group, reduced the total moment of inertia which denotes $\tilde{J}_{10}$ in the diagram and the torsional stiffness $c_{k_{10}}$ of the shaft section between the selected subgroups mechanisms. By VII—that group mechanisms assigned mechanisms of right receiving box, the total reduced moment of inertia $\tilde{J}_{11}$, and the torsional stiffness of the upper section of the shaft between the groups VI and VII mechanisms denoted $c_{k_{11}}$. This group covers mechanisms of braking, control planting and returns projectiles, opener of springs projectiles, projectiles ejection and stacking onto conveyor, right weft control and scissors. Their total reduced moment of inertia denotes $\tilde{J}_{12}$, and the torsional stiffness of the shaft section between the selected subgroups mechanisms denoted $c_{k_{12}}$. All mechanisms of the left and right upper boxes (groups VI and mechanisms VII) is driven by the upper shaft, is a cam-lever mechanism, fixed and variable structure with flat grooves and the cylindrical cams with cam speed corresponding to the speed of rotation of the main shaft, and a relatively small reduced mass the moving units. From the cross camshaft of left weft box, through a spur gear Π_4, the reduced moment of inertia which denotes J_{13}, driven chain conveyor of projectiles with constant mass of moving parts m_1 (group mechanisms—VIII). Torsional stiffness of the upper conveyor drive shaft and safety clutch torque limit is denoted $c_{k_{13}}$, the longitudinal stiffness of chain conveyor is denoted $c_4, c_2.c_4, c_2$. IX group of mechanisms are driven from the lower shaft machine, namely: (a) Mechanisms carriage (harness mechanism, shedding mechanism) and the mechanism of color change of weft with reduced total inertia $\tilde{J}_{14}$ are driven by dual chain drive Π_5. (b) Goods shafts with constant reduced moment of inertia $J_{15} = const$, torsional stiffness section of the drive shaft is denoted $c_{k_{15}}$; (c) Mechanisms of control and tension warp are driven from the rear end of the lower shaft, reduced the total moment of inertia which denotes $J_{16} = const$, and the torsional stiffness of the shaft section of the drive sprocket to the worm gear—$c_{k_{16}}$.

Mechanisms subgroup (b) and (c) in the group IX (goods shafts, control and tension of warp) have large mass of links, small speed and perceive large static load. We can obtain the differential equations describing the dynamics of the loom based on the dynamic model STB projectile (see Fig. 2) using the Lagrange equations of the 2nd kind with redundant coordinates [2]

$$\sum_{j=1}^{19} a_{ij}\ddot{q}_j + b_j(q,\dot{q}) + c_{ii}q_i = Q_i, \quad i = 1, 2, \ldots, 19. \tag{1}$$

where q_i—generalized coordinates, a_{ij}—inertial coefficients, c_{ij}—quasi-elastic coefficients, Q_i—generalized forces, b_i—dissipative coefficients.

Dynamic equation of asynchronous electric motor loom

$$\omega_0\left[1 - v_d(M_d + T_d\dot{M}_d)\right] = \dot{q}_1 \tag{2}$$

where ω_0—the angular velocity of idle speed, v_d—the steepness of the static characteristics of electric motor, T_d—the electromagnetic time constant of electric motor, M_d—the electric motor torque.

The solution of system of differential Eqs. (1, 2) and analysis of the results is a very complex task, which is shown in [11].

3 Dynamics Model of STB Projectile Loom on Software Package SimulationX

For convenience, we use to calculate the dynamics of the STB projectile loom software package SimulationX at the moment. SimulationX (ITI [14], is a multi-domain CAE simulation software for virtual prototyping of physical systems. It is developed and sold commercially by ITI GmbH, based in Dresden, Germany. Scientists and engineers in industry and education use the tool for the design, analysis and virtual testing of complex mechatronics systems, as the software models the interaction of components from a multitude of domains including their mutual interaction and feedback on one platform.

Figure 3 shows the dynamic model of the STB projectile loom on software package SimulationX.

3.1 The Simulation Results

Calculation of the dynamic model STB-180PN projectile loom conducted without external forces at motor speed is 1,440 revolutions per minute. Figure 4 shows a diagram of Campbell (ITI [14]).
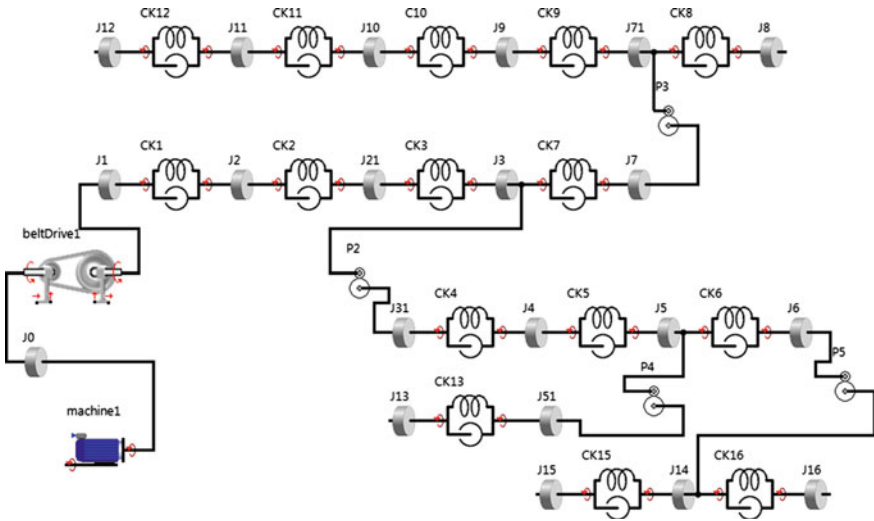
Fig. 3 Dynamic model of STB projectile loom on SimulationX

Fig. 4 Diagram of Campbell
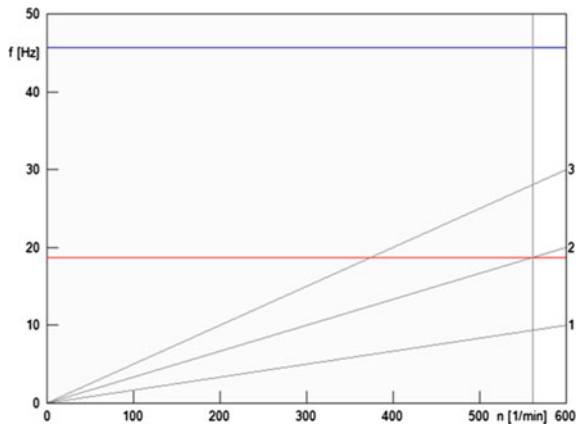
Figures 5 and 6 shows graphs the angular velocity and acceleration of the driving pulley of loom.

As can be seen from the diagram of Campbell (see Fig. 4), the resonances arise for 3rd harmonic of natural frequencies with revolutions of the main shaft of the loom $n = 380$ rev/min and the 2nd harmonic of natural frequencies with revolutions of the main shaft of the loom $n = 560$ rev/min. At present, Russian enterprises to develop new high-speed STB projectile looms with the number of revolutions of the main shaft to $n = 500$ rev/min. Therefore necessary to consider the 2nd and 3rd harmonic of natural frequencies of STB projectile looms at process of designing.

Fig. 5 The angular velocity
of the driving pulley
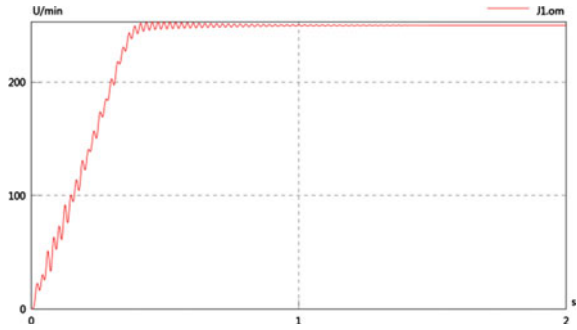
Fig. 6 The angular
acceleration of the driving
pulley
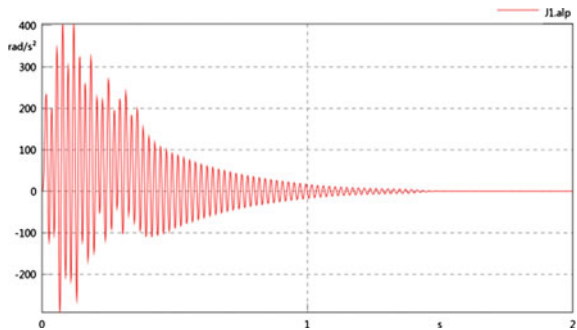
4 Conclusion

Dynamic model of STB projectile looms loom STB on software complex Simu-
lationX allow taking into account backlashes at the joints and links, forces of
resistance and characteristics of the electrical motor. Required results can be
obtained in graphical form and conduct automated analysis of natural frequencies
and mode shapes. Dynamic models on software complex SimulationX can be
applicable for the analyze of complex mechatronic systems.

References

1. Dresig, H., Holzweißig, F.: Dynamics of Machinery. Springer, Berlin (2010)
2. Wolfson, I.I.: Dynamic Calculations of Cycle Mechanisms. Mashinostroenie, Leningrad
   (1976)
3. Eckhardt, H.D.: Design of machines and mechanisms (1998)
4. Browne, J.W.: The Theory of Machine Tools. Cassell and Co. Ltd, London (1965)
5. Sandler, B.Z.: Robotics: Designing the Mechanisms for Automated Machinery. Academic
   Press, New York (1999)
6. Youssef, H.A., El-Hofy, H.: Machining Technology : Machine Tools and Operations. Taylor
   and Francis Group, LLC, Boca Raton (2008)

7. Shabana, A.A.: Dynamic of Multibody Systems, 2nd edn. Cambridge University Press, Cambridge (1998)
8. Jomartov, A.A.: Dynamic of machine-automaton on base of timing diagram. Proceedings of the 15th ITI Symposium, Dresden (2012)
9. Board, N.: Complete Technology Book on Textile, Spinning, Weaving, Finishing and Printing. Asia Pacific Business press Inc, Delhi (2009)
10. Topalbekiroglu, M., Celik, H.I.: Kinematic analysis of beat-up mechanism used for handmade carpet looms. Indian J. Fibre Text. Res. **34**, 129–136 (2009)
11. Jomartov, A.A., Ualiyev, G.: The dynamics of the mechanisms of automatic looms STB. Tauari, Almaty (2003)
12. Jomartov, A.A.: Dynamics of machine-automaton jointly with cyclegram. In: Proceedings of World Congress on Engineering, UK, London (2010)
13. Jomartov, A.A.: Multi-objective optimization of cyclogram mechanisms machine-automaton. In: Proceedings of World Congress on Engineering, UK, London (2011)
14. ITI GmbH: http://www.simulationx.com/ (2000)

Development of an Origami Type Robot to Realize Transformation and Movement

Kazuma Otani and Mitsuharu Matsumoto

Abstract In this research, we introduce a prototype of origami type robot to achieve free transformation of its shape. Although some transformation robots, which can adapt to the environmental change, have been proposed in the pasts, the structure of the robot is complicated and the robot is relatively big due to using gears and motors. To solve the problems, we have developed an origami type robot to miniaturize the robot and to reduce its weight. To achieve the origami type robot, we have employed a new material named biometal. The expansion and contraction of biometal can be controlled by giving an electric current to it. We conducted some experiments and confirmed that the developed robot not only could transform its shape but also could move unlike previous origami type robots.

Keywords Origami · Biometal · Miniaturization · Weight saving · Transformation robot

1 Introduction

Currently, there are many studies on the transformation robots that can adapt to the environmental change. For example, Nakai et al. have proposed the transformation robot that uses the phase change of low melting metal [10]. In this research, the robot is made of a low-melting-point alloy and its leg can be transformed by

K. Otani (✉) · M. Matsumoto
Department of Informatics, University of Electro-Communications, 1-5-1, Chofugaoka,
Chofu-shi, Tokyo, Japan
e-mail: otani@mm-labo.org

M. Matsumoto
e-mail: mitsuharu.matsumoto@ieee.org

softening the alloy by heating process. Kosett et al. have proposed a hybrid robot. It has two transforming modes, that is, wheel mode and helicopter mode [6]. Although it has flight capability and can achieve wheeled ground locomotion, the transformation range of the robot is limited.

Regarding reconfigurable robots, there are other approaches that aim to give robots several functions by combining plural robots called modules.

For example, Murata et al. have developed the robot called M-TRAN (Modular Transformer). The M-TRAN system can change its three-dimensional structure and its motion by connecting the modules in order to adapt itself to the geographical features [8]. Suzuki et al. also proposed a modular robot named CHOBIE [14]. They reported computational simulation of CHOBIE and developed some prototypes of modular robots.

Although module type robots can form various structures, the appropriate control is necessary to connect each module. In addition, the structure is complicated and the robots become relatively big due to the parts required in the connection mechanism such as gears, sensors and motors. To solve the problems, we aim to develop a robot that does not require the module connection with light weight. For this purpose, we pay attention to origami, and developed a prototype of the origami type robot whose shape can be transformed from two-dimensional sheet to three-dimensional structure. As origami type robot is basically a two-dimensional sheet, it does not require the large space to be placed. As all the parts of the origami type robot have been connected in advance, the origami type robot does not require the position adjustment between modules. Some authors proposed an origami type material using shape memory alloy related to this approach [5, 11]. This material can be transformed from two-dimensional sheet to three-dimensional structure by using the shape-memory alloy and magnet. However, the developed material is irreversible, that is, it is not possible to return to former shape when it is transformed once. As the authors also consider only shape transformation, the material cannot move itself to any direction.

There are also some related works from two-dimensional sheet from three-dimensional structure in self-assembly field. For example, Boncheva et al. realized a three-dimensional closed circuit from a sheet using magnetic force [2]. However, their research is basically self-assembly and the procedure is also irreversible.

In our previous trial, we employed a new material named biometal [15, 16] to realize reversible transformation [1]. Biometal is lighter and is smaller than the motor. The expansion and contraction of biometal can be controlled flexibly by applying electrical current to biometal. Although we could achieve simple reversible transformation, it still cannot move to any direction. In this paper, we show a prototype of an origami type robot that can not only do the simple transformation but also achieve the movement.

Fig. 1 Kawasaki rose and
Fujimoto cube [12, 13]
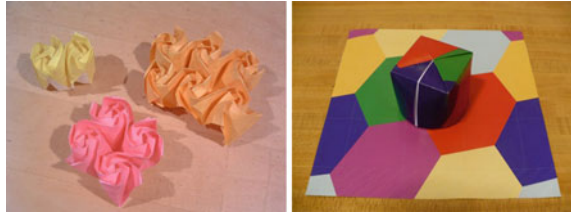
2 Origami Type Robot

Origami is a traditional Japanese art of paper folding. In origami art, we can form
many complex structures from a paper.

Kawasaki rose and Fujimoto cube shown in Fig. 1 are typical examples of
origami folding. Due to its complex and interesting topological features, geometry
of origami has been studied in mathematical area. In theoretical field, there are
some researches on computational origami and the conditions from a planar sheet
into a given three-dimensional shape are analyzed. Various complicated structures
can be created according to theoretical approaches [3, 9]. The studies on origami
also have some applications to engineering fields. For example, Miura-fold is a
famous folding, which can easily pack and unpack itself by pushing and pulling
the two ends of the paper [7]. Due to its easy packing and unpacking feature, it is
used for solar panel arrays for space satellites. Some authors focus on origami as
paper packaging and have developed some robots to fold origami using robotic
finger [4].

To clarify the feature of origami type robot, we describe the difference between
origami type robot and modular type robot. There are several differences between
modular type robot and origami type robot. Modular type robot requires the
position adjustment of each part. It is also necessary for the modules to commu-
nicate with each other. As the size of the parts is fixed, it requires the space to be
placed. On the other hand, origami type robot does not require the position
adjustment because phase structure is fixed and we only need to consider how to
fold the parts. Origami type robot also can miniature its size because it becomes
two-dimensional thin structures. Unlike modular type robot, it can be miniaturized
by folding.

3 System Implementation

The circuit diagrams of the developed origami type robot are shown in Fig. 2. The
number in Fig. 2 is to explain how to fold the parts of the robot in the experiment.
As shown in Fig. 2, we collected copper wires into the central position to avoid the
collision of the parts. The robot is composed by cardboard, biometal, copper wire,
copper foil, low density polyethylene film, and sticky mat. In our robot, we

Fig. 2 Circuit diagram of origami-robot. **a** Front side, **b** back side

Biometal ——— Copper
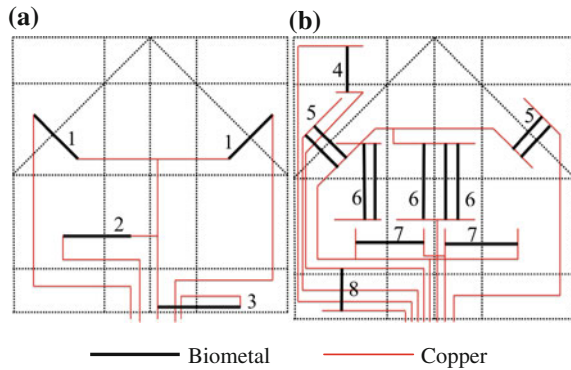
Table 1 Specification of the robot

Parameters	Value
Size (cm)	$19.5 \times 19.5 \times 0.1$
Weight (g)	24

Table 2 Specification of biometal (Toki corporation)

Parameters	Value
Length (mm)	20
Weight (g)	<0.1
Allowable upper temperature limit (K)	320–330
Standard electric resistance (Ω/m)	400
Standard drive current (mA)	200–300
Repeatability (times)	100,000

employed low density polyethylene film for lightening, flexibly and durability. As biometal is the important actuator in our robot, we briefly explain its feature. Biometal is the wire made from shape-memory alloy.

It is a thin soft actuator that shrinks by supplying electricity. Although it is soft and very flexible like the string of nylon in normal air temperature, it shrinks by strong power and becomes hardened like the piano wire if we pass an electric current to it. Biometal can be categorized into two types. One is BMF (BioMetal Fiber) and the other is BMX (BioMetal Herix). BMF is a thin line type actuator and the power is stronger than BMX. However, the displacement is 5 % of the total. On the other hand, BMX is a coil type actuator. Although the power is weaker than BMF, displacement is about 50 % of the total. As our robot does not require very strong force and the big displacement is preferable, we have employed BMX for our robot. The specification of the robot and biometal is shown in Tables 1 and 2, respectively. We also attached urethane elastomers to the robot as sticky mat material for gripping the ground. The control system is shown in Fig. 3. As shown in these figures, the robot is controlled by field-effect transistor (FET). Figure 4 shows Gainer and FET circuit for origami robot control, and the
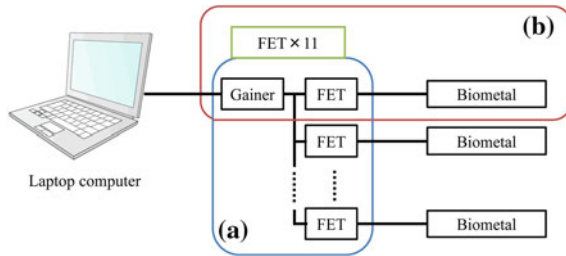
Fig. 3 System setup
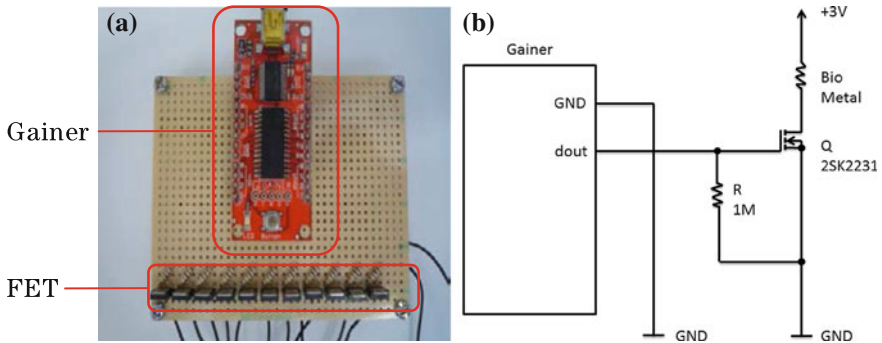
Fig. 4 Gainer and FET circuit for origami robot control. **a** Circuit for origami robot control, **b** circuit diagram for biometal control

circuit diagram for biometal control. The voltage to FET was controlled by I/O module named Gainer. Gainer is controlled through serial communications from the control computer, and the whole movement is managed. The program is developed by Microsoft Visual C#. DM-330MV of the ALINCO Company is used for power supply.

4 Experiments

We conducted fundamental experiments to evaluate the robot transformation and the movement. In our prototype, we designed both shape transformation and robot movement. For shape transformation, the robot first transforms its shape from two-dimensional sheet to the state of airplane. The robot next transforms its shape from the state of airplane to the state of folding up twice through two-dimensional sheet. For moving system, we referred inchworm motion in consideration of the torque of the biometal, and weight and performance of the robot.
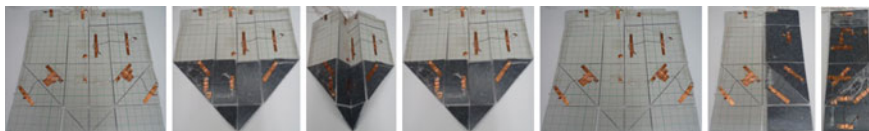
Fig. 5 Transformation process of the robot
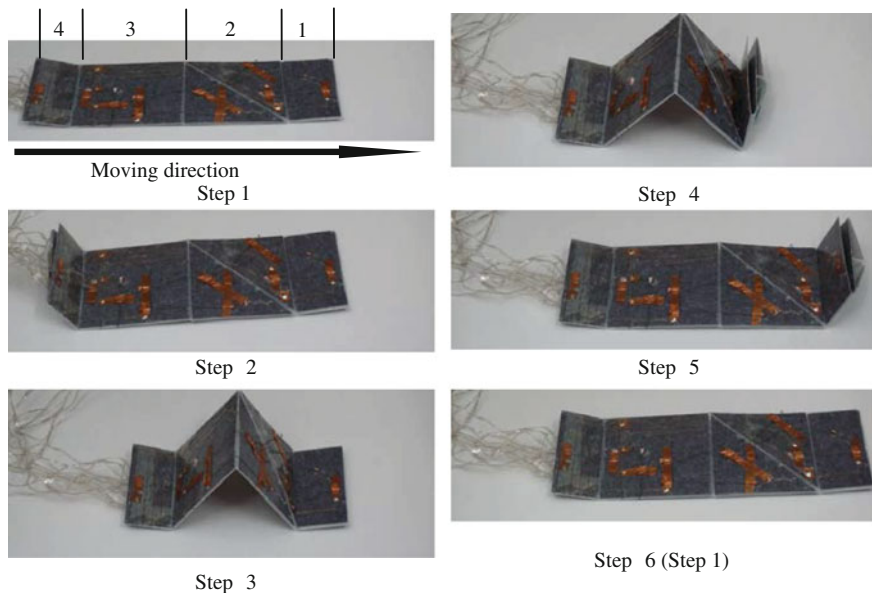
Fig. 6 Movement process of the prototype robot

The process of transformation and movement are summarized as follows:

Step (1) The robot first starts from a planar sheet.

Step (2) The robot is transformed from the sheet to the state of the airplane. (Power supply: biometal 1 and 7 in Fig. 2.)

Step (3) The robot is transformed from the state of the airplane to the two-dimensional sheet. (Power stop: biometal 1 and 7. Power supply: biometal 5.)

Step (4) The robot is transformed from the two dimensional sheet to the moving mode. (Current stop: biometal 5. Power supply: biometal 2 and 3.)

Step (5) The robot moves with inchworm motion.

The movement of the robot is inspired by inchworm motion. Figures 5 and 6 show the appearance of actual transformation and the procedure of the movement. The movement process is summarized as follows. The number of the explanation corresponds to the number in Fig. 2. The folding and unfolding are achieved by biometal.

Step (1) The robot first starts from the moving mode.
0Step (2) The fourth part is folded to reduce frictional force. (Power supply: biometal 8.)
Step (3) The second and third parts are folded to shrink the robot. (Power supply: biometal 6. Current stop: biometal 8.)
Step (4) The first part is folded to reduce frictional force. (Power supply: biometal 4.)
Step (5) The second and third parts are unfolded to move forward. (Power stop: biometal 6.)
Step (6) The first part returns its first position. (Power stop: biometal 4.)

The process from Step (1) to Step (6) is repeated. As shown in Fig. 5, we could confirm that the robot could transform from a plane to three fold via airplane in a series of operation. In these prototype, we did not implement the special function for bending 180 degrees except biometal. The paper was bent by its weight and inertia when we folded the paper using biometal. To be bent in two opposite directions, we set biometal on the front and back as shown in Fig. 2. We confirmed that the robot could perform the reversible operations unlike the past origami type material. We also confirmed the robot movement with inchworm motion.

5 Conclusion

In this research, we developed a prototype of an origami type robot that could achieve not only the transformation but also the movement. Although the transformation and movement are still beginning, we could achieve both functions, which could not be achieved in the past related works. In the future, it aims at the development of the origami type robot that achieves a further miniaturization and lightening. We also would like to achieve more complex shape transformation and a new movement model to do some tasks. For example, the picking up the object from narrow space will be suitable for origami type robot. Theoretical limitation due to the phase structure of origami should also be studied.

References

1. Ameda, K., Matsumoto, M.: Trial manufacture of an origami type robot enabling free transformation. In: Proceedings of the SSI2012, pp. 172–174 (2012)
2. Bocheva, M., Andreev, S.A., Mahadevan, L., Winkleman, A., Reichman, D.R., Prentiss, M.G., Whitesides, S., Whitesides, G.M.: Magnetic self-assembly of three-dimensional surfaces from planar sheets. Proc. Natl. Acad. Sci. **102–11**, 3029–3924 (2005)
3. Cerda, E., Mahadevan, L., Pasini, J.M.: The elements of draping. Proc. Natl. Acad. Sci. U.S.A. **101**, 1806–1810 (2004)

4. Dai, J.S., Caldwell, D.G.: Origami-based robotic paper-and-board packaging for food industry. Adv. Food Process. Packag. Autom. **21**(3), 153–157 (2010)
5. Hawkes, E., An, B., Benbernou, N.M., Tanaka, H., Kim, S., Demaine, E.D., Rus, D., Wood, R.J.: Programmable matter by folding. Proc. Natl. Acad. Sci. **107–28**, 12441–12445 (2010)
6. Kossett, A., Papanikolopoulos, N.: A robust miniature robot design for land/air hybrid locomotion. In: 2011 International Conference on Robotics and Automation, pp. 4595–4600 (2011)
7. Miura, K.: Science of Miura-ori—a review. In: 4th International Conference on Origami in Science, Mathematics, and Education (4OSME), A K Peters (2008)
8. Murata, S., Kakomura, K., Kurokawa, H.: Toward a scalable modular robotic system— navigation, docking, and integration of M-TRAN. IEEE Robot. Autom. Mag. **14**(4), 56–63 (2008)
9. Nagpal, R.: Programmable self-assembly: constructing global shape using biologically-inspired local interactions and origami mathematics. Dissertation (2001)
10. Nakai, H., Hoshino, Y., Inaba, M., Inoue, H.: Softening deformable robot: development of shape adaptive robot using phase change of low-melting-point alloy. J. Robot. Soc. Jpn. **20**(6), 625–630 (2002)
11. Paik, J., An, B., Rus, D., Wood, R.J.: Robotic origamis: self-morphing modular robots. In: Proceedings of the 2nd International Conference on Morphological Computation (2011)
12. Philip, C.B.: Fujimoto cube with 16-gon iris closure. http://www.flickr.com/photos/oschene/ (2008). Accessed 5 March 2014
13. Ryan, R.: Kawasaki rose crystallization. http://www.flickr.com/photos/infinite-origami/ (2006). Accessed 5 March 2014
14. Suzuki, Y., Inou, N., Kimura, H., Koseki, M.: Reconfigurable group robots adaptively transforming a mechanical structure (numerical expression of criteria for structural transformation and automatic motion planning method). In: Proceedings of the 2007 IEEE/ RSJ International Conference on Intelligent Robots and Systems, pp. 2361–2367 (2007)
15. Toki Corporation: BioMetal. http://www.toki.co.jp/biometal/english/contents.php (2010). Accessed 3 March 2014
16. Toki Corporation: BioMetal video library. http://www.toki.co.jp/biometal/video/index.php (2011). Accessed 10 March 2014

From Lawnmower Dynamics to Modeling, Simulation and Experiments of a Differentially Driven Robot

Qirong Tang and Werner Schiehlen

Abstract One kind of very useful service robots is the lawnmower, for example, the Automower® developed since two decades by the Swedish company Husqvarna. From a robotic point of view, this is a mobile platform driven by two big wheels along one axis and it has two small omnidirectional supporting casters. Thus, Automower® has three positional degrees of freedom in the plane, and two controllable velocity degrees of freedom subject to its nonholonomic constraint. Combined with a student project, the modeling, simulation and experiments of this kind of a differentially driven mobile robot is investigated in this study. The equations of motion are derived and the motion strategy is discussed. They are further tested on an experimental mobile platform on which the modeling assumptions for the nonholonomic robot dynamics is investigated, too.

Keywords Lawnmower · Differentially driven mobile robot · Nonholonomic constraint · Model validation

1 Introduction

Nowadays, service robots appear more and more in our daily surroundings and promise significant improvements to the quality of human life. Mobile robots may perform many service tasks [1]. Particularly the wheeled mobile robots play an important role in the service area and are well accepted by both, industry and

Q. Tang (✉) · W. Schiehlen (✉)
Institute of Engineering and Computational Mechanics, University of Stuttgart, Pfaffenwaldring 9, 70569 Stuttgart, Germany
e-mail: qirong.tang@itm.uni-stuttgart.de

W. Schiehlen
e-mail: werner.schiehlen@itm.uni-stuttgart.de

Fig. 1 Automower® (photo from [5])

Fig. 2 Robomow® (photo from [6])

domestic scenarios [2]. Moreover, wheeled robots are often used for understanding many of the robotic fundamentals during high school and university education [3, 4].

Nevertheless, for private use the service robots are still rare and currently under their developing. Very successful service robots are private robotic lawnmowers which are available on the market for about twenty years. The Swedish company Husqvarna generated and also made-up the word Automower® which is now their trademark, too. Another competitive product is the Robomow® from the Israeli company Friendly Robotics. Two exemplars of these products are shown in Figs. 1 and 2 respectively.

From a robotic point of view, differentially driven lawnmowers are nonholonomic mobile platforms carrying the cutting knives, the power unit with battery, as well as all the sensors and microelectronics. Nevertheless, they are just handy devices weighting several kilograms what are easy to be carried. Due to its nonholonomic constraint, this kind of mobile platform has unique features such as vanishing lateral motions along the drive axis, and control by two wheel inputs. Since it is oriented for grass cutting, the cutting strategy or in the robotic view the motion planning becomes important.

Motivated by above considerations, in this paper the modeling of lawnmowers is presented in Sect. 2 as a general differentially driven mobile robot and the simulations are presented in Sect. 3 while some experimental results on a platform developed and tested at the University of Stuttgart, Germany, is shown in Sect. 4. Conclusions and outlooks are given in Sect. 5 to close this paper.
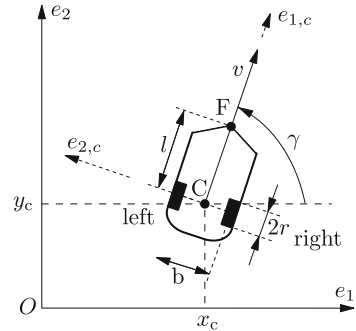
2 Modeling of a Lawnmower

2.1 Kinematics of a Differentially Driven Mobile Robot

The Automower® can be modeled as a typical differentially driven mobile robot,
see Fig. 3 for the basic kinematic relationships. This robot has two wheels
mounted along one axis. Additionally, it has two omnidirectional casters for the
support and balance of the robot body located at the front of the body. However,
for the analysis of the driving and motion mechanisms, only one caster is used at
the front sensor location 'F'. In the literature different support and balance designs
are found which are more or less consistent, see examples in [7–9].

One can easily derive the global velocity of the robot body as

$$
\begin{bmatrix} \dot{x}_c \\ \dot{y}_c \\ \dot{\gamma} \end{bmatrix} = \begin{bmatrix} \cos\gamma & 0 \\ \sin\gamma & 0 \\ 0 & 1 \end{bmatrix} \cdot \begin{bmatrix} v \\ \omega \end{bmatrix},
\tag{1}
$$

where x_c, y_c, γ describe the three positional degrees of freedom of the robot's
planar motion. Moreover, v is the robot body translational velocity with respect to
point 'C' and ω is its rotational velocity, representing the two velocity degrees of
freedom. Here 'C' coincides with both the center of mass and the wheels axial
center.

From (1) we can also obtain the nonholonomic constraint in implicit form as

$$
\dot{x}_c \cdot \sin\gamma - \dot{y}_c \cdot \cos\gamma = 0
\tag{2}
$$

what means vanishing lateral velocity of wheel axis $e_{2,c}$.

If the rotational velocities of the right and left wheels are denoted by ω_r and ω_l
separately, then it yields for the body local velocity

$$
\begin{bmatrix} v \\ \omega \end{bmatrix} = \begin{bmatrix} r/2 & r/2 \\ r/b & -r/b \end{bmatrix} \cdot \begin{bmatrix} \omega_r \\ \omega_l \end{bmatrix}, \tag{3}
$$

where r is the wheel radius and b represents the distance between the two wheel centers. Substituting (3) into (1) yields the kinematic model of the robot which is

$$
\begin{bmatrix} \dot{x}_c \\ \dot{y}_c \\ \dot{\gamma} \end{bmatrix} = \begin{bmatrix} (r\cos\gamma)/2 & (r\cos\gamma)/2 \\ (r\sin\gamma)/2 & (r\sin\gamma)/2 \\ r/b & -r/b \end{bmatrix} \cdot \begin{bmatrix} \omega_r \\ \omega_l \end{bmatrix}. \tag{4}
$$

2.2 Equations of Motion

In this study the dynamics model of the robot is derived by two methods. The first one is related to multibody system dynamics and based on Newton-Euler equations and Jourdain's principle. The second one is also briefly presented which is based on Lagrange's equations in conjunction with the constraint Eq. (2) from the traditional robotics point of view. The authors will show the different features of the two methods and seek the inspiration for the readers for different applications.

First, the robot mass is denoted by m, and the inertia tensor is written as

$$
I = \begin{bmatrix} I_{11} & I_{12} & I_{31} \\ I_{12} & I_{22} & I_{23} \\ I_{31} & I_{23} & I_{33} \end{bmatrix}. \tag{5}
$$

For this system, there are four generalized constraint forces. The normal forces g_1 and g_2 from the left and right wheels, respectively, and g_3 originates from the front caster. In addition, g_4 is the constraint force along the wheels axis. Therefore, the reaction forces and moments are

$$
f^r = \begin{bmatrix} 0 & 0 & 0 & -\sin\gamma \\ 0 & 0 & 0 & \cos\gamma \\ 1 & 1 & 1 & 0 \end{bmatrix} \cdot \begin{bmatrix} g_1 \\ g_2 \\ g_3 \\ g_4 \end{bmatrix},
$$

$$
l^r = \begin{bmatrix} \frac{b}{2}\cos\gamma & -\frac{b}{2}\cos\gamma & l\sin\gamma & 0 \\ \frac{b}{2}\sin\gamma & -\frac{b}{2}\sin\gamma & -l\cos\gamma & 0 \\ 0 & 0 & 0 & 0 \end{bmatrix} \cdot \begin{bmatrix} g_1 \\ g_2 \\ g_3 \\ g_4 \end{bmatrix}.
$$

In addition, the applied forces are the weight and the drive forces of the wheels. Thus, based on the six Newton-Euler equations and a transformation with the transposed global Jacobi matrix following Jourdain's principle

$$L^T = \begin{bmatrix} \cos\gamma & \sin\gamma & 0 & 0 & 0 & 0 \\ 0 & 0 & 0 & 0 & 0 & 1 \end{bmatrix} \tag{6}$$

in the inertial system, the equations of motion of the robot can be obtained as

$$\begin{bmatrix} m & 0 \\ 0 & I_{33} \end{bmatrix} \cdot \begin{bmatrix} \dot{v} \\ \dot{\omega} \end{bmatrix} = \frac{1}{r} \begin{bmatrix} 1 & 1 \\ b/2 & -b/2 \end{bmatrix} \cdot \begin{bmatrix} \tau_r \\ \tau_l \end{bmatrix}, \tag{7}$$

where τ_r and τ_l are the torques from the right and left wheels, respectively. For more details please refer to [8]. Thus, there are remaining with (1) five state equations as pure first order ordinary differential equations (ODE) without any constraint forces.

Based on the system's Lagrange function, the dynamics model can be described by

$$\begin{bmatrix} m\ddot{x}_c \\ m\ddot{y}_c \\ I_{33}\ddot{\gamma} \end{bmatrix} - \begin{bmatrix} 0 \\ 0 \\ 0 \end{bmatrix} = \frac{1}{r} \begin{bmatrix} \cos\gamma & \cos\gamma \\ \sin\gamma & \sin\gamma \\ b/2 & -b/2 \end{bmatrix} \cdot \begin{bmatrix} \tau_r \\ \tau_l \end{bmatrix} + \begin{bmatrix} -\lambda\sin\gamma \\ \lambda\cos\gamma \\ 0 \end{bmatrix}, \tag{8}$$

where λ is the Lagrange multiplier. Based on (8) the dynamics performance of the robot is governed, too. Due to the second derivatives in (8), now there remain six differential equations and in addition the unknown Lagrange multiplier λ characterizing differential algebraical equations (DAE). For the computational solutions of DAEs, one can refer to the monograph [10].

Equations (7) and (8) derived are based on two different methods. The first one uses the minimal coordinates of the system and there remains only ordinary differential equations and with (1) altogether has five unknowns, see (1) and (7). This brings a lot of computational convenience. The second is more standard, however it involves more unknown variables. In this case, it has differential algebraical equations with altogether seven unknowns which needs reasonable transformations to obtain the solutions. This is more challenging from the computational point of view, and more expensive. Nevertheless, this study gives both of the forms for the different applications according to different tasks of the readers. This study uses the minimal representation.

2.3 Cutting Strategy

The cutting strategy used in our simulation and experimental tests is straightforward and applied to validate our model, too. The robot is initially located in the grass area, and then begins to move meanwhile cutting grass by its equipped knives set. Once the robot detects any boundary or obstacle, it brakes and goes backward a little bit. Then, it rotates with certain degrees with respect to its forward direction for the next step. If it is still in the range with conflict to the

boundary or obstacle, it continues to rotate until it gets free for its forwarding. After the process of avoiding collisions, it continues its task. At the moment, the rotation degree taken by the robot in each step of obstacle avoidance is randomly. However, due to the users specific algorithms, it can be changed easily to improve the motion performance. More algorithms are currently under investigation.

3 Simulation

This section shows the cutting strategy within the simulation platform developed. Figure 4a demonstrates the simulation environment. Figure 4b is the beginning phase of one run, at which the robot is cutting the grass basically has no area to overwrite, whereas Fig. 4c is the phase after 30 min. The entire grass ground has been divided into many small segments and the robot begins to overwrite some areas which has been cut already, i.e., some areas are repeated for cutting. Nevertheless, at this phase the overwrite happens mainly because of trajectory crosses. Due to the nonholonomic feature and the non-zero rotation radius of this kind of robot, it generates a margin to the boundary. That is to say, a small stripe near each of the four boundaries are not reachable by the robot since the knife kit is usually not as wide as the robot body.

Figure 4d is the status after 1 h. Obviously, more areas are covered by the robot. However, the robot gets a higher chance to repeat some already cut places, even it happens the long trajectories overwrite not only crosses. Figure 4e is at the phase of closing the task. Due to the random walking strategy, there are still some small areas haven't been reached yet. The complete coverage is not guaranteed by this strategy. Some more advanced strategies with optimization are still under investigation. The coverage percentage is presented in Fig. 4f, from which we can see that the covered area is larger and larger.

This simulation platform includes a physical engine, thus many of the mechanical tasks are performed. By using this results, our model is verified via grass cutting experiments.

4 Experimental Differentially Driven Mobile Platform

4.1 Design and Construction Kits

The layout of the components of the designed robot is shown in Figs. 5 and 6 demonstrates the assembled robot in Pro/Engineer.
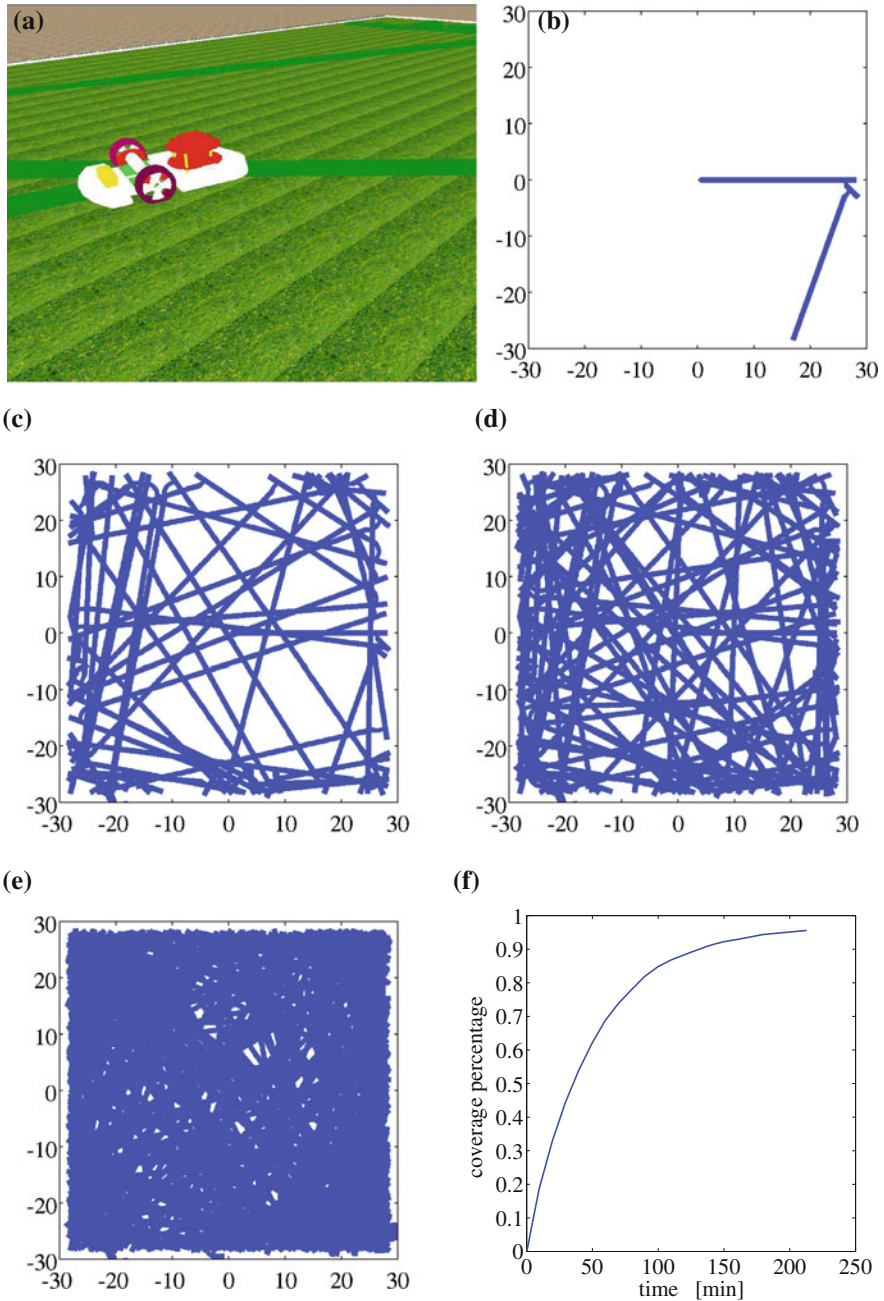
Fig. 4 A typical run of the simulation with four different phases demonstrated. **a** Simulation environment, **b** At the start phase (after 42 s), **c** After 30 min, **d** After 1 h, **e** Approaching goal (after 213 min), **f** Coverage rate over time

Fig. 5 Layout of construction kits of the designed robot

Fig. 6 Assembled in Pro/Engineer

Fig. 7 A typical run of the grass cutting experiment during the start phase. **a** Start from the center of the area, **b** meet boundary first time, **c** backwards a little bit, **d** turn to another direction
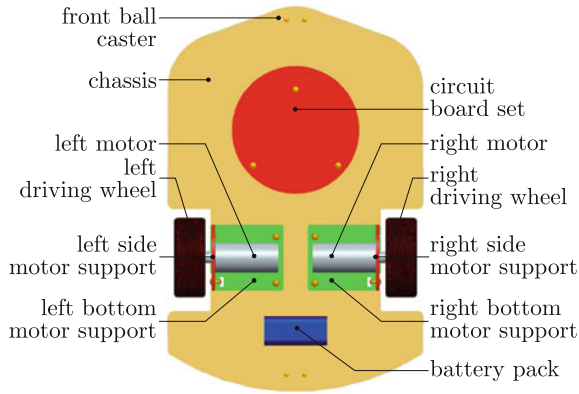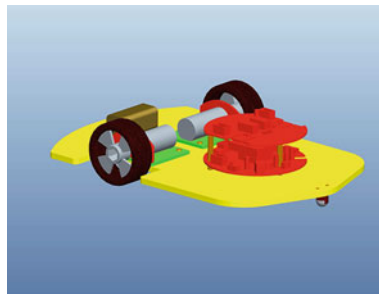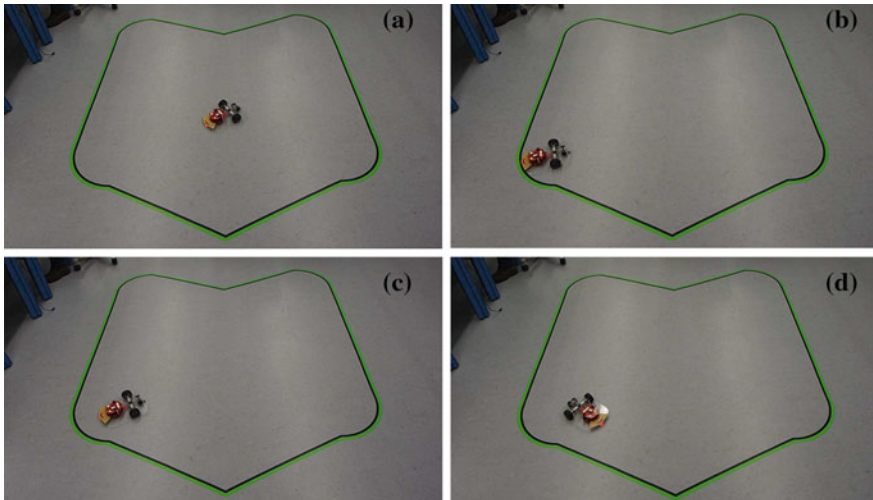
4.2 Experiments

The experiments of the grass cutting motion planning are also done in the laboratory, see Fig. 7 where the first set of critical motions are outlined.

The mechanical behaviors of the nonholonomic differentially driven robot in the laboratory environment is consistent to the simulations with the derived model. It moves forward (Fig. 7a), until it meets the boundary (Fig. 7b), where it backwards a little bit (Fig. 7c) and turns to another direction (Fig. 7d). This exactly reflects the behavior of the nonholonomic mobile robot under the aforementioned desired motion strategy.

5 Conclusions and Outlooks

This work is inspired from one kind of service robots, the lawnmower, specifically the Automower® and Robomow®. The kinematic and dynamic models of this kind of differentially driven mobile robots are first derived. Furthermore, the nonholonomic feature of this robot is emphasized and analyzed. The equations of motion are presented in minimal and Cartesian coordinates what gives more choices for robotic research. Based on these, a simulation platform which includes a physical engine is developed. The random cutting strategy of a lawnmower is analyzed with simulations and the results are compared with the motions of an experimental platform from a student project. Thus, the nonholonomic robot models are validated. More optimal motion planning strategies are currently under investigation with both simulations and experiments. Through this study, the authors highlighted the research tools for differentially driven mobile robots from both, multibody system dynamics and traditional robotic approaches, too.

References

1. Schraft, R., Schmierer, G.: Service Robots: Products, Scenarios, Visions. A K Peters, Natick (2000)
2. Ceccarelli, M., Cigola, M.: Service robots for restoration of goods of cultural heritage. In: Ceccarelli, M. (ed.) Service Robots and Robotics: Design and Application. IGI Global, Hershey (2012)
3. Lego Mindstorms: http://de.wikipedia.org/wiki/lego mindstorms. Accessed 30 Nov 2013
4. Schubert, T., Burchard, J., Sauer, M., Becker, B.: S-trike: A mobile robot platform for higher education. In: Proceeding of International Conference on Computers and Their Applications. 4–6 March, Honolulu, USA (2013)

5. Husqvarna: http://www.husqvarna.com. Accessed 30 Nov 2013
6. Friendly Robotics: http://www.robomow.com. Accessed 15 Dec 15 2013
7. Yang, J.M., Kim, J.H.: Sliding mode control for trajectory tracking of nonholonomic wheeled mobile robots. IEEE Trans. Robot. Autom. **15**(3), 578–587 (1999)
8. Schiehlen, W., Eberhard, P.: Applied Dynamics. Springer, Berlin (2014)
9. Tang, Q.: Cooperative search by mixed simulated and real robots in a swarm based on mechanical Particle Swarm Optimization. Doctoral thesis written at the Institute of Engineering and Computational Mechanics in University of Stuttgart, No. 25. Aachen: Shaker Verlag (2012)
10. Eich-Soellner, E., Führer, C.: Numerical Method in Multibody Dynamics. Teubner, Stuttgart (1998)

Kinematic Analysis Validation and Calibration of a Haptic Interface

Mehmet İsmet Can Dede, Barış Taner, Tunç Bilgincan and Marco Ceccarelli

Abstract Initial calibration tests of a novel hybrid-structured kinesthetic haptic device based on an R-CUBE mechanism is presented in this paper. Experimental validation of the kinematics along with the experimental test set-up description is provided for the manufactured R-CUBE mechanism.

1 Introduction

The word Haptic, based on an ancient Greek word, haptesthai, means related with touch [1]. As an area of robotics, haptics technology provides the sense of touch for robotic applications that involve interaction with human operator and the environment [1]. The sense of touch accompanied with the visual feedback is enough to gather most of the information about a certain environment. It increases the precision of teleoperation and sensation levels of the virtual reality (VR)

M. İ. C. Dede (✉) · B. Taner · T. Bilgincan
Department of Mechanical Engineering, İzmir Institute of Technology, 35430 İzmir, Turkey
e-mail: candede@iyte.edu.tr

B. Taner
e-mail: baristaner@iyte.edu.tr

T. Bilgincan
e-mail: tbilgincan@gmail.com

M. Ceccarelli
Laboratory of Robotics and Mechatronics, DICEM, University of Cassino and South Latium, Via Di Biasio 43, 03043 Cassino, FR, Italy
e-mail: ceccarelli@unicas.it

Table 1 Properties of HIPHAD v1.0 design

Properties of the design	
Sensation type	Kinesthetic
Mechanical structure	Hybrid
Control structure	Open-loop impedance
Application type	Desktop device
DoF of motion	6
Type of contact simulation	Point-type of contact (forces in 3D)
Continuous exertable force	>0.8 N in all directions
Nominal positional resolution	<0.1 mm
Workspace	120 W × 120 H × 120 D
Footprint	<200 mm^2

applications by exerting physical properties of the environment such as forces, motions, textures. Currently, haptic devices find use in many VR and teleoperation applications such as computer aided design [2], entertainment [3, 4], education [5], training [6], rehabilitation [7], nano-manipulation [8], virtual prototyping [9] and virtual sculpting [10].

Various types of haptic devices are developed, and they are employed in different types of tasks. Especially for accurate teleoperation [11] and precision required VR applications [12], high precision haptic systems are required with respect to the current commercially available haptic devices. In order to meet this precision criterion, a 6-DoF desktop haptic device, HIPHAD v1.0, was studied and constructed previously [13].

This paper focuses on the validation of mechanism analysis of the R-CUBE and the initial calibration tests. Next section of the paper is reserved for explanation of the HIPHAD v1.0 properties and kinematics. Later, the experimental test set-up for initial calibration is described. Finally, the test results are provided including the necessary calculation procedure for adaptation of the device in hardware-in-the-loop simulation environment.

2 Properties of HIPHAD v1.0

The device is designated to provide feedback signals to determine the pose of the tool handled by the user in space, therefore it is configured as a 6-DoF mechanism. Only point-type of contact is considered therefore, the motion and the force simulating activity of the tool can be grouped as 3-DoF active translational and 3-DoF passive rotation. The properties of the device designed are listed in Table 1.

In open-loop impedance type haptic devices, due to the random motion of the operator, no control can be employed to avoid singular positions. Therefore, motion through singular positions must be restricted. During the design procedure two singularity conditions are encountered and avoided by necessary precautions in design. Information on mechanical design can be found in [13].
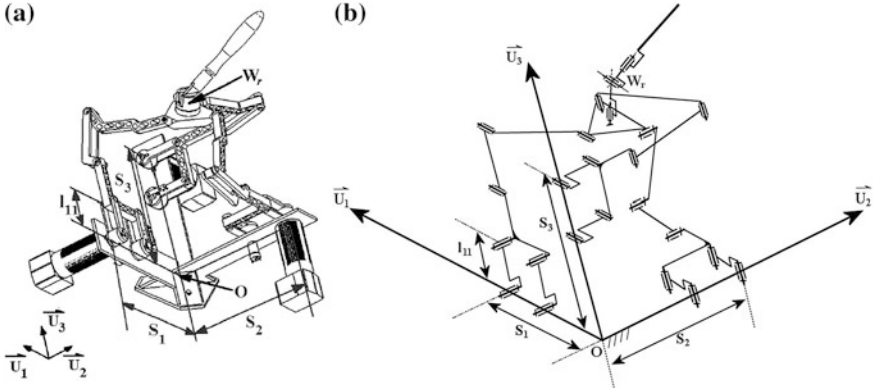
Fig. 1 Mechanism parameters: **a** CAD model, **b** sketch view

Fig. 2 a Link and joint parameters, **b** Joint limit
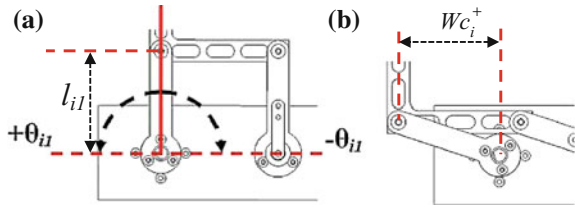
3 Kinematics Analysis of HIPHAD v1.0

Kinematics of the device can be easily obtained from the sketch representation of the device in Figs. 1 and 2.

The translational motion demand send to the slave system is based on the calculation of the Wr point by utilizing the real-time measurements from the positions sensors. Thus, direct kinematics is used to calculate the motion demand. In Eq. 1, the calculation of the position vector of the tip point, Wr, with respect to the global origin point, O, is described.

$$\vec{W}_r = \sum_{i=1}^{3} W_{ri}\vec{u}_i \qquad i = 1, 2, 3$$
$$W_{ri} = S_i + l_i \cdot \sin(\theta_{i1})$$

(1)

The zero position of the angle, θ_{i1}, is represented with solid red line in Fig. 2a. $\vec{W}c$ presented in Eq. 2 indicates the workspace limitation of the mechanism. Therefore, in Fig. 2, Wc_{i1} is theoretically half of the workspace limit along $\vec{u}_i$.

$$\vec{W}c = \sum_{i=1}^{3} Wc_i\vec{u}_i, \quad i = 1, 2, 3$$

(2)
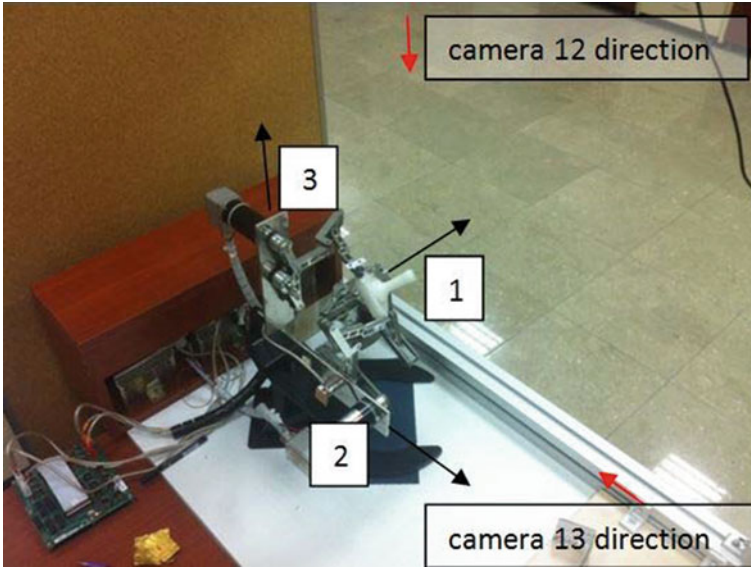
Fig. 3 Experimental test set-up

4 Experimental Test Set-up

The purpose of this experiment is to first find the absolute measurement of the mechanism's workspace. Later, this information will be transferred into joint space in order to find the joint motion limits. Finally, the joint limits will be matched with joint sensor reading (measured in V) to complete the calibration process.

Workspace is divided into two planes, $\vec{u}_1 - \vec{u}_2$ and $\vec{u}_1 - \vec{u}_3$. On those planes, we are able to measure three displacement values by two cameras, which are parallel to the normal of the selected planes as shown in the Fig. 1 with red arrows (Fig. 3).

Cameras are calibrated by finding the distance between two defined circles, whose distance in between their centers are known prior and attached on the end effector's vicinity. The translation of the end effector is measured by 2D-Cross Correlation in Matlab Simulink [14].

Total translation of the device along each direction, Wc_i, is divided into two. The two parts are denoted as Wc_i^+ and Wc_i^- representing the positive and negative translations that will be used for calculating θ_{i1}^+ and θ_{i1}^- angles.

Test procedure is initiated by finding the mid-position of the joint range, where $\theta_{i1} = 0°$, with a set-square. Then, the positive and negative limits, which are Wc_i^+ and Wc_i^-, of the mechanism are measured via cameras. Measured workspace limits are also used for calculating the joint limits θ_{i1}^+ and θ_{i1}^- as described in the Eq. 3.

Table 2 Measured values from cameras and calculated joint limits

Workspace limits	Means of measured values (mm)	Joint limits	Calculated values (°)
Wc_1^+/Wc_1^-	60.65/61.67	$\theta_{11}^+/\theta_{11}^-$	71.64/68.94
Wc_2^+/Wc_2^-	60.15/60.55	$\theta_{21}^+/\theta_{21}^-$	68.72/67.79
Wc_3^+/Wc_3^-	61.22/59.99	$\theta_{31}^+/\theta_{31}^-$	67.38/70.41

$$\begin{aligned}\theta_{i1}^+ &= \arcsin(Wc_i^+/l_{1i}) \\ \theta_{i1}^- &= \arcsin(Wc_i^-/l_{1i})\end{aligned}, \quad i = 1, 2, 3 \tag{3}$$

5 Test Results

Mechanism is located at its limits to measure workspace limits. Measured workspace limits and calculated joint limits are tabulated in the Table 2. Workspace limits are given as the mean value for six successive measurements with the same test procedure. Total angle swept by each joint within the workspace is calculated to have mean values of 140.58°, 136.50° and 137.79° for θ_{11}, θ_{21} and θ_{31} respectively. Standard deviation for value for each joint limit is calculated to be $s_{11} = 1.60$, $s_{21} = 1.26$ and $s_{31} = 1.47$. According to the statistics of data acquired from six sets of measured displacement values, error bounds are calculated for the 95.45 % of measurement as; first joint limit bounded within $\pm 3.20°$ error, second joint limit bounded within $\pm 2.94°$ error and third joint limit bounded within $\pm 2.51°$ error.

Voltage values measured from the potentiometers in each axis are given in the Table 3 with respect to the axis numbers. These values are measured at the joint limits, indicated with min and max, and also for the mid-position of the workspace, indicated by mid. In addition, the measurement ranges in between the joint limits are provided to be used in constant gain, K_i, calculation for converting the raw data into measured joint positions by using Eq. 4.

$$K_i = (\theta_{i1}^+ + \theta_{i1}^-)/Vr_i, \quad i = 1, 2, 3 \tag{4}$$

Finally joint angles at an instant during operation are calculated by the Eq. 5 by using measured voltage from the sensors of the joints, Vm_i for $i = 1, 2, 3$.

$$(Vm_i - Vmid_i) \times K_i = \theta_{i1}, \quad i = 1, 2, 3 \tag{5}$$

Table 3 Voltage values measured from joint sensors (potentiometers)

Pot$_1$		Pot$_2$		Pot$_3$	
Voltage values (V)	Voltage range, Vr (V)	Voltage values (V)	Voltage range, Vr (V)	Voltage values (V)	Voltage range, Vr (V)
Vmin$_1$ 2.68		Vmin$_2$ 2.20		Vmin$_3$ 0.86	
Vmid$_1$ 5.33	Vr$_1$ = 5.07	Vmid$_2$ 5.11	Vr$_2$ = 5.57	Vmid$_3$ 3.64	Vr$_3$ = 5.30
Vmax$_1$ 7.70		Vmax$_2$ 7.78		Vmax$_3$ 6.17	

6 Conclusions

The aim of this work was to calibrate and experimentally validate the kinematics of a novel haptic device, HIPHAD v1.0. External measurement of the absolute position of the mechanism is carried out by using a vision-aided algorithm. Calibration of the mechanism is done in accordance with the test results. Test results also indicate the precision errors in manufacturing and assembling the device which are accounted for by performing the calibration. As a result of the tests, repeatability of the device is calculated to be around 2°/100°. This performance can be improved for applications calling for increased precision by changing the joint sensors with encoder with higher resolutions. Future work includes the calibration of forces exerted by the mechanism to the human operator.

References

1. El Saddik, A.: The potential of haptics technologies. IEEE Instrum. Meas. Mag. **10**(1), 10–17 (2007)
2. Ott, R., Vexo, F., Thalmann, D.: Two-handed haptic manipulation for CAD and VR applications. Comput. Aided Des. Appl. **7**(1):125–138 (2010)
3. Faust, M., Yoo, Y.-H.: Haptic feedback in pervasive games. In: 3rd International Workshop Pervasive Gaming Applications, Dublin (2006)
4. Web. http://www.novint.com/index.php/novintfalcon. Accessed 27 July 2012
5. Kretz, A., Huber, R., Fjeld, M.: Force feedback slider (FFS): interactive device for learning system dynamics. IEEE Int. Conf. Adv. Learn. Technol. 457–458 (2005)
6. Basdogan, C., Ho, C.-H., Srinivasan, M.A.: Virtual environments for medical training: graphical and haptic simulation of laparoscopic common bile duct exploration. IEEE/ASME Trans. Mechatron. **6**(3), 269–285 (2001)
7. Broeren, J., Rydmark, M., Sunnerhagen, K.S.: Virtual reality and haptics as a training device for movement rehabilitation after stroke: a single-case study. Arch. Phys. Med. Rehabil. **85**(8), 1247–1250 (2004)
8. Sieber, A., Valdastri, P., Houston, K., Eder, C., Tonet, O., Menciassi, A., Dario, P.: A novel haptic platform for real time bilateral biomanipulation with a mems sensor for triaxial force feedback. Sens. Actuator. A Phys. **142**(1), 19–27 (2008)
9. Zhu, W., Lee, Y.-S.: Five-axis pencil-cut planning and virtual prototyping with 5-DOF haptic interface. Comput. Aided Des. **36**(13), 1295–1307 (2004)
10. Leu, M.C., Peng, X., Zhang, W.: Surface reconstruction for interactive modeling of freeform solids by virtual sculpting. CIRP Ann. Manuf. Technol. **54**(1):131–134 (2005)

11. Hokayem, P.F., Spong, M.W.: Bilateral teleoperation: an historical survey. Automatica **42**(12), 2035–2057 (2006)
12. Ferreira, A., Mavroidis, C.: Virtual reality and haptics for nanorobotics. IEEE Robot. Autom. Mag. **13**(3), 78–92 (2006)
13. Bilgincan, T., Gezgin, E., Dede, M.I.C.: (2010) Integration of the hybrid-structure haptic interface: HIPHAD v1.0. In: Proceedings of the International Symposium of Mechanism and Machine Theory
14. Pan, B., Qian, K., Xie, H., Asundi, A.: Two-dimensional digital image correlation for in-plane displacement and strain measurement. Meas. Sci. Technol. (2009). doi:10.1088/0957-0233/20/6/062001

Problems of Increasing Efficiency and Experience of Walking Machines Elaborating

E. S. Briskin, V. A. Shurygin, V. V. Chernyshev, A. V. Maloletov, N. G. Sharonov, Y. V. Kalinin, A. V. Leonard, V. A. Serov, K. B. Mironenko and S. A. Ustinov

Abstract The issues around problem of increasing efficiency of walking machine motion have been discussed in this paper. Among them: ground or bearing cross-country ability, profile cross-country ability, maneuverability, the energy consumption.

1 Introduction

It is well known and obvious that overwhelming majority of the ground transport and technological machines have wheeled or crawler mover. The usage and continuous perfection of such movers are based on the simplicity of the construction and the effectiveness in the work. However the exploiting situations take place when the usage of such movers is not effectively and sometimes even impossible.

The researches on the development of new types of movers for the transport and technological machines that meet the requirements of high profile and a bearing practicability, ecological compatibility with a ground, maneuverability, energy efficiency continuously carries out at present time. To such movers, in particular, belong walking mover [1].

However, it is known a limited number of walking machines, which are used or can be used in transportation and technological operations [2].

E. S. Briskin (✉) · V. A. Shurygin · V. V. Chernyshev · A. V. Maloletov · N. G. Sharonov ·
Y. V. Kalinin · A. V. Leonard · V. A. Serov · K. B. Mironenko · S. A. Ustinov
Volgograd State Technical University, 28, Lenin Ave, Volgograd 400005, Russia
e-mail: dtm@vstu.ru
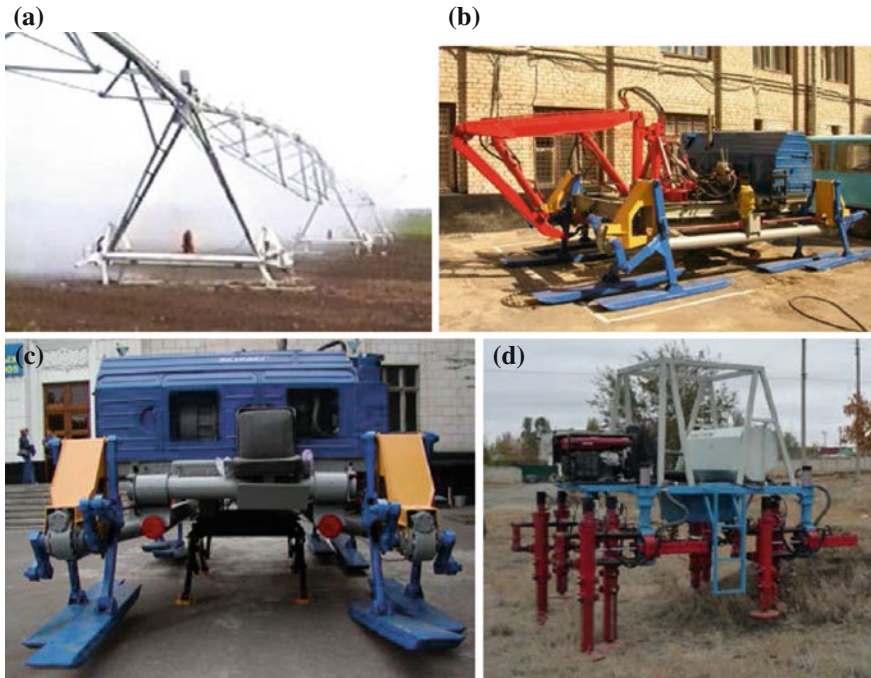
Fig. 1 Walking machines have developed in Volgograd State Technical University **a** Sprinkling machine "Kuban"with walking supports **b** Walking machine "Vosminog" **c** Walking machine "Vosminog -M" **d** Walking machine "Ortonog"

The reason of such situation is the relative complexity of the walking movers and control systems compared to traditional, and in this regard to their lower reliability. Therefore, main efforts of the developers of walking machines should be directed to the development of effective walking movers and control systems.

2 Statement of the Problem

The methods of increase efficiency of walking machine on the basis of mathematical modeling and experimental investigation real walking machine "Vosminog", "Vosminog-M", "Ortonog", sprinkling machine "Kuban" (Fig. 1) in real conditions [3] need to be developed.

Among them:

1. Problem improvement of ground practicability.
2. Problem of increase of profile cross-country ability for walking machines with cycle movers and machine with double orthogonal-rotating movers.
3. Problem of increase of the energy efficiency.
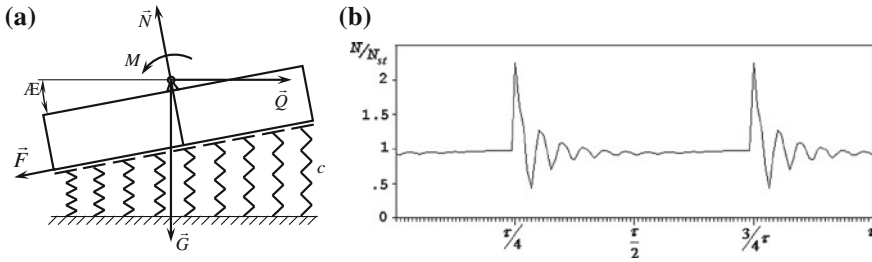
Fig. 2 The interaction of the foot with the ground. **a** Design scheme: G is load on foot; Q is resistance force; N is the normal reaction of the soil; F is the force grip; c is the stiffness of soil per unit length; M is moment of force; φ is rotation angle of the foot. **b** Cyclic dependence of the relative change in total normal reaction of soil N from its static value N_{st} for the cycle τ for elastic ground

3 Problem Solutions

3.1 Ground Practicability

For a walking machine average strength of the resistance movement is given by the expression

$$F = \sum_{j}^{NM} P_{j\max}^2 \theta / 2c_n L = \sum_{j}^{N} P_{j\max}^2 \Big/ 2kSL \tag{1}$$

where $P_{j\max}$ is the largest normal interaction force of walking mechanism of support with the ground, θ—rate regime; $c_n = kS$ is the normal rigidity of the system of soil-pacing mechanism; S is bearing area, k is coefficient of volume crumbling soil, L is the length of the pitch; M is number of mechanisms pacing; N is number of movers.

Thus, it can be concluded that resistant to the motion of walking machine the less than more the step length and the contact area with bearing surface.

The increase of bearing practicability for walking machines is possible even at the expense of two effects, which are impossible for wheeled and tracked vehicles.

First. In the study of the dependence of the coupling bearing mover and soil from the character of distribution of external forces, it is found that you can increase the trailer coupling properties of support, and even restore traction in its complete loss due to additional applications pair forces to a specific moment. The scheme of interaction of the foot with the ground is presented in Fig. 2. The effective coefficient of adhesion f_{ef} instead of f increases with growth of angle φ

$$f_{ef} \approx f + \text{tg}\varphi \tag{2}$$

This result was obtained with the help of preparing the equilibrium equations.

Fig. 3 The algorithms of overcoming obstacle
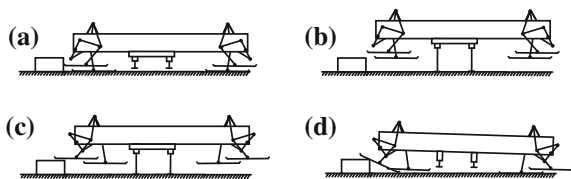
Fig. 4 The kinematical scheme of the double orthogonal rotating mover. *1* the body of walking machine, *2* the drive adaptation, *3* the drive of course motion, *4* the drive of rotation
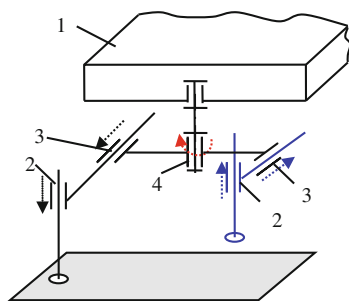
Second. When the shifting weight from one to other mover the oscillation occurs, influencing the value of a normal reaction. The characteristic of normal reaction dependence from time are presented in Fig. 2b.

The growth of the support reactions in some moments of the cycle is the reason of increased trailer coupling properties, and their decrease in other moments of the cycle contributes to the relative sliding of interacting bodies.

3.2 Profile Cross-Country Ability

A high lifting of walking mechanism pads can be based by the additional mechanisms of lifting of the walking machine "Vosminog-M" [4]. When it is necessary to overcome the rigid obstacle the motion of walking machine may be subdivided into some phases: first—stopping in front of the obstacle (Fig. 3a), second—lifting of walking machine with the help of mechanisms of lifting (Fig. 3b); third—putting on the driver of course motion, in this case the pads accomplish the motion and take position over the obstacle (Fig. 3c); fourth—sinking of the walking machine with the help of mechanisms of lifting (Fig. 3d).

Walking machine "Ortonog" (Fig. 1) is based on application of double orthogonal-rotating movers (Fig. 4)

The transition across the ledge by two pairs of legs is showed on Fig. 5.
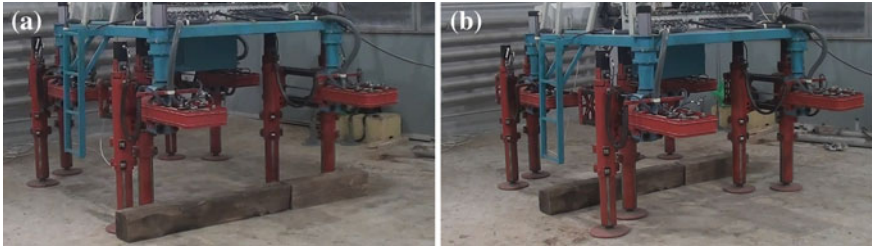
Fig. 5 Walking machine "Ortonog" across the ledge. **a** Start overcoming the ledge **b** completion of overcoming the ledge
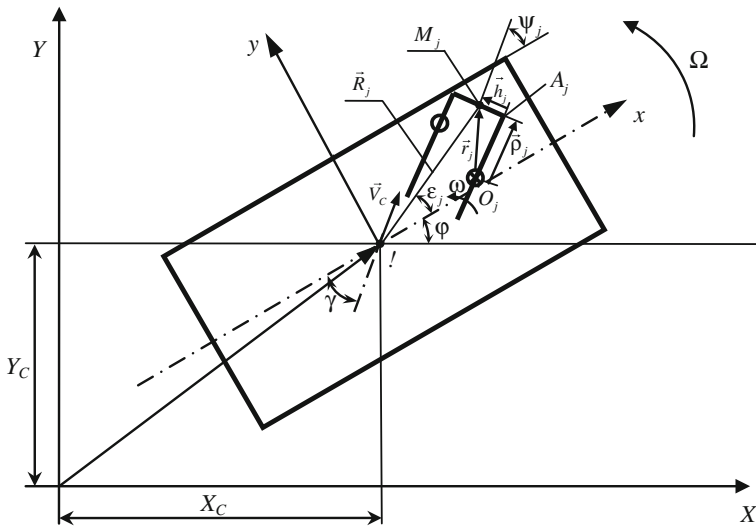
Fig. 6 The kinematic diagram of plane motion of housing and one of those in support of walking mechanisms

3.3 Maneuverability

In order to secure the kinematical exact turn for walking machine "Vosminog" the mechanisms of lifting have to be mounted on the turning circle. Such turning circle can accomplish the motion about fixed axis relatively the frame of the walking machine. The turn may be subdivided into three phases: first—lifting of the walking machine with the help of lifting mechanisms, second—turn of the walking machine frame relatively the turning circle, third—sinking of walking machine with the help of lifting mechanism.

The kinematic scheme of the machine "Ortonog" (Fig. 1) for definition of laws of motion is presented in Fig. 6.

The motion of the walking machine body in the plane Oxy (Fig. 6) is given by the speed $\vec{V}_C$ of the pole and the angular velocity of the rotational motion around the pole Ω. The position of the fastening points M_j on the body of the walking machine is set by radius-vector $\vec{R}_j$ relatively conventional centre C forming the angle ε_j of the longitudinal axis of the machine and the radius-vector $\vec{r}_j$ of points M relatively to the bearing point of the mover O_j. O_jA_j—the drive shaft of the longitudinal movement of walking mechanism which is in a supporting phase, $A_jM_j = h = \text{const}$—lever actuator mounting, ψ_j—is the angle of mover rotation relatively to the frame.

The programs laws of executive mechanisms motion are determined from these equations.

$$\begin{cases} V_{C\tau} - \Omega R_j \sin \varepsilon_j = \dot{\rho}_j \cos \psi_j + \left(\Omega + \dot{\psi}_j \right) \left(-\rho_j \sin \psi_j - h_j \cos \psi_j \right) \\ V_{Cn} + \Omega R_j \cos \varepsilon_j = \dot{\rho}_j \sin \psi_j + \left(\Omega + \dot{\psi}_j \right) \left(\rho_j \cos \psi_j - h_j \sin \psi_j \right) \end{cases} \tag{3}$$

where V_{Cn}, $V_{C\tau}$—is the projection of the velocity of the pole C on the normal and the longitudinal axis of the machine, ρ_j—relative displacement of j support.

3.4 Energy Efficiency

In the model estimation of power expenditures, the machine is a system of three solid bodies (Fig. 7): the body and two feet joined with each other by inertialess invertible mechanisms, and is set in motion by a single motor.

The motion equations of the considered mechanical system having a single common drive for walking mechanisms staying in the support phase and in the carrying phase contain differential equations of the motion of the machine body and feet regarded as rigid bodies, which move rectilinearly along the horizontal axis, the constraints equations that establish a dependence between movements of the leading link and the machine body with walking mechanism, and the motor equations under a constant velocity of its output link.

$$M\ddot{x}_1 = \lambda_1 - Q(x_1, \dot{x}_1), \quad m\ddot{x}_2 = \lambda_{2,1} - \Pi_1(\varphi) = 0, \quad x_2 - \Pi_2(\varphi) = 0,$$
$$L - \lambda_1 \frac{\partial \Pi_1}{\partial \varphi} - \lambda_2 \frac{\partial \Pi_2}{\partial \varphi} = 0 \tag{4}$$

where M and m are the mass of the machine body and the equivalent mass of links of the walking mechanism that are at the carrying state reduced to the support point; x_1 and x_2 are absolute horizontal coordinates of the machine body and the support point of the carried walking mechanism; λ_1 and λ_2 are indefinite Lagrange multipliers, Q is depending in the general case on its coordinates and body
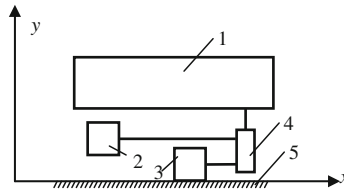
Fig. 7 Model diagram of the rectilinear motion of a walking machine: *1* is for the body, *2* is for the equivalent walking mechanism at the carrying stage, *3* is for the equivalent walking mechanism at the support stage, *4* is for the course motion drive, and *5* is for the ground

velocity; φ is the generalized coordinate of the drive motor (e.g., the angle of rotation), and $\dot{\varphi} = \omega = \text{const}$; $\Pi_1(\varphi)$, and $\Pi_2(\varphi)$ are transfer functions determining the holonomic stationary constraints between the motor and the considered bodies; and L is the generalized force generated by the motor (in the considered case, it is the torque). As a result of solving the variational isoperimetric problem we have [5, 6].

$$\dot{T} + Q\dot{x}_1 = \bar{Q}\,\bar{V}_1 \tag{5}$$

where T is kinematic energy, $\bar{Q}$ is average force, $\bar{V}$ is average velocity.

4 Conclusion

The performed analysis of the walking machine allows to make the following conclusion.

1. In order to increase the ground practicability it is necessary to increase the length of pitch, square feet, to be able to control the orientation of the foot and to be able quickly away from the ground at a moment of change feet.
2. It is possible to use additional lifting movers installed on the turn circle in order to increase the profile cross-country ability and insure kinematical exact turn for walking machines with circle movers (for example "Vosminog"). In order to increase the profile cross-country ability and ensure maneuverability for walking machines as "Ortonog" we must know how to choose the gait and control algorithm accordance with (3).
3. Energy efficiency of walking movers can be providing by the refusal of absolute comfort of motion in accordance with (5).

References

1. Silva M.F., MacHado J.A.T.: A literature review on the optimization of legged robots. J. Vib. Control **18**(12):1753–1767
2. Warren H.A.: CLAWAR2 - Mobile machines operating in outdoor unstructured terrains. In: Climbing and Walking Robots: Proceedings of the Fifth International Conference CLAWAR 2002, pp. 907–916. London, (2002)
3. Briskin E.S., Chernyshev V.V., Maloletov A.V., Sherstobitov S.V.: On dynamics of movement of walking machines with gears on the basis of cycle mechanisms theory and practice of robots and manipulators. In: ROMANSY 13: Proceedings of the 13th CISM-IFToMM Symposium/ International Centre for Mechanical Sciences, pp. 313–322. Wien, New York, (2000)
4. Briskin E.S., Zhoga V.V., Chernyshev V.V., Maloletov A.V., Kalinin Y.V., Sharonov N.G.: Walking machines (elements of theory, experience of elaboration, application). In: Emerging Trends in Mobile Robotics: Proceedings of the 13th International Conference on Climbing and Walking Robots and the Support Technologies for Mobile Machines, pp. 769–776. Nagoya Institute of Technology, Japan [Nagoya, Japan], 31 Aug–3 Sept (2010)
5. Briskin E.S., Zhoga V.V., Maloletov A.V.: Control of motion of a legged locomotion machine with minimal-power motor. Mech. Solids **44**(6):828–836 (2009)
6. Briskin E.S., Kalinin Y.V.: On energetically efficient motion algorithms of walking machines with cyclic drives. J. Comput. Syst. Sci. Int. **50**(2):348–354 (2011)

Stiffness Analysis of WL-16RV Biped Walking Vehicle

Giuseppe Carbone, Kenji Hashimoto and Atsuo Takanishi

Abstract This paper proposes a stiffness analysis of biped walking vehicle that is based on a parallel kinematics architecture. Namely, WL-16RV (Waseda Leg No.16 Refined V) is a biped walking vehicle that can carry on board a human while overcoming typical human environment barriers. Experimental tests have been carried out on a built prototype of WL-16RV by using a specific set up for validation purposes.

Keywords Stiffness analysis · Biped robots · Parallel mechanisms

1 Introduction

In the last decades several industrialized countries have experienced an increase of number of elderly and disabled wheelchair users. Accordingly, the avoidance of environmental barriers for elderly and disabled wheelchair users is getting more and more interest. In this frame, investigations at Waseda University have been carried out aiming to design a bipedal robot that may let a human overcoming the typical human environment barriers (stairs, obstacles), [1] and on 2003 WL-16 (Waseda Leg -No.16), has achieved the world first dynamic biped walking by carrying an adult human [2]. Several improved version have been proposed up to the current version named as WL-16 RV (Waseda Leg No.16 Refined V), Fig. 1.

G. Carbone (✉)
Laboratory of Robotics and Mechatronics, DiCEM, University of Cassino and South Latium, Via Di Biasio 43, 03043 Cassino, FR, Italy
e-mail: carbone@unicas.it

K. Hashimoto · A. Takanishi
Humanoid Robotics Institute, Waseda University, #41–204A, 17 Kikui-cho, Tokyo, Shinjuku-ku 162-0044, Japan
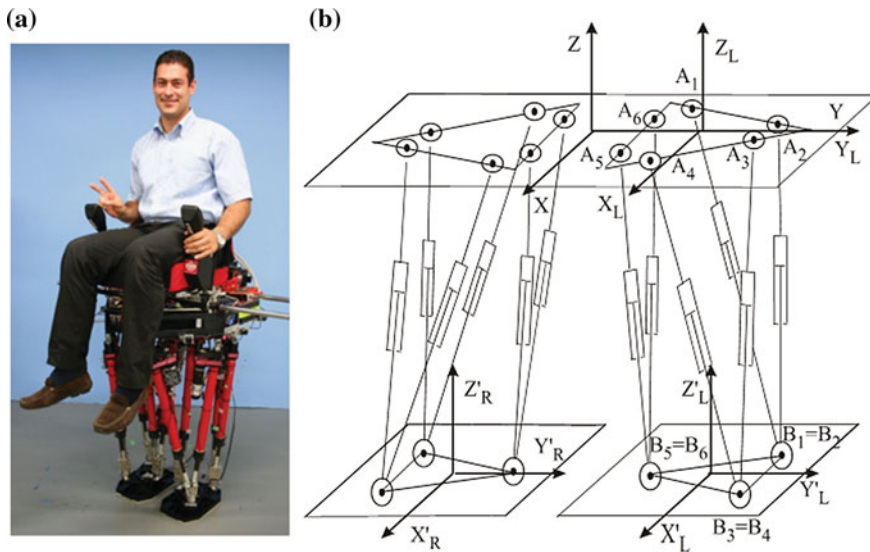
Fig. 1 WL-16RV: **a** a photo with a human on board; **b** a kinematic scheme

Also other research teams are investigating the use of walking robots for helping or assisting humans as reported for example in [3–5]. An electric wheelchair named "iBOT" capable of ascending and descending stairs and slopes is even available on the market, [6]. Nevertheless, these solutions have several drawbacks as compared with WL-16RV such as the need of a rigid stair rail to ascend and descend stairs or other special environment conditions also due to very high own weight and relatively low payload capacity.

Key aspects for achieving a successful human carrying walking vehicle are high payload to weight ratio as well as low compliant displacements. Thus, a careful stiffness analysis becomes a key issue for achieving a suitable design solution. Several analyses of stiffness performance have been carried out for different robotic architectures as reported for example in [7–9]. However, few stiffness models have been experimentally validated mainly due to the lack of a simple standard procedure for carrying out the necessary experimental tests.

The main goals of this paper are to define a suitable stiffness model for WL-16RV. Then, numerical simulations have been carried out in order to estimate its stiffness performance also in terms of compliant displacements. Additionally, a proper experimental set up as been defined as based on a simplified version of Milli-CaTraSys (Milli-Cassino Tracking System). The proposed set-up consists of two sets of three wire encoders and two six-axis force-torque sensors. This system can measure both applied wrench and resulting compliant displacements on a foot. Experimental tests have been carried out on a prototype of the biped walking vehicle WL-16RV under various operation conditions.

Table 1 Kinematic parameters for the left leg of WL-16RV

i-th link	x_{Ai} (mm)	y_{Ai} (mm)	z_{Ai} (mm)	x_{Bi} (mm)	y_{Bi} (mm)	z_{Bi} (mm)
1	55.0	−274.7	0.0	80.0	−31.0	59.0
2	−55.0	−274.7	0.0	80.0	−31.0	59.0
3	−224.7	−105.0	0.0	−80.0	−31.0	59.0
4	−120.0	−45.0	0.0	−80.0	−31.0	59.0
5	120.0	−45.0	0.0	0.0	62.0	59.0
6	224.7	−105.0	0.0	0.0	62.0	59.0

2 The Biped Locomotor WL-16RV

WL-16RV consists of two legs and a waist and is capable of walking independently. Each leg is composed of a 6-DOF Gough-Stewart parallel architecture, as also shown in the kinematic model of Fig. 1b. Main components of the mechanical design of WL-16RV prototype are a pelvis, 12 linear actuators, 12 conventional universal joints (upper joints), 6 customized spherical joints (lower joints). WL-16RV is actuated by 12 DC servomotors that are controlled by using 12 on-board servo drivers and an on-board master computer. An encoder and an optical photo micro sensor are embedded in the assembly of each linear actuator for control and calibration purposes. The mobility range of each linear actuator is about 350 mm from the maximum stretched configuration to the minimum stretched configuration. Other components such as batteries and control system are installed on-board. Table 1 reports the main kinematic parameters of WL-16RV by referring to the model in Fig. 1b. In particular, x_{Ai}, y_{Ai}, z_{Ai}, (i = 1∼6) are the Cartesian coordinates of the joints A_i on the waist and x_{Bi}, y_{Bi}, z_{Bi}, (i = 1∼6) define the location of the joints B_i on the left foot.

3 A Stiffness Model of WL-16RV

Considering Cartesian reference frames, 6×1 vectors can be defined for the compliant displacements $\Delta \mathbf{S}$ and for the external wrench $\mathbf{W}$ in the form

$$\Delta \mathbf{S} = (\Delta x, \, \Delta y, \, \Delta z, \, \Delta a, \, \Delta g, \, \Delta d)^t;$$
$$\mathbf{W} = (Fx, \, Fy, \, Fz, \, Tx, \, Ty, \, Tz)^t \tag{1}$$

where Δx, Δy, and Δz are the variations of Cartesian coordinates for the origin of a moving frame on manipulator extremity and $\Delta \alpha$, $\delta \gamma$, $\Delta \delta$ are the variations of angular coordinates for a moving frame; F_X, F_Y and F_Z are the force components acting upon a point on the moving frame along X, Y and Z directions, respectively; T_X, T_Y and T_Z are the torque components acting upon the same point on the

Fig. 2 A simplified stiffness
model of WL-16RV with
lumped parameters
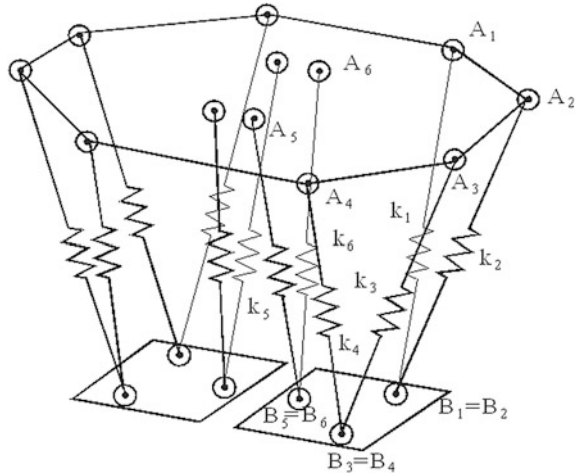
movable plate about X, Y, and Z directions, respectively. Under the assumption of small compliant displacements, one can write

$$\mathbf{W} = \mathbf{K}\,\Delta\mathbf{S} \tag{2}$$

where K is the so-called 6 × 6 Cartesian or spatial stiffness matrix.

Several different formulations can be used for the computation of the Cartesian stiffness matrix as discussed for example in [6–9]. A simplified approach widely used in robotics is based on the use of lumped stiffness parameters and Jacobian matrices so that the Cartesian stiffness matrix K can be computed as

$$\mathbf{K} = \mathbf{J}^t \mathbf{K_L} \mathbf{J} \tag{3}$$

where J is a 6 × 6 Jacobian matrix; t stands for the transpose operator, K_L is a diagonal matrix of the lumped stiffness parameters k_i (i = 1,...,6) in the form

$$K_L = \begin{bmatrix} k_1 & 0 & 0 & 0 & 0 & 0 \\ 0 & k_2 & 0 & 0 & 0 & 0 \\ 0 & 0 & k_3 & 0 & 0 & 0 \\ 0 & 0 & 0 & k_4 & 0 & 0 \\ 0 & 0 & 0 & 0 & k_5 & 0 \\ 0 & 0 & 0 & 0 & 0 & k_6 \end{bmatrix} \tag{4}$$

A simplified stiffness model with lumped parameters can be defined for WL-16RV as shown in Fig. 2 where six springs are used to represent the lumped stiffness properties of the six limbs in one leg. It is to note that the above mentioned simplified model can give convenient advantages in terms of reduced model complexity and in terms of computational costs while still giving a sufficient accuracy.

During the walking of WL-16RV, one can identify three main phases. Namely, single support phase on left leg, double supporting phase, and single supporting phase on right leg. The single supporting phase occurs most frequently. Moreover, in the double support phase WL-16RV is significantly stiffer since both legs are in contact with the ground. Thus, only the single support phase will be addressed in details in the followings.

The position and orientation of the movable frame that is attached to the standing leg can be defined through the rotation matrix

$$R = \begin{bmatrix} (c\phi\, c\theta) & (c\phi\, s\theta\, s\psi - s\phi c\psi) & (c\phi\, s\theta\, c\psi + s\phi s\psi) \\ (s\phi\, c\theta) & (s\phi\, s\theta\, s\psi + c\phi c\psi) & (s\phi\, s\theta\, c\psi + c\phi s\psi) \\ -s\phi & c\theta\, s\psi & c\theta\, c\psi \end{bmatrix} \qquad (5)$$

where $c\theta$, $s\theta$, $c\phi$, $s\phi$, $c\psi$, $s\psi$, are shorthands of $\cos\theta$, $\sin\theta$, $\cos\phi$, $\sin\phi$, $\cos\psi$, $\sin\psi$, respectively. It is to note that the rotation matrix in Eq. (5) has been defined by referring according to the notation Yaw–Pitch–Roll angle rotations, where a rotation ψ about the x axis (Yaw) is followed by a rotation θ about y axis (Pitch), and ending with a rotation ϕ about z axis (Roll).

The length of each limb can be defined as the distance between its initial and final coordinate. Thus, one can write

$$L_i = \sqrt{(x_{Bi} - x_{Ai})^2 + (y_{Bi} - y_{Ai})^2 + (z_{Bi} - z_{Ai})^2} \qquad (6)$$

where x_{Bi}, y_{Bi}, z_{Bi} ($i = 1,\ldots,6$) can be computed in the fixed reference frame by using the rotation matrix in Eq. (5). Then, the Jacobian matrix of the left leg of WL-16RV can be computed as

$$J = \begin{bmatrix} J_{ix}, & J_{iy}, & J_{iz}, & J_{i\varphi}, & J_{i\psi}, & J_{i\theta} \end{bmatrix}^t \qquad (7)$$

where $i = 1,\ldots,6$; t is the transpose operator, and

$$J_{ix} = \frac{\partial L_i}{\partial x}; J_{iy} = \frac{\partial L_i}{\partial y}; J_{iz} = \frac{\partial L_i}{\partial z}; J_{i\varphi} = \frac{\partial L_i}{\partial \varphi}; J_{i\psi} = \frac{\partial L_i}{\partial \psi}; J_{i\theta} = \frac{\partial L_i}{\partial \theta} \qquad (8)$$

4 Numerical simulations

Numerical evaluation of stiffness performance of WL-16RV has been achieved by implementing Eqs. (3)–(8) into a Matlab code to calculate the Cartesian stiffness matrix for a specific pose of WL-16RV. Additionally, Eq. (2) has been used for computing the compliant displacements ΔS at a given pose under the action of a specific wrench W. Required input data are the numerical values of kinematic parameters, the numerical values of the joint variables, the numerical values of
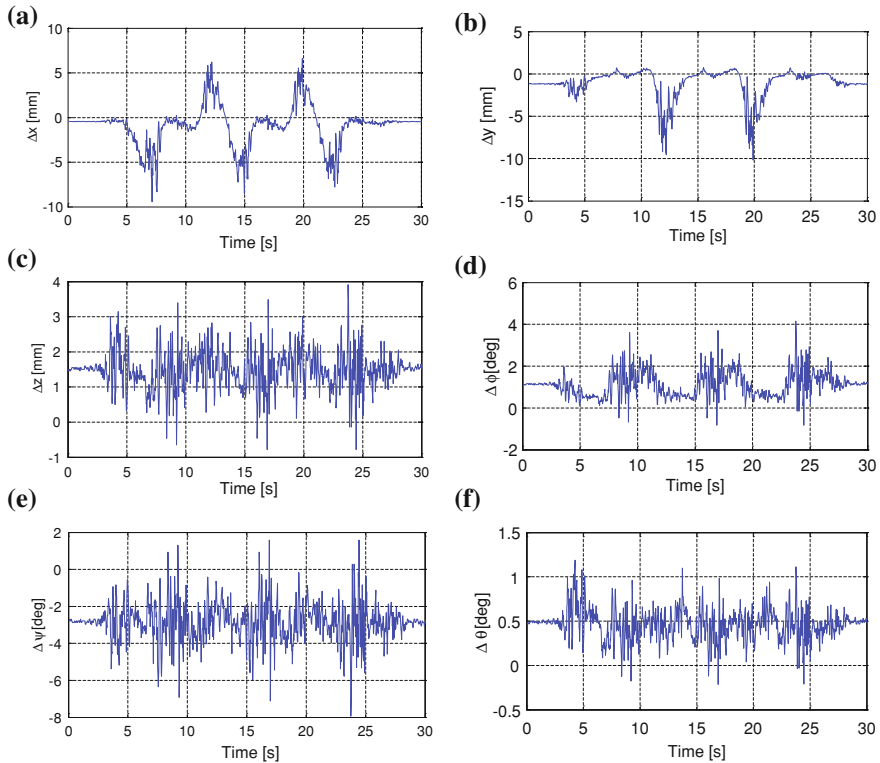
Fig. 3 Simulation of compliant displacements for a forward walking: **a** Δx; **b** Δy; **c** Δz; **d** $\Delta \varphi$; **e** $\Delta \psi$; **f** $\Delta \theta$

applied wrench at a given pose, the value of the lumped stiffness parameter of the limbs k_i ($i = 1,\ldots,6$).

The considered values of kinematic parameters have been those reported in Table 1 as referring to the real sizes of WL-16RV. The considered numerical values of the joint variables have been taken from the pattern generator of WL-16RV as referring to a real walking gait. Similarly, the numerical values of applied wrench at each given pose have been taken from measures during a real walking gait. Experimental tests have been carried out for estimating the lumped stiffness parameter of a limb k_i by means of a specific test-bed. The computed lumped stiffness parameter of a limb is equal to an average of 600 N/mm. Moreover, experimental tests show a clearance of the limb of about 0.3 mm at unloaded conditions.

Several simulations have been carried out in Matlab environment in different operation conditions. For example, Fig. 3 shows the plots of compliant displacements that have been obtained during a simulation of a four steps walking of WL-16 RV with the above-mentioned input value. Simulation results show maximum
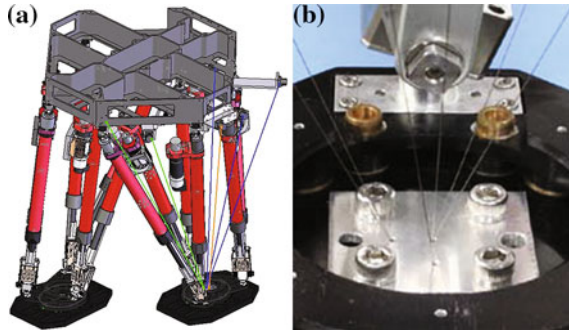
Fig. 4 Designed location of sensors on WL-16RV: **a** a 3D model; **b** a zoomed view of the foot with the attachment of wire sensors
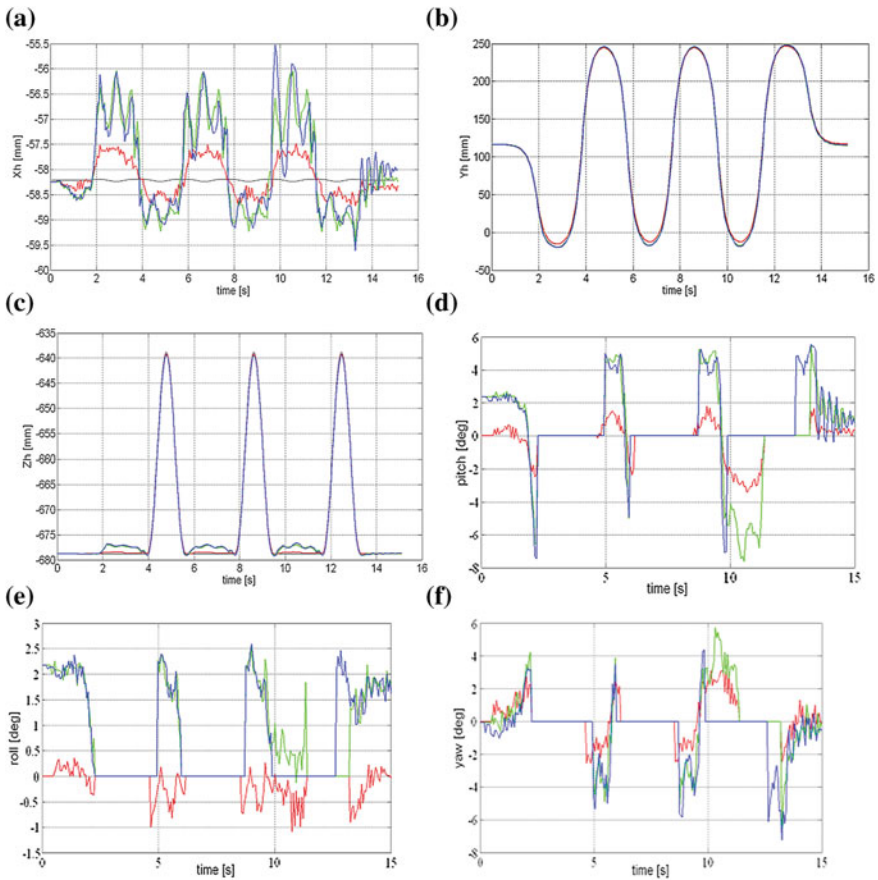
Fig. 5 Position and orientation of left foot of WL-16RV during a stamping experiment (*black dash line* is pattern data, *blue solid line* is no load case; *red dot line* is 9 kg load on waist case): **a** X-component; **b** Y-component; **c** Z-component; **d** pitch angle; **e** roll angle; **f** yaw angle

absolute values of linear compliant displacements as 6.62 mm along X direction, 10.14 mm along Y direction, 3.91 mm along Z direction. These values do not take into account the effect of clearance.

5 Experimental Setup and Tests

Figure 4 shows the proposed experimental set-up for stiffness tests. Its design and operation has been derived from Milli-CaTraSys design, [8]. It is composed of six Micritech MLS-12 linear encoder wire sensors for measuring the compliant displacements $\Delta \mathbf{S}$ of the foot via a trilateration technique, [8], and a Nitta IFS67M25T50 force/torque sensor that provides the values of the wrench $\mathbf{W}$ acting on the foot. Experimental tests have been carried out both in static and dynamic conditions for various configurations or walking operations of WL-16RV. The experimental data have been postprocessed in order to get the plots of compliant displacements such as shown in Fig. 5. These plots well match the shape of the numerically computed compliant displacements. Maximum measured compliant linear compliant displacements have been 9.63 mm along X direction, 21.17 mm along Y direction, 6.88 mm along Z direction. These values have the same magnitude order of the numerically computed maximum compliant displacements while absolute values are slightly higher also due to the effect of clearance.

6 Conclusions

This paper proposes a stiffness model for the biped walking vehicle WL-16RV. The proposed stiffness model has been implemented in Matlab environment for estimating the compliant displacements for various operation conditions. A specific experimental set-up has been proposed for measuring both linear and angular compliant displacements during the robot operation. Results of experimental tests provide a proof of the effectiveness of the proposed experimental set-up and a validation of the proposed stiffness model.

References

1. Sugahara Y., Hosobata T., Mikuriya Y., Sunazuka H., Lim H.O., Takanishi A.: Realization of dynamic human-carrying walking by a biped locomotor. In: IEEE International Conference on Robotics and Automation ICRA 2004, New Orleans, pp. 3055–3060 (2004)
2. Takanishi Lab. Webpage: http://www.takanishi.mech.waseda.ac.jp/top/index.htm (2014)
3. Konuma Y., Hirose S.: Development of the stair-climbing biped robot Zero Walker-1. In: Annual Conference of the RSJ, pp. 851–852. (2001) (in Japanese)
4. Takeda Y., Higuchi M., Funabashi H.: Development of a walking chair (Fundamental investigations for realizing a practical walking chair). In: 4th International Conference on Climbing and Walking Robots, CLAWAR2001, Karlsruhe, pp. 1037–1044 (2001)
5. Kim, J.Y., Lee, J.H., Oh, J.H.: Experimental realization of dynamic walking for a human-riding biped robot, HUBO FX-1. Adv. Robot. **21**(3–4), 461–484 (2007)
6. iBOT® 4000: http://www.ibotnow.com/home.html (2014)
7. Gosselin, C.: Stiffness mapping for parallel manipulators. IEEE Trans. Robot. Autom. **6**(3), 377–382 (1990)
8. Carbone, G.: Stiffness analysis and experimental validation of robotic systems. Front. Mech. Eng. **6**(2), 182–196 (2011)
9. Carbone, G., Ceccarelli, M.: Comparison of indices for stiffness performance evaluation. Front. Mech. Eng. China **5**(3), 270–278 (2010)

Compliance Based Characterization of Spherical Flexure Hinges for Spatial Compliant Mechanisms

Farid Parvari Rad, Giovanni Berselli, Rocco Vertechy and Vincenzo Parenti Castelli

Abstract In this paper, the closed-form compliance equations for spherical flexures are derived. Each element of the spatial compliance matrix is analytically computed as a function of both hinge dimensions and employed material. The theoretical model is then validated by relating analytical data with the results obtained through Finite Element Analysis. Finally, for a generic loading condition, spherical flexures are compared to circularly curved-beam hinges in terms of secondary compliance factors and maximum stress.

Keywords Spherical flexures · Compliance matrix · Finite element analysis · Parasitic motions

1 Introduction

Flexure hinges can profitably substitute traditional kinematic pairs in those articulated mechanisms which require absence of backlash and friction but restricted range of motion. Common applications span high precision manufacturing,

F. P. Rad (✉) · V. P. Castelli
Department of Mechanical Engineering, University of Bologna, Bologna, Italy
e-mail: farid.parvarirad2@unibo.it

V. P. Castelli
e-mail: vincenzo.parenti@unibo.it

G. Berselli
Department of Mechanical Engineering, University of Modena and Reggio Emilia,
Modena, Italy
e-mail: giovanni.berselli@unimore.it

R. Vertechy
Percro Laboratory, Scuola Superiore Sant'Anna, Pisa, Italy
e-mail: r.vertechy@sssup.it

Fig. 1 Circularly curved
flexures
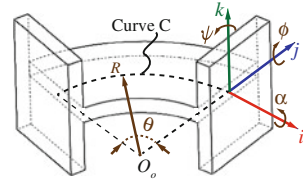
Fig. 2 Spherical flexures
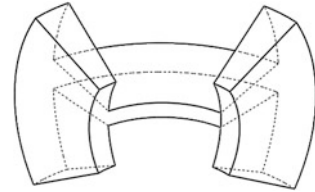
minimally invasive surgery and micro-electromechanical systems (MEMS). Several studies have been dedicated to the design, the characterization and the comparative evaluation of straight-beam flexures and compliant mechanisms formed therewith (see e.g. [1–3]). Lobuntiu and Cullin [4] have recently introduced the two-segment circular-axis symmetric notch flexure and compared its in-plane compliance with that of the straight-axis counterpart. Parvari Rad et al. [5] have evaluated the spatial compliance of Circularly Curved-Beam Flexures (CCBFs) that feature an arc of a circle as centroidal axis (see Fig. 1) and a rectangular cross-section. In addition, Berselli et al. [6] have qualitatively compared CCBFs with straight-beam flexures in terms of maximum achievable rotation and selective compliance.

Most of the aforementioned flexures have been conceived and applied to planar compliant mechanisms. Despite the practical relevance, investigations on compliant hinges for spatial mechanisms are instead quite limited. One of the most important classes of spatial mechanisms is the spherical linkage. In spherical mechanisms, all points of the end-link are constrained to move on concentric spherical surfaces that are fixed with respect to the base. With regard to compliant spherical mechanisms, Jacobsen et al. [7] studied a spherical bistable micro-mechanism for 2D mirror arrays that is based on lamina emergent torsional joints. Greenberg et al. [8] explored the analogy between flat-folding origami models and spherical lamina emergent mechanisms. Callegari et al. [9] employed the finite element method for designing and analysing a spherical micro-mechanism with flexure hinges. Li and Chen [10] proposed a pseudo rigid body model approach to obtain compliant spherical mechanism designs that are based on CCBFs with rectangular cross-section.

Here, Spherical Flexures (SFs), specifically designed for spherical compliant mechanisms, are first introduced and analyzed (Fig. 2). A SF features an arc of a circle as centroidal axis and an annulus sector as cross-section. Circle and annulus have a common center coinciding to that of the desired spherical motion. The axis

Fig. 3 SF loaded at the free end
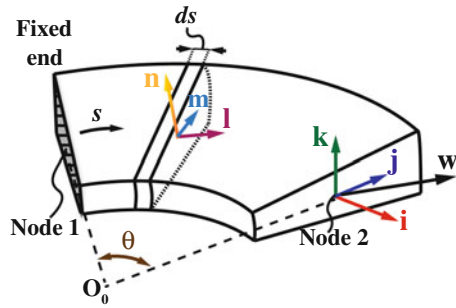
of the smaller SF central moment of inertia points towards the desired center of spherical motion. In the paper, the analytic expressions for the principal compliance factors of general SFs are obtained by using the method proposed by Jafari and Mahjoob [11]. After compliance factor verification via Finite Element Analysis (FEA), the proposed SF is compared in terms of parasitic motions and maximum stress to a CCBFs with rectangular cross section, that features equivalent compliant behavior with respect to moment-induced rotations.

2 Closed-Form Compliance Equations for Spherical Flexures

Similarly to [11], referring to Fig. 3, let one consider a cantilever curved beam with a uniform cross section and generically loaded at the free end. Node 1 and node 2 are located on the beam fixed and free end respectively. In addition, let one define a global coordinate system S_g, with axes **i**, **j** and **k**, located at Node 2, and a local coordinate system S_l, with axes **l**, **m** and **n** (namely the cross section tangent and principal unit vectors), located on the centroid of a generic beam cross section.

Let the external load, ${}^g\mathbf{w}$, and the corresponding deformation, ${}^g\mathbf{s}$, be expressed with respect to S_g as ${}^g\mathbf{w} = [f_x \quad f_y \quad f_z \quad m_x \quad m_y \quad m_z]^T$ and ${}^g\mathbf{s} = [u \quad v \quad w \quad \alpha \quad \phi\psi]^T$. The symbols u, v, w and α, ϕ, ψ denote, respectively, the three displacements and the three rotations of Node 2, whereas f_x, f_y, f_z and m_x, m_y, m_z denote, respectively, the forces and the three moments acting on the beam cross section along the **i**, **j** and **k** directions. The curve defining the centroidal axis (i.e. curve C with center O_0 in Fig. 1) is denoted as ${}^g r(s)$, the variable s referring to the coordinate variable along the same curve.

The relative orientation of the local and global coordinates can be expressed by means of the rotation matrix ${}^l\mathbf{R}_g(s)$, where s is the curvilinear coordinate describing curve C (see Fig. 1), so that ${}^l\mathbf{R}_g(s) = [\mathbf{l} \quad \mathbf{m} \quad \mathbf{n}]^T \cdot [\mathbf{i} \quad \mathbf{j} \quad \mathbf{k}]$.

The load ${}^g\mathbf{w}$ acting on the free end is balanced by a load ${}^l\mathbf{w}'$ acting on the element ds. This load ${}^l\mathbf{w}'$ produces a deformation per unit length, ${}^l\mathbf{E}$, on the same

element. The vectors $^l\mathbf{w}'$ and $^l\mathbf{E}$ and the corresponding analytical relation can be expressed as:

$$^l\mathbf{w}' = [\,f_l \quad f_m \quad f_n \quad m_l \quad m_m \quad m_n\,]^T; \quad ^l\mathbf{E} = [\,\varepsilon_{ll} \quad \gamma_{lm} \quad \gamma_{ln} \quad \kappa_{ll} \quad \kappa_{lm} \quad \kappa_{ln}\,]^T; \quad ^l\mathbf{w}' = \mathbf{K} \cdot{}^l\mathbf{E} \quad (1)$$

The matrix $\mathbf{K}$ is the stiffness matrix of the element ds that can be written as:

$$\mathbf{K} = \mathrm{Diag}\,[\,EA \quad b_m GA \quad b_n GA \quad GJ \quad EI_m EI_n\,] \tag{2}$$

where A, b_m, b_n, I_m, I_n, J, E and G are, respectively, cross section area, shear coefficients, principal moments of inertia and polar moment of inertia of the beam's cross section, Young's modulus and shear modulus of the employed material. The deformation, $d^l\mathbf{s}'$, of the element ds, due to the load $^l\mathbf{w}'$, is defined by:

$$d^l\mathbf{s}' = [\,du' \quad dv' \quad dw' \quad d\alpha' \quad d\phi' \quad d\psi'\,]^T = {}^l\mathbf{E} \cdot ds \tag{3}$$

where u', v', w' and α', ϕ', ψ' are respectively displacements and rotations of the element ds in the $\mathbf{l}$, $\mathbf{m}$ and $\mathbf{n}$ directions. The load $^l\mathbf{w}'$, acting on ds and due to the presence of a load $^g\mathbf{w}$ on the free end, can be computed via the adjoint transformation matrix $^l\mathbf{T}_g$ between global and local coordinates. In particular, the following relation holds:

$$^l\mathbf{w}' = {}^l\mathbf{T}_g \cdot {}^g\mathbf{w}, \quad \text{where} \quad {}^g\mathbf{T}_l = \begin{bmatrix} {}^g\mathbf{R}_l & \mathbf{0} \\ {}^g\mathbf{R}_l \cdot {}^g\widetilde{\mathbf{r}}_s & {}^g\mathbf{R}_l \end{bmatrix} \tag{4}$$

having defined $^g\mathbf{r_s}$ as the position vector connecting the centroid of the section to the center of S_g. In addition, the deformation of the element ds, denoted as $d^l\mathbf{s}'$, causes a deformation at the free end, $d^g\mathbf{s}$, that can be calculated by merging Eqs. 1, 3, and 4 as:

$$d^g\mathbf{s} = {}^l\mathbf{T}_g^T \cdot d^l\mathbf{s}' \Rightarrow d^g\mathbf{s} = {}^l\mathbf{T}_g^T \cdot \mathbf{K}^{-1} \cdot {}^l\mathbf{T}_g \cdot {}^g\mathbf{w} \cdot ds \tag{5}$$

By integrating Eq. 5, one can find the relation between the load $^g\mathbf{w}$ and the deformation $^g\mathbf{s}$ of the free node as follows:

$$^g\mathbf{s} = {}^g\mathbf{C} \cdot {}^g\mathbf{w}, \quad \text{where} \quad {}^g\mathbf{C} = \int_C^l \mathbf{T}_g^T \cdot \mathbf{K}^{-1} \cdot {}^l\mathbf{T}_g \cdot ds \tag{6}$$

Matrix $^g\mathbf{C}$ is the compliance matrix for a general cantilever curved beam loaded at the free end and represents the relationship between the applied loads and the corresponding deformations at the free end. Applying this method on a generic

cantilever circular beam (Fig. 1) with constant cross section, matrix $^g\mathbf{C}$ can be computed as follows:

$$^g\mathbf{C} = \begin{bmatrix} C_{x,f_x} & C_{x,f_y} & 0 & 0 & 0 & C_{x,m_z} \\ C_{y,f_x} & C_{y,f_y} & 0 & 0 & 0 & C_{y,m_z} \\ 0 & 0 & C_{z,f_z} & C_{z,m_x} & C_{z,m_y} & 0 \\ 0 & 0 & C_{\theta_x,f_z} & C_{\theta_x,m_x} & C_{\theta_x,m_y} & 0 \\ 0 & 0 & C_{\theta_y,f_z} & C_{\theta_y,m_x} & C_{\theta_y,m_y} & 0 \\ C_{\theta_z,f_x} & C_{\theta_z,f_y} & 0 & 0 & 0 & C_{\theta_z,m_z} \end{bmatrix} \tag{7}$$

where:

$$C_{x,f_x} = -\frac{R(-AR^2(3\theta + S(\theta)(C(\theta) - 4)) - I_n(EA^2Gb_m(\theta - S(\theta)C(\theta)) + \theta + S(\theta)C(\theta)))}{2EAI_n}$$

$$C_{x,f_y} = C_{y,f_x} = \frac{R((C(\theta) - 1)(-AR^2(C(\theta) - 1) + I_n(C(\theta) + 1)(EA^2Gb_m - 1)))}{2EAI_n}$$

$$C_{x,m_z} = C_{\theta_z,f_x} = \frac{R^2(S(\theta) - \theta)}{EI_n}$$

$$C_{y,f_y} = \frac{R(EA^2GI_nb_m(\theta + S(\theta)C(\theta)) + (AR^2 + I_n)(\theta - S(\theta)C(\theta)))}{2EAI_n}$$

$$C_{y,m_z} = C_{\theta_z,f_z} = -\frac{R^2(C(\theta) - 1)}{EI_n}$$

$$C_{z,f_z} = \frac{R(GJR^2(\theta - S(\theta)C(\theta)) + \frac{1}{2}EI_m(4AG^2\theta Jb_n + R^2(6\theta - 8S(\theta) + S(2\theta))))}{2EGJI_m}$$

$$C_{z,m_x} = C_{\theta_x,f_z} = \frac{R^2(GJ(\theta - S(\theta)C(\theta)) + EI_m(\theta + S(\theta)(C(\theta) - 2)))}{2EGJI_m}$$

$$C_{z,m_y} = C_{\theta_y,f_z} = -\frac{R^2\left(-GJC^2(\theta) + GJ + 4EI_mS^4\left(\frac{\theta}{2}\right)\right)}{2EGJI_m}$$

$$C_{\theta_x,m_x} = \frac{R(GJ(\theta - S(\theta)C(\theta)) + EI_m(\theta + S(\theta)C(\theta)))}{2EGJI_m}$$

$$C_{\theta_x,m_y} = C_{\theta_y,m_x} = \frac{S^2(\theta)R(-GJ + EI_m)}{2EGJI_m}$$

$$C_{\theta_y,m_y} = -\frac{R(-GJ(\theta + S(\theta)C(\theta)) + EI_m(S(\theta)C(\theta) - \theta))}{2EGJI_m}$$

$$C_{\theta_z,m_z} = \frac{\theta R}{EI_n}$$

with $S(\theta) = \sin(\theta)$ and $C(\theta) = \cos(\theta)$. In these equations, R and θ represent the radius and subtended angle of the centroidal axis.

As previously said, the SF cross section is an annular sector (Fig. 4). It can be considered as the common section of two concentric circular sectors with different radius. Let us consider r_i and r_o as the radius of the inner and the outer circular sectors respectively. The cross section properties can be obtained as follows:

Fig. 4 Cross section properties of SFs
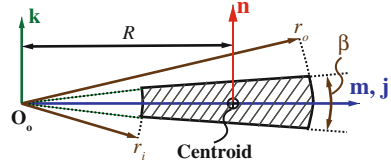
$$A = A_2 - A_1 = \frac{(r_o^2 - r_i^2)\beta}{2} \qquad (8)$$

$$I_m = \frac{1}{8}(r_o^4 - r_i^4)(\beta - \sin\beta) \qquad (9)$$

$$I_n = \frac{1}{8}(r_o^4 - r_i^4)(\beta + \sin\beta) - \frac{8}{9}\frac{(r_o^3 - r_i^3)^2 \sin^2(\beta/2)}{(r_o^2 - r_i^2)\beta} \qquad (10)$$

$$J = I_m + I_n = \frac{1}{4}(r_o^4 - r_i^4)\beta - \frac{8}{9}\frac{(r_o^3 - r_i^3)^2 \sin^2(\beta/2)}{(r_o^2 - r_i^2)\beta} \qquad (11)$$

Replacing Eqs. 8, 9, 10 and 11 in Eq. 7, the SF compliance matrix is determined as a function of the hinge geometric parameters and the employed material.

3 Numerical Example and Model Validation

The SF depicted in Fig. 2 is considered as a case study. The geometric parameters employed in the simulation are $r_o = 60$ mm, $r_i = 50$ mm, $\theta = \pi/3$ and $\alpha = \pi/180$. The hinge is made of Acrylic Plastic with Young's modulus $E = 3000$ MPa and Poisson's ratio $v = 0.33$. Being a slender beam hinge, shear induced deformations are reasonably neglected. The aforementioned theoretical procedure is adopted to estimate the SF compliance matrix. Results are then validated through FEA performed with the commercial software COMSOL. FEA simulations are executed by individually loading the flexure along the axes **i**, **j** and **k**. The compliance factors are simply computed as the ratios between each load and the corresponding deformations. Table 1 compares the results obtained via numerical model and FEA. The comparison shows a close agreement between the two methods.

In order to evaluate the flexure performance, we have compared the aforementioned SF with a rectangular cross section CCBF having identical centroidal axis and subtended angle. In addition, the two flexures are suitably dimensioned in order to present the same compliant behavior with respect to moment-induced rotations. The resulting CCBF width and thickness are $w = 9.98$ mm and $t = 0.963$ mm. By applying the method described in Sect. 2, the CCBF compliance matrix has been computed and numerical data are shown in Table 2. As we can

Table 1 Compliance factors for the SF and comparison between analytical and FEA results

Compliance factors	C_{x,f_x}	$C_{x,f_y}=C_{y,f_x}$	$C_{x,m_z}=C_{\theta_z,f_x}$	C_{y,f_y}	$C_{y,m_z}=C_{\theta_z,f_y}$	C_{z,f_z}
Analytic	4.0146e-5	−8.6900e-5	−0.0023	2.1584e-4	0.0064	0.0232
FEA	4.0149e-5	−8.6947e-5	−0.0023	2.1594e-4	0.0064	0.0232
Error(%)	7.5e-3	0.054	0	0.046	0	0
Compliance factors	C_{θ_x,m_x}	$C_{z,m_x}=C_{\theta_x,f_z}$	$C_{x,m_y}=C_{\theta_y,f_z}$	C_{θ_y,m_y}	$C_{\theta_x,m_y}=C_{\theta_y,m_x}$	C_{θ_z,m_z}
Analytic	8.0448	0.4147	−0.5158	18.4932	−9.0486	0.2413
FEA	8.0466	0.4148	−0.5159	18.4966	−9.0492	0.2413
Error (%)	0.022	0.024	0.019	0.018	6.6e-3	0

Table 2 Compliance factors for the similar CCBF

Compliance factors	C_{x,f_x}	$C_{x,f_y}=C_{y,f_x}$	$C_{x,m_z}=C_{\theta_z,f_x}$	C_{y,f_y}	$C_{y,m_z}=C_{\theta_z,f_y}$	C_{z,f_z}
Value	4.0144e-5	−8.6901e-5	−0.0023	2.1584e-4	0.0064	0.0232
Compliance factors	C_{θ_x,m_x}	$C_{z,m_x}=C_{\theta_x,f_z}$	$C_{x,m_y}=C_{\theta_y,f_z}$	C_{θ_y,m_y}	$C_{\theta_x,m_y}=C_{\theta_y,m_x}$	C_{θ_z,m_z}
Value	8.0448	0.4147	−0.5158	18.4932	−9.0486	0.2413

see, the compliance factors become identical for the two flexures with the exception of C_{x,f_x}, C_{x,f_y} and C_{y,f_x}, which represent undesired (secondary) compliances in all those application requiring a spherical motion. Naturally, unavoidable secondary compliances should be minimized in order to decrease parasitic motions as much as possible.

A quantitative comparison between SF and CCBF can then be achieved by defining two compliance ratios as follows:

$$r_{x,x} = \frac{C_{x,f_x}^{SF}}{C_{x,f_x}^{CCBF}}; \quad r_{x,y} = \frac{C_{x,f_y}^{SF}}{C_{x,f_y}^{CCBF}} = \frac{C_{y,f_x}^{SF}}{C_{y,f_x}^{CCBF}} \tag{12}$$

where each SF compliance factor (referred to with SF superscript) is divided by the corresponding CCBF compliance factor (referred to with CCBF superscript). In order to understand the behavior of SFs and CCBFs in terms of parasitic motions, we have assessed the influence of the geometric parameters on these two factors. This goal is achieved by evaluating the compliance ratios $r_{x,x}$ and $r_{x,y}$ for varying values of R and θ. Figures 5 and 6 respectively represent the values $(1 - r_{x,x}) \times 100$ and $(1 - r_{x,y}) \times 100$ as function of R and θ. From these two graphs, $r_{x,y}$ is always negative whereas r_{x,f_x} is always positive, meaning that it is impossible to assess which flexure presents the best selectively compliant behavior without considering a specific loading condition.

It is also worth mentioning that, by increasing the length of the flexures, the ratios $r_{x,x}$ and $r_{x,y}$ are tending to 1, which imply a similar deformation behavior for

Fig. 5 Influence of varying R on compliance ratios
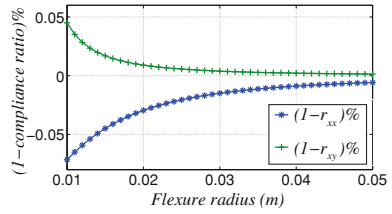
Fig. 6 Influence of varying θ on compliance ratios
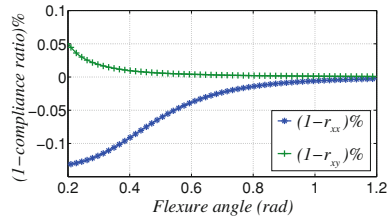
Fig. 7 SF deformed shaped under bending moment m_y
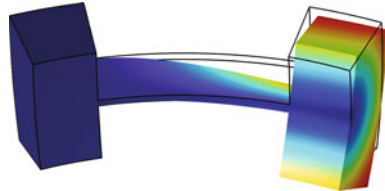
Fig. 8 Influence of varying θ on stress ratio
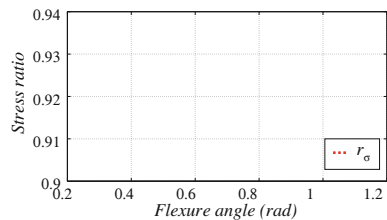
relatively large length-to-thickness ratios. For what concerns the overall Von Mises stress on each flexure when loaded with a (principal) bending moment m_y on the free end (see Fig. 7), the following stress ratio has been defined:

$$r_\sigma = \frac{\sigma_{max}^{SF}}{\sigma_{max}^{CCBF}} \tag{13}$$

Performing a series of FEA simulations, we have obtained this ratio for varying values of R and θ. In particular, the ratio r_σ assumes a constant value equaling 0.918 at varying R whereas the influence of θ is shown in Fig. 8. As we can see, SF

outperforms CCBF, being characterized by a lower stress level for equal load (meaning that the SF outperforms CCBF in terms of maximum achievable rotation).

4 Conclusions

The closed-form compliance equations for SFs as a function of both hinge dimensions and employed material have been presented and validated via FEA.

In addition, SFs have been compared to CCBFs in terms of secondary compliance factors and maximum stress. For what concerns secondary compliances, the selection of the best design solution strongly depends on the loading condition. Nonetheless, SFs always outperform CCBFs for what concerns maximum achievable rotations under the action of a principal bending moment.

References

1. Lobontiu, N., Paine, J., Garcia, E., Goldfarb, M.: Corner-filleted flexure hinges. J. Mech. Des. **123**(3), 346–352 (2001)
2. Paros, J.: How to design flexure hinges. Mach. Des. **37**, 151–156 (1965)
3. Tian, Y., Shirinzadeh, B., Zhang, D., Zhong, Y.: Three flexure hinges for compliant mechanism designs based on dimensionless graph analysis. Precis. Eng. **34**(1), 92–100 (2010)
4. Lobontiu, N., Cullin, M.: In-plane elastic response of two-segment circular-axis symmetric notch flexure hinges: the right circular design. Precis. Eng. **37**, 542–555 (2013)
5. Parvari Rad, F., Berselli, G., Vertechy, R., Parenti-Castelli, V.: Evaluating the spatial compliance of circularly curved-beam flexures. Computational Kinematics, Springer, Berlin, pp. 329–336 (2013)
6. Berselli, G., Parvari Rad, F., Vertechy, R., Parenti-Castelli, V.: Comparative evaluation of straight and curved beam flexures for selectively compliant mechanisms. In: IEEE/ASME International Conference on Advanced Intelligent Mechatronics (AIM), pp. 1761–1766 (2013)
7. Jacobsen, J.O., Chen, G., Howell, L.L., Magleby, S.P.: Lamina emergent torsional (LET) joint. Mech. Mach. Theory **44**(11), 2098–2109 (2009)
8. Greenberg, H.C., Gong, M.L., Magleby, S.P., Howell, L.L.: Identifying links between origami and compliant mechanisms. Mech. Sci. **2**(2), 217–225 (2011)
9. Callegari, M., Cammarata, A., Gabrielli, A., Ruggiu, M., Sinatra, R.: Analysis and design of a spherical micromechanism with flexure hinges. J. Mech. Des. **131**, 051,003 (2009)
10. Li, G., Chen, G.: Achieving compliant spherical linkage designs from compliant planar linkages based on prbm: a spherical young mechanism case study. In: IEEE International Conference on Robotics and Biomimetics (ROBIO), IEEE 2012, pp. 193–197 (2012)
11. Jafari, M., Mahjoob, M.: An exact three-dimensional beam element with nonuniform cross section. ASME J. Appl. Mech. **77**(6), 1–7 (2010)

Analysis and Synthesis of Thin-Walled Robot Elements with the Guided Deformation Law

S. Gavryushin

Abstract The numerical technique and practical experience are discussed in the field of analysis and designing of new generation of functional and executive elements of robotic devices and drives created on base of thin-walled mechanical structures. The distinctive features of examined elements is the realization of a principle of the guided deformation, allowing to create ordered law of moving. The results of the analysis and synthesis of real designs are exposed.

Keywords Actuators · Large displacements · Nonlinear deformation · Robot · Road · Thin shell · Numerical analysis

1 Introduction

Into the overall progress in the field of robotics and micro-technology acquisition subsystem information (sensors) and subsystems for mechanical object (actuators) are the weakest link. The main idea of the article—to present the new approach to the analysis and design of mechanical actuators and mechatronic systems. In the traditional sense robotic drive motors, hydraulic, pneumatic and other apparatus, are considered as rigid components movable relative to each other, which entails problems associated integrity, reduce friction, lubrication of the contacting surfaces, etc. In this respect, a special class of actuators may be considered deforming mechanical structures, i.e. structures capable to significantly change its original form without violating the integrity.

S. Gavryushin (✉)
Bauman Moscow State Technical University, Moscow, Russia
e-mail: gss@bmstu.ru

411

Such elements were essential when designing "white" robots, conclusions movement in vacuum, for the work of the aggressive and high temperature environments, including inside the human body [1–3]. The main property of actuators, using the principle of guided deformation, is obtaining movements. Deformation processes should provide a large displacements move [4]. It is known that in thin-walled structures large displacement can be implemented by means of small deformations. Deformation of such elements can be caused by pressure, temperature, or occur due to the effect of shape memory.

When implementing the proposal in article numerical methods of design construct is used, matching the two, in our opinion, the most promising design models: analytical model of spatial rod and design scheme ax symmetric thin-walled shell.

2 Multivariate Approach to the Study of Processes of Nonlinear Deformation of Thin-Walled Structures

To ensure the required operational characteristics in the process of numerical simulation and design of a deformable element is required to conduct a kind of programming properties of future construction, which laid the possibility of implementation of the required nonlinear deformation processes. To describe the current deforming state is vector-function of state $\mathbf{X}(s^0, q)$ depending on the Lagrangian coordinates s^0 and the q parameter has the meaning of the continuation parameter [5–7]. One method of calculation and designing components with the guided elastic deformation is based on the idea of multi parameter approach [5] at the mathematical modeling of computer essentially nonlinear processes. The numerical simulation is used the strategy of successive studies one parameters nonlinear problems belonging multi parameters family in which the task is immersed. Algorithm of the numerical research is based on the use of the parameter continuation method, in conjunction with the changing parameters subspaces technique [5].

The transition from problem analysis to synthesis of structures implemented in the framework of the multi parameters approach. The essence of which consists in the following. We write a system of resolving equations in operator form (1).

$$\mathbf{F}\left(\mathbf{X}^{(1)}, \mathbf{X}^{(2)}\right) = 0 \tag{1}$$

It is assumed that in the general case, the system (1), as the order of m has m unknown, $x_j^{(1)}(j = 1, 2, \ldots, m)$ which are internal parameters characterizing the state of the system, and depends on the variables $x_j^{(2)}(j = 1, 2, \ldots, m)$ which are treated as *external* parameters or control options. The number of independent external parameters defines the codimension of the problem.

Control parameters in an individual case may be design parameters, that is, parameters, which varies developer. Division of parameters of the two groups is

somewhat subjective. The ultimate aim of the synthesis problem is to find the rational values of parameters. Research of processes of deformation in solid mechanics, traditionally seen as a process dependent on external perturbation, the components of which constitute $\mathbf{X}^{(2)}$. If all functional components of the vector $\mathbf{X}^{(2)}$ we can express only through one independent parameter—q, we obtain the one parametric process with codimension equal to one.

The set of all solutions of (1) for a given number of $m + n$ external and internal parameters, for clarity could be interpreted as the equilibrium hyper surface built in the Euclidean space of parameters $\mathbf{R}^{(m+n)}$. Each one parameter process is interpreted as a trajectory belonging to this hyper surface.

When analyzing one parametric process controlling parameter q is conveniently considered equal with the rest of the parameters of the task, considering it as a $(m + 1)$-th unknown advanced vector $\mathbf{X}_{\text{ext}}$ and write the system of equations describing the single-parameter process in the form (2).

$$\mathbf{r}(\mathbf{X}_{\text{ext}}) = \mathbf{0} \tag{2}$$

$$f(\mathbf{X}_{\text{ext}}, \lambda) = 0 \tag{3}$$

Note that the order of the system (2) is equal to m, and its solution is carried out with the use of additional Eq. (3) that contains an independent value λ—called the continuation parameter.

It is known that in nonlinear mechanical systems even with simple types of disturbances can produce complex and difficult predictable transitions. The problems are studied in the framework of the catastrophe theory [8]. In the case of one-parameter family of systems in general position may be fatal features only type folds. Procedure of realization of calculations with the passage of the surroundings of limit points proposed in 1968 Valishvily and is known as the changing parameters technique [9]. The problem of choosing the optimal parameter for one-parametric problems considered in [6]. Features of codimension two and higher can be addressed through the *stirring* of the parameters of the system that basically allows you to select the path of the process that runs past the surroundings such singular points. Crawl around the singular point is carried out by means of the changing subspaces of parameters technique [5]. The essence of the technique is the following: at the approach to the neighborhood of a singular point, you should go to another parametric system, for which the projection of the equilibrium surface on the control parameter axis in the considered range of its variations has features of codimension not above the first. Strategy of numerical analysis is a piecewise-smooth continuation of the solution on the parameter of the space of states of all systems, with each smooth stretch of the process; numerical analysis is reduced to the one-parameter problem.

3 The Numerical Model of the Spatial Rod

At the analysis of spatial rod used equations describing a nonlinear deformation of a flexible tensile spatial rod assuming justice hypothesis Euler-Bernoulli. Analysis of deformation is reduced to the solution of a boundary problem for a system of nonlinear differential Eq. (5), supplemented by algebraic relations (6).

To describe the motion are two orthogonal right coordinate systems: the global system, and the local system. Axes of a local system coincide with the positive direction of the tangent to the centerline of the rod and the main axes of its cross section. As an independent variable used in the Lagrangian coordinate s^0, counted out along the unstrained the rod axis. Unknown geometric components are the coordinates of the center of gravity of section x_i and rotation angles θ_i necessary for transition from global coordinate system to the local. Use the following sequence of three rotations: rotation around a common axis i_2; turn around the new position of the axis i_3; turn a new position relative to the axis of i_1. As static unknown values were used internal efforts Q_i and M_i moments specified in the global basis. In (4) on the rights of the auxiliary unknown includes: the value of the deformation of the rod axis—ε and the components of the curvature of contemporary state—κ_i, calculated in local basis.

$$
\begin{cases}
\dfrac{dx_1}{ds^0} = (1 + \varepsilon) \cdot \cos(\theta_2) \cdot \cos(\theta_3) \\[2mm]
\dfrac{dx_2}{ds^0} = -(1 + \varepsilon) \cdot \sin(\theta_3) \\[2mm]
\dfrac{dx_3}{ds^0} = (1 + \varepsilon) \cdot \sin(\theta_2) \cdot \cos(\theta_3) \\[2mm]
\dfrac{dv_1}{ds^0} = (1 + \varepsilon) \cdot (\kappa_1 - \cos(\theta_1) \cdot tg(\theta_3) \cdot \kappa_2 + \sin(\theta_1) \cdot tg(\theta_3) \cdot \kappa_3) \\[2mm]
\dfrac{dv_2}{ds^0} = (1 + \varepsilon) \cdot \left(\dfrac{\cos(\theta_1)}{\cos(\theta_3)} \cdot \kappa_2 - \dfrac{\sin(\theta_1)}{\cos(\theta_3)} \cdot \kappa_3\right) \\[2mm]
\dfrac{dv_3}{ds^0} = (1 + \varepsilon) \cdot (\sin(\theta_1) \cdot \kappa_2 + \cos(\theta_1) \cdot \kappa_3) \\[2mm]
\dfrac{dQ_1}{ds^0} = -(1 + \varepsilon) \cdot q_1 \\[2mm]
\dfrac{dQ_2}{ds^0} = -(1 + \varepsilon) \cdot q_2 \\[2mm]
\dfrac{dQ_3}{ds^0} = -(1 + \varepsilon) \cdot q_3 \\[2mm]
\dfrac{dM_1}{ds^0} = -(1 + \varepsilon) \cdot (l_{21} \cdot Q_3 - l_{31} \cdot Q_2 + m_1) \\[2mm]
\dfrac{dM_2}{ds^0} = -(1 + \varepsilon) \cdot (l_{31} \cdot Q_1 - l_{11} \cdot Q_3 + m_2) \\[2mm]
\dfrac{dM_3}{ds^0} = -(1 + \varepsilon) \cdot (l_{11} \cdot Q_2 - l_{21} \cdot Q_1 + m_3)
\end{cases}
\tag{4}
$$
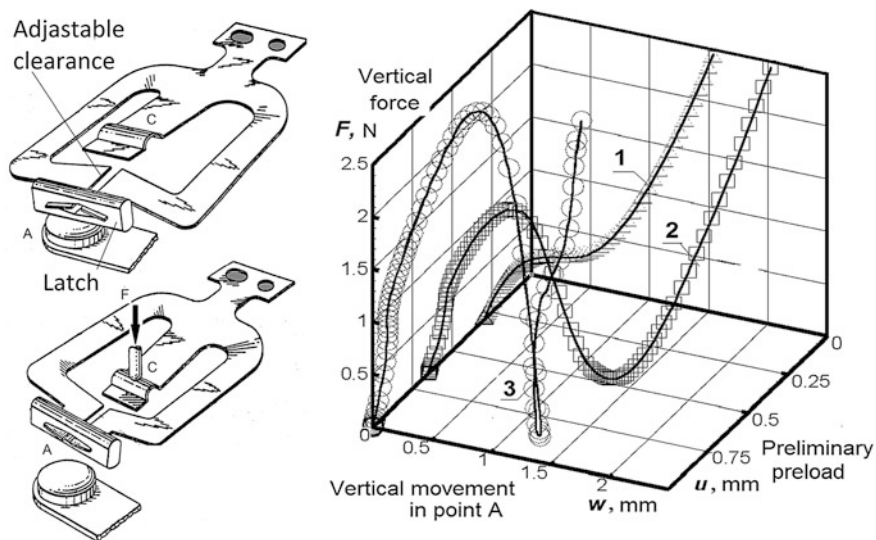
Fig. 1 Analysis of pre-strained spatial element with discrete feature of the switch

In the case of a linear-elastic behavior of the material under constant temperature, auxiliary equations take the form (5)

$$\varepsilon(s^0) = \frac{1}{B_0} \cdot (Q_1 \cdot l_{11} + Q_2 \cdot l_{21} + Q_3 \cdot l_{31})$$

$$\kappa_i(s^0) = \frac{1}{B_i} \cdot \sum_{j=1}^{3} M_j \cdot l_{ij} + (1 - \varepsilon) \cdot \kappa_i^0$$

(5)

In formulas (4 and 5) the following notation is used: q_i and m_i—projection distributed power and torque loads in the global system of coordinates, respectively;—functions curvatures, asked when describing the unstrained status bar; B_0, B_1, B_2, B_3—geometrical characteristics of the expansion-compression, torsion and bending around its local axes associated with the principal axes of the cross-section, respectively. If necessary, recalculation of forces, moments and loads in the local coordinate system is carried out using the matrix of rotation $[l(s^0)]$.

The results of numerical analysis of the elastic element on the switch [10] shown in Fig. 1. The element has a fairly complex form (Fig. 1). Characteristic size of the element sizes: length—10 mm, width—15 mm, thickness—0.3 mm.

Main operating characteristic element is its operating characteristics—the relationship between the vertical force—F, applied at the point C with vertical moving of contact w at point A. The operating characteristic element formed at the stage of preliminary deformation in the assembly. During this operation, the billet of the elastic element on the switch deform through the modification and subsequent fixing adjustable clearance. Thus, the elastic characteristic element is

formed at the stage of preliminary deformation. The elastic characteristic of the element depends from the size of preload For small values of the preload u elastic characteristic 1 has no singular points, and elastic element will not snap.

When increasing the preload, the operating characteristic two acquires a typical S-shaped character with the upper and lower critical points. Deformation of the elastic element with such elastic characteristic is implemented discretely (snap).

When reaching the force F and the upper critical values of the element snapping in the bottom position of equilibrium, and at lower values of power to the lower critical value of the force-returned to the top position. At the further increase in preload the operating characteristic three is complicated; the lower critical value of force may become negative, which corresponds to the so called "stuck" element in the lower equilibrium position. The problem of synthesis of the element consists in the selection of values preload at which the process switching is implemented with snap and without sticking. Found a rational value corresponds to about 0.65 mm.

4 The Numerical Model of the AxiSymmetric Shell

For description of nonlinear deformation of the used variant of the theory of thin elastic ax symmetric shells such Arnold [8]:

$$
\begin{cases}
\dfrac{du}{ds^0} = (1 + \varepsilon_{m0}) \cos \theta - \cos \theta_0, \\[2mm]
\dfrac{dv}{ds^0} = (1 + \varepsilon_{m0}) \sin \theta - \sin \theta_0, \\[2mm]
\dfrac{d\theta}{ds^0} = (1 + \varepsilon_{m0})\kappa_{m0} + \dfrac{d\theta_0}{ds^0} \\[2mm]
\dfrac{dU}{ds^0} = -(1 + \varepsilon_{m0})\left(\dfrac{\cos \theta}{X_0 + u} U - \dfrac{N_t}{X_0 + u} + q_u \right), \\[2mm]
\dfrac{dV}{ds^0} = -(1 + \varepsilon_{m0})\left(\dfrac{\cos \theta}{X_0 + u} V + q_v \right), \\[2mm]
\dfrac{dM_m}{ds^0} = -(1 + \varepsilon_{m0})\left[\dfrac{\cos \theta}{X_0 + u} (M_m - M_t) - U \sin \theta + V \cos \theta \right]
\end{cases}
\tag{6}
$$

Here s^0—independent coordinate, counted out along the arc unstrained meridian shell; u, v,—horizontal and vertical components of displacements of the points belonging to the middle surface; θ^0 and θ—angle tangent to the meridian in the original and current positions; e_{mo} and k_{mo}—linear deformations and curvature at the current point of the middle surface; U, V, M_m, and M_t—intensity of internal forces and moments; q_u and q_v—components of the external pressure. Values corresponding to the meridian direction, marked index—m and the circumferential ones—t. With regard to solving the problem on deformation of the bimetallic dome auxiliary values, included in (7) were determined by proportions [11].
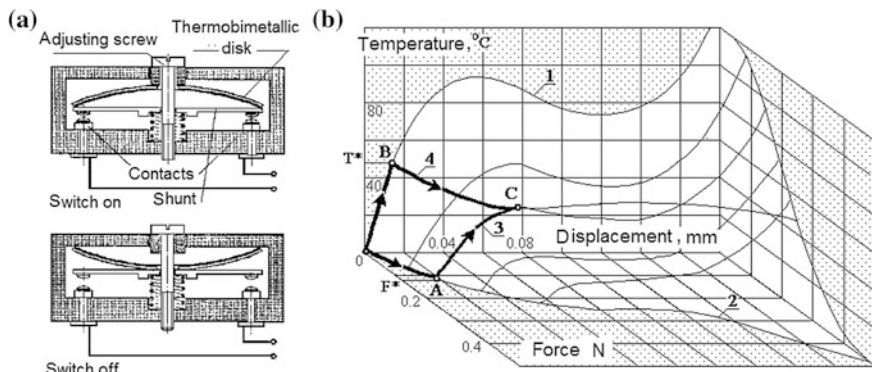
Fig. 2 Synthesis thermo bimetallic element for a temperature switching

Here X_0 and X—radial coordinate of the current point in the middle surface in the original and current position; E_1, E_2, h_1, h_2—modules of elasticity and thickness of the active and passive layers of the shell, respectively; μ—Poisson ratio.

$$\varepsilon_{m0} = \frac{1-\mu^2}{E_1h_1 + E_2h_2}(U\cos\theta + V\sin\theta) - \mu\frac{u}{X_0} + \frac{T(1+\mu)}{E_1h_1 + E_2h_2}(E_1h_1\alpha_1 + E_2h_2\alpha_2),$$

$$\kappa_{m0} = \frac{3(1-\mu^2)}{E_1h_1^3 + E_2h_2^3}M_m - \mu\frac{X_0 + u}{X_0}\left(\frac{\sin\theta}{X_0 + u} - \frac{\sin\theta_0}{X_0}\right) + \frac{3T(1-\mu)}{2(E_1h_1^3 + E_2h_1^3)}(E_1h_1^2\alpha_1 + E_2h_2^2\alpha_2),$$

$$N_t = \frac{E_1h_1 + E_2h_2}{1-\mu^2} + \left(\frac{u}{X_0} + \mu\varepsilon_{m0}\right) - \frac{T}{1-\mu}(E_1h_1\alpha_1 + E_2h_2\alpha_2),$$

$$M_t = \frac{E_1h_1^3 + E_2h_2^3}{3(1-\mu^2)}\left[\frac{X_0 + u}{X_0}\left(\frac{\sin\theta}{X_0 + u} - \frac{\sin\theta_0}{X_0}\right) + \mu\kappa_{m0}\right] - \frac{T}{2(1+\mu)}(E_1h_1^2\alpha_1 + E_2h_2^1\alpha_2).$$

$$\text{(7)}$$

The following design the snapping thermo bimetallic (TB) disk gives an idea of the implementation of the algorithm for numerical synthesis. By preliminary mechanical loading conducted with the help of the adjusting screw (see Fig. 2a), you need to configure the TB disk switching for given temperature T*.

In unstrained state the TB disk pressed to the plane of the outer perimeter of the force F, distributed along the contour holes in the top. The characteristics of the disk: diameter—5 mm radius of curvature in unstrained state—22.2 mm; thickness—0.04 mm, diameter of the central hole—0.5 mm. Physical characteristics of materials: $E_1 = 1.50 \times 10^5$ MPa, $E_2 = 1.35 \times 10^5$ MPa, $\mu_1 = \mu_2 = 0.3$, $\alpha_1 = 1.0 \times 10^{-6}$ 1/°C, $\alpha_2 = 18.0 \times 10^{-6}$ 1/°C. Results are presented in Fig. 2b. Curve 1 corresponds to the process of deformation of the disk in the absence of preload. Curve 2 corresponds to the power loading item at a constant temperature. Piecewise smooth curves 3 and 4 correspond to the complex process of deformation.

Technique of the changing subspaces of parameters was applied at points A and B. To determine the efforts preload ensures the operation at a given temperature, we used the following strategy to address the problem of synthesis.

At the first stage was done temperature loading along the curve 1 up to the set temperature T^*. The point B was made in a change of parameter continuation and further loading was carried by a force until it reaches a singular point C. Force F, corresponding point C, is equaled desired preload force F, which ensures the operating of element at the required temperature T^*. To check the problem solution we used the way of loading 3, which showed the identity of the results.

5 Conclusions

Use of elements of a guided elastic deformation, caused by pressure, temperature, or occur due to the effect of shape memory, opens up the prospect of creating new types of mechanical devices, sensors, actuators, functional elements of robotic systems. Elements may work in vacuum, high-purity or in aggressive environments and is subject to miniaturization. Using the principle of guided elastic deformation during designing of technical systems, including in the construction of robots will enhance their functionality and to leave on a new technical level corresponding to the needs of modern society.

References

 1. Aleksandrova, A.T.:New transmission and formation of the movement in vacuum. In: M: Vysshaya shkola, p. 69 (1979)
 2. Gavryushin, S.S.: Elements managed by the elastic deformation of functional devices robotic equipment. Mechatronics 5, 16–18 (2000)
 3. Patent of Russian Federation № 2218191 Endovasal mini-robot / G.V.Savrasov, A.V. Pokrovsky, S.S. Gavryushin,, O.S. Naraykin, A.S. Yuchenko, V.I. Pospelov– No. 200210938/14; Appl. 11.04.2002.; Publ. 10.12.2003, bul. №34
 4. Ponomarev, S.D., Andreeva, S.E.:Analysis of elastic elements of machines and devices. M: Machine-building, p. 326 (1980)
 5. Gavryushin, S.S.: Numerical simulation and analysis of processes of nonlinear deformation of flexible shells, Izv. In: USSR Academy of Science, MDS, vol. 1, pp. 109–119 (1994)
 6. Grigolyuk, E.I., Shalashin, V.I.: Problems of nonlinear deformation: method of continuation of the solution on the parameter in nonlinear problems of mechanics of deformable body. M: Nauka, pp. 232 (1988)
 7. Gavryushin, S.S.: Nonlinear analysis of elastic thin-walled shell structures. Commun. Nonlinear Sci Numer. Simul. 4, 223–233 (2002)
 8. Arnold, V.I.: Catastrophe yheory. M: Nauka, p. 128 (1990)
 9. Valishvily, N.V.: Methods of calculation of shells of rotation on computers. M: Mashinostroenie, p. 278 (1976)
10. Bogachev, M.V., Gavryushin, S.S.: Variational-differential method of analusis of flexible shallow elements of technical devices // Izv. Vuzov. Mashinostroenie 10–12, p. 14 (1997)
11. Karim, A.A., Gavryushin, S.S.: Numerical analysis of thermobimetallic elements of high speed electrical devices // Izv. Vuzov. Mashinostroenie 8, pp. 17–23 (2005)

HCLC Integration Design and High-Precision Control of a Joint for Space Manipulator

Zhihong Jiang, Hui Li, Que Dong, Xiaodong Zhang, Zixing Tang, Wei Rao, Yang Mo, Chenjun Ji and Qiang Huang

Abstract A novel method is presented to solve many problems of joints for space manipulator, such as large volume, large flexibility, complex routing and low system-control precision, which can realize integrated design for space manipulator joint with high-cohesion and low-coupling (HCLC) performance. Moreover, the mechanical and electrical interfaces of designed joint are especially suitable for space manipulator. First, To achieve higher system performance, the joint is designed as a whole for perfect match among components including permanent magnet synchronous motor (PMSM), motor controller and driver, sensors, space environment controller, reducer, routing and other mechanisms, which could eliminate redundant shell packages and mounting surfaces existed in traditional manipulator joint. Second, a new method is presented to design the rotors of two resolvers as joint sensors at the same axis shared with motor rotor, this kind of design has the advantages of redundant and high-precision sensing for the positions of motor rotor and joint, and joint position signal is differential sensing and has high robustness. Then, a kind of high-precision controller is presented for space manipulator based on a new PMSM model with model difference, and this controller is robust to joint nonlinear factors, such as friction and other disturbance torque. Finally, the experimental results showed the designed joint had fine

Z. Jiang · H. Li (✉) · Q. Dong · Y. Mo · C. Ji · Q. Huang
IRI, School of Mechatronical Engineering, Beijing Institute of Technology, Beijing, China
e-mail: lihui2011@bit.edu.cn

Z. Jiang · H. Li · Q. Dong · Y. Mo · C. Ji · Q. Huang
Key Laboratory of Biomimetic Robots and Systems, Ministry of Education, Beijing Institute of Technology, Beijing, China

Z. Jiang · H. Li · Q. Dong · Y. Mo · C. Ji · Q. Huang
Key Laboratory of Intelligent Control and Decision of Complex System, Beijing Institute of Technology, Beijing, China

X. Zhang · Z. Tang · W. Rao
Institute of Spacecraft System Engineering, CAST, Beijing, China
e-mail: zhangxiaodong@163.com

performances with high power density, high controlling precision and high operation stability and so on, and it is suitable for the application of space manipulator.

1 Introduction

Space manipulator is generally configured with the joints and connecting rod, and the joint is actuator, and space manipulator joint is a kind of complex mechatronic system. At present, main problems for space manipulator joint are as following. Low internal integration resulted in big size, low ratio of power to weight and low system precision, its reason is that there are so many discrete components for motor, reducer, sensors and others in space manipulator joint, each discrete component has its own shell and mounting interface, and these redundant shells and interfaces resulted in low joint performance. Moreover, space manipulator joint usually have complex mechatronic interface, this would cause that routing is difficult, reliability is low and standardization is poor. Sensors, driver and controller circuits and others usually are configured at the outside of the joint, and many cables need to be routed, so the external interface of the joint is complex. Because of the poor standardization, any change of joint may affect the whole space manipulator much, so it will increase developing cycle and cost on repetitive work. Figure 1 showed a typical space manipulator joints here.

To solve above problems to enhance space manipulator, several kinds of modular joints of CANADARM2 at the international space station in 2001, ROKVIS of German Aerospace Center in 2005 and so on [1–5] had been designed, and Harbin Institute of Technology and Beijing University of Posts and Telecommunications from China also designed some kinds of modular joints for space manipulator in 2007. However, modular joint only integrates the discrete components, and all redundant interfaces are still kept.

Disturbance torque compensation is an essential issue for high-precision servo system, for example, nonlinear friction generally existed in high-precision servo system, has very bad influence on servo system, it could mainly generate position tracking error, margin loop and crawl, especially in the velocity reversal, owing to the difference between the static friction moment and sliding friction moment, it could induce biggish tracking error. It is a barrier to improve the function of high-precision servo system, so the researchers have great concerns about it [6, 7]. Currently, the relative study methods to compensate for disturbance are mainly based on model and multi-parameters identification of disturbance torque model [8, 9], disturbance observation [10], PD regulator [11] and intelligent control methods [12, 13]. These methods are not easy to implement in application because of disturbance torque model not accurate, especially, velocity signal is not accurately measured in ultra-low velocity. Therefore, this paper presents a
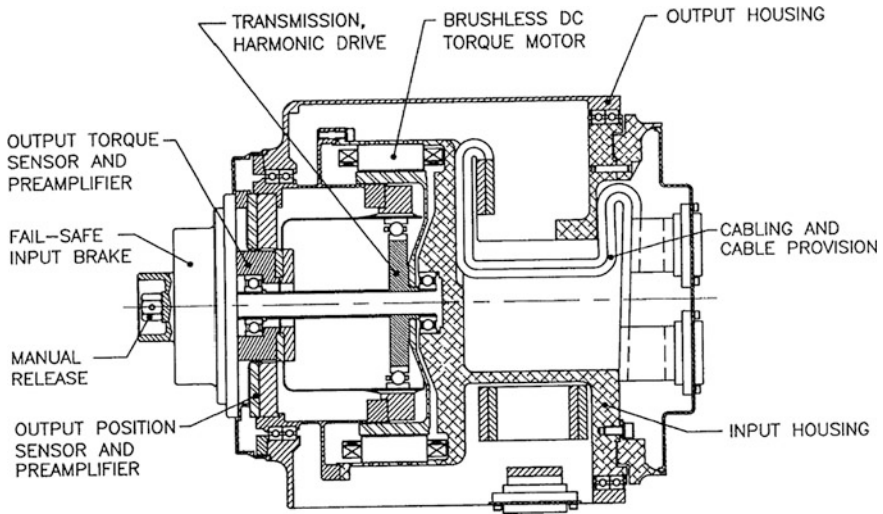
Fig. 1 Two typical joints for space manipulator

compensation method for disturbance torque, which does not depend on its model and is easy to implement in application. Based on model reference difference, we adopt AW-PI (Anti-Windup PI) regulator and high-pass filter to identify and compensate for disturbance torque in servo system.

The organization of this paper is as follows. In Sect. 2, we describe the details of HCLC designing method. A new method to design two resolvers' rotors at the same axis and its advantage will be presented in Sect. 3. In Sect. 4, the new PMSM model and model differential controller are introduced. Experiment results are given in Sect. 5. Finally, our conclusions are given in Sect. 6.

2 HCLC Integration Designing Method

In the space environment, the temperature changes drastically and electromagnetic environment is worse, moreover, during the process of launching with rocket, space manipulator has to sustain the impact, vibration, overload, and noise, so HCLC joint can meet this sharp requirement with double resolvers as sensors. As shown in Fig. 2, according to HCLC integration designing requirement, the motor, resolver and harmonic reducer are synchronously designed as a whole and integrated into the joint structure. The stators of motor and resolver have no shells only with cores and coils, and the joint shell is designed as their shells. The rotors of motor and two resolvers, harmonic generator of harmonic reducer are all integrated at the same motor axis. Controller and driver are installed inside the joint, cables can go through the hollow axis. The HCLC method can design all joint
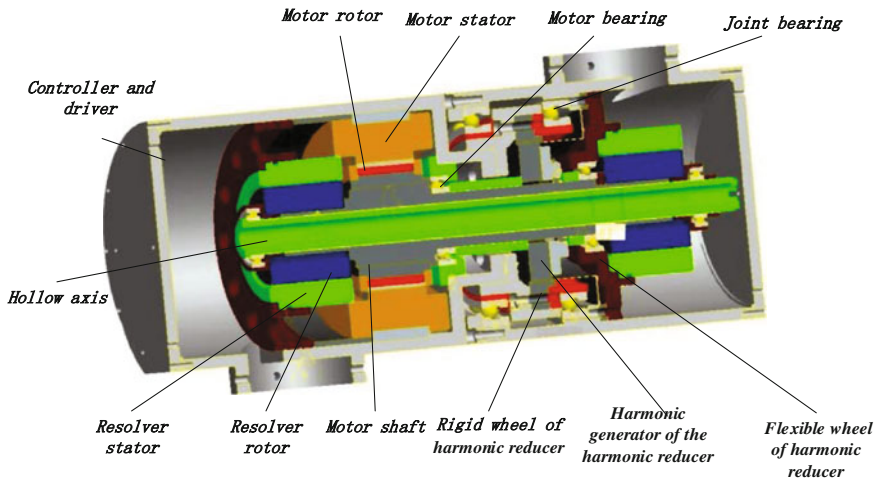
Fig. 2 Configuration of HCLC integrative joint of space manipulator

components with exact match to enforce joint cohesion and increase the ratio of weight to volume.

3 Redundant High-Precision Detection for Motor and Joint

This paper presents a method to design two rotors of two resolvers at the same axis share with motor, and one stator of resolver is fixed on motor side and the other is fixed on joint side, as shown in Fig. 2. On basis of this kind of mechanical designing, we can implement redundant high-precision detection for positions of motor and joint at the same time with the rotation difference of motor to joint. The relationship of the tested positions of motor and joint can be written in Eq. (1)

$$\theta_2 = \theta_1 + \frac{\theta_1}{n} = \frac{n+1}{n}\theta_1 \tag{1}$$

Where θ_2 is the position from the resolver on motor side, and θ_2 is the position of motor rotor; θ_1 is the position from the resolver on joint side; n (=160) is the ration of harmonic reducer, and ratio of harmonic reducer. The positions of motor rotor and joint can be written in Eq. (2) from (1),

$$\theta_{motor} = \theta_2 = \frac{n+1}{n}\theta_1 \ , \ \theta_{joint} = \theta_2 - \theta_1 = \frac{\theta_1}{n} \tag{2}$$

Actual Servo System

Fig. 3 Scheme of disturbance torque identification and compensation

Where θ_{motor} is the position of motor rotor, θ_{joint} the position of the joint. From Eq. (1), it can be found the positions of two resolver is very close, especially when n is big, so when one resolver is out of work, th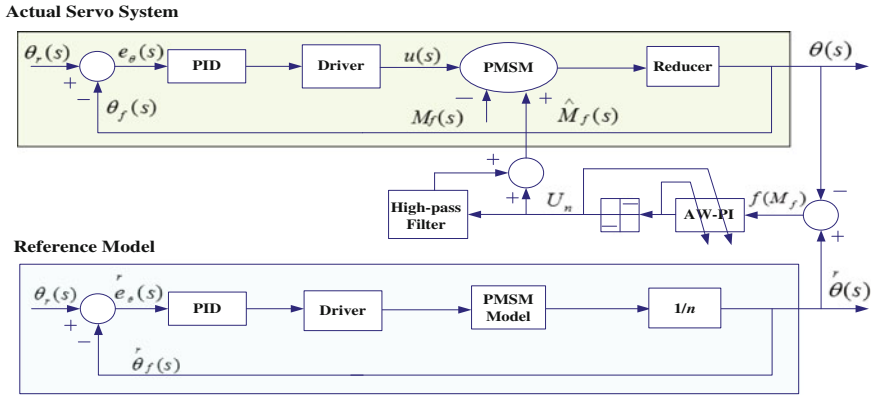e other one can also detect both positions in high accuracy. Therefore, redundant detection is achieved for motor and joint position.

4 High-Precision Controller Design

This paper presents a reference model difference method to eliminate the disturbance from nonlinear factors for high system precision, and it can guarantee that the control output error of reference mode and actual servo system only contains the disturbance torque information, so the disturbance torque in servo system can be identified. Moreover, in order to guarantee the speed of identification convergence and easy implementation in practice, AW-PI regulator is presented here for disturbance torque identification, and its scheme is shown in Fig. 3.

As shown in Fig. 3, $^r\theta(s) - \theta_f(s)$ is the output control difference of reference mode and actual servo system, namely $f(M_f)$, which is a function of the disturbance torque, and it is estimated by AW-PI regulator, then the output of AW-PI regulator is the disturbance torque of ideal reference model, when $^r\theta(s) - \theta_f(s)$ equals to zero, the ideal reference model output is equal to the actual output of servo system, namely $\hat{M}_f(s) = M_f(s)$, so $\hat{M}_f(s)$ could be used to compensate for the disturbance torque of the servo system and improve the servo precision.

In order to solve the influence that AW-PI regulator has on the controlled precision during the convergence process of identification when the disturbance torque of the servo system changes, a first-order high-pass filter to solve this problem.

Table 1 Performance parameters of HCLC integrated joint

Weight	Max torque	Standby torque	Routing lines	Positioning precision
3.0 kg	80 Nm	3.2 Nm	6	0.001°

Fig. 4 Designed HCLC joint for space manipulator

Table 2 Test results of joint

Performance	Experiment results
Stiffness (kN ·m/rad)	19.2
Velocity (rad/s)	2.5
Output torque (N ·m)	80.0
Ratio of power to size (W/m^3)	248679

5 Experimental Results and Analysis

The designed HCLC integrated joint was manufactured and its performance parameters were listed in Table 1, and the Designed HCLC integrated joint for space manipulator was shown in Fig. 4.

HCLC Joint is shown in Fig. 4. A series of performances test has been done, and the results were shown in Table 2.

The parameters of PMSM were listed in Table 3.

We added disturbance torque to servo system at 10 % of motor rating moment when tested, and disturbance torque equaled to 0.05 Nm, but in order to guarantee the stability of system and compensation margin, the max output of AW-PI regulator is limited to 20 % of motor rating moment and was set as 0.1 Nm, The experimental results were as shown in Fig. 5.

Figure 5a is the identification waveform of disturbance torques only with the AW-PI regulator. We can see that, during the convergence process of identification, it has big surge when the disturbance torque changes from one value to another. Therefore, first-order high-pass filter is introduced here to identify and compensate for the disturbance torque with AW-PI regulator together, and we can see from Fig. 5b, this method improves the convergence process of identification when the disturbance torque changes.

Figure 6a is the positioning error waveform with added disturbance torque into servo system without compensation, and the maximum control error is 0.03769°.

Table 3 Parameters of PMSM

Power supply	Max torque	Standby torque	Pole pairs	Phase resistance	Phase inductor
24 V	0.5 Nm	0.02 Nm	8	4.1/4.05/4.2 Ω	1.1/0.99/1.0 mH
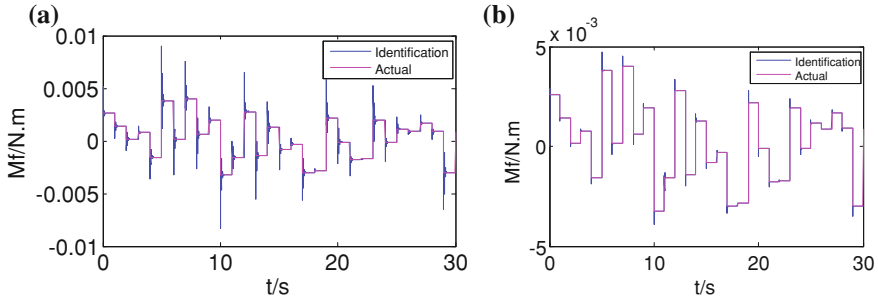
Fig. 5 Identified waveforms of added disturbance torque. **a** With AW-PI regulator. **b** With AW-PI regulator and high-pass filter
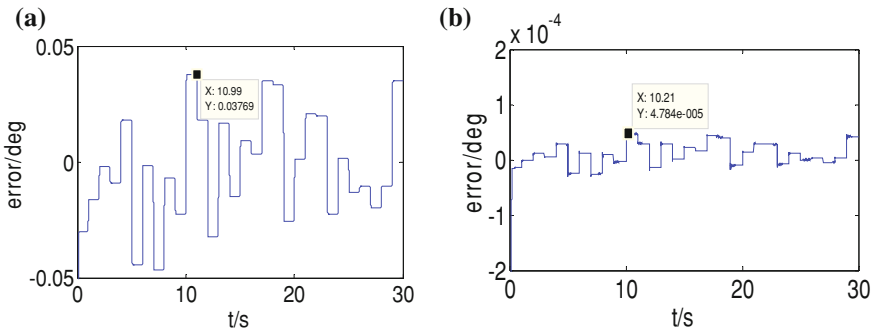
Fig. 6 Control error of servo system with friction compensation. **a** No disturbance compensation. **b** Disturbance compensation

Figure 6b is the positioning error waveform based on AW-PI regulator and first-order high-pass filter to identify and compensate for the disturbance torque, and the maximum control error is only $4.784 \times 10^{-5\circ}$.

6 Conclusion

The main results of this paper were as follows.

(1) A kind of HCLD integrative joint has been designed and manufactured for space manipulator. This joint was suitable for space manipulator with high ratio of power to size and very simple external interface & routings.

(2) The rotors of two resolvers have been designed at the same axis shared with motor rotor, this kind of mechanical designing realized redundant and high-precision sensing for the positions of motor rotor and joint, and joint-position signal sensing was differential sensing with high robustness.

(3) A novel and simple PMSM model was built, and it was suitable for microprocessor, and based on this PMSM model, a high-precision controller was presented based on model difference. The test results showed this controller was robust to nonlinear factors, such as friction or other disturbance torque.

Finally, the experimental results validated the presented HCLC integrative design and high-precision controller, and showed the designed joint was suitable for the application of space manipulator.

References

 1. Gibbs, G., Sachdev, S.: Canada and the international space station program: overview and status. Acta Astronaut. **51**(2), 591–600 (2002)
 2. Hirzinger, G., Albu-Schaffer, A., Hahnle, M., et al.: On a new generation of torque controlled light-weight robots. In: IEEE International Conference on Robotics & Automation. Piscataway, USA, pp. 3356–3363 (2001)
 3. Hirzinger, G., Landzettel, K., Brunner, B., et al.: DLR's robotics technologies for on-orbit servicing. Adv. Robot. **18**(2), 139–174 (2004)
 4. Hirzinger, G., Sporer, N., Albu-Schaffer, A., et al.: DLR's torque controlled light weight robot III—are we reaching the technological limits now? IEEE International Conference on Robotics and Automation. Piscataway, USA, pp.1710–1716 (2002)
 5. Yim, M., Roufas, K., Duff, D., et al.: Modular reconfigurable robot s in space applications. Auton. Robot. **14**(2), 225–237 (2003)
 6. Liu, Q., Er, L., Liu, J.: The summarization of characteristic of nonlinear Friction, modeling and control compensation. Syst. Eng. Technetronic **24**(11), 45–52 (2002)
 7. Basilio, B., Marina, I.: Friction compensation in robotics: an overview. In: IEEE Conference on Decision and Control, pp. 4360–4367 (2005)
 8. Canudas De Wit, C.: Comment on a new model for control of systems with friction. IEEE Trans. Autom. Contrdol **43**(8), 1189–1190 (1998)
 9. Zhang, W., Tai, X.: Friction moment self-adapting compensation of Artillery servo system based on the Lurge mode. Tsinghua Univ. Trans (natural science) **47**(S2), 1756–1760 (2007)
10. White, M.T., Tomizuka, M., Smith, C.: Improved track following in magnetic disk drives using a disturbance observer. IEEE/ASME Trans. Mechatron. **5**(1), 3–11 (2000)
11. Jeong-Yul, J., Seon-Woo, L., Hong-Kook, C., Jong-Hwan, K.: Low velocity friction identification and compensation using accelerated evolutionary programming. In: IEEE International Conference on Evolutionary Computation. Nagoya, pp. 372–377 (1996)
12. Huang, J., Ye, S.: Research of friction compensation based on the CMAC network. Chin. Mech. Eng. **10**(3), 269–271 (1999)
13. Sungchal, J.: A self-organizing fuzzy logic control for friction compensation in feed drives. In: American Control Conference. Seattle, WA, pp. 205–209 (1995)

A Novel Robotic Joint Actuation Concept: The Variable Mechanical Fuse, VMF

Yoichiro Dan and Oussama Khatib

Abstract This paper presents a novel robotic joint actuation concept, the Variable Mechanical Fuse, VMF. This actuation system realizes a rigid behavior for high control performance and an elastic behavior for safer human-robot interaction. The VMF adapts its behavior throughout a motion to ensure that both endpoints have high position accuracy and the intermediate trajectory maintains safety. Since the VMF changes its behavior passively from rigid to elastic, this actuation system is intrinsically safe even when unexpected collisions occur. A compact prototype has been designed and fabricated to verify its performance and safety.

Keywords Elastic joint · SEA · Variable stiffness joint · Compliant motion and torque control

1 Introduction

Industrial robots have been used in unmanned environments for a long time. Safety is enforced by not having humans within close proximity of robots in operation. However, applications that require robots to cooperate with humans are expected to increase in the near future. This has sparked a wide variety of research on safer robots. The research on human safe robot design started with SEA [1] developed by Pratt et al. SEA has springs as elastic components that allow compliant motions against external forces. Edsinger et al. developed a robot that is equipped with SEAs for safe human-robot interactions [2]. Due to the elasticity in SEAs, they
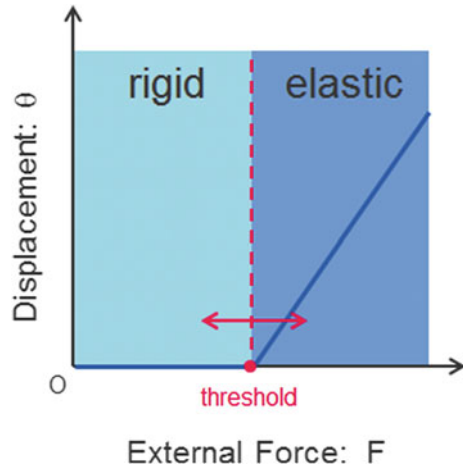
Y. Dan (✉) · O. Khatib
Artificial Intelligence Laboratory, Stanford University, Stanford 94305, CA, USA
e-mail: yoichir2@stanford.edu

O. Khatib
e-mail: ok@cs.stanford.edu

Fig. 1 Principle of VMF

usually have limited position accuracy. In order to overcome this problem, elastic mechanisms with variable elasticity were developed. Wolf et al. developed a variable stiffness joint [3, 4] and realized a mechanism that has variable elastic constants by non-linear cams and rollers. Morita et al. developed a variable stiffness joint that has a cantilever with a variable active length [5]. Tsagarakis et al. developed a variable stiffness joint that has springs and a lever [6]. Their design uses a separate mechanism to vary the pivot point of the lever that connects to the springs. Using a multi-stage elastic actuator concept, Kuan et al. developed a SEA with two springs of different constants [7]. However it is observed that these designs still do not have position accuracy that comes close to that of rigid joints.

A safe mechanism that does not sacrifice position accuracy while maintaining acceptable level of safety is required in industry. Zinn et al. developed a macro-mini actuation system that implements safety while being able to produce highly responsive position control [8]. However the performances such as position accuracy and frequency response are still not high enough compared to conventional rigid joints. The VMF concept attempts to solve the safety vs. performance trade-off by having two vastly different behaviors.

2 Principle

High position accuracy and safety of robot arms can be achieved in a single mechanism. The VMF actuation concept introduced here achieves both a rigid and elastic behavior by setting the threshold to external forces.

Figure 1 shows the basic elastic joint principle of the VMF. The VMF has a specific stiffness and a variable threshold to external forces. When the external force is lower than the threshold, the VMF shows a rigid behavior because the

Fig. 2 Schematic diagram of VMF model
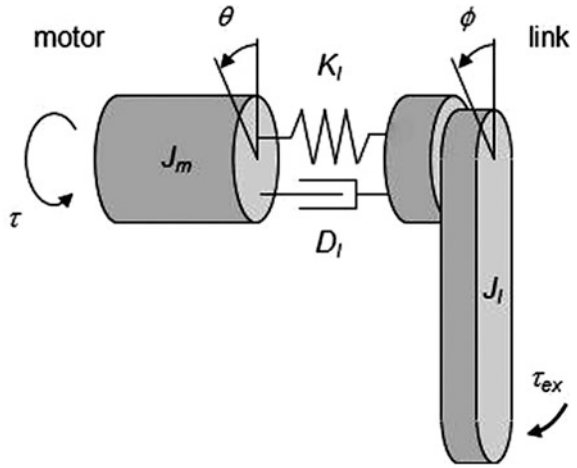
force is not large enough to produce a displacement. When the external force is higher than the threshold, the VMF shows an elastic behavior similar to that of an SEA. Since the threshold can be set to any value, the VMF can display a purely elastic behavior when the threshold is set to zero.

3 Analysis

Figure 2 shows a schematic diagram of a VMF model. The VMF has springs as elastic components between a motor and a link. The threshold is produced by applying preloads on the springs. The dynamic equation of the VMF is expressed by the following two equations.

$$
\begin{aligned}
J_m \ddot{\theta} - D_l\left(\dot{\phi} - \dot{\theta}\right) - f\left(\dot{\phi}, \dot{\theta}\right) &= \tau \\
J_l \ddot{\phi} - D_l\left(\dot{\phi} - \dot{\theta}\right) - f\left(\dot{\phi}, \dot{\theta}\right) &= \tau_{ex}
\end{aligned}
\tag{1}
$$

where J_m and J_l show inertia of the motor and the link respectively, D_l shows friction coefficient between the motor and the link. θ and ϕ show angle of the motor and the link respectively. τ and τ_{ex} show torque of the motor and external torque that is applied on the link respectively.

The torque applied by the springs is described by the function f that contains the preload on the springs.

$$
f\left(\dot{\phi}, \dot{\theta}\right) = \begin{cases} \tau_p \mathrm{sgn}\left(\dot{\phi} - \dot{\theta}\right) + K_l\left(\dot{\phi} - \dot{\theta}\right), & \left|\dot{\phi} - \dot{\theta}\right| > 0 \\ \left[-\tau_p \quad \tau_p\right], & \left|\dot{\phi} - \dot{\theta}\right| = 0 \end{cases}
\tag{2}
$$

Fig. 3 Position step response of VMF with different preloads
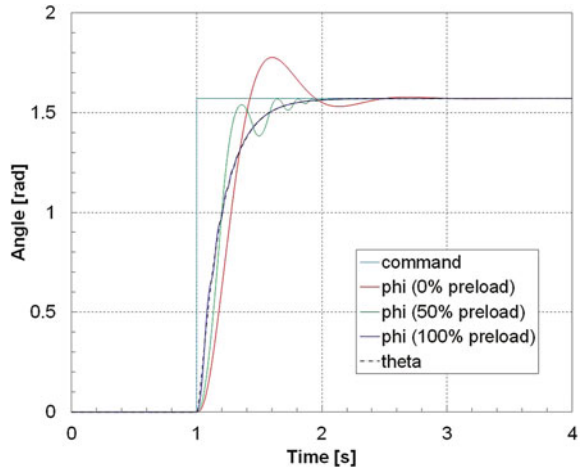
where sgn is the sign function implemented to express the preload on springs. τ_p and K_l show the preload and the spring constant respectively.

Figure 3 shows a simulation result of position step responses with various preload values. The preload can be set from zero to the maximum value that is large enough to cancel acceleration torque and holding torque of payloads. From the graph, the oscillation on the trajectory of ϕ is reduced with increased preloads. Eventually the trajectory of ϕ matches the trajectory of θ at 100 % preload which corresponds to the behavior of a rigid joint.

Figure 4 shows a comparison of impact forces between an ordinary rigid joint and the VMF. Here is assumed that a weight of 250 g is placed at the tip of the link of 250 mm length, and the weight is collided with an obstacle at the angular velocity πrad/s. The impact force of the VMF is reduced by approximately 40–60 % compared to a rigid joint. It indicates that the VMF is safer than ordinary rigid joints even when unexpected collisions are occurred while the VMF shows rigid behavior with the maximum preload.

4 Mechanism

4.1 Design of VMF

A VMF prototype for a single joint has been designed and assembled. Figure 5 shows a picture of the prototype. This joint has an elastic unit with springs and a mechanism to produce the preload on the springs for setting the threshold to external forces. The mechanism supports an encoder for sensing the angular
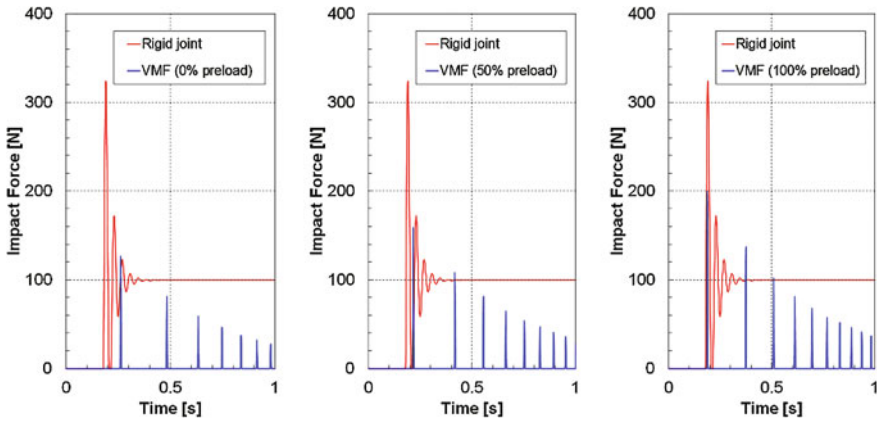
Fig. 4 Comparison of impact forces between a rigid joint and VMF

Fig. 5 Prototype of VMF
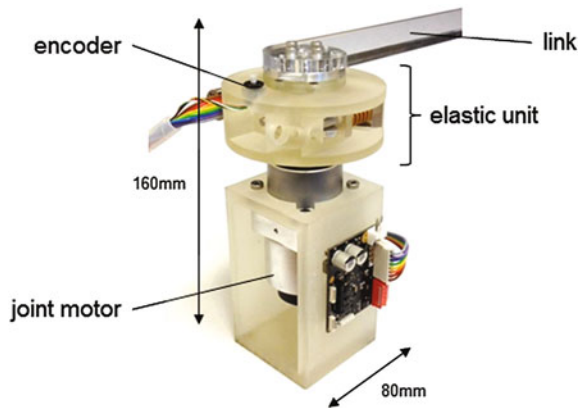
displacement of the elastic unit. An important characteristic of a VMF is that this unit also works as a torque sensor and allows compliant motions by torque control.

Figure 6 shows the cross-sectional CAD image of the elastic unit. This unit is equipped with a small geared electric motor coupled to a slide screw that is placed in the center of the unit. When the slide screw is rotated by the motor, it drives a preload generator downward in the picture to deform the springs and produce the preload. When an external force is applied to the link shown in Fig. 2, a pushing rotor that is placed in the center is rotated to the direction of the blue arrow since it is connected directly to the link. Then the pushing rotor pushes the spring on either side via a pushing plate to the direction of the red arrows. When the force applied to the spring by the pushing rotor is smaller than the preload, this unit shows a rigid behavior. When the force exceeds the preload, this unit shows an elastic behavior.
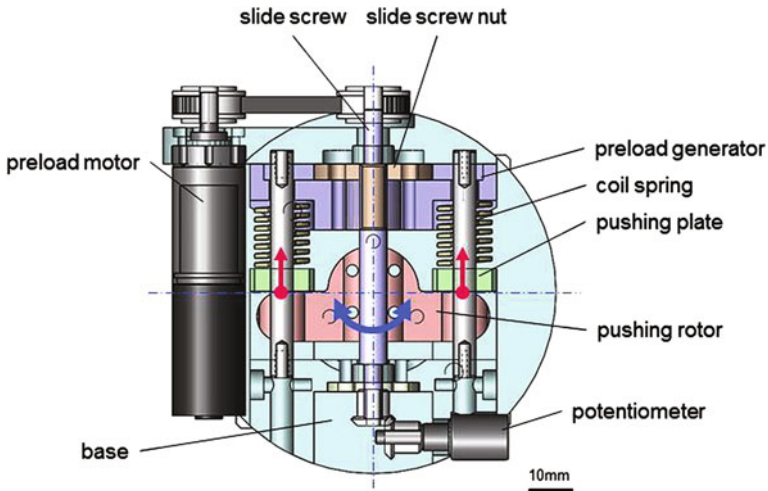
Fig. 6 Cross-sectional image of the elastic unit

This mechanism is applicable to joints of a robot arm. When precise motion is required such as for positioning, the arm can show high position accuracy by the VMF's rigid behavior. When safe motion is required during any interaction with the robot, the arm can show compliant motion by the VMF's elastic behavior.

4.2 Specification

Table 1 shows the specifications of the prototype. This prototype is designed to be incorporated into an elbow joint of a human sized robot arm. This design assumes a 0.5 kg payload at the tip of the link with a length of 0.25 m. The torque capacity is set at 1.3 Nm by the joint stiffness that is determined by the spring constant and the maximum angular displacement. The maximum preload is set at 1.1 Nm by the spring constant and the maximum stroke of preload generator. Since this value is large enough to cancel the holding torque and the acceleration torque of the payload, the unit can realize rigid behavior at any posture and velocity.

5 Experiment

An experiment of collisions was performed to investigate the VMF's safety. Figure 7 shows the experimental setup. A weight of 250 g is placed at the tip of the link of 250 mm length. The weight is collided with the load cell at the angular velocity πrad/s and stopped safely within the maximum displacement of the elastic

Table 1 Specifications of VMF

Parameters	Unit	Value
Max. payload	kg	0.5
Length of link	M	0.25
Joint stiffness	Nm/rad	7.3
Max. angular displacement	rad (deg)	0.17 (10)
Torque capacity	Nm	1.3
Max. preload	Nm	1.1
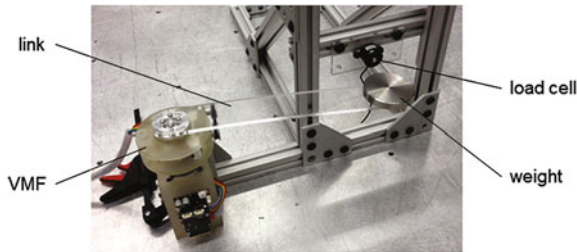
Fig. 7 Experimental setup
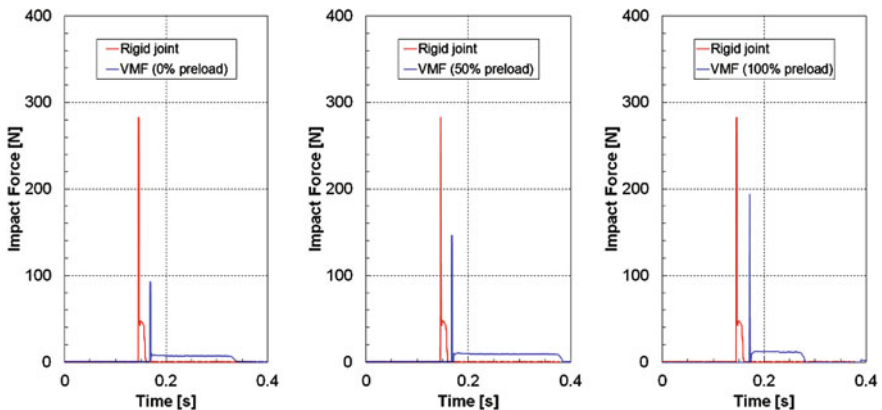
Fig. 8 Results of collision experiment with different preloads

unit. A rigid joint collision is also performed in the same condition. Figure 8 shows the results of the experiment. Depending on the preload value, the collision forces are reduced by 30–60 % compared to a conventional rigid joint. The collision forces vary from around 90–200 N linearly. These results correspond approximately to the simulation results described above. It was confirmed that the VMF has intrinsic safety in any value of the preload.

6 Conclusion

In this paper, we proposed the concept of VMF (Variable Mechanical Fuse) to address the challenge of achieving both performance and safety in an actuation system. Our study has shown this novel actuation system to realize high control performance while providing intrinsic safety. A compact single DOF prototype has designed and an experiment of collisions has been performed to confirm the intrinsic safety. The experiment has demonstrated reductions of 30–60 % of the collision forces compared to conventional rigid joints. Further experiments such as step response and frequency response are going to be performed soon.

References

1. Pratt, G.A., Williamson, M.M.: "Series elastic actuators" intelligent robots and systems 95. In: Proceedings, IEEE/RSJ International Conference on Human Robot Interaction and Cooperative Robots, vol. 1, pp. 399–406 (1995)
2. Edsinger, A.: Kemp, C.C.: Manipulation in Human Environments. In: 6th IEEE-RAS International Conference on Humanoid Robots, Page(s): 102–109 (2006)
3. Wolf, S., Eiberger, O., Hirzinger, G.: The DLR FSJ: energy based design of a variable stiffness joint. In: IEEE International Conference on Robotics and Automation (ICRA), pp. 5082–5089 (2011)
4. Wolf, S., Hirzinger, G.: A new variable stiffness design: matching requirements of the next robot generation. In: IEEE International Conference on Robotics and Automation (ICRA), pp. 1741–1746 (2008)
5. Morita, T., Sugano, S.: Development of one-DOF robot arm equipped with mechanical impedance adjuster. In: Proceedings IEEE/RSJ International Conference on Intelligent Robots and Systems 95, vol. 1, Human Robot Interaction and Cooperative Robots, pp. 407–412 , (1995)
6. Tsagarakis, N.G., Sardellitti, I., Caldwell, D.G.: A new variable stiffness actuator (CompAct-VSA): design and modeling. In: IEEE/RSJ International Conference on Intelligent Robots and Systems (IROS), pp. 378–383 (2011)
7. Jiun-Yih, K., Han-Pang, H., Yen-Tsung, C.: Coupled elastic actuation development for robots as an intrinsic compromise between performance and safety. In: IEEE/ASME International Conference on Advanced Intelligent Mechatronics (AIM), pp. 445–450 (2009)
8. Zinn, M.R., Khatib, O., Roth, B., Salisbury, J., Kenneth, J.: Playing it safe [human-friendly robots]. Robotics & Automation Magazine IEEE, pp. 12–21 (2009)

Internal Force-Based Impedance Control for Cable-Driven Parallel Robots

C. Reichert, K. Müller and T. Bruckmann

Abstract In this paper an internal force-based impedance controller for redundantly actuated cable-driven parallel robots (CDPRs) is proposed. For CDPRs, each actuated cable forms a manipulator equipped with the feature of an impedance to enforce a dynamical relationship between the end-effector (EE) velocity and the internal forces. No explicit position and force control loops are necessary. This approach can guarantee a desired tension level in the cable system for given EE movements. Additionally the platform dynamics do not cause tracking or steady state position errors. Non-linear effects like model uncertainties take a negative influence on the controller. The incorporated disturbance observers guarantee the necessary robustness for the impedance controller. To validate the described control approach, experiments with a 6-DOF CDPR with industrial BLDC-Motors are presented.

Keywords Cable-driven parallel robots · Redundant actuation · Internal force-based impedance control · Disturbance observer · Industrial BLDC-motors

1 Introduction

Cable-driven parallel robots (CDPR) have some advantages over serial manipulators like high end-effector (EE) accelerations over a wide workspace. The cables guiding the platform are usually wound up by winch drives attached to the base. Due

C. Reichert (✉) · K. Müller · T. Bruckmann
University of Duisburg-Essen, Duisburg, Germany
e-mail: reichert@imech.de

K. Müller
e-mail: mueller@imech.de

T. Bruckmann
e-mail: bruckmann@imech.de

to the unilateral properties of the cables, usually actuation redundancy is required to completely restrain the platform. This redundancy allows to enforce a desired tension level in the cable system and can be used to increase the stiffness of the mechanism. Moreover, it affects the dynamic performances of a redundantly actuated CDPR. To take full advantage from the capabilities of a CDPR, these properties must be supported by the controller. Preferred model-based control approaches like the computed torque control (CTC) or augmented PD (APD) control are designed to achieve accurate trajectory tracking. However, these approaches do not consider the regulation of the desired tension level in the cable system. Thus, force control strategies need to be integrated, having a significant influence on the dynamical behavior of the CDPR. Eppinger and Seering [1] provide an analytical overview of the involved dynamics and clarify possible influences which can lead to bandwidth limitations in robot force control. To overcome these limitations, the well-known impedance control approach introduced by Hogan [2] represents an elegant solution.

The paper is organized as follows: First the dynamics of a CDPR are formulated in EE coordinates. In Sect. 3 the derivation of the control law is introduced. In Sect. 4 experiments on a 6-DOF CDPR with industrial BLDC-Motors are presented and summarized in Sect. 5.

2 Manipulator Dynamics

2.1 Formulation in EE Coordinates

A CDPR consists of a working platform (end-effector) with δ degrees-of-freedom (DOF) constrained by m flexible cables in a parallel configuration which can be modeled as a multi-body system (MBS). The EE is described as a rigid body driven by constraint forces and task forces from the environment. The equations of motion for a CDPR can be formulated by Lagrange's equation of the first kind, with n generalized coordinates $\mathbf{q} \in \mathbb{V}^n$ describing the motion of the mechanism and $\delta \in \mathbb{N}$ EE coordinates $\mathbf{x} = \begin{bmatrix} \mathbf{r} & \psi \end{bmatrix}^\mathrm{T}$ (task-space) according to the EE position $\mathbf{r}$ and orientation ψ. As shown by Hufnagel et al. [3], these equations can be obtained by cutting each kinematic chain of the mechanism at the EE and introducing redundant geometric and kinematic closure conditions

$$\mathbf{0} = \mathbf{h}(\mathbf{q}, \mathbf{r}, \psi), \quad \mathbf{h}(\mathbf{q}, \mathbf{r}, \psi) \in \mathbb{R}^n, \tag{1}$$

$$\mathbf{0} = \mathbf{J}(\mathbf{q})\dot{\mathbf{q}} + \mathbf{J}_\mathrm{X}(\psi)\dot{\mathbf{x}}, \quad \mathbf{J}(\mathbf{q}) = \frac{\partial \mathbf{h}}{\partial \mathbf{q}} \in \mathbb{R}^{n \times n}, \ \mathbf{J}_\mathrm{X}(\psi) = \frac{\partial \mathbf{h}}{\partial \mathbf{x}} \in \mathbb{R}^{\delta \times n}, \tag{2}$$

where $\mathbf{h}(\mathbf{q}, \mathbf{r}, \psi)$ defines the forward kinematics of each kinematic chain between the cable exit point and the EE's center of mass. Typically, a CDPR is directly controlled by m external control forces $\mathbf{u}$ generated by the winch drives and the equations of motion become

$$\begin{bmatrix} \mathbf{D}\ddot{\mathbf{q}} + \mathbf{Q} \\ \mathbf{M}_X\ddot{\mathbf{x}} + \mathbf{K}_X + \mathbf{Q}_X \end{bmatrix} = \begin{bmatrix} \mathbf{u} \\ \mathbf{0}_d \end{bmatrix} + \begin{bmatrix} \mathbf{J}^T \\ \mathbf{J}_X^T \end{bmatrix} \lambda, \tag{3}$$

where $\mathbf{D}$ is the inertia matrix related to each winch and $\mathbf{Q}$ represents all remaining potential forces as friction forces. The subscript X denotes elements for the particular linear EE equations of motion. Accordingly, the generalized mass matrix is $\mathbf{M}_X$ and the generalized Coriolis and centrifugal forces are summarized in $\mathbf{K}_X$. The Lagrange multipliers λ represent the constraint forces. The set of all valid configurations of a CDPR, according to the constraints, defines the so-called configuration space (c-space) $V := \{\mathbf{q} \in \mathbb{V}^n | \mathbf{h}(\mathbf{q}, \mathbf{r}, \psi) = \mathbf{0}\}$ of the CDPR [3].

The constraint Jacobian $\mathbf{J}$ has locally full rank and its inverse is denoted as $\mathbf{J}^{-1}$. Hence, the generalized velocities can be expressed as

$$\begin{bmatrix} \dot{\mathbf{q}} \\ \dot{\mathbf{x}} \end{bmatrix} = \mathbf{F}\underline{\mathbf{x}}, \quad \mathbf{F} = \begin{bmatrix} -\mathbf{J}^{-1}\mathbf{J}_X \\ \mathbf{I}_\delta \end{bmatrix} \tag{4}$$

to parametrize all admissible configurations $\mathbf{q} \in \mathbb{V}^n$. Herein $\mathbf{F}$ represents an orthogonal complement of $[\mathbf{J} \quad \mathbf{J}_X]$, fulfilling $[\mathbf{J} \quad \mathbf{J}_X]\mathbf{F} \equiv \mathbf{0}$. The time derivative of Eq. (4) yields the accelerations $\ddot{\mathbf{q}} = \mathbf{F}\ddot{\underline{\mathbf{x}}} + \dot{\mathbf{F}}\underline{\mathbf{x}}$. By the use of the defined orthogonal complement, the unknown constraint forces λ can be eliminated by the projection of the equations of motion (3) onto the c-space V. Since the vector of external control forces $\mathbf{u}$ only comprises non-zero entries for the m actuated joints with generalized coordinates, a submatrix $\mathbf{A}$ of the orthogonal complement $\mathbf{F}$ can be identified so that

$$\mathbf{F}^T \begin{bmatrix} \mathbf{u} \\ \mathbf{0}_\delta \end{bmatrix} = \mathbf{A}^T\mathbf{c},$$

where $\mathbf{c} \equiv (c_1, \ldots, c_m)$ is a vector of generalized control forces corresponding to the actuator coordinates. The parameterization in Eq. (4) and its time derivative give rise to the equations of motion in EE coordinates

$$\overline{\mathbf{M}}(\mathbf{q})\ddot{\mathbf{x}} + \overline{\mathbf{K}}(\mathbf{q}, \dot{\mathbf{q}}) + \overline{\mathbf{Q}}(\mathbf{q}, \dot{\mathbf{q}}, t) = \mathbf{A}^T(\mathbf{q})\mathbf{c}, \tag{5}$$

where

$$\overline{\mathbf{M}} := \mathbf{F}^T[\text{diag}\{\mathbf{D}, \mathbf{M}_X\}]\mathbf{F},$$
$$\overline{\mathbf{K}} := \mathbf{F}^T\big[\text{diag}\{\mathbf{0}_m, \mathbf{K}_X\}\mathbf{F} + \text{diag}\{\mathbf{D}, \mathbf{M}_X\}\dot{\mathbf{F}}\big],$$
$$\overline{\mathbf{Q}} := \mathbf{F}^T\big[\mathbf{Q}^T \quad \mathbf{Q}_X^T\big]^T.$$

In Eq. (5), the matrix $\mathbf{A}^T$ is the so-called structure matrix which allows to classify the degrees-of-actuation (DOA) $\alpha = \text{rank}(\mathbf{A})$. Hufnagel et al. [3] define the degree of redundancy as follows $\rho := m - \alpha$. Hence the DOA determines how

many generalized accelerations are affected by the controller. To fulfill the requirements of a fully constrained CDPR, the DOA needs to lead to $\rho \geq 1$ guaranteeing that the cables can be tensed within the wrench-feasible workspace.

2.2 Inverse Dynamics in EE Coordinates

The inverse dynamics approach is used to determine the required cable forces for a given motion. For a redundantly actuated CDPR, the number of cables exceeds its DOF by ρ. The structure matrix is supposed to have full rank δ. Accordingly, $\mathbf{A}^{\mathrm{T}}$ is not square and its kernel (null-space) is of dimension ρ. Therefore Eq. (5) cannot be solved unambiguously for the control forces $\mathbf{c}$. It is possible to generate control forces lying in the kernel of $\mathbf{A}^{\mathrm{T}}$, which have no effect on the motion but can be used to generate a tension level. Let $\mathbf{c}^0 \in \mathbb{R}^m$ be a vector representing a desired tension level, a solution for $\mathbf{c}$ such that $\left[\mathbf{c} - \mathbf{c}^0\right]^{\mathrm{T}} \mathbf{W} \left[\mathbf{c} - \mathbf{c}^0\right] \to \min$ is

$$\left(\mathbf{A}^{\mathrm{T}}\right)_{\mathbf{W}}^{+}\left(\overline{\mathbf{M}}(\mathbf{q})\ddot{\mathbf{x}} + \overline{\mathbf{K}}(\mathbf{q}, \dot{\mathbf{q}}) + \overline{\mathbf{Q}}(\mathbf{q}, \dot{\mathbf{q}}, t)\right) + \mathbf{N}_{\mathbf{A}^{\mathrm{T}}, \mathbf{W}} \mathbf{c}^0. \tag{6}$$

Therewith $\left(\mathbf{A}^{\mathrm{T}}\right)_{\mathbf{W}}^{+} := \mathbf{W}^{-1}\mathbf{A}\left(\mathbf{A}^{\mathrm{T}}\mathbf{W}^{-1}\mathbf{A}\right)^{-1}$ is a weighted pseudo inverse, where $\mathbf{W}$ is a positive definite weighting matrix, with respect to the drive capabilities. The null-space projector $\mathbf{N}_{\mathbf{A}^{\mathrm{T}}, \mathbf{W}}$ generates the tension level in the cable system close to the desired value of $\mathbf{c}^0$ [4]. In the field of redundantly actuated CDPRs, the desired tension level must be chosen in a way that the unilateral properties of cables are met. Based on this requirement Müller et al. [5] delivers real-time capable force distribution algorithms based on geometrical approaches.

3 Internal Force-Based Impedance Control

3.1 Motivation

CDPRs can be considered as a multi-manipulator system handling an object, where every actuated cable forms a manipulator. Therefore, a control algorithm for CDPRs must feature the characteristic of achieving a cooperating interaction of the manipulators—contrary to controlling each manipulator without knowledge of the others—to eliminate contradicting (antagonistic) control forces. There are some further desirable properties, which should be provided within the design of the controller:

- Each manipulator features a compliance to eliminate contradicting control forces.
- Platform dynamics take no influence on tracking or steady state position errors.

All these properties can be considered in the design of an internal force-based impedance controller. This control approach represents a class of control algorithms where the controller directly gives each manipulator the property of an impedance and as proposed by Bonitz and Hsia [6]. This remarkable feature gives each manipulator the necessary robustness to cope with harsh interacting forces. Thus, impedance control becomes an attractive strategy for controlling CDPRs.

3.2 Derivation of the Control Law

The equation of motion for each winch drive is described by

$$\mathbf{u}_i = \overline{\mathbf{D}}_{i,i}(\mathbf{q})\ddot{\mathbf{q}}_i + \mathbf{Q}_i(\mathbf{q}_i, \dot{\mathbf{q}}, t_i) + \mathbf{f}_i, \tag{7}$$

where $\overline{\mathbf{D}} := \mathbf{D} + (\mathbf{A}^T)^+ \mathbf{M}_X (\mathbf{A})^+$ represents the joint space mass matrix. Under a perfect compensation of disturbances $\mathbf{Q}$ the external control forces $\mathbf{u}$ are exactly generated by the winch drives. Thus, the forces $\mathbf{f}$ can be replaced by the inverse dynamics solution (6) to improve the controller performance.

When multiple manipulators are connected to a platform, the forces $\tilde{\mathbf{f}}$ generated by each manipulator expressed in the cartesian space can be decomposed into motion-inducing forces $\tilde{\mathbf{f}}_M$ and internal forces $\tilde{\mathbf{f}}_I$, with

$$\tilde{\mathbf{f}} = \tilde{\mathbf{f}}_M + \tilde{\mathbf{f}}_I. \tag{8}$$

Internal forces $\tilde{\mathbf{f}}_I$ produce no net forces on the EE, however, a tension in the cable system and, thus, they must be chosen to lie in the range of the null-space projector $\mathbf{N}_{A^T}$. That means internal forces $\tilde{\mathbf{f}}_I$ are not affected by motion-inducing forces $\tilde{\mathbf{f}}_M$ and can be regulated simultaneously. Using this fact, following decomposition method to compute the internal forces for each manipulator can be used:

$$\tilde{\mathbf{f}}_{Ii} = \mathbf{A}_i^T \left(\mathbf{I}_m - (\mathbf{A}^T)^+ \mathbf{A}^T \right) \mathbf{f}. \tag{9}$$

As described by Bonitz and Hsia [6], impedance control in the application of cooperating manipulators must enforce a relationship between the EE velocity and the internal forces on the manipulated EE comparable to the interaction forces between the manipulators. Otherwise, if the total forces imposed by the environment onto the manipulator will be incorporated in the impedance relationship, platform dynamics will contribute to tracking and steady-state position errors.

Each manipulator is equipped with the following impedance describing a linear second-order function expressed in the cartesian space

$$\overline{\mathbf{M}}_i \delta \ddot{\mathbf{x}}_i + \overline{\mathbf{B}}_i \delta \dot{\mathbf{x}}_i + \overline{\mathbf{C}}_i \delta \mathbf{x}_i = \delta \tilde{\mathbf{f}}_{Ii}, \tag{10}$$

where

$\delta \mathbf{x}_i = \mathbf{x}_{id} - \mathbf{x}_i$ pose errors of the platform,

$\delta \tilde{\mathbf{f}}_{Ii} = \tilde{\mathbf{f}}_{Ii} - \tilde{\mathbf{f}}_{Iid}$ internal force errors,

$\overline{\mathbf{M}}_i, \overline{\mathbf{B}}_i, \overline{\mathbf{C}}_i$ desired mass-, damping- and stiffness matrices

Here d represents a desired quantity.

An interesting choice of the impedance mass $\overline{\mathbf{M}}$ is to set it equal to the projected mass matrix $\overline{\mathbf{M}} := \mathbf{M}_X + \mathbf{A}^T \mathbf{D} \mathbf{A}$. This choice of mass assures that the stability constraints shown by Bonitz and Hsia [6] are met. It should be mentioned that the selected mass matrix affects all EE coordinates simultaneously.

Each joint acceleration is related to the EE acceleration by its structure matrix

$$\ddot{\mathbf{q}}_i = \mathbf{A}_i \ddot{\mathbf{x}}_i + \dot{\mathbf{A}}_i \dot{\mathbf{x}}_i. \tag{11}$$

Solving Eq. (10) for $\ddot{\mathbf{x}}$, substituting into Eq. (11), and incorporating into each winch drive dynamic Eq. (7), yields the following control law for each manipulator:

$$\mathbf{u}_i = \overline{\mathbf{D}}_i \left\{ \mathbf{A}_i \left(\ddot{\mathbf{x}}_{id} + \overline{\mathbf{M}}_i^{-1} \left[\overline{\mathbf{B}}_i \delta \dot{\mathbf{x}}_i + \overline{\mathbf{C}}_i \delta \mathbf{x}_i - \delta \tilde{\mathbf{f}}_{Ii} \right] \right) + \dot{\mathbf{A}}_i \dot{\mathbf{x}}_i \right\} + \mathbf{Q}_i + \mathbf{f}_i \tag{12}$$

In general, the internal force-based impedance controller is governed by a CTC structure with a shaping of the internal forces resulting from the chosen mass matrix.

One advantage of the proposed impedance control scheme is that separate force and position control loops are not required. Therefore, the impedance parameters can be chosen almost freely in contrast to the mentioned bandwidth limitations shown by Eppinger and Seering [1]. Additionally, internal forces produce no net forces on the EE and therefore, the platform dynamics have no influence on tracking or steady state position errors.

4 Experimental Results

The presented internal force-based impedance controller was implemented on the 6-DOF SEGESTA prototype shown in Fig. 1. The CDPR is controlled by means of eight BLDC-Motors (Maxon RE 60) linked to the winches with a nominal torque generation of $c_{nom} = 0.85$ Nm. Thus $m = 8$, i.e. the CDPR is redundantly actuated. The winches are placed at the vertices of a nearly symmetric cuboid with an overall dimension of 1.2 m $\times$ 1.4 m $\times$ 1 m (l x L x h). The mass of the EE is approximately 0.825 kg. Strain-gauge beam arrangements (Megatron KM302) are
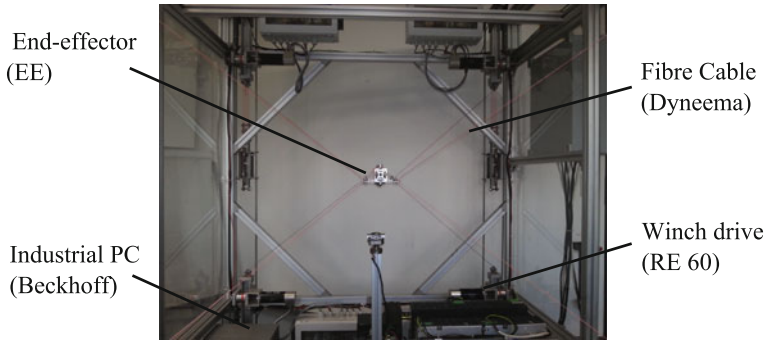
Fig. 1 SEGESTA prototype

Table 1 Coordinates of the chosen Pick-and-Place maneuver

Path	1	2	3	4	5
xyz-Pose in m	(0/0/0.5)	(−0.1/0.1/0.5)	(−0.1/−0.1/0.5)	(0.1/−0.1/0.5)	(0.1/0.1/0.5)
Radius in m	0	0	0.1	0.1	0.1

integrated into the winch drives and used to measure the cable forces. The applied encoders have a resolution of 2000 increments per turn.

To measure the EE pose the forward kinematics as proposed by von Zitzewitz et al. [7] is used. Additionally the cable stiffness to alter the cable length is in-cooperated in the forward kinematics. A high-gain observer as proposed by Khalil [8] is used to get all state variables to fulfill the requirements of the impedance controller. The BLDC-Motors have high stiction of about 0.1 Nm which makes it necessary to use an additional friction observer as proposed by Le Tien et al. [9] to support the internal force-based impedance controller. In addition, the compensation of further unmodelled effects as a variable mass matrix $\overline{\mathbf{M}}$ are handled by a disturbance observer presented by Reichert et al. [10]. To compute a desired tension level in the cable system, the so-called Puncture Method presented by Müller et al. [5] is used due to its property to deliver nearly minimum cable forces. Here, $\mathbf{f}_{min}$ is equal to 3 N.

Each manipulator impedance was chosen using the guidelines introduced by Bonitz and Hsia [6] examining the projected mass matrix $\overline{\mathbf{M}}$. The stiffness matrix $\overline{\mathbf{C}}$ was chosen such that an impedance bandwidth of approximately 3 Hz is achieved and $\overline{\mathbf{B}}$ was chosen to achieve critical damping: $\overline{\mathbf{C}} = 1000\overline{\mathbf{M}}$ and $\overline{\mathbf{B}} = 63\overline{\mathbf{M}}$.

The EE was controlled along the path shown in Table 1 with a maximum acceleration of 2.5 g and the maximum velocity was 1.5 m/s.

The parameter *Radius* describes the curve between the points in z-direction.

The evolution of the EE errors and the internal force errors expressed in the joint space, respectively, during the run are shown in Fig. 2.
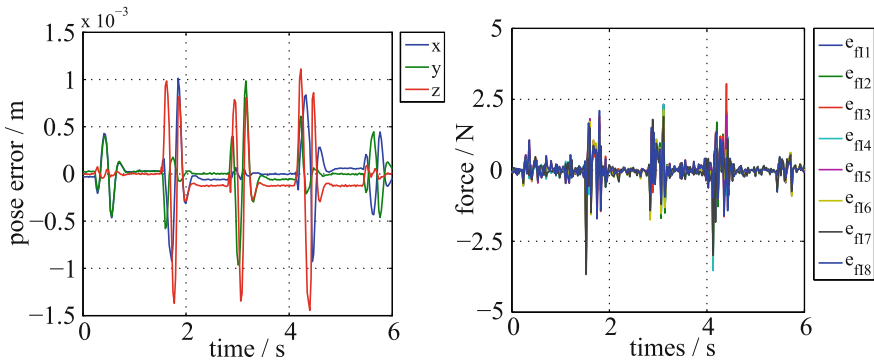
Fig. 2 EE errors (*left*) and internal force errors (*right*)

The results show that the controller has a good accuracy and the EE errors in Fig. 2 (left) are below 50 μm at the rest positions. During the run, peaks of about 1.25 mm due to the high stiction can be observed. The results demonstrate further (not shown in this paper) the importance of the disturbance observers, due to the elimination of steady state EE errors at the rest positions. In addition, the internal force errors shown in Fig. 2 (right) are going to zero at steady state, too.

5 Summary

In this paper, the equations of motion for CDPRs in terms of EE coordinates based on a projection method are presented. By using this formulation, an internal force-based impedance controller has been derived. No explicit position and force control loops are necessary. Its implementation is discussed and the feasibility is shown. Experimental results are reported for a 6-DOF CDPR, showing that an accurate trajectory tracking performance and a desired tension level in the cable system can be guaranteed during the EE movement.

References

1. Eppinger, S.D., Seering, W.P.: Understanding bandwidth limitations in robot force control. IEEE international conference on robotics and automation, pp. 904–909 (1987)
2. Hogan, N.: Impedance control: an approach to manipulation, part i—theory. ASME J. Dyn. Sys., Meas., Control **107**(1), 1–7 (1985)

3. Hufnagel, T., Reichert, C., Schramm, D.: Centralized non-linear model predictive control of a redundantly actuated parallel manipulator. In: Viadero, F., Ceccarelli, M. (eds.) New Trends in Mechanism and Machine Science, vol. 7 of Mechanisms and Machine Science, pp. 621–629. Springer, Netherlands (2013)
4. Müller, A.: Problems in the control of redundantly actuated parallel manipulators caused by geometric imperfections. Meccanica **46**(1), 41–49 (2011)
5. Müller, K., Reichert, C., Bruckmann, T.: Analysis of geometrical force calculation algorithms for cable-driven parallel robots with a threefold redundancy. In: Lenarčič J., Khatib O. (eds.) Advances in Robot Kinematics. Springer, Dordrecht (2014)
6. Bonitz, R.G., Hsia, T.C.: Internal force-based impedance control for cooperating manipulators. IEEE Trans. Robot. Autom. **12**(1), 78–89 (1996)
7. von Zitzewitz, J., Rauter, G., Vallery, H., Morger, A., Riener, R.: Forward kinematics of redundantly actuated, tendon-based robots. In: IEEE/RSJ international conference on intelligent robots and systems, pp. 2289–2294 (2010)
8. Khalil, H.K.: High-gain observers in nonlinear feedback control. In: IEEE international conference on control and automation, pp. 1527–1528 (2009)
9. Le Tien, L., Albu-Schäffer, A., De Luca, A., Hirzinger, G.: Friction observer and compensation for control of robots with joint torque measurement. In: IEEE/RSJ international conference on intelligent robots and systems, pp. 3789–3795 (2008)
10. Reichert, C., Hufnagel, T., Schramm, D.: Regelung redundant angetriebener parallelmanipulatoren mit reibungsbehafteten motoren. In: 16. VDI Getriebetagung, pp. 118–130 (2012)

Time Sub-Optimal Path Planning for Hyper Redundant Manipulators Amidst Narrow Passages in 3D Workspaces

Elias K. Xidias and Nikos A. Aspragathos

Abstract A novel approach is proposed for the time sub-optimal motion of a hyper redundant manipulator used for manipulations in a 3D workspace with narrow passages. This method is based on the Hyper-Bump Surface concept to represent the entire 3D workspace. A number of feature points randomly scattered on the surface of each link are used to estimate the degree of intruding into obstacles, which is obtained by the "flatness" function. An optimization problem is formulated including the error to the desired pose of the end-effector, the time spent for the motion and the flatness, which is solved by a GA. Simulation results are presented for manipulations in 3D complex environments to show the efficiency of the proposed method.

Keywords Hyper-redundant manipulator · Three dimensional workspace · Hyper bump-surface · Flatness · Time sub-optimal · Genetic algorithm

1 Introduction

In recent years, efforts have been made to develop manipulators with high numbers of degrees of freedom (DoF) that can be used in rescue missions, inspection and manipulation in quite complex pipe and nuclear energy installations [1] either moving autonomously or by remote control. In these applications, apart from free motion requirements, the time to complete a manipulation or inspection is crucial.

E. K. Xidias (✉)
Department of Product and Systems Design Engineering, University of the Aegean,
84100 Syros, Greece
e-mail: xidias@aegean.gr

N. A. Aspragathos
Department of Mechanical and Aeronautics Engineering, University of Patras,
26500 Patras, Greece
e-mail: asprag@mech.upatras.gr

445

The extra number of DoFs increases the motion capabilities and the dexterity of the manipulator in highly cluttered environments with narrow passages, while the complexity of the motion planning problem is increased, so approaches for high dimensional motion planning spaces are required.

The motion planning algorithms can be classified into three categories: cell decomposition, roadmap and potential field methods, which are used in the motion planning of hyper redundant manipulators too. Cell decomposition based methods [2] are computationally very expensive and for higher dimensional Configuration Spaces require large storage means. Potential field based approaches [3] are computationally efficient, but the manipulator can be trapped at local minima. Techniques have been introduced to overcome these local minima trapping at a high computational cost.

The roadmap techniques and particularly the Probabilistic Roadmap [4] approach proved successful in finding feasible paths in a wide range of path planning problems involving robots with high DoFs. However, the generated path often involves redundant movements, which is far from optimal in any sense and has poor quality.

In this paper a process is developed for planning time sub-optimal collision free motions for a hyper redundant manipulator in a 3D workspace able to move via narrow passages based on the Hyper-Bump Surface (H-BS) concept to represent the entire 3D workspace by one mathematical entity [5]. The motion planning problem is formulated as a global optimization problem which is solved using a Genetic Algorithm with multiple populations (MPGA). The main innovations and contribution of the proposed approach are the following: (i) the workspace is presented as one entity analytically; (ii) the determination of the H-BS is fast and independent of the manipulator, so there is no need for high storage capacities, (iii) Any shape of the obstacles and of the robot can be accommodated. The collision avoidance checking is not combinatorial, since the algorithm does not find the distance between the various combinations of objects. In fact, it checks the flatness of the H-BS in the coordinates of a set of points by simply comparing two numbers, and the deviation from the flatness is punished in the searching procedure.

2 General Assumptions and Notations

In this paper, we assume a hyper redundant manipulator (Fig. 1a) operating in a 3D workspace cluttered with static obstacles of arbitrary size and shape. In addition: (i) the links are represented by identical (length and diameter) cylinders, (ii) each joint has 2-dofs described by two rotation angles: yaw and pitch so the joint variables are denoted by $q = [q_1, \ldots, q_j, \ldots, q_{2n}]$, where n is the overall number of links and (iii) the velocity of each joint is constant. The joints of the manipulator are moving simultaneously and the travel time between two configurations is determined by the joint that takes longer. The hyper-redundant kinematics is trivial so their derivation is omitted.
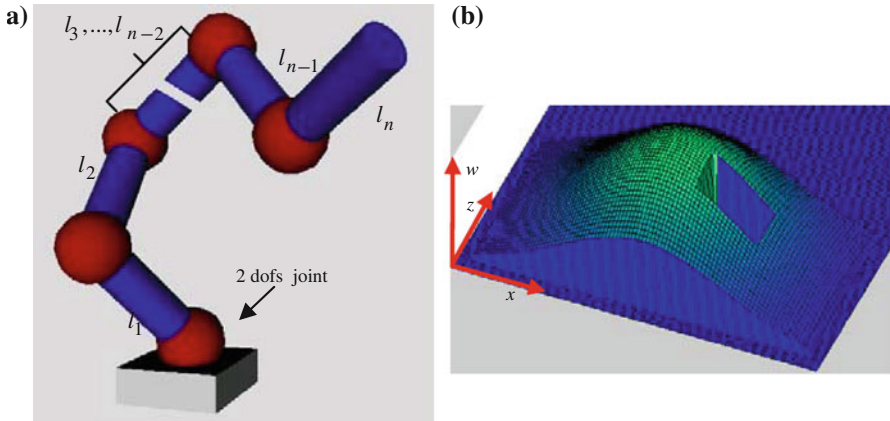
Fig. 1 a The hyper redundant manipulator. **b** The projection of the H-BS on x − z plane of the wall with a window

The obstacles have fixed and known geometry and are static. The initial and the desired position and orientation of the end-effector are fixed and known.

3 Time Sub-Optimum Path Planning in 3D Workspace

In order to provide an optimum or even a near-optimum path for the manipulator's end-effector an objective function is formulated including: (a) the clearance between the robot and the obstacles and (b) the time required for executing the required kinematics mode motion by the hyper redundant manipulator to reach the goal. In this section, the formulations of the objective function and the Genetic Algorithm with multiple populations (MPGA) for the determination of the sub-optimal solution are presented.

Given a 3D workspace the construction of the Hyper-Bump Surface (H-BS) is an application of the Z-value algorithm [5], where the fourth coordinate of each grid point takes a value in the interval (0, 1] if the corresponding grid point lies inside an obstacle and the value 0 otherwise. A tensor product B-Spline surface with uniform parameterization [6] represents the H-BS S:$[0, \ 1]^3 \rightarrow [0, \ 1]^4$. Figure 1b illustrates the projection of the H-BS on x − z plane of a wall obstacle with a window (Fig. 2). It must be noticed that, the initial discretization is used for the definition of the control points net and it is not used in the definition of the objective function and in searching for the optimum. Furthermore, the computational time required to construct the H-BS depends only on the algorithm, which is used to determine the location [5] of the grid point and especially on the algorithm, which is used to determine the fourth coordinate of each grid point. The H-BS is independent from the anatomy and the shape of the manipulator so it is not
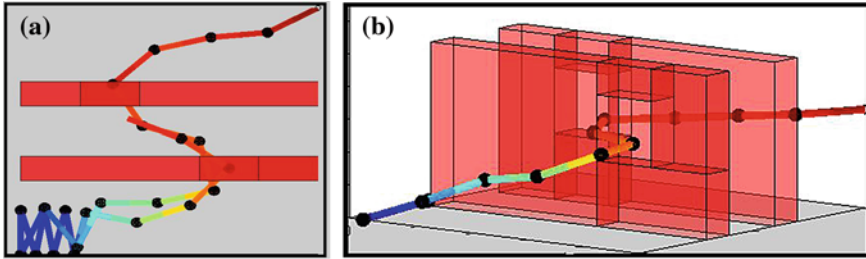
Fig. 2 a An intermediate and a final configuration, respectively. **b** Another point of view

necessary to reconstruct the H-BS when the manipulator is moving in the work-space or when the manipulator structure is changed.

On the surface of each manipulator's link a set of N random points a_v^μ with $v = 1, \ldots, N$, and $\mu = 1, \ldots, n$. Larger value for N represents the links more accurately, but increases the computational time, thus a trade-off is required.

The objective for collision avoidance implies points a_v^μ on $S(x, y, z)$ with minimal "flatness" given by:

$$H = \max_{\boldsymbol{q}_{total}} \left(S_w\left(a_1^1\right), \ldots, S_w\left(a_N^1\right), \ldots, S_w\left(a_1^n\right), \ldots, S_w\left(a_N^n\right) \right) \qquad (1)$$

with respect to the joint variables $\boldsymbol{q}_{total} = (\boldsymbol{q}^1, \ldots, \boldsymbol{q}^m, \ldots, \boldsymbol{q}^{R+2})$, with $\boldsymbol{q}^m \in [0, \frac{11\pi}{6}]^{2n}$, and $S_w\left(a_v^\mu(s)\right)$ denotes the w-coordinate (fourth coordinate) of each point a_v^μ on $S(x, y, z)$. R is the number of intermediate manipulator configurations between the initial and final goal defined by the user.

The time optimal motion of the manipulators could be considered as a two stage process [7]. In the first stage the kinematics and the geometry of the environment are considered so the time required to move from one configuration to another one depends on the path in the configuration space and on the velocity of each joint. In the next stage of trajectory implementation on the determined optimal path the time could be further reduced based on the dynamics of the manipulator. The joints of the current industrial manipulators are moving simultaneously with a trapezoidal profile of velocity from configuration to configuration. Since the major part of the motion has constant joint speed and the acceleration of the actuators is increasing, the joint velocity is approximated by a constant for the first stage of the path planning [8, 9].

Considering that the joints of the manipulator are moving simultaneously with constant velocity, a simple approximation of the time t required for executing a path from the initial goal to the desired goal passing through a number R of intermediate configurations is given by,

$$t = \sum_{m=2}^{R+2} \max_j \left(\frac{\left| \boldsymbol{q}_j^m - \boldsymbol{q}_j^{m-1} \right|}{\dot{\boldsymbol{q}}_j} \right), \quad j = 1, \ldots 2n \qquad (2)$$

where q_j^m expresses the intermediate mth configuration, and $\dot{q}_j$ is the average velocity of the jth-joint that is assumed to be constant.

Considering the metrics for the rigid body pose in SE [7], in order to represent the orientation of the hyper redundant manipulator's end-effector we use unit quaternions due to their advantages [10]. We define as $D = \|p_c - p_d\|$ the position error between the current position p_c of the manipulator's end-effector and desired one p_d, and $Rot = \arccos(R_c \cdot R_d)$ expressing the angle (orientation error) between the two unit quaternions the current R_c and the desired orientation R_d. The requirement for the manipulator's end-effector to reach the desired pose (position and orientation) is defined by the following weighted metric:

$$DR = w_d D + w_r Rot, \quad w_d + w_r = 1, \ 0 \leq w_d, w_r \leq 1 \tag{3}$$

Considering the collision free motion and the time required for moving along the determined path, he following combined objective function is formulated:

$$E(q_{total}) = t * e^{w_1 DR + w_2 H}, \ w_1 + w_2 = 1, \ 0 \leq w_1, w_2 \leq 1 \tag{4}$$

The scalars w_d, w_r, w_1, w_2 are weights factors. For example higher values for w_2 and w_d enforce the optimization method to search for paths with optimum clearance and the smallest position error ignoring to some degree the end-effector's orientation and the required time for executing the path and vice versa. It should be noted that, if we do not take into account the required time t then we find a collision free path which connect the initial goal with the desired goal.

Equation (4) presents a penalized time function, which takes a value in the interval $(t, +\infty)$, if the manipulator collide with the obstacles and the value t, otherwise. Furthermore, E expresses the total cycle time obtained taking into account the manipulator's configurations at the initial and desired states and the R intermediate configurations and simultaneously ensures that no collision occurs during the motion between these configurations.

Considering that our objective function is procedural, non-linear and multimodal, a GA with parallel populations and migration [11] technique has been implemented to search for sub-optimal solution. This GA has multiple, independent populations, and at each generation, some individuals migrate from one population to another. When migration occurs, the best individuals from one population replace the worst individuals in another population (the nth population migrates into both the (n − 1)th and the (n + 1)th population). The master population is updated in each generation with best individuals from each population. It is worth to notice that, each chromosome represents the strat, goal and intermediate configurations q_{total} of a path. The fitness function of the problem is expressed by the inverse of the objective function (Eq. 4), thus the maximization of the fitness function leads to the minimization of the objective function.
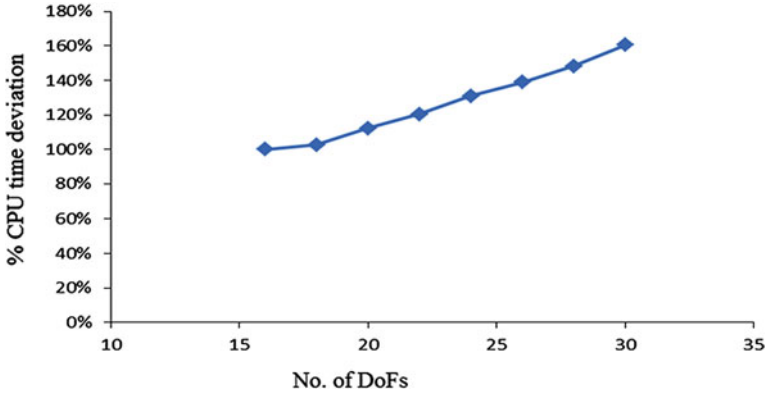
Fig. 3 The effect of DOFs in CPU time

4 Experiments

The performance of the proposed method was investigated through simulation examples for a hyper-redundant manipulator operating in a 3D environment. Due the space limits we present only one test case of manipulation with Hyper Redundant manipulators. The length of each link is equal to $l_i = 0.5$, $i = 1,\ldots, 12$, ($n = 12$ is the total number of the links) the radius of each cylinder is equal to $r = 0.1$. Suitable setting for number of feature points N on the surface of each manipulator's link and for the GA's parameters were experimentally determined in preliminary tests and defined as follow: feature points $N = 20$, *population size* = 50, *number of generations* = 80, *crossover rate* = 0.7, *probability of boundary mutation* = 0.003, *Migration-Interval* = 10 and *Migration-Fraction* = 0.1. The grid size for the construction of the H-BS is $80 \times 80 \times 80$ and the manipulator's base is lying on (0.5, 0, 0).

In the present test case, the environment is cluttered with obstacles forming narrow passages (one window on each wall) from where the manipulator is requested to pass, in order to reach the desired state, shown in Fig. 2. The hyper redundant manipulator initially is lying on the floor. The end-effector should approach the desired point with a rotation of a 60° angle about the global axis z where the corresponding quaternion is (0.866, 0, 0, 0.5). Figure 2a, shows an intermediate configuration and the final configuration of the hyper redundant manipulator. The total travel time is equal to 18.03 and when the time optimization is not taken into account the total travel time is equal to 25.06.

It must be noticed that, in all our experiments the mean square error for the position is 0.34 % and for the orientation is 0.43 %,respectively. Furthermore, Fig. 3, shows the increase of the CPU time versus the number of DoFs for the second case. The percentage increase of the CPU time is calculated with respect to the computational time required for a manipulator with 16 DoFs. It could be

noticed that the increase of computational time is almost linear which shows the efficiency of the proposed algorithm for redundant manipulators with even quite high number of DoFs.

5 Conclusions

This paper proposes a method for time sub-optimal path planning of a hyper redundant manipulator for manipulations or inspection in complex 3D environments. The proposed method is based on the H-BS concept for representing the 3D workspace. The path planning problem is transformed to a global optimization problem which is solved using a GA with multiple populations. Simulated experiments are conducted showing the effectiveness and efficiency of the proposed method for high DoF manipulators. Apart from avoiding the obstacles and reaching the desired pose with very good accuracy, the manipulator saves about 32 % of the time to reach the desired pose with respect of the time required when the time optimization is not taken into account. Thus the proposed method could be used in time crucial handling and inspection operation either autonomously or by remote control.

Future work will be concentrated on applying the proposed concept in more complicated environments where a hyper redundant manipulator is requested to serve a set of task points while is moving safely in its environment.

References

1. Wolf, A., Brown, H.B., Casciola, R., Costa, A., Schwerin, M., Shamas, E., Choset H.: A mobile hyper redundant mechanism for search and rescue tasks. In: Proceedings of the 2003 IEEE/RSJ International Conference on Intelligent Robots and Systems, Las Vegas (2003)
2. Lingelbach, F.: Path planning using probabilistic cell decomposition. In: Proceedings of IEEE International Conference on Robotics and Automation (2004)
3. Lin, C.-C., Chuang, J.-H.: A potential based path planning algorithm for hyper redundant manipulators. J. Chin. Inst. Eng. **33**(3), 415–427 (2010)
4. Kavraki, L., Svestka, P., Latombe, J.C., Overmars, M.H.: Probabilistic roadmaps for path planning in high-dimensional configuration spaces. IEEE Trans. Robot. Autom. **12**(4), 566–580 (1996)
5. Xidias, E.K., Aspragathos, N.A.: Motion planning for multiple non-holonomic robots: A geometric approach. Robotica **26**(4), 525–536 (2008)
6. Piegl, L., Tiller, W.: The NURBS Book. Springer, Heidelberg (1997)
7. Verscheure, D., Demeulenaere, B., Swevers, J., De Schutter, J., Diehl M.: Practical time-optimal trajectory planning for robots: a convex optimization approach. IEEE Trans. Autom. Control **30**, 531–541 (2008)
8. Ellekilde, L.-P., Petersen, H.G.: Motion Planning efficient trajectories for industrial bin-picking. Int. J. Robot. Res. **32**, 9–10 (2013) (published online 20 June 2013)

9. Zacharia, P.T., Xidias, E.K., Aspragathos, N.A.: Task scheduling and motion planning for an industrial manipulator. Robot Comput-Integr Manuf **29**(6), 449–462 (2013)
10. Kuffner, J.J.: Effective sampling and distance metrics for 3D rigid body path planning. In: Proceedings of the 2004 IEEE International Conference on Robotics & Automation (2004)
11. Luque, G., Alba, E., (2011) Parallel genetic algorithms: theory and real world applications. In: Studies in Computational Intelligence. Springer, Berlin

A Blocking Plate Manipulation Robot System Based on Image Recognition

Yonggui Wang, Xingguang Duan, Amjad Ali Syed, Meng Li, Xiangzhan Kong, Chang Li, Yang Yang and Ningning Chen

Abstract Since the intricate and dangerous working environment of steam generator, it's risky for staffs to complete fastening bolts of blocking plate. This paper introduces the blocking plate manipulation robot system based on image recognition. The mechanical design was proposed gradually to satisfy the requirement of compact structure, light weight and quick installation. Then the control system is displayed to guarantee precise control and safe operation. In addition, the center coordination values of the bolt based on the image recognition are extracted to guide the robot to fasten the bolts. Finally the experiment validates the effectiveness of the image recognition.

Keywords Robot · Image recognition · Mechanical design · Blocking plate

1 Introduction

As the development of nuclear power automation, the robot, image processing has been widely applied to play an important role in the dangerous environment. In the nuclear power plants, the equipment and operating environment are radioactive. Therefore, the robot application is not only lower the cost of artificial protective equipment and management, but also reduce the staff radiation dose and labor intensity [1]. After the Chernobyl disaster and Fukushima disaster, the more attention has been taken to nuclear safety by government and other related organization.

Y. Wang (✉) · X. Duan · A. A. Syed · M. Li · X. Kong · C. Li · Y. Yang · N. Chen
Intelligent Robotics Institute, Key Laboratory of Biomimetic Robots and Systems, Ministry of Education School of Mechatronical Engineering, Beijing Institute of Technology, 5 Nandajie, Zhongguancun, Haidian, Beijing 100081, China
e-mail: wangyg1025@163.com

Fig. 1 Blocking plate and fastening the bolt
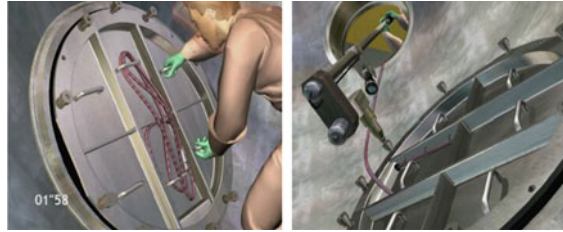
In recent years, many robots have been applied in the nuclear plant. The Pioneer (RedZone robot company), which has 6 DOFs arm, was an electric tracked vehicle and used for reprocessing nuclear accident [2]. The radiation-resistant robot RaBOT (JAERI Robot Company) was a mobile robot with double arm and equipped seven CCD cameras [3]. It could work under the γ radiation field of 105 Sv and complete switching valves, sample collections. The PackBot robot (iRobot company, American) aimed to detect the working condition, analyzing and recording the parameters [4]. In addition, it could provide tipping self-adjusting, self-recovery communication and GPS positioning. The TWS system (AREVA company, French) including robot, ultrasonic phased array module and analysis system, was a general detection tools for reactor pressure vessel. Furthermore, other robot has also been used under the complex environment of nuclear power plant.

During the maintenance period of the nuclear power plant, the inlet and outlet of steam generator, which are on the 40° slope, should be blocked in order to protect the maintenance staff and guarantee the normal work of other steam generator. Now the seal of inlet and outlet of steam generator allows for the rubber inflatable capsule and blocking plate. The aluminum blocking plate, which is divided into three parts to be convenient to carry and attaches 14 bolts in order to connect with the steam generator, is delivered into the steam generator one by one from the manhole, then the staff put the blocking plate and rubber inflatable capsule on the inlet of steam generator, as shown in Fig. 1. In the current way, the staff would fasten the bolt from the manhole by using a long fastening tool on which the camera was installed. This process spends much time in fastening bolt and the staff also would be long time exposure to the radioactive environment [5–7].

So this paper proposes a blocking plate manipulation robot system based on the image guide to deal with current difficulties, which has the characteristics of compact structure, light weight and easy to handle. The system overview is introduced in Sect. 2. The mechanical design and control system of robot are recommended by Sects. 3 and 4. The Sect. 5 provides a center coordinate recognition method.
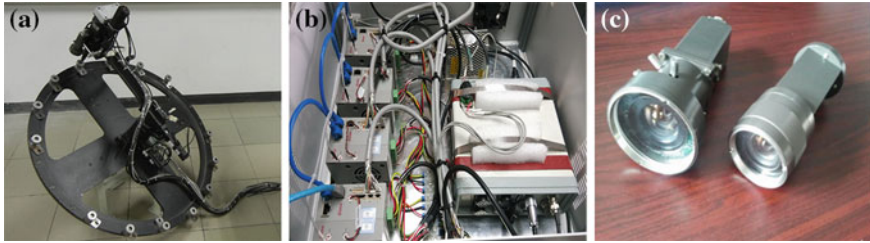
Fig. 2 The blocking plate manipulation robot system. **a** Manipulation robot. **b** Control system. **c** Image recognition

2 System Overview

In this section the designed and implemented system components are discussed. The blocking plate manipulation robot system includes the robotic manipulator, control system and image recognition system, as shown in Fig. 2.

The manipulation robot being a system carrier completes fastening 14 bolts in the steam generator. Because of the limitation of work space, the mechanical structure of robot is compact and light weight. Taking account for the function of fastening bolt, the manipulation robot adapts a typical structure of cylindrical arm with roll wrist. So the robot allows for four DOFs, three DOFs of them determine the target positions, another one is used for fastening bolt through the cooperation of first three DOFs.

The control system aims to control the robot to move stably and smoothly. In order to improve the control quality and safety, a reliable control system must be needed. Therefore, distributed control system is selected built on CAN-bus. Because of reliable communication, real-time, flexibility, strong robustness, long transmission distance, CAN-bus is widely applied in all kinds of industry control field [8].

The image recognition system played an important role in entire system. As the blocking plate consists of three parts, each bolt position of blocking plate is uncertain. Through processing the image from the camera, which is installed in the robot arm in order to keep the constant distance from the camera to the surface of blocking plate so that the image recognition system could acquire the bolt center coordinates by designed algorithm. Then convert and transfer the center coordinates to the blocking plate manipulation robot so that the manipulation robot completes the bolt fastening.
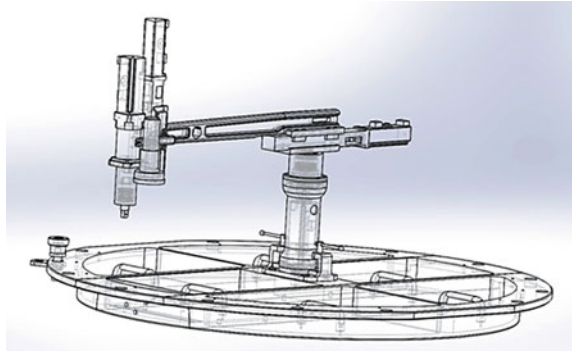
3 Mechanical Structure

The blocking plate manipulation robot aims to be easy to carry into the steam generator, and quick installation on the blocking plate. So the robot should be the characteristic of compact structure, light weight, quick installation and safety. By analyzing the working space, the typical structure of cylindrical coordinate system with roll wrist was used for completing the task on the blocking plate. The robot has four DOFs driven by four AC servo motor, three of them are used for determining the position and another for fastening the bolts, as shown in Fig. 3.

Based on analyzing the dexterous workspace, some parameters about the manipulation robot could be confirmed. The first joint is supported by the servo motor and harmonic reducer realizes the circular motion of robot in order to control the robot to every bolt. The second joint is maintained by the motor and linear module allows for the radial movement to adapt the bolt position. The three joint is just as the second joint, aiming to be used for lifting motion. The fourth joint realized to fasten bolts, so the servo motor and reducer are chosen to output the required torque.

4 Control System

Communications among these electric devises are required to be stable and fast. Compared with other sort of communication bus, CAN field bus is remarked as a competent choice. Whole structure of the system is shown in Fig. 4. Control system consists of an industry computer, a CAN card with PCI slot, motor controller and other devises as mount points on the CAN bus.

CAN open protocol, a high-layer protocol base on CAN field bus, is widely accepted in industry uses. Promoted by BOSCH company, it is a serial bus protocol with outstanding properties, such as high reliability, strong interference immunity, low cost and development simplicity. CAN open is object-oriented, and

Fig. 4 control system of blocking plate manipulation robot
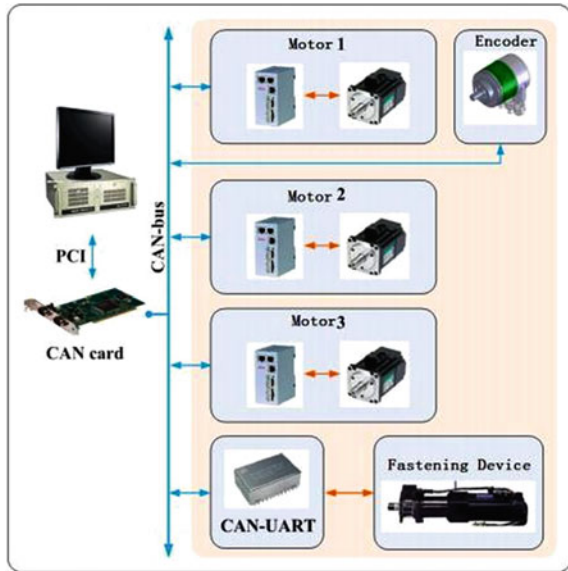
is characteristic of modularization and remarkable adaptability make it widely used in plenty of fields. The hardware of control system is displayed in Fig. 5.

According to the motion sequence of real time and workflow, firstly control the motor 1 to the proper position. Then acquire the image and detect the coordination values of bolt's center, calculate the angle and distance of motor 1 and motor 2 in order to guarantee the robot to move just above the bolt. Finally the motor 3 and motor 4 could complete the fastening and loosening bolts.
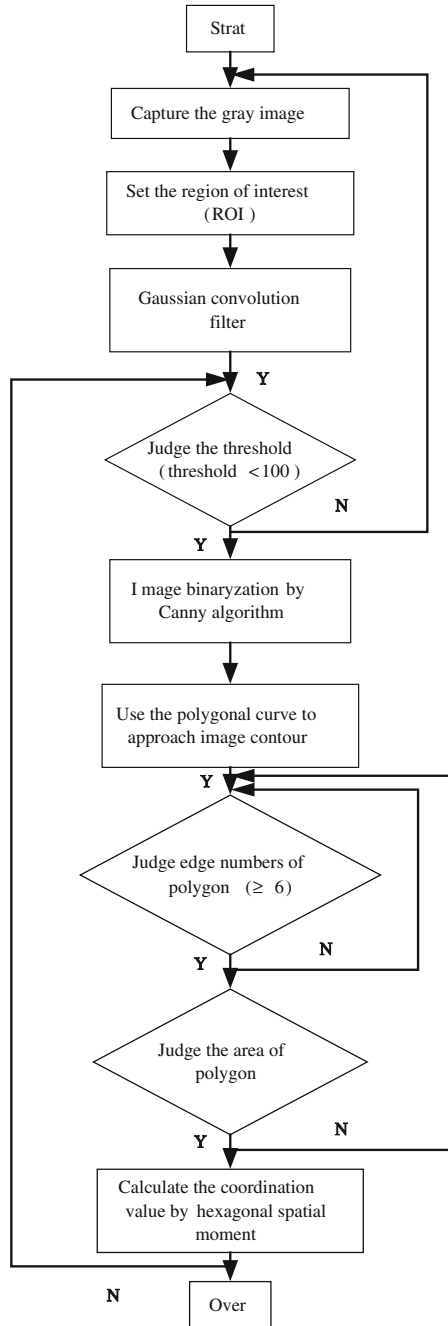
5 Image Recognition

The image recognition system goals to capture the image, extract that bolt center coordinate values and convert into the joint angles [9–11]. As the structure of bolts is special, identifying hexagon is more effective than the circle in the process. Because the blocking plate could have a number of circular structures and it is prone to recognize other center coordinate values rather than the bolts, circle isn't an ideal recognition feature. The camera is special designed for radiation protection due to complex working environment.

As acquiring bolts image in real-time, the light, uneven exposure and other factors brought to the image noise. Without noise removal, image segmentation, image enhancement and image analysis and judgment would be affected. So the corresponding approach is applied in order to realize the image recognition and acquire the center coordinate values [12, 13].

Fig. 5 The process of image recognition
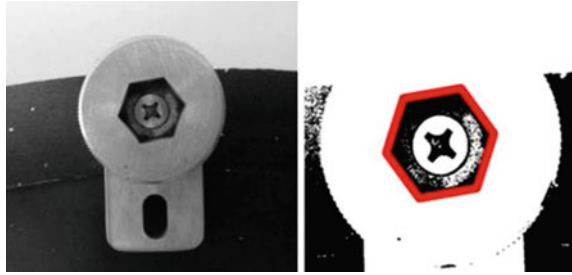
Fig. 6 The result of image recognition

Image recognition aims to acquire the center coordinate values of bolts. Through the procedure as shown in Fig. 5, the center values calculated. In this procedure, the image binaryzation and identification of the center become key steps.

Through the analysis of different image recognition algorithms, Canny operator could obtain optimum efficiency of edge detection. High signal noise ratio, better positioning performance and only a single response to a single edge are the advantages of Canny algorithm. The basic principle of Canny algorithm is to calculate the gradient magnitude and direction of the Gaussian filter impulse response [14].

Supposing gradient vectors is $\nabla f(x,y) = \begin{bmatrix} f_x(i,j) \\ f_y(i,j) \end{bmatrix}$, boundary strength is $\nabla_{i,j} = \sqrt{f_x^2(i,j) + f_y^2(i,j)}$, and the gradient direction angle is $\theta = \arctan\left(\frac{f_y(i,j)}{f_x(i,j)}\right)$.

However, geometrical figure is incomplete, which will make a difficult to find the center of bolt. Besides that, the light direction and illumination have a great influence on image recognition. Non-maximum suppression method and two threshold judgment are applied in edge detection.

After the adjustment of threshold, a satisfy result can be obtained, as shown in Fig. 6.

Through the analysis of the hexagonal spatial moment, the center values of the hexagonal could be calculated by

$$\bar{x} = \frac{\sum_{i=1}^{n} x_i p(x_i, y_i)}{\sum_{i=1}^{n} p(x_i, y_i)} \quad \bar{y} = \frac{\sum_{i=1}^{n} y_i p(x_i, y_i)}{\sum_{i=1}^{n} p(x_i, y_i)} \tag{1}$$

Then transform the center values to joint angles which enable manipulation robot to get the target position, and complete fastening the bolts.
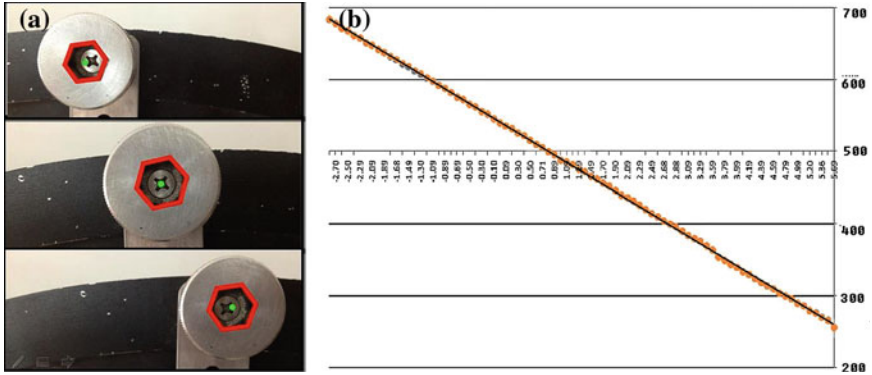
Fig. 7 Result of precision experiment. **a** The different position. **b** The relationship between the pixel and joint 1

6 Experiment

The experiment aims to validate the image acquisition and processing system, affirm the scope of taking image and calculation the relationship between the pixel and joint angle. The image recognition plays an important role on the robot system so that the camera guides the robot to the suitable position. Because it is difficult for camera to acquire image just above the bolt, we need to calculation the scope in which the algorithm of image recognition could detect the bolt's center. The procedure of experiment is presented as follows:

(1) Move the camera to just above the bolt and recode the center coordination values of the bolt, such as (500, 500). So when the joint 1 moves θ_b, the fastening device could be moved to just above of the bolt and complete fastening and loosening the bolt.
(2) The joint 1 rotates 0.2° each time along the clockwise direction. Recode the center coordination values of bolt by the image recognition system.
(3) Along the counterclockwise direction, the joint 1 rotates 0.2° each time and recodes the values, as shown in Fig. 7.

The result shows in the Fig. 7 that the relationship between the camera location and center coordination values is linear in certain scope. Given the location of the above bolt as the zero point, the scope of taking image is $(-2.70, 5.69)$. In addition, the relationship between the joint angle and pixels could be calculated.

$$\theta = (x) - 500 \times 0.1/2 + \theta_b$$
$$l = (y - 540) * 0.5/3 \tag{2}$$

Where, the coordination value (x, y) is the bolt center when the camera moves to above the scope. The relationship is used to guide the robot to complete that task.

7 Discussion

A blocking plate manipulation robot is designed and implemented in this paper in order to protect the staffs and reduce the radiation duration. Through the requirements of the blocking plate manipulation, the mechanical design and control system are introduced to achieve this function. At last the image recognition system is narrated to display the process of identifying the center values of the bolt. The robot has the characteristic of small volume, light weight and easy-to-handle. After a lot of experiments were conducted, the system has been proved to be effective. But the image recognition is not enough stable because of the light intensity. Now the system is used for low torque, the high torque unloading problems should be considered. So it still has a lot of work to make the system better and higher reliability.

References

1. Hogan, M.K.: Anti-radiation clothing. Tech. Text. Int. **4**, 1899–2014 (1995)
2. Charles, J.: Rosie: a worker for the nuclear age. IEEE **11**, 82–83 (1996)
3. Kiyoshi, O., Kiyoshi, S.: Development of a radiation-proof robot. VSP BV **16**, 493–496 (2002)
4. Yamauchi, B.M.: PackBot: a versatile platform for military robotics. SPIE-int. Soc. Opt. Eng. **5422**, 228–237 (2004)
5. Hayasaka, Y.: R&D of advanced robot for nuclear power plant facilities. Robot (Japan) **62**, 0387–1940 (1988)
6. Maki, H.: The concept of the advanced robot for nuclear power plants. Japan Ind. Robot Assoc. **1985**, 497–505 (1985)
7. Rohrabacher, A., Carlton, R., Gelhaus, F.: Considerations in the development and implementation of a maintenance robot for nuclear power facilities. Trans. Am. Nucl. Soc. **54**, 186–190 (1987)
8. Herpel, T., Hielscher, K.-S., Kelhmet, U., et al.: Stochastic and deterministic performance evaluation of automotive CAN communication. Comput. Netw. **53**, 1171–1185 (2009)
9. Hutchinson, S., Hager, G.D., Corke, P.I.: A tutorial on visual servo control IEEE Transactions on robotics and automation **12**, 651–670 (1996)
10. Chaumette, F., Hutchinson, S.: Visual servo control—Part II: advanced approaches. IEEE Robot. Autom. Mag. **14**, 109–118 (2007)

11. Corke, P.I., Hutchinson, S.A.: A new partitioned approach to image-based visual servo control. IEEE Trans. Robot. Autom. **17**, 507–515 (2001)
12. Zhou, C.: Wei Fu (2011) A study of robot control technology based on stereo vision. Int. Conf. Electron. Optoelectron. **2011**, 152–155 (2011)
13. Kroger, T., Padial, J.: Simple and robust visual servo control of robot arms using an on-line trajectory generator. IEEE Int. Conf. Robot. Autom. **2012**, 4862–4869 (2012)
14. Panetta, K. A., Agaian, S. S., et al.: Shape-dependent canny edge detector. Opt. Eng. 50, 087008 (2011)

Walking Mobile Robot with Manipulator-Tripod

**V. Zhoga, A. Gavrilov, V. Gerasun, I. Nesmianov, V. Pavlovsky,
V. Skakunov, V. Bogatyrev, D. Golubev, V. Dyashkin-Titov
and N. Vorobieva**

Abstract This paper describes the design of an autonomous mobile robot of a small class, equipped with manipulator-tripod with a swivel block. The robot movements software optimization methods are shown here. The positional problem of manipulator pickup device changing over from the starting position to the set finite one was solved. The trajectory and the law of motion along the trajectory from the minimum pickup device acceleration were synthesized.

Keywords Mobile robot with walking movers · Manipulator-tripod with a swivel block

1 Introduction

Mobile robots equipped with manipulators are used to monitor and predict the state of the environment, disaster management. The vast majority of mobile robots have wheeled or caterpillar movers. However there are operational situations where the use of such movers is impossible. Application of robots with walking mechanism

V. Zhoga (✉) · A. Gavrilov · V. Skakunov
Volgograd State Technical University, Volgograd, Russia
e-mail: dtm@vstu.ru

V. Gerasun · I. Nesmianov · V. Dyashkin-Titov · N. Vorobieva
Volgograd State Agrarian University, Volgograd, Russia
e-mail: ivan_nesmiyanov@mail.ru

V. Pavlovsky
Keldysh Institute of Applied Mathematics of RAS, Moscow, Russia
e-mail: vpavl@mail.ru

V. Bogatyrev · D. Golubev
JSC CCB Titan, Khimki, Russia
e-mail: denisgolubev21@rambler.ru

allows to improving the robot's flotation, to navigate along the flights of stairs, as well as to reduce the damaging influence on the soil fertile layer [1].

Usually manipulators are installed on the robot, which represent consequently connected chain links. These manipulators have a low weight-lift index and are characterized by high static and dynamic errors. One of the ways of overcoming these shortcomings is to use the manipulator-tripod with parallel kinematics [2].

In this regard it is relevant to study mobile robots with walking propellers equipped with manipulators-tripods.

1.1 Mobile Robot

The Fig. 1 shows a robotic system consisting of a mobile robot equipped with a manipulator-tripod [3].

The robot consists from a top frame 1, connected by the rotation mechanism with the bottom body 2. Each of the body parts are connected with pair of guide blocks 3, 4 made in the form of a splined shaft with a ball screw LBST30 DD CL, with a stroke of 942 mm and 1,042 mm, with the horizontal displacement drives [4, 5]. The drives of the company «Maxon motors» are used as horizontal displacement drives and rotation drive. Each drive includes a servo motor RTG060, planetary gear, brake, position sensor (encoder HEDL9140, 500 imp/rev). Twisting moment on the drive shaft of horizontal movement is 4 Nm; angular velocity is 425 rev/min. Maximum twisting moment on the rotating drive shaft is 34 nm; the angular velocity of the output shaft is 17 rev/min. Robot vertical adaptation drives 5 to the supporting surface are mounted at the ends of the rods. The linear actuators CAT33Hh400h4AG1F, «SKF group» are used as drives. Bearing rod dynamic load is 500 N; the speed is 0.174 m/s; the stroke is 400 mm. The robot is powered by the battery with the voltage of 24 V.

The robot is equipped with sensors to determine when to touch the surface support stand; guide block motion sensors, infrared distance meter, two-axis inclinometer and video cameras.

1.2 Manipulator-Tripod

Manipulator gripper movement is provided by variable-length units (actuators SKF). One ends of the links are secured via two movable pivot points on the support base. Opposite ends of the links are connected by the spherical joint assembly [2], whereby the longitudinal axes of the links converge at a single point. Support base has a possibility to rotate the expense of a variable-length link 4 (actuator SKF).

The task of the operating gripper movement consists of three stages—the positioning of the gripper, its trajectory synthesis and determination of the motion law along the trajectory.

2 Robot Dynamic Model

Mechanical part of the robot is resented in the form of six absolutely rigid bodies of mass m_1, m_2, m_3, m_4 connected with moving drives (Fig. 2).

The robot motion relative to a fixed reference system $O\xi\eta\varsigma$ is considered. The coordinate axes C_1XYZ are connected with the mass center of the lower main body. The mass center location is determined by the radius—vector $\vec{r}_1$, velocity vector $\vec{V}$ and angular velocity vector $\vec{\omega}$. The movable coordinate system $C_kX_kY_kZ_k$, $(k = 1 \div 6)$ are closely connected with each of solid bodies. Their position relatively to the axis C_1XYZ is defined by using Euler ship angles φ, ψ, θ.

The equations of motion are written in the form of Lagrange equations of the 2nd kind

$$A\,\ddot{q} = B(q,\dot{q}) + F(q,\dot{q},t) + N(q,\dot{q}), \tag{1}$$

where A is 10×10 a symmetric matrix of inertia coefficients; $B(q, \dot{q})$ is a matrix column terms depending on generalized coordinates and velocities; $F(q, \dot{q}, t)$ is a column matrix of control forces; $N(q, \dot{q})$ is the matrix column of supporting surface reaction forces.

The mathematical model describing the dynamics of the robot spatial movement is implemented as a set of programs written in C# using .NET Framework 4.
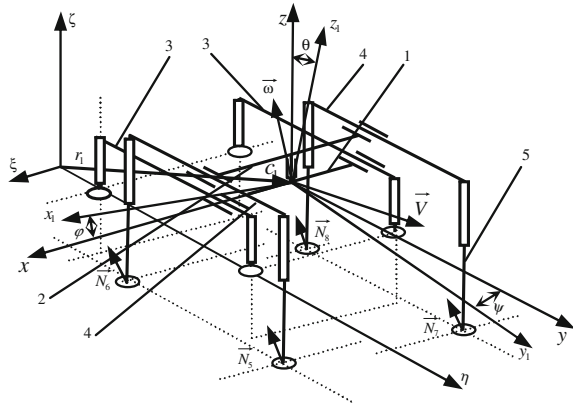
The main objective of the program is the calculation and visualization of the robot
based on the differential motion equations integration results.

In the robot movements' numerical simulation the cyclic gait with a constant
factor regime was defined. The carried out numerical study allowed us to for-
mulate technical requirements for the mobile robot drives experimental model.

Along with discrete algorithms of movement (start-stop), the robot's kinematic
scheme allows us to implement the algorithm in which a robot moves uniformly in
a straight line. Unaccented robot adaptation to uneven support surface is provided
by a software laws relatively to its links movement [6].

3 Optimization of Robot Program Motion

The robot prototype experimental studies showed that basic energy consumption
for movement is caused by friction in the joints of its parts.

One of the methods of reducing energy consumption to overcome the frictional
forces is the realization of the software moving optimum laws of robot frames
found by minimizing a criterion for determining irreversible losses in electric
motors. The set problem is solved by the methods of classic calculus of variations
[6, 7].

$$I_1 = \int\limits_0^{t_1} \left[F_1^2(t) + F_2^2(t) \right] dt$$

F_1, F_2—driving force control actuators

When implementing the got motion optimal law, the energy on the robot
movement is reduced, compared with the "triangular" law by 25 %. Figure 3
shows the coordinates velocity and acceleration of the frame change program laws.

Fig. 3 Optimal kinematic parameters of portable frame $x\dot{}(t)$—speed, $x(t)$—coordinate
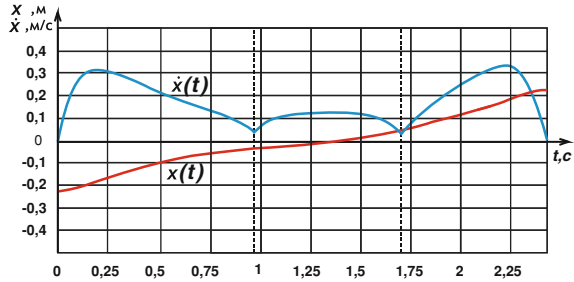
4 Manipulator Research

4.1 Structural Analysis

Manipulator-tripod structural analysis from the conditions required movements' realization without redundant links and local mobility was carried out. Figure 4 is a block diagram of the manipulator, wherein the linear movement axes geometrically converge via the universal spherical five-flexible pivoting unit.

Links of slave cylinders with kinematic pairs are 2–3, 5–6, and 8–9 V class, while at the points of attachment A, B, C must be installed two-flexible pivoting units. In this case manipulator has 3 degree of freedom.

The required robot platform working area and dimensions parameters are adopted as basic geometric constraints in the synthesis of a manipulator based on the spatial mechanism.

Static loads affecting on the manipulator links, depending on the position and the pickup device are determined from its equilibrium under the influence of the spatial system reaction $\overline{N_1}, \overline{N_2}, \overline{N_3}$ forces converging manipulator links and the force applied to grab G. Effort $\overline{N_4}$ in the link L_4 is determined from the equilibrium conditions of the rotary base (Fig. 5). Point M equilibrium equation is obtained from the principle of virtual movements in the projections on the axes of the fixed coordinate system. Efforts in the manipulator links for each point M_i (y_i, z_i) of manipulator service areas were determined (Fig. 6).

4.2 Positioning Task

Manipulator gripper positioning is to move it from the initial state $M_0(x_{M0}, y_{M0}, z_{M0})$ to the finite position $M_k(x_{Mk}, y_{Mk}, z_{Mk})$ [2]. As the number of generalized manipulator coordinates exceeds the number of generalized gripper coordinates that has a non-zero maneuverability, and the target position corresponds to a variety of configurations.

Fig. 4 Manipulator-tripod with universal spherical pivot point scheme
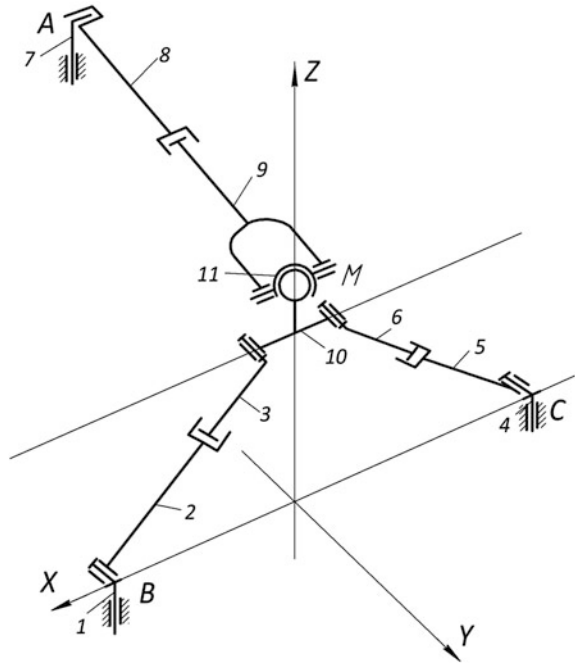
Fig. 5 Manipulator-tripod power analysis design scheme
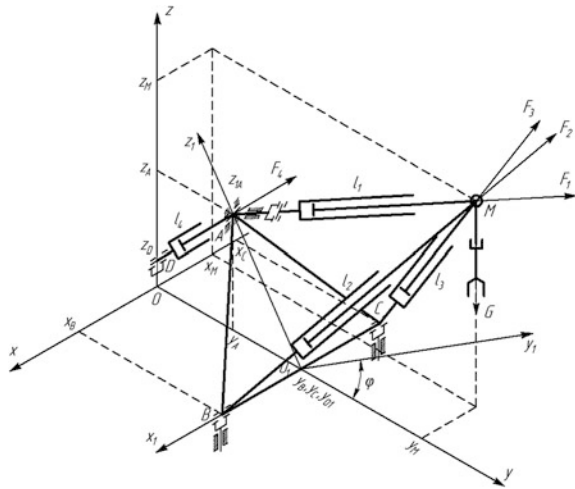
Coordinates of the gripper center x_M, y_M, z_M units and manipulator links 1–4 in the coordinate system $OXYZ$ are connected by the equations

$$\begin{cases} x_M^2 + (y_M - y_A)^2 + (z_M - z_A)^2 = l_1^2, \ (x_M - x_B)^2 + (y_M - y_B)^2 + z_M^2 = l_2^2, \\ (x_M - x_C)^2 + (y_M - y_C)^2 + z_M^2 = l_3^2, \quad y_M^2 + (z_A - z_D)^2 = l_4^2, \end{cases} \quad (2)$$

Fig. 6 Efforts change in manipulator links at the link length change $L_{1min} \le L_1 \le L_{1max}$ at $L_{2min}, L_{3max}, \varphi = 30°$

Links length l_{2k}, l_{3k} uniquely determined from Eq. (2), and the segments lengths $l_{1k}(y_A, z_A)$, $l_{4k}(y_A, z_A)$ are found according to the by quadratic function [7] minimizing problem setting [7]
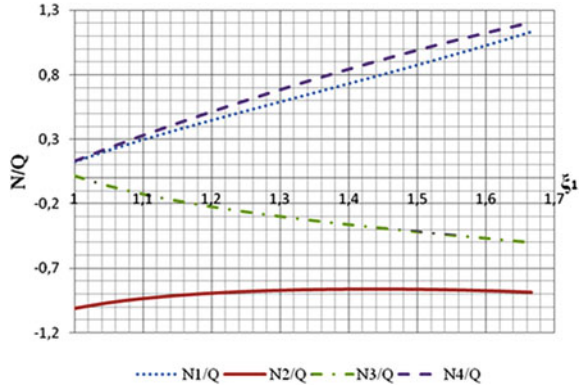
$$\Phi(y_A, z_A) = C_1(l_{1k} - l_{10})^2 + C_4(l_{4k} - l_{40})^2$$

equality constraints, $f(y_A, z_A) = z_A^2 + (y_B - y_A)^2 - O_1A^2 = 0$
and inequalities $L_{1min} \le L_1 \le L_{1max}$, $L_{4min} \le L_4 \le L_{4max}$.

In accordance with the Kuhn-Tucker theory the necessary problem setting for stationary are written in the form [7]

$$\frac{\partial \Phi^*}{\partial Y_A} = C_1 \frac{\partial(L_{1k} - L_{10})^2}{\partial Y_A} + C_4 \frac{\partial(L_{4k} - L_{40})^2}{\partial Y_A} + \lambda_1 \frac{\partial f(Y_A, Z_A)}{\partial Y_A} - \lambda_2 - \lambda_3 = 0$$

$$\frac{\partial \Phi^*}{\partial Z_A} = C_1 \frac{\partial(L_{1k} - L_{10})^2}{\partial Z_A} + C_4 \frac{\partial(L_{4k} - L_{40})^2}{\partial Z_A} + \lambda_1 \frac{\partial f(Y_A, Z_A)}{\partial Z_A} = 0$$

$$(3)$$

Here $\lambda_2 \begin{cases} \ge 0, & \text{if } Y_A = Y_{Amin}, \\ = 0, & \text{if } Y_A > Y_{Amin}, \end{cases}$ $\lambda_3 \begin{cases} \ge 0, & \text{if } Y_A = Y_{Amax}, \\ = 0, & \text{if } Y_A < Y_{Amax}. \end{cases}$

From which the values $L_{1k}(Y_A, Z_A), L_{4k}(Y_A, Z_A)$ are found.

4.3 Trajectory Synthesis

The system of differential equations describing the manipulator motion with holonomic constraints (1) can be written using the Lagrange equations with undetermined multipliers.

The notations $x_1 = x$, $x_3 = y$, $x_5 = z$, $x_7 = \varphi$, F_k, $k = 1, 2, 3, 4$ are introduced; they control efforts in the manipulator links. Functions that transform

manipulator gripper from the initial position to the finite position during the time T are found from the minimum of the functional [7].

$$J = \Phi(x_7(T)) + \frac{1}{2} \int_0^T \left[\dot{x}_2^2 + \dot{x}_4^2 + \dot{x}_6^2 + O_1 A^2 \cdot \dot{x}_8^2 \right] dt. \tag{4}$$

Unknown functions must satisfy the following boundary conditions $x_{2S-1}(0) = x_{2S-1,0}$, $x_{2S-1}(T) = x_{2S-1,T}$, $x_{2S}(0) = x_{2S}(T) = 0$. The function value $x_7(T)$ is unknown. Writing the necessary conditions of stationary for $x_k(t)$, $k = 1, 3, 5$ taking into account the boundary conditions, we have

$$x_k(t) = \frac{-2[x_k(T) - x_k(0)]}{T^3} t^3 + \frac{3[x_k(T) - x_k(0)]}{T^2} t^2 + x_k(0). \tag{5}$$

According to [1, 4] the boundary condition for the influence function is

$$\lambda_7(T) = \frac{\partial \Phi[(x_7(T)]}{\partial x_7(T)}, \ \Phi(x_7(T)) = -\frac{\mu x_7^2(T)}{2T^3}$$

μ—constant factor which value is determined by the result of obtained solution analysis. Then $\dddot{x}_7(T) = const = \dddot{x}_7(t) = \frac{x_7(T)}{T^3}$, and after the integration we obtain

$$\varphi(t) = \frac{\mu \varphi(T)}{6T^3} t^3 - \frac{\mu \varphi(T)}{4T^2} t^2 + \varphi(0). \tag{6}$$

For $t = T$ we define the unknown basis rotation angle at the finite time $x_7 = \varphi \cdot O_1 A$, and from Eq. (2) we can find manipulator links $l_k(t)$ length changes laws.

Programmatic efforts are found from the dynamics equations solution.

5 Management Control

The robot control system (CS) is based on a modular microprocessor system ROBOCON-1 [8]. The system realizes 16 channels of control drives with analog and digital feedback and includes four 4-channels controllers and, respectively, 16 channels to control DC drives. The format of the drive control unit boards is PC104. The computers connection with the drive control unit is provided via RS-232 or USB. The robot's control system is built under the scheme with speed feedback and solves the problem of contouring control actuators on the robot. The robot sensors are connected to the drive control unit modules. The control system realizes synthesized and described above software laws of the robot movement. The system supports autonomous, semi-autonomous (with the possibility of operator intervention) and remote modes of the robot control.

6 Conclusions

Scientific and technical principles of energy efficient, high profile patency autonomous mobile robot systems with orthogonal walking movers had been developed. On their basis experimental sample of robot have been designed and built. Robot has curb weight about 184 kg and carrying capacity about 300 N. It's dimensions (LxWxH): 1890 × 764 × 1257 mm—(operating position), 1290 × 764 × 857—transport position. Max speed—1.35 km/h. Surmountable obstacle height)—up to 400 mm, pace—600 mm. Max soil bearing pressure—0.84 kg/cm^2. Movement on a slope (maintaining the horizontality)—24°.

References

1. Mao, W., Qin, G., Lee. J.: Humanoid push recovery strategy for unknown input forces. In: The 2009 IEEE International Conference on Mechatronics and Automation, Changchun, Jilin, Aug 9–12, 2009, pp. 1904–1909
2. Gerasun, V.M., Zhoga, V.V., Nesmiyanov, I.A., Vorobjeva, N.S., Dyashkin-Titov, V.V.: Research of manipulator-tripod with rotary base optimal configuration. Mechatron. Autom. Manage. **6**, 21–26 (2013)
3. Zhoga, V.V., Skakunov,V.A., Eremenko,A.V., Fedchenkov,P.V., Gerasun, V.M., Nesmiyanov,I.A., Dyashkin-Titov, V.V.: Patent 2476372 RF, МПK C1. Accident rescue vehicle. Volgograd State Technical University (2013)
4. E. Gavrilov, E., Zhoga,V.V., Pavlovskiy, V.E., Fedchenkov, P.V.: Patent 2435693 RF, МПK B 62 D 57/032. Walking propeller of cross-country capacity. Volgograd state Technical University (2011)
5. Zhoga, V.V., Gavrilov, A.E., Shurygin, V.A., Danshin, A.S., Golubev, D.V.: Mobile walking robot of light class. Mod. Eng. Sci. Edu. **3**, 718–724 (2013)
6. Gavrilov, A.E., Zhoga, V.V., Fedchenkov, P.V.: Synthesis of optimal program law for movement of a robot with orthogonal walking drives. J. Comput. Syst. Sci. Int. **50**(5), 847–857 (2011)
7. Bryson, Jr E., Ho, Y.-C.: Applied Optimal Control. Wattham, London, p. 544 (1969)
8. Pavlovsky, V.E., Pavlovsky, V.V.: Modular microcontroller robots control system ROBO-CON-1. Keldysh Institute of Applied Mathematics of RAS (KIAM), 86, 32 (2012)

Brain Flow in Application for New Robotic POLIMI Platform

Alberto Rovetta

Abstract This paper deals with Locobot and Polimi Platform, a new robotic platform, able to interpret the actions of the persons operating in its environment. It uses not a deterministic logic, as usually in industrial and not industrial robotics. It adopts a structuralistic logic, where reality experience is executed with the personal structure, which is different from person to person. Polimi Platform uses nodes structures, with a total participation of all sensors and actuators. Application and realization is reported here, in its first phase. Polimi—Platform is the development of one of the first voice controlled robots, called Gilberto, in 1981 (see Refs. [1], [2]), after that LOCOBOT European Union Project, (see Ref. [3]) proposed an intelligent Platform, performed in the applicative results. Locobot means LowCost Robot and the platform performed in Politecnico di Milan had practical demonstrations on 14th March 2013 and July 2013 in AUDI Co., Partner in the Project. Now Polimi—Platform is a subsequent development, after 1st August 2013, for increasing a new type of intelligence in the system, substantially in the platform, which is equipped with a new nano microphone system for high level performances and new logical and emotional software to have the participation and cooperation of the worker(s) with the robotic system.

Keywords Robotics · Brain · Emotional robotics · Interface · Robotic special intelligence

A. Rovetta (✉)
Dipartimento di Meccanica, Politecnico di Milano, Via Lamasa 1, 20156 Milan, Italy
e-mail: alberto.rovetta@polimi.it

1 Introduction

In 1981 (see Ref. [1, 2]) the Author designed and developed Gilberto, which was able to recognize voice, to speak, and to have a vision system to recognize objects. It was controlled by a microprocessor, as reported by Isaac Asimov in its book on Robotics. As presented in [2], the movies show the flexibility and reliability of the robot Gilberto in 1983. Polimi—Platform Platform is the development of one of the first voice controlled robots, called Gilberto, in 1981 (see Refs. [1, 2]). In 2010–2013 in LOCOBOT European Union Project, (see Ref. [3]) Politecnico di Milano, Laboratory of Robotics, proposed an intelligent Platform, performed in the applicative results. Locobot means Low Cost Robot and the platform performed in Politecnico di Milan had practical demonstrations, as in the contract, in 2013 in AUDI Co., Partner in the Project. The Polimi Platform for Locobot is able to have speech recognition, voice control, vision recognition, lidar and vision control, autonomous motion with exploration and navigation, an a high level sensor fusion. It is applied in tests in Audi Co. for the best improvement of manufacturing activities in cooperation between workers and robotic systems.

Polimi Platform (which is the previous design and practical working application of Polimi—Platform) performs a controlled motion, in synchronization with production line, according to the planning of Locobot Project, as reported in Ref. [3]. Movies, photographs, tests and analytical developments of studies are reachable in EU Commission. Polimi Platform for Locobot was presented officially in the Celebration Day of European Union in Bruxelles, in the event called EU Open Doors, as honored example of one of the best (15 on 3700) research scientific results of all European Union Projects. Locobot is a new step towards the future of robotics. Its dissemination is running now and the research on Locobot Platform will lead to real new steps in real robotics, out of the old and surpassed ways and methods, which must be day by day adjourned. Now Polimi Platform is a subsequent development of Locobot, after 1st August 2013. It wants to increase a new type of intelligence in the system, substantially in the platform, which is equipped with a new nano microphone system for high level performances and new logical and emotional software to have the participation and cooperation of the worker(s) with the robotic system. Robotics till 2000 developed mainly industrial robots, and research followed. Now it is time of a new research, and the research must have immediate applications, as Polimi Platform for Locobot with Audi, towards a real reality of cooperation man/robots in the real environment. Laboratory of Robotics of Politecnico di Milano dedicated the years from 1992 to 2013 also to develop substantial research and applications (see Ref. [2]) to the neurological aspects of human behaviour, with studies on neuromotor control in cooperation with Nobel Prizes (see Ref. [5, 6]). References [7–10] can give a survey of the problems. Now we present our results in new robotics, and new robotics means also low cost, high performances, great reliability, as Polimi Platform and its development Polimi—Platform offer in great measure.

From 1981 to today we have developed the useful (and patented) robotics (see Ref. [2]) and Polimi Platform is one of the best trends which Politecnico di Milano, Dept. of Mechanics, is developing.

2 Special Intelligence

The POLIMI Platform has developed the new version, characterized by special intelligence. The structure of the platform is defined by many independent sensors connected to a central PC via software, which uses independent and interconnected nodes. Any information of each sensor reaches directly the central computer and, based on the data processing, controls the movement. The entire system is monitored on the screen of the Platform and can also be seen from the remote computer, from tablet, from cellphones, on the Internet. Polimi Platform goes a step further, and adapts to the new frontiers of bio robotics and modern neurology.

Polimi acts in presence of human intellectual perception and logic, feelings and emotions. Polimi Platform uses a special node with logic, born from structuralism, which is pervading in recent years all the human sense, natural and theoretical sciences, philosophical and engineering disciplines, neurological and physical knowledge.

The logic of materialism considers as the only reality is external nature to man, who lives this reality as a passive protagonist. The idealist logic (especially by Plato and Aristotle [4] as many works in Thomas Aquinas and Kant to Hegel) considers instead the IDEAS as existing and reality must adapt to the ideas that encloses the whole. Today neither setting is accepted. Today is born structuralism, where perception and intelligent understanding of things and reality are different from individual to individual. Everyone structures own life according to the experience of every moment. Structuralism knows that reality is perceived and felt differently by each person, depending on his/her sensory system, nervous system, memory capacity and interpretation, conscious and unconscious experience. Materialism and idealism do not consider unconscious and instinctive, which instead have a great importance in human life. Polimi—Platform wants to be the first robot (or robotic system) that works with structuralism. It uses the same hardware used by POLIMI PLATFORM, uses the same nodes, as if they were the dendrites of the human brain, and uses them in a new way, by interpreting the patterns of structuralism. Polimi Platform behaves differently depending on the reality surrounding human beings who interact. The human person interprets reality, not with digital values, but with models created by each person through the senses, and the models are filtered and modified in each step by the sense organ. They transduce signals to the brain analysis, providing synthetic information, short and compact, so that the information is present in few elements. Polimi Platform uses self-learning to grow and increase its basic statistical information and to become more and more safe and reliable. The perception of Polimi Platform limi can be changed according to the environment, to the people around, to the

developed and expected events. Polimi Platform will have its own special intelligence, adaptive, not as a machine but as an object built by man for man, with a special intelligence gained from reality and life through restructuring.

The restructurism involves processing signals, derived from each sensor in order to provide the values of the models and the signals as indices of perception and communication. They are sent to all nodes of the computer to be processed by the network of nodes, passing through the nodes of the "special intelligence" that uses new logical models of interpretation.

The "new logic models" are nothing more than the recovery of some aspects of formal logic, ancient and ever born alive. They connect logic action, affection, emotion, without any distinction between quality and quantity, and application of brain control goes back to the basic principles of Aristotle, who first spoke. The first consideration is that the formal logics has filled completely the robotics and the systems engineering, till some years ago, starting from ancient Egyptian and Chinese cultures. Today the technical determinism has been transformed in an operational activity, which is very interrelated, and no more sequential. Only formal logics and traditional engineering are maintaining a rigid structuralism. The modern science is communication between disciplines, is emotional participation towards the progress of mankind, and is a political and strategical choice for the driving of society towards the development and best quality of life. Ref. [5] by Sir John Eccles, Nobel Prize, represents the first step for the new developments in Robotics in Dept. Mechanics, Politecnico di Milan. After his visit and comments on 1992, the Robotic Lab. took care of the real neurological aspects of intelligence, searching for the behavior of the human body. Grasping of the hand is a very complicated process, and robotic really can only reproduce a part of the human grasping process, with alfa and gamma circuits of the brain in parallel actions. The same neurological aspects have been considered and Daphne results, with neurological aspects, have been developed, with very active and practical results (See Refs. [2]), [6] by Montalcini, Nobel Prize, is very well considered after her visit and cooperation in new ideas and design towards new frontiers of robotics, of new robotics. Her skill on neurology was the first support to have the courage to over go the traditional robotic logics, where the mechanisms obey the software, according to deterministic laws, which really do not exist in life.

3 Description of Polimi Platform

The Fig. 1 shows the Polimi Platform, with the webcam, the lidar, the infrared sensors, the ultrasonic sensors, the Kinect, the stereo camera, the omnidirectional mecanum wheels. The safety is guaranteed.

The mental spaces that led to the design of Polimi—Platform were born in the search for a robotic system that interprets the face, words, movements, and also the intentions and actions of human beings, adding a real active cooperation to the robotic machine. The concepts are spatial, in the sense that concepts are not

Fig. 1 Polimi Platform Locobot—Polimi, with the webcam, the lidar, the infrared sensors, the ultrasonic sensors, the Kinect, the stereo camera, the omni directional mecanum wheels
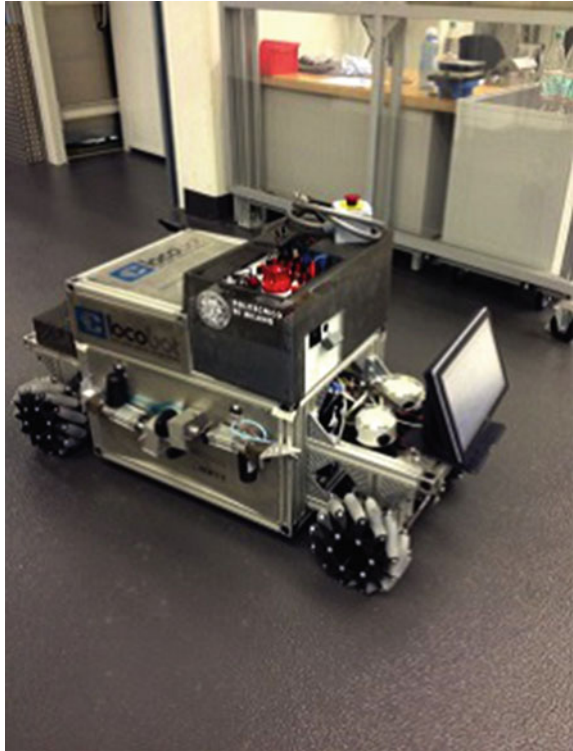
running the traditional engineering method, the consequentiality after execution of the project, but working for cyclic rings linked together, as in a necklace. The strength of the series lies in its ability to add rings, and bring new systems, attached to the preferred or more suitable ring. Polimi Platform does not want to look like a humanoid robot, with face, legs, arms (see Author website, multipurpose hand 1979 Gilberto, 1981, prosthesis, 1984, etc.). Its genetic shape is to have a horizontal drooped body, that is linked to a movement parallel to the ground. The movement in the version examined here occurs with 4 wheels, and have been studied and developed versions with 6 legs, also at a stage of intelligence so far.

Polimi Platform has four omnidirectional wheels, such that the robot platform can move in any direction in the floor, with a control that allows the pure rotation or pure translation, and of course the rotation and translation motion.

The main feature of the software developed in Polimi Platform is linked to the use of software packages referred to as Robot Operating System (ROS). They have been downloaded from the network in a very short time, have been adapted to the different needs of the platform and were integrated into the controller board. The management of the movement occurs with the use of packages modular, simple, developed only for Locobot. The signals come from Lidar radar and allow the mapping of the surrounding area, with fixed objects, obstacles, people still and

people on the go. The map appears on the touchscreen of the platform. With the use of a mouse or of the computer keyboard and also with smart phones and tablet computer, the platform is controlled in all its functions. A significant point is the use of nodes in the structure. The whole system has been designed in a parametric way, and also each sensor node is connected in a network to the main program. All nodes are working in a parallel manner, and this property makes platform Locobot as very flexible and adaptable. All sensors act together and therefore the security of the system is absolutely guaranteed. We have 16 infrared sensors and ultrasonic sensors, 3 cameras, radar and also all the positioning information of the system through GPS and odometry measurements of the movement, voice control, kinect interface. The intelligence of the platform is also in the sharing of data, as a GPRS card allows to transmit via satellite all the relevant information. The control circuits take the fuzzy logic and neural circuits to control, to decide what action to perform. The number one priority is safety. The safety of the highest priority concerns humans, the second priority is on the machines, on the platform and on the environment. The integration of the software for the movement with all other controls is done through the property of nodes, which activate the individual parts of the platform. In addition, the icons are taken to have an easily manageable handling. There are no written phrases, but only icons without words.
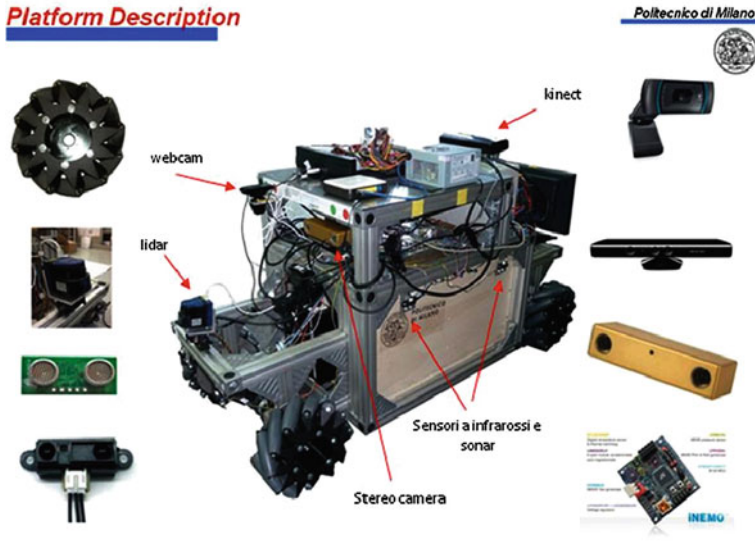
3.1 Exploration and Automatic Navigation, with Perfect Understanding of the Environment and People

The Fig. 2 shows Polimi Platform during its navigation, after exploration, with the action of all sensors and actuators.

Polimi Platform explores by the radar 3D (and 2D) the whole environment, a webcam explores the ceiling and stores the main data; a stereo camera explores stores and analyzes all side walls and pulls out the main features. All results come in the memory of the PC board and are stored. A special tool widely used, called Kinect, is adopted to recognize people in their handling of arms, legs, and also to recognize the faces and expressions. These data are part of the exploration of the environment where Polimi Platform is chosen to operate. If the environment changes, Polimi Platform runs a new scan and stores all the obtainable data.

Simple algorithms traditional as well as new ones are applied, beyond the formal logic that is expressed with usual logical determinism, even with statistical forecasts.

Each received, read and interpreted data must pass through the filter of a logical structure non-formal and must obtain an index of validity and truth, which is now used in the application. In this way, it is like building a "mental space" for the robot with a "special intelligence" that must be filled, and must be made active and positive. The new "intelligent special robotics" can free the worker, the designer, the user, every person who interacts with the robot, from the bondage of the obligation of an asset.

Fig. 2 Polimi Platform during its navigation, after exploration, with the action of all sensors and actuators

3.2 Emotions in Action and Sharing

Polimi Platform presents a software connection to the sensors and actuators using the system ROS, applied with operating "nodes", so as each sensor runs independently of the other. In the same time Polimi Platform integrates data into an active and simple network, and each new sensory element can be added. Polimi Platform shall participate in personal, emotional state of the person with whom it interacts, or with the emotional state of the group of people who interact, and also to the physical environment in which it operates. To perform these operations in an interactive way, it must be used a non-deterministic logic that has been designed and built in a "special node" of the network of data and commands in the computer. This node only performs with algorithms, which are enriched by the experience of Polimi Platform. The structure of the "intelligent node" can be expanded with the experience of Polimi—Platform and all other similar robots in operation, which are networked via the Internet and via satellite with active tabs positioned in intelligent robot.

3.3 Expression of Emotion and Participation by Polimi Platform

Polimi Platform can express itself in relation to the input it receives from the outside world, consisting of the persons, from environment, from other Polimi—Platform and

other machines. The expression of Polimi Platform used, possibly with music, flashing and stained with led, by action of mechanical and mechatronic systems placed on the platform, and also from any external interfaces to the Polimi Platform platform placed in the environment of existence. It must therefore be build a reaction protocol of Polimi Platform that best shows its expressions and makes clear its reactions.

4 Applications

The application of Polimi Platform is devoted to the systems and environments where there is an interaction of the machines, the robots with the human presence. Locobot applications are performed in a manufacturing Company, which is Audi, as a Partner in Locobot project. Locobot can synchronize its motion with the automotive production line, where different cars are produced. It is very smart and nice to see the cooperative motion of the Polimi Platform for Locobot with the suspended production line, where cars are moved. Locobot supports the assembly line increasing the efficiency and the velocity of all the line. The web site of Locobot Project (see Ref. [3]) shows all the actions and demonstrations, which are spectacular in front of the traditional robotics. The meaning of "robot" must change. Up to now, in industrial field "robot" is a system to be programmed, which can perform programmed tasks, and no autonomous existence. Some research robots look as independent and it is not correct, because all the behaviors of robot depend on a line of a software program. When we mean "emotional and intelligent robot" we mean clearly that a new kind of internal controlled logic can be used, and this "internal logic" considers also the psychological effects that the human behaviour induces in the robot itself. The effect of human psychology always acts in all our actions, and robots, which are the most sophisticated production machines, can participate of this reality in an optimizing and performing way.

Possible Polimi Platform applications for normal use are here reported.

1. Manufacturing industry for moving parts
2. Neurodegenerative cares
3. Cleaning of supermarkets
4. Cleaning of offices
5. In restaurants
6. In the stations
7. Robotics platform for space exploration
8. Building construction
9. Replacement of items in supermarkets
10. Industry: logistics
11. Mobility in hospitals
12. Transport in airports
13. Assembly in manufacturing industry
14. Buggy self-guided.

5 General Specifications of Polimi: Platform for Normal Applications

The Input may be endless, and yet the main categories are the following: type of person view, with levels of hierarchy and authority on the type of movement; type of voice command embossed, with level of significance on the function of Polimi Platform; type of emergency declared from zero to maximum, with action on the type of movement of Polimi Platform; kind of Safety imposed and verified, with management of the movement of Polimi Platform.

Polimi Platform enters in a logical manner to obey commands, takes them into account and performs the necessary operations, not like a robot but as an object with its special intelligence. "Intelligence" is born from the embedded logic in the computer and experience growth is based on the actions carried out. The safety immediately reduces speed and acceleration, almost cancels the jerk, slows down and stops the movement, to assume a position of verification. The Safety engages an automatic trajectory, if necessary, even in extreme conditions of operation. The safety index ranges from 0, when the situation is critical and dangerous to the value 1 one when the system is always in the best possible safety.

For voice, Polimi Platform receives voice commands with a few keywords and executes the corresponding orders. The way to zero 0, is completely passive and the execution is not critical. Level 1 is a budget higher and the software manages the voice as a manifestation of human phenomenon, to create a deep interaction between Polimi—Platform, the human beings who speak, and the equipment which plays the sound. When the output is followed by a voice response system on Polimi—Platform, the position of the source is identified by the system that calculates the GPS coordinates of the local source, and repeats in a loud voice, as well as write them on PC monitor process. The answer is vocally in the base language, which is English or other language according to the country chosen as the base of Polimi Platform. The vocal response of the position is clear and unambiguous. If the Input is a command word or phrase with words declaring control, Polimi Platform takes inputs and actuates links also to motion and to vision, sends the signal in the subsequent "Node of special intelligence" and executes orders in sequence, according to the rules in the node. Consequently, orders are executed by Polimi Platform in a way like an intelligent way.

References

1. Rovetta, A.: Voice Control. In: Dorf (ed.) Encyclopedia of Robotics, vol. III (1987)
2. http://robotica.mecc.polimi.it
3. http://www.locobot.eu
4. Aristotle, (330 b.C.), Categories, 8; 9
5. Eccles, J.C.: Brain and Conscious Experience. Springer, Heidelberg (1966)
6. Montalcini Levi, R.: Abbi il coraggio di conoscere. Rizzoli, Milan (2004)

 7. Sherrington, C.S.: The Integrative Action of the Nervous System. Yale University Press, New Haven, London (1906)
 8. Sperry, R.W.: Cerebral dominance in perception. In: Early Experience in Visual Information Processing in Perceptual and Reading Disorders, National Academy Sciences, Washington (1970)
 9. Eccles, J.C.: The Physiology of Synapses. Springer, Gottingen (1964)
10. Edelman, G.M.: Neural Darwinism. New York (1987)

A Dual Formation Constraint Mechanism of Mobile Sensor Network Based on Congestion Will

Cheng Yang, Ping Song, Chuangbo Hao, Guang Wang, Lin Xie and Wenjuan Guo

Abstract For the weakness of formation adjustment in formation control of mobile sensor network nodes and formation disorder caused by long distance travel, a dual formation constraint mechanism based on congestion will is proposed in this paper. The mobile nodes use both general constraint and local constraint to maintain a stable formation based on the analysis of the kinematics model of the mobile node. The general constraint makes the nodes coordinated and improves the efficiency. The local constraint ensures the balanced position of each node in the formation. Simulation results show that the mobile nodes can move to the target in a stable and regular formation utilizing this method.

Keywords Dual constraint mechanism · Mobile sensor network · Congestion will

C. Yang (✉) · P. Song (✉) · C. Hao · L. Xie · W. Guo
Intelligent Robotic Institute, Beijing Institue of Technology, Beijing 100081, China
e-mail: ycthink@gmail.com

P. Song
e-mail: Sping2002@bit.edu.cn

C. Hao
e-mail: haochuangbo@sina.com

L. Xie
e-mail: xiel16@bit.edu.cn

W. Guo
e-mail: ir06bit@bit.edu.cn

G. Wang
65052 Units of PLA Shenyang Military Area, Shenyang 110001, China
e-mail: guang_wang212@163.com

1 Introduction

Mobile sensor network combines the wireless sensor network with mobile robot technology. The wireless sensor network expands the perceived space of mobile robot and provides the possibility of improving collaboration of the mobile robot and extending application scope.

Formation control is a significant research context for mobile sensor network and mobile robot. Most formation control methods are mainly applied to the field of mobile robot, such as leader-follower method, virtual structure method, behavior-based method and graph theoretic method [1].

However, there are two prominent different points between mobile sensor network and mobile robot.

On one hand, since most actuators of mobile sensor nodes are designed to be simple in order to reduce both energy consumption and size, the control accuracy is not high. For instance, the execution errors due to differences of mechanical properties between each nodes will be introduced. These errors will result that some nodes may deviate from their balanced positions in the formation.

On the other hand, the amount of nodes in the mobile sensor network is much larger than that in traditional muti-mobile robots system. System perception and communication robustness is achieved by the wide layout of cheap nodes [2]. On account of the complex communication and wide distribution range, some nodes may miss the instruction, which cause collisions with other nodes.

A constraint mechanism to the mobile sensor network based on congestion will has been presented in Ref. [3] for formation control. The kinematic model, however, is not taken into account in simulation. Each mobile node is supposed as an omnidirectional platform, the local constraint is demanded in the actual formation control in order to preserve the holistic motion state of the node group.

Above that, a dual formation constraint mechanism based on congestion will is proposed in this paper, taking the kinematics model of the four-wheel mobile node into account, in which the general constraint and the local constraint are designed for mobile nodes to keep a stable formation with existence of the problems described as above.

2 Mobile Sensor Network Nodes

2.1 The Group of Mobile Sensor Network Nodes

The group of mobile nodes consists of one leading node and several following nodes. The former is responsible for starting a network, while the others can join this network utilizing self-organizing and multi-hop through the wireless module based on ZigBee protocol [4].

Every node is equipped with hall sensor and electronic compass. The hall sensor is used to measure the mileage, while the electronic compass is used to get the information of course. Dead reckoning method [5] based on these two sensors is utilized to obtain the node's coordinate.

The leader-flower method [6, 7] is utilized as the formation control strategy. The formation of the node group is determined by the leading node, which also transmits instructions to other nodes together with their positions in the formation. Next, the following nodes successively move to their coordinate points determined by the leading node. Then, all nodes of the group move to the target in the established formation.

2.2 Kinematics Model of the Mobile Node

The mobile platform discussed here is a four-wheel car, controlled by two PWM signals, one of which is for steering action, while the other is for forward-backword action. All motion control behaviors are carried out by changing the speed of rear wheels and the deflection angle of front wheels. Therefore, it should be allowed firstly for the relation between the pose of the car and the speed of wheels.

Figure 1a depicts the kinematics model, d is a wheel base between the front and rear wheels. The dashed line represents the veer of front wheel in arc movement, φ denotes deflection angle. So, the radius of circular motion, r, is calculated in Eq. (2.2.1)

$$r = \frac{d}{\sin \varphi} \tag{2.2.1}$$

Figure 1b depicts the arc model, where arc AB is the movement locus of a mobile node. The line segment AB is the displacement, which calculated through the radius r by Eq. (2.2.2).

$$dl = v \cdot T$$
$$ds = 2 \cdot r \cdot \sin(\frac{dl}{2r}) \tag{2.2.2}$$

where, dl is the arc length, T is the moving time. v and φ are respectively the speed and deflection angle of the mobile node, which conform to the constraint condition of Eq. (2.2.3).

$$v_{min} < v < v_{max}$$
$$-\varphi_{max} < \varphi < \varphi_{max} \tag{2.2.3}$$
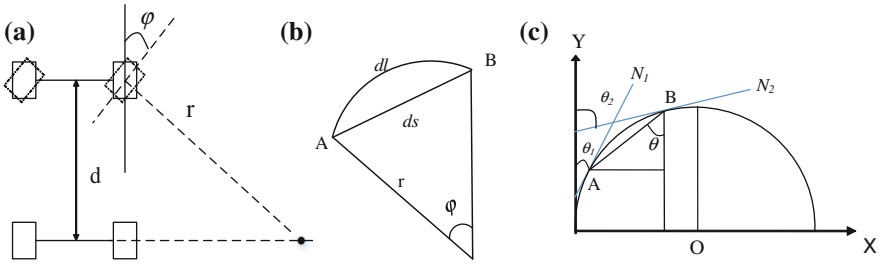
Fig. 1 Kinematics model of a mobile node. **a** depicts the kinematics model, d is a wheel base between the front and71 rear wheels. The dashed line represents the veer of front wheel in arc movement, u72 denotes deflection angle, **b** depicts the arc model, where arc AB is the movement locus of amobile node, **c** arc AB is a portion of a circle, $\theta 1$is the angle between the tangent N_1 across point A and Y-axis, θ_2 is the anglebetween the tangent N_2 across point B and Y-axis

We assume that arc AB is a portion of a circle, as is illustrated in Fig. 1c. θ_1 is the angle between the tangent N_1 across point A and Y-axis, θ_2 is the angle between the tangent N_2 across point B and Y-axis. θ can be calculated by Eq. (2.2.4).

$$\theta = \frac{\theta_1 + \theta_2}{2} \tag{2.2.4}$$

The displacements of a mobile node along X-axis and Y-axis are separately derived from Eq. (2.2.5)

$$x = ds \ \sin \theta$$
$$y = ds \ \cos \theta \tag{2.2.5}$$

3 Dual Formation Constraint Mechanisms

3.1 General Constraint Mechanism

General constraint mechanism adjusts the moving step based on the congestion will between the group of mobile nodes and the target. The moving step regulated by the speed and deflection angle of a mobile node is increased with the distance between the group of mobile nodes and the target, which also means that the congestion will becomes stronger.

Firstly, the leading node calculates the distance from its current position to the target.

$$d_{st} = \sqrt{(x_s - x_t)^2 + (y_s - y_t)^2} \tag{3.1.1}$$

where, (x_s, y_s) is the current coordinate of the leading node. (x_t, y_t) denotes the target position.

Secondly, the moving step determined by general constraint is defined as Eq. (3.1.2)

$$step(d_{st}) = \begin{cases} step_{\min}(1 + b \cdot lg \dfrac{W_{group}^k}{d_0}) & d_{st} \geq d_0 \\ step_{\min} & d_{st} < d_0 \end{cases} \qquad (3.1.2)$$

where, $W_{group}^k = a*d_{st}$ is the strength of congestion will, a is congestion coefficient, $step_{min}$ is the smallest step determined by the smallest actuating speed, b is rate factor which can regulate the change rate between each step. If the distance between the leading node and the target is smaller than d_0, $step(d_{st})$ equals the smallest step. Otherwise, $step(d_{st})$ varies with the d_{st}. The output of $step(d_{st})$ is the speed and deflection angle of the mobile node.

Finally, the leading node gets the next position $X_i^{k+1} = X_i^k + step(d_{st})$. i means the ith node. Then, the rest nodes move to their respective positions in accordance with the established formation.

3.2 Local Constraint Mechanism

Sometimes the following nodes will miss the instruction of the leading node, or produce the execution error because the control accuracy of servo and motor is not very high. In addition, nodes might not arrive at the desired position because of restrict of kinematics features. Local constraint mechanism adjusts the position of a node based on the congestion will of its neighbour nodes to eliminate these deviations and avoid affecting the holistic movement. Adjustment is not required when the node is in balanced position where the congestion will strength is very small.

The node group moves toward with the step determined by general constraint, and the strength of congestion will is calculated by the distance between node i and node j as is shown in Eq. (3.2.1)

$$W_{ij} = W_1 + W_2 \qquad (3.2.1)$$

where, W_{ij}, W_1, W_2 are all vectors. The value of W_1 is the attract constant u, whose direction is from i to j. The value of W_2 is k/d_{ij}^2, whose direction is from j to i. k is repulsive coefficient, d_{ij} means the distance between i and j.

$\sum_{j}^{neighbor} W_{ij}^k$ is the sum of congestion will strength of all neighbors to node i. $adjust\_step(\sum_{j}^{neighbor} W_{ij}^k)$, named as *adjustment step*, is required when $\sum_{j}^{neighbor} W_{ij}^k$ is larger than the threshold value m.

Adjustment step is proportional to the sum of congestion will strength, which is not necessary if $\sum_{j}^{neighbor} W_{ij}^k$ is smaller than m, that is to say,
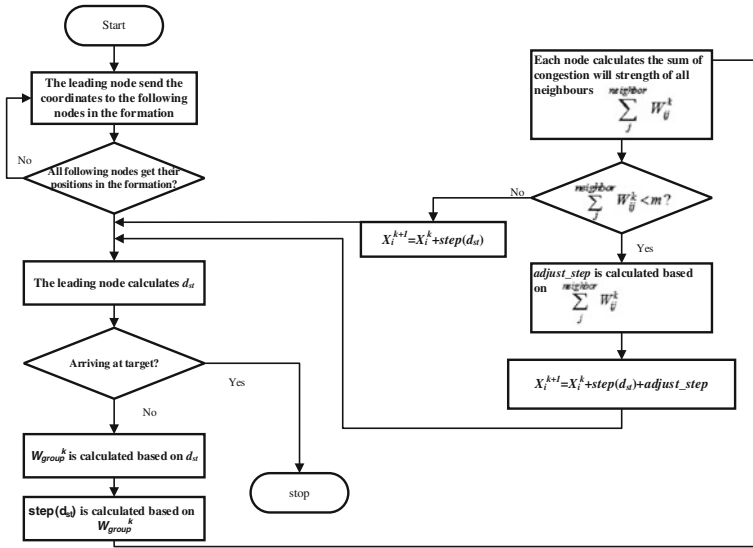
**Fig. 2** The flow chat of the dual formation constraint mechanism

$adjust\_step(\sum_j^{neighbor} W_{ij}^k) = 0$. The nodes demanding adjustment step move to their next positions according to Eq. (3.2.2).

$$X_i^{k+1} = X_i^k + step(d_{st}) + adjust\_step(\sum_j^{neighbor} W_{ij}^k) \tag{3.2.2}$$

$adjust\_step(\sum_j^{neighbor} W_{ij}^k)$ is controlled by speed v and angle φ which have to conform to Eq. (2.2.3). φ is determined by the direction of $\sum_j^{neighbor} W_{ij}^k$ and v is confirmed by the value of $\sum_j^{neighbor} W_{ij}^k$. v is increased with $\sum_j^{neighbor} W_{ij}^k$, which is maximum when $\sum_j^{neighbor} W_{ij}^k$ is larger than threshold value p, as is defined by Eq. (3.2.3)

$$v = \begin{cases} v_{max} & \text{if } (\sum_j^{neighbor} W_{ij}^k > n) \\ \dfrac{\sum_j^{neighbor} W_{ij}^k}{c} \cdot v_{max} & \text{else} \end{cases} \tag{3.2.3}$$

The flow chat of the dual formation constraint mechanism is shown in Fig. 2.
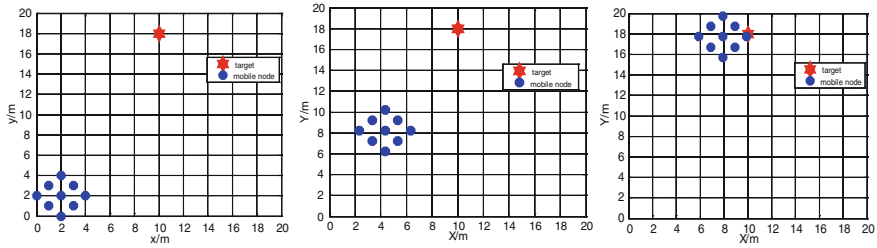
Fig. 3 Moving process based on general constraint mechanism. The blue dots denote the mobile nodes, the red star denotes the target position
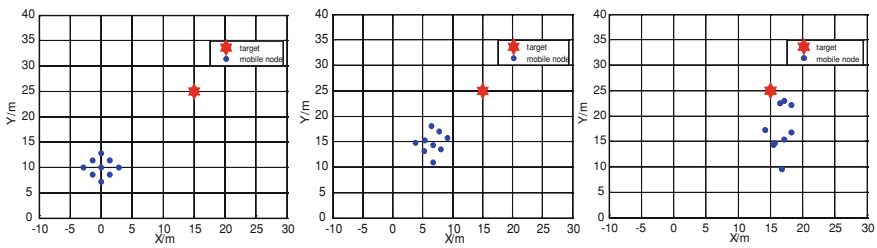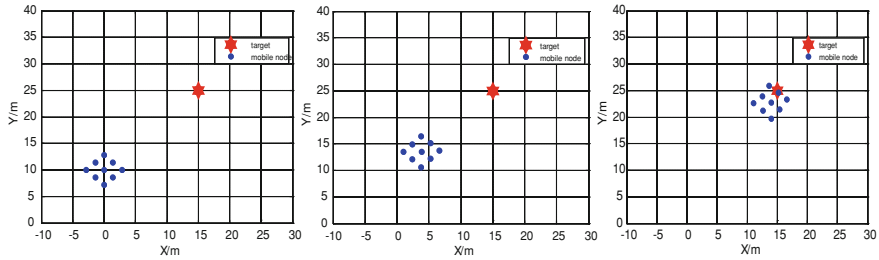

Fig. 4 The moving process without local constraint mechanism with all nodes having random errors

4 Simulation

The node group moves to the target in 3×3 formation and stops when arriving at the target. The step is adjusted according to the general mechanism during the moving process. The congestion coefficient $a = 3$, the rate factor $b = 0.2$, $d_0 = 3$, $step_{min} = 0.9$, the abstract constant $u = 3$, the repulsive coefficient $k = 12$ and the coefficient of speed $c = 5.v_{min} = 0.2$, $v_{max} = 0.5$, $\varphi_{min} = -20$, $\varphi_{max} = 20$.

The simulation results are shown in Fig. 3 where circle points denote the mobile nodes and hexagon denotes the target. Figure 3a shows the initial state, b shows the moving state and c shows final state. The step is 1.1219 when the nodes start to move from the initial state where d_{st} equals 17.088. Then, the step reduces with the decrease of d_{st}.

When the random errors of speed and angle are introduced in each mobile node, the moving state without local constraint mechanism is depicted in Fig. 4. As we can see, the nodes gradually deviate from its balanced position and eventually disorder. When the constraint mechanism is introduced, the nodes can move to the target staying their balanced position within the formation, as is shown in Fig. 5.

Fig. 5 The moving process utilizing local constraint mechanism with all nodes having random errors

5 Conclusion

We propose a dual formation constraint mechanism based on the analysis of the kinematics model of mobile sensor network node. The node group, whose formation is controlled by the general and local constraint mechanism, can move to the target stably and efficiently. The simulation verified the feasibility of the dual mechanism.

References

1. Li, W. et al.: Wireless Sensor Networks and Mobile Robot Control. Science Press, Beijing (2009). ISBN: 978-7-03-023548-0
2. Ren, L., Wang, W., Du, Z.: The key technology and development for mobile robot formation control. CAAI Trans. Intel. Syst. (2013). doi:10.3969/j.issn.1673-4785.201302011
3. Song, P., Wang, Y., Wang, X., Pan, Z.: A congestion will based constraints mechanism of mobile sensor network. In: IEEE Conference on Multisensor Fusion and Integration for Intelligent Systems 2012 (2012). doi: 10.1109/MFI.2012.6343069
4. NXP Laboratories UK Ltd: ZigBee PRO Stack User Guide. http://www.nxp.com/documents/user_manual/JN-UG-3048.pdf (2013). Accessed 12 Jan 2014
5. Cho, B.-S., Moon, W., Seo, W.-J., Baek, K.-R.: A dead reckoning localization system for mobile robots using inertial sensors and wheel revolution encoding. J. Mech. Sci. Technol. **25**(11), 2907–2917 (2011). doi: 10.1007/s12206-011-0805-1
6. Gu, D., Wang, Z.: Leader–follower flocking: algorithms and experiments. IEEE Trans. Control Syst. Technol. **17**(5), 1211–1219 (2009). doi:10.1109/TCST.2008.2009461
7. Consolini, L., Morbidi, F., et al.: Leader–follower formation control of nonholonomic mobile robots with input constraints. Automatica **44**, 1343–1349 (2008). doi:10.1016/j.automatica.2007.09.019

Kinematic Uncertainties in Human Motion Tracking and Interaction

Qilong Yuan and I-Ming Chen

Abstract Human kinematic model is crucial for precise human motion tracking and representation. While using wearable sensors to track the human motion, the human kinematics cannot be measured exactly due to the complexity of the human body and the sensor measurement errors. For the existence of these uncertain parameters in the human kinematics, the contact interactions with the environment during the activity cannot be correctly captured. Research works on the kinematic uncertainty problem for motion tracking is still lacking. In this paper, after discussing on the kinematic uncertainties, a method to re-adjust the body posture for correct motion and interaction tracking is introduced. In the preliminary experiment validation, an IMU based motion and interaction tracking system is used to capture the human motion with contact interactions in the environments. After considering the kinematic uncertainties in the tracking, motions like climbing ladders, rock climbing, gym etc., can be captured and represented with correct interactions with the environment.

Keywords Human kinematic uncertainty · Human motion tracking

1 Introduction

Motion capture technology has been important research topics during the past decades. Applications in biomechanics [1–3], gait analysis [4–6] entertainment (dancing, gaming est.) [7–9], sports etc. [10–12] have been developed using the existing off the shelf tracking systems. Nowadays, tracking the human movement

Q. Yuan (✉) · I.-M. Chen
School of Mechanical and Aerospace Engineering, Nanyang Technological University, Singapore
e-mail: QLYUAN@ntu.edu.sg

I.-M. Chen
e-mail: MICHEN@ntu.edu.sg

Fig. 1 Climbing a ladder
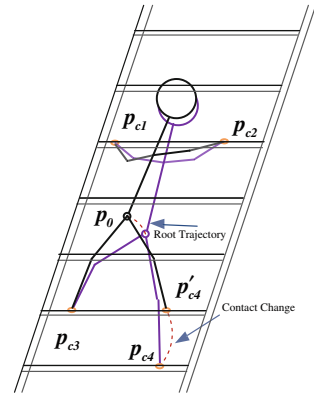
is technically quite common and there are many types of capture systems available [7, 9, 13, 14, 15]. However, while considering the physical interaction between human and the acting environments, only tracking the body movement of the human subject cannot fully describe the motion interaction with the surroundings. For example, when a human subject is climbing a ladder as shown in Fig. 1, the human uses hands to hold on the ladder and uses the feet to stand on the steps. The hands holding the ladder and the feet standing on the steps represent the contacts between the ladder and the human. From the kinematic point of view, these contact interactions in the environment become the *kinematic constraints* imposed on the human body motion, which needed to be satisfied in the captured human motion— interaction.

Unlike the robotic systems whose kinematic parameters are very precise, the human body kinematic model has uncertain parameters in the description: (1) Uncertainties in the dimensions of the limbs. (2) Uncertainties in the orientation of limbs. (3) Uncertainties in the joint motions. Due to this uncertain parameters, although the body movement can be accurate captured, the kinematic constraints from the physical interaction may not be satisfied in the captured motions.

For a human motion and interaction tracking system, the research problem is: How to use appropriate sensor systems and corresponding tracking methodologies to accurately track the human motion and interaction with the environment *based on a proper human kinematic model of the human subject.* In order to correctly capture the motion interactions like ladder climbing, we need to study the property of the body kinematic uncertainty and the corresponding methods to re-adjust the postures to satisfy the kinematic constraints from the environment are very crucial.

In this paper, we introduce the uncertainties of the kinematic parameters in motion tracking. Then, based on the kinematics and uncertain model of the human, a posture re-adjustment model is introduced to correctly describe the motion and interaction with the environment.

2 Kinematics and Uncertainties

The Local POE formula is applied to model the kinematics of human body in this work [16, 17]. Let a pair of adjacent limbs be itemized as i-1 and i and connected by joint i. If we denote the body coordinate frame on the limb i by frame i, then the relative pose of frame i with respect to frame i-1, under a joint displacement q_i can be described by a 4 by 4 homogeneous matrix, such that $T_{(i-1),i}(q_i) = T_{(i-1),i}(0)e^{\widehat{\xi}_i q_i}$, where $T_{(i-1),i}(0)$ represents the initial pose of frame i in frame i-1 which depends on

the constant limb link parameters. $e^{\widehat{\xi}_i q_i}$ is the joint motion which need to be determined based on the sensor measurement in the motion capture.

For convenience, in the initial standing posture, all the body coordinate systems of the subject are chosen such that X-axis points forward, the Z-axis points downward. The Y-axis is determined such that a right-handed coordinate frame is formed. Thus, in the kinematic model, the initial relative postures between the frame i in frame $i-1$ are pure translational matrix which can be determined using a calibration procedure, as discussed in [18, 19]. This calibration can provide a skeleton model with around 1 cm accuracy. The joint motion is represented by a

twist motion $e^{\widehat{\xi}_i q_i}$ which is captured by the sensors. The general case is that a complex body joint can include both rotational motion $R_{(i-1),i}$ and translational motion δp_i. Therefore, the twist motion of each joint is a 6 DOF displacement in general that can be represented by a SE (3) matrix,

$$T_i = e^{\widehat{\xi}_i q_i} = \begin{bmatrix} R_{(i-1),i} & \delta p_i \\ 0_{1\times 3} & 1 \end{bmatrix} \tag{1}$$

In this simplified human kinematic model, it is assumed that the limb joints only have rotational motion: $\delta p_i = \mathbf{0}$. A root frame is defined at this point on the pelvis. The posture of this frame represents the absolute location and orientation of the person in the environment. The relative posture between the root frame and the distal limbs (feet, hands and head etc.) frame n are defined by the kinematic chain between them. The POE formulas of the kinematic chains depend on the initial relative posture of the body frames $T_{(i-1),i}(0)$ and the joint twist motions as follow,

$$T_{0n}(q_1, q_2, \ldots, q_n) = T_{0,1}(0)e^{\widehat{\xi}_1 q_1} T_{1,2}(0)e^{\widehat{\xi}_2 q_2} \cdots T_{(n-1),n}(0)e^{\widehat{\xi}_n q_n} \tag{2}$$

2.1 Uncertainty in Human Kinematics Model

After determining the dimensions of the limbs, a proper kinematic model to describe the human motion can be generated. The limb dimensions and orientations bound to have measurement errors. This is crucial because such uncertainty

would affect the accuracy of the body postures and also the correct presentation of the contacts with the environment. Firstly, we assume that the skeleton dimensions are imprecise, and let $\delta l_{i-1,i}$ represent the slight dimension errors of the limb i. Then, we assume that the limb orientation is also imprecise. Let $\delta R_{0,i}$ represent the rotational error of joint i with respect to the base root frame.

Because of the complexity in the human kinematics, having an exact uncertainty model for the complex human body mechanism is almost impossible. *In this paper, the properties of these parameters are assumed to be normally distributed with the standard deviation of $2°$ and 1.5 cm for position and orientation. Because the simplified model does not consider collarbone inside, the shoulders joint positioning uncertainty is set to be larger* (3 cm).

2.2 Uncertainty in Position

Due to the kinematic uncertainty, the relative posture between the root and the distal limbs are also inaccurate. With the orientation error of limb i $\delta R_{0,i}$, and the link length error $\delta l_{i-1,i}$, and according to Eq. (1), we have:

$$p'_{0n} = \sum\nolimits_{i=1}^{n} R'_{0,i-1}(l_{i-1,i} + \delta l_{i-1,i}) \tag{3}$$

Note that $R'_{0,i} = \delta R_{0,i} R_{0,i} = e^{\delta \hat{\omega}_i} R_{0,i}$, $\delta R_{0,i}$ represents the orientation measurement errors and $\delta \hat{\omega}_i$ denotes the corresponding *se* (3) skew-symmetric matrix.

Thus, the position error on this distal limb is

$$p'_{0n} - p_{0n} = \sum\nolimits_{i=1}^{n} [(e^{\delta \hat{\omega}_{i-1}} - I)R_{0,i-1}l_{i-1,i} + R'_{0,i-1}\delta l_{i-1,i}] \tag{4}$$

Note that when $\delta \omega_i$ is small, $(e^{\delta \hat{\omega}_i} - I) \approx \delta \hat{\omega}_i$, and $R'_{0,i-1} \approx R_{0,i-1}$. Thus, we have

$$\delta p_n = p'_{0n} - p_{0n} \approx \sum\nolimits_{i=1}^{n} [-(R_{0,i-1}l_{i-1,i}) \times \delta \omega_i + R_{0,i-1}\delta l_{i-1,i}] \tag{5}$$

Rearrange the above Equation, we have, $\delta p_n = BX$.

Where $B = diag(-(R_{0,1}l_{1,2})^{\wedge}, -(R_{1,2}l_{2,3})^{\wedge}, \ldots, -(R_{0,n-1}l_{n-1,n})^{\wedge}, I, R_{0,1}, \ldots, R_{0,n-1})$, $B \in \Re^{6n \times 6n}$, and $X = [\delta \omega_1^T, \delta \omega_2^T, \ldots, \delta \omega_n^T, \delta l_{0,1}^T, \delta l_{1,2}^T, \ldots, \delta l_{(n-1),n}^T]^T$, $X \in \Re^{6n \times 1}$.

For posture correction, the location of the person presented by the root point is quite crucial since this frame is the central base representing the spatial location of the person. Details on the human localization can be found in [12]. Once the root location is known, the location constraint points can be estimated from the forward kinematics of the limbs.

Fig. 2 Demonstration of contact constraint correction
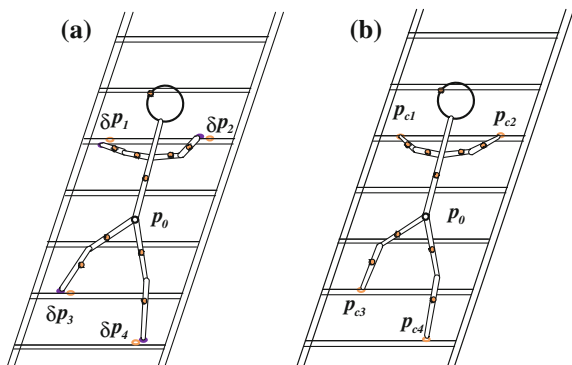
3 Posture Fine-Tuning

It is known that once the location of the root point is calculated, the absolute positions of the distal limbs (feet and hands) on the body are directly available from the forward kinematics of the human body. Meanwhile, the actual positions of the contact points on the ladders are fixed (In this paper the contact points are assumed to be known.). Then, the location errors of the contacting points (hands and feet) δP_n can be calculated by comparing the difference between the position of the distal limbs and the contacting positions on the ladder. The posture fine tuning is to re-adjust the parameters inside the kinematic chains to eliminate these position errors on the distal limbs (Fig. 2, (1)). The properties of these parameters are important in the posture re-adjustment because the amounts of readjustment on the limb parameters are much dependent on their accuracy. Thus, it is closely related to the kinematic uncertainty model of the human body.

3.1 Posture Fine Tuning Algorithm

In the ladder climbing example, there are multiple contact constraints to be satisfied. In this posture fine tuning, the human skeleton should be considered as an integrated kinematic system instead of separated kinematic chains. Otherwise, *the symmetry of the skeleton model will be broken and* the dimension of the limbs shared by two or more chains cannot be uniquely determined. Thus, in the posture fine tuning, the human body should be considered as one mechanism with all the distal limbs satisfying the kinematic constraints from the contacts. Thus, referring to Eq. (2), we have

$$P_A = B_A X_{all} \tag{6}$$

where $P_A = [\delta P_{rh}^T, \delta P_{lh}^T, \delta P_{rf}^T, \delta P_{lf}^T]^T \in \mathbb{R}^{12 \times 1}$ is the vector representing the distal limb location errors (the hands and the feet with the subscript *rh, lh, rf, lf* denoting the chain of the right hand, the left hand, the right foot and the left foot respectively).

$X_{all} \in \mathbb{R}^{69 \times 1}$ is the column vector of the uncertain error parameters for all limbs.

$B_A = [B_{rh}^T, B_{lh}^T, B_{rf}^T, B_{lf}^T]^T \in \mathbb{R}^{12 \times 69}$ is the matrix that maps the uncertain parameters to the location errors of the distal limbs based on the forward kinematic of the human body.

Although the lengths of humans' legs and arms on different sides can have some slight difference, for a healthy human subject, the skeleton model of the body can be considered as symmetric on the right and the left sides. Therefore, the symmetric relationship of all the corresponding limbs in the kinematic model is defined based on the following equation, $0 = B_S X_{all}$. Where $B_S \in \mathbb{R}^{18 \times 69}$ is a constant matrix defining the symmetric relationship. Then, the constraint equations of the uncertain parameters become $P_F = B_F X_{all}$.

Based on the distribution of these error parameters, the optimal posture should be determined such that the following probability is optimized under the *constraint equations*: $P_F = B_F X_{all} \cdot P(X_{all}) = \prod_{i=1}^{m} P(x_i)$.

Based on the assumed uncertain model of the kinematic parameters, all the uncertain parameters (x_i) are normally distributed with a variance σ_{x_i} representing the uncertainty. Thus, we have $P(X_{all}) = \prod_{i=1}^{m} P(x_i) = C \cdot \exp(-\sum_{i=1}^{m} \frac{x_i^2}{2\sigma_{x_i}^2})$, where C is a constant defining the normalized coefficient.

The solution of X_{all} should be the values that maximize the probability $P(X_{all})$ under the constraint equations from the human kinematic model: $P_F = B_F X_{all}$. It means that the solution is most likely to be X_{all} among all the possible solutions. The solution that maximize the probability $P(X_{all})$ corresponds to the solution minimizing the following function $f = \sum_{i=1}^{m} \frac{x_i^2}{2\sigma_{x_i}^2}$ under the constraint equation: $P_F = B_F X_{all}$. For the minimization of f under the constraint equation $P_F = B_F X_{all}$, the solution can be found using the Lagrange multiplier method [20]. The analytical solution is as follows,

$$y = \begin{bmatrix} \lambda & B_F^T \\ B_F & 0 \end{bmatrix}^{-1} \begin{bmatrix} 0 \\ P_F \end{bmatrix}, \text{where } \lambda_{i,j} = \frac{\partial}{\partial x_j}(\frac{\partial f}{\partial x_i}) \cdot y = [X_{all}^T, \zeta^T]^T \qquad (7)$$

In this way, all the parameters X_{all} are determined for the posture fine tuning. The computation time is very quick, almost immediate because the solution is analytical. All the constraints are satisfied after the posture refinement.

Fig. 3 Movements with constraints
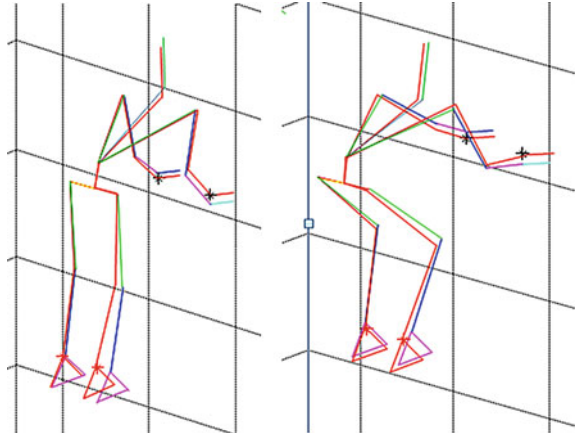

4 Experiments

4.1 Devices and Skeleton Model

In this demonstration, the IMU sensors are used as the orientation measurement devices for posture measurement. As shown in Fig. 3, totally 15 IMUs are used to measure the posture of the body. Sensors are tightly attached on the limbs (head, chest, pelvis, upper arms, forearms, hands, shanks, thighs, and feet). This IMU sensors [21] measures its own orientation with respect to the global frame. From [12] we know that the orientation of limbs can be calculated from the sensor orientation after a coordinate mapping calibration. The skeleton dimensions can be calibrated before actual capturing.

4.2 Experiments of Re-adjustment

To verify the posture refinement method, four fixed contact constraints with known locations are arranged in the environment to constrain the location of the feet and the hands. These locations are pre-defined with the measured dimensions. The experiment procedure of the posture fine tuning experiment is as follows. **Step 1** The subject wears the sensors, and calibrates the full body skeleton dimension model. **Step 2** He stands in front of the table and conducts the system calibration. **Step 3** The subject locates his feet and hands to match the constraint points. The footprints are used to constraint the location of the feet and the markers on the table are used to define the location of the wrists. **Step 4** The subject changes some postures while maintaining the contact positions as shown in Fig. 3.

Fig. 4 Postures before and after refinement

The system tracks the motions of the subject based on the sensor measurement and the calibrated human kinematic model. Based on the experiment, before posture refinement, the error on the distal limbs (hands and feet) can be as large as 4 cm. The captured postures and the postures after the fine tuning are shown Fig. 4. The black stars indicate the reference location of the constraint points. The multi-color models indicate the captured motions. The fine-tuned posture is presented as the red-color models. As shown in Fig. 4, all the contact interactions are satisfied after the posture fine tuning.

5 Conclusion

This paper discusses on the human kinematic uncertainty model for motion tracking. To correct the posture errors in the captured motions resulted from these uncertainties, a method to re-adjust the body motion for correct motion and interaction tracking is introduced afterward. Experimental results show that the introduced method can correctly represent the contact interactions with the environment. This method statistically takes the uncertainty of the errors into account. Thus, the posture can be refined with respect to the accuracy of the error parameters. The geometric constraint conditions and the symmetry of the human kinematic model are satisfied after the posture refinement.

Since the IMU sensor based MoCap systems are now widespread, this method can be useful to correctly monitor the correct interaction between the human and the environments. Especially for those applications in daily environments where the lab-based system cannot handle, this method can help the IMU based system to achieve accurate motion tracking with contact interactions. Therefore, after considering the kinematic uncertainties in the tracking, motions like climbing ladders, rock climbing, gym etc., can be captured and represented with correct interactions with the environment.

References

1. Frigo, C., Rabuffetti, M., Kerrigan, D., Deming, L., Pedotti, A.: Functionally oriented and clinically feasible quantitative gait analysis method. Med. Biol. Eng. Compu. **36**(2), 179–185 (1998)
2. Goodvin, C., Park, E., Huang, K., Sakaki, K.: Development of a real-time three-dimensional spinal motion measurement system for clinical practice. Med. Biol. Eng. Comput. **44**(12), 1061–1075 (2006)
3. Schepers, H.M., van Asseldonk, E., Buurke, J.H., Veltink, P.H.: Ambulatory estimation of center of mass displacement during walking. IEEE Trans Biomed Eng **56**(4), 1189–1195 (2009)
4. Besier, T., Sturnieks, D., Alderson, J., Lloyd, D.: Repeatability of gait data using a functional hip joint centre and a mean helical knee axis. J. Biomech. **36**(8), 1159–1168 (2003)
5. Mariani, B., Hoskovec, C., Rochat, S., Büla, C., Penders, J., Aminian, K.: 3D gait assessment in young and elderly subjects using foot-worn inertial sensors. J. Biomech. **43**(15), 2999–3006 (2010)
6. Scapellato, S., Cavallo, F., Martelloni, C., Sabatini, A.M.: In-use calibration of body-mounted gyroscopes for applications in gait analysis. Sens. Actuators A **123**, 418–422 (2005)
7. Vlasic, D., Adelsberger, R., Vannucci, G., Barnwell, J., Gross, M., Matusik, W., Popovi, J.: Practical motion capture in everyday surroundings. ACM Trans Graph (TOG) **26**(3), 35–44 (2007)
8. Fujimori, Y.Y., Harada O.T., Kuniyoshi Y.: Wearable motion capture suit with full-body tactile sensors. In: IEEE International Conference on Robotics and Automation, ICRA '09 (2009)
9. Roetenberg, D., Luinge, H., Slycke, P.: Xsens MVN: full 6DOF human motion tracking using miniature inertial sensors. Xsens Technologies (2009)
10. Brodie, M.A.D.: Development of fusion motion capture for optimization of performance in alpine ski racing. PhD Thesis, Massey University (2009)
11. Yuan, Q., Chen I.-M.: Simultaneous localization and capture with velocity information. IEEE/RSJ International Conference on Intelligent Robots and Systems, San Francisco (2011)
12. Yuan, Q., Chen I.-M., Lee S.P.: SLAC: 3D localization of human based on kinetic human movement capture. IEEE International Conference on Robotics and Automation (ICRA), Shanghai (2011)
13. Bachmann, E.: Inertial and magnetic tracking of limb segment orientation for inserting humans into synthetic environments. Ph.D. Thesis (2000)
14. MetaMotion. http://www.metamotion.com (2014)
15. Vicon. http://www.vicon.com (2014)
16. Chen, I.M., Yang, G., Tan, C.T., Yeo, S.H.: Local POE model for robot kinematic calibration. Mech. Mach. Theory **36**(11–12), 1215–1239 (2001)
17. Yang, G.: Kinematics, dynamics, calibration, and configuration optimization of modular reconfigurable robots. Ph.D., Nanyang Technological University (2011)
18. Yuan, Q., Chen I.-M.: Human velocity and dynamic behavior tracking method for inertial capture system. Sensors and Actuators A: Physical (2012)
19. Yuan, Q., Chen I.-M., Sin A.W.: Method to calibrate the skeleton model using orientation sensors. In: Proceedings of IEEE International Conference on Robotics and Automation, Karlsruhe (2013)
20. Bretscher, O.: Linear algebra with applications. Prentice Hall, Eaglewood Cliffs (1997)
21. InterSense. www.intersense.com (2014)

Experiments of a Human-Robot Social Interactive System with Whole-Body Movements

Gan Ma, Qiang Huang, Zhangguo Yu, Xuechao Chen, Weimin Zhang, Junyao Gao, Xingguang Duan and Qing Shi

Abstract One crucial problem for a humanoid service robot is to be able to communicate with humans naturally. This study focuses on this issue and develops a social interactive system for a humanoid robot to interact with human beings. The interactive system features hearing, voice conversation, and facial and full body emotional expression capability. Experiments are conducted on the robot to interact with humans in a real human indoor environment, and the effectiveness of the system is evaluated.

Keywords Human-robot interaction · Whole-body movement · Humanoid robot

1 Introduction

Humanoid robots feature humanlike appearance and structure; they have the advantage to perform tasks without changing the mankind environment [1]. Therefore, they have a wide application prospect in serving people in future.

Face-to-face communication plays a major role in our daily communications. Only 7 % of information is transferred using spoken language, whereas 38 % is transferred using paralanguage and 55 % using facial expressions [2]. Therefore,

G. Ma (✉) · Q. Huang · Z. Yu · X. Chen · W. Zhang · J. Gao · X. Duan · Q. Shi
IRI, School of Mechatronical Engineering, Beijing Institute of Technology,
Beijing, China
e-mail: magan@bit.edu.cn

G. Ma · Q. Huang · Z. Yu · X. Chen · W. Zhang · J. Gao · X. Duan · Q. Shi
Key Laboratory of Biomimetic Robots and Systems, Ministry of Education,
Beijing Institute of Technology, Beijing, China

Q. Huang
Key Laboratory of Intelligent Control and Decision of Complex System,
Beijing Institute of Technology, Beijing, China

in order to interact with people more effectively, it is better for a humanoid robot to have a human-like face and interact with humans in a way similar to humans.

Numerous face robots have been presented in recent years. Some researchers [3–10] present robots that can make basic humanlike facial expressions with a mechanical head. Some of them can indeed interact with humans through facial and body emotional expressions, but the mechanical head cannot express facial expressions vividly. Meanwhile, android-type robots have been developed [11–17]. These robots can vividly interact with humans as they are generally designed to have an appearance with human-like skin, teeth, hair and clothes.

However, few of these reports focus on the study of the interactive system with whole-body android-type emotional expressions. In this study, an interactive system for android-type humanoid robot is introduced. The system, which can make a humanoid robot to communicate with humans through full body movements, is implemented on a humanoid robot platform.

The remainder of this paper is organized as follows: First, the overview of a humanoid robot is presented. Then, the implementation of an interactive system on the robot is presented. Finally, experiments are carried out to validate the effectiveness of the interactive system.

2 The Implementation of a Human-Robot Interactive System

2.1 The Overview of Humanoid Robot BHR-4

In this study, a humanoid android robot named BHR-4 [18] is used as the platform to design our social interactive system. Thus, this section will make a short description of the platform BHR-4.

BHR-4 is a humanoid service robot developed by our institute. It is unveiled in 2010 with its nickname of "Xiao Gao". This robot features hearing, voice conversation, force sensing capability. It can walk straight and sideways, go around, negotiate stairs, perform Taiji (a Chinese traditional Kongfu), and some other complex motions, without resorting to external cables. Also, it can speak as well as make some facial expressions like humans.

This robot consists of a torso, a head, a waist, two arms and two legs. The height of the robot is 1.65 m and the weight is approximately 60 kg. This robot has 51 degrees of freedom (DOF), including 13 facial joints to make vivid facial expressions. The maximum walking speed is 1.5 km/h.

2.2 Structure of the Interactive System

In this section, an interactive system is developed for the humanoid robot BHR-4 to communicate with humans in human domestic environment. The interactive system is composed of the speech recognition module, the dialogue control module, the mouth control module, the emotional control module and the body movement control module. There are two computers in this system; one is a main control computer used to control the motion of the robot; the other is a speech recognition computer.

1. The speech recognition module: In this study, Microsoft Speech SDK is employed to recognize diverse voices from different individuals. When an individual speaks certain dialogue through microphone, the program receives and recognizes the words spoken. Then the program would compare the words with keywords stored in advance. If the words are similar to one of the keywords in the database, the robot would then send certain protocol to the main control computer through Socket Communication.

2. The dialogue control module: When the main control computer receives certain protocol from the speech recognition computer, it begins to work. In the dialogue control module, the system extracts the specified dialogue results from the voice library, and plays the dialogue using a speaker mounted inside the mouth of the robot. The voices from the voice library are recorded from a real person in advance, and correspond to questions which include the keywords in the speech recognition module.

3. The mouth control module: In order to make the interaction more vividly, a mouth control module is designed. When the robot is speaking, the mouth of the robot would be opened and closed according to the rates of the dialogue.

4. The emotional control module: In order to vividly interact with humans, it is crucial for the robot to have humanlike appearance and make facial expressions similar to humans. The facial design methods were originally proposed in [18, 19]. In the current study, when the interactive program is executing, the robot would make the six vivid facial emotions, along with winking from time to time. The six basic emotions, which are happiness, sadness, surprise, anger, fear and disgust, would be made by the robot based on the contents of the interaction.

5. The body movement control module: When the robot is executing the interactive program, a real-time program is utilized to control the body movement to make the interaction more vivid. In this study, the body movement includes the movements of arms, legs, and waist of a humanoid robot.

2.3 Planning of Full Body Motion Trajectories for Communication

In this study, we intend to design a humanoid robot to be able to communicate with humans in a way similar to humans. Thus, human facial and body motions when communicating are adopted as the basic database for humanoid robots. We presented a method to generate humanoid motion from a human actor based on motion capture system in our previous studies [20], and it is employed here.

Two professional actors (one man and one woman, Chinese, 22 years old) are invited to perform social interactive movements. They are informed to communicate based on the contents of the dialogue database. Motion capture system is utilized to record the movements of the arms, legs and waist of the actors. Once the data from motion capture system are obtained, we can generate the emotional movement trajectories of the robot according to similarity analysis and evaluation method [20].

In this study, body motion trajectories when making some basic social interactions are made, such as social hand gesture, bow, walk, goodbye gesture. These trajectories are saved in the body motion trajectories library. When one trajectory is needed, the control system would call it to execute.

3 Experiments

In this section, two experiments are designed to evaluate the effectiveness of the interactive system. In the first experiment, the robot is controlled to communicate with human subjects using only facial expressions and verbal behavior; while in the second one, the robot would communicate with human subjects with facial expressions, verbal behavior and body movements. Figure 1 indicates the interactive screen.

3.1 Experimental Procedures

For each one of the two experiments, ten subjects (five men and five women, Chinese, average age: 25) were invited to communicate with the robot. These subjects held a microphone into the room. Once the robot heard "Hello" from the microphone, the interactive system began to work. Then, the subject can chat with the robot using the preset questions. Once the robot recognized one of the questions, it would response to humans. Table 1 shows a simple demo of the interaction. Note the body movements accompanied with the communication are only implemented in the second experiment.

Fig. 1 The interactive screen

Table 1 Demo of a social interaction

	Verbal communication	Facial expressions	Body motion
Subject	Hello		
Robot	Hello, I am Xiao Gao and I am glad to talk with you	Happiness	Bow
Subject	Thank you. Where are you from?		
Robot	I came from Beijing Institute of Technology, China	Happiness	
Subject	Do you have hobbies?		
Robot	I am really into the Chinese Kongfu, Taiji	Winking	Gesticulate
Subject	Who do you like most?		
Robot	I like the teachers and students in our lab the most	Happiness	Gesticulate
Subject	That's it for today, see you later		
Robot	OK, goodbye	Happiness	Wave hands

Table 2 Questions to the subjects

Q.1	How did you feel at first glance of the robot?
Q.2	Did you feel more nervous than normal communication?
Q.3	Did the robot chat with you vividly?
Q.4	Did you have a good time when chatting with the robot?
Q.5	Do you wish to communicate with the robot again?
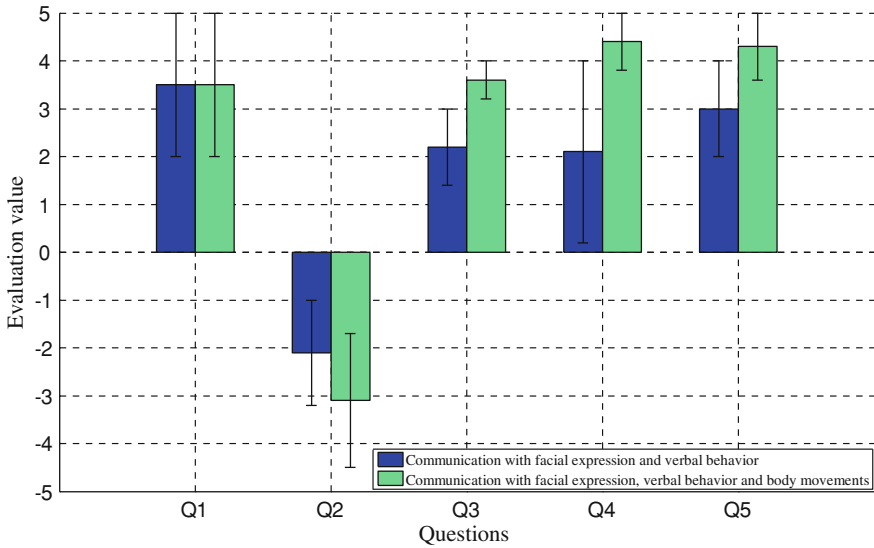
Fig. 2 The evaluation value of the questionnaire

3.2 Evaluation Methods

The aim of this study is to develop an interactive system for humanoid robots to vividly interact with humans. Thus, the object of the evaluation is to evaluate the verisimilitude and naturality of the robot compared with humans.

Five questions were prepared for the subjects to evaluate the results of the interaction (Table 2). These questions were evaluated on a scale from −5 to 5, values over zero mean positive evaluation, while when the values were less than zero, it means negative. The answers to these questions by the subjects are shown in Fig. 2.

3.3 *Experimental Results*

It is seen from Fig. 2 that the results are acceptable, and the results of the experiment 2 are better than that of the experiment 1. Specifically, the overall rates of both the systems are acceptable. Also, subjects feel the robot system with body motions are more vivid than without it, and they are also tend to chat with the robot with body motions.

Meanwhile, some subjects are a little bit nervous when communicating when the robots. We consider this is because it is the first time the subjects participate in the communication, and although the voices from the robot are recorded from a real person, it is still very different from the voices of a real person.

4 Conclusion

This study aims to develop a social interactive system for a humanoid robot to interact with humans in a way similar to humans. The contributions of this study are as follows.

1. A human-robot social interactive system with whole-body movements is introduced.
2. Experiments are made for the robot to interact with humans in the indoor environment to validate the effectiveness of the system.

References

1. Sakamoto, D., Kanda, T., Ono, T.: Cooperative embodied communication emerged by interactive humanoid robots. Int. J. Hum. Comput. Stud. **62**, 247–265 (2005). doi:10.1109/ROMAN.2004.1374801
2. Mehrabian, A.: Communication without words. Psychol. Today **2**, 53–55 (1968)
3. Fukuda, T., Tachibana, D., Arai, F., Taguri, J., Nakashima, M., Hasegawa, Y.: Human-robot mutual communication system. In: Proceedings of the IEEE International Workshop on Robot and Human Interactive Communication. Paris, France, pp. 14–19 (2001). doi:10.1109/ROMAN.2001.981870
4. Breazeal, C.: Emotion and sociable humanoid robots. Int. J. Hum. Comput. Stud. **59**, 119–155 (2003). doi:10.1016/S1071-5819(03)00018-1
5. Breemen, A.V.: Bringing robots to life: applying principles of animation to robots. In: Workshop on Shaping Human-Robot Interaction-Understanding the Social Aspects of Intelligent Robotic Products. Vienn (2004)

6. Bartneck, C., Reichenbach, J., Breemen, A.: In your face, robot! The influence of a character's embodiment on how users perceive its emotional expressions. In: Proceedings of the Design and Emotion Conference. Ankara, Turkey, pp. 32–51 (2004). doi:10.1.1.58.2622

7. Zecca, M., Mizoguchi, Y., Endo, K., Iida, F., Kawabata, Y., Endo, N., Itoh, K., Takanishi, A.: Whole body emotion expressions for KOBIAN humanoid robot-preliminary experiments with different emotional patterns. In: IEEE International Symposium on Robot and Human Interactive Communication, pp. 381–386 (2009). doi:10.1109/ROMAN.2009.5326184

8. Destephe M, Henning A, Zecca M, Hashimoto K, Takanishi A (2013) Perception of Emotion and Emotional Intensity in Humanoid Robots Gait. Proceedings of the IEEE International Conference on Robotics and Biomimetics. Shenzhen, China. 1276-1281

9. Cosentino, S., Kishi, T., Zecca, M., Sessa, S., Bartolomeo, L., Hashimoto, K., Nozawa, T., Takanishi, A.: Human-humanoid robot social interaction: laughter. In: Proceedings of the IEEE International Conference on Robotics and Biomimetics. Shenzhen, China, pp. 1396–1401 (2013)

10. Tasaki, T., Ogata, T.G., Okuno, H.: The interaction between a robot and multiple people based on spatially mapping of friendliness and motion parameters. Adv. Robot. 28, 39–51 (2014). doi:10.1080/01691864.2013.854457

11. Hashimoto, T., Kato, N., Kobayashi, H.: Development of educational system with the android robot SAYA and evaluation. Int. J. Adv. Robot. Syst. **8**, 51–61 (2011)

12. Hara, F., Akazawa, H., Kobayashi, H.: Realistic facial expressions by SMA driven face robot. In: Proceedings of the IEEE International Workshop on Robot and Human Communication. Paris, France, pp. 504–511 (2001). doi:10.1109/ROMAN.2001.981954

13. Oh, J.H., Hanson, D., Kim, W.S., Han, I.Y., Kim, J.Y., Park, I.W.: Design of android type humanoid robot Albert HUBO. In: Proceedings of the IEEE/RSJ International Conference on Intelligent Robots and Systems. Beijing, China, pp. 1428–1433 (2006). doi:10.1109/IROS.2006.281935

14. Nishio, S., Ishiguro, H., Hagita, N.: Geminoid: teleoperated android of an existing person. Humanoid Robots: new Developments. Vienna, Austria. pp. 343–352 (2007). doi:10.5772/4876

15. Sakamoto, D., Kanda, T., Ono, T., Ishiguro, H., Hagita, N.: Android as a telecommunication medium with a human-like presence. In: Proceedings of 2nd ACM/IEEE International Conference on Human-Robot Interaction. Washington, USA. pp. 193–200 (2007). doi:10.1145/1228716.1228743

16. Becker-Asano, C., Ishiguro, H.: Intercultural differences in decoding facial expressions of the android robot Geminoid F. J. Artif. Intell. Soft Comput. Res. **1**, 215–231 (2011)

17. Lin, C.C., Huang, H.P.: Design of a face robot with facial Expression. In: Proceedings of the IEEE International Conference on Robotics and Biomimetics. Guilin, China, pp. 492–497 (2009)

18. Gao, J.Y., Huang, Q., Yu, Z.G., et al.: Design of the facial expression mechanism for humanoid robots. In: 18th CISM-IFToMM Symposium on Robot Design, Dynamics and Control, vol. 524. Udine, Italy, pp. 433–440 (2010)

19. Yu, Z.G., Ma, G., Huang, Q.: Modeling and design of a humanoid robotic face based on an active drive points model. Adv. Robot. **28**, 379–388 (2014). doi:10.1080/01691864.2013.867290

20. Huang, Q., Yu, Z.G., Zhang, W.M., et al.: Design and similarity evaluation on humanoid motion based on human motion capture. Robotica **28**, 737–745 (2010). doi:10.1017/S0263574709990439

Distributing the Supporting Heads for Robotized Machining

Teresa Zielinska, Wlodzimierz Kasprzak, Cezary Zielinski and Wojciech Szynkiewicz

Abstract The paper presents a method of placement for the movable supporting heads of a self-reconfigurable robotic fixture system. The whole system consists of two mobile platforms carrying parallel type manipulators equipped with deformable heads. The heads are providing the dynamic support for large flexible workpieces during machining. The two heads consecutively relocate and affix themselves to the supported thin metal sheet, so that one of them supports the workpiece while the other relocates itself in such a way as to precede the working tool. The method for heads positioning for circular contours is presented. Formulas are derived and the results are summarized.

Keywords Robotized machining · Motion planning · Mobile manipulators · Supporting heads

1 Introduction

Components made of thin metallic or composite sheets are common in automotive and aircraft manufacturing, they are also becoming increasingly popular in other sectors. Traditional processing of such parts is costly, it requires non-reconfigurable,

T. Zielinska (✉)
Faculty of Power and Aeronautical Engineering (FPAE), Warsaw University of Technology (WUT), ul. Nowowiejska 24, 00–665 Warsaw, Poland
e-mail: teresaz@meil.pw.edu.pl

W. Kasprzak · C. Zielinski · W. Szynkiewicz
Faculty of Electronics and Information Technology, WUT, ul. Nowowiejska 15/16, 00–665 Warsaw, Poland

especially shaped supporting molds. In the case of frequent modifications of the workpieces a reconfigurable fixture composed of robots is much cheaper. With still dominating classical approach in the industry which is applying the molds, in the engineering research it can be noticed the increasing interest in flexible fixturing. The method for fixturing using small number of supports is presented in [1]. The localization of supports is not trivial and requires specific solutions, typically it is viewed as a global optimization problem. Thus nonlinear programming is often applied to obtain the fixture layout with an optimum value of some objective function taking into account the material properties [1, 2]. Most of the research related to fixture modeling and design considers fixturing in static conditions, but often the tool is in motion. Coordinated displacement of mobile bases and manipulators propelling the heads provides an adequate support to the thin-sheet workpiece, it is enabling the dynamic machining. Moreover, the controlled flexibility of the heads facilitates their adaptation to the diverse local shapes of the supported sheets. In our system stationary thin-sheet workpiece is subjected to a sequence of machining actions (such as milling or drilling) executed by a moving machine tool. The workpiece is kept in place by a limited number of static fixtures that support its weight, but cannot adequately resist both sagging due to gravitation and the significant dynamic machining forces.
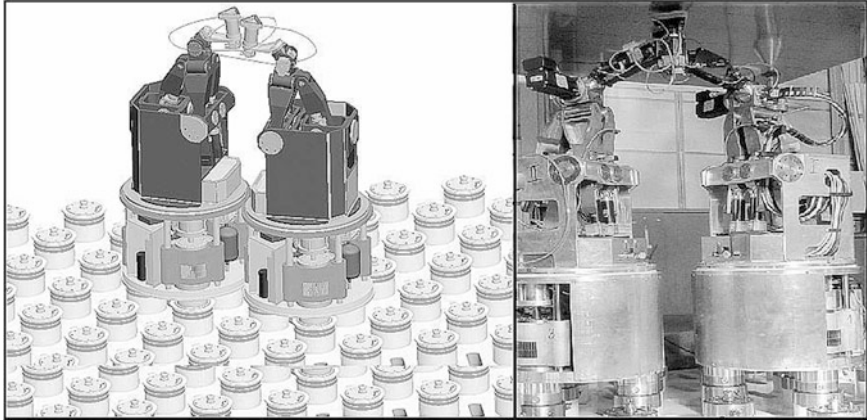
2 Robotic System

Every supporting element is a robot composed of: a mobile base, a parallel manipulator mounted on the base and an adaptable head being the end-effector of the manipulator (Fig. 1).

The mobile base is docked to a flat bench with protrusions (pins) [3]. During machining it is docked to three pins forming an equilateral triangle. When the mobile base has to translocate itself two docking elements are released and lifted so that the base can rotate itself around the third pin. Once the rotation is complete the docking elements are lowered and secured to the new pins. The parallel manipulator positions and orients the supporting head thus assuring a rigid support. The head is able to adapt to the local geometry of the sheet by using a phase-change fluid and vacuum adhesion [4, 5]. The problem is decomposed into three hierarchical subproblems which all together constitute the planner:

- the head placements,
- mobile base positioning,
- manipulator positioning.

Obtaining an admissible sequence of head placements is the most difficult part of the planning process. The overall solution, properties of developed and implemented control system are outlined in [6–8]. The planning task is solved off-line.

Fig. 1 Robotic system; graphical representation—*left*, system during the work—*right*

The plan fulfilling constraints for head, manipulator and mobile base positioning (including the limits due to motion dynamics) is implemented and realized by developed control system [8].

3 Heads Positioning

When the tool is in the vicinity of the head, this head provides the support and the second head moves to the next location. When the tool leaves the proximity of the first head the next part of the edge is already supported by the second head, there are brief periods when the support is provided by two heads. The head positioning constraints result from the FEM (Finite Elements Method) analysis of deformations of thin workpieces [3]. The following constraints are considered: d_{min}—the minimum distance of the supporting head from the contour edge, or from the drilled point (safety margin to avoid the head damage by the tool), d_{max}—the maximum distance of the head from the edge, or from drilled point (both are the limits for providing sufficient support), dh_{max}—the maximum permissible distance between two adjacent head locations for sufficient support. The head is a regular triangle with the length of edge equal to a. Machined is circular contour with radius r. The two extreme cases are: the small circles, and the contours with small curvatures (with big radius). The drilled points are located in constant distance from the edge, the milling is performed on the contour edge. Depends on machining operation r is denoting the radius of drilled or milled contour. For satisfactory support the distance c between the drilling tool (or milling tool) and the head edge must be in range $<d_{min}, d_{max}>$. This value can be different for drilling and for milling. Two reference frames are defined, the frame $O_B X_B Y_B$ attached to the head in the point being in minimum allowable distance to driller

(for drilling point), or to the milling tool (for milling), and reference frame $O_A X_A Y_A$ with origin attached to the center of circular contour. The frame $O_B X_B Y_B$ changes its position and orientation according to the heads placement. Its origin is attached to the point O_B on the head edge which is in minimum permissible distance $d_{\min}$ from the machined edge or from the drilling point. Let us consider the situation when the initial head position is symmetrical towards $O_A X_A$ axis— Fig. 2. The tool moves counterclockwise along circular contour. Point M, being in distance $d_{\max}$ from the head, marks end of fragment supported by this head. As it is illustrated in Fig. 2 the upper half of the head gives the satisfactory support between points P_1 and P_2 (and symmetrically the similar situation will be for its lower half). Coordinates of those points are:

$$
\begin{aligned}
{}^A x_{P_1} &= r + d_{\min} \\
{}^A y_{P_1} &= 0 \\
{}^A x_{P_2} &= r + d_{\min} = r\cos(\phi) + d_{\max} \\
{}^A y_{P_2} &= r\sin(\phi)
\end{aligned}
\tag{1}
$$

${}^A x_{P_1} = {}^A x_{P_2}$ (Fig. 2a). Using (1) the angle ϕ marking the supported fragment is obtained:

$$
\cos(\phi) = 1 + \frac{d_{\min} - d_{\max}}{r}
$$
$$
\phi = \arccos(1 + \frac{d_{\min} - d_{\max}}{r})
\tag{2}
$$

When r is much bigger than the head edge, the head support is ended before the maximum permissible distance $d_{\max}$ is reached (see Fig. 2b). In this situation ${}^A y_P > {}^A y_c$ (${}^A y_c$ is coordinate of head upper vertex) and ϕ is evaluated using:

$$
\phi = a\sin({}^A y_c / r)
\tag{3}
$$

Note: in our graphical representation ${}^A y_P$ and ${}^A y_c$ are in the upper part od reference frame, therefore they are positive. The distance d_o to the machined point where the head ends its support is equal to:

$$
d_o = r + d_{\min} - r\cos(\phi)
\tag{4}
$$

After obtaining ϕ from (2) or (3) ${}^A y_{P_2}$ is evaluated using (1).

The vertex of next supporting head is located in the point P_p on the circle with the radius $r + d_s$ where $d_{\min} < d_s < d_{\max}$. The coordinates of P_p are:
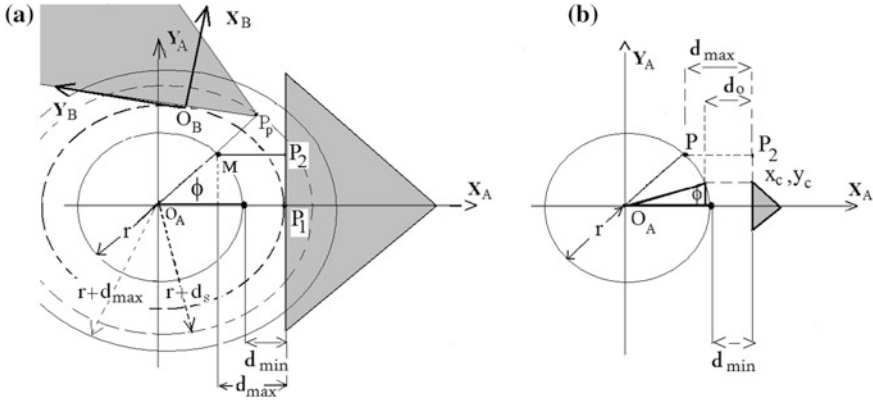
Fig. 2 Coordinate frames and heads placements (**a**, **b**)

$$
\begin{aligned}
{}^A x_{P_p} &= (r + d_s)\cos(\phi) \\
{}^A y_{P_p} &= (r + d_s)\sin(\phi)
\end{aligned}
\tag{5}
$$

Next the coordinates of O_B are expressed in frame $O_A X_A Y_A$. Let us define the frame $P_p X_C Y_C$ with origin in point P_p and rotated towards the frame A by angle ϕ—Fig. 3a. Having in mind that the supporting edge of next head is tangent to the circle $r + d_{\min}$, we can get the rotation angle ϕ_0 of the frame $O_B X_B Y_B$ towards the frame $P_p X_C Y_C$.

$$
\phi_0 = a\cos((r + d_{\min})/d)
\tag{6}
$$

where d is the distance from the center of the circle to the point P_p—Fig. 3, $d = \sqrt{{}^A x_P^2 + {}^A y_P^2}$.
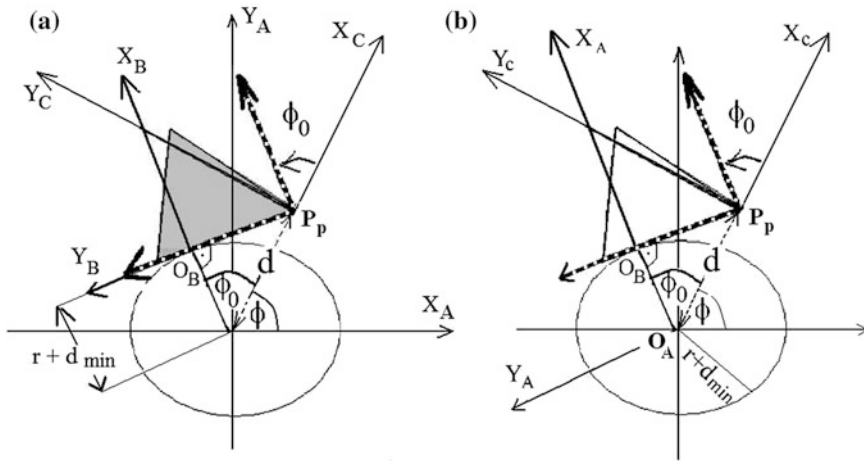
The coordinates of O_B (origin of frame $O_B X_B Y_B$) are:

$$
\begin{aligned}
{}^A x_{O_B} &= (r + d_{\min})\cos(\phi + \phi_o) \\
{}^A y_{O_B} &= (r + d_{\min})\sin(\phi + \phi_o)
\end{aligned}
\tag{7}
$$

Introducing $\gamma = \phi + \phi_o$ we express transformation matrix from frame $O_B X_B Y_B$ to frame $O_A X_A Y_A$:

$$
{}^A_B \mathbf{T} =
\begin{bmatrix}
\cos(\gamma) & -\sin(\gamma) & {}^A x_{O_B} \\
\sin(\gamma) & \cos(\gamma) & {}^A y_{O_B} \\
0 & 0 & 1
\end{bmatrix}
\tag{8}
$$

With this transformation coordinates of head points (e.g. head vertices) given in frame $O_B X_B Y_B$ can be expressed in frame $O_A X_A Y_A$.

Fig. 3 Rotated reference frames: **a** frame $O_B X_B Y_B$, **b** the new $O_A X_A Y_A$ frame

$$^A\mathbf{P_i} =^A_B \mathbf{T}\ ^B\mathbf{P_i} \tag{9}$$

This brings:

$$
\begin{aligned}
^A x_{P_i} &= \cos(\gamma)^B x_i - \sin(\gamma)^B y_i +^A x_{O_B} \\
^A y_{P_i} &= \sin(\gamma)^B x_i + \cos(\gamma)^B y_i +^A y_{O_B}
\end{aligned}
\tag{10}
$$

The first head localization in frame $O_A X_A Y_A$ is symmetrical towards X_A axis (Fig. 2). The coordinates of next head vertex—P_p (rel. (5)) and point O_B (rel. (7)) on its edge are obtained in frame $O_A X_A Y_A$. This is sufficient for the next head positioning. Knowing head geometry we obtain easily the coordinates of two remaining vertices in frame $O_B X_B Y_B$. For the purpose of graphical representation we transform it to $O_A X_A Y_A$. Next we consider the new reference frame $O_A X_A Y_A$ which is rotated by $\gamma = \phi + \phi_0$ towards the previous one—Fig. 3b. Coordinates of P_p and O_B marking the third head position are evaluated taking into account the new $O_A X_A Y_A$ frame. Procedure is repeated with every new $O_A X_A Y_A$ until the plan is ready for the whole contour. The distance between the previous and next head is $d_{heads} = |r + d_{\min} - (r + d_s)\cos(\phi)|$. It must be checked towards the maximal permissible $dh_{\max}$. Taking into account (2) we obtain this distance for circular fragments with smaller radiuses:

$$
d_{heads} = abs(d_{\max} - d_s + d_s \frac{d_{\max} - d_{\min}}{r}) \leq dh_{\max} \tag{11}
$$

When the minimal distance $_{\min}d_{heads} = dh_{\min}$ is also given, then the following must be fulfilled

$$dh_{\min} \leq abs(d_{\max} - d_s + d_s \frac{d_{\max} - d_{\min}}{r}) \leq dh_{\max} \qquad (12)$$

For $r = 75$ and the other parameters as considered d_{heads} changes from 1.33 mm (for $d_s = d_{\min} = 1$ mm) to 9.13 mm (for $d_s = d_{\max} = 10$ mm) what is acceptable. For the contours with big r angle ϕ is expressed by (3), $\cos(\phi) = \sqrt{1 - (^A y_c/r)^2}$. Applying it in $d_{heads} = |r + d_{\min} - (r + d_s)\cos(\phi)|$ we obtain:

$$d_{heads} = abs(r + d_{\min} - (r + d_s)\sqrt{1 - (^A y_c/r)^2} \qquad (13)$$

For r much bigger than y_c it can be estimated by $d_{heads} = abs(d_{\min} - d_s)$, d_s must fulfill $dh_{\min} \leq abs(d_{\min} - d_s) \leq dh_{\max}$.

4 Results

Described method was tested in MATLAB. For the real implementation the mobile bases and manipulators positioning assuring the head positions must be obtained, this is discussed in [7]. In MATLAB program the following parameters were used: head edge—$a = 70$ mm, $d_{\min} = 1$ mm, $d_{\max} = 10$ mm, $dh_{\max} = 10$ mm. The smallest circle had the radius $r = 75$ mm. In P_p calculations the distance d_s was gradually increased from $d_{\min}$ do $d_{\max}$. For each d_s the heads placement was evaluated. Depends on d_s (influencing the head twist towards the edge) needed number of supporting head positions can differ. Solution with smallest number of heads covering the whole machined edge is the candidate for realization. Figure 4 illustrates two plans of heads positioning. Every odd number marks first head and even number marks the second one. The planning starts with given position of head denoted by 1, in Fig. 4a this position is symmetrical towards the horizontal axis as it was considered in our transformations. In Fig. 4a dotted edges are marking the plan obtained for $d_s = 0.436 d_{\max}$, and the solid ones—for $d_s = 0.96 d_{\max}$. For the more twisted heads position with $d_s = 0.436 d_{\max}$ 8 positions is needed, what is by one more than for $d_s = 0.96 d_{\max}$. The second plan (for $d_s = 0.96 d_{\max}$) saving the number of head displacements therefore saving the time and energy is the proper one. In Fig. 4b for small curvature the greater distance is covered by dotted heads with $d_s = 0.1 d_{\max}$.
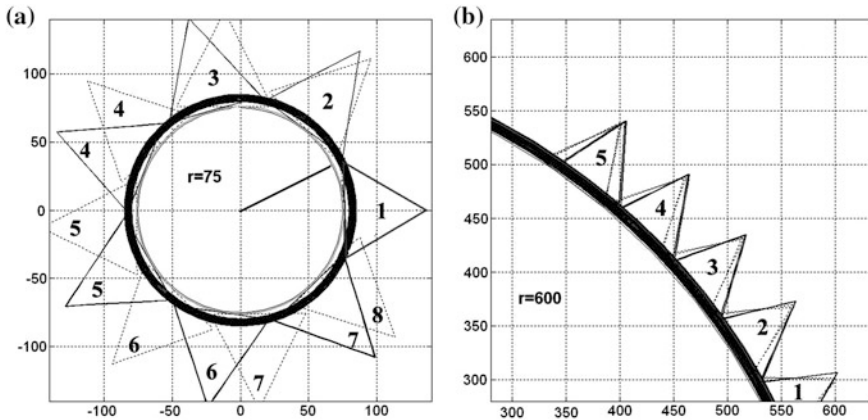
Fig. 4 Heads distribution: **a** for $r = 75$ mm and with $d_s = 0.436 d_{max}$ (*dotted edges*) and $d_s = 0.96 d_{max}$ (*solid edges*), **b** $r = 600$ mm, $d_s = 0.1 d_{max}$ (*dotted edges*), $d_s = d_{max}$ (*solid edges*)

5 Conclusion

In our works several strategies for heads position planning were proposed. The most universal one (applied to all possible workpiece shapes) is formulated as the Constraint Satisfaction Problem [6]. In CSP there is no formal description of the heads transfers. The CSP program rearranges the heads allocation fulfilling defined constraints. Presented methods applies geometrical approach, it is dedicated for the regular contours with defined curvature positioning. The first developments of this method were described in [9] without testing it and without analyzing the distances between the heads. The generated heads positioning plan together with manipulators and mobile bases position is stored as an XML data file which is subsequently supplied to the real-time control system. The developed control system is presented in [8], and a detailed description of robot kinematics is presented in [10]. The whole system including the mobile robots was launched successfully and its work was tested with drilling and milling operations performed on thin metal sheets.

References

1. Qin, G., Zhang, W., Wan, M.: A mathematical approach to analysis and optimal design of a fixture locating scheme. Int. J. Adv. Manuf. Technol. **29**, 349–359 (2006)
2. Vallapuzha, S., Meter, E.D., Choudhuri, S., Khetan, R.: An investigation of the effectiveness of fixture layout optimization methods. Int. J. Mach. Tools Manuf. **42**, 251–263 (2002)
3. Li, X., Molfino, R., Zoppi, M.: Fixture layout optimization for flexible aerospace parts based on self-reconfigurable swarm intelligent fixture system. Int. J. Adv. Manuf. Technol. **66**, 1305–1313 (2013)

4. Gagliardi, S., Li, X., Zoppi, M., De Leonardo, L., Molfino, R.: Adaptable fixturing heads for swarm fixtures: discussion of two designs. In: Proceedings of the ASME 2012 11th Biennial Conference on Engineering Systems Design and Analysis (ESDA2012), pp. 99–106 (2012)
5. Zoppi, M., Gagliardi, S., Molfino, R.: Multi-agent fixtures for automotive and aeronautical industries: design and prototyping of agent adaptable heads. In: 5th International Conference on Integrated Modeling and Analysis in Applied Control and Automation (IMAACA) 2011
6. Kasprzak, W., Zlatanov, D., Szynkiewicz, W., Zielinska, T.: Task planning for cooperating self-reconfigurable mobile fixtures. Int. J. Adv. Manuf. Technol. **69**, 2555–2568 (2013)
7. Zielinska, T., Kasprzak, W., Zielinski, C.: Path planning for robotized mobile supports. Mach. Mech. Theory **78**, 51–64 (2014)
8. Zielinski, C., Kasprzak, W., Kornuta, T., Szynkiewicz, W., Trojanek, P., Walecki, M., Winiarski, T., Zielinska, T.: Control and programming of a multi-robot-based reconfigurable fixture. Ind. Robot Int. J. **40**(4), 329–336 (2013)
9. Szynkiewicz, W., Zielinska, T., Kasprzak, W.: Robotized machining of a big work pieces: localization of supporting heads. Front. Mech. Eng. China (Springer) **5**(4), 357–369 (2010)
10. Zoppi, M., Zlatanov, D., Molfino, R.: Kinematics analysis of the Exechon tripod. In: Proceedings of ASME DETC, 34th Annual Mechanisms and Robotics Conference (MR), pp. 15–18 (2010)

The Founder of Russian School of a Robotics (to the 100 Anniversary Since the Birth of Academician E. P. Popov)

Evgeny Kotov, Anaid Nazarova and Sergey Vorotnikov

Abstract This article is devoted to the main stages of life of E. P. Popov (1914–1999), the engineer and the mathematician, the outstanding scientist in the field of mechanics, the theory of automatic control and a robotics, the academician of the Russian Academy of Sciences, the major general, the winner of the state awards of USSR 1949, 1972 and 1984.

Keywords Elasticity and deformation of rod structures · Nonlinear systems of automatic control · Method of harmonic linearization · Chart of quality of oscillatory processes · Robotics

Evgeny Pavlovich Popov was born on February 14, 1914 in Moscow. In 1934 he became the student of Moscow Institute of Mechanical Engineering, as was called Bauman Moscow State Technical University (BMSTU) at that time. E. P. Popov started his scientific work in the second year of Institute in the course of resistance of materials. By the results of a number of academic projects he published two articles in the magazine of Academy of Sciences of the USSR "Applied mathematics and mechanics". One of the solved tasks was connected with deformation of not cylindrical springs, and another—with research of a bend of thin loaded rods. While investigating deformation of springs, he found out that rigidity of a spring at its compression increases, and dependence of movement on compressing force becomes nonlinear, and this is characteristic for springs of any form.

The second task was a finding of big movements of a bend of thin rods and plates when the general deformation of a bend turns out very high so the ends of a

E. Kotov (✉) · A. Nazarova (✉) · S. Vorotnikov (✉)
Bauman Moscow State Technical University, Moscow, Russia
e-mail: kotov-831@mail.ru

A. Nazarova
e-mail: avn@bmstu.ru

S. Vorotnikov
e-mail: vorotn@bmstu.ru

rod receive movements, comparable with length of the rod. It was first obtained by Euler, who also suggested that the appropriate mathematical method in general terms. E. P. Popov developed the universal method of calculation including all special cases.

Essential development of a material of the first of these student's works become the master's dissertation, and the second—the doctor's.

After the Institute graduation in 1939 E. P. Popov was going to leave to postgraduate study, but mass mobilization at this time began, and he was called up to the army, where served in technical units of the Air Force. The Finnish war began soon, and after it—the Great Patriotic War. Sergeant E. P. Popov had to share with the colleagues all burdens of service on time of hostilities. However even in these conditions he found possibility to write serious scientific articles, which academic magazines continued to print. In 1942 his unit was transferred to Ioshkar Ola. There the Leningrad military and air engineering academy, created in 1941, was evacuated, feeling need for the qualified teaching personnel. In a rank of the senior sergeant E. P. Popov was transferred to teaching work in Academy. The young scientist received the first officer rank in 1943.

Here, in the conditions of military academy, E. P. Popov's ability had extremely fast and powerful development. On the basis of the tasks solved in a student time, in 1944 in Bauman Institute he made a master's dissertation: "The theory of deformation of twisted springs taking into account the phenomenon of screws connections". Reworked dissertation materials were published in 1950 in the collection of Academy of Sciences of the USSR "Dynamics and durability of springs" [6].

After finishing of the master's dissertation, E. P. Popov, despite big pedagogical load, began to prepare the doctoral dissertation. It was theoretical work: the classical task set by L. Euler was solved. However it was necessary not only to find mathematically beautiful decision, but also to create engineering methods of research and calculation of flexible structures. Work was complete already in Leningrad where academy returned in autumn of 1944.

The dissertation was called "Calculation of flexible parts of devices and machines (the applied theory of a flat bend of a direct and curve bar of small rigidity)". The scientific works, which were available in this area, came to an end with the basic mathematical decisions, which were not allowing to the engineer the possibility to apply them in the calculations. E. P. Popov found the universal equations and the ratios, allowing to solve practically any special problem in this area with a uniform method. For convenience of engineering calculations special numerical tables and nomograms were made. In 1946 at the age of 32 E. P. Popov successfully finished the doctoral dissertation, and the military rank the engineer major was appropriated to him.

The main scientific results of the performed work were published in 1947 in the form of the book "The theory and calculation of flexible elastic parts" for which the author in 1949 was awarded the Stalin award. In 1948 an academic status of the professor of theoretical mechanics was appropriated to E. P. Popov, and in 1949— the military rank the engineer lieutenant colonel.

By the results received in the doctoral dissertation, E. P. Popov published in 1948 the monograph "Nonlinear problems of statics of thin cores" in a series "Modern problems of mechanics". The outstanding scientist–mechanic the professor A. I. Lurye was the title editor of this series.

Science development often makes tasks, which decision demands development of new areas of research. Automatic equipment and telemechanics became such areas in the 50th years. In 1949 E. P. Popov received a task to create in Academy automatic equipment and telemechanics department, the first among military higher education institutions. Automatic equipment and telemechanics at that time did not develop yet as a science. There were no textbooks, which could be offered to listeners. Having processed a large quantity of available literature, mainly magazine articles, E. P. Popov builds, in essence, a new science—the theory of automatic control. The first books written by him in this subject were published as the manual in the Leningrad Military and Air Academy: "The theory of automatic control" p. 1 in 1952 and p. 2 in 1953. The book—"Dynamics of systems of automatic control" was published by Gostekhizdat in 1954 [6]. It's essentially extended and reworked version "Automatic control and management" sustained five editions in publishing house Fizmatgiz from 1956 to 1966 [6]. During this period the book was translated to foreign languages and published in Germany, England and the USA. Let's note that a large number of the books which have been released subsequently according to the theory of automatic control and regulation generally follows sections of this theory, offered by E. P. Popov, accepts his definitions and basic provisions. Thus, it is possible to consider the author as one of founders of this science in Russia and in the world.

E. P. Popov's particular interest was caused by the theory of nonlinear systems of automatic control. Probably, it was connected with its previous works in the field of mechanics as it there were essentially nonlinear tasks. In the 60-th years he published some works, which have founded methods of harmonic linearization. This method till this day remains to one of the most effective methods of research and design of automatic systems with essential nonlinearities. Being based on decomposition of signals on an exit of a nonlinear element in a Fourier row, and being limited to the first harmonic, it is possible to receive rather simple equations for determination of parameters of self-oscillations in nonlinear automatic systems. In 1960 E. P. Popov's and Paltov's book "Approximate methods of research of nonlinear automatic systems" was published containing mathematical justification of a method of harmonic linearization, the analysis of symmetric self-oscillations and their stability, an assessment of quality of nonlinear transients and calculation of the highest harmonics of self-oscillations [7]. This book also was published abroad—in Germany, USA and Poland.

The next ten years E. P. Popov continued work on the theory of nonlinear automatic systems. In 70-th the researches in this area were generalized in the monograph "The applied theory of control processes in nonlinear systems" [3]. He and his students solved new tasks for a separate class of systems, in particular, analysis of multi-frequency fluctuations, and also harmonic linearization of systems with several non-linearities. Charts of quality of the oscillatory processes,

Fig. 1 Research of nonlinear systems by means of charts of quality of oscillatory processes: **a** the block diagram, **b** family of charts of quality
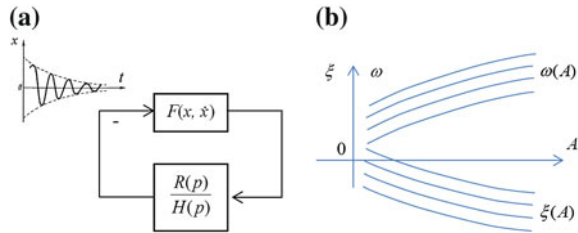
generalizing a method of harmonic linearization, and giving the chance not only to analyze, but also to design nonlinear systems of automatic control should be noted especially. The main idea of charts consists in consideration of oscillatory processes with variable amplitude. The signal arriving on an entrance of a nonlinear node *of F(x, ẋ)*, in the system shown on Fig. 1a, is represented in a form:

$$x(t) = A(t) \sin \Theta(t),$$

$$\frac{dA}{dt} = A\xi(A), \quad \frac{d\Theta}{dt} = \omega(A),$$

where $\xi(A)$ and $\omega(A)$—an indicator of attenuation and frequency, defined as functions of variable amplitude A from the characteristic equation of system after its harmonic linearization:

$$H(p) + R(p)\big[q(A) + q'(A)(p - \xi)\omega^{-1}\big] = 0,$$

$$p = \xi + j\omega$$

$R(P)$, $H(P)$—polynomials of any degree of numerator and a denominator, respectively, of the linear part, $q(A)$, $q'(A)$—factors of harmonic linearization.

Thus, charts of quality (or charts of attenuation) allow to investigate dynamics of nonlinear systems in all range of amplitudes. From the engineering point of view they give information about system in such form that creation of the equivalent model representing closed single circuit system and consisting of considered nonlinearity and some oscillatory node with variable parameters is possible. It follows from the main idea of a method of harmonic linearization according to which dynamic process in the closed nonlinear system is defined by the roots next to an imaginary axis. Equivalent model can be useful for purposeful change of parameters of system. If, for example, we want construct family of charts for various values of any parameter of system (Fig. 1b), it is possible to choose such values of this parameter at which the system of automatic control will meet the requirements shown to it. These diagrams are useful in the design of separate drives manipulation systems.

Use of charts of attenuation is of special interest for research of multilink (multi-axial) manipulators. If in some of n of degrees of movability of the manipulator are include same essential nonlinearity, for example, elastic

Fig. 2 a The block diagram
of multilink nonlinear
manipulator system,
b multi-frequency oscillatory
processes
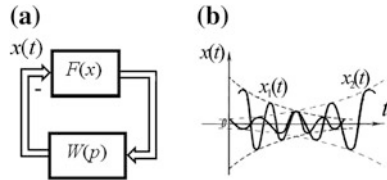
mechanical gear backlash, the model of system can be presented in the form of the block diagram (Fig. 2a):

Here $F(x)$—the diagonal matrix $(n \times n)$ which elements are, in general, essential nonlinearity; $W(p)$—a functional matrix $(n \times n)$ of the linear part; $x(t)$—the vector $(n \times 1)$, which coordinates—the dynamic signals arriving on an input of nonlinearities (Fig. 2b):

$$x(t) = \sum_{i=1}^{l} A_i(t) \sin \theta_i(t)$$

$$\frac{dA_i}{dt} = A_i \xi_i(A_1, A_2, \ldots A_l), \quad \frac{d\theta_i}{dt} = \omega_i(A_1, A_2, \ldots A_l)$$

where l—quantity of harmonics in considered process.

For a certain class of systems with the aid of diagrams damping parameters can be defined harmonic components and their stability. For this purpose harmonic linearization of each of nonlinearity, for example, by a method of minimization of a mean square of a difference between the valid and approximate values of signals is carried out.

The results of these investigations were implemented in the program package "Robot", developed in Bauman Institute for simulation, research and design of complex manipulation systems together with a set of drivers.

The Popov's researches in the theory of nonlinear control systems have been reflected in a number of monographs. Under E. P. Popov's edition and with his participation the Mashinostroenie publishing house in 1978–1980 released a series from 10 books according to the theory of nonlinear systems of automatic control [6]. In 1972 E. P. Popov was awarded the second state award for works on the theory of nonlinear control systems.

In 1960 E. P. Popov was elected as the member–correspondent of Academy of Sciences of the USSR in section of mechanics and control processes. In 1964 in a rank of the major general it was transferred to work to Moscow in Scientific and technical committee of the General Staff and appointed as the chairman of just created Section of applied problems at Presidium of Academy of Sciences of the USSR. On this post he was from 1964 to 1971. Despite of big organizational work and continuous business trips, E. P. Popov continues the scientific activity. In 1966 the new book written together with V. A. Besekersky "The theory of automatic control systems", which was three times republished and became the main

textbook for several generations of students, was released [2]. For work in Section of applied problems of E. P. Popov it was awarded the order a labor Red Banner.

After demobilization from army in 1971 E. P. Popov returned to Bauman Institute. One of the initiators of this transition was the rector of Institute—the academician G. A. Nikolayev, which E. P. Popov regularly met at meetings of Academy of Sciences. In the beginning he became heads of the department of applied mathematics, but soon was appointed as the head of the department "Automatic systems" with which collective started to create bases of a new science—robotics. At the initiative of E. P. Popov in the list of the USSR scientific specialties there was a new specialty—"Robots, manipulators and robotics systems". In the 80-th years the state programs providing wide introduction of a robotics in the industry were accepted. The need of the industry for engineers—developers of new robotics systems essentially increased. Regarding to this, it was decided to start the new specialty "Robotics systems and complexes". Scientific and methodical council was created on this specialty, headed by E. P. Popov. One of the first monographs in this area in the USSR was "Manipulation Robots. Dynamics and Algorithms" [8].

In 1984 E. P. Popov created in Bauman Institute new department—"Robotics systems" which became head in "Robotics Systems and Complexes" specialty.

One of principles which E. P. Popov follows in his pedagogical work consisted in combining actually educational process with active scientific work of students. Creation in 1981 of Scientific Training Center "Robotics" became an important initiative in this direction. It was one of the first scientific and pedagogical establishments in Russia in which the idea of integration of the academic science with a high school science and with educational process was realized. In 1991 the Center was transformed to Scientific Training Center of a robotics and automation of BMSTU and the Russian Academy of Sciences. Association of the scientific and pedagogical forces working on common problems, allowed to solve many actual problems of the industry and the national economy, connected with a robotics. Principles of creation of robotic system were developed for service of the thermonuclear reactor Tokamak, the mobile robots which were taking part in elimination the consequences of the Chernobyl, researches for the Center of preparation of cosmonauts of Y. Gagarin were carried out. Researches on application of robotic systems in mining industry were carried out. For the practical results connected with introduction in practice of robotic systems, including flexible production systems in the industry, E. P. Popov was awarded by the third state award in 1984.

In the 90-th years the new tendencies connected with use of methods of artificial intelligence were outlined in a robotics, and also in control of groups of robots. E. P. Popov actively supported these new directions of scientific research. The staff of the Center with his direct participation developed ways of adaptive control for robots with use of system of the technical vision, introduced in production. The main results of scientific work in the field of a robotics in BMSTU found the reflection in a multivolume series of engineering monographs "Automatic manipulators and robotic systems" under Popov's edition [9].

Being the head of Scientific Training Center "Robotics" of BMSTU, E. P. Popov constantly cared about scientific and business connections of the

Center with Academy of Sciences of the USSR. In Academy coordination council on scientific researches in the field of a robotics which headed E. P. Popov was created.

E. P. Popov combined qualities of the outstanding scientist and the wonderful teacher. His textbooks, written during work in BMSTU "The theory of linear systems of automatic control" [5] and "The theory of nonlinear systems of automatic control" [4] have not equal so far on laconicism and clarity of a statement. These books were the first in a series of textbooks according to the theory of automatic control under Popov's edition in publishing house "Nauka".

In 1990 E. P. Popov left the position of the head of the department "Robotic systems", remaining the research supervisor of the Center of a robotics of BMSTU. In 1992 he was elected the full member of the Russian Academy of Sciences.

In the 90-th years there came hard times for a science and for University. Robotics Center did not avoid these processes. The industry lost any interest to a robotics for a while. But Evgeny Pavlovich kept the Centre. Educational process and scientific researches did not stop. It was possible to keep and the main scientific and pedagogic collective in department "Robotic systems".

Interest to new paths in a science, ability to notice this new in time did not abandon E. P. Popov till the end of life. The last large monograph in which writing he participated as the author and as the editor, was the multivolume encyclopedia "Mechanical engineering" [1]. Volume 1–4 of this edition is entirely devoted to the theory of automatic control. In the section "Theory of nonlinear systems" written by him it is possible to find absolutely new fragments, such as phase space of system of a high order and processes of emergence of chaotic movements with strange attractor in dynamic systems. It seems that the author faced new opening and only withdrawal from life in 1999 stopped continuous process of scientific search.

References

1. Astapov, Y.M., Popov, E.P., et al.: Encyclopedia mechanical engineering, vol. 1–4. Mashinostroenie, Moscow (2000)
2. Besekersky, V.A., Popov, E.P.: The Theory of Automatic Control Systems. Nauka, Moscow (1975)
3. Popov, E.P.: The Applied Theory of Control Processes in Nonlinear Systems. Nauka, Moscow (1973)
4. Popov, E.P.: The Theory of Nonlinear Systems of Automatic Control. Nauka, Moscow (1979)
5. Popov, E.P.: The Theory of Linear Systems of Automatic Control. Nauka, Moscow (1989)
6. Popov, E.P.: Memories. BMSTU, Moscow (1996)
7. Popov, E.P., Paltov, I.P.: Approximate Methods of Research of Nonlinear Automatic Systems. Fizmatgiz, Moscow (1960)
8. Popov, E.P., Vereshchagin, A.F., Zenkevich, S.L.: Manipulation Robots. Dynamics and Algorithms. Nauka, Moscow (1978)
9. Popov, E.P., Yurevich, E.I., et al.: Automatic Manipulators and Robotic Systems. Mashinostroenie, Moscow (1984)

Scaffold with Improved Construction Rigidity

Y. S. Temirbekov and S. U. Joldasbekov

Abstract A scaffold system has been developed; practically coinciding by its kinematic parameters with the scaffold based on the "Nurenberg Scissors". The construction based on this system is superior by its rigid characteristics to an analogical construction based on the "Nurenberg Scissors". An experimental construction of such scaffold (PMD-2.2) has been created, with an elevated working platform up to 4 m. A comparative analysis of the rigidity and condition on the stability of the—PMD-2.2 construction and the analog on the basis the "Nurenberg Scissors" has been presented.

Keywords Scaffold · Nuremberg scissors · Rigidity

1 Introduction

The hinge-lever scaffold on the kinematic basis of "Nurenberg Scissors" (NS) is widely used abroad. The analysis of the kinematic diagram of the "Nurenberg Scissors" has shown that, along with all its advantages, it still has rooms for increasing its rigidity. The authors have developed a kinematic system that is better than the kinematic system of the "NS", in terms of the rigidity characteristics. While possessing all the merits of the "NS", this system also has an increase longitudinal and lateral rigidity, on account of the introduction of a sliding coupling, located on the additionally inserted vertical strut rail. Several Patents of the
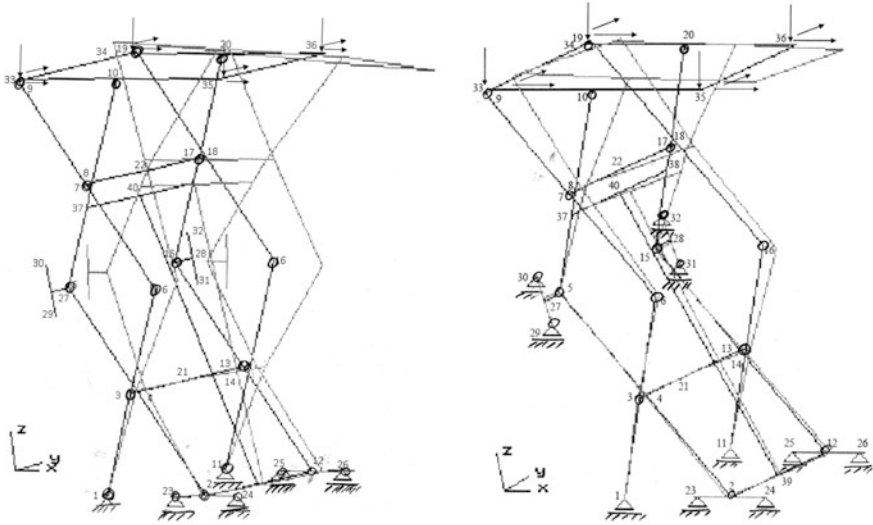
Y. S. Temirbekov (✉)
Institute of Mechanic and Mechanical Engineering, Almaty Technological University,
Almaty, Kazakhstan
e-mail: temirbekove@mail.ru

S. U. Joldasbekov
Institute of Mechanic and Mechanical Engineering, Almaty, Kazakhstan
e-mail: skanderbek55@mail.ru

Fig. 1 End-component models of the "nuremberg scissors" and the PMD-2.2

Republic of Kazakhstan have been obtained on this engineering solution, on the functional model and Industrial specimen [1–4]. The insertion of an additional sliding coupling creates an anchor point for constructing its movement in space. While the various well-known foreign scaffold constructions based on the "NS", have anchor points only on the plane of the horizontally lying frame. To show the advantages of the scaffold system developed by the authors, a comparative rigidity analysis is given of the end-component models of the scaffold construction PMD-2.2 and their analog on the basis of "NS".

For the rigidity analysis of the scaffold construction, their end-component models (ECM), consisting of 40 joints have been built (Fig. 1).

Two end-components models are being considered here (Fig. 1), all the joints are the same but they differ only in the fact that, for the construction designed by the authors, the additional sliders move on rigidly fixed vertical guideways, and for the second, they are free from them (Table 1).

2 Structure and Cross-Sectional Geometry, Material Properties

To carry out the calculation; the elastic and geometric characteristics of the constructions are set, the geometry of the cross sections and properties of the material (the same for both ECM): the area of the cross section of all end core components

Table 1 Joint coordinates of the models

N	X	Y	Z	N	X	Y	Z
1	0.00000e+00	−0.40000e−01	0.00000e+00	21	0.29686e+00	0.30000e+00	0.55000e+00
2	0.59372e+00	0.00000e+00	0.00000e+00	22	0.29686e+00	0.30000e+00	0.16500e+01
3	0.29686e+00	−0.40000e−01	0.55000e+00	23	0.39372e+00	0.00000e+00	0.00000e+00
4	0.29686e+00	0.00000e+00	0.55000e+00	24	0.79372e+00	0.00000e+00	0.00000e+00
5	0.00000e+00	0.00000e+00	0.11000e+01	25	0.39372e+00	0.60000e+00	0.00000e+00
6	0.59372e+00	−0.40000e−01	0.11000e+01	26	0.79372e+00	0.60000e+00	0.00000e+00
7	0.29686e+00	−0.40000e−01	0.16500e+01	27	0.00000e+00	−0.10000e+00	0.11000e+01
8	0.29686e+00	0.00000e+00	0.16500e+01	28	0.00000e+00	0.70000e+00	0.11000e+01
9	0.00000e+00	−0.40000e−01	0.22000e+01	29	0.00000e+00	−0.10000e+00	0.96667e+00
10	0.59372e+00	0.00000e+00	0.22000e+01	30	0.00000e+00	−0.10000e+00	0.12333e+01
11	0.00000e+00	0.64000e+00	0.00000e+00	31	0.00000e+00	0.70000e+00	0.96667e+00
12	0.59372e+00	0.60000e+00	0.00000e+00	32	0.00000e+00	0.70000e+00	0.12333e+01
13	0.29686e+00	0.60000e+00	0.55000e+00	33	0.00000e+00	0.00000e+00	0.22000e+01
14	0.29686e+00	0.64000e+00	0.55000e+00	34	0.00000e+00	0.60000e+00	0.22000e+01
15	0.00000e+00	0.60000e+00	0.11000e+01	35	0.12500e+01	0.00000e+00	0.22000e+01
16	0.59372e+00	0.64000e+00	0.11000e+01	36	0.12500e+01	0.60000e+00	0.22000e+01
17	0.29686e+00	0.60000e+00	0.16500e+01	37	0.22561e+00	0.00000e+00	0.15180e+01
18	0.29686e+00	0.64000e+00	0.16500e+01	38	0.22561e+00	0.60000e+00	0.15180e+01
19	0.00000e+00	0.64000e+00	0.22000e+01	39	0.59372e+00	0.30000e+00	0.00000e+00
20	0.59372e+00	0.60000e+00	0.22000e+01	40	0.22561e+00	0.30000e+00	0.15180e+01

N—number of joints
(X, Y, Z)—coordinates of the joints

Table 2 Concordance of ECC numbers and joints

ENR	KNR1	KNR2	ENR	KNR1	KNR2	ENR	KNR1	KNR2	ENR	KNR1	KNR2
1	1	3	14	13	15	26	2	24	38	10	35
2	2	4	15	14	16	27	12	25	39	20	34
3	3	4	16	15	38	28	12	26	40	20	36
4	4	5	17	16	18	29	5	27	41	33	34
5	3	6	18	17	18	30	15	28	42	35	36
6	5	37	19	18	19	31	27	29	43	8	37
7	6	7	20	17	20	32	27	30	44	17	38
8	7	8	21	4	21	33	28	31	45	37	40
9	7	9	22	13	21	34	28	32	46	38	40
10	8	10	23	8	22	35	9	33	47	39	40
11	11	14	24	17	22	36	19	34	48	2	39
12	12	13	25	2	23	37	10	33	49	12	39
13	13	14									

ENR—number of RFE

KNR1, KNR2—beginning and end numbers of joints ECC

Table 3 Boundary coupling of joints along the axis (differs for both by ECM addition)

KNR	VX	VY	VZ	DX	DY	DZ	KNR	VX	VY	VZ	DX	DY	DZ
1	1	2	3	4	5	6	Negative addition for the construction PMD-2.2:						
11	1	2	3	4	5	6	29	1	2	–	4	5	6
23	–	2	3	4	5	6	30	1	2	–	4	5	6
24	–	2	3	4	5	6	31	1	2	–	4	5	6
25	–	2	3	4	5	6	32	1	2	–	4	5	6
26	–	2	3	4	5	6							

KNR—number of the joint being fixed

(VX, VY, VZ) and (DX, DY, DZ)—direction of linear and corner coupling

(ECC) is equal to A $= 12000e-02$, moments of inertia, $I_V = 198e-05$, $I_W = 0.1790e-06$, $E = 2*10^{11}$, $v = 0.3$. Concordance of numbers of the ECC and ECM joints (same for both ECM) is given in Table 2,

To calculate the boundary fixers and the geometry of the models in the corresponding joints, limitations have been set and in the joints between the elements, rotational and translational kinematic couplings have been introduced (Tables 3 and 4).

The weight of the construction does not take into consideration the external forces for both models and it is given in the form of complex loading of the working platform (Table 5).

Table 4 Calculation of hinge joints (the same for both ECM)

ENR	KNL	KZ	ENR	KNL	KZ	ENR	KNL	KZ
1	1	5	6	1	5	9	2	5
11	1	5	16	1	5	36	1	4
3	1	4	5	2	5	19	2	5
13	2	4	15	2	5	10	2	5
2	1	5	7	1	5	20	2	5
12	1	5	17	1	5	37	1	1
4	2	5	8	1	4	38	1	1
1	2	5	18	2	4	39	1	1
			35	1	4	40	1	1

ENR—ECC with hinge; KNL—local joint (1—begining, 2—end) ECC; KZ—local degree of freedom

Table 5 Joint loading (the same for both ECM)

NUMM	X	Y	Z	NUMM	X	Y	Z
33	0.25e+03	0.25e+03	−0.375e+03	35	0.25e+03	0.25e+03	−0.375e+03
34	0.25e+03	0.25e+03	−0.375e+03	36	0.25e+03	0.25e+03	−0.375e+03

NUMM—number of joint loading; (X, Y, Z)—joint coordinates

3 Elastic Displacement ECM Nodes

Therefore, one end-component model corresponds to the scaffold PMD-2.2, and the other scaffold on the basis of the "NS", is that which is widely used abroad. The rigidity is calculated using the computer software "LIRA" and "INVEN-TOR" [5, 6]. The elastic movements of the joints of the models have been found (Tables 6 and 7).

Elastic linear displacement has been found for the extreme upper position of both constructions, since this the most dangerous position when the operator is working on height. The relations of corresponding elastic displacement of joints have been taken for both ECM "NS" and ECM PMD-2.2 (Table 8).

As seen from the presented results, the rigidity of the PMD-2.2 construction as compared to that of the construction based on "NS" increased on the average by not less than two times, and the lateral rigidity (displacement along axis OY) was even more. Therefore, introduction of additional sliding coupling allowed for increase in rigidity of the construction as a whole, and especially "lateral" rigidity. The authors have designed and built an experimental specimen of the scaffold PMD-2.2 construction with elevated working platform of up to 4 m (Fig. 2).

Table 6 Elastic displacement of joints of ECM "NS" (Fig. 1)

N	X	Y	Z	N	X	Y	Z
1	0.0000E+00	0.0000E+00	0.0000E+00	21	6.4600E−05	2.3840E−04	−2.8052E−05
2	−1.0234E−04	1.7849E−06	−2.3637E−07	22	3.2241E−04	1.4912E−03	−5.2760E−05
3	−5.9553E−05	2.3843E−04	4.0525E−05	23	−1.0234E−04	0.0000E+00	0.0000E+00
4	−5.2743E−05	2.3845E−04	2.9854E−05	24	−1.0234E−04	0.0000E+00	0.0000E+00
5	3.1050E−04	8.5604E−04	2.3132E−04	25	3.4307E−04	0.0000E+00	0.0000E+00
6	−1.3055E−04	7.8744E−04	7.8712E−05	26	3.4307E−04	0.0000E+00	0.0000E+00
7	2.8027E−04	1.4911E−03	3.0043E−04	27	2.9320E−04	8.5604E−04	3.4050E−04
8	2.7255E−04	1.4911E−03	2.5638E−04	28	7.0005E−05	8.5560E−04	−2.8329E−04
9	7.0906E−04	2.2394E−03	5.3205E−04	29	2.9320E−04	7.1048E−04	3.4050E−04
10	4.1190E−04	2.5215E−03	1.7988E−04	30	2.9320E−04	1.0016E−03	3.4050E−04
11	0.0000E+00	0.0000E+00	0.0000E+00	31	7.0005E−05	7.0547E−04	−2.8329E−04
12	3.4307E−04	1.8228E−06	−2.6585E−06	32	7.0005E−05	1.0057E−03	−2.8329E−04
13	1.8459E−04	2.3834E−04	−9.3418E−05	33	6.9687E−04	2.2394E−03	4.7592E−04
14	1.9189E−04	2.3832E−04	−1.0620E−04	34	3.8460E−04	2.2395E−03	−3.6043E−04
15	4.2043E−05	8.5560E−04	−1.7069E−04	35	0.0000E+00	3.1708E−03	−2.7794E−04
16	5.6570E−04	7.7321E−04	−3.1045E−04	36	−3.6411E−04	3.1707E−03	−1.1211E−03
17	3.9519E−04	1.4913E−03	−3.6217E−04	37	2.5712E−04	1.3462E−03	2.6429E−04
18	3.9312E−04	1.4913E−03	−4.0622E−04	38	3.0751E−04	1.3460E−03	−3.1429E−04
19	3.7438E−04	2.2395E−03	−4.1700E−04	39	1.3962E−04	1.8322E−06	−1.6348E−05
20	8.7195E−04	2.5041E−03	−6.2232E−04	40	2.5703E−04	1.3461E−03	−4.5339E−06

N—number of joint; (X,Y,Z)—direction of linear displacement

Table 7 Elastic displacement of joints ECM PMD-2.2 (Fig. 1)

N	X	Y	Z	N	X	Y	Z
1	0.0000E+00	0.0000E+00	0.0000E+00	21	1.1540E−05	1.9593E−06	−6.1919E−06
2	−9.6255E−05	−8.9390E−07	1.1116E−07	22	1.0626E−04	3.0529E−04	−7.2099E−05
3	−5.6460E−05	2.0043E−06	3.0490E−05	23	−9.6255E−05	0.0000E+00	0.0000E+00
4	−5.4738E−05	1.9998E−06	2.7127E−05	24	−9.6255E−05	0.0000E+00	0.0000E+00
5	6.5962E−06	2.0944E−06	6.7645E−05	25	1.5765E−04	0.0000E+00	0.0000E+00
6	−3.2745E−05	1.3027E−04	1.6295E−05	26	1.5765E−04	0.0000E+00	0.0000E+00
7	6.0637E−05	3.0516E−04	6.5380E−05	27	4.1895E−07	1.8194E−06	7.3721E−05
8	5.4355E−05	3.0512E−04	4.7616E−05	28	−1.6055E−07	1.6200E−06	−9.7723E−05
9	2.5147E−04	6.9941E−04	1.6871E−04	29	0.0000E+00	0.0000E+00	7.3721E−05
10	2.3535E−04	9.0925E−04	−5.1497E−05	30	0.0000E+00	0.0000E+00	7.3721E−05
11	0.0000E+00	0.0000E+00	0.0000E+00	31	0.0000E+00	0.0000E+00	−9.7723E−05
12	1.5765E−04	−8.5157E−07	−1.4423E−06	32	0.0000E+00	0.0000E+00	−9.7723E−05
13	8.3699E−05	1.9188E−06	−4.3201E−05	33	2.4721E−04	6.9941E−04	1.4495E−04
14	8.7135E−05	1.9234E−06	−4.7589E−05	34	1.5032E−04	6.9949E−04	−2.0004E−04
15	−3.6498E−06	1.8649E−06	−9.1293E−05	35	0.0000E+00	1.5132E−03	−4.0588E−04
16	2.7793E−04	1.1183E−04	−1.5186E−04	36	−3.2172E−04	1.5131E−03	−7.8247E−04
17	1.7726E−04	3.0546E−04	−1.9097E−04	37	2.7848E−05	2.3852E−04	6.1272E−05
18	1.7573E−04	3.0549E−04	−2.0844E−04	38	1.2199E−04	2.3826E−04	−1.6035E−04
19	1.4788E−04	6.9949E−04	−2.2430E−04	39	4.8067E−05	−8.8614E−07	−1.5366E−05
20	5.2330E−04	8.9390E−04	−3.8043E−04	40	5.3820E−05	2.3840E−04	−3.0277E−05

N—number of joint; (X, Y, Z)—direction of linear displacement

Table 8 Relation of corresponding elastic displacement of joints of ECM PMD-2.2

N	X	Y	Z
1	0.000	0.000	0.000—Fixed column
2	1.063	−1.997	−2.126—minus sign indicate opposite displacement along Y and Z
3	1.055	118.959	1.329
4	0.964	119.237	1.101
5	47.073	408.728	3.420
6	3.987	6.045	4.830
7	4.622	4.886	4.595
8	5.014	4.887	5.384
9	2.820	3.202	3.154
10	1.750	2.773	−3.493
11	0.000	0.000	0.000—fixed column
12	2.176	−2.141	1.843
13	2.205	124.213	2.162
14	2.202	123.906	2.232
15	−11.519	458.791	1.870
16	2.035	6.914	2.044
17	2.229	4.882	1.896
18	2.237	4.882	1.949
19	2.532	3.202	1.859
20	1.666	2.801	1.636
21	5.598	121.676	4.530
22	3.034	4.885	0.732
23	1.063	0.000	0.000—displacement only along X
24	1.063	0.000	0.000—displacement only along X
25	2.176	0.000	0.000—displacement only along X
26	2.176	0.000	0.000—displacement only along X
27	699.845	470.507	4.619
28	−436.032	528.148	2.899
29	0.000	0.000	0.000—displacement along Z
30	0.000	0.000	0.000—displacement along Z
31	0.000	0.000	0.000—displacement along Z
32	0.000	0.000	0.000—displacement along Z
33	2.819	3.202	3.283
34	2.559	3.202	1.802
35	.000	.000	0.000
36	1.132	2.095	1.433
37	9.233	5.644	4.313
38	2.521	5.649	1.960
39	2.905	−2.068	1.064—minus sign indicate opposite displacement along Y
40	4.776	5.646	0.150

Number of joint; (X, Y, Z)—relations of directional linear displacement

Fig. 2 Experimental specimen PMD-2.2. In raised and transport positions

4 Conclusions

As the seen from the calculation obtained, the rigidity of the PMD-2.2 construction, is on the average two times greater than the rigidity of "NS" construction, and the lateral rigidity is even greater. Thus, introduction of an additional sliding coupling, located on a rigid vertical guideway, increases the rigidity of the scaffold construction as a whole and especially the "lateral" rigidity.

References

1. Temirbekov, Y.S., et al.: Utility model patent. Official Bulletin №5(1), Astana. MoJ RSE "NIIS", Mobile Mechanized Scaffold (2009)
2. Temirbekov, Y.S., Joldasbekov, S.U., et al.: Utility model patent №127 from 06.12.2002, 12c. Mechanized Scaffold (2002)
3. Temirbekov, Y.S., et al.: Decision on the granting of a prepatent for invention. Kazpatent of 10.09.2001 №1174. The copyright certificate №11543. Rectilinear-Guide Mechanism (2001)
4. Temirbekov, Y.S., Joldasbekov, S.U., et al.: Prepatent for industrial design №306 from 10.02.2003. 6c. Mobile Scaffold (2003)
5. Digital Prototyping: Autodesk Inventor 2010 Official training course, 944 p. M.: DMK Press, (2010)
6. Software complex for calculation and design "Lira", version 9.0. Guide User. Book 1: Basic Theoretical and Calculated Position. Some of the recommendations. Kiev, NIIASS, 147 p (2002)

Force Capability Polytope of a 3RRR Planar Parallel Manipulator

L. Mejia, H. Simas and D. Martins

Abstract This paper shows how the characteristic *force capability polytope* of a 3RRR parallel manipulator can be obtained from the optimization of its static equations. The objective function of the optimization problem of force capability is defined by employing the Screws Theory and Davies's method as a primary mathematical tool. In order to solve the problem regarding the global optimization, an evolutionary algorithm known as Differential Evolution (*DE*) is used. Finally, some force capability polytopes are obtained for different kinematic positions and different working modes of the manipulator.

Keywords Force capability polytope · Optimization · Screws theory · Davies's method

1 Introduction

The increased complexity of the tasks of industrial manipulators requires further studies on robots interaction with the environment. When the movement of the manipulator is slow, as it is common in force interaction tasks, it is possible to consider the interaction as quasi-static, [8].

The task space capabilities of a manipulator to perform motion and/or to exert forces and moments are of fundamental importance in robotics. Their evaluation can be useful to determine the structure and the size of a manipulator that best fit

L. Mejia · H. Simas (✉) · D. Martins (✉)
Federal University of Santa Catarina, Florianópolis, Brazil
e-mail: hsimas@gmail.com

D. Martins
e-mail: daniel.martins@ufsc.br

L. Mejia
e-mail: leonardo.mejia.rincon@posgrad.ufsc.br

the designer's requirements or they can be used to find a better configuration or a better operation point for a manipulator to perform a given task [2].

In robotics, the ***force capability*** of a manipulator is defined as the maximum wrench that can be applied (or sustained) by a manipulator for a given pose based on the limits of the actuators. By considering all possible directions of the applied wrench or by considering specific directions along spatial trajectories, a force capability plot can be generated for the given pose [5].

The force capability of a manipulator depends on its design, posture and actuation limits [9]. The scaling factor method and the explicit method to evaluate the force capabilities of parallel manipulators have been presented in [11], Nokleby et al. [4] used those methods to show some results for 3-RRR, 3-RPR and 3-PRR parallel architectures with redundant and non-redundant actuation. The main objective of this study is to develop a method to obtain the force capability polytope of a 3RRR parallel manipulator in static or quasi-static conditions.

2 Geometric Representation of a 3RRR Planar Parallel Manipulator

Parallel manipulators usually consist in a mobile platform connected to a fixed platform by several branches in order to transmit the movement. Generally, the number of branches of parallel manipulators is equals to their degree of freedom (DoF), and the motors are usually located near the fixed base [7].

In this paper, a *"3RRR Planar Parallel Manipulator (PPM)"* is studied. In this parallel manipulator, the fixed and mobile platforms are joined by using three branches. Each branch has three rotational joints whose axes are perpendicular to the $(x - y)$ plane, and the first of the three joints in each branch is actuated, as shown in Fig. 1.

Furthermore, the mobile and fixed platforms are formed by equilateral triangles with sides l_m and l_f respectively. The branches are formed by two links with lengths l_1 and l_2 respectively, the distance between one of the mobile platform vertices and its centroid is called l_3 and the angle ϕ represents the orientation of the mobile platform. For the studied manipulator, the link lengths and platform edge lengths are specified as $l_1 = l_2 = l_m = 0.2$ m, $l_f = 0.5$ m, the manipulator's final effector is located in $[0.25 \text{ m}, 0.144 \text{ m}]$, the mobile platform is oriented in $\phi = 0°$ and the maximum torque capability for each actuated joint of the manipulator is ± 4.2 Nm.

3 Statics of the Manipulator

In the static analysis of manipulators, the goal is to determine the force and moment requirements in the joints. It is possible to apply forces and moments in the mechanism joints to analyse the efforts obtained in the final actuator, or to
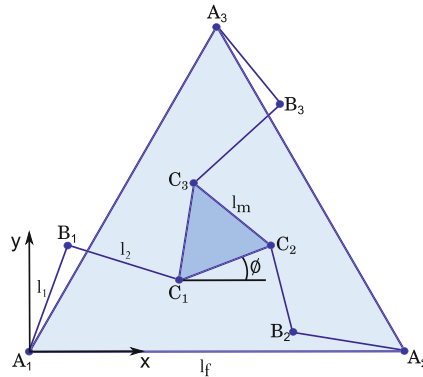
Fig. 1 Schematic representation of a 3RRR PPM

apply external forces and calculate the necessary forces and moments in the joints to balance these external forces.

The wrenches (force and moments) applied (or sustained) can be represented by the vector $F = [F_x, F_y, M_z]^T$, where F_x and F_y denotes the force in the directions "x" and "y" respectively, and M_z denotes the moment around the "z" axis. The actuator torques of joints A_1, A_2 and A_3 (denoted by the vector τ) are respectively τ_{A_1}, τ_{A_2} and τ_{A_3}. The manipulator does not have actuation redundancy and knowing the three independent variables the manipulator is statically solved.

Using the formalism presented in ***Davies*** [3], the primary variables are known, and the secondary variables are the unknown variables. Considering the actuation torques as the primary variables, the $\widehat{A}_N$ matrix can be obtained using ***graph theory***, ***screw theory*** and ***Kirchhoff-Davies cutset law*** [1], where $\widehat{A}_N$ is the diagonalized unitary action matrix and V is a vector comprising all the unknown wrenches in the manipulator as shown in this equation: $[\widehat{A}_N]_{21 \times 24} \tau_{24 \times 1} = V_{21 \times 1}$.

The complete manipulators action graph is shown in Fig. 2, where the vertices are the manipulator links and the edges are the joints. Existing wrenches in each joint are represented by the symbol $. In this model the gravitational effects were not considered.

The cutset law states that: when a manipulator is in static equilibrium, the sum of wrenches acting in a single cut must be zero. Each one of the k cuts divides the manipulator in subsets of links and joints, where in each subset, the static equilibrium must be preserved [9].

Since the manipulator is planar, the space dimension λ is three and only the F_x, F_y, and M_z wrench components are considered, while F_z, M_x, and M_y are always equal to zero [9] and will not be represented in this paper. For revolute joints, the wrench can be written as shown in Eq. (1), where x and y are the location of the joint axis given in Cartesian coordinates, F_x and F_y are respectively the forces in
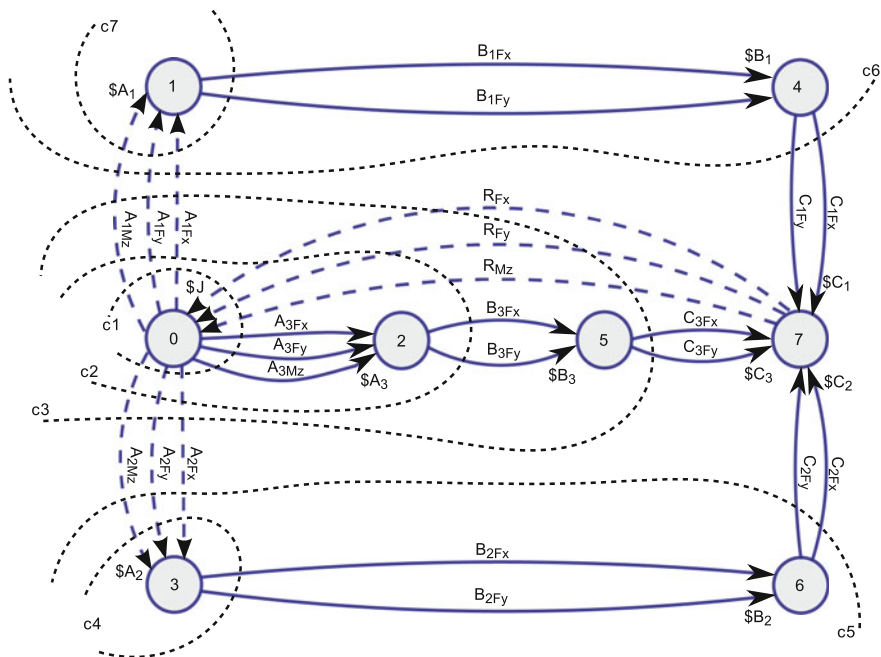
Fig. 2 Manipulator action graph of a 3RRR PPM

directions x and y, and τ is the actuation torque. If the joint is passive, τ is zero and the last term of equation Eq. (1) vanishes [9].

$$\$ = \begin{bmatrix} -y \\ 0 \\ 1 \end{bmatrix} F_x + \begin{bmatrix} x \\ 0 \\ 1 \end{bmatrix} F_y + \begin{bmatrix} 1 \\ 0 \\ 0 \end{bmatrix} \tau \tag{1}$$

For each cutset there are three independent equations that can be written in the matrix as shown in Eq. (2), where A_D is the cut action matrix, $\widehat{A}_N$ is the unitary cut action matrix, Ψ is the vector comprising the wrenches magnitudes, λ is the space dimension, and C represent the manipulator's gross [1, 3, 9].

$$\Sigma\$ = [A_D]_{\lambda \times C} = [\widehat{A}_N]_{\lambda \times C} \{\Psi\}_{C \times 1} = \{0\}_{\lambda \times 1} \tag{2}$$

Algebraic manipulation of Eq. (2) allows us to obtain the expressions for the forces and the moment in the manipulator's final effector as shown in Eq. 3, in these equations the $k_1, \ldots, k_9$ terms represent the kinematic expressions as functions of the manipulators joints positions, and the $\tau_{A_1}, \tau_{A_2}, \tau_{A_3}$ terms represent the torques in the actuated joints.

$$
\begin{bmatrix} F_x \\ F_y \\ M_z \end{bmatrix} = \begin{bmatrix} k_1 & k_2 & k_3 \\ k_4 & k_5 & k_6 \\ k_7 & k_8 & k_9 \end{bmatrix} \cdot \begin{bmatrix} \tau_{A_1} \\ \tau_{A_2} \\ \tau_{A_3} \end{bmatrix} \tag{3}
$$

4 Optimization Problem

The aim of the optimization problem studied in this paper, is to maximize the force F_m applied or sustained for the manipulator in a given direction by the angle θ, while the moment is imposed as a constant. As shown in Fig. 3, a force capability map is obtained when all the possible directions of the maximum force F_m are considered. The force capability map shown in Fig. 3 was first studied by Nokleby [4, 5].

The optimization problem can be described as the process in which the torque in the actuators τ_{A_1}, τ_{A_2}, and τ_{A_3} must be optimized in order to maximize the pure force and minimize the error in the imposed value for the moment in the manipulator's final effector. This optimization must be done in all possible directions given for the angle θ. In our simulations, were used 360 repetitions, one repetition per degree of the angle θ, and the imposed moment was increased positively and negatively until the force in any direction was zero.

4.1 Objective Function and Differential Evolution Algorithm

The objective function used in the optimization process is shown in Eq. (4), where the terms F_x and F_y are the components of the force obtained in each iteration of the optimization, α_d is the desired angle of the application of the force, α_o is the obtained angle of the application of the force as a function of the F_x and F_y components, M_z is the moment obtained in the manipulator's final effector, M_k is the constant moment imposed in the manipulator's final effector and finally the "P" term is the penalization of the objective function.

In Eq. (4), the $|\alpha_d - \alpha_o / \alpha_d|$ term minimizes the normalized error between the obtained and desired force direction, the $\left| 3l_1 \tau_{An_{max}} / \sqrt{F_x^2 + F_y^2} \right|$ term maximizes the normalized force obtained, and the $|M_z - M_k / M_k|$ term minimizes the normalized error between the obtained moment and the desired moment in the manipulator's end effector.

$$
F_{obj} = \left| \frac{\alpha_d - \alpha_o}{\alpha_d} \right| + \left| \frac{3l_1 \tau_{An_{max}}}{\sqrt{F_x^2 + F_y^2}} \right| + \left| \frac{M_z - M_k}{M_k} \right| + P \tag{4}
$$
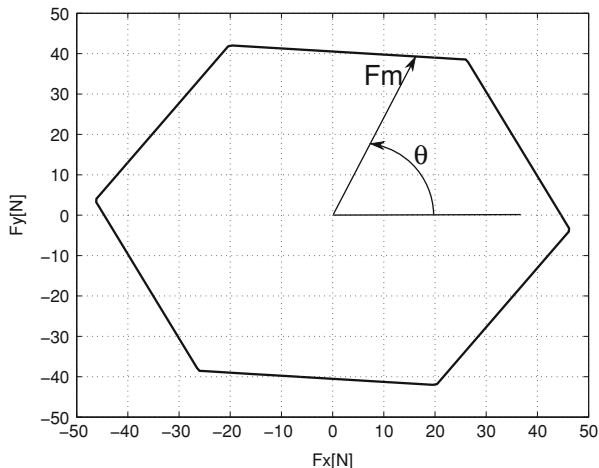
Fig. 3 Force capability map of a 3RRR PPM

The penalization term "P" included in Eq. (4) is activated when the condition $[\tau_{An_{\min}} \leq \tau_{An} \leq \tau_{An_{\max}}]$ is not satisfied, this condition is imposed as the maximum admissible torque in the actuators τ_{An}. In this paper was used $\tau_{An_{\min}} = -4.2\,\text{Nm}$ and $\tau_{Anmax} = 4.2\,\text{Nm}$.

In order to solve the problem regarding the global optimization, an evolutionary algorithm known as Differential Evolution (*DE*) was used. *DE* is a very simple population based, stochastic function minimizer and very powerful at the same time.

DE optimizes a problem by maintaining a population of candidate solutions, and creating new candidate solutions by combining existing ones, according to its simple formula, and then keeping whichever candidate solution has the best score or fitness on the optimization problem at hand. In this way, the optimization problem is treated as a black box that merely provides a measure of quality given a candidate solution, and therefore, the gradient is not needed [10].

The performance of the DE algorithm is sensitive to the mutation strategy and respective control parameters, such as the population size (NP), crossover rate (CR), and the mutation factor (MF). The best settings for control parameters can be different for different optimization problems, and the same functions with different requirements, for consumption time and accuracy [9]. In this study the parameters $NP = 30$, $MF = 0.5$, $CR = 0.8$ were used, as suggested in [6], and the maximum iteration number was established in 4,000.

5 Results

From the optimization of the objective function shown in Eq. (4) and using the topology shown in Sect. 2, is possible to obtain the maximum force in a desired direction. By repeating the optimization process for each possible direction the
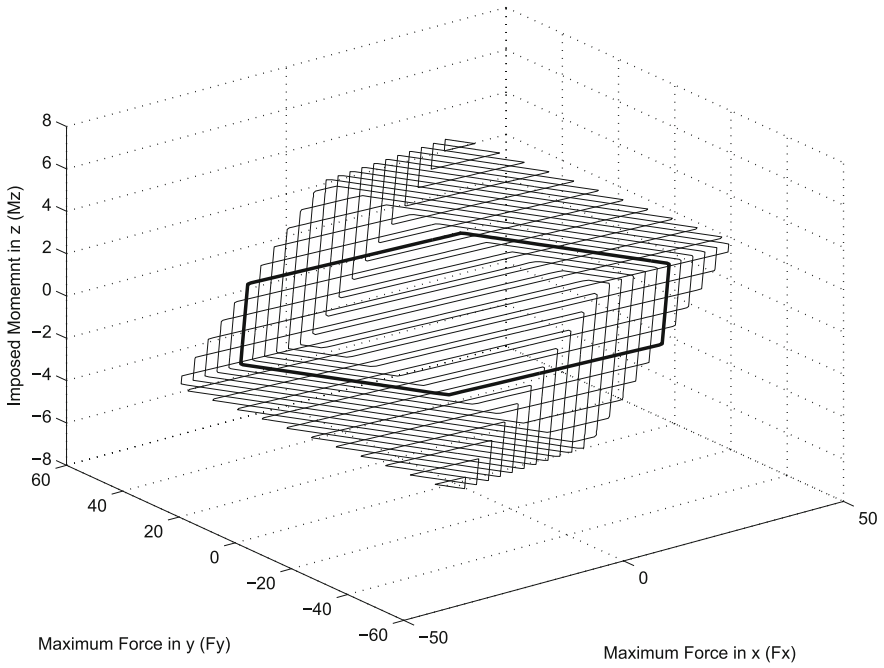
Fig. 4 Force capability polytope of a 3RRR PPM (first studied case)
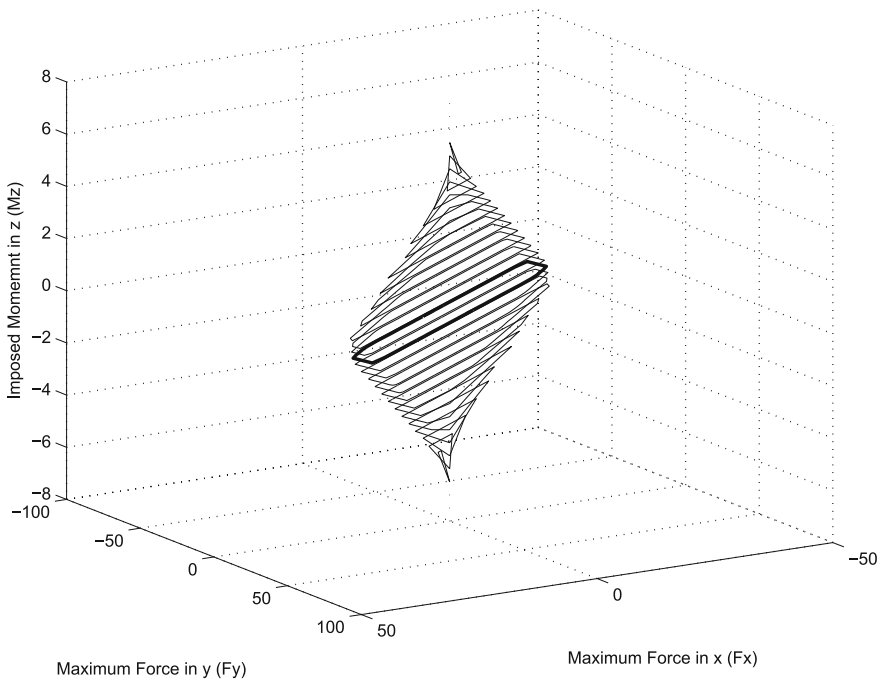
Fig. 5 Force capability polytope of a 3RRR PPM (second studied case)

force capability map as shown in Fig. 3 is obtained. Finally, by varying the value for the imposed moment in the manipulator's final effector, the manipulators force capability polytope as shown in Fig. 4 is obtained.

Using the same manipulator shown in Fig. 1, but changing the final effector's position to $[0.35\,\text{m}, 0.244\,\text{m}]$, the orientation of the mobile platform to $\phi = 12°$, and inverting the working mode of the branch A_1, B_1, C_1, is obtained the manipulator's force capability polytope shown in Fig. 5.

6 Conclusions

This paper presents a method to obtain the force capability polytope in a 3RRR parallel manipulator optimizing the torque in the actuators of the manipulator and imposing the moment in the manipulator's final effector.

The force capability polytope is composed by the superposition of several force capability maps and depends on several parameters as their kinematic position, orientation and working mode. Two study cases were shown in order to illustrate these dependencies, but, using the same strategy, is possible to obtain the manipulator's force capability polytope for each position into the manipulator's workspace.

The present study may be extended in various ways. Manipulators with different DOFs, kinematic chains and including dynamic behavior may be studied, and the minimization of the force and the maximization of the moment may be considered.

References

1. Cazangi, H.R.: Aplicação do método de davies para análise cinemática e estática de mecanismos de múltiplos graus de liberdade. Ph.D. thesis, Universidade Federal de Santa Catarina, Brazil (2008)
2. Chiacchio, P., Bouffard-Vercelli, Y., Pierroto, F.: Evaluation of force capabilities for redundant manipulators. In: IEEE International Conference on Robotics and Automation, pp. 3520–3525 (1996)
3. Davies, T.H.: Mechanical networks: wrenches on circuit screws. Mech. Mach. Theory **18**, 107–112 (1983)
4. Nokleby, S.B., Firmani, F., Zibil, A., Podhorodeski, R.P.: Force moment capabilities of redundantly actuated planar parallel architectures. In: 12th IFToMM 2007 World Congress, pp. 17–21 (2007)
5. Nokleby, S.B., Fisher, R., Podhorodeski, R.P., Firmani, F.: Force capabilities of redundantly-actuated parallel manipulators. Mech. Mach. Theory **40**, 578–599 (2004)
6. Storn, R., Price, K.: Differential evolution: a simple and efficient adaptive scheme for global optimization over continuous spaces. Technical Report TR-95-012, International Computer Science Institute (2005)
7. Tsai, L.W.: Robot Analysis and Design: The Mechanics of Serial and Parallel Manipulators, 1st edn. Wiley, New York (1999)

8. Weihmann, L.: Modelagem e otimização de forças e torques aplicados por robôs com redundância cinemática e de atuação em contato com o meio. Ph.D. thesis, Universidade Federal de Santa Catarina, Brazil (2011)
9. Weihmann, L., Martins, D., Coelho, L.S.: Force capabilities of kinematically redundant planar parallel manipulators. In: 13th World Congress in Mechanism and Machine Science, p. 483 (2011)
10. Weihmann, L., Martins, D., dos Santos Coelho, L.: Modified differential evolution approach for optimization of planar parallel manipulators force capabilities. Expert Syst. Appl. **39**, 6150 (2012). doi:http://dx.doi.org/10.1016/j.eswa.2011.11.099
11. Zibil, A., Firmani, F., Nokleby, S.B., Podhorodeski, R.P.: An explicit method for determining the force moment capabilities of redundantly actuated planar parallel manipulators. Mech. Design **129,** 1046–1056 (2007)

Interactive Design of a Controlled Driving Actuator

G. V. Kreinin and S. Yu. Misyurin

Abstract The interactive design of a fast driving actuator consisting of a motor, transferring mechanism and control system is considered. The design procedure is based on a set of a normalized, mathematical model with increasing complexity. The procedure is illustrated as an example of the positioning actuator. The initial model of the actuator represented by an ideal motor and an ideal transferring mechanism gives the opportunity to determine approximate power parameters of the motor and to construct the controlling algorithm. The dates obtained at the first stages are corrected further by taking into account the motors characteristics, structure of the mechanism, a time lag of the control system and others factors.

Keywords Dialog mode · Design procedure · Motor · Transfer mechanism · Control system · Mathematical models · Normalization · Similar criteria

The fast acting driving actuator is a combination of a power and control units. The first one consists of a power source, power converter and an actuating device (a motor plus transfer mechanism), where the primary power is transformed in a motion mechanical power of the actuating parts of a drive. The control unit (error sensors, signal transformers etc.) controls the power ensuring the specified motion mode of the output link. The actuator considered is used for the transfer control of an object, its positioning and other goals.

The mode of the actuator behavior can deviate from the specified mode if: (1) the power unit does not provide the required power; (2) the control unit does not cope with the power control. In the last case the problem is solved by optimizing of the control algorithm. It is possible only under one condition that the power unit

G. V. Kreinin
Institute of Machines Science of the Russian Academy of Sciences,
M. Kharitonievskiy p. 4, 101990 Moscow, Russia

S. Yu. Misyurin (✉)
National Research Nuclear University "MEPhI", Kashirskoye shosse 31,
115409 Moscow, Russia
e-mail: ssmmrr@mail.ru

has to deliver the required rates, accelerations, driving forces (or moments) at the output link of the drive.

At the initial stage of a synthesis the driving actuator structure is presented as a constructive suggestion. Owing to a relative complex mathematical model a dialog mode using is to be sensible. Its efficiency contributes the following regulations [1, 2, 6].

At individual steps of the design one should use most simple mathematical model gradually complicated step by step.

The use of the normalized (dimensionless) models is recommended insistently since the real parameters and other characteristics of the system transforms to the generalized dimensionless complexes and simulations criteria. As a result the number of the basic parameters is reduced what facilitates the analysis and synthesis of the system considered.

The structure of the driving actuator is shown in Fig. 1.

The motor can be electric, hydraulic, pneumatic or other types. The motion to the controlled object is performed by a mechanical system with a constant or varying ratio. As at initial stage the structure of the components is either not determined or is presented in the form of the structure analogies, one should consider the motor as an ideal unit and to start the constructing of the controlling system structure from a relatively simple algorithm proceeding from the actuators function. The driving force of an ideal motor is completely identified by the controlling signal and does not depend on the motor speed or other factors. A motor current driving force $P_x = P_{x\max}\gamma$, where γ is a controlling action, is determined the driving force mode. The actuator dynamic equations, written relatively of the output link, are

$$\begin{cases} m\ddot{y} = P_y - c_{\dot{y}} \cdot \dot{y} + P_L \\ P_y = P_x \cdot i \\ P_x = P_x(\gamma) = P_{x\max} \cdot \gamma \end{cases} \tag{1}$$

where y is the position coordinate of the object (output link), m is the inertial load of the moving object, P_y is the driving force (moment) applied to the object, P_L is the constant resistance force (moment). An alternating resistance force (moment) that is proportional to the speed is also included in (1); $c_{\dot{y}}$ is a coefficient of proportionality. If needed, others types of load can be taken into consideration. The inertial load of the motor is accepted here relatively small.

A transfer mechanism in the Eq. (1) is represented by the transfer ratio $i = \dot{x}/\dot{y}$, (x is the position coordinate of the input link); x and y can be linear or angular coordinate. Their cooperation is determined by the ratio i, which in general depends on the position of the mechanism, for an example, as a $i(y)$. If $i = const$, we have $i = s_x/s_y$, where $s_{x,\,y}$ are a corresponding travels of the motor and object.

By the synthesis of the actuator with a transfer mechanism with the $i = var$, not only its parameters, but also the structure of the mechanism, previously were either not determined, or presented as some analog. Therefore it is suggested at the first stages of the synthesis to use a kinematic model $i(y)$ of the mechanism. For
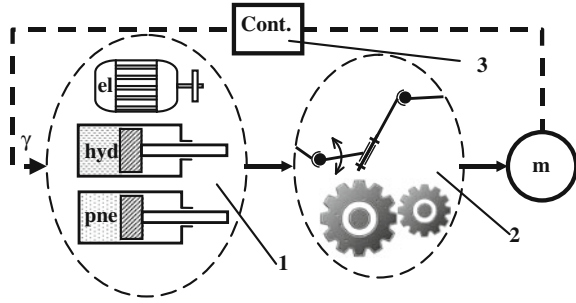
convenience a concept of an equivalent ratio $i_e = \bar{s}_x/\bar{s}_y$ is introduced, where $\bar{s}_{x,y}$ are basic travels of the input and output links of the mechanism. If the function $i(y)$ is known, then

$$i_e = \frac{1}{\varDelta s_y} \cdot \int_{y_1}^{y_2} i(y)dy$$

where $y_{1,2}$ are coordinates of initial and final positions of the output link,
$\varDelta s_y = y_2 - y_1$ is its travel. The displacement of the input link of the mechanism is

$$\varDelta x = \int_{y_1}^{y_2} i(y)dy$$

By the construction of the ratio function $i(y)$ and estimation its influence on the actuator dynamics it is expedient to use a relative transfer ratio $I = i/i_e = I(y)$ as a function of y. On the first step $i = i_e$ is defined. It gives the way to construct gradually an approximate $I(y)$ function using the simplified form for its representation included the complex linear form. At the final stages of the designing procedure the real mechanism can be realized using the method of the stepwise approximation of a real transfer function to a function preliminary accepted.

The system (1) is reduced to a normalized state by replacing variables: $y = s_y v_y$, $P_y = P_y^* \chi_y$, $P_y^* = P_{xmax} i_e$, $P_x = P_{xmax} \gamma$, $P_L = P_y^* \chi_L$, $t = \tau t^*$, $i = i_e I$, where $t^* = (ms_y/P_y^*)^{0,5} s_y$ is the travel of the output link accepted as a scale. As a result we have the normalized dynamic equations of an actuator.

$$\begin{cases} \ddot{v} = \chi_y - \lambda_{\dot{v}} \cdot \dot{v} + \chi_L \\ \chi_y = \gamma \cdot I \end{cases} \qquad (2)$$

where $\lambda_{\dot{v}} = c_{\dot{y}} \cdot (s_y/mP_y^*)^{0,5}$. If ratio $i = const$, then we have $i_e = i$ and $I = 1$.

The controlling action γ (a relative driving force of the motor) is generated by the income control signal γ_C of the controlling system. Under real conditions $\gamma \neq \gamma_C$ due to a time lag factor. The controlling algorithm γ_C is set depending on the function of the actuator. For example, for the position sensing mechanism the following simple controlling algorithm can be used

$$\gamma_C = K_1(y_e - y) - K_2\dot{y} - K_3\ddot{y} \tag{3}$$

where K_1, K_2 and K_3 are the feedback position, velocity and acceleration gains; y_e is a final position sensing coordinate of the object. Using accepted relations between dimensioned and dimensionless values, we obtain the normalized form of the controlling algorithm

$$\gamma_C = \kappa_1(v_e - v) - \kappa_2 \cdot \dot{v} - \kappa_3 \cdot \ddot{v} \tag{4}$$

where $k_1 = s_y K_1$, $k_2 = (s_y /t^*)K_2$, $k_3 = (s_y /t^{*2})K_3$. The (2–4) equations are a model of the lowest level used to start the designing. At the beginning $\lambda_{v'} = 0$, $\chi_L = 0$ and $I = 1$ can be accepted, i.e. taking into account only the inertial load and a constant mechanism ratio.

A preliminary analysis showed, that the controlling algorithm (4) does not guarantee a smooth mode without the considerable jerk by the transferring into the deceleration motion. To eliminate this defect and provide simultaneously the high feedback position gain in position sensing point, k_1 is made variable from the k_{1i} in the start of the motion to the k_{1e} in the end of the positioning, why $k_{1i} << k_1$

$$\kappa_1 = 1/(1/\kappa_{1e} + (1/\kappa_{1i} - 1/\kappa_{1e}) \cdot |v_e - v|) \tag{5}$$

The current values of k_2 are determined according to the fixed relation $k_1/k_2 = \theta$, which were established owing to a simulation results.

In Fig. 2 the simulation results of the two positioning processes of the electric motor actuator are presented. In Fig. 2a where $k_{1i} = k_{1e} = 100$ the abrupt jump of the acceleration takes place. In the second case where $k_{1i} = 2$ and $k_{1e} = 100$, this defect is absent. The rational values of the feedback gains and relation θ were defined as a result of the simulation.

At the next stages of the designing process other addition characteristics of the actuator model are to be taken into consideration. The first one is the dependence of the motor moving force (moment) on its velocity. If the mechanical characteristic is linear (a direct current motor), then the motion equation is

$$\ddot{v} = \chi_y - (1/\tilde{\Lambda} + \lambda_{\dot{v}})\dot{v} + \chi_L \tag{6}$$

where $\tilde{\Lambda} = \Lambda/i$, $\Lambda = \dot{x}_{id}t^*/s_y$, $\dot{x}_{id}$ is the idle velocity of the motor. The criterion $\tilde{\Lambda}$ depends on the behavior of the motor mechanical characteristic reduced to the output link. In the area of low values of $\tilde{\Lambda}$ the motion of the object is close to
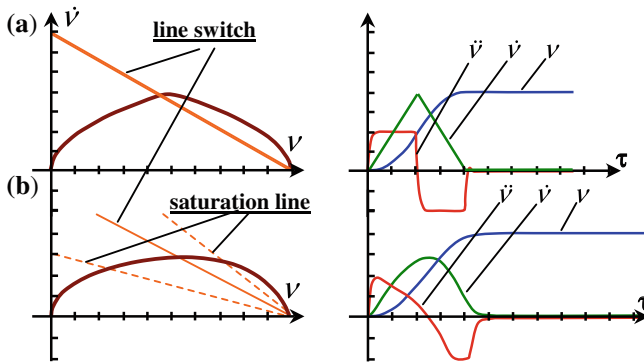
Fig. 2 Dynamics of an actuator with constant **a** and variable **b** gain χ_1: *1* the switching line, *2* the saturation line

uniform motion. As a value of $\tilde{\Lambda}$ increases the system strives to uniform accelerated motion.

The actuators with the motor having nonlinear mechanical characteristic are described by a more complex equation. For example, the actuator with the hydraulic piston motor, which has the quadratic mechanical characteristic, is described at first approximation by

$$\ddot{v} = 1 - ((1/\beta\tilde{\Lambda})\dot{v})^2 - \lambda_{\dot{v}}\dot{v} - \chi_L \tag{7}$$

where $\beta(\gamma)$ is the relative opening mode of the hydraulic operating channels. In details the mathematical models of the actuators with the motors of different types were considered in [2–5].

The next feature which has an effect on the actuator dynamics is the dynamic flexibility of the motor. Its flexibility can be measured by an elasticity index ς_y, included in the equation describing the transformation of the primary power to the mechanical power of the moving parts

$$\dot{\chi}_y = \varsigma_y(W - \dot{v}) \tag{8}$$

where W is the controlling action generated by the control unit. The ς_y value depends on the type of the motor and actuator parameters [2–4]. As a rule, the greatest value of ς_y has an actuator with the hydraulic motor, followed by the system with the electric motor. The lowest value of ς_y has the system with pneumatic motor.

In Fig. 3 the $v(\tau)$, $\dot{v}(\tau)$, $\sigma_1(\tau)$ and $\sigma_2(\tau)$ curves are shown as the functions of the normalized time τ. They illustrate the positioning process worked out by the actuators employed an electric, hydraulic and pneumatic motors; σ_1 and σ_2 are the relative pressures in the motors chambers; $\tau_s = t_s/t^*$ is travel time factor, t_s— the real travel time. The curves show the motion of the object from the start point $v_i = 0$ to the end position sensing point $v_e = 1$. The considered processes should
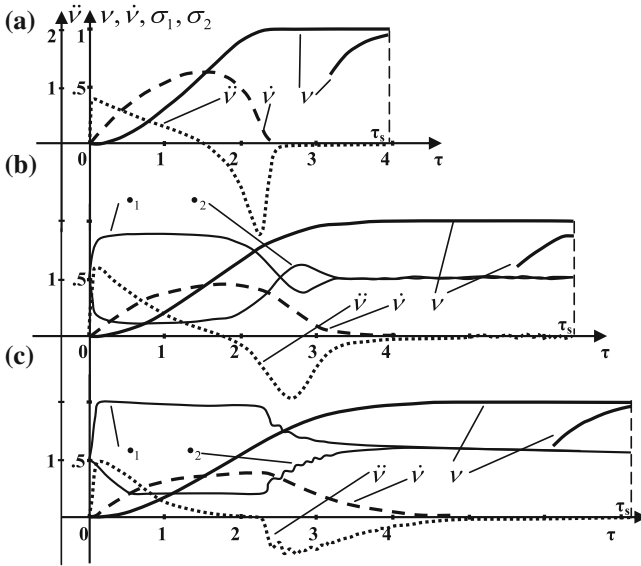
Fig. 3 Positioning processes of an actuators with the motors: **a** electric; **b** hydraulic; **c** pneumatic

be appreciated in some degree as optimal. The $\dot{v}(\tau)$ curves are symmetric relating to the speed up and slow down parts, the abrupt jerks absent, the high operating rate is realized, the differential pressure acting on the piston is fully employed and final sensing position is successfully achieved.

The rational values of κ_1, κ_3 and ϑ (Table 1) were determined according to the simulation results of the dynamic processes.

The $k_{1e} = 100$ were selected for all types of motors to provide the same resolution ability. The k_{1e} value defined is optimal: its further increasing gives no positive effect, but its decreasing can lead to the loss of the system stability. The other dates presented in the Table 1 are needed in some commentary.

The actuators with the electric and hydraulic motors have close dynamic characteristics. In both cases the value $k_{1i} = 1$ provides sufficiently smooth transferring to the decelerated motion of the output link. The deceleration gain k_3 is relatively low and in many cases may be presumed as $k_3 = 0$. The controlling parameters k_{1e}, k_{1i}, k_3 are stable and practically do not depend on the parameter $\bar{\Lambda}$.

The controlling parameters of the actuator with the pneumatic motor are different in a great extend. First of all, here $k_{1i} = k_{1e} = 100$ is reasonable; at the second place the parameter k_3 should be rather high and it considerably depends on the criterion $\bar{\Lambda}$. The both factors are the consequence of the poor dynamic rigidity of a pneumatic motor, which provides the smooth motion mode, but makes the problem in the resolution ability at the final position sensing point. The problem should be solved by means of an acceleration gain realized by the feedback circuit with acceleration sensor or an observer system [5].

Table 1 Data for the motors

Motor type	k_{1e}	k_{1i}	k_3	θ
Electric	100	1	1	2.5
Hydraulic	100	1	1	1.5
Pneumatic	100	100	10–75	0.6–1.5

The next step in the mathematical model verification is to take into consideration the time lag effect typical for the transition stage $\gamma_C \rightarrow \gamma$. The time lag effect can be described by the relatively simple relation

$$\dot{\gamma} = (1/\tau_e)(\gamma_C - \gamma) \qquad (9)$$

where τ_e is a time constant of the controlling circuit. The value of τ_e should be at last one order lower than the travel time factor τ_s. The more detailed relations can be used if necessary.

1 Conclusion

An employment of the gradually complicated dynamical models presented in the normalized state, opens the way to form a set of the simulation criteria which should be useful in the designing procedures of a different systems. A typical example is the parameter synthesis of the position system considered in this paper.

As a result of the simulation its normalized models there were revealed some basic relations, for example the highly important law-governed nature of the $\tau_s(\bar{\Lambda})$ function. By the $\bar{\Lambda}$ increasing above some limit ($\bar{\Lambda} \geq \bar{\Lambda}^*$) we have nearly constant value $\tau_s \approx \bar{\tau}_s$. This gives an opportunity to formulate the optimal value $i = \dot{x}_{id} t_s / \bar{\tau}_s \bar{\Lambda}_{opt} s_y$ of the transfer ratio which gives the minimal value $\bar{P}_{x\max} = m s_y^2 \eta / \dot{x}_{id} t_s^3$ of the motor starting force (moment), where t_s is the set travel time of the object, η is equal to $(\bar{\Lambda} \tau_s^3)_{\min}$. For example for the electric motor actuator we have $\eta = 28 - 30$.

It should be noted that the values of the normalized controlling parameters practically do not depend much on the $\bar{\Lambda}$ criterion and this fact considerably simplifies the selection of control system.

References

1. Cotsaftis, M., Keskinen, E.: Smooth high precision contact position control of rotating cylinder with hydraulic actuator. In: 12th IFToMM World Congress, Besancon (France), 18–21 June 2007
2. Kreinin, G.V., Misyurin, S.Y.: Dynamics and synthesis of the parameters of a positioning drive. J. Mach. Manuf. Reliab. **38**(6), 523–530 (2009). ISSN 1052-6188

3. Kreinin, G.V., Misyurin, S.Y.: A systematic approach to synthesis of a drive system. J. Mach. Manuf. Reliab. **40**(6), 507–511 (2011). ISSN 1052-6188
4. Kreinin, G.V., Misyurin, S.Y.: On some general laws in drive dynamics. J. Mach. Manuf. Reliab. **37**(6), 546–551 (2008). ISSN 1052-6188
5. Krivits, I.L., Krejnin, G.V.: Pneumatic Actuating Systems for Automatic Equipment. Structure and Design. CRC Press, Boca Raton, p. 345 (2006)
6. Samin, J.C., Bruls, O., et al.: Multiphisic modeling and optimization of mechatronic multibody system. Multibody Sys. Dyn. **18**(3), 345–373 (2007)

Design and Implementation
of Self-Balancing Camera Platform
for a Mobile Robot

Mehmet Volkan Bukey, Emin Faruk Kececi and Aydemir Arısoy

Abstract One of the most common sensors used on mobile robots are cameras. An important issue of the image obtained from the camera on the mobile robot is that the image is affected by the posture of the robot. In this study, a camera is placed on a mobile robot and the equilibrium of the camera system is achieved by a camera tower system. In this way, the impact of the changing robot orientation on the image obtained from the camera is reduced. In order to measure the orientation of the robot body, an inertial measurement device is used and the sensory data is corrected with a Kalman filter. With the field test, the effectiveness of the camera stabilization system is proven.

Keywords Camera stabilization · Kalman filter

1 Introduction

Robots use sensors to detect both the outside environment and their own situation. According to these sensory data, they achieve their tasks. The optimization of the sensory data in a robotic system and the calibration of the system are very important.

M. V. Bukey · E. F. Kececi (✉)
Department of Mechanical Engineering, Istanbul Technical University, Istanbul, Turkey
e-mail: kececi@itu.edu.tr

M. V. Bukey
e-mail: vbukey@itu.edu.tr

A. Arısoy
Department of Electronics Engineering, Turkish Air Force Academy, Istanbul, Turkey
e-mail: aarisoy@hho.edu.tr

Since using a camera system the motion of the robot can be detected, in mobile robot applications the camera systems are widely used. One of the biggest problems with camera systems on a mobile robot is that the image received changes depending on the posture of the robot. When the camera is tilted or facing to a different angle, it becomes very difficult to control the robot. In order to overcome this problem the image needs to be corrected to show the interested area.

There are number of methods to fix the image distortion caused by the mobile robot orientation change. These methods can be grouped as image processing [1], optical methods [2] and mechanical methods [3].

In this study, in order to balance the camera placed on the mobile robot a mechanical system powered by servo motors is utilized. With the help of this system roll, pitch and yaw angles of the camera are controlled. The orientation of the mobile robot body is measured by an inertial measurement unit. In order to optimize the sensory data, a Kalman filter is used, which provides the Euler angles for the orientation of the robot body. By using the orientation angles, the roll and pitch angles are corrected automatically, leaving the yaw angle to be controlled by the operator to select the interested area for the user.

2 System Design

In this study, a camera tower is designed and placed in between a tracked mobile robot base and a wireless camera. The robot is remotely controlled and the camera tower powered by servo motors adapts to the orientation changes of the mobile robot and provides an undistorted image. The camera tower system is explained in two sections: mechanical and electronic.

2.1 Mechanical Components

The mechanical parts of the system consist of a tracked robot powered by two DC motors and the tower structure powered by the servo motors. The servo motors are automatically controlled to adapt to the motion of the robot to control the roll and pitch angles of the wireless camera. Three servo motors capable of 180 degrees of rotation are used to control the orientation of the camera. Two of the servo motors control the roll and pitch angles while the third servo motor is controlled by the operator manually. Figures 1 and 2 show the robot base and the camera tower system. During this study, it is assumed that the orientation of the camera is only changing with the orientation of the mobile robot body. This assumption eliminates the translational components of the kinematic equations and only a rotation matrix is used to derive the kinematic equations. It is also assumed that the rotation axes of the robot and the camera intersect. Since the yaw angle is not intended to be controlled automatically, a rotational matrix is not calculated for this axis.
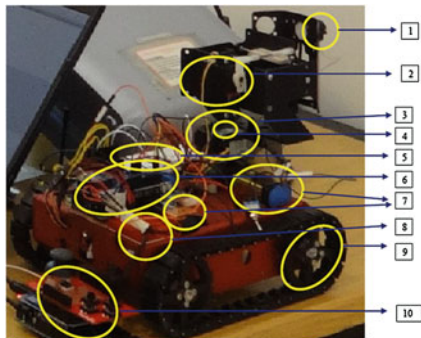
Fig. 1 Camera stabilization system components
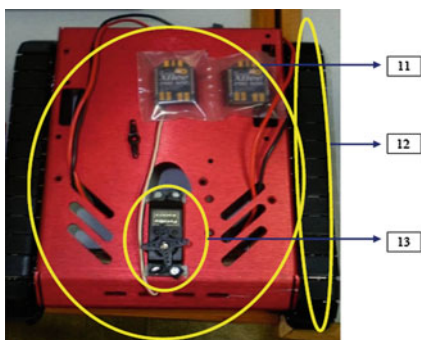
Fig. 2 Mobile robot base components

The orientation of the camera related to the earth is given in Eq. 1. The equation is a combination of rotational movements in three axes, Since the yaw angle is not controlled, the value of the yaw angle is considered as zero. In this equation θ denotes the pitch angle and ψ denotes the roll angle.

$$R_{12}(\theta, \psi, 0) = \begin{bmatrix} \cos\theta & \sin\psi\sin\theta & \cos\psi\sin\theta \\ 0 & \cos\psi & -\sin\psi \\ -\sin\theta & \sin\psi\cos\theta & \cos\psi\cos\theta \end{bmatrix} \quad (1)$$

Since the pitch angle is only controlled with one servo which rotates about the y axis and the roll angle is only controlled with the second servo which rotates about the x axis, two matrices are defined to show the rotational motion as Eqs. 2 and 3.

$$R_{Yservo}(\theta_1) = \begin{bmatrix} \cos\theta_1 & 0 & -\sin\theta_1 \\ 0 & 1 & 0 \\ \sin\theta_1 & 0 & \cos\theta_1 \end{bmatrix} \quad (2)$$

Part	Task
Arduino UNO	Microprocessor
MinIMU-9 v2	IMU
MC33926 Dual Motor Driver	Motor driver
XBee Pro 50 mW Wire Antenna-Series 2	Wireless communication
DL-007 WS + Receiver	Wireless camera
Arduino Uno + Joystick Shield	Control unit

Table 1 Robot electronic components and their tasks

Fig. 3 Control method of the camera stabilization system
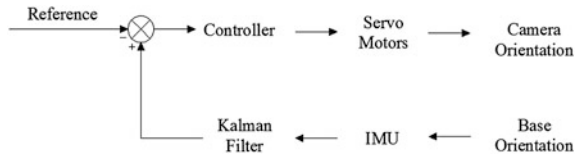
$$R_{Xservo}(\psi_1) = \begin{bmatrix} 1 & 0 & 0 \\ 0 & \cos\psi_1 & \sin\psi_1 \\ 0 & -\sin\psi_1 & \cos\psi_1 \end{bmatrix} \qquad (3)$$

It is assumed that at the beginning of the robot motion the earth's coordinate and the camera coordinates are superimposed. At the initial position all the Euler angles at Eq. 1 become zero and the rotation matrix is equal to identity matrix.

During the robot motion the orientation changes causing different values to the Euler angles. The two servo motors, controlling the roll and the pitch angle move the camera towards the initial position. This motion is achieved by actuating the servo motors in reverse direction with the same angle values of roll and pitch angles.

2.2 Electronic Components

Table 1 summarizes the electronic components used in this robotic system to create a remote controlled robot with a camera stabilization system.

2.3 System Operation

After the prototyping stage; the mobile base, camera tower and control unit are shown in Figs. 1 and 2.

The different parts of the robotic system are: 1-wireless camera, 2-pitch direction servo motor, 3-yaw direction servo motor, 4-inertial measurement sensor, 5-servo motors battery, 6-microprocessor 7-wireless camera and microprocessor battery, 8-circuit board for connections, 9-motor connections, 10-control unit, 11-mobile base, 12-tracks and 13-yaw servo.

The camera stabilization system's control scheme is given in Fig. 3. When the user is driving the mobile base, he can change the camera orientation by using the yaw servo motor. The orientation of the mobile base is measured by the inertial measurement unit and with a Kalman filter the sensor data is fed to the controller to move the roll and pitch servo motors.

3 Kalman Filter

In order to increase the performance of the camera stabilization system, the data received from the IMU unit must be accurate. In the measurement of the pitch and roll angles both a accelerometer and gyroscope are used [4]. The vibration of the mobile base causes noise in the IMU system. A gyroscope is more immune to the vibration of the system. On the other hand since the gyroscope data must be integrated, for an extended time the error in a gyroscope system increases.

A Kalman filter is used in this study to eliminate the sensor data. Euler angles obtained from the accelerometers are updated by using the gyroscope data. At the same time with the help of accelerometer data, the gyroscope error has been corrected. The filter equation given in Eq. 5 is written in consideration of the relationship between the gyroscope offset value and the rotation angle.

$$a_k = a_{k-1} + (u_k - b_{k-1})T \tag{5}$$

In this equation the variables are defined as k step size, a Euler angle parameter, u the angular velocity obtained from the gyro variable and b the offset of the gyroscope. The T value represents the microprocessor code specifies a fixed cycle time. This constant is used in the calculation of the integral value in Eq. 5. The dynamical equations are simplified to decrease the calculation time on the microprocessor. Consequently, the state and measurement equation to be used in Eq. 5 is formulated as:

$$x_k = \begin{bmatrix} a \\ b \end{bmatrix}_k = \begin{bmatrix} 1 & -T \\ 0 & 1 \end{bmatrix} x_{k-1} + \begin{bmatrix} T \\ 0 \end{bmatrix} u_k + w_{k-1} \tag{6}$$

$$z_k = \begin{bmatrix} 1 & 0 \end{bmatrix} x_k + v_k \tag{7}$$

Fig. 4 Euler angle values measured by the accelerometer
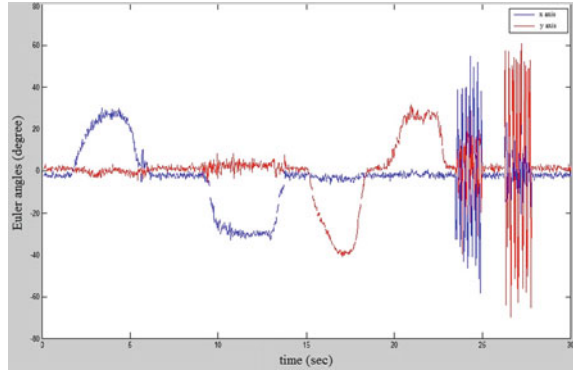
3.1 Kalman Filter Application

First of all, the Euler angles are calculated by using the accelerometer. Figure 4 shows the effect of the vibration on the calculated angle. Since with a single accelerometer there is also sensor noise in the system, the effectiveness of the control will be limited.

In this study, a Kalman filter is used to eliminate the error in the inertial navigation unit. From Eq. (5) for both of the axes Euler angles and gyroscope offset values are used for system state. When a Kalman filter is used, noise covariance matrices should be selected as an initial condition. By adjusting these parameters, the speed of the convergence and accuracy can be improved.

Measurement noise covariance shows the reliability of the measured sensor data. When the value of this covariance decreases, it is possible to trust the sensor data during the estimation. It means that the sensor data error is small. Since the measurement noise covariance depends on the sensor error it can be measured experimentally. With the experiments for x axis, it is found as 0,4461 and for y axis it is found as 0,4369.

Process noise covariance can be described as the effect of system states to the Kalman filter outputs. Smaller values of the process noise covariance increase the system stability whereas the bigger values cause better adaptation to the changes in the system states.

Since the current Kalman filter has two states the process noise covariance is written as a matrix, Eq. (8).

$$Q = \begin{bmatrix} Q_a & Q_{ab} \\ Q_{ba} & Q_b \end{bmatrix} \tag{8}$$

Q_a and Q_b are system state covariance whereas Q_{ab} and Q_{ba} are proportional to the standard deviation of these two values. Since the noise values are independent of each other for two states, Q_{ab} and Q_{ba} values are zero. Q_a and Q_b values are

Fig. 5 x axis Kalman filter output
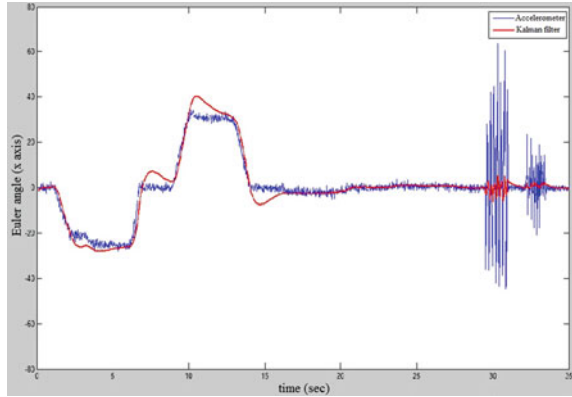
Fig. 6 y axis Kalman filter output
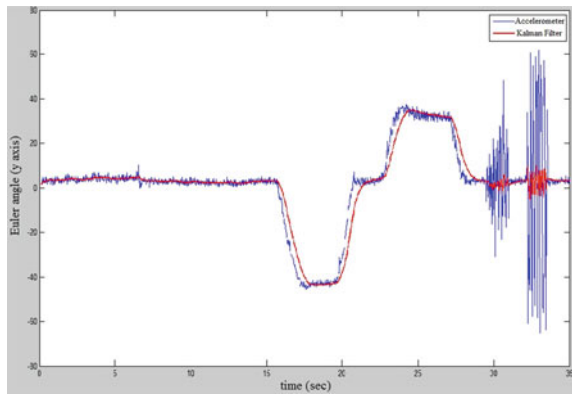
found experimentally and when they are smaller than 0,0001 the stabilization of the camera is achieved.

Figures 5 and 6 shows the results of the Kalman filter. With the help of the Kalman filtering, the effects of the vibration on the accelerometer measurements are decreased and system stability is achieved.

4 Conclusion

By using a Kalman filter the camera stabilization is achieved. By adapting the system parameters, the speed and the stability of the controller is adjusted. Since the inertial measurement unit is placed on the mobile base, the current system controls the camera position depending on the robot orientation. By placing a second IMU on the camera, the control of the camera angles can be improved. However, the usage of two IMU will require higher processing performance.

In this application the noise covariance values are considered as constants. This implies that standard deviation at the system states and sensor working conditions are constant. In order to improve the Kalman filter performance, noise covariance values can be updated with a control algorithm.

References

1. Miyauchi, R., Shiroma, N., Matsuno, F.: Compact image stabilization system using camera posture information. J. Field Robot. **25**, 268–283 (2008)
2. Sato, K., Ishizuka, S., Nikami, A., Sato, M.: Control techniques for optical image stabilizing system. IEEE Trans. Consum. Electron. **39**, 461–466 (1993)
3. Lee, D.B., Chitrakaran, V., Burg, T., Dawson, D., Xian, B.: Control of a remotely operated quadrotor aerial vehicle and camera unit using a fly-the-camera perspective. In: Proceedings of the IEEE Conference on Decision and Control, pp. 6412–6417 (2007)
4. Colton, S.: The Balance Filter. Massachusetts Institute of Technology, Boston (2007)

Action of Robot with Adaptive Electric Drives of Modules

Konstantin S. Ivanov

Abstract Action of robot with modules which have adaptive electric drives is considered. Adaptive electric drive contains electric motor and adaptive connecting gear with two degrees of freedom. The adaptive gear has a form of closed differential mechanism and is extremely simple. It changes a transfer ratio depending on loading continuously only at the expense of mechanical properties and does not demand any control. The equations of adaptive mechanism parameters interconnection are worked out. Definability of the adaptive electric drive motion is confirmed by experimental research. Stop regime of the module motion takes place when working body of the module is motionless. This regime allows to avoid an overloading and to overcome emergencies. In the robot with adaptive drives of modules the stop regime of motion can be overcome at the expense of motions of other modules leading to decrease of resistance.

Keywords Module · Drive · Adaptation · Parameters · Interconnection

1 Introduction

Adequate to loading drive of manipulator module should have the variable transfer ratio. However application of the adjustable gear box in the manipulator drive is impossible. Recently there were compact adaptive mechanical stepless adjustable transfers [1–3]. Such transfer provides ideal conformity to variable load and allows choosing the propeller on average power of resistance. The adaptive electric drive of the manipulator module is now developed and bases of its research are created [4, 5]. Adaptive mechanical transfer is investigated in Ivanov's works [6, 7]. It is

K. S. Ivanov (✉)
Djoldasbekov Institute of Mechanics and Machine Science, Almaty University of Power Engineering and Telecommunications, Almaty, Kazakhstan
e-mail: ivanovgreek@mail.ru

the elementary adjustable transfer as it contains only a wheelwork with constant cogging of toothed wheels (without the gear change). Transfer has small gabarits and weight. Power adaptation of the module creates possibility of sampling of the electric motor not on maximum and on average loading power.

Definability of motion takes place in the absence of friction account. Presence of definability of motion of the adaptive electric drive is confirmed by an experimental research of adaptive transfer [8]. Motion of modules at a steady load is uniform.

The present work is devoted describing of action of robot with adaptive drives of modules. Work is executed on the basis of mechanics laws.

2 Design of Adaptive Drive

The module of the manipulator with the adaptive drive of translational motion [5] is presented on Fig. 1.

A—module stationary part: 1. Plate. 2. Butt for joint with previous module. 3. Guides for screw nut. 4. Electric motor. 5. Adaptive reducer. 6. Working screw.

B—module moving part: 7. Running screw nut. 8. Butt for joint with the subsequent module.

In operating time the electric motor with constant power 4 transfers rotation through the adaptive reducer 5 to the working screw 6. Working screw 6 moves the running screw nut 7 together with the module moving part on guides 3. The adaptive reducer 5 provides rotation of the working screw 6 with a speed inversely proportional to resistance moment which is conforming to external loading of module.

Module of manipulator with adaptive drive of rotary movement has mobile part which is fixed directly on output reducer shaft (instead of working screw 6).

The adaptive mechanism (reducer) of the manipulator module (Fig. 2.) contains frame 0, input carrier H_1, input satellite 2, block of central wheels 1–4, block of ring wheels 3–6, output satellite 5 and output carrier H_2.

Number of degrees of freedom of the kinematic chain is equal 2.

3 Interconnection of Parameters of a Wheelwork in Operating Conditions

Interconnection of parameters in operating regime for the wheelwork with two degrees of freedom is defined by theorem: mobile closed contour in kinematic chain with two degrees of freedom under action of any way set superposed forces is in equilibrium [6, 7]. Basic equations of parameters interconnection of wheelwork with two degrees of freedom have following form.
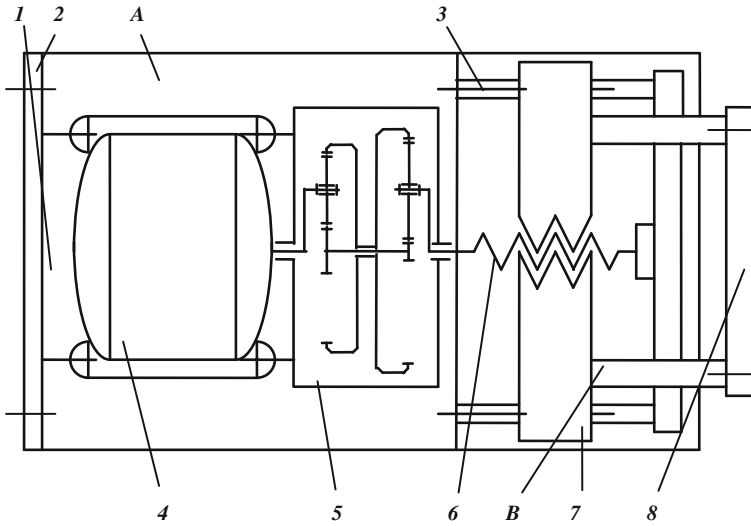
Fig. 1 Manipulator module of translational motion

Fig. 2 Adaptive mechanism
of manipulator module
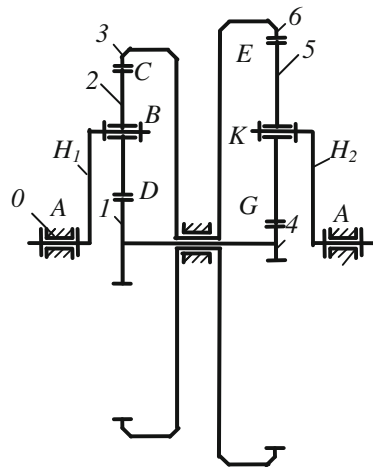
Sum of powers of internal forces is equal to null

$$M_{1-4}\omega_1 + M_{3-6}\omega_3 = 0 \tag{1}$$

Sum of powers of external forces is equal to null

$$M_{H1}\omega_{H1} + M_{H2}\omega_{H2} = 0 \tag{2}$$

From formula (2) follows

$$\omega_{H2} = \frac{M_{H1}\omega_{H1}}{M_{H2}} \tag{3}$$

Formula (3) defines effect of force adaptation: at constant input power $N_{H1} = M_{H1}\omega_{H1}$ output angular speed ω_{H2} is inverse proportional to external output resistance moment M_{H2}. The effect of power adaptation characterizes the major property for machines with variable technological resistance—ability independently and continuously to adapt for variable technological loading.

4 Experimental Testing of the Drive

Testing of force adaptation effect in the mechanism presented on Fig. 2 has been executed on the test-bed in LARM of university Cassino [8].

On Fig. 3 experimental tractive characteristic of the gear adaptive mechanism presented as function of output traction moment (or resistance moment) in Nm from output angular speed in rpm at constant input angular speed and engine torque. On the graph of function the following curve pieces take place: 0A—motion in condition with one degree of freedom in absence of internal mobility in gear mechanism contour (start up), ABC—motion with two degrees of freedom (operating regime), B—intermediate point, C—operating regime end (maximum resistance moment and stop).

5 Interconnection of Robot Adaptive Modules

Let's consider the robot with two adaptive modules (Fig. 4) containing basis 0, module of lifting 1 with the adaptive drive of rotary motion in point A and module of pulling out of the arm 2 with the adaptive drive of translational motion in point B. In capture 3 (point C) the moved product with weight G is placed. Product lifting is made by the module 1. The drive of the module 1 provides rotation in direction of an circular arrow and overcomes resistance moment $M = Gh$ (h—variable shoulder of resistance force G relatively point A). In an initial position the module of turn 1 has vertically position and shoulder $h = 0$.

During turn of module 1 relatively point A when $AC = const$ the shoulder h is increasing and resistance moment M is increasing. At achievement of maximum resistance moment for drive $M = M_{max}$ the module 1 is stopped and the drive of module 1 passes in stop regime. The drive electric motor continues to work and the module 1 as line AC remains motionless. The point C of tractive characteristic (Fig. 3) takes place. In this moment a motion sensor of robot control system is switching on the drive of translational motion of module 2. This drive starts to
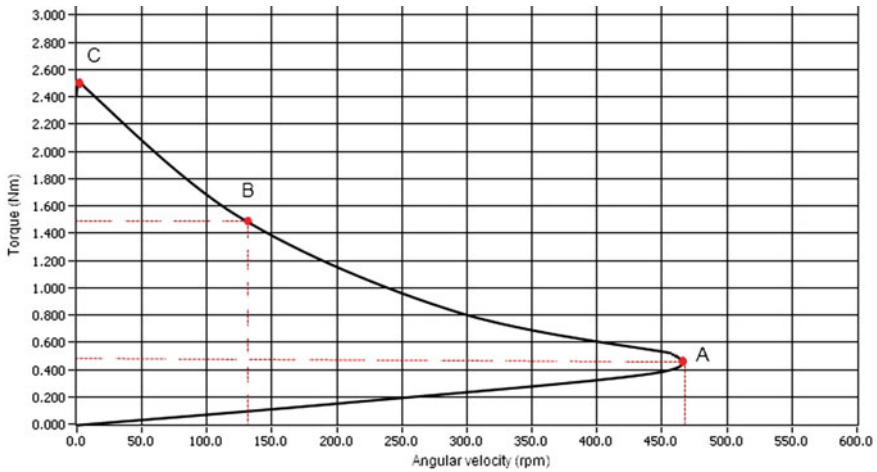
Fig. 3 Experimental tractive characteristic of gear adaptive mechanism

Fig. 4 Robot with two adaptive modules
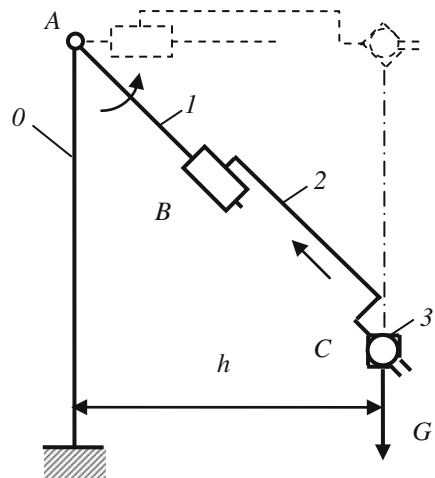
move capture 3 with product in an linear arrow direction. Shoulder *h* begins to decrease. Drive of the rotary motion module 1 gets out from stop regime of motion and provides product lifting together with the translational motion module 2 of the arm. Sensors of angular moving of module 1 and linear moving of module 2 in common are controlling by moving of capture 3 under the set program. Final position of the robot is shown by a dotted line. Thus, there is a continuous adaptation of the robot to motion conditions. Separate movement of modules (at first turn of module 1 in horizontal position and then linear horizontal moving of module 2 in final position) would demand use of more powerful engine of turn of module 1.

6 Conclusion

Regularity of interconnection of power and kinematic parameters of the robot in which each module has the adaptive electric drive are developed. The adaptive electric drive contains the electric motor and the adaptive connecting gear with two degrees of freedom. The adaptive mechanism provides motion of module mobile part with a speed inverse to force loading at constant power of electric motor. The adaptive mechanism has the variable transfer ratio which depends on loading. The adaptive drive provides at first a regime of start-up or start with one degree of freedom and then operating regime of motion with two degrees of freedom. It is proved that the adaptive mechanism has definiteness of motion in a condition with two degrees of freedom and in a condition with one degree of freedom because it contains the closed mobile contour which imposes additional constraint on motion of links under action of forces. The mechanism analysis can be executed a classical method without a friction. Presence of definability of motion of the adaptive electric drive is confirmed by the drive experimental research. The experimental tractive characteristic containing a regime of start-up and operating regime is gained. The tractive characteristic matches to the theoretical characteristic.

The adaptive drive is extremely simple in design. It changes the transfer ratio depending on loading independently only at the expense of mechanical properties and does not demand control of the transfer ratio. Power adaptation allows reducing sizes and weight of the drive at the expense of decrease of a required power of the electric motor. The equations of interconnection of parameters of motion of the adaptive mechanism are developed. The adaptive drive of the module of the robot provides a stop regime of motion at achievement of the maximum value of variable resistance. In this moment the module mobile part appears as motionless and the electric motor continues motion with former speed. Stop regime allows to avoid an overloading and to overcome emergencies. In the robot with adaptive drives of modules stop regime can be overcome at the expense of motion of other modules leading to decrease of resistance.

The adaptive drive of the robot provides a high efficiency.

References

1. Harries, J.: Power transmission system comprising two sets of epicyclic gears. Patent of Great Britain GB2238090 (A) (1991)
2. Ivanov, K.: Almaty, KAZ—owner of the registered sample. The name—device of automatic and continuous change of a twisting moment—and changes of a corrected speed of output

shaft depending on a tractive resistance. The deed on registration of the registered sample $N^{\underline{o}}$ 20 2012 101 273.1. Day of Registration 02.05.2012. The German patent and firm establishment. Federal Republic Germany (2012)

3. Ivanov, K.S.: Theory of continuously variable transmission (CVT) with two degrees of freedom: paradox of mechanics. In: Proceedings of the American Society of Engineers Mechanics (ASME) International Mechanical Engineering Congress and Exposition (IMECE 2012), pp. 543–562. Houston (2012)

4. Ivanov, K.S.: Principles of creation of manipulator adaptive drive. Theses of papers of the first international Dzholdasbekov symposium. MON RK, Kaz. National University of Al-Farabi, Almaty 74 (2011)

5. Ivanov, K.S et al.: Dynamic synthesis of adaptive drive of manipulator. In: 3rd IFToMM International Symposium on Robotics and Mechatronics (ISRM 2013), pp. 191–200, Singapore (2013)

6. Ivanov, K.S.: Continuously variable transmission: adaptive gear stepless mechanical CVT. In: Proceedings of International Conference of Gears with Exibition. VDI Wissensforum GmbH, Technical University of Munich (TUM), pp. 984–987. Garching (near Munich) (2013)

7. Ivanov, K.S., Jilisbaeva, K.: Paradox in the mechanism science. Mechanisms and machine science 19: new trends in educational activity in the field of mechanism and machine theory, pp. 129–136. Springer (2013)

8. Ceccarelli, M, Balbayev, G.K.: Design and characterization of a new planetary gear box. Mechanism and machine science, vol. 17. New advances in mechanics, transmissions and applications. In: Proceedings of the Second Conference MeTrApp 2013, vol. 17. pp. 91–98. Springer (2013)

Author Index

571